JOINT TRANSPORTATION
RESEARCH PROGRAM
INDIANA DEPARTMENT OF TRANSPORTATION
AND PURDUE UNIVERSITY

Increasing Bridge Deck Service Life

Volume I—Technical Evaluation

Robert J. Frosch, Samuel Labi, Chungwook Sim

SPR-3422 • Report Number: FHWA/IN/JTRP-2014/16 • DOI: 10.5703/1288284315516

RECOMMENDED CITATION

Frosch, R. J., Labi, S., & Sim, C. (2014). *Increasing bridge deck service life: Volume I—Technical evaluation* (Joint Transportation Research Program Publication No. FHWA/IN/JTRP-2014/16). West Lafayette, IN: Purdue University. http://dx.doi.org/10.5703/1288284315516

AUTHORS

Robert J. Frosch, PhD
Professor of Civil Engineering
Lyles School of Civil Engineering
Purdue University
(765) 494-5904
frosch@purdue.edu
Corresponding Author

Samuel Labi, PhD
Associate Professor of Civil Engineering
Lyles School of Civil Engineering
Purdue University

Chungwook Sim
Graduate Research Assistant
Lyles School of Civil Engineering
Purdue University

JOINT TRANSPORTATION RESEARCH PROGRAM

The Joint Transportation Research Program serves as a vehicle for INDOT collaboration with higher education institutions and industry in Indiana to facilitate innovation that results in continuous improvement in the planning, design, construction, operation, management and economic efficiency of the Indiana transportation infrastructure. https://engineering.purdue.edu/JTRP/index_html

Published reports of the Joint Transportation Research Program are available at: http://docs.lib.purdue.edu/jtrp/

NOTICE

COPYRIGHT

Print ISBN: 978-1-62260-332-9
ePUB ISBN: 978-1-62260-333-6

TECHNICAL REPORT STANDARD TITLE PAGE

1. Report No.	2. Government Accession No.	3. Recipient's Catalog No.
FHWA/IN/JTRP-2014/16		

4. Title and Subtitle	5. Report Date
Increasing Bridge Deck Service Life: Volume I—Technical Evaluation	December 2014
	6. Performing Organization Code

7. Author(s)	8. Performing Organization Report No.
Robert J. Frosch, Samuel Labi, Chungwook Sim	FHWA/IN/JTRP-2014/16

9. Performing Organization Name and Address	10. Work Unit No.
Joint Transportation Research Program Purdue University 550 Stadium Mall Drive West Lafayette, IN 47907-2051	
	11. Contract or Grant No. SPR-3422

12. Sponsoring Agency Name and Address	13. Type of Report and Period Covered
Indiana Department of Transportation State Office Building 100 North Senate Avenue Indianapolis, IN 46204	Final Report
	14. Sponsoring Agency Code

15. Supplementary Notes

Prepared in cooperation with the Indiana Department of Transportation and Federal Highway Administration.

16. Abstract

Deterioration of bridge decks is a primary factor limiting the lifespan of bridges especially in cold climates where deicing salts are commonly used. While controlling deck cracking or decreasing the permeability and porosity of concrete can improve performance and service life, chloride and moisture ingress as well as cracking cannot be eliminated. Full-depth cracks which are caused by restrained shrinkage allow for corrosive conditions at early ages for both the top and bottom reinforcement mats. Therefore, the use of corrosion-resistant reinforcement is essential to mitigate deterioration of bridge decks. The objective of this research program to examine the efficacy of using alternative materials in a bridge deck from both technical and economic perspectives. For the technical evaluation (Volume 1), a three phase experimental investigation was conducted considering a wide range of corrosion-resistant reinforcing materials. These materials included stainless steels, microcomposite steel, and coated steels considering a variety of metallic and nonmetallic coatings. The first phase evaluated the bond between corrosion-resistant reinforcement and concrete using lap splice tests. The second phase evaluated the cracking behavior of slabs reinforced with corrosion-resistant reinforcement. Finally, the third phase evaluated corrosion resistance under uncracked and cracked conditions using macrocell test specimens. Transverse steel was also tied to the longitudinal steel to simulate actual bridge deck conditions. Recommendations are provided on development and splice lengths for both conventional black and corrosion-resistant reinforcing steel, control of cracks widths, as well as the selection, design, and construction of corrosion-resistant reinforcement. For the economic evaluation (Volume 2), a decision support methodology and associated spreadsheet tool for robust analysis of the cost-effectiveness of alternative material types for bridge deck reinforcement was developed. The two evaluation criteria are agency and user costs, and the input data that influence this criteria include the deck service life, material process, discount rate, detour length, and bridge size. The methodology incorporates analytical techniques that include life cycle analyses to evaluate the long-term cost and benefits of each material over the bridge life; Monte Carlo simulation to account for the probabilistic nature of the input variables; stochastic dominance to ascertain the probability distribution of the outcome that a specific reinforcement material is superior to others; and analytical hierarchical process to establish appropriate weights for the agency and user costs. The study methodology is demonstrated using a case study involving three reinforcement material alternatives: traditional (epoxy-coated) steel, zinc-clad steel, and stainless steel. Through this study, it is demonstrated that the use of corrosion-resistant reinforcing materials can significantly increase bridge deck life, reduce agency and user costs associated with bridge deck rehabilitation and maintenance, and thus lower the financial needs for long-term preservation of bridges.

17. Key Words	18. Distribution Statement
corrosion-resistant reinforcing steel, stainless steel reinforcing bars, high-strength reinforcing steel, coated reinforcing steel, bridge deck service life, structural concrete, bond strength, development and splice length, bridge deck cracking, crack control, cracking performance, corrosion-resistance, galvanic corrosion	No restrictions. This document is available to the public through the National Technical Information Service, Springfield, VA 22161.

19. Security Classif. (of this report)	20. Security Classif. (of this page)	21. No. of Pages	22. Price
Unclassified	Unclassified	285	

Form DOT F 1700.7 (8-69)

EXECUTIVE SUMMARY

INCREASING BRIDGE DECK SERVICE LIFE: VOLUME I—TECHNICAL EVALUATION

Introduction

Deterioration of bridge decks is a primary factor limiting the lifespan of bridges especially in cold climates where deicing salts are commonly used. Research has been previously performed to mitigate deterioration by controlling deck cracking using improved design methods such as bar spacing and cover requirements or by decreasing the permeability and porosity of concrete through the use of high performance concrete. While these methods can improve performance and extend service life, chloride and moisture ingress as well as cracking cannot be eliminated. Full-depth cracks which are caused by restrained shrinkage allow for corrosive conditions at early ages in both the top and bottom reinforcement mats. Therefore, corrosion of the reinforcing steel ultimately occurs. However, the service life of the deck has the potential of being significantly improved if corrosion resistant reinforcement is used.

While epoxy-coated reinforcement has become standard practice to improve corrosion resistance, this reinforcement type is not immune to corrosion. Its performance is highly dependent on the condition of coating. The coating can be damaged even with special care during manufacturing, transportation, and construction. Therefore, the use of other corrosion reinforcing materials has significant potential to provide improved performance. The objective of this research program to examine the efficacy of using alternative materials in a bridge deck from both technical and economic perspectives. Technical criteria include bond strength, cracking performance, and corrosion resistance while economic criteria comprise agency and user costs associated with construction, replacement, and rehabilitation over the life cycle.

Findings

Volume I: Technical Evaluation

The technical evaluation was conducted in three phases and considered a wide range of corrosion resistant reinforcing materials. These materials included stainless steel (316LN, Duplex 2205, Duplex 2304, XM-28), MMFX II microcomposite steel, and coated steel (epoxy, dual-coated zinc and epoxy (Z-bar), hot-dipped galvanized, and zinc-clad).

Bond Strength.

The bond strength of corrosion resistant reinforcing materials were tested to ensure that current design procedures for the calculation of splice and development lengths are appropriate. Stainless-steel, MMFX II microcomposite, hot-dip galvanized, and Zbar (dual-coated) reinforcing bars have bond strengths comparable to black bars. Coated bars other than galvanized and dual-coated have reduced bond strengths. Epoxy-coated bars had on average 11% less bond strength than black while unplated zinc-clad and tin-plated zinc-clad bar had on average 18% and 26% less bond strength than black bars, respectively. Modification factors were developed for development and splice length calculations when other bar types are used. The test data were also combined with other data available in literature to construct a simple model for development and splice length calculations that consider a wide range of corrosion resistant bar types as well as unconfined and confined conditions.

Cracking Performance.

Because the variations in the surface roughness of different corrosion-resistant reinforcement, cracking performance was evaluated by testing slab specimens. The effect of bar spacing and the effect of high reinforcement stresses that can be obtained by high-strength reinforcement (stainless steel or MMFX II) were evaluated. The bar types affected the spacing and width of primary cracks. For the control of crack widths, it is recommended that crack widths be calculated based on black bars and multiplying modification factors. Design code approaches can directly incorporate these factors to reduce the spacing of corrosion-resistant bars by dividing the black bar spacing by the modification factors. Epoxy-coated, galvanized, and MMFX II microcomposite reinforcing bars do not need modification. Recommendations are provided for the control of crack widths for the other bars evaluated in this study. Spacing of the reinforcement affected both crack spacing and crack widths. As the reinforcement spacing increased, the number of primary cracks decreased and the crack spacing increased. This trend is consistent with previous test results. Crack spacing and crack width, however, did not increase significantly after spacing of the reinforcement became greater than 12 in. For design purposes, the crack spacing can be considered to be constant for bar spacing greater than 12 in. For a given stress, this results in the same crack widths for spacings greater than 12 in. In addition, crack widths of high-strength bars (stainless steel and MMFX II) which have a roundhouse stress-strain curve will increase nonlinearly at high stresses ($>$80 ksi). However, the crack widths of high-strength bars can be conservatively calculated using the model for conventional black bars up to bar stresses of 80 ksi.

Corrosion Resistance.

While all uncracked specimens showed relatively very low currents at 503 days of exposure, several cracked specimens demonstrated high corrosion activity which was electronically measured by the macrocell test and confirmed by visual examination through an autopsy of the specimen. Autopsy results demonstrated that the longitudinal steel (secondary reinforcement in a bridge deck) corroded at the intersection with the transverse steel (primary reinforcement in a bridge deck) while the transverse reinforcement corroded over its entire length. The transverse steel, typically located parallel to the cracks, was under direct chloride exposure over its entire length while the longitudinal steel had direct exposure only at the location of the cracks. When corrosion-resistant chromium based reinforcing steel is used in the top mat and black bars are used in bottom mats, a galvanic couple resulted where the bottom black steel corroded to protect the top corrosion-resistant reinforcement. This galvanic couple occurred because the cracks in the macrocells were formed full depth where chlorides can easily reach the bottom black bars from the first day of testing. This condition is realistic as bridge decks have full-depth cracks which are formed at early ages ($<$28 days) due to restrained shrinkage. Both the electrical current measurements and autopsy results demonstrated that mixing reinforcement where black bars are provided in the bottom mat is detrimental to corrosion resistance. Specimens that were tied with black ties indicated more corrosion than specimens with plastic ties. In addition, tying reinforcing steel with dissimilar metallic materials results in galvanic coupling. When stainless steel tie were used to connect black reinforcement, increased damage of the black bars resulted. In addition, black ties used to connect stainless bars resulted in crevice corrosion and pitting of the stainless steel bar. Only similar metallic or inert (plastic) materials should be used to tie reinforcement.

Volume II: Economic Evaluation

The study developed a systematic framework for evaluating these alternative reinforcing materials on the basis of their life-cycle cost. Case studies involving different scenarios of bridge and operating characteristics were used to demonstrate the methodological framework and to develop nomograms (decision support charts) for the material selection. On the basis of the results of the analysis and the case studies, it is

recommended that deck reinforcement material for any future INDOT bridge deck design should be selected only after carrying out a life-cycle cost analysis among other considerations; such analysis should be preceded by establishment of the decision contexts and consequently, values of the identified input parameters for the life-cycle cost analysis. From a general perspective, it is recommended that INDOT considers for inclusion in its bridge design or rehabilitation manual, the decision support nomograms that specify the conditions at which each material is optimal from a life-cycle perspective.

Nevertheless, there exist avenues that could be addressed or explored further to fine-tune the selection process for appropriate deck reinforcement material alternative for any specific bridge project. First, mathematical models describing the time-dependent chloride-induced corrosion deterioration processes could be incorporated to provide more precise estimates of the life-cycle activity profiles for each material type.

Secondly, the laboratory experiments carried out as part of this research (see Volume I of the report) could be followed by full-scale field studies. For this, it is recommended that a few bridge reconstruction or deck replacement projects should be selected from INDOT's long-range plan or bridge program through an experimental design; for these bridges or decks, INDOT should apply the three material types in a controlled experimental setting. The costs (initial construction and subsequent maintenance), work durations, and the physical condition and service lives of the bridges or decks having each alternative material should be closely monitored and recorded over several decades. Doing this would validate or refine the assumptions made in this study. The experimental design could be designed carefully to include climatic region (northern and southern Indiana), highway classes, traffic volume, and bridge size.

Implementation

Based on the research conducted in the technical evaluation, a number of recommendations were developed that address the selection and design of corrosion-resistance reinforcing bars and are appropriate for adoption into the INDOT Bridge Design Manual. First, guidance is provided to assist in the selection of corrosion-resistant reinforcement based on the duration of testing completed in this study. Extended corrosion exposure is required to provide improved estimates as well as differentiation of the materials. It is recommended that both the top and bottom mats of the bridge deck be constructed of the same reinforcing material. Mixing of reinforcing material causes galvanic corrosion. It is recommended that reinforcement be tied with only inert (plastic) ties or ties made of the same material as the reinforcing bar to avoid galvanic coupling between tie material and reinforcement. Second, design recommendations are provided for the calculation of development and splice lengths including modification factors required for the use of corrosion-resistant reinforcement. It was found that stainless-steel, MMFX II, hot-dipped galvanized, and Zbar perform similarly to black bars and do not require modification. Finally, design recommendations are provided for the control of cracking and the calculation of crack widths. The control of cracking is also of importance even with the use of corrosion-resistant reinforcement and is essential for durability of the bridge deck.

Based on the research conducted in the economic evaluation, a software tool, RM-LCCA, was developed that can be used by INDOT and design consultants. The economic evaluation methodology presented in this study provides a platform to assess the life-cycle costs of different types of bridge deck reinforcement materials based on their corrosion resistance as well as their economic efficiency. The analysis outcome from the RM-LCCA electronic tool can help bridge engineers and practitioners identify the optimal reinforcement alternative for a given bridge on the basis of its expected service life, schedules for rehabilitation and deck replacement, and the accompanying costs to the highway agency and bridge users. The service life of bridge deck, even for the same reinforcement alternative, can change due to factors such as increased loading, rapid changes in the surrounding environment, and upcoming new policy decisions that can affect the short-term and long-term service life of preservation treatments. For the estimated preservation years, the user can incorporate the probability that the treatment timings will be different than what is specified as the average. By running the tool several times for different values of the input variables, the user can carry out simulate the outcome corresponding to different combinations of the input variables. It is envisioned that as the benefits of corrosion-resistant reinforcement alternatives are tested and become recognized, their demand will increase, leading to higher production and lower unit prices.

CONTENTS

LIST OF TABLES

LIST OF FIGURES

1. INTRODUCTION

1.1 Introduction

The deterioration of bridge decks is a major concern for bridge structures. The bridge deck is directly exposed to traffic loading, deicing salts on roads, and environmental conditions. Serving as a roof to the bridge, a typical reinforced concrete bridge deck in cold climates with conventional mild or epoxy-coated steel reinforcement usually has a service life of 20–30 years. This life expectancy is based upon experience in Indiana. At this point, the bridge deck has to be replaced, and the rest of the superstructure can be retained depending on its condition. In worst case scenarios, bridge deck deterioration can lead to or be accompanied by advanced degradation of girders and the substructure, which may require replacement of the entire bridge. Other difficulties such as removing the deck from the girders can also lead to complete superstructure replacement.

Research has been performed to mitigate deterioration in reinforced concrete bridge decks by controlling deck cracking using improved design methods (Frosch, Blackman, & Radabaugh, 2003; Frosch, Bice, & Erickson, 2006a) or by decreasing the permeability and porosity of concrete, typically referred to as high-performance concrete. While these methods can improve performance and extend service life, cracking of the deck cannot be eliminated. In addition, chloride and moisture ingress also cannot be eliminated. Therefore, corrosion of the reinforcing steel ultimately occurs as shown in Figure 1.1. However the service life of a bridge deck has the potential of being improved if corrosion-resistant reinforcement is used.

1.2 Background

1.2.1 Corrosion Resistance

Protective measures to prevent chloride-induced corrosion have been studied over the last three decades. Among the protective measures, epoxy-coated reinforcing steel has become standard practice to inhibit corrosion in susceptible structures such as bridge decks and parking garages in cold regions where deicing salts are used or in marine environments. While epoxy-coated reinforcement became standard practice, this reinforcement is not immune to corrosion as shown in Figure 1.1.

Kahhaleh (1994) tested epoxy-coated reinforcement in various conditions and concluded that these bars are susceptible to chloride induced corrosion. Corrosion can result from debonding of the rebar coating and depends on the level of damage to the coating.

Similarly, Smith and Virmani (1996) also reported that epoxy coatings might become brittle and delaminate from the steel reinforcement through years of exposure to high chloride concentrations. Small breaks, cracks, or holidays in the epoxy coating can result in corrosion at early stages of service life as demonstrated by a bridge substructure in the Florida Keys where chloride-induced corrosion was discovered six years after construction (Sagüés, Powers, & Kessler, 1994).

Samples and Ramirez (1999) stated that the performance of epoxy-coated reinforcement is highly dependent on construction practices during fabrication, transportation, construction, and maintenance. In summary, research has illustrated problems with the use of epoxy coating as a protective measure.

Alternative materials such as solid stainless steel, fiber reinforced polymers (FRP), MMFX II microcomposite steel, hot-dip galvanized, dual coated (zinc and epoxy), and zinc-clad reinforcement are considered as potential solutions to increase bridge deck service life. A number of research projects within the last ten years focused on evaluating the corrosion performance of these corrosion-resistant reinforcing steels under the support of the Federal Highway Association (FHWA) and state DOTs (Darwin et al., 2001; Kahl 2007; Hartt et al., 2009; Phares, Fanous, Wipf, Lee, & Jolley, 2006). In a number of these studies, macrocell tests have been used to evaluate the corrosion performance of some of these reinforcement types. These tests typically use macrocells outlined in ASTM G109 (2005) or ASTM A955 (2009). These standard macrocells shown in Figure 1.2, however, have a number of limitations which include: uncracked specimens (ASTM G109), artificial cracks formed by stainless steel shim

Figure 1.1 Corrosion of epoxy-coated reinforcing steel (photos courtesy of INDOT).

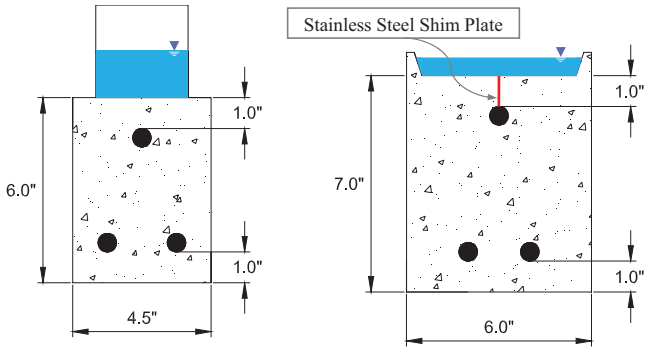

(a) ASTM G109 Macrocell (b) ASTM A955 Macrocell

Figure 1.2 Macrocells used in Other Corrosion Studies.

plates (ASTM A955) only down to the top bar, and no transverse reinforcement (ASTM G109 and ASTM A955).

To put these limitations in perspective, concrete bridge decks are always cracked, and cracks are full depth. When concrete is cracked, chloride exposure is immediate and high concentrations of chlorides at these locations are likely. High chloride ion concentrations at crack locations can lead to localized pitting corrosion of the reinforcing steel. Cracks also typically occur at locations of the transverse reinforcement. At the connection between transverse and longitudinal bars, crevice corrosion is also possible. Finally, full depth cracks (Figure 1.3) allow for full penetration of chlorides and exposure of both top and bottom mats. Limitations of standard macrocells lead to concerns regarding the translation of laboratory results into field performance.

1.2.2 Structural Peformance

Unlike corrosion, there has been very limited research on the structural performance of the different reinforcement types. Of particular interest when considering different bar types is development and splice lengths as well as crack control.

Ahlborn and DenHartigh (2003) conducted a study comparing the bond strengths of stainless steel and conventional mild steel through beam-end tests and suggested that no development length reduction factor is required for 316LN and Duplex 2205 stainless steel reinforcement. Johnson and Moen (2010) also concluded that the bar types which they evaluated (Duplex 2205 stainless steel, 316LN stainless steel, stainless steel clad bar, MMFX, epoxy-coated, and Zbar (dual coated)) through pull-out and beam-end tests well exceed calculated values considering the ACI 318-08 (2008) design equations.

While these limited tests exist for bars other than epoxy-coated, it should be noted that ACI Committee 408 (2001) does not recommend using pullout test results as the basis for determining development length because the bond stress developed is different from the stress state of most reinforced concrete members. In addition, beam-end specimens can duplicate the stress state in reinforced concrete members if the rebar and the surrounding concrete are simultaneously placed in tension, but, if the compressive force is placed relatively close to the bar, higher bond strengths can be reached. Therefore, a splice test is recommended to evaluate the bond strength and development length of reinforcing steel. Unfortunately, splice tests have not been conducted for the majority of these alternative bar types.

As previously noted, crack control remains important when considering corrosion resistant reinforcement. Even if corrosion of the reinforcement is eliminated, it is important to minimize leakage from the bridge deck to both the superstructure and substructure. Cracking of the bridge deck can also lead to other durability concerns such as freeze-thaw damage of the concrete. Based on previous research, it is clear that the reinforcement type can affect both crack widths and spacing. For example, a study by Frosch et al. (2003) demonstrated that epoxy coating thickness affects both crack widths and spacings. Considering that the surface roughness is quite different for various corrosion resistant rebar types even when coatings

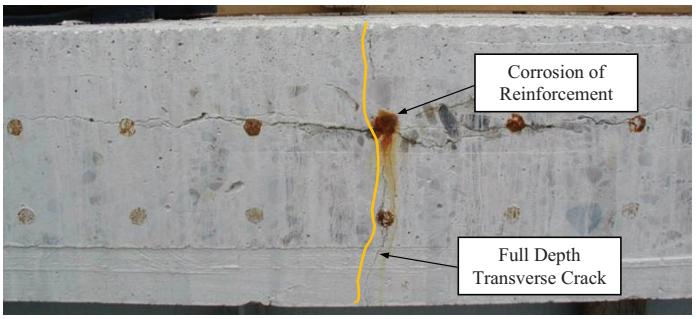

Figure 1.3 Full-depth shrinkage crack in bridge deck.

are not used, differences in cracking performance are expected and should be evaluated.

1.3 Research Objective

The objective of this research program is to evaluate both the structural and corrosion performance of concrete bridge decks reinforced with corrosion-resistant reinforcement.

1.4 Research Scope

This research program was conducted in three phases and considered a wide range of corrosion resistant reinforcing materials. These materials included stainless steel (316LN, Duplex 2205, Duplex 2304, XM-28), and MMFX II micro-composite steel, and coated steel (epoxy, dual-coated zinc and epoxy (Z-bar), hot-dipped galvanized, and zinc-clad)). The first phase of research evaluated the bond strength of the corrosion resistant bars using full-scale splice tests. The second phase evaluated cracking behavior using regions of slab specimens subjected to constant moment. Finally, the third phase evaluated corrosion resistance of the various bars using macrocell specimens specially designed to simulate cracked and uncracked bridge deck behavior. The results of the three phases are used to assist in the selection of corrosion resistant reinforcement and provide design recommendations regarding development and splicing as well as crack control when these reinforcement types are selected.

2. CORROSION-RESISTANT REINFORCING STEEL

2.1 Research Summary

Eleven different reinforcing steels shown in Figure 2.1 are used in this study. Of the eleven, ten are corrosion-resistant reinforcing bars and one is conventional black steel. The ten corrosion-resistant reinforcing bars include epoxy-coated, hot-dip galvanized, tin-plated zinc-clad, un-plated zinc-clad, Zbar (dual-coated with epoxy and zinc), MMFX II microcomposite, and four different types of stainless steel.

Epoxy-coated reinforcing steel protects the steel inside by functioning as a barrier to keep oxygen, water, and chloride ions from reaching the surface of the steel. Hot-dip zinc-coated galvanized and zinc-clad reinforcing steel protects the steel inside by acting as a sacrificial anode that corrodes faster than the protected base metal. Dual-coated reinforcing steel, Zbar, has an epoxy layer on the exterior and an underlying zinc layer over the base metal. The dual-coated reinforcing steel provides both barrier and sacrificial protection. MMFX II microcomposite steel is designed to have no carbides and have 9% chromium to increase corrosion-resistance. Stainless steels are known to be corrosion-resistant and contain more than 12% chromium. Complete details including literature review of each corrosion resistant reinforcement and the properties of the reinforcement used in this study are provided in Appendix A.

3 EVALUATION OF BOND STRENGTH

3.1 Research Summary

The objective of this phase of research was to investigate the bond between corrosion-resistant reinforcing bars and concrete. Forty five beam specimens with tension lap splices were tested to evaluate the effect of bar type, bar size, bar spacing, splice length, transverse reinforcement, and axial rigidity on bond strength. Lap-splice beam tests were selected for this study because these specimens are commonly used to ascertain the development and splice lengths of reinforcement and are the basis for development length design expressions. The test data were combined with other data available in literature to construct a simple model for development and splice length considering the range of corrosion resistant bar types as well as unconfined and confined conditions. Complete details of the experimental program are provided in Appendix B. The details of the test results and analysis are provided in Appendix C.

3.2 Conclusions

Based on the results of this phase of research, the following conclusions are provided:

1. Stainless-steel, MMFX II microcomposite, hot-dip galvanized, and Zbar (dual-coated) reinforcing bars have bond strengths comparable to black bars.
2. Coated bars other than galvanized and dual-coated have reduced bond strengths. Epoxy-coated bars had on average 11% less bond strength than black. Un-plated zinc-clad and Tin-plated zinc-clad bar had on average 18% and 26% less bond strength than black bars, respectively.

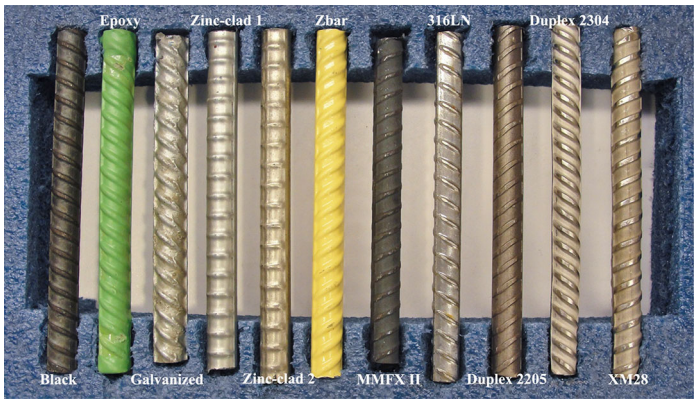

Figure 2.1 Corrosion-resistant steel used in this study.

3. Relative rib area had essentially no correlation with the bond strength of the bars tested. The relative rib area of the tested bars ranged from 0.059 to 0.117 for the #5 bars (only 3 bars larger than 0.1) and 0.045 to 0.095 for the #8 bars.
4. As the surface roughness of the uncoated bars increased, the bond strength increased. All uncoated bars in this study had at least a surface roughness of 100 peak and valley pairs. For every 20 peak and valley pair increase in surface roughness beyond 100, a 1 ksi increase in bar stress was observed.
5. Coated bars with a coating thickness more than 10 mils were observed to have reduced bond strengths. For every 2 mils increase in thickness beyond 10 mils, a 1 ksi decrease in bar stress was observed.
6. As the splice length increases, the bar stress reached at failure increases nonlinearly. Bar stresses reached at bond failure, f_s, was observed to be increased proportional to the square root of splice length, $\sqrt{l_s}$.
7. Providing transverse reinforcement in the center of the splice region is not effective. Only minimal increase in bond strength were observed using this configuration.
8. Confinement of the splice region can be used to increase bond strength. The additional force capacity of one splice bar is proportional to the force capacity of the transverse reinforcement crossing the splitting plane $A_{tr}f_{yt}N_s/N_b$. It is observed that the increased longitudinal force is 1/2 the transverse force F_{tr}.

4. EVALUATION OF CRACKING PERFORMANCE

4.1 Research Summary

The objective of this phase of research was to investigate the cracking behavior of slabs reinforced with corrosion-resistant reinforcing steel. Although the reinforcing bars considered in this testing program are corrosion-resistant, the control of crack widths in reinforced concrete structures still remain important not only for aesthetics but also for durability. Twelve slab specimens were tested to 1) identify how cracking is affected by the distribution of the longitudinal reinforcement, 2) investigate if current crack width calculation procedures are adequate for these different products, and 3) evaluate crack widths at high stress levels considering that many of these material have higher strengths that may be utilized in design. The specimens were tested in four-point bending with an 8 ft long constant moment region provided to generate a sufficient number of cracks. Primary variables considered included the reinforcement type and bar spacing. The influence of reinforcement stress was also of primary interest as high reinforcement stresses can be obtained using the high-strength provided by some of the reinforcement products considered. Complete details of the experimental program are provided in Appendix D. The details of the test results and analysis are provided in Appendix E.

4.2 Conclusions

Based on the results of this phase of research, the following conclusions were made:

1. The bar types affected the spacing and width of primary cracks.
2. Spacing of the reinforcement affected both crack spacing and crack widths. As the reinforcement spacing increased, the number of primary cracks decreased and the crack spacing increased. This trend is consistent with previous test results.
3. Crack spacing and crack width, however, did not increase very much after spacing of reinforcement became greater than 12 in. For design purposes, the crack spacing can be considered to be constant for bar spacing greater than 12 in. For a given stress, this results in the same crack widths for spacings greater than 12 in.
4. Crack widths of high-strength bars (MMFX II and stainless steel) which have a roundhouse stress-strain curve will increase nonlinearly at high stresses ($>$ 80 ksi). However, the crack widths of high-strength bars can be conservatively calculated using crack width models for conventional black bars up to bar stresses of 80 ksi.

5. EVALUATION OF CORROSION-RESISTANCE

5.1 Research Summary

The objective of this experimental program was to evaluate the corrosion-resistance of various types of reinforcing steel. The performance of these materials was compared with conventional black reinforcing bar which was used as the control. One hundred and twelve (112) modified macrocell specimens were constructed evaluating corrosion resistance under uncracked and cracked conditions. Transverse reinforcing bar was also tied to the longitudinal reinforcing bar to simulate actual bridge deck conditions. A testing procedure identical to ASTM G109 including a sodium chloride concentration of 3%-by-weight solution and a test regime with two weeks of wet cycle followed by the two weeks of dry cycle was followed. Corrosion was monitored by measuring the electrical current flowing across the mats. After 503 days of testing, one specimen out of three replicates was autopsied to visually correlate corrosion measurements. Complete details of the experimental program are provided in Appendix F. The details of the test results and analysis are provided in Appendix G.

5.2 Conclusions

Based on the results of this phase of research, the following conclusions were made:

1. While all uncracked specimens showed relatively very low currents at 503 days of exposure, cracked specimens demonstrated high corrosion activity which was electronically measured by the macrocell test and confirmed by visual examination through an autopsy of the specimen.
2. Autopsy results demonstrated that the longitudinal steel (secondary reinforcement in a bridge deck) corroded at the intersection with the transverse steel (primary reinforcement in a bridge deck) while the transverse reinforcement corroded over its entire length. The transverse steel, typically located parallel to the cracks, was under direct chloride exposure over its entire length while the longitudinal steel had direct exposure only at the location of the cracks.
3. When corrosion-resistant chromium based reinforcing steel is used in the top mat and black bars are used in bottom mats, a galvanic couple resulted where the bottom black steel corroded to protect the top corrosion-resistant reinforcement. This galvanic couple occurred because the cracks in the macrocells were formed full depth where chlorides can easily reach the

bottom black bars from the first day of testing. This condition is realistic as bridge decks have full-depth cracks which are formed at early ages (<28 days) due to restrained shrinkage. Both the electrical current measurements and autopsy results demonstrated that mixing reinforcement where black bars are provided in the bottom mat is detrimental to corrosion resistance.

4. Specimens that were tied with black ties indicated more corrosion than specimens with plastic ties. In addition, tying reinforcing steel with dissimilar metallic materials results in galvanic coupling. When stainless steel tie were used to connect black reinforcement, increased damage of the black bars resulted. In addition, black ties used to connect stainless bars resulted in crevice corrosion and pitting of the stainless steel bar. Only similar metallic or inert (plastic) materials should be used to tie reinforcement.

6. DESIGN RECOMMENDATIONS

6.1 Development Length Equation

The following model is recommended for the calculation of development and splice lengths for both conventional black and corrosion resistant reinforcing steel:

$$l_s = \frac{(f_s - f_{tr})^2}{\sqrt{f'_c}} d_b \cdot \psi_b \qquad (6.1)$$

where:

l_s = *splice or development length (in.)*
f_s = *bar stress at failure (ksi)*
f_{tr} = *bar stress contribution from confinement (ksi)* $= \frac{1}{2}\frac{A_{tr} f_{yt}}{A_b N_b} N_s$
A_b = *area of spliced bar (in.^{2})*
A_{tr} = *total area of transverse reinforcement crossing the potential splitting plane ($A_{tr} = A_{tr_{1bar}} \cdot N_l$) (in.^{2})*
$A_{tr_{1bar}}$ = *area of one transverse reinforcement (in.^{2})*
N_l = *number of legs of transverse reinforcement that cross the splitting plane*
f_{yt} = *yield strength of transverse reinforcement (ksi)*
N_s = *number of spliced bars*
N_b = *number of spliced or developed bars*
f'_c = *specified compressive strength of concrete (psi)*
d_b = *nominal diameter of spliced bar (in.)*
ψ_b = *modification factor for different bar types (Table 6.1)*

6.2 Crack Width Calculations

For the control of crack widths, it is recommended that crack widths be calculated based on black bars and multiplied using the following factors (Table 6.2). Design code approaches can directly incorporate these factors to reduce the spacing of these bars. The maximum allowed bar spacing for crack control of black bars should be divided by these factors.

6.3 Corrosion-Resistant Reinforcing Steel and Tie Material

- It is recommended that both the top and bottom mats of the bridge deck be constructed of the same reinforcing material. Mixing of reinforcing material causes galvanic corrosion.

TABLE 6.1
Recommended Modification Factor

Bar Type		Modification Factor ψ_b
Black		1.0
Coated Bars	Epoxy	1.3
	Galvanized	1.0
	Zinc-clad I	1.4
	Zinc-clad II	2.0
	Zbar	1.0
MMFX II		1.0
Stainless Steel Bars	316 LN	1.0
	Duplex 2205	
	Duplex 2304	
	XM-28	

TABLE 6.2
Recommended Modification Factor for Crack Width Calculations

Bar Type		Modification Factor X_{Crack}
Black		1.0
Coated Bars	Epoxy	1.0
	Galvanized	1.0
	Zinc-clad	2.0
	Zbar	1.3
MMFX II		1.0
Stainless Steel Bars	316 LN	1.3
	Duplex 2205	
	Duplex 2304	
	XM-28	

- It is recommended that reinforcement be tied with only inert (plastic) ties or ties made of the same material as the reinforcing bar to avoid galvanic coupling between tie material and reinforcement.
- To assist in the selection of corrosion resistant bars, the following ranked order in terms of corrosion resistance in concrete is provided (Table 6.3). These estimates are preliminary and extended corrosion testing is required to provide improved estimates as well as differentiation.

TABLE 6.3
Corrosion Resistance of Reinforcing Bars

Rank	Bar Type	Corrosion Performance
1	316LN	Best
2	Duplex 2304	↑
3	Duplex 2205	
4	Zinc-clad	
5	Galvanized	
6	XM-28	
7	Zbar	
8	Epoxy	
9	MMFX II	↓
10	Black	Worst

REFERENCES

AASHTO. (2010). *AASHTO LRFD Bridge Design Specifications*. Washington, DC: American Association of State Highway and Transportation Officials.

Abrams, D. A. (1913). *Tests of bond between concrete and steel* (Engineering Experiment Station Bulletin No. 71). Urbana: University of Illinois.

ACI 318. (2008). *Building code requirements for structural concrete and commentary* (ACI 318-08). Farmington Hills, MI: American Concrete Institute.

ACI 318. (2011). *Building code requirements for structural concrete and commentary* (ACI 318-11). Farmington Hills, MI: American Concrete Institute.

ACI 408. (2003). *Bond and development of straight reinforcing bars in tension* (ACI 408R-03). Farmington Hills, MI: American Concrete Institute.

ACI 408. (2009). *Guide for lap splice and development length of high relative rib area reinforcing bars in tension and commentary* (ACI 408.3R-09). Farmington Hills, MI: American Concrete Institute.

Ahlborn, T., & DenHartigh, T. (2003). Comparative bond study of stainless and high-chromium reinforcing bars in concrete. *Transportation Research Record*, *1845*, 88–95.

ASME B46.1. (2009). *Surface texture (surface roughness, waviness, and lay)*. New York, NY: American Society of Mechanical Engineers.

ASTM A1035. (2007). *Standard Specification for Deformed and Plain, Low-carbon, Chromium, Steel Bars for Concrete Reinforcement*. West Conshohocken, PA: American Society for Testing and Materials.

ASTM A370. (2012). *Standard Test Methods and Definitions for Mechanical Testing of Steel Products*. West Conshohocken, PA: American Society for Testing and Materials.

ASTM A615. (2009). *Standard Specification for Deformed and Plain Carbon-Steel Bars for Concrete Reinforcement*. West Conshohocken, PA: American Society for Testing and Materials.

ASTM A767. (2009). *Standard Specification for Zinc-Coated (Galvanized) Steel Bars for Concrete Reinforcement*. West Conshohocken, PA: American Society for Testing and Materials.

ASTM A775. (2007). *Standard Specification for Epoxy-Coated Reinforcing Bars: Materials and Coating Requirements*. West Conshohocken, PA: American Society for Testing and Materials.

ASTM A934. (2007). *Standard Specification for Epoxy-Coated Prefabricated Steel Reinforcing Bars*. West Conshohocken, PA: American Society for Testing and Materials.

ASTM A955. (2009). *Standard Specification for Deformed and Plain Stainless-Steel Bars for Concrete Reinforcement*. West Conshohocken, PA: American Society for Testing and Materials.

ASTM C39. (2012). *Standard Test Method for Compressive Strength of Cylindrical Concrete Specimens*. West Conshohocken, PA: American Society for Testing and Materials.

ASTM C496. (2011). *Standard Test Method for Splitting Tensile Strength of Cylindrical Concrete Specimens*. West Conshohocken, PA: American Society for Testing and Materials.

ASTM D3963. (2011). *Standard Specification for Fabrication and Jobsite Handling of Epoxy-Coated Steel Reinforcing Bars*. West Conshohocken, PA: American Society for Testing and Materials.

ASTM D7091. (2005). *Standard Practice for Nondestructive Measurement of Dry Film Thickness of Nonmagnetic Coatings Applied to Ferrous Metals and Nonmagnetic, Nonconductive Coatings Applied to Non-Ferrous Metals*. West Conshohocken, PA: American Society for Testing and Materials.

ASTM D7127. (2005). *Standard Test Method for Measurement of Surface Roughness of Abrasive Blast Cleaned Metal Surfaces Using a Portable Stylus Instrument*. West Conshohocken, PA: American Society for Testing and Materials.

ASTM E376. (2011). *Standard Practice for Measuring Coating Thickness by Magnetic-Field or Eddy-Current (Electromagnetic) Testing Methods*. West Conshohocken, PA: American Society for Testing and Materials.

ASTM G109. (2005). *Standard Test Method for Determining the Effects of Chemical Admixtures on the Corrosion of Embedded Steel Reinforcement in Concrete Exposed to Chloride Environments*. West Conshohocken, PA: American Society for Testing and Materials.

Azizinamini, A., Stark, M., Roller, J. J., & Ghosh, S. K. (1993). Bond performance of reinforcing bars embedded in high-strength concrete. *ACI Structural Journal*, *90*(5), 554–561.

Azizinamini, A., Pavel, R., Hatfield, E., & Ghosh, S. K. (1999). Behavior of spliced reinforcing bars embedded in high-strength concrete. *ACI Structural Journal*, *96*(5), 826–835.

Beeby, A. (1983). Cracking, cover, and corrosion of reinforcement. *Concrete International: Design and Construction*, *5*(2), 35–41.

Bertolini, L., Gastldi, M., Pedeferri, M., Pedeferri, P., & Pastore, T. (1998). Effects of galvanic coupling between carbon steel and stainless steel reinforcement in concrete. In *Proceedings of International Conference on Corrosion and Rehabilitation of Reinforced Concrete Structures* [CD-ROM]. Federal Highway Administration, Dec. 7–11, Orlando, FL.

Bianchini, A. C., Kesler, C. E., & Lott, J. (1968). Cracking of reinforced concrete under external load. *Causes, mechanism, and control of cracking in concrete, ACI publication SP-20* (pp. 73–85). Farmington Hills, MI: American Concrete Institute.

Blackman, D. (2002). *Evaluation of design methods for the control of early age bridge deck cracking* (Master's thesis). West Lafayette, IN: Purdue University.

Broms, B. B. (1965a). Technique for investigation of internal cracks in reinforced concrete members. *ACI Journal Proceedings*, *62*(1), 35–43.

Broms, B. B. (1965b). Crack width and crack spacing in reinforced concrete members. *ACI Journal Proceedings*, *62*(10), 1237–1255.

Broms, B. B., & Lutz, L. A. (1965). Effects of arrangement of reinforcement on crack width and spacing of reinforced concrete members. *ACI Journal Proceedings*, *62*(11), 1395–1410.

Burns, C. (2011). *Serviceability analysis of reinforced concrete based on the tension chord model* (Doctoral dissertation). Zurich, Switzerland: Swiss Federal Institute of Technology.

Cairns, J., & Abdullah, R. (1994). Fundamental tests on the effect of an epoxy coating on bond strength. *ACI Materials Journal*, *91*(4), 331–338.

Canbay, E., & Frosch, R. J. (2005). Bond strength of lap-spliced bars. *ACI Structural Journal*, *102*(4), 605–614.

Chamberlin, S. J. (1956). Spacing of reinforcement in beams. *ACI Journal Proceedings*, *53*(1), 113–134.

Chamberlin, S. J. (1958). Spacing of spliced bars in beams. *ACI Journal Proceedings*, *54*(8), 689–698.

Chinn, J., Ferguson, P. M., & Thompson, J. N. (1955). Lapped splices in reinforced concrete beams. *ACI Journal Proceedings*, *52*(10), 201–213.

Clark, A. P. (1946). Comparative bond efficiency of deformed concrete reinforcing bars. *ACI Journal Proceedings*, *18*(4), 381–399.

Clark, A. P. (1949). Bond of concrete reinforcing bars. *Journal of Research of the National Bureau of Standards*, *43*, 565–579.

Clark, A. P. (1956). Cracking in reinforced concrete flexural members. *ACI Journal Proceedings*, *27*(8), 851–862.

Clear, K. C. (1981). *Time-to-corrosion of reinforcing steel in concrete slabs, vol. 4. galvanized reinforcing steel* (Publication No. FHWA/RD-82/028). McLean, VA: Federal Highway Administration.

Clear, K. C. (1992). Effectiveness of epoxy-coated reinforcing steel. *Concrete International*, *14*(5), 58–62.

Cleary, D. B., & Ramirez, J. A. (1993). Epoxy-coated reinforcement under repeated loading. *ACI Structural Journal*, *90*(4), 451–458.

Clemeña, G. G., & Virmani, Y. P. (2004). Comparing the chloride resistance of reinforcing bars. *Concrete International*, *25*(11), 39–49.

Clifton, J. R., Beeghly, H. F., & Mathley, R. G. (1975). *Nonmetallic coatings for concrete reinforcing bars* (Publication No. NBS BSS-65). Washington, DC: Federal Highway Administration.

Cook, A. R., & Radtke, S. F. (1977). Recent research on galvanized steel for reinforcement of concrete. In D. E. Tonini & S. W. Dean (Eds.), *Chloride Corrosion of Steel in Concrete: ASTM STP 629* (pp. 51–60). Philadelphia, PA: American Society of Testing and Materials.

Darwin, D., Manning, D., Hognestad, E., Beeby, A., Rice, P., & Ghowrwal, A. (1985). Debate: Crack width, cover, and corrosion. *Concrete International*, *7*(5), 20–35.

Darwin, D., & Graham, E. K. (1993). Effect of Deformation Height and Spacing on Bond Strength of Reinforcing Bars. *ACI Structural Journal*, *90*(6), 646–657.

Darwin, D., Browning, J., Nguyen, T. V., & Locke, C. Jr. (2001). *Evaluation of corrosion resistance of different steel reinforcement types* (Report No. SD2001-05-F). Pierre, SD: South Dakota Department of Transportation.

Darwin, D., Browning, J., O'Reilly, M., Xing, L., & Ji, J. (2009). Critical Chloride corrosion threshold of galvanized reinforcing bars. *ACI Materials Journal*, *106*(2), 176–183.

Darwin, D., Tholen, M. L., Idun, E. K., & Zuo, J. (1996). Splice strength of high relative rib area reinforcing bars. *ACI Structural Journal*, *93*(1), 95–107.

DeVries, R. A., Moehle, J. P., & Hester, W. (1991). *Lap splice of plain and epoxy-coated reinforcements: An experimental study considering concrete strength, casting position, and anti-bleeding additives* (Report No. UCB/SEMM-91/02, Structural Engineering Mechanics and Materials Program). Berkeley: University of California.

Di Bella, C., Villani, C., Hausheer, E., & Weiss, J. (2012). Chloride transport measurements for a plain and internally cured concrete mixture. In A. K. Schindler, J. G. Grygar, & W. J. Weiss (Eds.), *The economics, performance, and sustainability of internally cured concrete: SP-290*. Farmington Hills, MI: American Concrete Institute.

El-Hacha, R., El-Agroudy, H., & Rizkalla, S. H. (2006). Bond characteristics of high-strength steel reinforcement. *ACI Structural Journal*, *103*(6), 771–782.

Ferguson, P. M., & Thompson, J. N. (1962). Development length for large high strength reinforcing bars in bond. *ACI Journal Proceedings*, *59*(7), 887–922.

Ferguson, P. M., & Breen, J. E. (1965). Lapped splices for high-strength reinforcing bars. *ACI Journal Proceedings*, *62*(9), 1063–1078.

Ferguson, P. M., & Thompson, J. N. (1965). Development length for large high strength reinforcing bars. *ACI Journal Proceedings*, *62*(1), 71–94.

Ferguson, P. M., & Briceno, A. (1969). *Tensile Lap Splices—part 1: Retaining wall type, varying moment zone* (Center for Highway Research Report No. 113-2). Austin: The University of Texas at Austin.

Fontana, M. G. (1986). *Corrosion engineering*. New York, NY: McGraw Hill, Inc.

Frosch, R. J. (1999). Another look at cracking and crack control in reinforced concrete. *ACI Structural Journal*, *96*(3), 437–442.

Frosch, R. J., Blackman, D. T., & Radabaugh, R. D. (2003). *Investigation of bridge deck cracking in various superstructure systems* (Joint Transportation Research Program Publication No. FHWA/IN/JTRP-2002/25). West Lafayette, IN: Purdue University http://dx.doi.org/10.5703/1288284313257

Frosch, R. J., Bice, J. K., & Erickson, J. B. (2006a). *Design methods for the control of restrained shrinkage cracking* (Joint Transportation Research Program Publication No. FHWA/IN/JTRP-2006/32). West Lafayette, IN: Purdue University http://dx.doi.org/10.5703/1288284313363

Frosch, R. J., & Pay, A. C. (2006b). *Implementation of a nonmetallic reinforced bridge deck, volume 1: Bond behavior* (Joint Transportation Research Program Publication No. FHWA/IN/JTRP-2006/15). West Lafayette, IN: Purdue University http://dx.doi.org/10.5703/1288284313383

García-Alonso, M. C., González, J. A., Miranda, J., Escudero, M. L., Correia, M. J., Salta, M., & Bennani, A. (2007). Corrosion behavior of innovative stainless steels in mortar. *Cement and Concrete Research*, *37*(11), 1562–1569.

Gergely, P., & Lutz, L. A. (1968). Maximum crack width in reinforced concrete flexural members. *Causes, mechanism, and control of cracking in concrete: SP-20* (pp. 87–117). Farmington Hills, MI: American Concrete Institute.

Goto, Y. (1971). Cracks formed in concrete around deformed tension bars. *ACI Journal Proceedings*, *68*(4), 244–251.

Hadje-Ghaffari, H., Choi, O. C., Darwin, D., & McCabe, S. L. (1994). Bond of epoxy-coated reinforcement: Cover, casting position, slump, and consolidation. *ACI Structural Journal*, *91*(1), 59–68.

Hamad, B. S., & Itani, M. S. (1998). Bond strength of reinforcement in high-performance concrete: The role of silca fume, casting position, and superplasticizer dosage. *ACI Materials Journal*, *95*(5), 499–511.

Hamad, B. S., & Jirsa, J. O. (1993). Strength of epoxy-coated reinforcing bar splices confined with transverse reinforcement. *ACI Structural Journal*, *90*(1), 77–88.

Hamad, B. S., & Machaka, M. F. (1999). Effect of transverse reinforcement on bond strength of reinforcing bars in silica fume concrete. *Materials and Structures*, *32*(220), 468–476.

Hamad, B. S., & Mansour, M. Y. (1996). Bond strength of noncontact tension lap splices. *ACI Structural Journal*, *93*(3), 316–326.

Hartt, W. H., Powers, R. G., Marino, F. P., Paredes, M., Simmons, R., Yu, H., ... Virmani, Y. P. (2009). *Corrosion resistant alloys for reinforced concrete* (Publication No. FHWA-HRT-09-020). Washington, DC: Federal Highway Administration.

Hasan, H. O., Cleary, D. B., & Ramirez, J. A. (1996). Performance of concrete bridge decks and slabs reinforced with epoxy-coated steel under repeated loading. *ACI Structural Journal*, *93*(4), 397–403.

Hester, C. J., Salamizavaregh, S., Darwin, D., & McCabe, S. L. (1993). Bond of epoxy-coated reinforcement: Splices. *ACI Structural Journal*, *90*(1), 89–102.

Hewitt, J., & Tullmin, M. (1994). Corrosion and stress corrosion cracking performance of stainless steel and other reinforcing bar materials in concrete. In R. N. Swamy (Ed.), *Corrosion and corrosion protection of steel in concrete* (pp. 527–539). Sheffield, UK: Sheffield Academic Press.

Hoffman, J. S. (2008). *Control and repair of bridge deck cracking* (Master's thesis). West Lafayette, IN: Purdue University.

Hognestad, E. (1951). *A study of combined bending and axial load in reinforced concrete members* (Engineering Experiment Station Bulletin No. 399). Urbana: University of Illinois.

Hognestad, E. (1962). High-strength bars as concrete reinforcement—part 2: Flexural cracking. *Journal of the PCA Research and Development Laboratories*, *4*(1), 46–63.

Hwang, S. J., Lee, Y. Y., & Lee, C. S. (1994). Effect of silica fume on the splice strength of deformed bars of high-performance concrete. *ACI Structural Journal*, *91*(3), 294–302.

Idun, E. K., & Darwin, D. (1999). Bond of epoxy-coated reinforcement: Coefficient of friction and rib face angle. *ACI Structural Journal*, *96*(4), 609–615.

International Federation for Structural Concrete. (2013). *fib model code for concrete structures 2010*. Lausanne, Switzerland: Ernst & Sohn.

Johnson, J., & Moen, C. (2010). *Bond strength of corrosion resistant steel reinforcement in concrete* (Virginia Transportation Research Center Publication No. FHWA-VTRC-10-CR). Washington, DC: Federal Highway Administration.

Jones, D. A. (1996). *Principles and prevention of corrosion*. New York, NY: Macmillan Publishers.

Kadoriku, J. (1994). *Study on behavior of lap splices in high-strength reinforced concrete members* (Doctoral dissertation). Kobe, Japan: Kobe University.

Kahhaleh, K. Z. (1994). *Corrosion performance of epoxy-coated reinforcement* (Doctoral dissertation). Austin: The University of Texas at Austin.

Kahl, S. (2007). *Corrosion resistant alloy steel (MMFX) reinforcing bar in bridge decks* (Publication No. MDOT R-149). Lansing, MI: Michigan Department of Transportation.

Karr, P. H., & Mattock, A. H. (1963). High-strength bars as concrete reinforcement—part 4: Control of flexural cracking. *Journal of the PCA Research and Development Laboratories*, *5*(1), 15–38.

Kim, N., & Thomas, G. (1984). Effects of the constituents on the mechanical behavior of low carbons steel. *Scripta Metallurgica*, *18*(8), 817–820.

Kimura, H., & Jirsa, J. O. (1992). *Effects of bar deformation and concrete strength on bond on reinforcing steel to concrete* (Phil M. Ferguson Structural Engineering Laboratory Publication No. 92-4). Austin: The University of Texas at Austin.

Kluge, R. W., & Tuma, E. C. (1945). Lapped bar slices in concrete beams. *ACI Journal Proceedings*, *42*, 13–33.

Kobayashi, K., & Takewaka, K. (1984). Experimental studies of epoxy-coated reinforcing steel for corrosion protection. *The International Journal of Cement Composites and Lightweight Concrete*, *6*(2), 99–116.

Koo, J., & Thomas, G. (1977). Design of duplex Fe/X/0.1C steels for improved mechanical properties. *Metallurgical Transactions A*, *8*(3), 525–528.

Lee, S., & Krauss, P. D. (2004). *Long-term performance of epoxy-coated reinforcing steel in heavy salt-contaminated concrete* (Publication No. FHWA/HRT-04/090). McLean, VA: Federal Highway Administration.

Macias, A., & Andrade, C. (1990). The behavior of galvanized steel in chloride-containing alkaline solutions—I. *The influence of the cation. Corrosion Science*, *30*(4–5), 393–407.

Mathey, R., & Clifton, J. R. (1976). Bond of coated reinforcing bars in concrete. *Journal of the Structural Division, ASCE*, *102*(1), 215–229.

Mathey, R., & Watstein, D. (1961). Investigation of bond in beam and pull-out specimens with high-yield-strength deformed bars. *ACI Journal Proceedings*, *58*(9), 1071–1090.

McCrum, R. L., & Arnold, C. J. (1993). *Evaluation of simulated bridge deck slabs using uncoated, galvanized, and epoxy-coated reinforcing steel* (Publication No. R-1320). Lansing, MI: Michigan Department of Transportation.

McDonald, D. B., Pfeifer, D. W., & Blake, G. T. (1996). *The corrosion performance of inorganic-organic and metallic-clad reinforcing bars and solid metallic reinforcing bars in accelerated screening test* (Publication No. FHWA/RD-96/085). McLean, VA: Federal Highway Administration.

McDonald, D. B., Pfeifer, D. W., & Sherman, M. R. (1998). *Corrosion evaluation of epoxy-coated, metallic-clad and solid metallic reinforcing bars in concrete* (Publication No. FHWA/RD-98/153). McLean, VA: Federal Highway Administration.

McKenzie, M. (1993). The effect of defects on the durability of epoxy-coated reinforcement. *Transportation Research Circular*, *403*, 17–28.

Mindess, S., Young, J. F., & Darwin, D. (2002). *Concrete* (2nd ed.). Upper Saddle River, NJ: Prentice Hall.

Morita, S., & Fujii, S. (1982). Bond capacity of deformed bars due to splitting of surrounding concrete. In P. Bartos (Ed.), *Proceedings of the International Conference on Bond in Concrete* (pp. 331–341). London, UK: Applied Science Publishers.

Mosley, C. P. (2000). *Bond performance of Fiber Reinforced Plastic (FRP) reinforcement in concrete* (Master's thesis). West Lafayette, IN: Purdue University.

Neuhart, B. N. (2000). Use of stainless steels 316LN and Duplex 2205 in bridge deck construction in North America. *Repair, rehabilitation, and maintenance of concrete structures, and innovations in design and construction proceedings: SP-193* (pp. 1027–1050). Farmington Hills, MI: American Concrete Institute.

Nürnberger, U. (1996). *Stainless steel in concrete—state of the art report* (European Federation of Corrosion Publication No. 18). Cambridge, UK: The Institute of Materials.

Orangun, C. O., Jirsa, J. O., & Breen, J. E. (1975). *The strength of anchored bars: A reevaluation of test data on development length and splices* (Center for Highway Research Publication No. 154-3F). Austin: The University of Texas at Austin.

Orangun, C. O., Jirsa, J. O., & Breen, J. E. (1977). Reevaluation of test data on development length and splices. *ACI Journal Proceedings*, *74*(3), 114–122.

O'Reilly, M., Darwin, D., Browning, J., & Locke, C. E. Jr. (2011). *Evaluation of multiple corrosion protection systems for reinforced concrete bridge decks* (SM Report No. 100). Lawrence: University of Kansas.

Pay, A. C. (2005). *Bond behavior of unconfined steel and Fiber Reinforced Polymer (FRP) bar splices in concrete beams* (Doctoral dissertation). West Lafayette, IN: Purdue University.

Pavelchak, M. A. (2009). *Factors for improving the design and construction of U-beam bridges: Live load distribution and prestressing strand debonding effectiveness* (Master's thesis). West Lafayette, IN: Purdue University.

Phares, B. M., Fanous, F. S., Wipf, T. J., Lee, Y., & Jolley, M. J. (2006). *Evaluation of corrosion resistance of different steel reinforcement types* (Center for Transportation Research and Education Project 02-103). Ames, IA: Iowa Department of Transportation.

Pianca, F., & Schell, H. (2005). *The long term performance of three ontario bridges constructed with galvanized reinforcement*. Downsview, ON: Ontario Ministry of Transportation.

Qian, S., Qu, D., & Coates, G. (2006). Galvanic coupling between carbon steel and stainless steel reinforcements. *Canadian Metallurgical Quarterly*, *45*(4), 475–484.

Reynolds, G. C., & Beeby, A. W. (1982). Bond strength of deformed bars. *Proceedings of the International Conference on Bond in Concrete* (pp. 434–445). London, UK: Applied Science Publishers.

Rezansoff, T., Akanni, A., & Sparling, B. (1993). Tensile lap splices under static loading: A review of the proposed ACI 318 code provisions. *ACI Structural Journal*, *90*(4), 374–384.

Rezansoff, T., Konkankar, U. S., & Fu, Y. C. (1992). Confinement limits for tension lap splices under static loading. *Canadian Journal of Civil Engineering*, *19*(3), 447–453.

Richter, B. P. (2012). *A new perspective on the tensile strength of lap splices in reinforced concrete members* (Master's thesis). West Lafayette, IN: Purdue University Retrieved from http://docs.lib.purdue.edu/dissertations/AAI1535137/

Rondelli, G., Vicentini, B., & Cigada, A. (1995). Influence of nitrogen and manganese on localized corrosion behavior of stainless steels in chloride environments. *Materials and Corrosion*, *46*, 628–632.

Russell, H. G. (2004). *Concrete bridge deck performance* (NCHRP Report 333). Washington, DC: Transportation Research Board.

Sagüés, A., & Powers, R. (1990). *Effect of concrete environment on the corrosion performance of epoxy-coated reinforcing steel* (Paper No. 311). Paper presented at NACE Corrosion 90, Apr. 23–27, Las Vegas, NV.

Sagüés, A., Powers, R., & Kessler, R. (1994). *Corrosion processes and field performance of epoxy-coated reinforcing steel in marine substructures* (NACE Paper No. 299). NACE International Corrosion Conference, Feb. 28–March 4, Baltimore, MD.

Samples, L. M., & Ramirez, J. A. (1999). *Methods of corrosion protection and durability of concrete bridge decks reinforced with epoxy-coated bars—Phase I* (Joint Transportation Research Program Publication No. FHWA/IN/JTRP-98/15). West Lafayette, IN: Purdue University http://dx.doi.org/10.5703/1288284313268

Sederholm, B., & Almqvist, J. (2008). *Stainless steel in concrete—galvanic effects on carbon steel* (Report No. KIMAB-2008-133). Stockholm, Sweden: Swedish Corrosion Institute.

Sederhom, B., Almqvist, J., & Randström, S. (2009). *Corrosion properties of stainless steels as reinforcement in concrete in Swedish outdoor environment* (NACE Paper No. 09203). NACE International Corrosion Conference, March 22–26, Atlanta, GA.

Seibert, P. J. (1998). *Galvanic corrosion aspects of stainless and black steel reinforcement in concrete* (Master's thesis). Kingston, Ontario: Queen's University.

Seliem, H. M., Hosny, A., Rizkalla, S., Zia, P., Briggs, M., Miller, S., ... Jirsa, J. O. (2009). Bond characteristics of ASTM A1035 steel reinforcing bars. *ACI Structural Journal*, *106*(4), 530–539.

Shahrooz, B. M., Miller, R. A., Harries, K. A., & Russell, H. G. (2011). *Design of concrete structures using high-strength steel reinforcement* (NCHRP Report No. 679). Washington, DC: Transportation Research Board.

Sim, C. (2014). *Structural and corrosion performance of concrete bridge decks reinforced with corrosion-resistant reinforcing steel* (Doctoral dissertation). West Lafayette, IN: Purdue University. Retrieved from http://docs.lib.purdue.edu/dissertations/AAI3636520/.

Smith, J. L., & Virmani, Y. P. (1996). *Performance of epoxy coated rebars in bridge decks* (Publication No. FWHA-RD-96-092). Washington, DC: Federal Highway Administration.

Sonin, A. A. (2001). *The physical basis of dimensional analysis*. Cambridge, MA: Massachusetts Institute of Technology.

Sozen, M. A., & Moehle, J. P. (1990). *Development and lap-splice lengths for deformed reinforcing bars in concrete* (Report No. 1891). Skokie, IL: Portland Cement Association.

Sozen, M. A. (2009). An idealized representation of bond stress distribution along a deformed bar. [CE 676 class handout]. School of Civil Engineering, Purdue University, West Lafayette, IN.

Swamy, R. N., Koyama, S. T., Arai, T., & Mikami, N. (1988). Durability of steel reinforcement in marine environment. *Concrete in Marine Environment, Proceedings, 2nd International Conference, St. Andres by-the-sea, Canada, SP-109* (pp. 147–161). Detroit, MI: American Concrete Institute.

Tepfers, R. (1973). *A theory of bond applied to overlapped tensile reinforcement splices for deformed bars* (Division of Concrete Structures Publication 73:2). Goteborg, Sweden: Chalmers University of Technology.

Thompson, M. A., Jirsa, J. O., Breen, J. E., & Meinheit, D. F. (1975). *The behavior of multiple lap splices in wide sections* (Center for Highway Research Report No. 154-1). Austin: The University of Texas at Austin.

Treadaway, K. W. J., Brown, B. L., & Cox, R. N. (1980). Durability of galvanized steel in concrete. In D. E. Tonini & J. M. Gaidis (Eds.), *Corrosion of reinforcing steel in concrete, ASTM STP 713* (pp. 102–131). Philadelphia, PA: American Society of Testing and Materials.

Treadaway, K. W. J., Cox, R. N., & Brown, B. L. (1989). Durability of corrosion resisting steels in concrete. *Proceedings of the Institution of Civil Engineers, Part 1*, *86*(2), 305–331.

Treadaway, K. W. J., & Davies, H. (1989). Performance of fusion-bonded epoxy-coated steel reinforcement. *Structural Engineer*, *67*(6), 99–108.

Trejo, D., Monteiro, P. J., Thomas, G., & Wang, X. (1994). Mechanical properties and corrosion susceptibility of dual-phase steel in concrete. *Cement and Concrete Research*, *24*(7), 1245–1254.

Trejo, D., Monteiro, P. J., Gerwick, J. r., B, C., & Thomas, G. (2000). Microstructural design of concrete reinforcing bars for improved corrosion performance. *ACI Materials Journal*, *97*(1), 78–84.

Trejo, D., & Pillai, R. G. (2004). Accelerated chloride threshold testing: Part II—corrosion-resistant reinforcement. *ACI Materials Journal*, *101*(1), 57–64.

Warren, G. E. (1969). *Anchorage strength of tensile steel in reinforced concrete beams* (Doctoral dissertation). Ames: Iowa State University.

Virmani, Y. P., Clear, K. C., & Pasko, T. J. (1983). *Time-to-corrosion of reinforcing steel in concrete slabs, vol. 5: Calcium nitrite admixture or epoxy-coated reinforcing bars as corrosion protection systems* (FHWA/RD-83/012). Washington, DC: Federal Highway Administration.

Yeomans, S. R. (1994). Performance of black, galvanized, and epoxy-coated reinforcing steels in chloride-contaminated concrete. *Corrosion*, *50*(1), 72–81.

Yeomans, S. R. (1995). Coated steel reinforcement for corrosion protection in concrete. *Transactions*, *2*(2), 17–27.

Zekany, A. J., Neumann, S., Jirsa, J. O., & Breen, J. E. (1981). *The influence of shear on lapped splices in reinforced concrete* (Research Report 242-2). Center for Transportation Research, Bureau of Engineering Research. Austin: University of Texas.

Zsutty, T. C. (1968). Beam shear strength prediction by analysis of existing data. *ACI Journal Proceedings*, *65*(11), 943–951.

Zuo, J., & Darwin, D. (1998). *Bond strength of high relative rib area reinforcing bars* (SM Report No. 46). Lawrence, KS: University of Kansas Center for Research.

Zuo, J., & Darwin, D. (2000). Splice strength of conventional and high relative rib area bars in normal and high-strength concrete. *ACI Structural Journal*, *97*(4), 630–641.

APPENDICES

APPENDIX A: CORROSION-RESISTANT REINFORCING STEEL

A.1. INTRODUCTION

Eleven different reinforcing steels shown in Figure A.1 are used in this study. Of the eleven, ten are corrosion-resistant reinforcing bars and one is conventional black steel. The ten corrosion-resistant reinforcing bars include epoxy-coated, hot-dip galvanized, tin-plated zinc-clad, un-plated zinc-clad, Zbar (dual-coated with epoxy and zinc), MMFX II microcomposite, and four different types of stainless steel.

Epoxy-coated reinforcing steel protects the steel inside by functioning as a barrier to keep oxygen, water, and chloride ions from reaching the surface of the steel. Hot-dip zinc-coated galvanized and zinc-clad reinforcing steel protects the steel inside by acting as a sacrificial anode that corrodes faster than the protected base metal. Dual-coated reinforcing steel, Zbar, has an epoxy layer on the exterior and an underlying zinc layer over the base metal. The dual-coated reinforcing steel provides both barrier and sacrificial protection. MMFX II microcomposite steel is designed to have no carbides and have 9% chromium to increase corrosion-resistance. Stainless steels are known to be corrosion-resistant and contain more than 12% chromium. This chapter provides a literature review regarding corrosion resistant reinforcement and presents the properties of the reinforcement used in this study.

A.2. LITERATURE REVIEW

A.2.1 Coated Reinforcing Steel

Coated reinforcing steel is widely used to reduce the risk of corrosive attack in concrete structures and can be defined as conventional reinforcing steel to which either a metallic, non-metallic coating, or a combination of these surface coatings are applied to the reinforcement (Yeomans, 1995). Both metallic and non-metallic coatings act as a barrier to the environment and prevent oxygen, water, and chlorideions from reaching the substrate metal. Among various non-metallic coatings, epoxy-coated reinforcing steel is the most widely used, developed, and studied. In this study, fusion-bonded epoxy-coating is included as a non-metallic coated bar.

Unlike non-metallic coatings, metallic coatings serve another function and protect the substrate steel by following electrochemical principles of being more anodic (active) or more cathodic (noble) than the substrate steel depending on the chemical alloy used (Jones, 1981; Yeomans, 1995). Based on corrosion potentials, when alloys such as aluminum, zinc, and magnesium that are more active than steel are used as a coating, the metallic coating sacrifices itself and the steel inside remains cathodic (Yeomans, 1995). On the other hand, when alloys such as tin, nickel, copper, and stainless steel are used for coatings, the metallic coatings remain noble (cathodic) and protect the substrate steel. Due to the economic cost in using other alloys, the most common alloy used for metallic coating is zinc. Zinc can be applied by immersion, plating, cladding, or arc-spraying (Jones, 1996). In this study, hot-dip galvanized (zinc coating), tin-plated zinc-clad, and un-plated zinc-clad reinforcing bars are evaluated as metallic coatings.

Dual-coated reinforcing bars (Zbar) which combine fusion bonded epoxy coating over an arc-sprayed zinc layer are also included in this study. This type of dual coated reinforcing steel acts first as a barrier. If the epoxy coating is damaged, zinc provides a secondary protection layer acting as an active anode to protect the underlying steel. A number of studies have evaluated this type of dual coated reinforcing steel and have demonstrated the synergic effect of the dual coating.

A.2.1.1 Epoxy-coated reinforcing steel. Epoxy-coated reinforcing steel has been the standard practice for protective measures to prevent chloride-induced corrosion for the last four decades since it was first used in 1973 as reinforcing steel for a bridge deck in Philadelphia

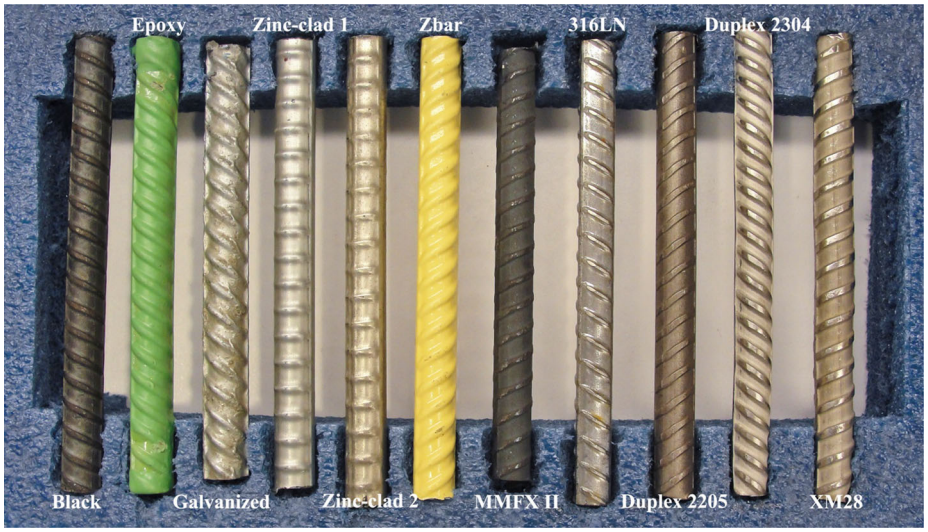

Figure A.1 Corrosion-resistant steel used in this study.

(Humphreys, 2004). Epoxy-coated reinforcing steel provides excellent corrosion protection as a non-metallic coating where the coating is not consumed during the protection. The idea of using non-metallic, organic coatings such as epoxy was initially supported by Clifton, Beeghly, & Mathley (1975) from a study supported by the National Bureau of Standards (NBS).

Virmani, Clear, and Pasko (1983) performed an outdoor exposure test on 31 large concrete slabs reinforced with epoxy-coated reinforcing steel, uncoated black steel, and with calcium nitrite admixture added to the concrete. The slabs were constructed in two lifts. The bottom was chloride-free and the top was contaminated with 15 lb/yd^3 of chloride ions added during concrete mixing. The study found that both epoxy-coated reinforcing steel and calcium nitrite admixtures reduced the corrosion rate. The study reported that it is more effective to have both mats of reinforcing steel coated to provide better corrosion protection than only coating the top mat. This study also concluded that epoxy-coated reinforcing steel is several times more corrosion-resistant than uncoated reinforcement although the coating thickness was not as thick as specified in specifications.

Kobayashi and Takewaka (1984) have monitored beam specimens with epoxy-coated reinforcing steel, galvanized steel, and black steel exposed in marine splash zones for three years. The beams were loaded in four point bending to form cracks at midspan with a maximum crack width of approximately 4 to 8 mils in the tension region. The beams had two different concrete covers of 0.8 and 1.2 in. and the epoxy-coated reinforcing steel had two different coating thicknesses of 4 mils and 8 mils. The test results demonstrated that metal loss and corrosion depth is substantially reduced relative to black steel when epoxy-coated reinforcing steel is used. However, after three years of exposure, the epoxy-coating completely peeled off from large areas and the base steel was corroded significantly for the case with epoxy-coated reinforcing steel with coating thickness of 4 mils. On the other hand, with a coating thickness of 8 mils, the corroded areas and corrosion losses were small and considerably less compared to the use of uncoated or galvanized steel. This research recommended a minimum 8 mils of coating thickness to provide corrosion protection.

Swamy, Koyama, Arai, and Mikami (1988) carried out three years of exposure testing in a natural splashing tidal zone and two years of accelerated corrosion testing with wet and dry cycles under the support of Sumitomo Metal Industries Ltd. in Japan to evaluate the durability of steel reinforcement under marine environment. The specimens were square concrete prisms with reinforcing steel located in the center. Three covers (0.8, 1.6, and 2.8 in.) and three epoxy coating thicknesses (4, 8, and 12 mils) were chosen as variables. The specimens were pre-cracked and kept under permanent load through a load-reaction jig that stressed the bars in tension at approximately 29 ksi during exposure. The average crack widths on the specimens were 4-5 mils for specimens with 0.8 in. cover, 6–7 mils for specimens with 1.6 in. cover, and 8–9 mils for specimens with 2.8 in. cover. Although, the study does not provide specific details on the amount of damage to the coating, some epoxy-coated reinforcing steel was damaged prior to casting. This research reported that 4 mils of epoxy coating was not adequate to provide good corrosion protection. The test results showed that uncoated black steel will corrode in a marine environment even with a 2.8 in. cover. Galvanized reinforcing steel performed better than black steel but did not provide complete protection while epoxy-coated reinforcing steel with coating thicknesses greater than 8 mils was capable of providing long-term protection under severe conditions (cracked specimens with coating damage).

Treadaway and Davies (1989) also demonstrated from a five year exposure test that the use of fusion-bonded epoxy coatings on steel reinforcement provides significant reduction in the corrosion rate of reinforcing steel under high levels of chloride attack. However, the research did report that corrosion is spreading from points of defects in the coatings and stated that the long-term experiments on underfilm corrosion requires further studies.

Epoxy-coated reinforcing bars gained further attention through the observations on bridge substructures located in the Florida Keys. Sagüés and Powers (1990) reported that extensive corrosion was observed on epoxy-coated reinforcing steel less than ten years after construction. The damage was reported to be accompanied by disbonding of the epoxy coating, corrosion of the underlying metal, and formation of large pits.

Clear (1992) changed his view from previous research on epoxy-coated reinforcing steel and raised concerns regarding the longevity of the corrosion protection it provides under aggressive environments. The Concrete Reinforcing Steel Institute (CRSI) and Clear reported their discussions on the effectiveness of epoxy-coated reinforcing steel. Other researches (Kahhaleh, 1994; Sagüés, Powers, & Kessler, 1994; Smith & Virmani, 1996) stated that when epoxy coating is damaged, debonded, or delaminated from the steel reinforcement, coated reinforcement will no longer serve as an effective protection.

Based on this history, research in the early 1990s to current time (Darwin et al., 2001; Kahhaleh, 1994; McDonald, Pfeifer, & Sherman, 1998; McKenzie, 1993; Samples & Ramirez, 1999) focused on the corrosion performance of epoxy-coated reinforcing steel that is artificially damaged prior to testing which not only simulates field conditions better but also creates a more severe condition for corrosion.

Samples and Ramirez (1999) documented the results of a field evaluation which found examples of excessive damage to epoxy-coated reinforcing steel created during fabrication, transportation, construction, and maintenance. The field and laboratory evaluations recommended an increase of the minimum coating thickness from 6 mils to 12 mils which could limit the amount of damage to the coating and increase the mat to mat corrosion resistance of epoxy-coated reinforcing steel.

In response to the concerns for the Florida Keys bridges and research regarding the performance of epoxy-coating steel reinforcement, ASTM committees for steel reinforcement have updated multiple ASTMs (ASTM A775, 2007; ASTM A934, 2007; ASTM D3963, 2011). These ASTMs have carefully stated the requirements for coating thickness

(minimum 7 mils), surface preparation, coating continuity, coating flexibility, and coating adhesion. In addition, the coating damage incurred during handling, fabrication, and transportation that is permitted to be repaired is 1% of the total surface area in a linear one foot length of the bar. Starting from 1991, the Concrete Reinforcing Steel Institute (CRSI) introduced a Voluntary Certification Program for Epoxy Coating Applicator Plants which sets quality control procedures to ensure that fabricators produce epoxy-coated reinforcing steel in accordance with industry standards and recommendations.

Lee and Krauss (2004) continued monitoring and testing slabs that were not autopsied during the 1993–1998 Federal Highway Administration (FHWA) research project completed by McDonald et al. (1998) which contained 12 different bar types including epoxy-coated reinforcing steel. The study concluded that bent epoxy-coated reinforcing steel in the top mat with black bars in the bottom mat performed worst among all other cases that used epoxy-coated reinforcing steel. However, when epoxy-coated reinforcing steel (coating pre-damaged) was used in the top mat with black bars in the bottom mat, the corrosion activity was reduced by at least 50% compared to the case of both mats reinforced with black bars. When both top and bottom mat were reinforced with epoxy-coated steel (coating pre-damaged), the average macrocell currents were less than 2% of the highest black bar case. This study revealed that when specimens with epoxy-coated reinforcing steel show high macrocell currents, coating deterioration due to corrosion was observed during autopsy. In addition, numerous hairline cracks and blisters were found while some areas displayed coating disbonding and underlying steel corrosion. Because no consistent trend was found between the level of macrocell currents and coating adhesion loss, the study concluded that there is no direct relationship between loss of adhesion of the coating and the effectiveness of epoxy-coated reinforcing steel. Therefore, it was determined that adhesion tests are a poor indicator of long-term performance of coated bars.

Although, FHWA has been initiating research since the early 90s to develop steel reinforcement that is more corrosion-resistant than fusion-bonded epoxy-coated reinforcement, research on epoxy-coated reinforcing bars continues (Darwin et al., 2001; Kahl, 2007; Lee & Krauss, 2004; McDonald et al., 1998; O'Reilly, Darwin, Browning, & Locke, 2011; Phares et al., 2006; Smith & Virmani, 1996) and their performance is commonly compared with other corrosion-resistant reinforcing bars.

Many studies (Darwin et al., 2001; Kahl, 2007; Lee & Krauss, 2004; McDonald et al., 1998; O'Reilly et al., 2011; Phares et al., 2006; Smith & Virmani, 1996) support the continued use of epoxy-coated reinforcing bars as the common corrosion-protection system used in the U.S. This system requires high quality control in manufacturing, transportation, and to prevent coating damage (ASTM A755, ASTM A934, ASTM D3963, ACI 301, and the Voluntary Certification Program by CRSI).

A.2.1.2 Hot-dip galvanized reinforcing steel. Zinc coating can be applied to steel by various processes including electroplating, mechanical adhesion, arc-sprayed, or hot-dipped (Yeomans, 1995). Hot-dip galvanizing is the most common method and is widely used. The term galvanizing refers to a process where iron or steel is hot-dipped into a bath with molten zinc (Porter 1991). This type of galvanized reinforcement has been used since the 1930s in concrete construction (ILZRO 1981). ASTM A767 (2009) specifies the required mass of zinc coating per surface area in which the mass of the zinc coating is calculated based on the coating thickness measured through the process introduced in ASTM E376 (2011). For bars larger than #4, the minimum amount of 3.5 oz/ft^2 of zinc coating (equivalent to coating thickness of approximately 6 mils) is required for Class I coatings applied to structural or load bearing reinforcement (ASTM A767).

Cook and Radtke (1977) performed tests on bridges ranging in ages from 3 to 23 years to resolve the question whether or not galvanized bars perform superior to ordinary black bars. The study concluded that galvanized bars were only superficially affected by chloride attack although the chloride levels were several times higher than the thresholds of black bar corrosion. The study considered galvanized bars to be outstanding compared to black bars.

Treadaway, Brown, and Cox (1978) reported from a 14-year study on the durability of galvanized bars in concrete that the use of galvanized reinforcement delays corrosion. However, the research stated that the greatest benefit of using galvanized bars would occur when chloride content is low while the concrete quality is poor (being relatively permeable). When chloride levels were above 1.9% by weight, the research stressed out that there was serious corrosion on both galvanized and black steel and that the delay in corrosion-induced cracking of the cover was only limited to a period ranging from six to twelve months longer than black steel.

Clear (1981) conducted 10 years of comparative testing of large slabs to determine the time-to-corrosion of reinforcing bars in concrete slabs. The research contained conventional black bars and galvanized reinforcing bars. From this long-term outdoor exposure testing, it was found that galvanized reinforcing bars only benefited when the quality of concrete was relatively poor with a high water-to-cement ratio. When the water-to-cement ratio was 0.4, the research stated that there is no benefit of using galvanized bars because it has a comparable corrosion rate with conventional black bars. When the water-to-cement ratio was 0.5 and both top and bottom mats of concrete slab were reinforced with galvanized bars, the rate of corrosion was reduced 34% and the reduction in metal loss was 22%. However, the study found that when the galvanized reinforcing bars were only used in the top mat of the slab and coupled with black bars in the bottom, the rate of corrosion was more than twice that provided when black bars were used in both top and bottom mats.

McCrum and Arnold (1993) summarized results of long-term tests made by the Michigan Department of Transportation on evaluating the corrosion performance of slabs reinforced with galvanized, epoxy-coated, and conventional black reinforcing steel. The test slabs were designed as a small section of a bridge deck (3 ft wide and 4 ft long with a

thickness of 7-1/2 in.) including both longitudinal and transverse reinforcing bars in the top and bottom mats. The slabs were exposed to natural weather conditions with a weekly salt application during winter. The uncoated reinforcement performed the worst. The next worst case was when the top mat was reinforced with galvanized steel and the bottom mat black steel. When both top and bottom mats were reinforced with galvanized steel, the corrosion performance was comparable with the case with both mats reinforced with epoxy-coated reinforcing steel. This result is consistent with Clear's (1981) observations. The authors also reported that although the galvanized reinforcing steel performed better than black bars, galvanized portions of the slabs deteriorated at a faster rate than the uncoated portions of the slab specimens for the later half of the project. The authors pointed out that galvanized reinforcement corrodes in the same fashion as black steel in which expansion of the corrosion products can exceed the tensile strength of the concrete cover. Although, the oxides created by zinc may not expand as fast as iron oxides, the study stated that expansion issues associated with the use of metallic coatings such as zinc are still possible.

Yeomans (1994, 1995) performed tests on galvanized, epoxy-coated, and conventional black reinforcing bars using half-cell potential measurements and using concrete cylinders that have each reinforcing bar embedded and exposed to wet and dry cycles in a salt fog environment. The study concluded that the time to initiation of corrosion takes 4–5 times longer when using galvanized bars compared to black bars. In addition, galvanized reinforcement was shown to tolerate chloride levels in concrete at least 2.5 times higher than that required to corrode black bars in an equivalent condition.

Macias and Andrade (1990) concluded that the discrepancies reported by different researchers on the performance of galvanized reinforcing bars are due to the behavior of zinc in concrete. During the initial stages of curing, concrete is in a high alkaline state where zinc reacts with hydroxyl ions to form zinc oxide and hydrogen gas. Further on, zinc oxide reacts with calcium ions to form calcium hydrozincate, $Ca(Zn(OH)_3)_2 \cdot 2H_2O$. This passivates the galvanized bar and provides corrosion protection. However, the study found that the desired protective layer of calcium hydroxyzincate forms at a pH below 13.3. When the pH is higher than 13.3, the calcium hydroxyzincate layer does not form uniformly and a galvanized bar will have local areas where corrosion protection is not provided. In addition, the study also noted that the behavior of a galvanized bar is controlled by the medium pH which depends on the parent salt (either from $CaCl_2$ or NaCl) providing the chloride ions. Therefore, the discrepancies on whether galvanized steel is effective as corrosion protection can be explained from the use of various salt solutions or from the use of various types of concrete with varying pH values that may have affected the formation of the passivation product (calcium hydroxyzincate layer). Based on their test results, it may be anticipated that the lower the alkali content, the better the performance of galvanized reinforcement.

McDonald, Pfeifer, and Blake (1996) noted that the service life of galvanized reinforcing bars might decrease since the alkali contents in cements are increasing due to the environmental regulations in the U.S. In addition, McDonald et al. (1998) reported that galvanized reinforcing bars are less effective than fusion-bonded epoxy-coated reinforcing bars in terms of resistance to chloride ions.

Pianca and Schell (2005) summarized field studies performed in Ontario, Canada where they monitored the performance of three different bridge structures for 30 years that contain both layers of galvanized reinforcement. The study reported that galvanized reinforcement showed marginally better performance than conventional black reinforcement but started to corrode and resulted in delamination of the concrete soon after the chloride corrosion threshold for black steel was reached at the top reinforcement.

Recently, Darwin, Browning, O'Reilly, Xing, and Ji (2009) evaluated the critical chloride corrosion threshold of galvanized reinforcing steel through laboratory tests with macrocell specimens. Although, there has been controversial views on the performance of galvanized reinforcement, this study shows that specimens with both mats of galvanized reinforcement provides a higher critical chloride corrosion threshold than companion specimens of conventional black steel. The study found that the average time to corrosion initiation at crack locations for conventional black steel is 2.3 years and 4.8 years for galvanized steel with 3 in. concrete cover. However, the study did point out that galvanized steel exhibits some values of chloride contents that are similar in magnitude to those shown in black steel, although the overall range of values of chloride content is greater for galvanized reinforcement than black steel, and explained that this might be the reason for various views on galvanized steel. The study additionally reported that zinc corrosion products were observed on the surface of reinforcing steel including some exposure of the intermetallic layer during the autopsy process.

A.2.2 Microcomposite Steel Reinforcement

The prototype of the current microcomposite steel was initially developed and patented by a research group in the department of materials science and mineral engineering at the University of California at Berkeley (Kim & Thomas, 1984; Koo & Thomas, 1977). They were designed as dual-phased ferritic martensitic (DFM) steel with no carbides. Conventional reinforcing steels have ferrite-carbide microstructures in which the carbides can become cathodic to ferrite and develop microcorrosion when the protective oxide film or mill scale is depassivated. The developers claimed that dual-phased ferritic martensitic steels are more corrosion-resistant than conventional steel by having no pearlite microstructure which is a combination of ferrite and carbides (Trejo, Monteiro, Thomas, & Wang, 1994; Trejo, Monteiro, Gerwick, & Thomas, 2000). This DFM steel had a low amount of chromium (0.1%) and was produced by heat-treatment and quenching to transform the austenite to martensite (Trejo et al., 1994). However, the DFM steel was later developed as a microcomposite MMFX steel by the MMFX Steel Corporation of America without having the quenching operation which required additional facilities.

MMFX II is the current brand name of this microcomposite steel and this steel contains approximately 9% chromium which increases the corrosion resistance of the steel (also referred to 9% Cr rebar).

Darwin, Browning, Nguyen, and Locke (2001) tested the mechanical and corrosion properties of MMFX steel for the South Dakota Department of Transportation and reported that the microscopic evaluation after the rapid macrocell test shows that similar corrosion products are deposited on the surfaces of MMFX and conventional reinforcing steel. The study also reported that MMFX steel corrodes at a rate equal to 60% of that observed in conventional steel while epoxy-coated reinforcing steel corroded at a rate equal to or less than half that of MMFX steel. With cracked beam tests and southern exposure tests, the research also observed that epoxy-coated steel with damage (holes in coatings) corrodes at the lowest rate while MMFX steel corrodes faster than epoxy-coated steel but at a lower rate than conventional black steel.

Trejo and Pillai (2004) evaluated the corrosion-resistance of MMFX steel through accelerated chloride threshold (ACT) tests which they developed to determine the critical chloride threshold level of reinforcement embedded in cementitious materials. The study reported that the MMFX steel, 304, and 316 stainless steel have significantly higher critical chloride threshold values than the conventional black steel having 8.6, 9.4, and 20 times higher values than black steel.

Clemeña and Virmani (2004) also evaluated R304, 316LN, 316L clad bar, dual coated rebar with zinc and epoxy, 2101 LDX stainless steel, MMFX microcomposite steel, and black bar through macrocell test specimens subjected to weekly cycles of ponding in NaCl solution (cycles of 3 days wet and 4 days dry). The measured chloride threshold concentrations were in the order of 316LN, R304, 316L clad, dual coated rebar, 316L clad with cut, MMFX micro-composite, 2101 LDX stainless steel, and black steel. The MMFX microcomposite had threshold ratios of 4.7 to 6.0 higher when normalized to the threshold values of black steel. The best performing, 316LN had a ratio of 11.2 to 14.2. From the various studies, MMFX II steel is shown to have higher corrosion-resistance than black steel but provides lower corrosion protection than most of the stainless steel reinforcing bars as well as coated and dual coated reinforcing steel.

A.2.3 Stainless Steel Reinforcement

A.2.3.1 Types of stainless steel reinforcement. Stainless steel reinforcing bars have a low carbon content and include chromium as the main alloying element. Stainless steel is defined as a group of corrosion-resistant iron alloys with chromium content of at least 11%–12% (definition of minimum amount of chromium varies upon researcher (Nürnberger, 1996; Sedriks, 1996). Among the various methods to classify stainless steel, the most common way to categorize them is based on their metallurgical microstructure.

The microstructure is mainly dependant on the type of stabilizing elements used in composing the stainless steel alloy (Sederholm & Almqvist, 2008). Pure iron (ferritic) forms an austenitic structure during the heating process and will stabilize to an austenite by adding carbon, nitrogen, manganese, or nickel. On the other hand, pure iron that undergoes a heat process stabilizes to ferrite by applying chromium, molybdenum, or silicon. Depending on what stabilizing alloys are added, the microstructure can be ferritic, austenitic, ferritic-austenitic (duplex), or martensitic. Table A.1 shows the type of stainless steel reinforcing bars that are available for concrete reinforcement as specified in ASTM A955 (2009).

Nürnberger (1996) stated that ferritic stainless steels are low carbon with no or lower nickel contents, and chromium less than 17%. The American Iron and Steel Institute (AISI) designates ferritic stainless steel within the 400 series, and the designation is shown in the first three numbers of the unified numbering system (UNS) used in Table A.1.

Austenitic stainless steels are low carbon steels that contain chromium and nickel and are designated by 200 or 300 series. Austenitic stainless steels generally contain 17–19% of chromium in the alloy. The 304 and 316 stainless steels are the most well known austenitic stainless steels. The letter L that follows these AISI designated numbers 304 and 316 stands for low carbon content, which increase the weldability of steel by decreasing the maximum allowable carbon content from 0.08% to 0.03%. The letter N that follows L stands for additional nitrogen, which significantly provides higher yield and tensile strength without affecting ductility, corrosion-resistance, or non-magnetic properties. Austenitic stainless steels are non-magnetic while ferritic or ferritic-austenitic (duplex) stainless steel are magnetic.

TABLE A.1
Examples of Stainless Steel Reinforcement (provided by ASTM A955)

			Chemical Composition (%)						
Micro-structure	UNS Designation	Type	Carbon	Chromium (Cr)	Nickel (Ni)	Molybdenum (Mo)	Nitrogen (N)	Manganese (Mn)	PREN
Ferritic	S40977	3CR12	0.03	12.5	1	–	0.03	1.5	13
Austenitic	S24100	XM-28	0.15	16.5–19	2.25–3.75	–	0.2–0.45	11–14	23
	S30400	304	0.08	18–20	8–10.5	–	0.1	2	21
	S31600	316	0.08	17	12	2.5	0.1	2	27
	S31653	316L	0.03	16–18	10–14	2–3	0.1	2	27
	S31653	316LN	0.03	16–18	10–14	2–3	0.1–0.16	2	27
Ferritic-Austenitic	S31803	Duplex 2205	0.03	21–23	4.5-6.5	2.5–3.5	0.08–0.2	2	37

The ferritic-austenitic (duplex) stainless steels primarily contain more chromium but less nickel than austenitic steels. These duplex stainless steel bars contain 22-28% chromium and 4-8% nickel. Because, nickel and molybdenum increase the price of stainless steel compared to other steels, duplex stainless steels that contain less nickel are generally less expensive than general austenitic stainless steels (García-Alonso et al., 2007) except the newly developed XM-28 austenitic stainless steel that contains less nickel and no molybdenum (contains high manganese content as a substitute of nickel). XM-28 is one of the lowest cost stainless steels currently available on the market.

Although ferritic stainless steels can also be used as reinforcing bars in concrete structures, they are shown to be less corrosion-resistant than austenitic or duplex stainless steels. Research by Treadaway, Cox, and Brown (1989) reported on their long-term (10-year) study on uncracked concrete specimens that 405 and 430 ferritic stainless steels in the test specimens exhibited substantial pitting corrosion while 302, 315, and 316 austenitic stainless steels embedded in concrete containing 3.2% admixed chloride ion by weight of cement did not encounter any serious corrosion. Hewitt and Tulmin (1994) also reported that after one year of simulated marine exposure, ferritic stainless steel (3CR12) experienced localized corrosion (although the amount is minimal compared to black steel) while 304 or 316 austenitic stainless steels did not display any corrosion damage when the specimens were opened.

Austenitic or ferritic-austenitic stainless steels are preferred types for use as concrete reinforcement (Nürnberger, 1996) because they can be produced as ribbed bars within normal ranges of strength and deformability.

A.2.3.2 Chemical composition of stainless steel reinforcement. Chromium is the most important alloy in stainless steel and is responsible for forming an iron-chromium oxide layer. This layer has the ability to self-repair through a process called passivation. When stainless steel is damaged under excessive or continuous chloride attack, chromium in stainless steel reacts with oxygen and forms a thin invisible passive layer that protects the material from corrosion. This chromium stabilizes the iron to ferrite and 17 to 18% is required to obtain the strength desired for reinforcement.

Nickel is the next most important alloy in stainless steel which increases corrosion resistance in acid media (Nürnberger, 1996). When the supply of nickel was low, manganese was added to make austenitic stainless steel (Sederholm & Almqvist, 2008). García-Alonso et al. (2007) evaluated stainless steel that included more manganese and less nickel (XM-28) which potentially cost less than common austenitic stainless and duplex stainless steels.

Other important alloys for stainless steel include molybdenum and nitrogen which increase resistance against pitting and crevice corrosion. Rondelli, Vicentini, and Cigada (1995) proposed the pitting resistance equivalent formula, which is slightly modified as the pitting resistance equivalent number (PREN). This number which is widely used by researchers to evaluate the risk of pitting corrosion (Nürnberger, 1996) quantifies how much chromium, molybdenum, and nitrogen the alloy carries ($1 \times \%Cr + 3.3 \times \%Mo + 16 \times \%N$) (Sederholm & Almqvist, 2008). The PREN summarized in Table A.1 clearly demonstrates that ferritic stainless steel is not desired in highly aggressive environments such as carbonated concrete or exposed to chlorides. Because the objective of the testing program in this study is to evaluate corrosion-resistant reinforcing steel for bridge decks exposed to deicing salts, ferritic stainless steels were not selected for use.

A.2.3.3 Corrosion resistance of stainless steel reinforcement. The PREN is important because pitting and crevice corrosion are the most common forms of corrosion for stainless steels in concrete (Nürnberger, 1996). General corrosion is not a problem for a passivated steel in concrete. Stress corrosion is likely to take place in welded austenitic structures placed in carbonated concrete under high temperature with excessive chloride attack, however, this is not likely to occur for stainless steel reinforcing bars in typical concrete that has a high pH and relatively low temperatures in service (Neuhart, 2000; Nürnberger, 1996).

Because of the price differences between stainless steel and conventional carbon steel, mixing stainless steel as a top mat and black steel as a bottom mat has been considered. Therefore, a number of research studies have focused on the possibility of galvanic corrosion. Various research (Bertolini, Gastldi, Pedeferri, Pedeferri, & Pastore, 1998; Cochrane, 1999; Qian, Qu, & Coates, 2006; Sederholm, Almqvist, & Randström, 2009) reported that galvanic coupling of stainless steel with carbon steel will not increase the risk of corrosion of carbon steel reinforcement. Although, Bertolini et al. (1998) stated that the influence of galvanic coupling between stainless steel rebar and black bar is less than the coupling between a corroding black bar at the anode and a noble black bar at the cathode, the research reported that stainless steel can enhance the corrosion rate of active carbon steel reinforcement under particular conditions such as in carbonated or chloride contaminated concrete.

Andrade (1992) reported that galvanic coupling between stainless steel and black steel could be appreciable if the cathode surface area is located in a higher location height-wise than the anode surface area. This case can occur for instance when bottom black bars in cracked concrete are exposed to chloride attack. Then the bottom black bars which become anodes can relatively be located at a lower position than the top stainless steel bars that are serving as cathodes. This view is also supported by Seibert (1998) who did not recommend mixing the use of stainless steel and carbon steel because he concluded that galvanic coupling will initiate corrosion of the mild carbon steel.

McDonald et al. (1998) demonstrated that 304 stainless steel experienced significant corrosion when coupled with a black bar cathode. Approximately 50% of the bars that were tested in pre-cracked concrete showed significant corrosion under galvanic coupling conditions.

Although there are conflicting views on galvanic coupling and the amount of corrosion that can occur due to this condition, the previous tests even under pre-cracked conditions were not conducted under the worst conditions a bridge deck can encounter. Bridge decks typically crack due to restrained shrinkage at early ages, and these cracks

TABLE A.2
Chemical Composition as Reported

Bar Type	Bar Size	Composition (%)									
		C	Mn	P	S	Si	Cu	Cr	Ni	Mo	N
MMFX II	#4	0.08	0.68	0.008	0.015	0.20	0.19	9.30	0.11	0.02	150 ppm
	#5	0.09	0.70	0.009	0.010	0.16	0.17	9.89	0.12	0.02	150 ppm
	#8	0.07	0.63	0.007	0.006	0.17	0.17	9.04	0.09	0.01	100 ppm
316 LN	#4	0.03	1.47	0.030	0.023	0.61	–	16.8	11.02	2.53	0.07
	#5	0.02	1.09	0.030	0.023	0.60	–	17.9	10.60	2.03	0.14
	#8	0.02	1.35	0.029	0.024	0.50	–	16.7	10.10	2.00	0.13
Duplex 2205	#4	0.02	1.71	0.025	0.003	0.27	–	22.5	4.73	3.36	0.19
	#5	0.02	1.72	0.025	0.001	0.37	0.26	21.4	4.76	2.56	0.18
	#8	0.02	1.76	0.026	0.006	0.36	0.19	21.5	4.62	2.57	0.18
Duplex 2304 (all same heat)	#4	0.02	1.54	0.026	0.0003	0.47	0.21	22.6	4.24	0.15	0.17
	#5	0.02	1.54	0.026	0.0003	0.47	0.21	22.6	4.24	0.15	0.17
	#8	0.02	1.54	0.026	0.0003	0.47	0.21	22.6	4.24	0.15	0.17
XM-28	#4	0.05	12.0	0.020	0.001	0.44	0.06	17.5	0.89	0.24	0.30
	#5	0.05	12.1	0.020	0.001	0.33	0.10	17.4	1.64	0.14	0.30
	#8	0.05	12.1	0.020	0.001	0.33	0.10	17.4	1.64	0.14	0.30

are full depth. The macrocells that were tested in a cracked state or a macrocell introduced in ASTM A955 (2009), which is intended for corrosion testing of stainless steel reinforcement contains an artificial crack that is formed only to the level of the top bar.

A.3. MATERIAL PROPERTIES

This section presents the various material properties for the bars used in this study including chemical composition, material strength, deformation geometry (rib height and spacing), coating thickness (for coated bars), and surface roughness. Throughout this study, three sizes of rebar are mainly used which include #4, #5, and #8. Properties are presented for these specific bars. Additional sizes of rebar (#6, #7, and #11) were used for a few beam specimens constructed to evaluate the bond performance.

A.3.1 Chemical Composition

The chemical compositions of the uncoated corrosion-resistant reinforcing steel used in this study are presented in Table A.2. The compositions are as reported by the producing mills. Of particular note, the different sizes of reinforcement for Duplex 2205 reinforcing steel were produced all from the same heat.

A.3.2 Mechanical Properties

A.3.2.1 Yield and tensile strength. Three samples of each type of bar were tested in tension in accordance with ASTM A370 (2012) using a Baldwin 120-kip capacity universal testing machine with an Instron control and data acquisition system.

Strains were measured using an Epsilon extensometer (3543-0800-200T-ST, Large Gage Length Model), which has an 8 in. gage length. The test setup is shown in Figure A.2 and the bar samples of #5 and #8 bars tested are shown in Figure A.3. Stress-strain curves of the #8 reinforcing steel for one sample of each bar are provided in Figure A.4(a) and (b).

Complete stress-strain curves (Figure A.4(a)) of the reinforcing steel demonstrate that the rupture strain of stainless steel reinforcing steel is between 20% and 40% while conventional black steel and coated steel have rupture strains of approximately 18%. As shown in the close-up view of the stress-strain curves in Figure A.4(b), MMFX II and stainless steel reinforcement do not have a well-defined yield point or yield plateau. MMFX II reinforcement which is produced according to ASTM A1035 (2007) and stainless steel reinforcement produced in accordance with ASTM A955 (2009) both require that the yield strengths be determined by the offset (0.2% offset) method introduced in ASTM A370 (2012). In addition, both ASTM A1035 and ASTM A955 require a minimum stress for a specified tensile

Figure A.2 Test setup for rebar coupon tension test.

(a) #5 Reinforcement Samples

(b) #8 Reinforcement Samples

Figure A.3 Tension test reinforcement samples.

strain. ASTM A1035 requires a minimum of 80 ksi for Grade 100, and 90 ksi for Grade 120 steel, at a tensile strain of 0.0035.

ASTM A955 requires a minimum of 60 ksi for Grade 60, and 75 ksi for Grade 75, at a tensile strain of 0.0035. Both standards require that the value of stress corresponding to a tensile strain of 0.0035 be reported. The mechanical properties (average of three samples) including the modulus of elasticity, stress at 0.0035 tensile strain, yield strength, tensile strength, ultimate strain, and rupture strain are listed in Table A.3 for all reinforcing steel used in this research program.

A.3.2.2 Deformation height and spacing. The deformation height, spacing, and relative rib ratio of the reinforcing steel were measured. The average height of deformations is based on three typical deformations with at least one located on the opposite side of the bar. Five measurements were made per deformation as shown in Figure A.5 (grey area is deformation) with one at the center of the overall length (location 3), two at the ends (locations 1 and 5), and two located halfway (quarter points; locations 2 and 4) between the center and the ends. The measurements are reported in Appendix A. This procedure is in accordance to Section 6.6.1 of ACI 408 (2003) which exceeds the requirements of ASTM A615 (2009), A1035 (2007), and A955 (2009).

The average spacing of deformations was determined in accordance with ASTM A615 (2009), A1035 (2007), and A955 (2009) by measuring the length of a minimum of ten spaces between the deformations and dividing the length by the number of spaces included. None of the spacing measurements were made over the bar surface area that contains the bar marking.

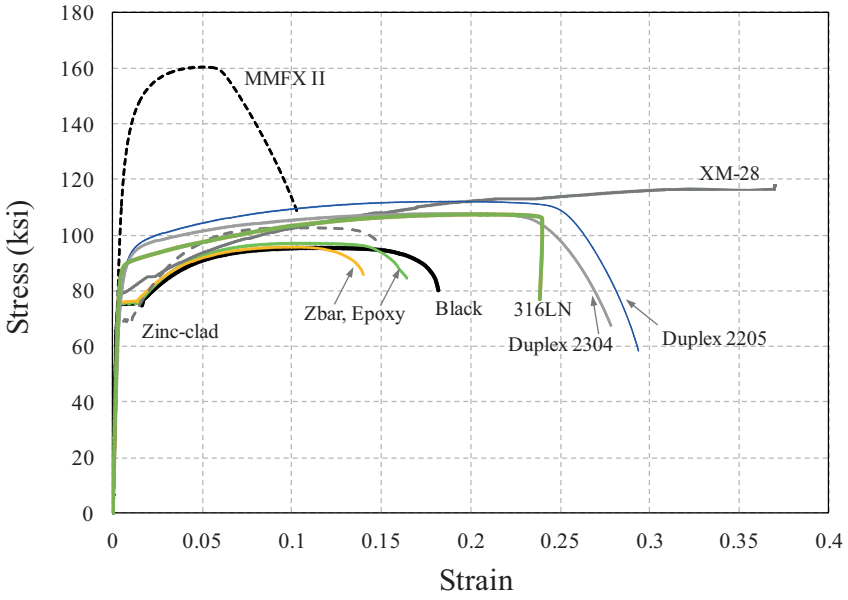

(a) Stress-Strain Curve

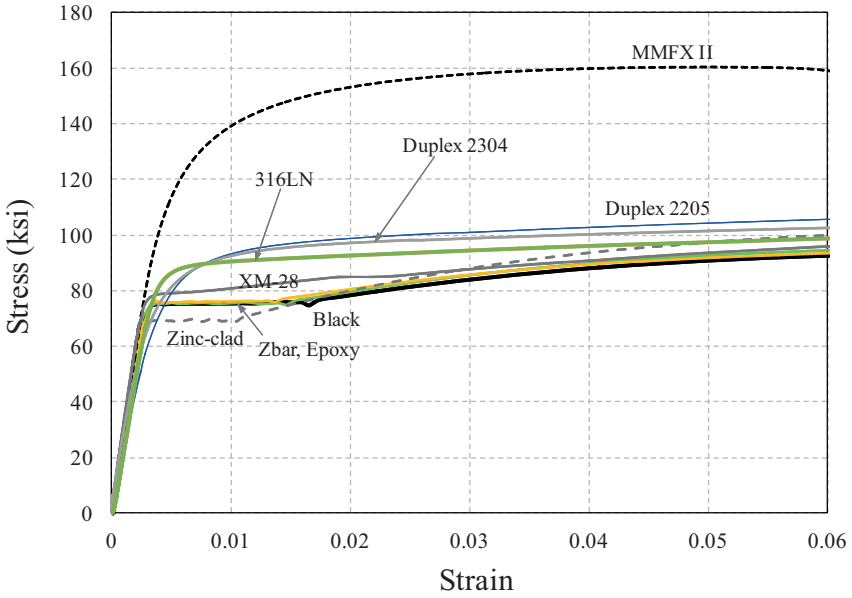

(b) Close-Up View of Stress-Strain Curve

Figure A.4 Stress-strain relationships of reinforcement samples (#8).

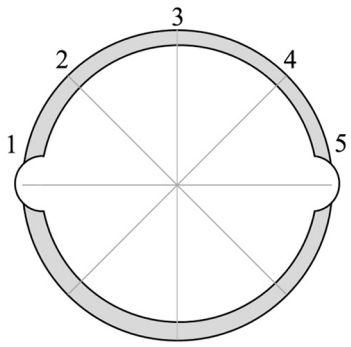

Figure A.5 **A.5** Deformation height measurement locations.

The relative rib area was calculated following the procedure described in ACI 408r-03, which is approximately the ratio of bearing area over shearing area. Note that the relative rib area of each bar is provided in Table A.3.

A.3.2.3 Coating thickness. The coating thickness of reinforcement containing coatings (galvanized, un-plated zinc-clad, tin-plated zinc-clad, epoxy-coated, and dual-coated (epoxy and underlying zinc) were measured with a magnetic pull-off dry-film gage as shown in Figure A.6 in accordance with ASTM D7091 (2011) and ASTM E376 (2011). This gage measures the tension force required to pull and overcome the

TABLE A.3
Mechanical Properties of Corrosion-Resistant Reinforcing Steel

Bar Type	Bar Size	Modulus of Elasticity E (ksi)	Yield Strength f_y (ksi) 0.0035 strain	Yield Strength f_y (ksi) 0.2% offset	Tensile Strength f_u (ksi)	Ultimate Strain ε_u	Rupture Strain $\varepsilon_{rupture}$	Rib Height (in.)	Rib Spacing (in.)	Relative Rib Area	Coating (mils)	No. of Peak and Valleys
	#4	28,200	64	60	106	0.101	0.124	–	–	–	–	–
Black	#5	28,310	79	78	96	0.090	0.099	0.046	0.3928	0.106	–	229
	#8	28,720	76	76	96	0.114	0.178	0.065	0.6163	0.095	–	160
	#4	27,080	84	86	101	0.070	0.089	–	–	–	–	–
Epoxy	#5	28,220	84	87	105	0.082	0.105	0.051	0.3947	0.128	12.3	42
	#8	27,950	76	76	96	0.114	0.178	0.061	0.6155	0.089	11.7	37
	#4	27,840	67	67	104	0.104	0.132	–	–	–	–	–
Hot-Dip Galv.	#5	29,230	68	67	104	0.113	0.166	0.037	0.4048	0.086	4.6	112
	#8	29,340	71	71	106	0.108	0.162	0.057	0.6708	0.076	3.8	111
	#4	30,270	68	68	105	0.089	0.100	–	–	–	–	–
Zinc-clad 1	#5	29,370	66	66	103	0.078	0.087	0.031	0.4267	0.062	18.2	68
	#8	29,330	69	69	103	0.110	0.149	0.046	0.6766	0.057	22.8	39
	#4	29,570	78	83	100	0.044	0.046	–	–	–	–	–
Zinc-clad 2	#5	29,370	66	66	103	0.078	0.087	0.029	0.4212	0.059	23.0	56
	#8	29,940	67	68	105	0.086	0.149	0.034	0.6739	0.045	44.0	89
	#4	28,580	84	85	105	0.084	0.110	–	–	–	–	–
Zbar	#5	27,870	78	79	100	0.089	0.104	0.051	0.3992	0.015	10.7	52
	#8	28,230	76	76	96	0.095	0.115	0.065	0.6281	0.093	11.6	45
	#4	30,410	95	121	153	0.042	0.065	–	–	–	–	–
MMFX	#5	29,650	90	115	156	0.044	0.060	0.040	0.4238	0.087	–	195
	#8	29,500	93	123	161	0.051	0.107	0.063	0.6461	0.090	–	110
	#4	22,120	75	111	122	0.018	0.040	–	–	–	–	–
316LN	#5	–	80	89	113	–	0.180	0.032	0.3234	0.093	–	137
	#8	26,070	78	87	107	0.219	0.302	0.051	0.5638	0.085	–	152
Duplex 2205	#4	25,330	78	98	122	0.147	0.213	–	–	–	–	–
	#5	23,110	71	90	119	0.194	0.301	0.043	0.4269	0.094	–	126
	#8	21,541	65	83	112	0.186	0.293	0.061	0.5700	0.094	–	168
	#4	19,380	59	70	96	0.230	0.262	–	–	–	–	–
Duplex 2304	#5	24,690	69	78	104	0.222	0.273	0.028	0.3676	0.068	–	127
	#8	23,822	72	79	108	0.179	0.264	0.048	0.6697	0.061	–	140
	#4	–	–	–	–	–	–	–	–	–	–	–
XM-28	#5	25,360	60	61	100	0.370	0.402	0.030	0.4193	0.065	–	105
	#8	28,790	77	79	117	0.370	0.370	0.068	0.6894	0.087	–	207

magnetic attraction to the substrate steel beneath the coating. Five individual gage measurements were obtained from different locations on the surface of the reinforcing steel and reported in Appendix A. The average of these measurements is reported in Table A.3.

A.3.2.4 Surface roughness. The surface roughness of the various types of reinforcing steel was measured using a portable stylus instrument as shown in Figure A.7. The measurements were made at an epoxy-coating plant located in Bourbonnais, Illinois. In accordance with ASTM D7127 (2005) and ASME B46.1 (2009), the number of peak/valley pairs defined per unit length and the largest peak to valley measurement were measured. Five measurements were made from different locations on the surface of the reinforcing steel (measurements reported in Appendix A), and the average of these measurements is reported in Table A.3.

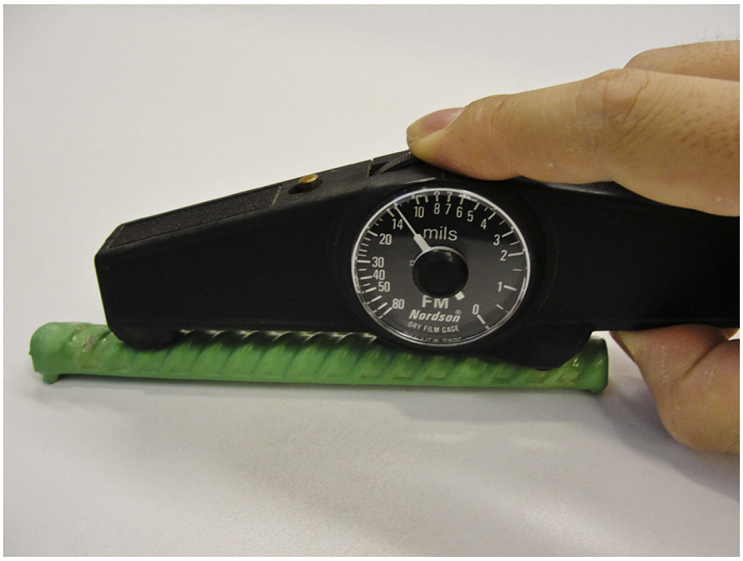

Figure A.6 Coating thickness measurements (pull-off dry film gage).

Figure A.7 Surface roughness measurement (profiliometer).

APPENDIX B: BOND STRENGTH—EXPERIMENTAL PROGRAM

B.1. INTRODUCTION

The objective of this phase of research is to investigate the bond between corrosion-resistant reinforcing bars and concrete. Forty five beam specimens with tension lap splices were tested to evaluate the effect of bar type, bar size, bar spacing, splice length, transverse reinforcement, and axial rigidity on bond between corrosion-resistant reinforcing steel and concrete.

B.1.1 Factors Influencing Bond Behavior

The geometry of the bar (deformation height and spacing), surface condition of the bar, splice length, concrete cover, bar spacing, and presence of transverse reinforcement are known as major factors that influence the bond behavior between reinforcing steel and concrete. The following section provides a literature review on these factors.

B.1.1.1 Bar type. The forces that contribute to bond transfer between reinforcement and concrete can be divided into adhesion and friction forces along the surface and bearing forces on the ribs as shown in Figure B.1. Bond is transferred through chemical adhesion between the bar and concrete until initial slip of the bar. After adhesion is lost, bearing forces on the ribs and friction forces along the surface and ribs transfer the bond forces.

As early as 1913, Abrams tested 1,500 pullout and 110 beam specimens to investigate the bond between concrete and steel, and more than 15 variables were evaluated in this monumental study. Among many of his findings, Abrams (1913) reported that chemical adhesion consists with approximately 60% of the maximum bond resistance while friction consists with 40% of the bond resistance in plain bars. Therefore, when plain bars are polished, bond resistance is mostly governed by adhesion producing only 60% of the bond resistance shown for bars with an ordinary surface (unpolished). He also reported that rusted bars produce approximately 15% higher bond resistance than similar bars with ordinary mill scale. These findings indicate that the surface condition of various bars will provide different bond strengths.

B.1.1.2 Bar size. For a given development and splice length, the bond force increases as the bar size increases. However, bond stresses have been measured lower for larger diameter bars because the rate of increase in the bond force is lower than the rate of increase in bar area which requires longer development lengths (Chinn, Ferguson, & Thompson, 1955; Ferguson & Thompson, 1965; Mathey & Watstein, 1961).

B.1.1.3 Splice length. The bar stress distribution along short splices has been shown to be relatively linear which is in agreement with the assumption of a uniform distribution of bond stress along the bonded length. However, the bar stress distribution along long splices demonstrates nonlinearity resulting in a decrease in effectiveness of force development as the splice length is increased (Ferguson & Briceno, 1969). In other words, the total bond force transferred between the concrete and steel reinforcement will increase as the development or splice length increases but the relative increase in bond strength reduces with increasing splice length. Therefore, the unit bond strength decreases as splice length increases. This behavior has been demonstrated in many previous studies which are discussed below.

Chinn et al. (1955) demonstrated that steel stress increases with splice length but the bond stress decreases as the splice is lengthened. Ferguson and Thompson (1962, 1965) demonstrated that the unit bond strength decreases as the development length increases. However, Ferguson and Thompson (1965) also pointed out that the bond strength did not appear to decrease significantly as the development length increased for development lengths in excess of 50 in. Azizinamini, Stark, Roller, and Ghosh (1993) similarly found that the unit bond strength decreases as the splice length

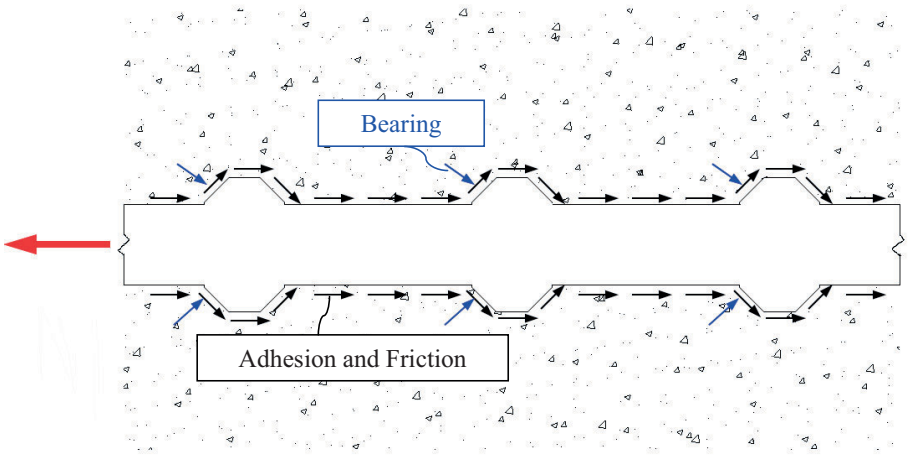

Figure B.1 Bond force transfer mechanism.

increases for specimens with reinforcing bars embedded in high-strength concrete.

Other tests demonstrate that the increase in bond force is not proportional to the increase in development length or splice length. Pay (2005) studied the bond behavior of unconfined steel and fiber reinforced polymer (FRP) bar splices in concrete beams. By using the concept of an equivalent splice length that accounts for various bars with different axial stiffness, the study demonstrated that for both steel and FRP bars, the bond force nonlinearly increases as the equivalent splice length increases. El-Hacha, El-Agroudy, and Rizkalla (2006) studied bond characteristics of high-strength steel reinforcement and also demonstrated that bond force is not linearly related with the splice length.

B.1.1.4 Concrete cover and bar spacing. If there is not sufficient development length to yield the bar, the specimen will fail in bond by either a bar pullout failure or concrete splitting failure. The parameters that determine the type of bond failure are the cover and bar spacing dimensions and the presence of transverse reinforcement.

The force between the reinforcing bar and concrete is first transferred through chemical adhesion. Once adhesion is lost, the force is transferred through friction along the surface and bearing against the deformations. These friction forces along the surface and bearing forces against the deformations are balanced by the compressive and shear stresses on the surrounding concrete surface. Goto (1971) explained that these compressive stresses on the surrounding concrete surface can not only serve to tighten the concrete around the reinforcing bar and increase the frictional resistance between the steel and concrete but also cause ring tension as a reaction to the tightening force and result in cracking planes horizontal and perpendicular to the reinforcement. If the concrete cover and spacing between the bars are small, these splitting cracks can form a plane to eventually cause a splitting failure. Depending on the concrete cover and bar spacing dimensions, the splitting failure can either become a side splitting failure, face splitting failure, or face and side splitting failure as shown in Figure B.2.

If there is sufficient concrete cover, a wide spacing, and transverse reinforcement to prevent these splitting failures, but inadequate development length, the specimen will fail in a pullout failure mode.

Concrete cover and bar spacing are important parameters that not only determine the type of bond failure but also influence the bond behavior of a specimen. Chinn et al. (1955) reported that increasing the cover increases the bond strength and resistance against splitting failure. Chamberlin (1956) found that the unit bond strength increases as the clear spacing/bar diameter ratio increases. Ferguson and Thompson (1962) indicated that there is an increase in bond strength as the cover increases. However, they also reported that the increase in bond strength is less for larger bars and for longer splice lengths. Thompson, Jirsa, Breen, and Meinheit (1975) found that the bond strength of splices increases as the ratio of the clear cover to clear spacing increases. Orangun, Jirsa, and Breen (1977) demonstrated that large side cover or wide clear spacing increases the bond strength. Hadje-Ghaffari, Choi, Darwin, and McCabe (1994) studied both uncoated black bars and epoxy-coated bars and found that the bond strength of both coated and uncoated bars increase as the cover increases.

B.1.1.5 Transverse reinforcement. Stirrups in the splice region will arrest the progression of side or face splitting cracks, and therefore, provide ductility to the beam and increase splice strength. Chinn et al. (1955) found that ties around the splice increased the bond strength by 45%. Ferguson and Breen (1965) observed that minimum stirrups increased the splice strength as much as 20% and heavy stirrups increased the splice strength as much as 50%. Warren (1969) found that stirrups arrest crack propagation and provide ductility, but the variation of stirrup size did not substantially affect the anchorage capacity. Thompson et al. (1975) reported that splice strength increases and the number of splitting cracks reduce with the addition of transverse reinforcement. Morita and Fujii (1982) stated that the major role of transverse reinforcement is to increase ductility by maintaining bond resistance of surrounding concrete after splitting takes place. Morita and Fujii observed that bond strength increases with the addition of transverse reinforcement. However, they observed that the efficiency of stirrups in improving bond behavior depends on the splitting failure mode which is controlled by the bar spacing and cover dimensions. Zuo and Darwin (2000) stated that the higher the quantity of coarse aggregate, the greater the contribution of transverse reinforcement to splice strength. Zuo and Darwin (2000) also observed that bond strength confined by transverse reinforcement increases with an increase in relative rib ratio or bar size of longitudinal reinforcement. Without transverse

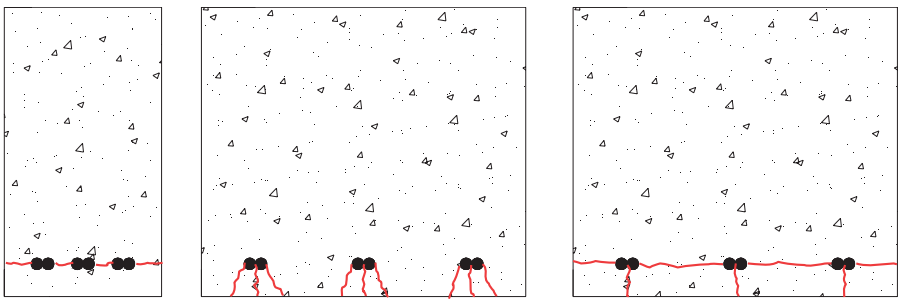

(a) Side Splitting (b) Face Splitting (c) Face and Side Splitting

Figure B.2 Type of splitting cracks.

reinforcement, the influence of relative rib ratio to bond strength reduces.

The advantage of providing transverse reinforcement in the splice region was also observed in epoxy-coated reinforcement. Hamad and Jirsa (1993) found that the bond strength of epoxy-coated bar splices relative to uncoated bar splices improved from 74% to 80–85% when transverse reinforcement was provided. Hester, Salamizavaregh, Darwin, and McCabe (1993) also observed that the strength of splices containing both coated and uncoated bars increased by adding transverse reinforcement.

Orangun et al. (1977) observed that bond stress increases as the amount of transverse reinforcement increases. With increasing transverse reinforcement, the failure mode can be changed from a splitting to pull-out failure. Orangun et al. (1977) found that extremely heavy transverse reinforcement does not increase the bond strength further and an upper limit is needed due to this change in failure mode. Rezansoff, Konkankar, and Fu (1992) found that short lap lengths with heavy confinement were as effective as long lap lengths with less confinement. They also reported that confinement provided by increasing the concrete cover is less efficient than the equivalent confinement provided by stirrups. Azizinamini, Pavel, Hatfield, and Ghosh (1999) evaluated the bond strength of lap-spliced beams using high-strength concrete and similarly observed that requiring some minimum amount of stirrups at the ends of splices over the development length is more effective than increasing the splice length to increase bond strength. In addition, Azizinamini et al. (1999) found that even with large concrete covers, a minimum amount of stirrups should be provided over the splice length to develop #8 or #11 bars.

Based on the previous test results and studies regarding the influence of transverse reinforcement to bond strength, transverse reinforcement will prevent splitting failures and provides not only ductility but also an increase in bond strength. An upper limit for confinement based on the studies of Orangun et al. (1977) is used in design codes to account for the fact that adding transverse reinforcement beyond a certain amount will not increase bond strength once adequate confinement is produced to prevent a splitting failure and produces a pullout failure.

Because the bar stress distribution is not linear along the splice (Azizinamini et al., 1999; Ferguson & Briceno, 1969; Kluge & Tuma, 1945; Richter, 2012), and because stirrups are not stressed to yield and reach higher stresses in regions of higher shear (Reynolds & Beeby, 1982), the location where transverse reinforcement is provided can be critical in providing efficient confinement.

B.1.1.6 Axial rigidity. Axial rigidity (AE) has been investigated by Pay (2005) as a parameter that influences bond strength. Pay evaluated the influence of axial rigidity by (1) varying the cross-sectional area (using the same diameter bar) while maintaining the modulus of elasticity constant and (2) varying the modulus of elasticity of the reinforcement while maintaining the cross-sectional area constant. Pay (2005) found that the higher the modulus of elasticity of the reinforcement, the higher the bond force reached at failure. He also concluded that axial rigidity of the bar is a major parameter influencing splice strength.

B.2. SPECIMEN DESIGN

B.2.1 Specimen Dimensions

Beam splice tests were selected for this study because these specimens are commonly used to ascertain the development and splice lengths of reinforcement and are the basis for development length design expressions. A typical test specimen and test setup are shown in Figure B.3. The test setup produces a constant moment region between the supports subjecting the entire splice region to a constant force. The splice lengths (L_s) were selected based on the estimated bond strengths to ensure that the reinforcement would not reach yield prior to bond failure and provide valid results.

Sufficient length is provided between the support and end of the splice to permit evaluation of the development of cracking and evaluation of crack spacing and widths. Because bond strength is known to influence cracking, these measurements can provide additional insight regarding the overall bond performance. In addition, the splice region was located where the assumption that plane sections remain

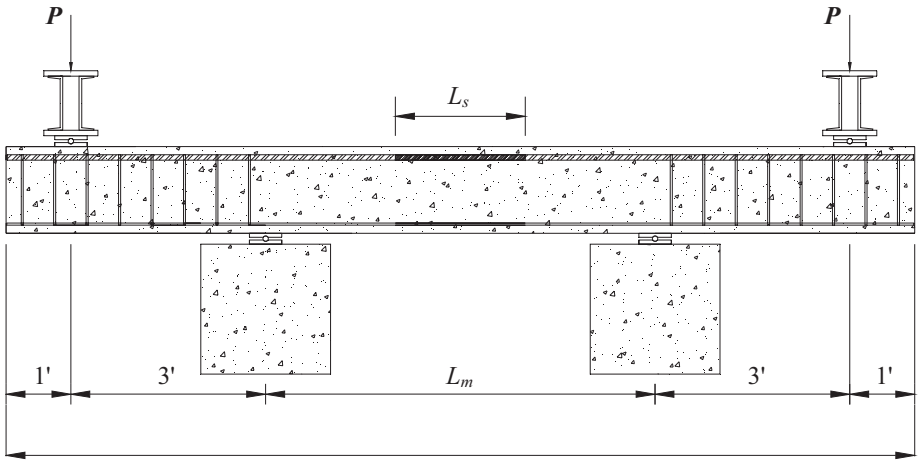

Figure B.3 Lap-splice specimen and loading system.

plane from flexural theory is valid. Based on St. Venant's Principle, the stress at a section from a distance equal to the overall height of the member away from the section where load changes will have a linear distribution. Therefore, the length of the constant moment region (L_m) was selected such that the splice end is at least h (the overall height of the member) away from the supports. As a result, the constant moment region was 6 ft long for specimens with 12, 15, 18, 24, and 36 in. splices, while the constant moment region was constructed as 8 ft long for specimens with 48 in. splices. All specimens had a 3 ft shear span and 1 ft added to each end to accommodate the dimensions of the loading system. Considering these requirements, the specimen was designed to have an overall length (L) of 14 ft for specimens with 12, 15, 18, 24, and 36 in. splices and an overall length of 16 ft for specimens with 48 in. splices.

The 14 ft long specimen includes #3 stirrups at a 6 in. spacing in the shear span with two #3 longitudinal bars provided in the compression side to assist in the fabrication of the reinforcement cage. The 16 ft long specimens include #4 stirrups at 6 in. spacing in the shear span with two #3 longitudinal bars provided in the compression side. In general, no transverse reinforcement was provided throughout the constant moment region which provides a worst case scenario and provides clarity in results in evaluating the influence of the corrosion-resistant reinforcement on bond strength. In addition, the absence of transverse reinforcement is consistent with bridge deck applications. Transverse reinforcement was provided in the constant moment region for six specimens that were constructed to specifically investigate the influence of splice confinement.

Two bar-spacing arrangements were selected to ensure consistency in behavior considering two different failure modes: side-face splitting and top-face splitting. Furthermore, it was decided to test the reinforcement in critical layouts where minimum cover and spacing requirements are provided. Therefore, two bar-spacing arrangements were selected as shown in Figure B.4. Specimens that were designed to produce a side-face splitting failure mode were

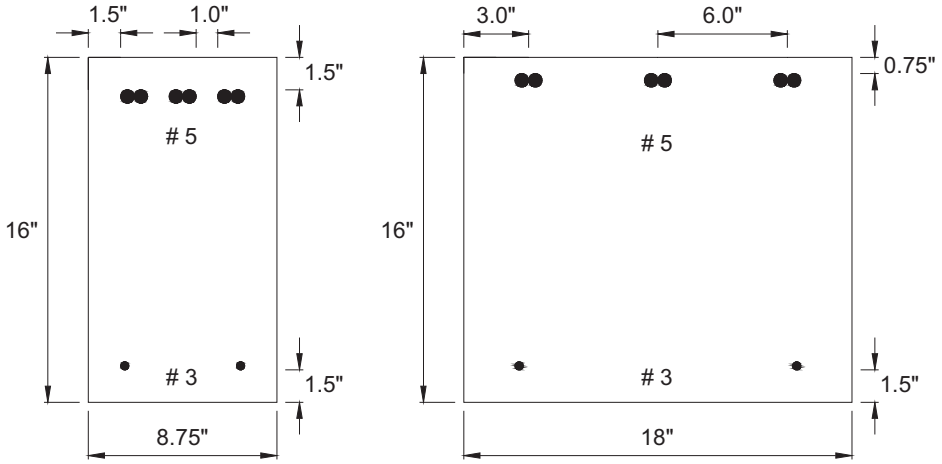

(a) Side Splitting Beams (#5) (b) Face Splitting Beams (#5)

(c) Side Splitting Beams (#6) (d) Face Splitting Beams (#6)

Figure B.4 Cross section details at splice region. *(Figure continued on next page.)*

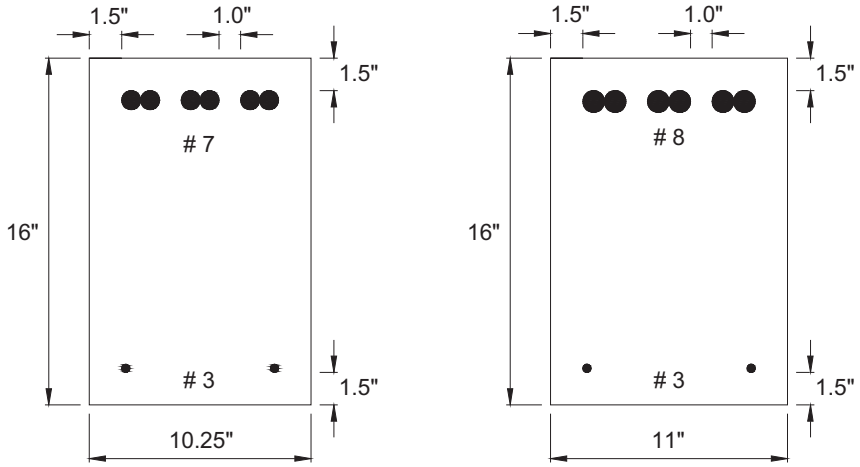

(e) Side Splitting Beams (#7) (f) Side Splitting Beams (#8)

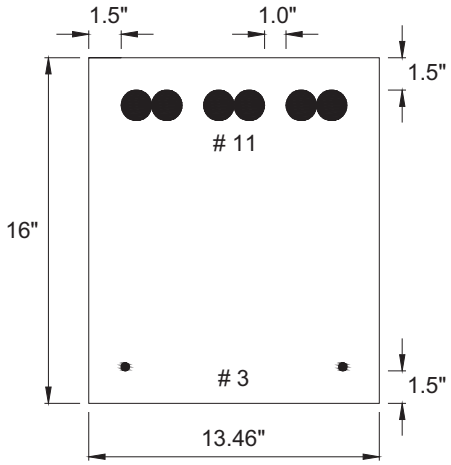

(g) Side Splitting Beams (#11)

Figure B.4 *Continued.*

provided a minimum top and side clear cover of 1.5 in. and a clear spacing of 1 in. between the bars located in the splice region. These dimensions represent the minimum clear cover allowed by ACI 318-11 (2011) and AASHTO (2010) LRFD (primary reinforcement not exposed to weather) and minimum clear spacing allowed by ACI 318-11. Specimens that were designed to produce a top-face splitting failure mode were provided a reduced top cover of 0.75 in. or 1.0 in. and a wide bar spacing of 6.0 in. between bars. With the identical cover and spacing dimensions, the width of the specimens was finally determined by the size of reinforcement used (#5, #6, #7, #8, and #11 bars were tested in this study). Cross section details of the specimens are provided in Figure B.4. These bar sizes encompass the range of the most common bar sizes used as primary reinforcement in flexural members.

All beams were rectangular in cross section, and the total depth was selected as 16 in. to permit comparisons with previous test data. This depth was selected in previous studies to allow the reinforcement to be cast in top position by having more than 12 in. of fresh concrete cast in the member below the reinforcement. However, all beam specimens in this study were bottom cast and flipped before testing to produce tension on the top surface using the loading system shown in Figure B.3. This loading direction produces cracking on the top surface, providing ease in both mapping cracks and measuring crack widths in the splice region.

B.2.2 Specimen Variables

Forty-five reinforced concrete beam specimens with tension lap splices located in the constant moment region were tested to evaluate bond between the corrosion-resistant reinforcing steel and concrete. Test variables included bar type, bar size, bar spacing, splice length, transverse reinforcement, and axial rigidity. A summary of the specimens is provided in Table B.1.

Tests were conducted in five series. The first series consisted of four specimens with #6 un-plated zinc-clad bars. Specimens were constructed and tested to evaluate the bond

TABLE B.1
Lap-Splice Specimen Test Matrix

Series	Designation	Bar Type	Bar Size	Splice Length L_s (in.)	Cover and Bar Spacing (in.)
I	B-6-S-15	Black	#6	15	top, side cover: 1.5; clear spacing: 1.0
	ZC1-6-S-15	Zinc-clad 1	#6	15	
	B-6-F-15	Black	#6	15	top cover: 1.0; bar spacing: 6.0
	ZC1-6-F-15	Zinc-clad 1	#6	15	
II	B-5-S-12	Black	#5	12	top, side cover: 1.5; clear spacing: 1.0
	E-5-S-12	Epoxy	#5	12	
	G-5-S-12	Galvanized	#5	12	
	ZC1-5-S-12	Zinc-clad 1	#5	12	
	ZC2-5-S-12	Zinc-clad 2	#5	12	
	Z-5-S-12	Zbar	#5	12	
	M-5-S-12	MMFX II	#5	12	
	S316LN-5-S-12	316LN	#5	12	
	S2205-5-S-12	Duplex 2205	#5	12	
	S2304-5-S-12	Duplex 2304	#5	12	
	SXM28-5-S-12	XM-28	#5	12	
III	B-8-S-24	Black	#8	24	top, side cover: 1.5; clear spacing: 1.0
	E-8-S-24	Epoxy	#8	24	
	G-8-S-24	Galvanized	#8	24	
	ZC1-8-S-24	Zinc-clad 1	#8	24	
	ZC2-8-S-24	Zinc-clad 2	#8	24	
	Z-8-S-24	Zbar	#8	24	
	M-8-S-24	MMFX II	#8	24	
	S316LN-8-S-24	316LN	#8	24	
	S2205-8-S-24	Duplex 2205	#8	24	
	S2304-8-S-24	Duplex 2304	#8	24	
	SXM28-8-S-24	XM-28	#8	24	
IV	B-5-F-12	Black	#5	12	top cover: 0.75; bar spacing: 6.0
	ZC2-5-F-12	Zinc-clad 2	#5	12	
	Z-5-F-12	Zbar	#5	12	
	S2205-5-F-12	Duplex 2205	#5	12	
	B-8-S-24-C1	Black w/stirrups	#8	24	top, side cover: 1.5; clear spacing: 1.0
	B-8-S-24-C2	Black w/stirrups	#8	24	
	B-8-S-24-C3	Black w/stirrups	#8	24	
	M-5-S-24	MMFX II	#5	24	
	M-5-S-36	MMFX II	#5	36	
	S2205-5-S-24	Duplex 2205	#5	24	
	S2205-5-S-36	Duplex 2205	#5	36	
V	M-5-S-48	MMFX II	#5	48	top, side cover: 1.5; clear spacing: 1.0
	M-7-S-24	MMFX II	#7	24	
	M-7-S-18	MMFX II	#7	18	
	M-8-S-48	MMFX II	#8	48	
	M-11-S-24	MMFX II	#11	24	
	M-8-S-48-C1	MMFX II w/stirrups	#8	48	
	M-8-S-48-C2	MMFX II w/stirrups	#8	48	
	M-8-S-48-C3	MMFX II w/stirrups	#8	48	

Note: Zinc-clad 1 (un-plated), Zinc-clad 2 (tin-plated), Zbar (dual-coated).

strength of un-plated zinc-clad reinforcing bars as compared with ASTM A615 (2009) black bars in two different bar spacings. In the second series, specimens with 11 different #5 bars were tested to evaluate how different bar types influence bond strength. In the third series, specimens with 11 different bar types but with larger #8 bars were tested to evaluate if bar size changes the behavior observed in the previous test series. After evaluating the performance of the various bar types, four reinforcement types were selected and further investigated in the fourth series to evaluate if beams with

wider bar spacings and smaller covers influence the relative bond strengths. In addition, variables such as transverse reinforcement in the splice region and specimens with longer splice lengths were investigated through testing seven additional specimens. Finally, in the fifth series, eight specimens with MMFX II bars were added to further investigate the effect of longer splices, the effect of transverse reinforcement in the splice region, and the effect of axial rigidity of lapped reinforcement.

Specimens in Table B.1 are identified by the initial of the reinforcement type followed by the bar size (#5, #6, #7, #8, and #11), the failure mode (S if designed to fail in side-face splitting and F if designed to fail in top-face splitting mode), and finally by the splice length in inches. Specimens with confinement in the splice region are appended with the letter C and the type of confinement (1 for the case with one stirrup tied at each end of the splice, 2 for the case with two stirrups tied together at the center of the splice, and 3 for the case with one stirrup tied at each end and one stirrup tied in the center). The following sections discuss the variables selected for this study which are known to affect bond strength.

B.2.2.1 Bar type. The effect of different bar types on bond strength was investigated. Eleven types of reinforcement were included to evaluate how the different surface conditions and geometries of the various corrosion-resistant reinforcing bars affect bond strength. Conventional black steel was considered as a control. The reinforcement types include epoxy-coated, hot-dip galvanized, un-plated zinc-clad, tin-plated zinc-clad, dual coated reinforcement, MMFX II, and four different types of stainless steel (316LN, Duplex 2205, Duplex 2304, and XM-28). These eleven bars have different surface conditions such as various coating thicknesses for coated bars, different surface roughness which may affect adhesion and friction, and different deformation height and spacing which may affect the bearing resistance from the ribs.

B.2.2.2 Bar size. The effect of bar size was investigated. Two bar sizes (#5 and #8) were used to evaluate the effect of bar size on bond strength for the eleven bar types. In addition, #6 bars were tested for un-plated zinc-clad bars and #7 and #11 bars were additionally included in evaluating the MMFX II bars.

B.2.2.3 Splice length. The effect of splice length was investigated. Splice length was varied from 12 to 48 in. In terms of bar diameters, these splice lengths are $19d_b$ to $77d_b$ for the #5 bar. To investigate the effect of splice length on bond strength without yielding the bars, MMFX II microcomposite high-strength bars were selected for the long splices. All specimens were designed to fail in splitting prior to yielding.

B.2.2.4 Concrete cover and bar spacing. The effect of concrete cover and bar spacing were investigated. The concrete cover and bar spacing were varied in three different arrangement as follows: (1) top and side cover of 1.5 in. and clear spacing of 1 in. between the bars, (2) top cover of 1.0 in. and center-to-center bar spacing of 6 in., and (3) top cover of 0.75 in. and center-to-center bar spacing of 6 in. Specimens with a clear spacing of 1 in. between the bars are expected to fail in side-face splitting failure while specimens with center-to-center bar spacing of 6 in. are expected to fail in top-face splitting failure mode. The wider specimens are also expected to have higher bond strength than narrower beams. Specimens that were designed to fail in a top-face splitting failure mode provide a minimum face cover (1.0 in.) for a bridge deck according to AASHTO (2010) or provide a minimum face cover (0.75 in.) for a slab according to ACI 318 (2011).

B.2.2.5 Transverse reinforcement. The effect of having transverse reinforcement in the splice region was investigated. This study considered three stirrup layouts

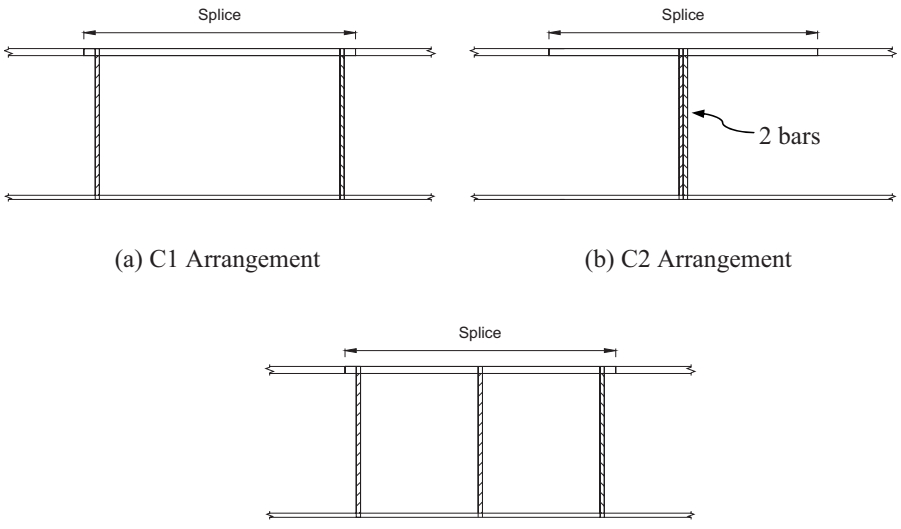

(a) C1 Arrangement (b) C2 Arrangement

(c) C3 Arrangement

Figure B.5 Transverse reinforcement arrangement.

using two different splice lengths for #8 bars: 24 in. and 48 in. The three arrangements are shown in Figure B.5. The first layout (C1) has one stirrup tied at each end of the splice. The second layout (C2) has two stirrups tied together at the center of the splice. These two layouts provide an identical amount of transverse reinforcement, A_{tr}, but at different locations along the splice. The third layout (C3), includes one stirrup tied at each end of splice similar to C1, but adds one stirrup in the center of the splice to evaluate the effectiveness of the stirrup in the center in increasing bond strength.

It was hypothesized that providing confinement in the middle of splice region will not have a large influence on bond strength. Therefore, the C2 arrangement and the specimen with no confinement provided in the splice region are expected to have comparable bond strengths. Similarly, by providing an identical amount of transverse reinforcement in C1 and C2, the C1 arrangement is expected to provide a higher bond strength than the C2 arrangement. In addition, although more transverse reinforcement is provided in the C3 arrangement compared to the C1 arrangement, the two layouts are expected to have comparable bond strengths.

The hypothesis that transverse reinforcement in the middle of the splice region will not have much influence on bond strength is based on the assumption that the bond stress distribution is not uniformly distributed along the splice length as shown in Figure B.6. This assumption is supported by test results that measured the bar stress along the splice (Azizinamini et al., 1999; Ferguson & Briceno, 1969; Kluge & Tuma, 1945; Richter, 2012).

The assumption can also be visualized by modeling the splice region with multiple springs as shown in Figure B.7 that have both longitudinal and transverse stiffness (Sozen, 2009). The transverse stiffness was half of longitudinal stiffness.

For a unit load at the end, the normalized bar force and bond stress distribution along short lap-splices (with 5 nodes at the top and bottom) and long lap-splices (with 15 nodes at the top and bottom) can be presented as shown in Figure B.8. From a simple spring model, a similar conclusion can be made that for a longer splice, there is approximately no change in bar force in the center of splice region as shown. Therefore, it should be less effective to place confinement where bond stresses are close to zero.

B.2.2.6 Axial rigidity. The effect of axial rigidity (AE) was also investigated. In this study, MMFX II microcomposite reinforcing steel was selected for the test bar to evaluate the influence of axial rigidity due to its high yield strength. With the hypothesis that $A_1E_1L_1 = A_2E_2L_2$, maintaining the modulus of elasticity of the bar as constant, the bar size and splice length was paired in the following three combinations to investigate the effect of axial rigidity on bond strength: It is expected that the paired splice length and bar size will produce the same total bar force.

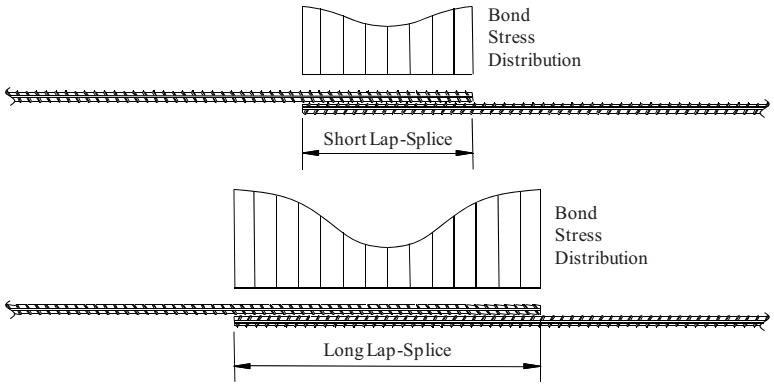

Figure B.6 Bond stress distribution (retrieved from Canbay & Frosch, 2005).

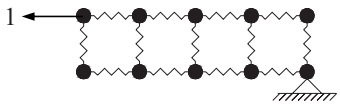

(a) Linear Spring Model with 5 Nodes at Top and Bottom

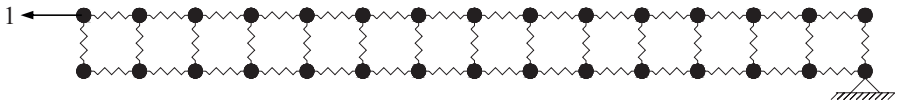

(b) Linear spring model with 15 nodes at top and bottom

Figure B.7 Linear spring model of short and long splices.

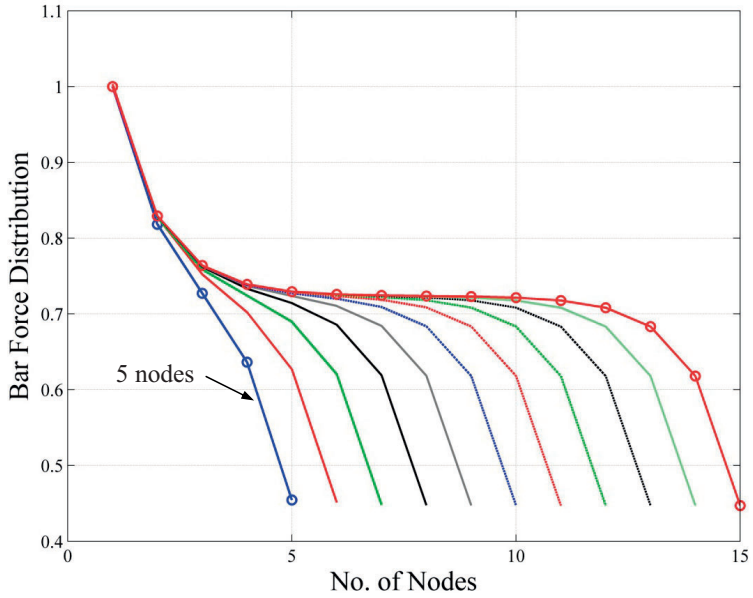

(a) Normalized Bar Force Distribution

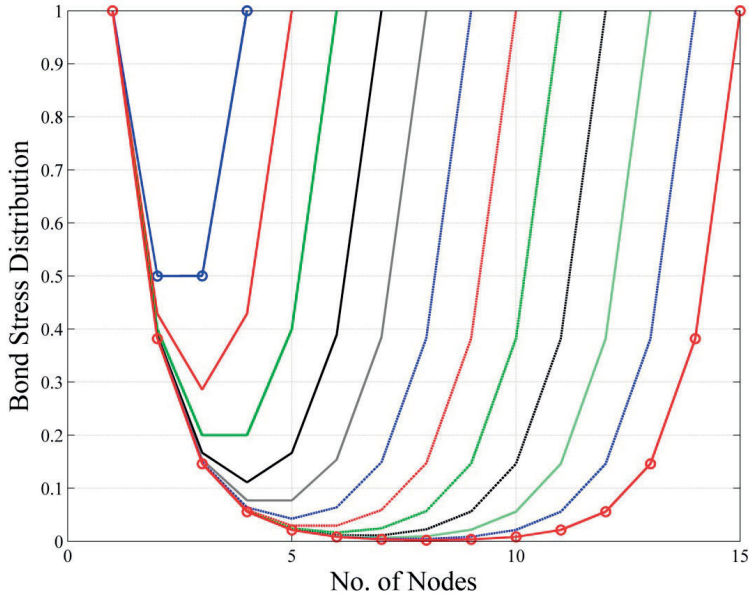

(b) Normalized Bond Stress Distribution

Figure B.8 Bond stress distribution from linear spring model.

1. 48 in. splice and #5 bars (A_1L_1=14.9) vs. 24 in. splice and #7 bars. (A_2L_2=14.4)
2. 36 in. splice and #5 bars (A_1L_1=11.2) vs. 18 in. splice and #7 bars (A_2L_2=10.8)
3. 48 in. splice and #8 bars (A_1L_1=37.9) vs. 24 in. splice and #11 bars (A_2L_2=37.4)

B.3. MATERIALS

B.3.1 Concrete

Specimens were cast in five different batches (Table B.2) of the same concrete mix design, all of which had a target strength of 4000 psi. This strength was selected because it is commonly used in bridge decks as well as flexural members. Concrete was provided by a local ready-mix concrete supplier, Irving Materials Inc. (IMI), located approximately 1.5 miles from Bowen Laboratory.

A concrete mix that contains river gravel with a 3/4 in. maximum aggregate size was selected. The concrete mix proportions, batch weights per cubic yard, and slump prior to casting are provided in Table B.3. A target slump of 5 in. was requested for each of the casts and was measured upon arrival at the laboratory. Actual values achieved are listed.

The compressive strength of concrete cylinders for each concrete batch was monitored by testing three standard 6 by 12 in. cylinders at 3, 7, 14, 21, and 28 days after casting.

TABLE B.2
Cast History

Casting Data	Series I	Series II	Series III	Series IV	Series V
Beam Specimens	B-6-S-15	B-5-S-12	B-8-S-24	B-5-F-12	M-5-S-48
	ZC1-6-S-15	E-5-S-12	E-8-S-24	ZC2-5-F-12	M-7-S-24
	B-6-F-15	G-5-S-12	G-8-S-24	Z-5-F-12	M-7-S-18
	ZC1-6-F-15	ZC1-5-S-12	ZC1-8-S-24	S2205-5-F-12	M-8-S-48
		ZC2-5-S-12	ZC2-8-S-24	B-8-S-24-C1	M-11-S-24
		Z-5-S-12	Z-8-S-24	B-8-S-24-C2	M-8-S-48-C1
		M-5-S-12	M-8-S-24	B-8-S-24-C3	M-8-S-48-C2
		S316LN-5-S-12	S316LN-8-S-24	M-5-S-24	M-8-S-48-C3
		S2205-5-S-12	S2205-8-S-24	M-5-S-36	
		S2304-5-S-12	S2304-8-S-24	S2205-5-S-24	
		SXM28-5-S-12	SXM28-8-S-24	S2205-5-S-36	
Cubic yards	3.75	7.25	9.5	11	6
Date of Casting	01/19/10	07/12/11	08/05/11	02/08/12	10/09/12

TABLE B.3
Mix Proportions per Cubic Yard

Material	Series I	Series II	Series III	Series IV	Series V
Cement (lbs/yd^3) (ASTM C-150 Type 1)	423	423	423	423	423
Coarse Aggregate (lbs/yd^3) (Gravel, Vulcan Materials, Lafayette, IN)	1850	1850	1850	1850	1850
Fine Aggregate (lbs/yd^3) (#23 Sand, Vulcan Materials, Lafayette, IN)	1455	1455	1455	1455	1455
Water (lbs/yd^3)	215	235	225	233	233
Water Reducer (oz/yd^3) (BASF Glenium 3030 NS)	2	2	2	2	2
Air Entrainer (oz/yd^3) (ASTM C-260)	0.5	0.5	0.5	0.6	0.8
Water-to-Cement Ratio	0.51	0.56	0.53	0.55	0.55
Measured Slump (in.)	4	4	5	6.5	5

Additional testing was performed on the day specimen testing started and ended. A 600 kip capacity Forney F-60C-DFM/I compression testing machine was used for the tests. The cylinders were capped with neoprene pads and loaded in compression at a loading rate of 35 psi/sec (approximately 59,000 lb/min), in accordance with ASTM C39 (2012). All cylinders were made during each cast and cured 7 days in an identical manner as the beam specimens (covered with wet burlap and plastic sheathing). Cylinder molds were removed when the formwork for the specimens was removed. In addition, split-tensile strength was monitored by testing three standard 6 by 12 in. cylinders at 7 and 28 days after casting and on the day specimen testing started or ended. Load was applied at a rate of 150 psi/min (approximately 17,000 lb/min), the average rate in accordance with ASTM C496 (2011). The compressive strength growth curves for each cast are provided in Figure B.9, and a summary of results is given in Table B.4. The strength at test day in Table B.4 indicates the average of strength measured when testing started and ended.

B.3.2 Reinforcing Steel

The sizes, types, ASTMs, and the suppliers of the primary reinforcement used in the bond test program are summarized in Table B.5. Three reinforcement samples of each type of bar were tested in tension in accordance with ASTM A370, and the yield strength, tensile strength, and rupture strain were determined.

The primary reinforcement used in Series I was supplied by Jarden Zinc Products and included both #6 zinc-clad and ordinary black bars of Grade 60. Both bars were obtained from the same mill and conformed with ASTM A615 (2009). Tension tests of the black bars and zinc-clad for Series I were performed and indicated yield strengths of 63,600 and 64,900 psi, respectively. Test results are presented in Table 2.3.

The primary reinforcement used in Series II, III, and IV includes eleven types of reinforcing steel for both #5 and #8 bars.

Reinforcement used in Series V includes MMFX II microcomposite steel as indicated. Tension tests of the #7 MMFX II bars (results of #5 and #8 bars are provided in Table 2.3) indicate yield strengths of 125 psi (by 0.2% offset).

Reinforcement required for the stirrups and longitudinal compression bars were obtained from a local supplier (Indiana Steel Fabricating, Inc.). No.3 Grade 60 bars conforming to ASTM A615 and prefabricated with standard bends and details as required by ACI 318-11 were used for test specimens in Series I to Series IV. No. 4 bars were used for stirrups in Series V.

B.4. SPECIMEN CONSTRUCTION

B.4.1 Formwork and Reinforcing Steel Layout of Series I

The forms shown in Figure B.10 were constructed on a plywood base of sufficient width to accommodate the different beam widths. The center divider was fastened to the base while the outside forms were attached to the base with

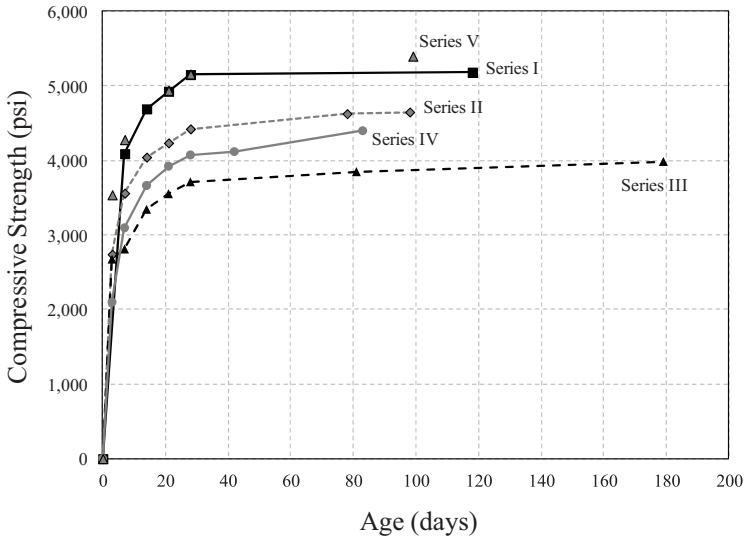

Figure B.9 Concrete strength growth.

TABLE B.4
Compressive and Split-Tensile Strength Data

Age	Series I				Series II				Series III				Series IV				Series V			
	f'_c (psi)		f_t (psi)		f'_c (psi)		f_t (psi)		f'_c (psi)		f_t (psi)		f'_c (psi)		f_t (psi)		f'_c (psi)		f_t (psi)	
	Ea.	Avg.	Ea.	Avg.	Ea.	Avg.	Ea.	Avg.	Ea.	Avg.	Ea.	Avg.	Ea.	Avg.	Ea.	Avg.	Ea.	Avg.	Ea.	Avg.
7	4240	4090	–	–	3650	3560	450	440	2890	2810	390	370	3160	3100	420	400	4510	4280	460	400
	4000				3500		440		2750		380		3000		420		4270		380	
	4030				3530		420		2810		330		3130		350		4060		380	
28	5520	5150	–	–	4420	4420	460	440	4420	4420	360	360	4000	4070	480	480	5190	5160	500	490
	4990				4430		460		4430		350		4140		490		5140		420	
	4950				4420		410		4420		350		4080		480		5180		550	
Test Day	5100	5180	540	510	4670	4650	400	420	4080	3990	430	450	4390	4400	430	420	5350	5400	420	490
	4670		490		4630		430		3900		480		4570		400		5450		540	
	4990		510		4650		420		3980		450		4240		420		5410		500	

TABLE B.5
Reinforcing Steel Information

Series	Bar Size	Bar Type	ASTM	Provided
I	#6	Black	ASTM A615	Jarden Zinc Products
		Zinc-clad 1	–	Jarden Zinc Products
II	#5	Black	ASTM A615	Gerdau Co.
III	#8	Epoxy	ASTM A934	Gerdau Co.
IV		Galvanized	ASTM A767	South Atlantic
		Zinc-clad 1	–	Jarden Zinc
		Zinc-clad 2	–	Jarden Zinc
		Zbar	ASTM A1055	Gerdau Co.
		MMFX II	ASTM A1035	MMFX Tech. Co.
		316LN	ASTM A955	Valbruna Stainless, Inc.*
		Duplex 2205	ASTM A955	Talley Metals Tech., Inc.**
		Duplex 2304	ASTM A955	American Arminox, Inc.
		XM-28	ASTM A955	Talley Metals Tech., Inc.**
V	#5, #8, #7, #11	# IIMMFX	ASTM A103	MMFX Tech. Co.

* Purchased from Tell Steel, Inc.

** Purchased from Salit Speciality Rebar.

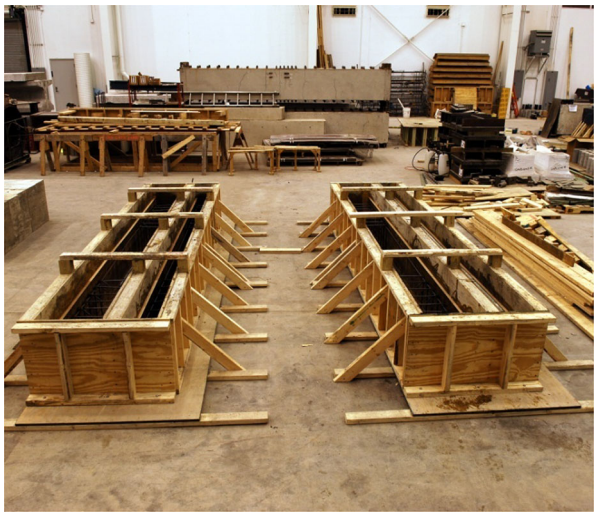

Figure B.10 Formwork for series I.

lag-screws to accommodate the two beam widths. Two sets of forms were constructed. The beams with zinc-clad bars were constructed in one set, and the beams with black bars in the other. The form surfaces were coated with release agent, and the joints were sealed with silicone. Chamfer strips were used to provide the desired beam height of 16 in. because the forms were also used to produce different height beams for another research study.

The steel cages were fabricated outside the forms as shown in Figure B.11 and were placed on individual chairs to provide the correct cover. Details of the reinforcement

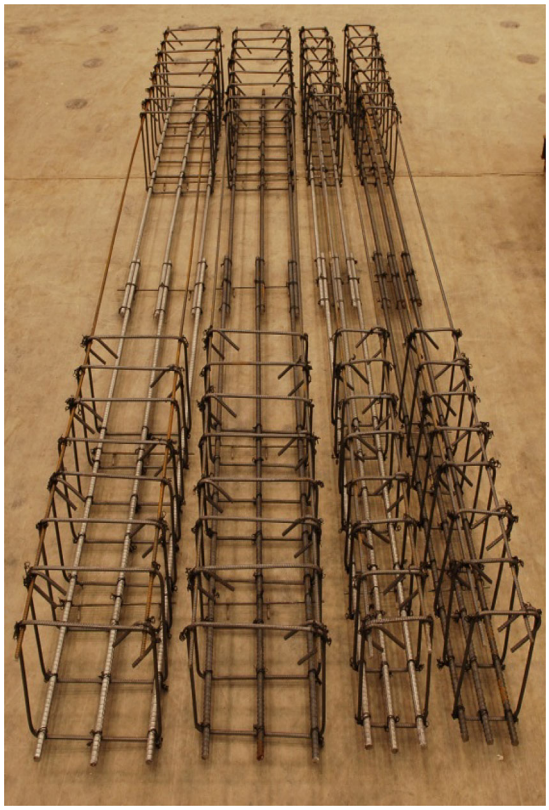

Figure B.11 Steel cages (series I).

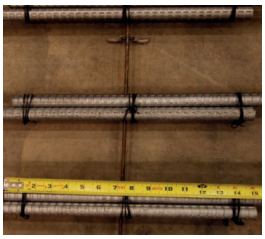

(a) Splice Length (15 in.)

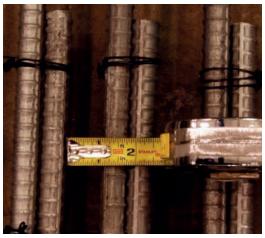

(b) Clear Spacing (1 in.)

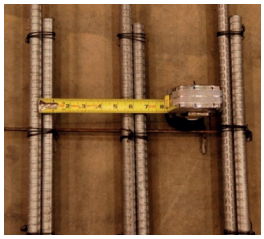

(c) Center-to-Center Spacing (6 in.)

Figure B.12 Spacing details (series I).

layouts are shown in Figure B.12. All specimens had a splice length of 15 in. as shown in Figure B.12(a). The specimens designed to produce a side-splitting failure included a 1 in. clear spacing between the bars in the splice region as shown in Figure B.12(b) while the specimens designed to cause face splitting failure included a 6 in. center-to-center spacing of the bars as shown in Figure B.12(c).

Closed stirrups with #3 bars were used in the shear span to prevent shear failure during loading. No stirrups were provided in the splice region, as discussed earlier, to eliminate any influence of transverse reinforcement on the splice (Figure B.11). Two #3 bars were provided as compression steel for the entire length of the beam to assist with holding the cages together as well as prevent complete collapse of the specimen upon failure. Because the beams were designed to be bottom cast, the two #3 bars are shown on the top side in Figure B.11 with the primary reinforcement located in the bottom-cast position.

B.4.2 Formwork and Reinforcing Steel Layout of Series II through V

Twelve specimens were cast simultaneously (eleven and one extra specimen for each series) using six sets of formwork

Figure B.13 Assembled formwork (series II).

constructed as shown in Figure B.13. Each set allows two specimens to be cast side-by-side. All forms were constructed with 3/4 in. plywood and 2×4 in. lumber. The base form had a width of 4 ft and a length of 16 ft which was constructed with two 4×8 ft plywood sheets (3/4 in. thickness) supported by 2×4 in. lumber spaced at 12 in. The center divider, side forms, and end forms were assembled having a skeleton structure with 2×4 in. lumber on top and bottom supported by 2×4 in. studs spaced at 12 in. Plywood sheets (3/4 in. thickness) were attached to the skeletons with screws and attached to the base using lag screws to allow ease in formwork removal and to allow constructing various widths of beams used throughout the experimental program.

To prevent formwork failure during casting and to maintain the shape of formwork for multiple casting operations, 2×4 in. diagonal braces were attached to the side forms and 4×4 in. blocks were fixed on top of side and center forms to attached 2×4 in. cross-braces. All joints between the forms were sealed with silicon caulking and backing rods to prevent leakage during casting. After the formwork was completed, form oil was sprayed one day prior to the cast before rebar placement. The same formwork was reused during the experimental program to cast specimens in Series II through V.

The steel cages were fabricated outside the forms as shown in Figure B.14 and Figure B.15 and placed on individual

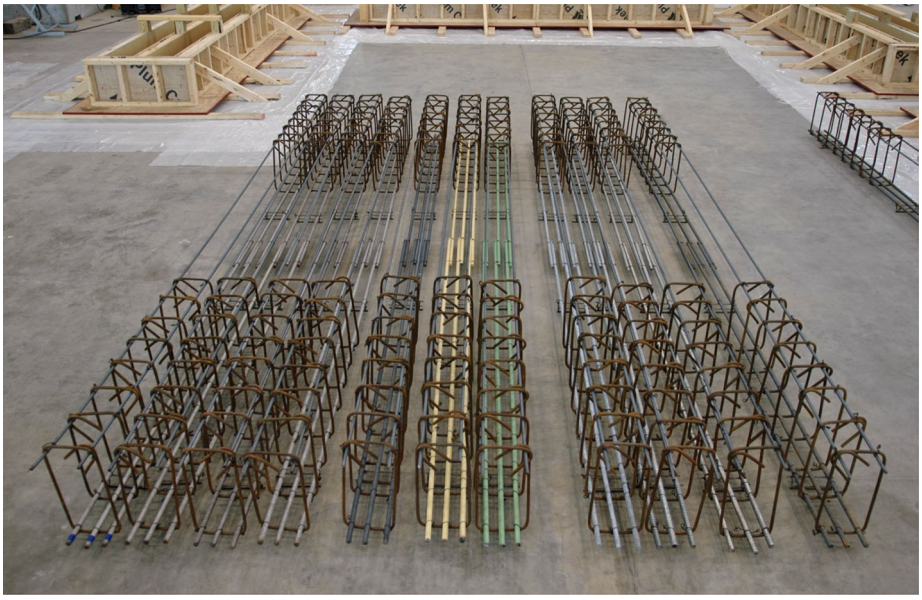

Figure B.14 Assembled reinforcing cage (series II).

Figure B.15 Assembled reinforcing cage (series IV).

chairs to provide the correct cover. Because, all specimens were bottom cast, the reinforcement for the tension side is shown at the bottom (Figure B.14 and Figure B.15). Two #3 bars were provided in the compression zone to assist with fabrication of the reinforcement cage and prevent collapse of the specimen upon failure.

The steel cages were placed on 1.5 in. chairs for specimens in Series II through V designed to cause side splitting failure and on 0.75 in. chairs for specimens in Series IV designed to cause face splitting failure. All chairs were located outside the splice region to prevent any influence on bond strength as shown in Figure B.16. The steel cages were secured in the formwork using plastic spacer wheels to provide the correct side cover and to prevent movement during casting as shown in Figure B.17. They were further secured by tying the cages to the nails that were attached at the end forms (Figure B.17).

B.4.3 Casting and Curing

Specimens in each series were cast simultaneously from the same batch of concrete. Concrete was placed in two lifts directly from the chute of the ready-mix truck into the forms as well as using a bucket and overhead crane as shown in Figure B.18. The beams were screeded first with 2×4 in. lumber or magnesium screeds. Then, the surface was finished using a magnesium float as shown in Figure B.19. Two coil loop inserts manufactured from Dayton Superior Co. (Type B-16, 0.5" diameter, 4" insert length) were installed for lifting purposes. After initial set of the concrete, the slabs were covered with wet burlap, and plastic sheets were placed on top of the burlap to prevent moisture loss during curing. The specimens were cured for 7 days. Immediately following the end of wet curing, the forms were removed.

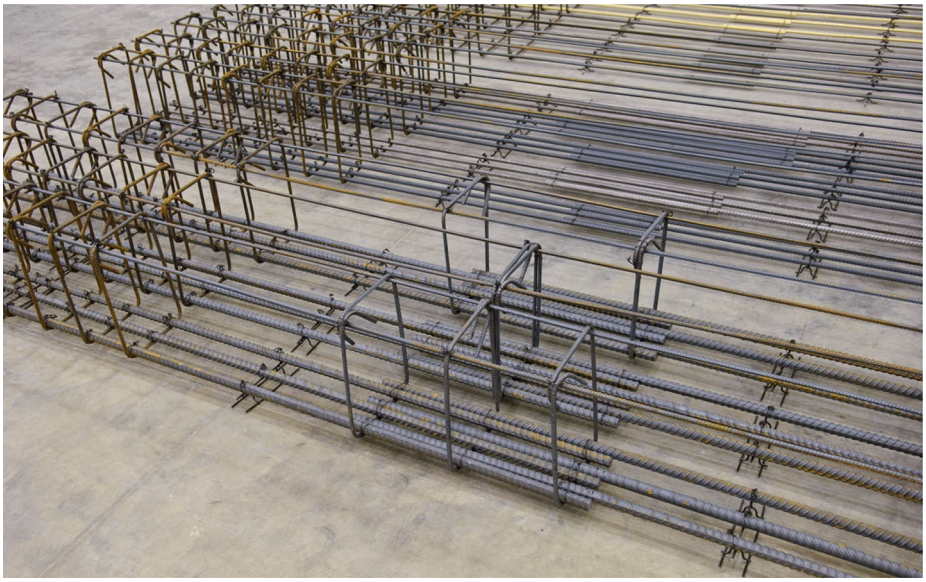

Figure B.16 Details of the reinforcing bar in splice region (series IV).

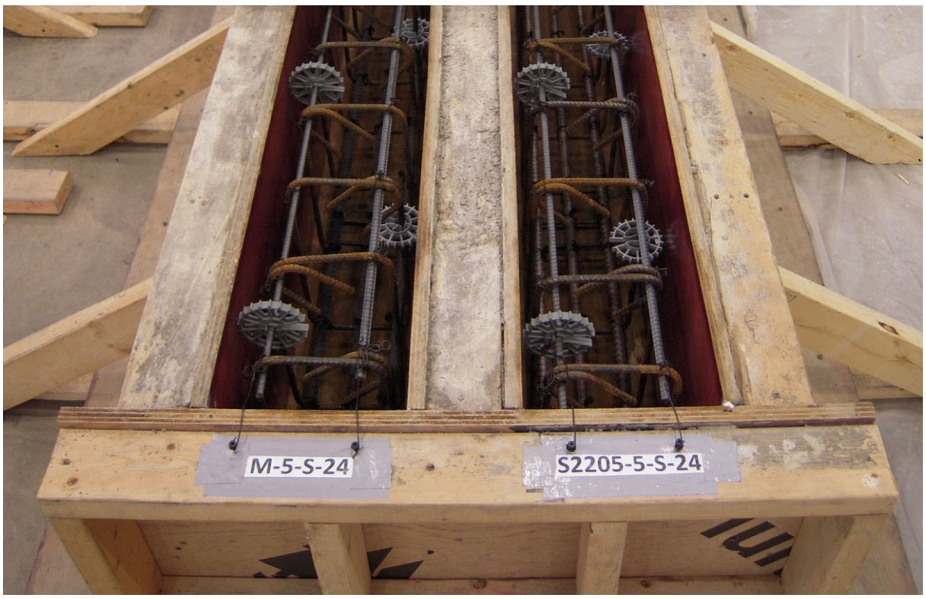

Figure B.17 Plastic spacer wheels (series IV).

Concrete cylinders were also cast at the same time and placed into cylinder molds with steel scoups in two lifts. The cylinders were consolidated using an internal vibrator. The identical curing procedure used for the beams specimens was followed for the cylinders, and the molds were removed after 7 days of curing. The test specimens were stored for 28 days prior to testing.

B.5. TEST SETUP AND TEST PROCEDURE

The testing setup was designed to load the beams at the ends producing a constant moment region in the center. The beams were supported by concrete blocks. At the reaction points, steel bearing plates were attached to the concrete block and the test specimen using hydrostone to provide uniform load distribution and control bearing stresses in the concrete. A roller support was obtained by placing a 1 in. diameter and 14 in. long steel rod between $0.5 \times 6 \times 14$ in. flat steel plates while a pin support was obtained by placing a 1 in. diameter and 36 in. long steel rod between $0.75 \times 6 \times 14$ in. steel plates that were grooved 0.25 in.

Although all beams were identically loaded at the ends, the test setups varied slightly between each series of testing due to the availability of hydraulic rams in the laboratory at the moment of testing. For Series I and

Figure B.18 Casting (series II).

Figure B.19 Finishing the concrete (series II).

Series V, load was applied by two 60 ton, two-way, center-hole hydraulic rams with a 5 in. stroke capacity at each end of the specimen. The loading system is shown in Figure B.20.

For Series II and Series III, load was applied by placing one 60 ton, two-way, center-hole hydraulic ram with a 5 in. stroke capacity on the center of the beam between the steel beam and test specimen. When loading with one hydraulic ram, a special wooden frame was constructed to provide stability and prevent rotation or lateral movement of the steel reaction frame as shown in Figure B.21.

For Series IV, load was applied using two 60 ton one-way center-hole hydraulic rams with a 3 in. stroke capacity at each end of the specimen as shown in Figure B.22.

Hydraulic pressure was supplied with a manual pump through a manifold to the four rams (Series I, IV, and V) or to the two rams (Series II and III). Two 1 in. diameter, high strength steel, threaded rods were provided at each end to resist the applied load and transfer the load directly to the strong floor in all cases. Two grooved bearing plates ($0.75 \times 6 \times 14$ in.) with a 1 in. diameter steel rod was installed between the loading beams and the specimen to locate and concentrate the load.

The load for the beam specimens in which the calculated yield load was below 20 kips was applied in 1 kip intervals. Beam specimens that had calculated yield loads under 30 kips had a 2 kip load increments. Specimens that had calculated yield loads under 40 kips had a 4 kip load increments. Finally, beams with long splices or transverse

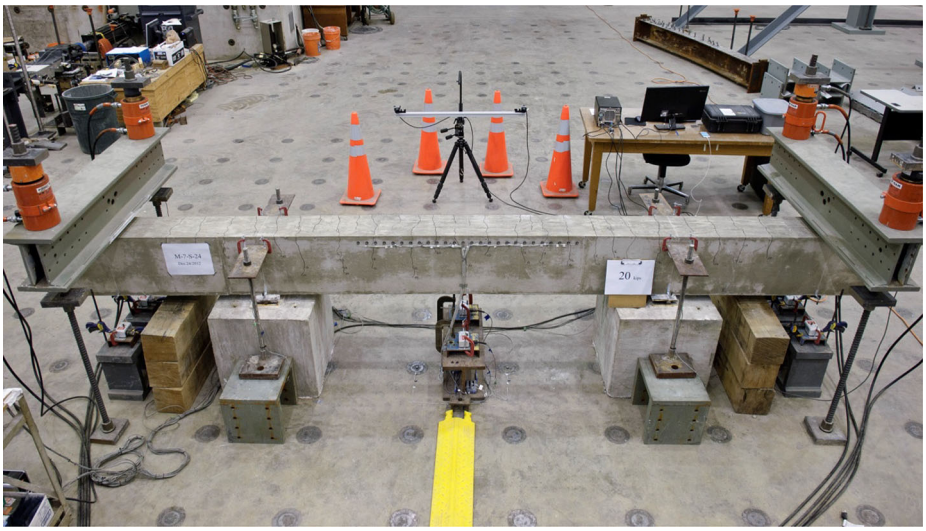

Figure B.20 Beam specimen test setup (series I and V).

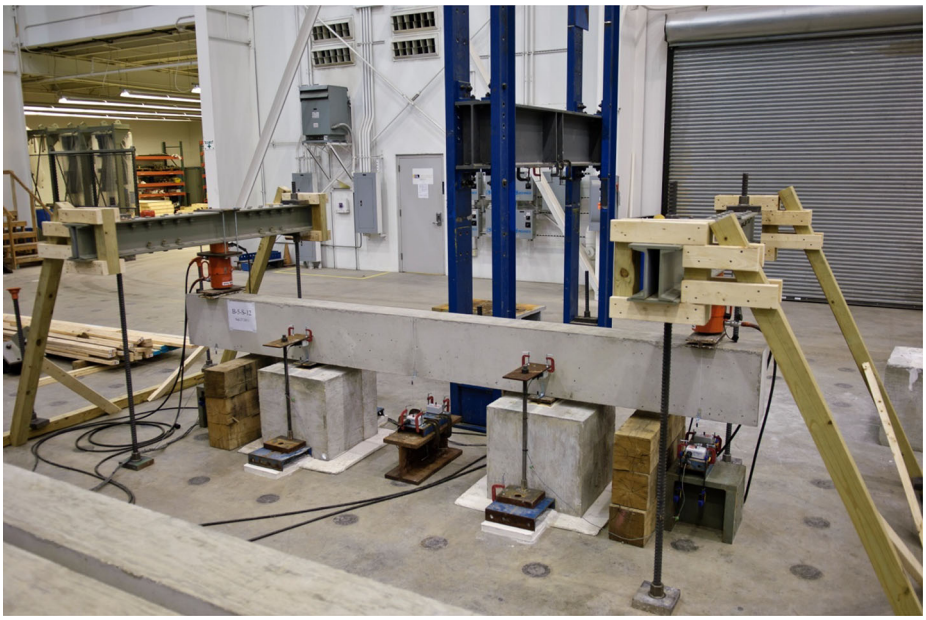

Figure B.21 Beam specimen test setup (series II and III).

reinforcement in Series V which were expected to yield beyond 40 kips were loaded in 5 kip load increments.

B.6. INSTRUMENTATION

A summary of the entire instrumentation used in this testing program is provided in Table B.6.

B.6.1 Load Measurements

The load from each ram was monitored by load cells manufactured from Tokyo Sokki Kenkyujo Co., Ltd. and from Honeywell Inc. The loading system was calibrated on a Baldwin 120-kip capacity universal testing machine with an Instron control and data acquisition system.

B.6.2 Deflection Measurements

Deflections were monitored using ten string potentiometers manufactured by UniMeasure Inc. (range and sensitivity in Table B.6). Two string potentiometers were installed at midspan, two at each support, and two at loading points. Average of the two measurements from each location was reported. Load and deflection data were collected through a

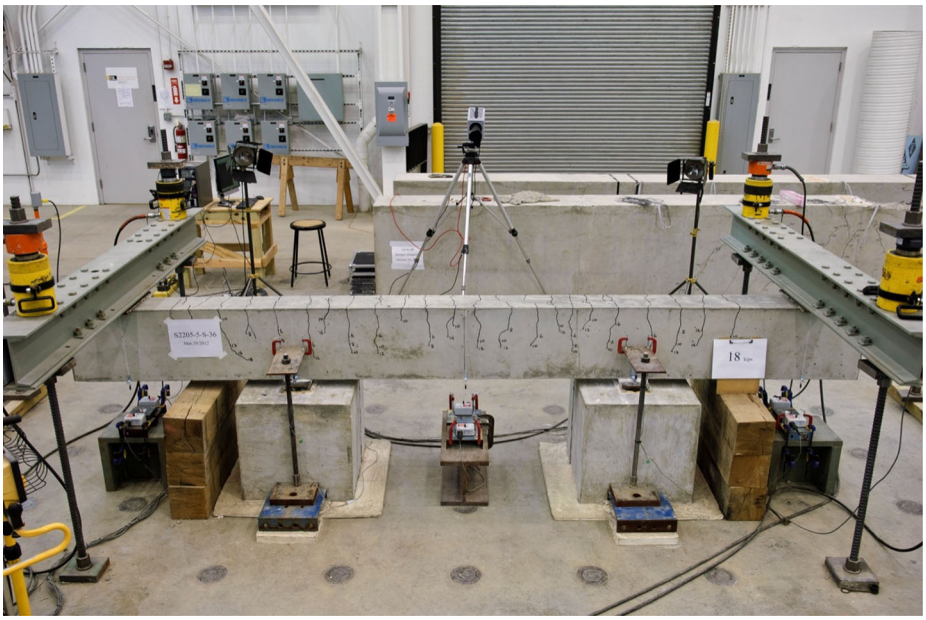

Figure B.22 Beam specimen test setup (series IV).

TABLE B.6
Summary of Instrumentation

Type of Application	Manufacturer	Model	Accuracy or Range
Data Acquisition	Vishay	System 7000-128-SM	Measurement accuracy of ± 0.05%
Hydraulic Ram1	SPX Co.	Power Team RH605	60 ton Push 25 ton Pull 5 in. stroke
Hydraulic Ram2	Enerpac	RCH-603	60 ton capacity 3 in. stroke
Load Cell	Tokyo Sokki	KCB-500kN	±125,000 lb
	Honeywell	3632-100k	±100,000 lb
String Potentiometer	UniMeasure	PA-10-DS	±10 in.
		PA-25-DS	±25 in.
Crack width microscope	Edmunds Industrial Optics	50X Direct Measuring	Reading accuracy of 1/1000 in.
Digital Image Correlation (DIC) Device	Correlated Solutions, Inc.	Vic-3D Vic-Snap	Strain accuracy $50 \times 10^{(6}$
Camera for DIC	Point Grey Research, Inc.	Grasshopper GRAS-5055M	2448 × 2048 at 15 fps
Lens for DIC	Schneider Optics	35mm f/1.4	–
Motion Capture System	Northern Digital Inc.	OptoTRAK Dynamic Measuring Machine	Reading Resolution: $\pm 4 \times 10^{(4}$in.
Demountable Mechanical Strain Gage	Mayes Instruments Limited	DEMEC strain gage gage length: 100 mm	$\pm 5 \times 10^{6}$in.
High-Speed Camera	Photron, Inc.	FASTCAM-APX RS	1024 × 1024 at 3000 fps
Lens for High-Speed Camera	Tokina	28-70mm f/2.8	–

VISHAY data acquisition System 7000-128-SM and monitored at 0.1-second intervals during testing using VISHAY StrainSmart Ver. 4.7.25. The string potentiometers for deflection measurements were calibrated using a Fowler Trimos height gage (Model 600+, 24 in. travel) with an accuracy of 0.00005 in.

B.6.3 Crack Measurements

At each load stage, cracks were marked and crack widths in the constant moment region were measured using an Edmund Direct Measuring 50X pocket microscope and crack comparator. The microscopes allowed for crack measurement within an accuracy of 1/1000 of an inch. Only cracks located between the support and end of the splice region were considered for measurement because they were not influenced by the splice or the support. Crack widths at specific locations were measured throughout the test up to a critical load for which it was deemed unsafe to continue measurements.

B.6.4 Strain Measurements

Strain measurements were made for specimens in Series IV and Series V for two cases: 1) strain measurements on the legs of transverse reinforcement 2) concrete surface strains on the beam side in the region surrounding the sliced bars. Strain gages were used to measure the strains on stirrups while a mechanical strain gage, motion capture system, and a digital image correlation device was used to measure the strains on the concrete surface in the splice region. The following sections discuss each measurement system in detail.

B.6.4.1 Strain gages. Specimen B-8-S-24-C1, B-8-S-24-C2, and B-8-S-24-C3 in Series IV include strain gages attached on the outside of each stirrup leg at the location where side splitting cracks were expected to propagate towards the concrete surface. The location where the strain gages were expected to be installed on the #3 stirrup leg were prepared by mechanical and chemical means to achieve appropriate bond between the strain gages and the substrate metal. Strain gages obtained from Tokyo Sokki Kenkyujo Co. (120 Ohm strain gages with 5 meter lead wires attached) were installed.

First the mill-scale on the rebar and the deformations were removed and grinded with a high-speed electrical sand paper grinding machine to provide a flat bonding site on the reinforcing bar leg. The surface was treated and the strain gages were installed with products from Vishay Micro-Measurements in the following procedure: 1) Degrease the surface using CSM-2 Degreaser, 2) Dry abrade the surface using 220-grit silicon carbide paper, 3) Abrade the surface with 320-grit silicon carbide paper wetted with M-Prep Conditioner A, 4) Dry the surface with GSP-1 gauze sponges and draw alignment marks on the cleaned surface, 5) Apply M-Prep Conditioner A again with cotton tips and slowly dry with gauze sponges, 6) Apply M-Prep Neutralizer 5A with cotton tips and carefully dry the surface again with gauze sponges, 7) Attach the PCT-2M gage installation tape on the strain gage and install the gage at the location of interest, 8) By lifting the tape where the strain gage is attached, apply a few drops of Vishay M-Bond AE-10 adhesive and press with thumb to properly install the strain gage, and 9) Take off the PCT-2M tape.

After the strain gages were installed they were coated with Vishay M-Coat D, an acrylic waterproofing agent to prevent the electrical resistance strain gages from becoming short circuited by the moisture or water in concrete. On top of the strain gage painted with M-Coat D, an additional M-Coat FB butyl rubber was attached to provide not only environmental protection but also mechanical protection.

B.6.4.2 Digital Image Correlation (DIC). Specimens in Series V with long splices, large bars, and confinement were monitored using an optical method, Digital Image Correlation (DIC), to measure strain on the concrete surface in the splice region. The DIC device, Vic-snap and Vic-3D measurement system developed by Correlated Solutions, Inc. was used to track the sprayed paint speckle patterns while specimens were tested. By using two cameras,

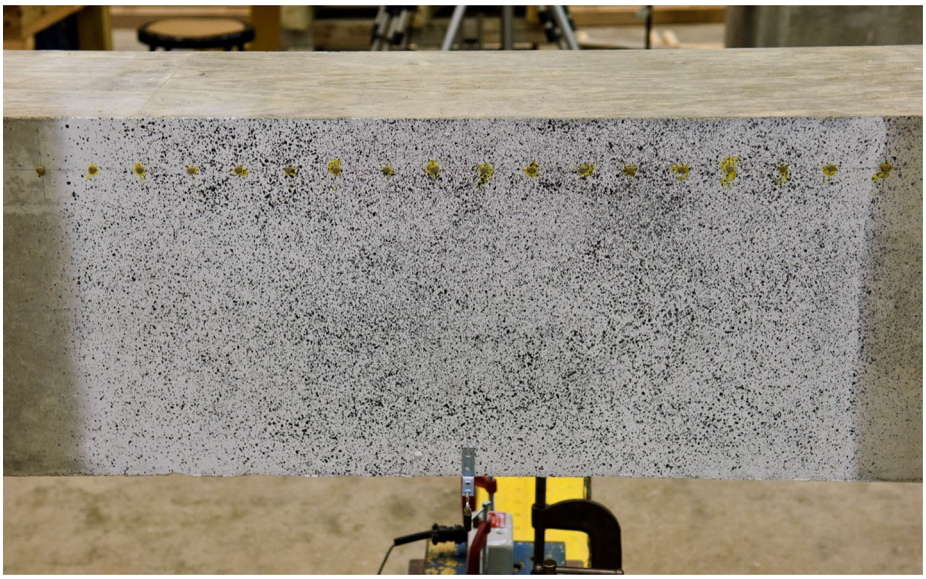

Figure B.23 Black and white speckle patterns.

this optical method allows measurement of both in-plane and out-of-plane displacement and strain in 3-dimensions at every point on the specimen's surface where a random speckle pattern is applied. This optical device was used to investigate the bar stress in the splice region without influencing the bond strength as is done when strain gages are installed on the lap spliced bars. To achieve the best results from the digital image correlation technique, the pattern should be high contrast and non-repetitive. Therefore, black and white spray paint was used to apply the speckle patterns as shown in Figure B.23. To avoid wet paint flow caused by gravity, test specimens were flipped 90° so that the side surface of interest was facing upward. The splice region was first painted with white spray paint. After the white paint dried, black spray paint was applied in a sweeping motion with the spray nozzle barely pushed and angled 45° upwards from the horizontal surface. This allowed black paint with larger dots and produce the appropriate size of speckles on the surface.

Two Grasshopper GRAS-5055M cameras with Schneider 35mm f/1.4 lens attached were positioned at a location where the centerline between the two cameras is in alignment with the center of painted surface, symmetrically as shown in Figure B.24. After the camera and tripod were setup at the proper location, a calibration board with black grid dots was used to initiate the calibration procedure prior to testing. Vic-snap software was used to capture the images from the two cameras every second. After all images were acquired,

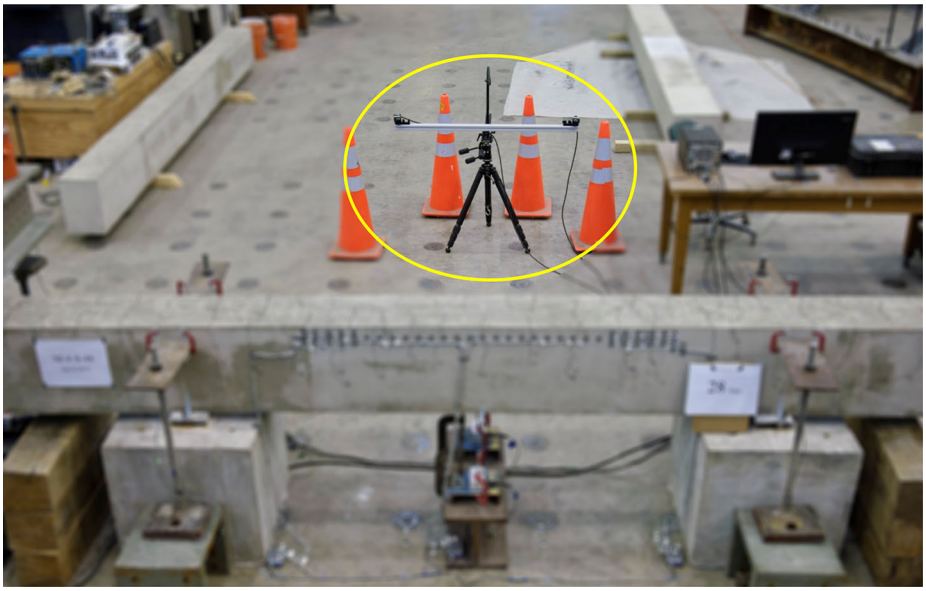

Figure B.24 Two cameras setup for digital image correlation.

Figure B.25 Infrared position trackers.

Vic-3D software was used to analyze the full-field displacement or strain on the concrete surface measured during the bond test.

B.6.4.3 Optical tracking of infrared position markers. Specimens in Series V with long splices, large bars, and confinement were also monitored using an optical motion capture system that tracks infrared position markers to evaluate the strain on the concrete surface in the splice region and to compare the measurements with the DIC results. The OptoTRAK Dynamic Measuring Machine (DMM) motion capture system developed by the Northern Digital Inc. was used to track the small infrared (IRED) position markers attached to the test specimen in the splice region. The system provides 3D coordinates of each target in real-time. However, to minimize the amount of data, the 3D coordinates of each target was only recorded once per load increment. The x, y, and z coordinates were used to compute the displacement and strain at each load step. The location where the targets were planned to be attached was scraped with a razor blade in advance and a hot glue gun was used to attach the plastic moldings that hold the IRED position markers (Figure B.25) on the concrete surface. The overall setup is shown in Figure B.26.

B.6.4.4 Demountable mechanical strain gage. To verify the strain measurement results obtained from the optical methods (OptoTRAK and DIC) introduced earlier, a demountable mechanical strain gage was used in this investigation. The demountable mechanical strain gage (DEMEC) was developed by the British Cement and Concrete Association to enable strain measurements using a single instrument as shown in Figure B.27. The DEMEC digital mechanical strain gage system assembled by Mayes Instruments Limited consists of a Mitutoyo 543 digital dial gage attached to an Invar bar. A fixed conical point is mounted on one end of the Invar bar while a moving conical point is mounted on a knife edge pivot at the opposite end.

Figure B.26 OptoTRAK motion capture system.

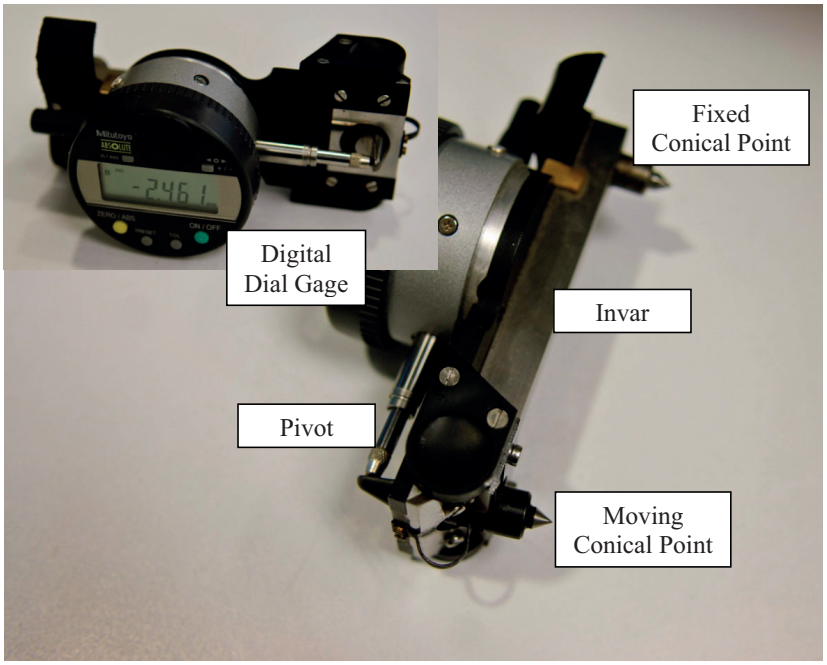

Figure B.27 Demountable mechanical strain gage.

The pivoting movement of this conical point is measured by the digital dial gage.

DEMEC locating stainless steel disks with pre-drilled conical holes in the disk center were attached at the measurement location as shown in Figure B.28 using a layout bar shown in Figure B.29 which is 50 mm apart between the two conical locating points. The measurement location was the concrete surface at the level of reinforcement in the lap-splice region. The BondAway 2011A/2012B system developed by Fielco Adhesives was used to bond the locating disks to the specimen. This epoxy adhesive was used because it was proven from previous studies at Purdue (Pavelchak, 2009) to be efficient and painless in eliminating the epoxy from the locating disks after testing is completed by dipping them in boiling water. Therefore, all disks can be easily reused.

The mechanical strain gage measurements using the DEMEC gage were taken by the same operator throughout the investigation as shown in Figure B.30. Because the locating disks were installed at 50 mm and the mechanical strain gage has a 100 mm gage length, each measurement was made between alternative disks and not between consecutive

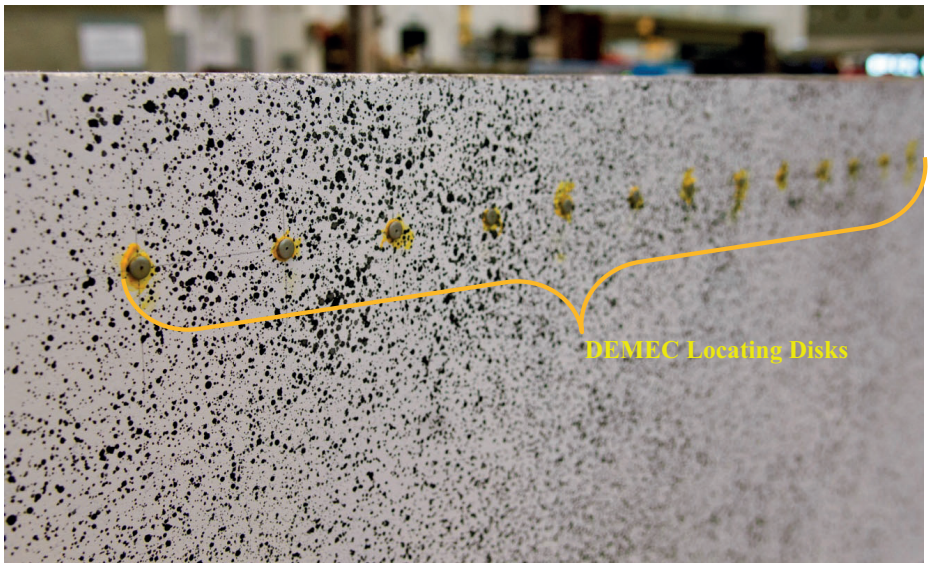

Figure B.28 Stainless steel locating disks installed.

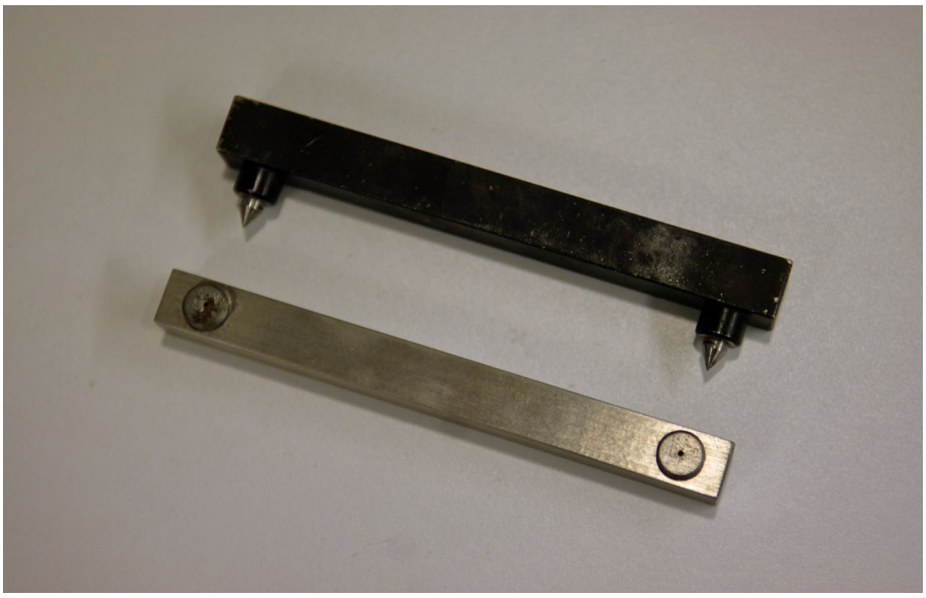

Figure B.29 Installation layout bar.

Figure B.30 Demountable mechanical strain gage measurements.

disks. Therefore, to obtain strain between two consecutive points, the average of strain measurements from two intervals is taken.

B.6.5 Failure Observation

A high-speed camera was used to capture the moment of brittle failure and observe how the side or top face splitting cracks propagate and branch out at failure. The high-speed camera, FASTCAM SA3 manufactured by Photron, Inc. was used to take 6,000 frames per seconds. A Tokina 28-70mm f/2.8 lens was mounted on the camera and manually focused prior to testing. Although, failure is brittle, the loading step that caused failure of the specimen was able to be predicted by monitoring the progress of horizontal splitting cracks shown on the side or top surface. The system constantly takes 6,000 photos per seconds and records the photos of the 3 seconds prior to pushing the trigger at failure. The trigger was pushed slightly after hearing the explosive failure.

APPENDIX C: BOND STRENGTH—TEST RESULTS AND ANALYSIS

C.1. INTRODUCTION

The experimental results of each test are presented to evaluate the effect of bar type, bar size, splice length, concrete cover, bar spacing, transverse reinforcement, and axial rigidity on the bond behavior of the specimens. The test results are discussed through consideration of the general behavior, failure modes, load-deflection behavior, crack width measurements, crack patterns, and bond strength.

The bond strength of each corrosion-resistant reinforcing bar was first evaluated and analyzed considering current design recommendations. The bar stress of each test specimen was computed according to Section 12.2.3 of ACI 318 Building Code Requirements for Structural Concrete (2011), Section 4.3 of the ACI Committee 408 Recommendations (2003), Section 5.11.2 of the AASHTO LRFD Bridge Design Specifications (2010), and a behavior model. The achieved bar stress at failure was compared with the computed values. After the test results of the experimental program were analyzed using these methods, the effects of parameters investigated in the experimental program were analyzed. Based on the analysis results, a simple model considering the various corrosion-resistant reinforcing bars with and without transverse reinforcement is proposed.

C.2. GENERAL BEHAVIOR

C.2.1 Flexural and Splitting Cracking

Flexural cracks first occurred over or near the support, the location where the highest moment is produced due to the applied loading condition and self-weight of the beam. All specimens have the same depth and shear span and only vary by width. Therefore, specimens with identical widths in a given series cracked at approximately the same load because the section properties and stiffness of the specimens up to first cracking is primarily controlled by the concrete section.

The number of flexural cracks developed in the constant moment region subsequently increased as loading increased. Due to the fact that reinforcement is effectively twice as much in the splice region, flexural cracks in the splice region appeared when the steel stress was approximately twice the bar stress achieved at the cracking load.

After a certain load was reached, the number of flexural cracks did not increase further, but the existing cracks extended and widened. Cracks in the splice region did not extend down as far as the other cracks outside the splice region because there is twice as much steel in this section of the beam. The steel stress at this stage (when the number of flexural cracks did not increase after a certain load) on average was approximately 80% (40 ksi) of the bar stress at failure for specimens with #5 bars and 70% (30 ksi) of the bar stress at failure for specimens with #8 bars. Of particular note, longitudinal (horizontal) cracks on the side or top surface were first observed during this stage approximately 80% and 70% of the bar stress at failure for specimens with #5 bars and #8 bars, respectively. For specimens with wide bar spacings, long splices, or transverse reinforcement, the bar stress in which all cracks were formed and longitudinal cracks first appeared was approximately 50% of the bar stress at failure.

The longitudinal (horizontal) cracks that were observed either on the side surface or on the top tension face of the beams were observed in all specimens except three specimens with zinc-clad reinforcing bars. These longitudinal cracks parallel to the reinforcing bars are an indication that splitting cracks are forming on the concrete surface, and an early warning that bond failure is approaching. However, the bar stresses when the first longitudinal splitting cracks were observed was about 70-80% of the steel stresses at failure, and bond failure normally occurred after a few additional load steps. For beams with long splices or transverse reinforcement, these splitting cracks initially formed at lower stresses approximately 50% of the steel stresses at failure. Therefore, as loading increased for these beams, the splitting cracks extended further, parallel to the reinforcing bar, or formed branches at the end of splice prior to bond failure as shown in Figure C.1. Splitting cracks were observed primarily on the top tension face (Figure C.2) for the specimens with wide bar spacings and small top cover, while specimens with smaller clear spacings between the bars exhibited splitting cracks on both the side and top surface as shown in Figure C.3.

Flexural cracking was also observed in the shear span. The number of flexural cracks increased as loading increased in a symmetric fashion with respect to the centerline of the beam in both shear spans. The first flexural cracks occurred near the supports and continued toward the loading point as

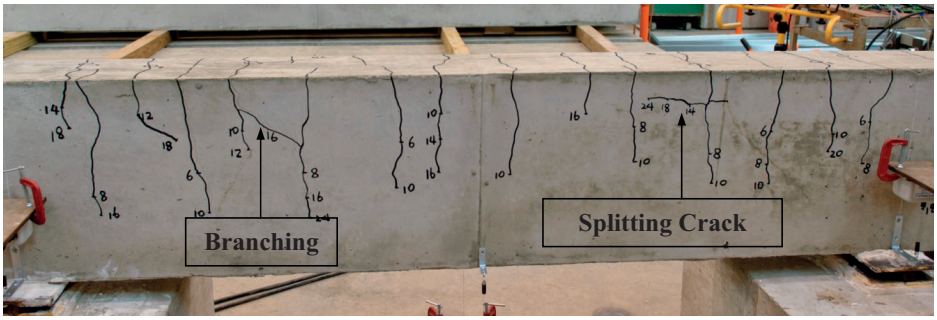

Figure C.1 Splitting crack and branching (M-5-S-36).

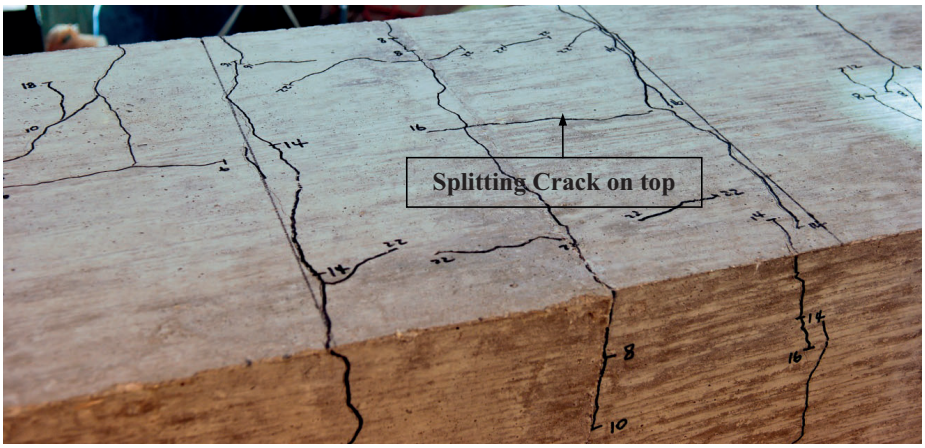

Figure C.2 Splitting crack on top cover (ZC1-6-F-15).

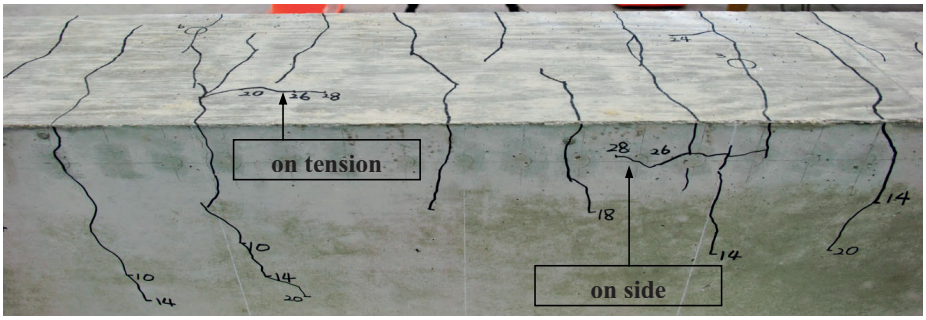

Figure C.3 Splitting crack on both side and top cover (M-7-S-18).

loading increased. These cracks were vertical in the early stages of loading and propagated towards the supports as an inclined shear crack as loading increased (Figure C.4). However, a sufficient number of stirrups were provided in the shear span to prevent shear failure prior to the designed bond failure in the constant moment region. The flexural cracking pattern and the number of primary flexural cracks were symmetric with respect to the centerline of the beam specimen and also resembled the bending moment diagram of the beam as shown in Figure C.4. However, the number of primary flexural cracks varied depending on specimens.

The number of primary cracks at the last load step prior to the bond failure is shown in Figure C.5. The specimen with Duplex 2304 stainless steel bars shown in Figure C.5(b) had a comparable number of cracks as the companion specimen with black bars (Figure C.5(a)). Specimens with epoxy shown in Figure C.5(c) had a similar number of cracks but less than the specimen with black bars. The zinc-clad specimen (Figure C.5(d)) had the least number of primary flexural cracks indicating that there is less bond between the bars and concrete and that stress is not being transferred as efficiently as the specimen with black bars.

C.2.2 Bond Failure

All specimens failed by splitting of the concrete in the splice region. The specimens failed in an explosive, brittle manner as shown in Figure C.6 when the loaded energy was released from the splice region at the time of failure. Three different types of splitting failure modes shown in Figure C.7 were captured using the high-speed camera at the time of failure. The first type was failure by splitting of the cover which initiated from the longitudinal cracks on the side surface as shown in Figure C.7(a). The second type was failure by splitting of the cover which initiated from the top face cracks at the tension face as shown in Figure C.7(b). This failure type occurred in specimens with a wide spacing between bars. The third type was failure by splitting of the cover which initiated

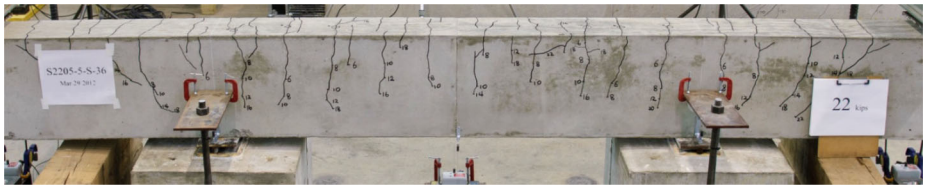

Figure C.4 Crack pattern (S2205-5-S-36).

(a) Black (B-5-S-12)

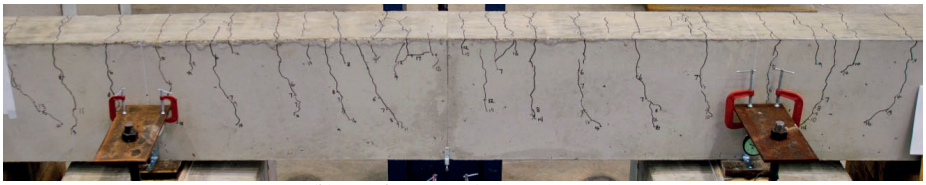

(b) Duplex 2304 (S2304-5-S-12)

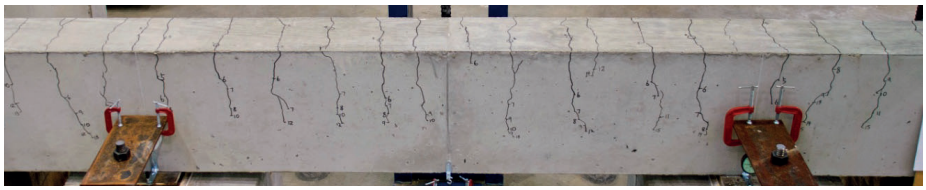

(c) Epoxy (E-5-S-12)

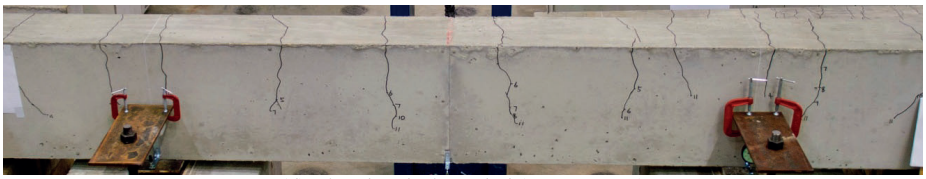

(d) Tin-Plated Zinc-Clad (ZC2-5-S-12)

Figure C.5 Primary flexural cracks prior to bond failure.

from both the top and side splitting cracks as shown in Figure C.7(c). This failure occurred in specimens with long splices or with transverse reinforcement in the splice region. Signs of warning were observed through side splitting or top-face splitting cracks at approximately 50–70% bar stress of failure prior to these bond failures in 42 out of 45 specimens tested.

C.2.3 Appearance After Failure

The splice region of all specimens was carefully investigated after the test was completed. The fragments of the cover from the brittle failure were collected, and the remaining parts of the cover were removed with special care to inspect both the bars and the reassembled concrete cover as shown in Figure C.8.

The concrete cover of each specimen was inspected as shown in Figure C.9 to determine if the as-built dimensions were in good agreement with the designed dimensions. The as-built dimensions are documented in Appendix B.

By inspecting the uncoated bars (stainless steel, black, and MMFX II bars), it was noticed that concrete was well attached to the bar at the deformations indicating good adhesion between the concrete and uncoated bars as shown in Figure C.10 through Figure C.13. The bottom of Figure C.12

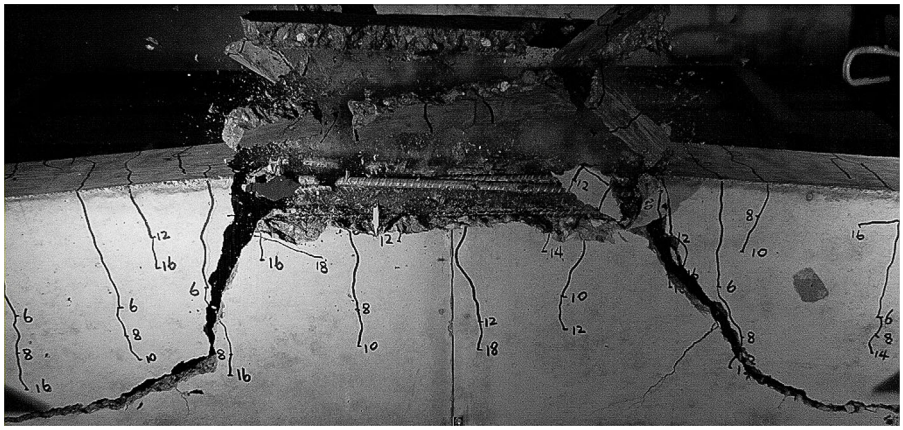

Figure C.6 Explosive splitting failure of unconfined specimens (S2205-5-S-36).

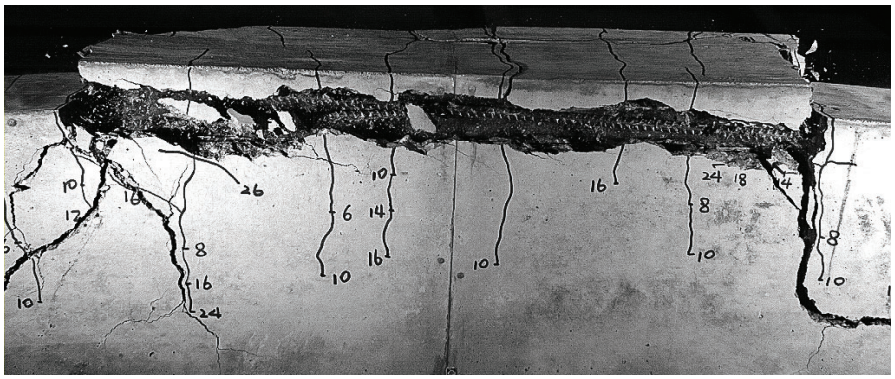

(a) Side Splitting (M-5-S-36)

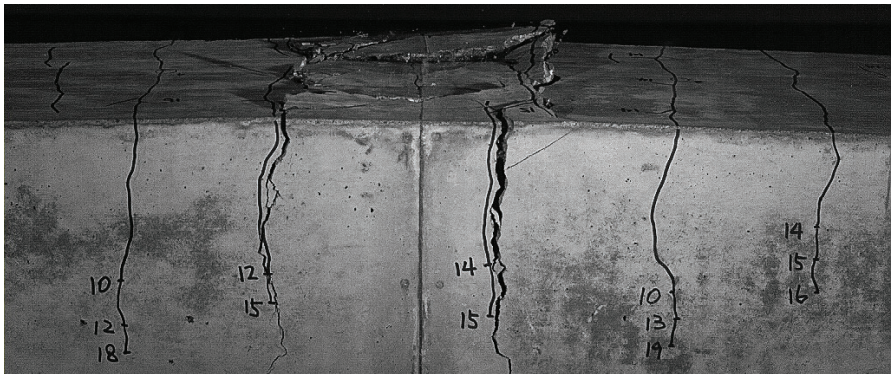

(b) Face Splitting (B-5-F-12)

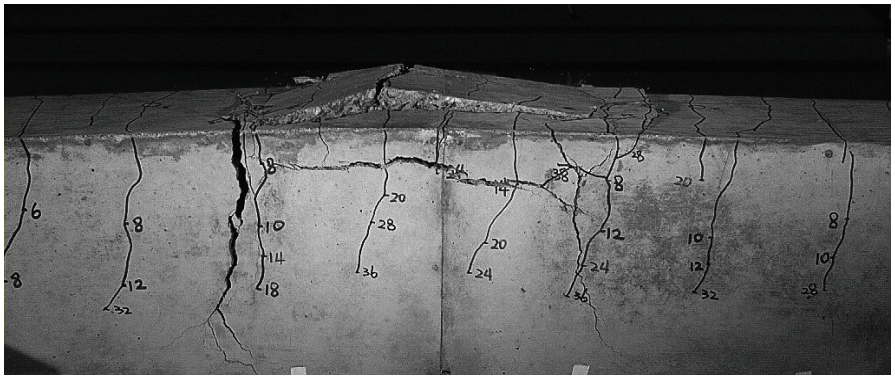

(c) Face and Side Splitting (B-8-S-24-C1)

Figure C.7 Splitting failure modes.

shows crushed concrete on the bar deformations indicating how each bar was being pulled inside the concrete. For the MMFX II bars shown in Figure C.13, it was noticed that there were several spots where the black mill scale of MMFX II bar was removed and attached to the concrete cover.

Upon removal of the cover from the coated bars, it was noticed that less concrete was adhering to the bar as shown in Figure C.14. Of particular note, concrete was attached to the bars more at the cut ends that was patched with epoxy touch-up paint as shown for Zbar.

Figure C.8 Reassembled concrete cover (specimen M-5-S-36).

(a) Top Cover (1.5 in.)

(b) Bar Clear Spacing (1.0 in.)

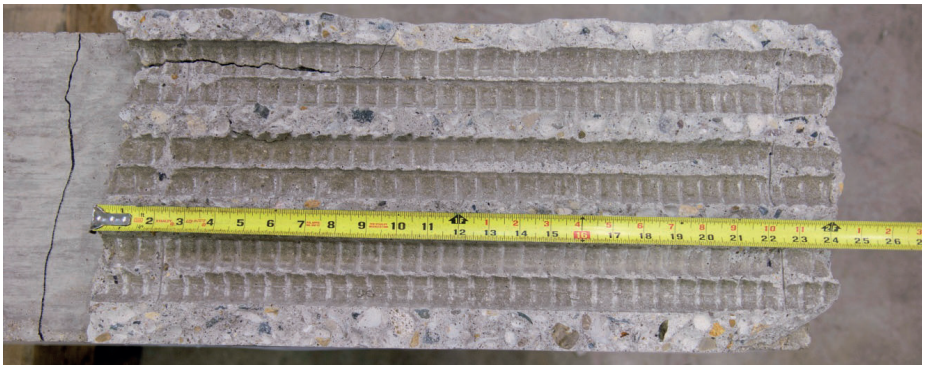

(c) Splice Length (24 in.)

Figure C.9 As-built dimension check.

Figure C.10 Adhesion of concrete to Duplex 2304 stainless steel bars.

Figure C.11 Adhesion of concrete to XM-28 stainless steel bars.

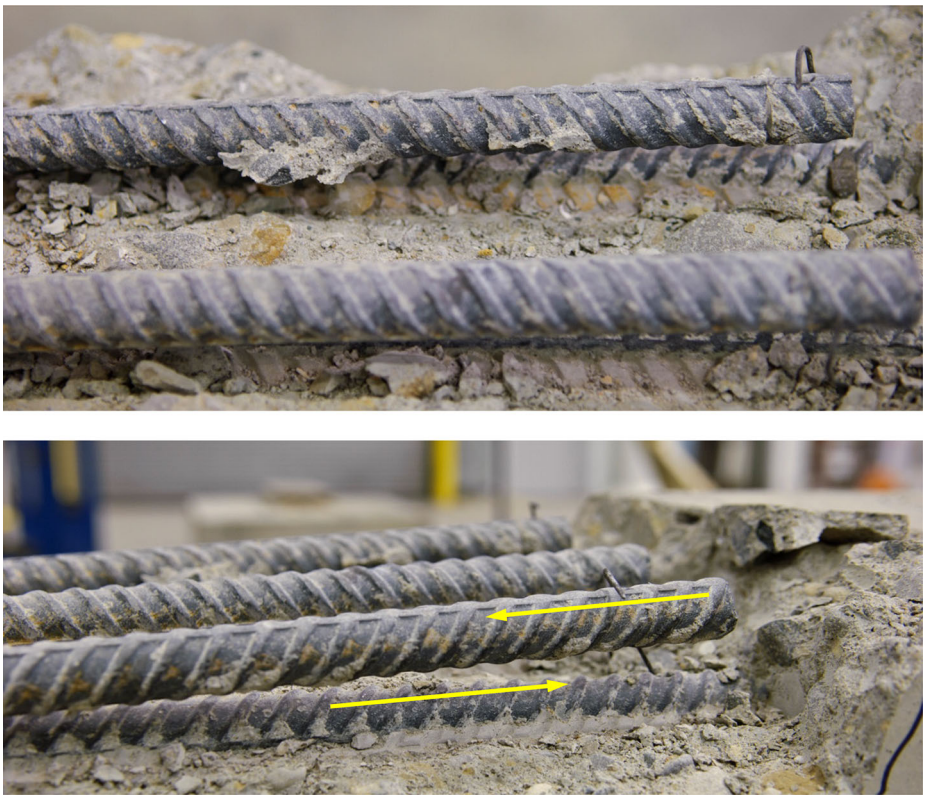

Figure C.12 Adhesion of concrete to black bars.

By removing the cover from the zinc-clad bars, poor adhesion with the concrete was noted. For the un-plated zinc-clad bars, the concrete cover which was in contact with the bars was greenish in color as shown in Figure C.15(b) and Figure C.16(a). More air voids were observed in the concrete that was in contact with the zinc-clad bars. It appears that a chemical reaction occurred between the zinc and concrete during hydration. It is known that during the initial stages of curing, concrete is in a high alkaline stage and can react with zinc to form hydroxyl ions and form zinc oxide and hydrogen gas (Macias & Andrade, 1990).

Zinc oxide reacts with calcium ions to form calcium hydrozincate, $Ca(Zn(OH)_3)_2{\cdot}2H_2O$ which results in poor bond between zinc coated reinforcement and concrete as discussed earlier in Section 2.2.1.2 (Macias & Andrade, 1990). Tin-plated zinc-clad bars were also provided from the manufacturer to eliminate this reaction. It was observed that more zinc (silver color) was remaining on the bar for the tin-plated zinc-clad bars and the discoloration of the concrete air voids did not occur as shown in Figure C.16(b). However, as shown in Figure C.17, only minimal concrete was attached to the rebar indicating poor bond between the tin-plated zinc-clad bars and concrete.

A similar appearance was observed on the concrete covers removed from hot-dip galvanized bars as from the un-plated zinc-clad bars. Figure C.18 indicates that zinc on the hot-dip galvanized bars reacted as the un-plated zinc-clad bars reacted with the concrete during the hydration process. Due to the fact that the coating thickness is significantly thinner for hot-dip galvanized bars (less than 5 mils), only a small amount of zinc was remaining when the concrete cover was removed. The bars looked similar to conventional black bars rather than galvanized bars.

C.3. TEST RESULTS

The results of the bond tests are given in Table C.1. The maximum applied load at the ends of the beam (P_{max}) and corresponding reinforcing steel stress (f_{su}) achieved for each test specimen is provided. Compressive concrete strength (f'_c), splice length (l_s), side cover (c_{so}), half of clear spacing (c_{si}), and bottom cover (c_b) are provided for the ease of comparison.

All calculations were based on the design cross-sectional dimensions. The steel stresses presented in Table C.1 were calculated using moment-curvature analysis based on the load achieved during testing. The concrete stress-strain relationship was represented using the Hognestad (1951) stress-strain curve while the reinforcing steel stress-strain relationship was based on measured values. The actual stress-strain data of the steel reinforcement was used to account for the fact that some reinforcing material (stainless steel bars and high-strength MMFX II bar) do not have a distinct modulus. Reinforcing bar stresses at failure calculated using cracked section analysis were approximately the same as those computed using moment-curvature analysis only for the reinforcing material that behaves linearly elastic up to yield strength (black, epoxy, galvanized, zinc-clad, and Zbar). Values from both analyses were slightly different for specimens with reinforcing materials that have a round-

Figure C.13 Exposed MMFX II bars and concrete cover.

house stress-strain relationship or specimens that were tested to high stress levels. For instance, specimens in Series V reached high stress levels (Specimen M-5-S-48 reached a stress of 105 ksi) and the bar stresses computed from both analyses had difference ranging from 0.5 to 1.7 ksi. Therefore, bar stresses from moment-curvature analysis are used to report the test results for bars that behave nonlinearly.

C.3.1 Load-Deflection Behavior

The stiffness of beams containing different reinforcing steel is compared to that of the specimens with black bars to investigate whether the reinforcing material influences the load-deflection behavior. The average load applied to each end measured from calibrated load cells and the average end deflection values obtained from string potentiometer measurements are used to plot the load-deflection curves. Figure C.19 and Figure C.20 show the load-deflection response of the specimens tested in Series II with #5 stainless-steel bars and #5 coated bars relative to the companion beams with black bars. Up to cracking, the stiffness of the specimens is primarily controlled by concrete, and the behavior is elastic. Therefore, the load-deflection curves are linear, and the slope of the curves are approximately identical. As evident from both figures, the flexural cracking load was also not influenced by the type of reinforcement. No change was

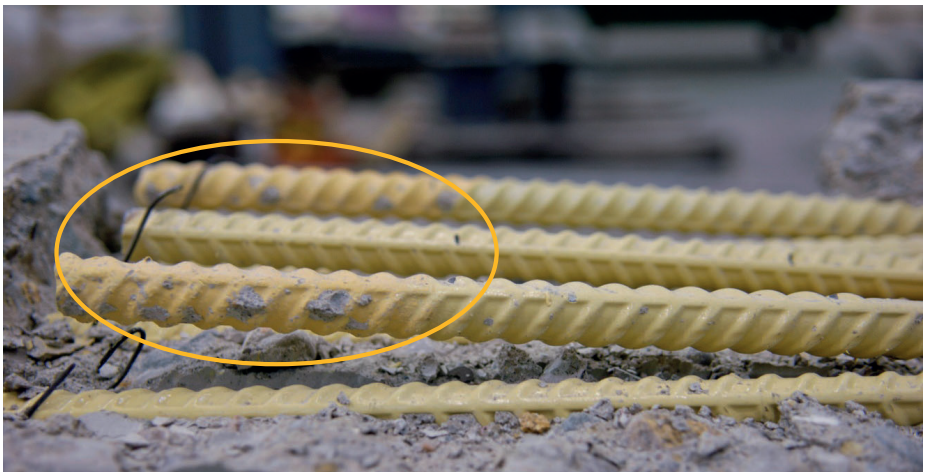

Figure C.14 Adhesion of concrete to dual coated Zbars.

expected because the cracking load is primarily influenced by concrete strength, geometric section, and shear span. This overall behavior also demonstrates that the concrete strength in companion specimens was essentially identical.

The slope of the load-deflection curve changes after cracking where the stiffness of the structure is governed primarily by the reinforcement. Although the stiffness changes after cracking, the behavior remains approximately linear up to yielding. In this stage, specimens with Duplex 2205 and Duplex 2304 bars demonstrated a lower beam stiffness as shown in Figure C.19. The modulus of elasticity of these beams is lower (shown in Table 2.3) which explains this behavior. As shown in Figure C.20, no difference in stiffness was observed between coated bars and companion black specimen.

The specimens followed the post-cracking stiffness up to failure. All specimens failed in a brittle mode by splitting of the concrete in the splice region. It is clearly evident that coated reinforcing bars reached lower loads than that of the companion black bar specimen, while duplex stainless steel bars reached failure loads comparable to the black bar specimen.

The same overall observations were made for specimens tested with #8 bars (Series III) as shown in Figure C.21 and Figure C.22. First cracking was not influenced by the type of reinforcement, and the stiffness of the specimens reduce after cracking. Similarly, the stiffness of the specimens with duplex stainless steels were lower than that of the other specimens. However, in all cases, the #8 stainless steel bars reached higher failure loads than that of the black bar. In addition, galvanized

(a) Black Bar (B-6-S-15) (b) Un-plated Zinc-Clad Bar (ZC1-6-S-15)

Figure C.15 Concrete covers removed after lap-splice test.

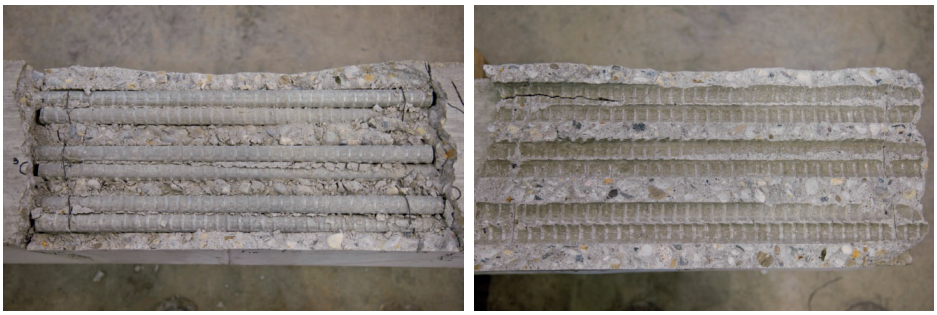

(a) Un-plated Zinc-Clad Bar (ZC1-8-S-24)

(b) Tin-plated Zinc-Clad Bar (ZC2-8-S-24)

Figure C.16 Concrete covers removed from zinc-clad bars.

and Zbar had comparable bond strength to black bar while other coated bars had lower strength (Figure C.22).

The load-deflection response of specimens with confinement in the splice region is shown in Figure C.23. There is no difference in stiffness as expected. Failure was sudden and brittle in all specimens. The results demonstrate that when confinement is concentrated in the center of the splice (M-8-S-48-C2), the failure loads are similar to the companion specimen with no splice. When the confinement was located at the ends (M-8-S-48-C1) still having the identical amount of transverse reinforcement as M-8-S-48-C2, the failure load increased approximately 30% compared to specimen without confinement. In addition, when the confinement was located at the ends, identical to M-8-S-48-C1, but with additional transverse reinforcement in the center of splice (M-8-S-48-C3), the failure load was comparable. These results indicate that providing transverse reinforcement in the center of the long splice is not an effective method of increasing bond strength.

C.3.2 Crack Widths

Crack widths of beams associated with each type of reinforcement were compared by plotting the bar stress versus the average and maximum crack widths in the constant moment region. The calculation of reinforcing bar stress was based on the load measured at the time the crack widths were measured using moment-curvature analysis. Both the Hognestad concrete stress-strain curve and the actual reinforcing steel stress-strain relationship were used. Crack widths were measured using the Edmund Direct Measuring 50X pocket microscope that allows crack measurement within an accuracy of 1/1000 of an inch. Crack widths were measured, and photographs were taken

Figure C.17 Concrete attached to tin-plated zinc-clad bars (ZC2-8-S-24).

(a) Hot-Dip Galvanized Bars (G-8-S-24)

(b) Concrete Cover Removed from Hot-Dip Galvanized Bars

Figure C.18 Appearance after failure of hot-dip galvanized bars.

to record the crack patterns at each load step until it was considered unsafe to approach the beam. Crack width measurements and crack patterns for each specimen are reported in Appendix B. Crack widths were measured on the top surface of the beam only in the constant moment region outside the splice zone. Crack widths were measured at the same location for each selected crack. Cracks that are in the shear span, over the support, at the ends of the splice region, and in the splice region were not included considering that the bar stress in the shear span is not constant, the cracks over the support or at the ends of splice region are affected by the configuration of the test setup, and crack widths measured in the splice region are significantly smaller because there is twice amount of reinforcement in this region. Average and maximum crack widths for selected cracks in the constant moment region were plotted against the calculated bar stress in the constant moment region and presented in Figure C.24 through Figure C.28.

For the #5 bar, specimens with stainless steel bars (Figure C.24), the crack widths are comparable to those of the black bar specimen at a given stress level. In addition, although, specimens with Duplex 2205 stainless steel had larger crack widths around 30-40 ksi, during most of the other stress levels, the crack widths were comparable with the black specimen. The curves obtained from specimens with coated reinforcement, however, are remarkably different from the curves of the black specimen as shown in Figure C.25. At a given stress level, specimens with tin-plated zinc-clad bars (Zinc-clad 2) had average and maximum crack widths significantly larger than the black bar. In fact, all coated bars other than the galvanized showed increased crack width indicating decreased bond.

For the #8 bars, specimens with stainless steel bars (Figure C.26) showed comparable crack widths with black specimens. At stresses over 25 ksi, specimens with MMFX II and XM28 stainless steel bars actually produced smaller crack widths than the companion black specimen. For the coated reinforcement (Figure C.27), there was less scatter in the average and maximum crack widths for galvanized, epoxy, and Zbar with #8 bars relative to the #5 bars (Figure C.25). The epoxy-coated, Zbar, and galvanized bars performed similarly to black bars. However, zinc-clad bars produced significantly larger crack widths compared to that of black bar at the same stress level clearly indicating less bond.

Specimens with wide bar spacings and small cover also showed similar results (Figure C.28). The average crack width at 40 ksi for specimens with tin-plated zinc-clad bars (Zinc-clad2) was twice that of the black bars. Considering average and maximum crack widths, side-splitting and top-face splitting failure beams, and #5 and #8 bars, it is evident that larger crack widths were observed with zinc-clad bar specimens indicating that the bars do not bond as well as the companion black bar specimens or any of the other bars for that matter.

C.3.3 Bond Strength

The bond strength for the specimens from each series is presented in Table C.2. The strengths were determined by

TABLE C.1
Bond Test Results

Series	Specimen	f'_c (psi)	l_s (in.)	c_{so} (in.)	c_{si} (in.)	c_b (in.)	P_{max} (kips)	f_{su} (ksi)
I	B-6-S-15	5,180	15	1.5	0.5	1.5	22.4	48.3
	ZC1-6-S-15	5,180	15	1.5	0.5	1.5	17.0	36.6
	B-6-F-15	5,180	15	2.375	2.375	1.0	26.1	52.8
	ZC1-6-F-15	5,180	15	2.375	2.375	1.0	22.1	44.5
II	B-5-S-12	4,650	12	1.5	0.5	1.5	18.1	55.5
	E-5-S-12	4,650	12	1.5	0.5	1.5	16.2	49.6
	G-5-S-12	4,650	12	1.5	0.5	1.5	16.7	50.9
	ZC1-5-S-12	3,990	12	1.5	0.5	1.5	15.1	46.4
	ZC2-5-S-12	4,650	12	1.5	0.5	1.5	12.2	37.6
	Z-5-S-12	4,650	12	1.5	0.5	1.5	16.9	51.9
	M-5-S-12	4,400	12	1.5	0.5	1.5	18.1	55.6
	S316LN-5-S-12	4,650	12	1.5	0.5	1.5	16.9	51.5
	S2205-5-S-12	4,650	12	1.5	0.5	1.5	17.8	54.1
	S2304-5-S-12	4,650	12	1.5	0.5	1.5	17.9	54.7
	SXM28-5-S-12	4,650	12	1.5	0.5	1.5	17.0	51.8
III	B-8-S-24	3,990	24	1.5	0.5	1.5	34.0	44.2
	E-8-S-24	3,990	24	1.5	0.5	1.5	30.1	38.9
	G-8-S-24	3,990	24	1.5	0.5	1.5	33.9	43.9
	ZC1-8-S-24	3,990	24	1.5	0.5	1.5	29.1	37.6
	ZC2-8-S-24	3,990	24	1.5	0.5	1.5	26.1	33.8
	Z-8-S-24	3,990	24	1.5	0.5	1.5	33.8	43.8
	M-8-S-24	3,990	24	1.5	0.5	1.5	40.2	52.7
	S316LN-8-S-24	3,990	24	1.5	0.5	1.5	36.7	47.5
	S2205-8-S-24	3,990	24	1.5	0.5	1.5	35.5	45.3
	S2304-8-S-24	3,990	24	1.5	0.5	1.5	35.7	45.9
	SXM28-8-S-24	3,990	24	1.5	0.5	1.5	34.1	44.5
IV	B-5-F-12	4,400	12	2.375	2.375	0.75	21.6	61.0
	ZC2-5-F-12	4,400	12	2.375	2.375	0.75	17.2	54.6
	Z-5-F-12	4,400	12	2.375	2.375	0.75	19.1	53.8
	S2205-5-F-12	4,400	12	2.375	2.375	0.75	21.9	61.4
	B-8-S-24-C1	4,400	24	1.5	0.5	1.5	39.7	51.5
	B-8-S-24-C2	4,400	24	1.5	0.5	1.5	37.7	48.7
	B-8-S-24-C3	4,400	24	1.5	0.5	1.5	41.8	54.3
	M-5-S-24	4,400	24	1.5	0.5	1.5	25.5	78.6
	M-5-S-36	4,400	36	1.5	0.5	1.5	29.1	89.7
	S2205-5-S-24	4,400	24	1.5	0.5	1.5	23.6	71.7
	S2205-5-S-36	4,400	36	1.5	0.5	1.5	27.4	83.3
IV	M-5-S-48	5,400	48	1.5	0.5	1.5	34.3	104.5
	M-7-S-24	5,400	24	1.5	0.5	1.5	40.8	66.3
	M-7-S-18	5,400	36	1.5	0.5	1.5	32.2	52.1
	M-8-S-48	5,400	18	1.5	0.5	1.5	58.6	74.7
	M-11-S-24	5,400	48	1.5	0.5	1.5	53.5	35.6
	M-8-S-48-C1	5,400	48	1.5	0.5	1.5	73.5	97.1
	M-8-S-48-C2	5,400	48	1.5	0.5	1.5	60.1	76.6
	M-8-S-48-C3	5,400	48	1.5	0.5	1.5	75.2	97.0

Notation:
f'_c = *concrete cylinder strength (psi).*
l_s = *splice length (in.).*
c_{so} = *side cover (in.)* c_{si} = *half of clear spacing (in.)* c_b = *bottom cover (in.).*
P_{max} = *load at failure (kips).*
f_{su} = *bar stress is calculated based on moment curvature analysis (ksi).*

calculating the average bond stress (Equation (C.1)) with the assumption that the tension force in the bar is resisted by a uniform distribution of stress along the surface of the splice length. The nominal bar diameter and design dimensions were used in all calculations.

$$u_{avg} = \frac{f_s \cdot d_b}{4 l_s} \tag{C.1}$$

where:

u_{avg} = *average bond stress, bond strength (psi)*
f_s = *bar stress (psi)*
d_b = *nominal diameter of bar (in.)*
l_s = *splice length (in.)*

The bond ratio presented in Table C.2 represents the ratio of bond stress for the specimen in comparison to the bond stress of the control specimen (black bar) within that series (control specimens noted in shaded rows). From comparison of the bond stresses between various reinforcing materials, it is evident that zinc-clad bars had the lowest bond strength regardless of bar size. On average, tin-plated zinc-clad bars had 26% less, un-plated zinc-clad bars had 18% less, epoxy-coated had 11% less, Zbars had 6% less, and galvanized bars had 4% less bond strength than black bars. Stainless steel bars or MMFX II reinforcing steel had comparable or greater bond strength than black bar. In addition, bond strength increased when confinement was provided at the splice ends while it decreased as the splice length was increased.

C.4. DATA ANALYSIS

C.4.1 Bond Strength

C.4.1.1 ACI 318 design provisions. Design for bond anchorage was based on a limiting bond stress of 800 psi until a development length equation was first adopted in ACI 318-71. The first version of the code development length equation was:

$$l_d = 0.04 \frac{a_b f_y}{\sqrt{f'_c}} \tag{C.2}$$

where:

l_d = *development length of reinforcement (in.)*
a_b = *cross-sectional area of reinforcing bar (in.^{2})*
f_y = *specified yield stress of reinforcement (psi)*
f'_c = *specified compressive strength of concrete (psi)*

The equation consisted of the area of the reinforcing bar in tension, the specified yield strength of the reinforcement, and the specified compressive strength of the concrete. The equation was designed so that the calculated development length achieves a stress 25% higher than the yield strength of the reinforcement to ensure ductility.

Revisions to the ACI 318-71 design equation for development length were made in the 1989 design provisions to include the various factors that influence bond strength. The ACI 318-89 design expression was based on a study conducted by Orangun, Jirsa, and Breen (1975, 1977). Orangun et al. (1975) collected 116 lap-splice beam test results and evaluated the factors that influence bond

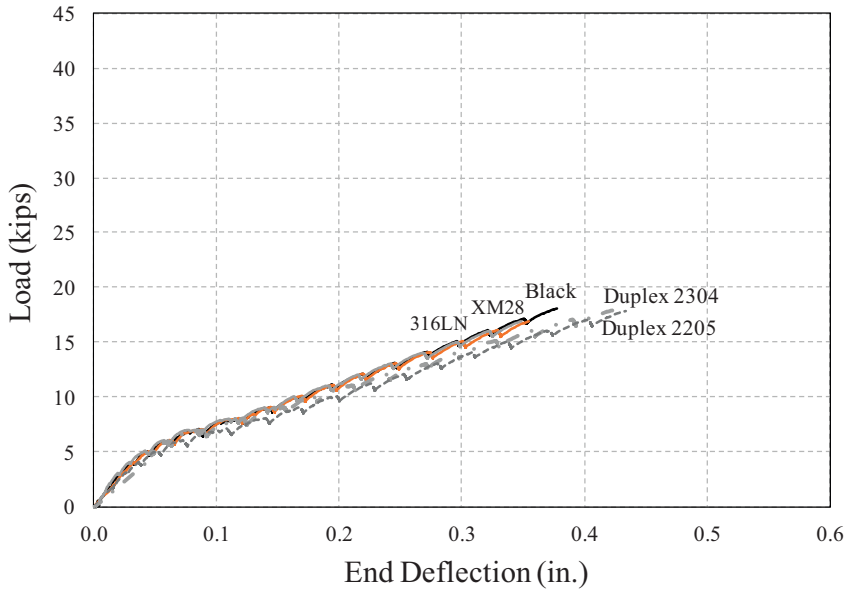

Figure C.19 Load-deflection response of stainless-steel bars (#5 bars).

strength. The effect of splice length, concrete cover, bar diameter, concrete strength, and transverse reinforcement on the strength of the anchored or developed bar were considered in this study. As a result, the expression shown in Equation (C.3), a measure of the average bond stress over the splice length, was derived from a nonlinear regression analysis of the beam splice test results.

$$\frac{u}{\sqrt{f'_c}} = 1.2 + \frac{3C}{d_b} + \frac{50d_b}{l_d} + \frac{A_{tr}f_{yt}}{500sd_b} \qquad \text{(C.3)}$$

where:

u = *average bond stress, psi*
f'_c = *concrete cylinder strength (psi)*
C = *the smaller of clear bottom cover to main reinforcement and half clear spacing between bars or splices (in.)*
d_b = *nominal diameter of bar (in.)*
l_d = *development or splice length (in.)*
A_{tr} = *area of transverse reinforcement normal to the plane of splitting (in.^{2})*
f_{yt} = *yield strength of transverse reinforcement (psi)*
s = *spacing of transverse reinforcement, center-to-center (in.)*

Plugging in the average bond stress (Equation (C.1)) to this expression and re-organizing Equation (C.3) as the ratio of the development length to the diameter of the bar (l_d/d_b)

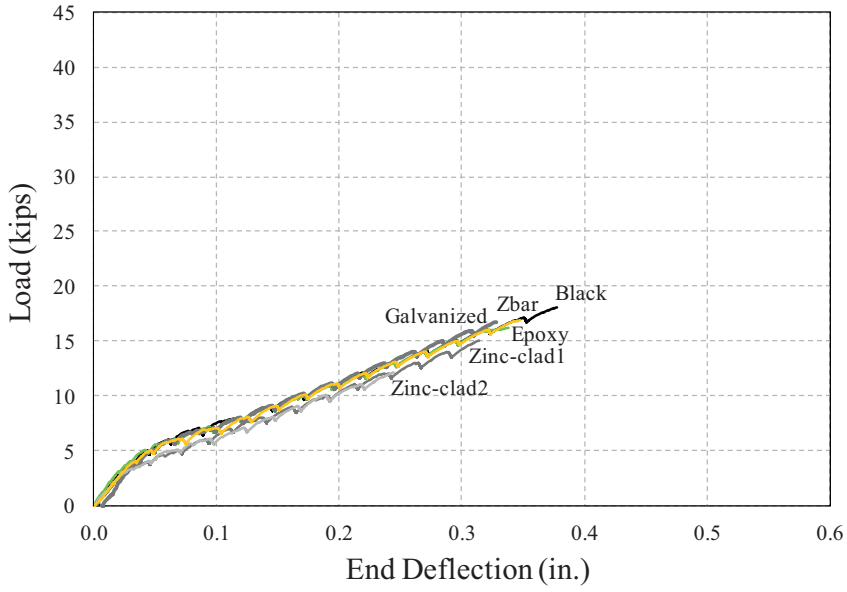

Figure C.20 Load-deflection response of coated bars (#5 bars).

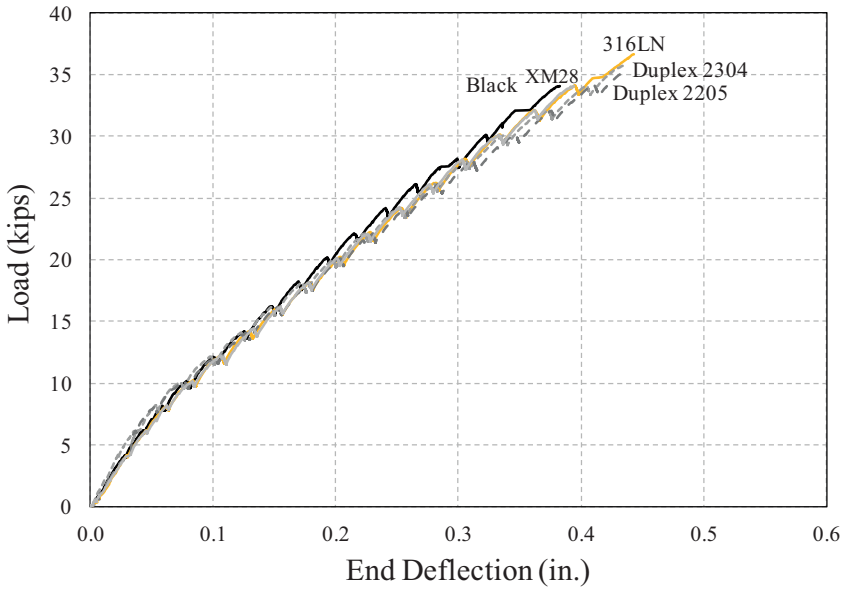

Figure C.21 Load-deflection response of stainless-steel bars (#8 bars).

results in the following equations:

$$\begin{aligned}\frac{l_d}{d_b} &= \frac{\frac{f_s}{4\sqrt{f'_c}} - 50}{\left(1.2 + \frac{3C}{d_b} + \frac{A_{tr}f_{yt}}{500sd_b}\right)} \\ &= \frac{f_s - 200\sqrt{f'_c}}{4\sqrt{f'_c}\left(1.2 + \frac{3C}{d_b} + \frac{A_{tr}f_{yt}}{500sd_b}\right)} \\ &= \frac{f_s - 200\sqrt{f'_c}}{12\sqrt{f'_c}\left(0.4 + \frac{C}{d_b} + \frac{A_{tr}f_{yt}}{1500sd_b}\right)} \\ &= \frac{\frac{f_s}{12\sqrt{f'_c}}\left(1 - \frac{200\sqrt{f'_c}}{f_s}\right)}{\frac{1}{d_b}(0.4d_b + C + K_{tr})}\end{aligned} \tag{C.4}$$

where:

$$K_{tr} = \frac{A_{tr}f_{yt}}{1500sn} \tag{C.4}$$

By substituting $f'_c = 3000$ psi, and $f_s = 60,000$ psi (values from Orangun et al., 1977) for the terms in the parentheses of numerator in Equation (C.4) and using the yield strength of the reinforcing bars, f_y to fully develop the bar gives the following expression:

$$\frac{l_d}{d_b} = \frac{0.068\frac{f_y}{\sqrt{f'_c}}}{\frac{1}{d_b}(0.4d_b + C + K_{tr})} \tag{C.5}$$

Considering that the cover to the center of bar, $c_c = C + 0.5d_b$, the term $0.4d_b + C$ can be approximated as c_c resulting in:

$$\frac{l_d}{d_b} = \frac{0.068\frac{f_y}{\sqrt{f'_c}}}{\frac{1}{d_b}(c_c + K_{tr})} \tag{C.6}$$

To account for deviations in material properties, dimensional errors, and the uncertainty involved in calculation, Orangun et al. (1977) suggested that Equation (C.6) divided by a capacity reduction factor of 0.8 (factor of safety = 1.25).

$$\frac{l_d}{d_b} = 0.085\frac{f_y}{\sqrt{f'_c}}\frac{1}{\left(\frac{c_c + K_{tr}}{d_b}\right)} \tag{C.7}$$

To be conservative, multiplying Equation (C.7) by $\phi = 0.9$ used in flexure gives:

$$\frac{l_d}{d_b} = 0.0765\frac{f_y}{\sqrt{f'_c}}\frac{1}{\left(\frac{c_c + K_{tr}}{d_b}\right)} \tag{C.8}$$

Based on Equation (C.8), the current development length equation used in the ACI 318-11 building code is given as the following expression:

$$\frac{l_d}{d_b} = \frac{3}{40}\frac{f_y}{\lambda\sqrt{f'_c}}\frac{\psi_t\psi_e\psi_s}{\left(\frac{c_b + K_{tr}}{d_b}\right)} \tag{C.9}$$

where:

l_d = *development length in tension of deformed bar (in.)*
d_b = *nominal diameter of bar (in.)*
f_y = *specified yield strength of reinforcement (psi)*
λ = *modification factor for lightweight concrete*
f'_c = *specified compressive strength of concrete (psi)*
ψ_t = reinforcement location factor
ψ_e = reinforcement coating factor

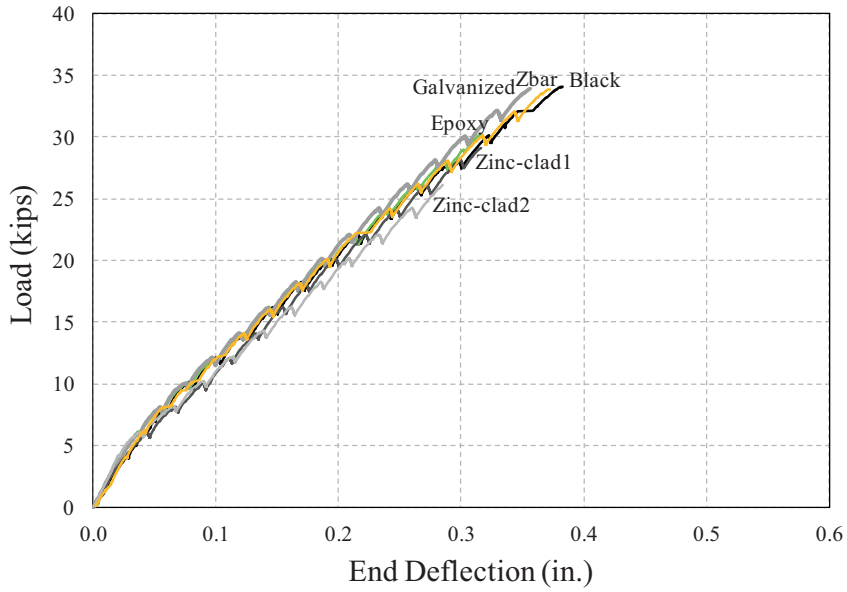

Figure C.22 Load-deflection response of coated bars (#8 bars).

ψ_s = reinforcement size factor
c_b = *smaller of (a) the distance from center of a bar to nearest concrete surface, and (b) one-half the center-to-center spacing of bars being developed (in.)*
K_{tr} = *transverse reinforcement index* = $\frac{40A_{tr}}{s \cdot n}$ *(Note: based on* f_{yt} *= 60,000 psi plugged into* K_{tr} *in page 137)*
A_{tr} = *total cross-section area of all transverse reinforcement within spacing s that crosses the potential plane of splitting (in.*^{2}*)*
s = *center-to-center spacing of transverse reinforcement (in.)*
n = *number of bars being spliced or developed along the plane of splitting*

To ensure the bond failure mode is controlled by splitting, $(c + K_{tr})/d_b$ should not be taken greater than 2.5. In addition, the value of $\sqrt{f'_c}$ is limited to 100 psi due to the lack of data on test specimens with concrete compressive strength in excess of 10,000 psi. Modification factors are added to the design equation to account for bar location ψ_t, bar coating ψ_e, bar size ψ_s, and lightweight concrete λ.

Because the ACI-318 design equation is derived from a limited amount of test data and is an empirical expression, it is important to point out that the equation may not reflect actual bond behavior and should be used with caution beyond the limits of the variables included in the supporting research. For example, the ACI 318-11 equation is limited by code to f_y = 80ksi. Therefore, it may not be applicable for the high-strength steel used in this test program (MMFX II and

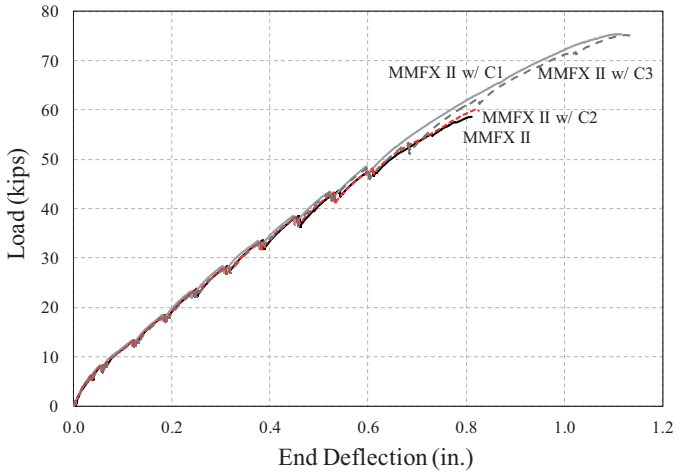

Figure C.23 Load-deflection response of beams with confinement (#8 bars).

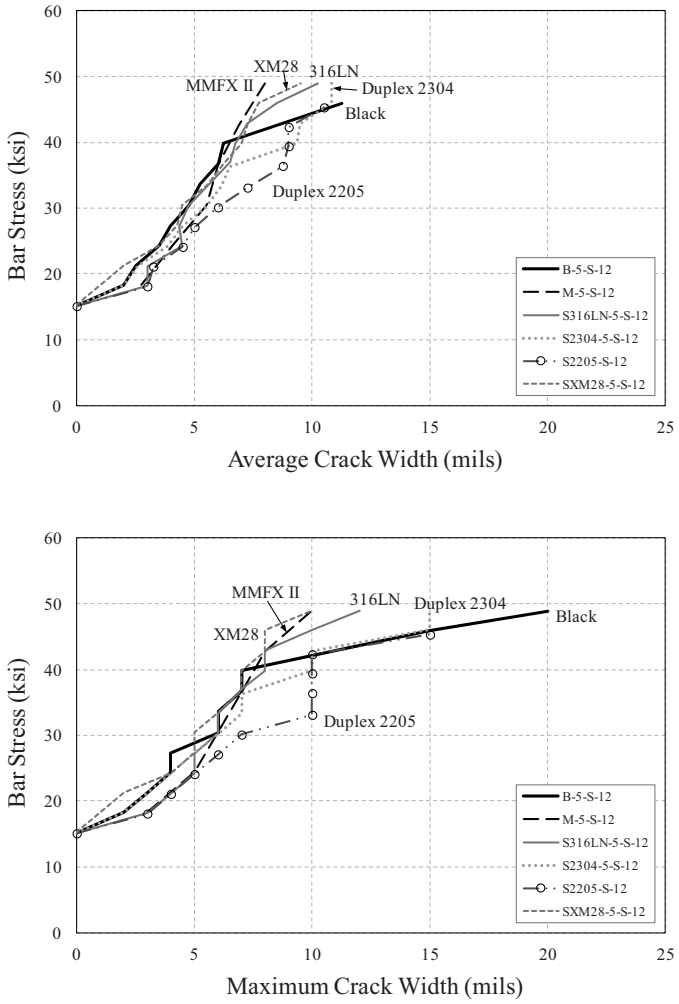

Figure C.24 Bar stress vs. crack width (#5 bars, stainless-steel and MMFX II).

stainless-steel reinforcement). However, to evaluate the performance of the equation through the full range of variables, these limits were neglected in this analysis. The purpose of this analysis is to investigate results outside of this range.

The test data were analyzed using the ACI 318-11 design equation to compare how the bond strength developed from the various corrosion-resistant reinforcing bars vary from the calculated strength. It should be noted that the database from which Equation (C.9) was developed includes only uncoated mild steel bars. The ratio of measured to calculated bar stresses at failure is presented in Figure C.29 through Figure C.34. The calculated values were obtained by solving Equation (C.9) with the design splice length, design cover dimensions, nominal bar diameter, and average concrete compressive strength for each series while considering the bar size (ψ_s = 0.8 for #6 and smaller bars), and bar coating (ψ_e = 1.5 for epoxy-coated, and zinc and epoxy dual coated Zbars) through the modification factors. The transverse reinforcement index, K_{tr} was also used for specimens with confinement in the splice region.

The ACI 318-11 development length equation yielded conservative bond strengths for all specimens with #5 bars (12 in. splice) and #8 bars (24 in. splice) shown as in Figure C.29. Considering that the test/calculated ratio was close to 2.0 for both the #5 and #8 black bars (dashed line provided to illustrate relative values), the tin-plated zinc-clad bar specimen (#5 bar) was the only type of bar that stands out with a test to calculated ratio of 1.3. Excluding the tin-plated zinc-clad bars, the test/calculated ratio is conservative between 1.9 to 3.3 with an average of 2.2. Epoxy-coated and dual-coated bars had the highest ratio which resulted from the use of the epoxy multiplication factor.

It is interesting to note that for wider beams (larger bar spacing but less cover, Figure C.30), the test/calculated ratio drops compared to that for narrower beams with less bar spacing between the bars. Figure C.30 presents both cases where the narrower beams are noted as side split and the wider beams are noted as face split. This drop occurred in all specimens except for ZC2 which has the lowest bond strength. On average, the test/calculated ratio was 1.5.

The level of conservatism drops further as the splice length increases (Figure C.31). Because the equation derived from regression analysis included only a limited amount of data with long splices, the equation may not be a reflection of the actual

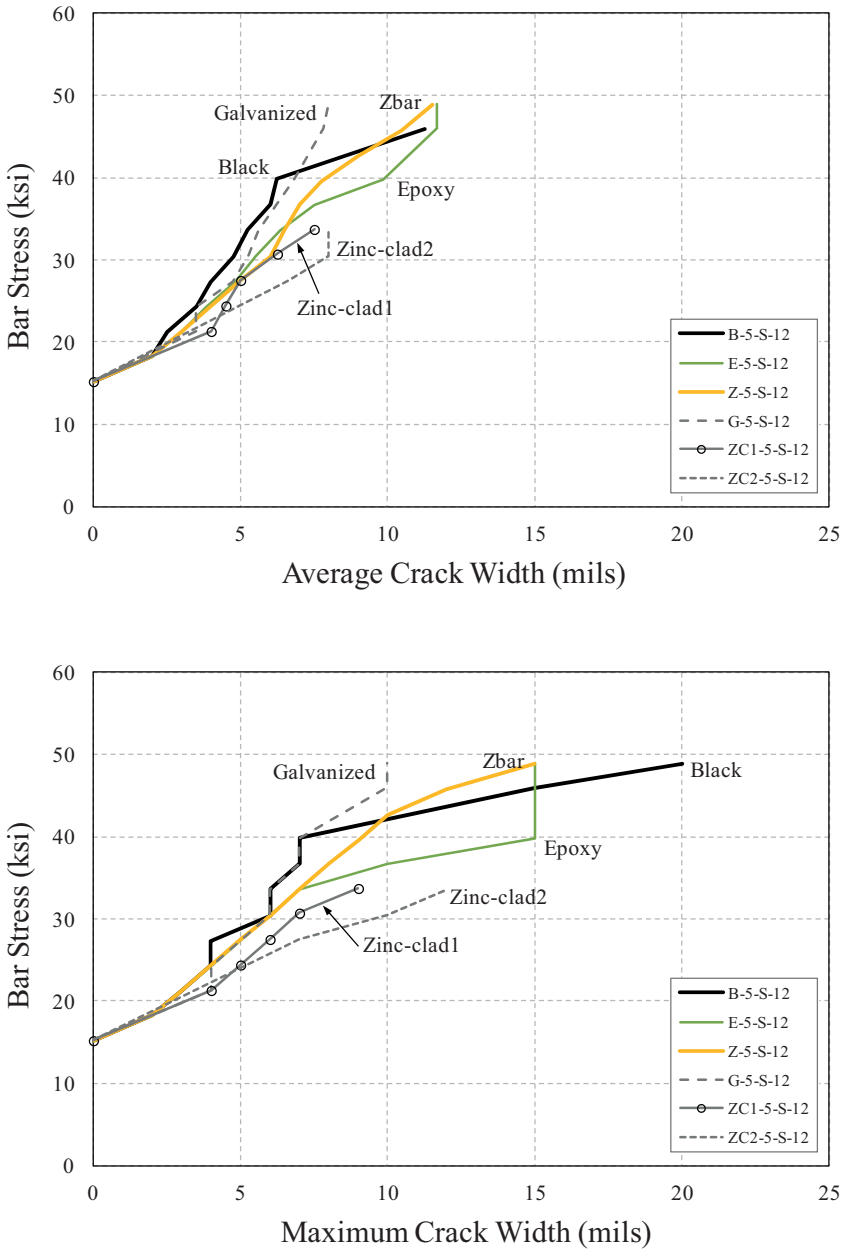

Figure C.25 Bar stress vs. crack width (#5 bars, coated reinforcement).

bond behavior for long splices. The test to calculated ratio for long splices on average was 1.3 considering long splices as lengths equal to or greater than $40d_b$. When the splice length of #5 MMFX II bar increased to 48 in. ($77d_b$), the equation provided unconservative results (test/calculated ratio ≤ 1).

The specimens that included confinement were also not calculated with the same conservatism as observed for the splices with no confinement (Figure C.32). The test to calculated ratio dropped in most cases except for one specimen (M-8-S-48-C1). It should be noted that this specimen reached a bond strength comparable to M-8-S-48-C3 which had additional confinement in the center of splice. Although, the ACI 318-11 calculates a higher bond strength with additional transverse reinforcement, the two arrangements C1 and C3 reached the same bar stress. While ACI 318-11 calculates a higher bond strength with arrangement C2 than the case with no confinement, the bar stress reached at failure was comparable for Specimen M-8-S-48-C2 and M-8-S-48 (no confinement). This result indicates that providing transverse reinforcement in the center of splice region is not effective which is in disagreement with the design expression.

Specimens with identical bar axial rigidity were compared in Figure C.33. The bond force obtained from testing is shown in Figure C.33(a) while the test to calculated ratio is presented in Figure C.33(b). Although, the difference in force is not substantial (Figure C.33(a)), the ratio of bond force tested to that calculated for each specimen is significantly different (Figure C.33(b)). As discussed earlier, the level of conserva-

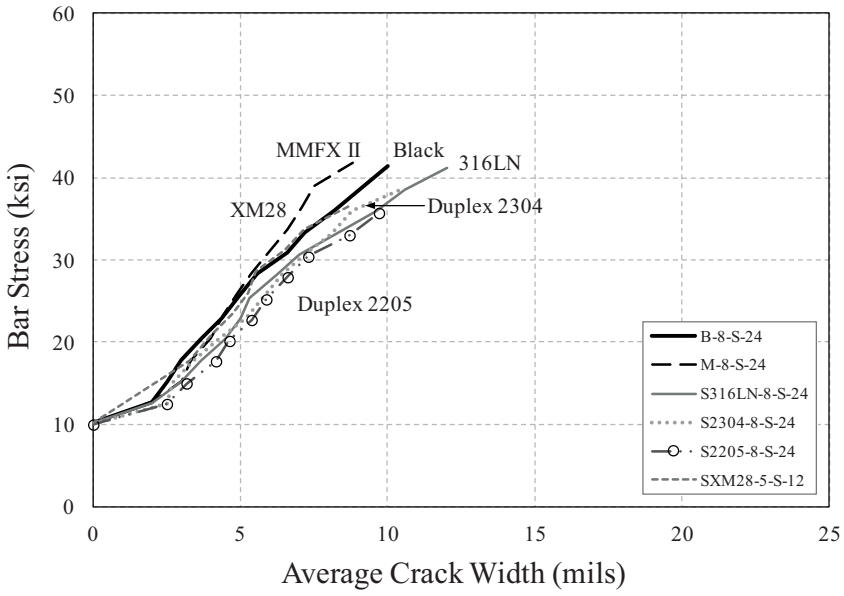

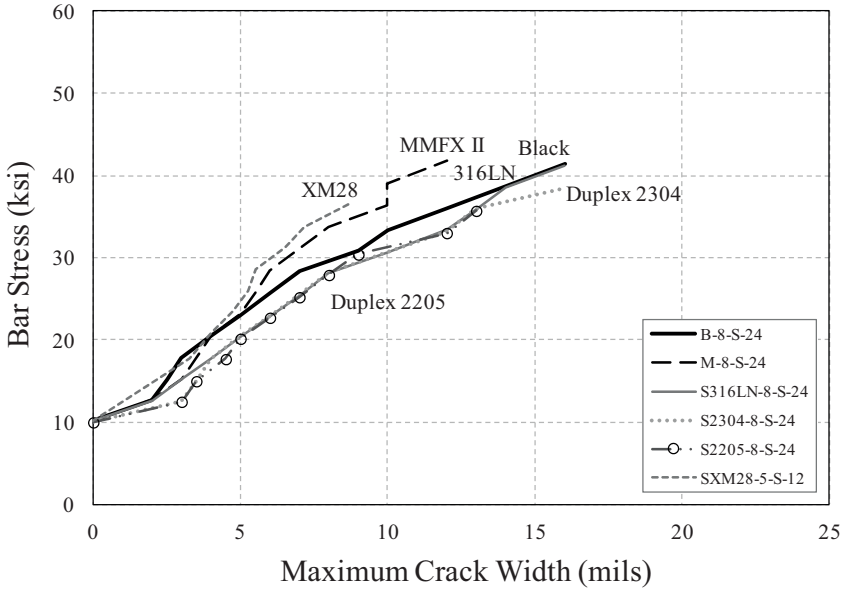

Figure C.26 Bar stress vs. crack width (#8 bars, stainless-steel and MMFX II).

tism drops as the splice length increases (Figure C.31). Therefore, the ACI 318 expression is overestimating the bond force for long splices which explains the differences observed.

In summary, several trends were observed by analyzing Figure C.29 through Figure C.33. Among the various corrosion-resistant reinforcing steel, zinc-clad bars had the smallest test to calculated ratios. As the specimens became wider (larger clear spacings between bars) and the failure modes change from side-splitting failure to top-face splitting failure, the test results to calculated values decreases. Furthermore, as the splice length increases, low test to calculated ratio are obtained.

All tested values to calculated values are presented in Figure C.34. In general, the results are conservative. However, an unconservative result is observed for Specimen M-5-S-48 (splice length = $77d_b$). Specimen S2205-5-S-36 (splice length = $58d_b$) and Specimen ZC1-6-F-15 with a wide bar spacing produced a test to calculated ratio of 1.0.

C.4.1.2 ACI 408R-03 recommendations. The splice and development length equation recommended by ACI Committee 408 (2003) is as follows:

$$\frac{l_d}{d_b} = \frac{\left(\frac{f_y}{\sqrt[4]{f'_c}} - 2210\omega\right)\alpha\beta\lambda}{70\left(\frac{c\omega + K_{tr}}{d_b}\right)} \tag{C.10}$$

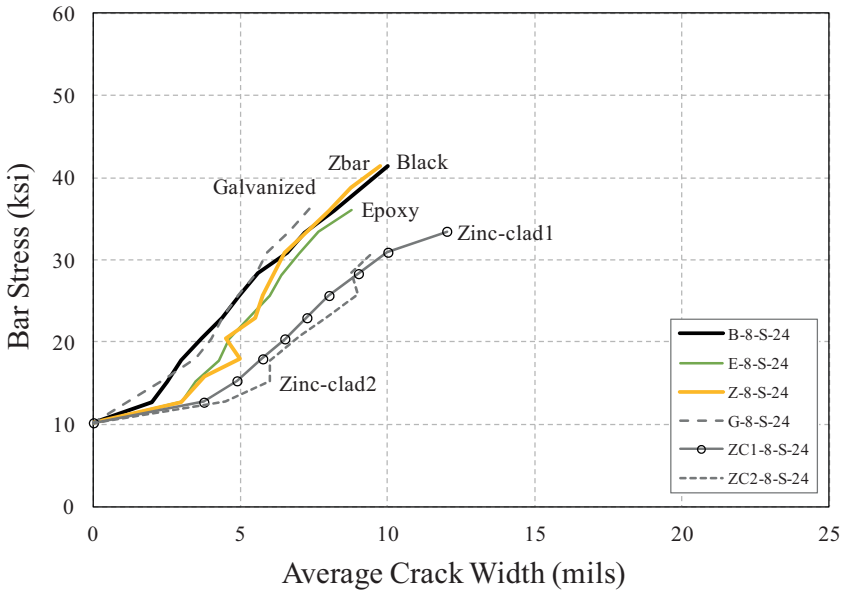

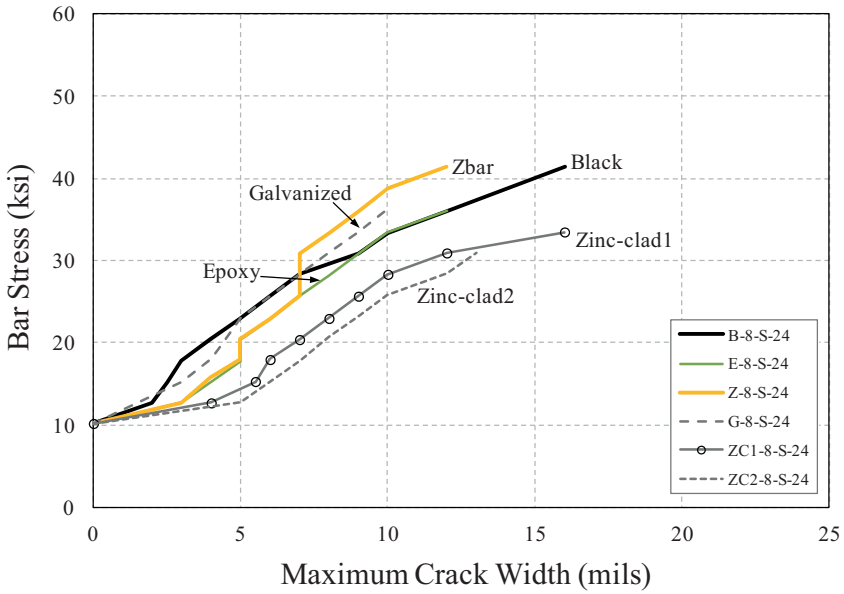

Figure C.27 Bar stress vs. crack width (#8 bars, coated reinforcement).

where:

l_d = *development or splice length (in.)*
d_b = *nominal diameter of bar (in.)*
f_y = *specified yield strength of reinforcement (psi)*
f'_c = *specified compressive strength of concrete (psi)*
ω = $0.1c_{max}/c_{min} + 0.9 \leq 1.25$
c_{max} = *maximum of bottom concrete cover, side cover,* $\frac{1}{2}$ *of bar clear spacing*
c_{min} = *smaller of minimum concrete cover or* $\frac{1}{2}$ *of bar clear spacing*
c = $c_{min} + 0.5d_b$
α = *reinforcement coating factor*
β = *reliability index*
λ = *Lightweight aggregate concrete factor*
K_{tr} = *transverse reinforcement index* $\left(0.52t_r t_d A_{tr}/sn\right)\sqrt{f'_c}$
t_r = $9.6R_r + 0.28 \leq 1.72$ *(the effect of relative rib ratio)*
t_d = $0.78d_b + 0.22$ *(the effect of bar size)*
A_{tr} = *Area of each stirrup crossing the potential plate of splitting (in.*^{2}*)*
s = *center-to-center spacing of transverse reinforcement (in.)*
n = *number of spliced or developed bars*
R_r = *relative rib area of reinforcement*

This equation is based on the work performed by Zuo and Darwin (1998, 2000). Zuo and Darwin's equation is based on

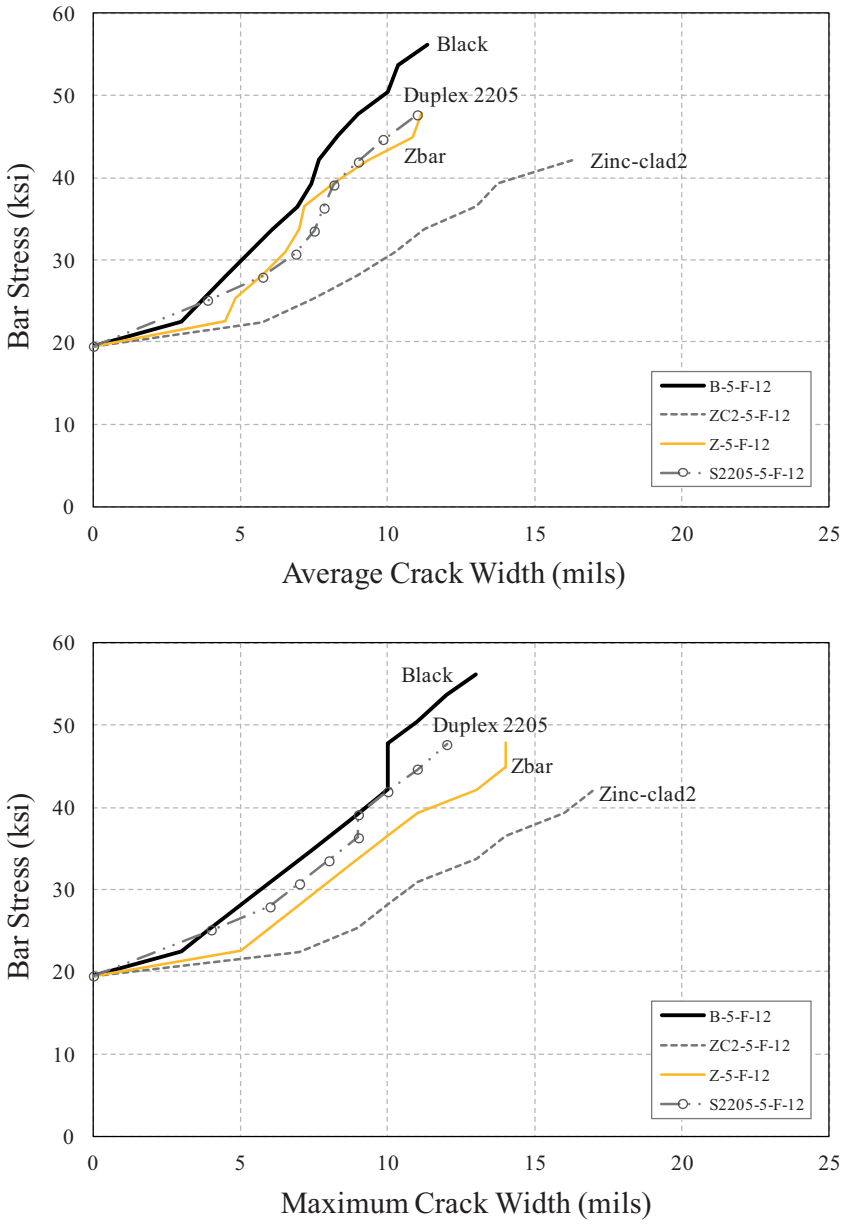

Figure C.28 Bar stress vs. crack width (#5 bars, top-face splitting).

171 unconfined and 196 confined splice tets reinforced with deformed steel bars. The database consisted of only bottom cast specimens and includes specimens with high-strength concrete. Zuo and Darwin (1998, 2000) incorporated the effect of the ratio of cover dimensions and relative rib ratio. In addition, the concrete compressive strength was included, however, the fourth roots is considered instead of the use of the square root as used in ACI 318.

Strength-reduction ϕ factors that depend upon the strength-reduction factor used for tension, and the load factors used in design can be incorporated to Equation (C.10) to convert this empirical equation to a design expression (ACI 408R-03). Based on the load combinations used (1.4D + 1.7L to 1.2D + 1.6L), two different ϕ factors for bond (0.92 for 1.4D + 1.7L and 0.82 for 1.2D + 1.6L) were suggested in ACI 408R-03 (2003). With that said, the ACI 318-11 development length equation was not modified when the load combination was converted from 1.4D + 1.7L to 1.2D + 1.6L. Therefore, Equation (C.10) can be evaluated directly without considerations of a strength reduction factor with the test results. This expression is commonly used without a ϕ factor.

The test data were analyzed (Equation (C.10)) which has been shown to provide better results relative to ACI 318-11. The ratio of experimental to calculated bar stresses at failure is presented in Figure C.35 through Figure C.39. The comparison between the experimental results and calculated values demonstrate that Equation (C.10) performs reasonably well and has less conservatism than the ACI 318-11 equation. Regarding the various material shown in Figure C.35, the zinc-

TABLE C.2
Lap-Splice Bond Strength

Series	Specimen	P_{max} (kips)	f_{su} (ksi)	u (psi)	*Bond Ratio*
I	B-6-S-15	22.4	48.3	603	1.00
	ZC1-6-S-15	17.0	36.6	458	0.76
	B-6-F-15	26.1	52.8	660	1.00
	ZC1-6-F-15	22.1	44.5	556	0.84
II	B-5-S-12	18.1	55.5	722	1.00
	E-5-S-12	16.2	49.6	645	0.89
	G-5-S-12	16.7	50.9	663	0.92
	ZC1-5-S-12	15.1	46.4	604	0.84
	ZC2-5-S-12	12.2	37.6	490	0.68
	Z-5-S-12	16.9	51.9	675	0.94
	M-5-S-12	18.1	55.6	724	1.00
	S316LN-5-S-12	16.9	51.5	671	0.93
	S2205-5-S-12	17.8	54.1	704	0.98
	S2304-5-S-12	17.9	54.7	713	0.99
	SXM28-5-S-12	17.0	51.8	674	0.93
III	B-8-S-24	34.0	44.2	460	1.0
	E-8-S-24	30.1	38.9	405	0.88
	G-8-S-24	33.9	43.9	457	0.99
	ZC1-8-S-24	29.1	37.6	392	0.85
	ZC2-8-S-24	26.1	33.8	352	0.76
	Z-8-S-24	33.8	43.8	456	0.99
	M-8-S-24	40.2	52.7	549	1.19
	S316LN-8-S-24	36.7	47.5	494	1.07
	S2205-8-S-24	35.5	45.3	472	1.03
	S2304-8-S-24	35.7	45.9	479	1.04
	SXM28-8-S-24	34.1	44.5	464	1.01
IV	B-5-F-12	21.6	61.0	794	1.00
	ZC2-5-F-12	17.2	54.6	629	0.79
	Z-5-F-12	19.1	53.8	701	0.88
	S2205-5-F-12	21.9	61.4	799	1.01
	B-8-S-24*	34.0	44.2	460	1.00
	B-8-S-24-C1	39.7	51.5	536	1.17
	B-8-S-24-C2	37.7	48.7	508	1.10
	B-8-S-24-C3	41.8	54.3	565	1.23
	M-5-S-12*	18.1	55.6	724	1.00
	M-5-S-24	25.5	78.6	512	0.71
	M-5-S-36	29.1	89.7	389	0.54
	S2205-5-S-12*	17.8	54.1	704	1.00
	S2205-5-S-24	23.6	71.7	467	0.66
	S2205-5-S-36	27.4	83.3	362	0.51
IV	M-5-S-48	34.3	104.5	340	1.00
	M-7-S-24	40.8	66.3	604	1.78
	M-5-S-36*	29.1	89.7	389	1.00
	M-7-S-18	32.2	52.1	633	1.63
	M-8-S-48	58.6	74.7	389	1.00
	M-11-S-24	53.5	35.6	523	1.34
	M-8-S-48-C1	73.5	97.1	506	1.30
	M-8-S-48-C2	60.1	76.6	399	1.03
	M-8-S-48-C3	75.2	97.0	505	1.30

* Specimens that were tested as part of a different series are included because they are the control specimen.

clad bars (ZC 1 and ZC 2) is the only bar type that is significantly different from the black bar.

While the ratio dropped for larger bar spacings using Equation (C.9), the ACI 408 committee recommendations calculated bar stress for these wider beams with similar conservatism as shown in Figure C.36. This result is different with that observed for the ACI 318 expression where a more significant decrease was noted. Again, the ZC2 bars were an outlier.

The test to calculated ratio was also computed for the specimens where the splice length was increased (Figure C.37). These results demonstrate that bar stress is not linear with splice length as assumed by the ACI 408 equation. As shown, there is a decreasing trend with longer splice lengths.

For the case of transverse reinforcement, although the bar stresses achieved at failure were similar for arrangements C1 and C3, the design expression calculates higher bond strength with the case with additional confinement (C3). As a result, the test to calculated ratio drops for the case with C3 (Figure C.38). The same observation was made in the earlier section when comparing the results from the ACI 318-11 expression. Again, the design expression does not account for varying effectiveness of the transverse reinforcement based on location in the splice zone.

In summary, Equation (C.10) compares reasonably well with experimental data. The calculated results using the ACI 408 expression for the wide specimens with larger bar spacings as well as specimens with longer splices are more consistent than the ACI 318-11 expression. In addition, even with the modification factors included for coated reinforcement, the results were not overly conservative as shown in the case of using the ACI 318-11 equation. However, two issues were noted. First, the conservatism decreases as the splice length increased, and second, the influence of transverse reinforcement can be overestimated depending on its location in the splice zone.

All tested values to calculated values are presented in Figure C.39. The results have less scatter than the ACI 318-11 expression, and calculations were improved for longer splices. The only specimens that produced unconservative results were those with the un-plated and tin-plated zinc-clad coatings.

C.4.1.3 AASHTO bridge design specifications. The tension development length requirement in Article 5.11.2.1.1 of the AASHTO LRFD Bridge Design Specifications (2010) is identical to the requirements included in the ACI 318-71 building code (Equation (C.2)).

In ACI 318-63, the maximum bond stress was set at:

$$u = 0.305\frac{\sqrt{f'_c}}{d_b} \leq 0.8(ksi) \qquad \text{(C.11)}$$

where:

u = *bond stress (ksi)*
d_b = *nominal diameter of bar (in.)*
f'_c = *specified compressive strength of concrete (ksi)*

Combining Equation (C.1) and Equation (C.11), solving for l_d, and multiplying by 1.2 (factor of safety) results in Equation (C.12) which is the basic development length equation for #11 and smaller bars in the AASHTO LRFD specifications (units in ksi). The coefficient is different from Equation (C.2) because the AASHTO specification use base units of ksi while ACI 318 uses psi. Otherwise, these expressions are identical.

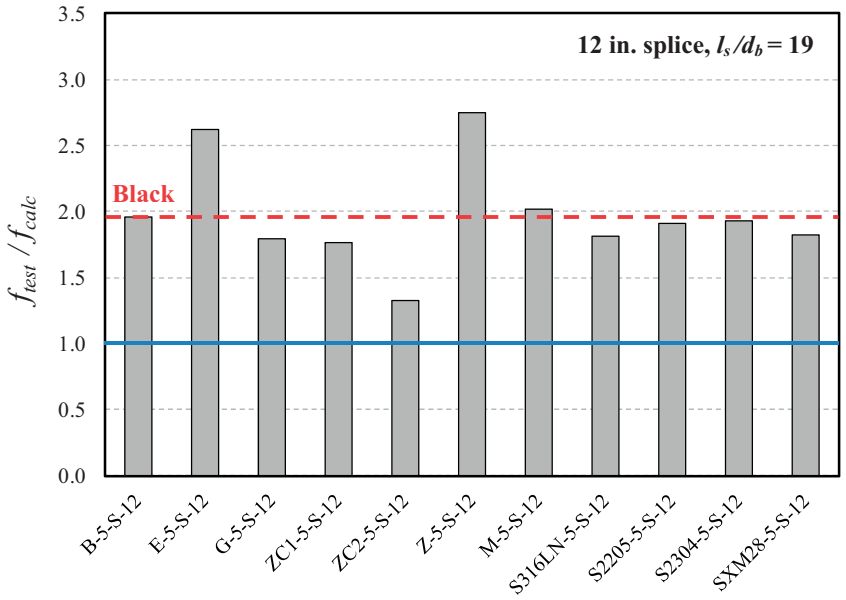

(a) #5 Bars

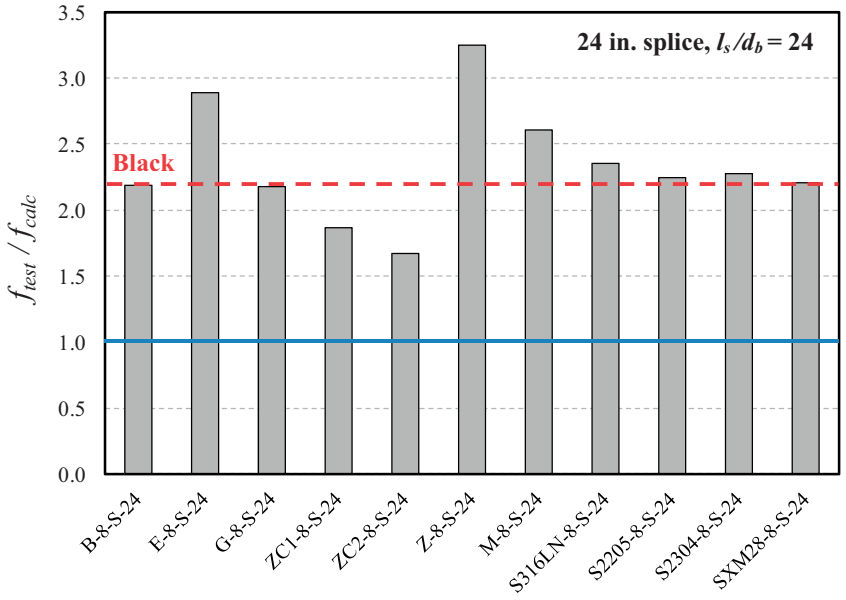

(b) #8 Bars

Figure C.29 Comparison of strength calculations of corrosion-resistant reinforcing bars by ACI 318-11.

$$l_d = \frac{1.25 A_b f_y}{\sqrt{f'_c}} \qquad \text{(C.12)}$$

where:

l_d = *development length (in.)*
A_b = *cross-sectional area of reinforcing bar (in.^{2})*
f_y = *specified yield strength of reinforcement (ksi)*
f'_c = *specified compressive strength of concrete (ksi)*

Although there are modification factors (to consider top bar, lightweight aggregate, coating, cover, and bar spacing) to Equation (C.12) to increase or decrease the development length, there is no adjustment for the addition of transverse reinforcement in the splice region. The AASHTO expression limits the development length to be longer than $0.4 d_b f_y$ and the steel stress is limited to 75 ksi.

All tested values to calculated values are presented in Figure C.40. Test results with transverse reinforcement were not included because AASHTO does not account for the confinement. All specimens containing bars larger than #5 and those with long splices ($l_s > 40 d_b$) were observed to have unconservative test/calculated ratios. This result was not unexpected considering that ACI discontinued use of the expression in 1989 due to its unconservative nature.

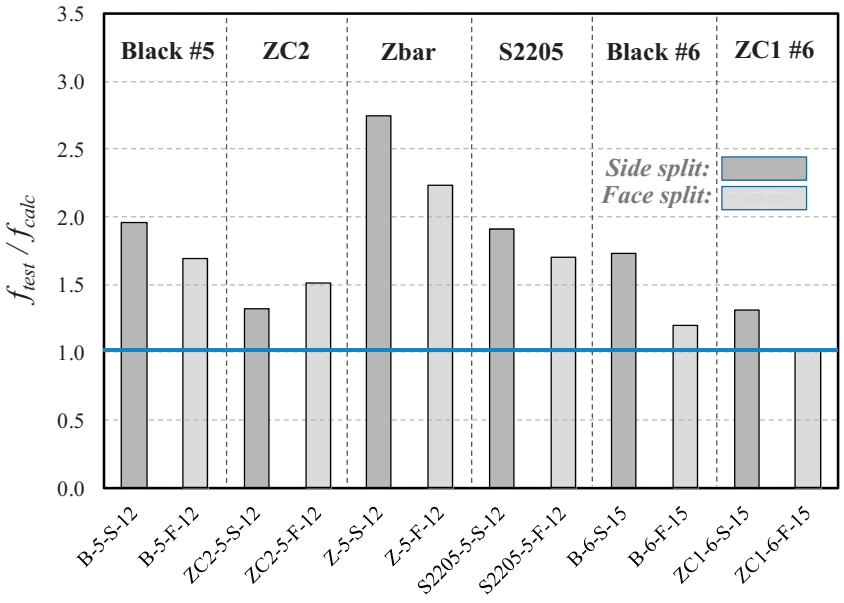

Figure C.30 Bond strength calculations of beams with different splitting failure modes by ACI 318-11.

C.4.1.4 Descriptive equation (Canbay & Frosch, 2005 Model). Canbay and Frosch (2005) developed an expression based on a physical model of tension cracking in the lap-spliced region of concrete. The equation is a function of splice length, bar diameter, cover and spacing dimensions, number of spliced bars, and concrete compressive strength. The expression is presented as follows:

$$f_b = \frac{F_{splitting}}{\tan\beta \cdot nA_b} \tag{C.13}$$

Side-splitting failure:

$$F_{splitting} = l_s^* \left[2c_{so}^* + (n-1)2c_{si}^*\right] 6\sqrt{f'_c} \tag{C.14a}$$

Face-splitting failure:

$$F_{splitting} = l_s^* \left[2c_b^* \left(0.1\frac{c_{so}}{c_b} + 0.9\right) + 2_b^*(n-1)\left(0.1\frac{c_{so}}{c_b} + 0.9\right)\right] 6\sqrt{f'_c} \tag{C.14b}$$

where:

f_b = *bar stress at failure (ksi)*
l_s = *splice length (in.)*
c_b = *bottom concrete cover (in.)*
c_{so} = *clear side cover of reinforcing bars (in.)*
c_{si} = *half of clear spacing between bars (in.)*
c_s = *min(c_{si} + 0.25, c_{so})*

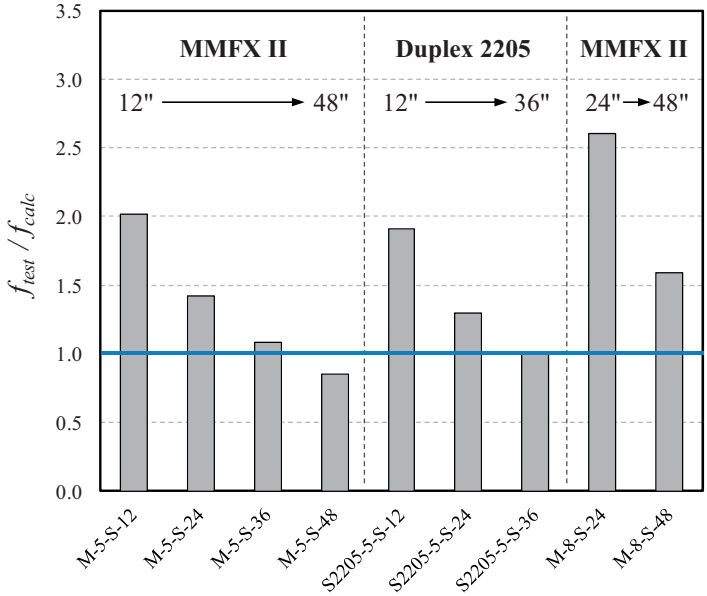

Figure C.31 Bond strength calculations of beams with varying splice lengths by ACI 318-11.

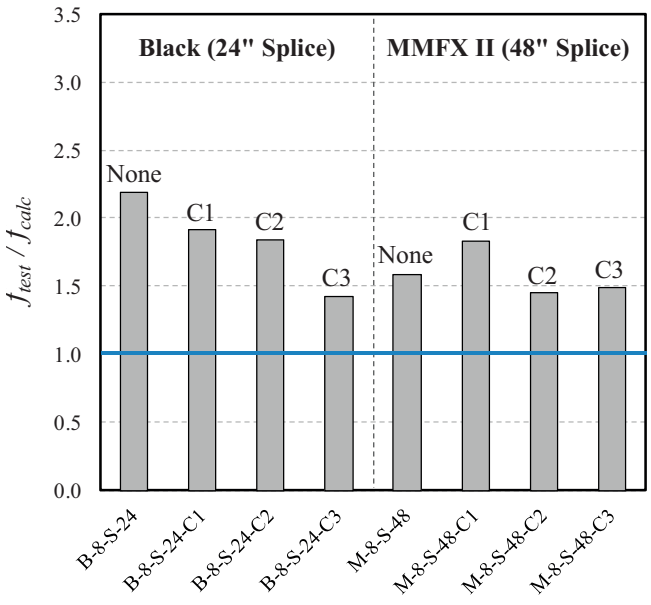

Figure C.32 Bond strength calculations of beams with confinement in splice region by ACI 318-11.

f'_c = *specified compressive strength of concrete (psi)*
n = *number of spliced bars*
A_b = *area of spliced reinforcement (in.^{2})*
β = *20 degrees (angle between resultant force of longitudinal and splitting forces and longitudinal force)*

where:

$$l_s^* = l_s \cdot \min\left(\frac{33}{\sqrt{\frac{l_s}{d_b}} \cdot \sqrt[4]{f'_c}}, 1\right) \tag{C.15}$$

$$\left(0.1\frac{c_s}{d_b} + 0.9\right) \geq 1 \tag{C.16}$$

$$c_b^* = c_b \cdot \min\left(\frac{0.8}{\sqrt{\frac{c_b}{d_b}}}, 1\right), \quad c_{so}^* = c_{so} \cdot \min\left(\frac{0.8}{\sqrt{\frac{c_{so}}{d_b}}}, 1\right),$$
$$c_{si}^* = c_{si} \cdot \min\left(\frac{0.8}{\sqrt{\frac{c_{si}}{d_b}}}, 1\right) \tag{C.17}$$

All tested values to calculated values are presented in Figure C.41. Unlike design expressions (ACI 318-11, ACI 408R-03, AASHTO-LRFD) which are meant to provide conservative estimates, the physical bond model proposed by Canbay and Frosch (2005) is a predictive (descriptive) equation and as expected provides reasonably accurate estimates of failure stresses. The results were more compressed, and the measured bar stresses at failure was close to that calculated. The few specimens that were overestimated (unconservative with test/calculated <1) were the specimens with un-plated and tin-plated zinc-clad bars which are observed to have 20–30% less bond strength than conventional black steel. It should also be noted that coating modification factors were not included in this analysis as the expression was developed for black bars.

C.5. INFLUENCE OF INVESTIGATED PARAMETERS

The variables investigated for the forty-five reinforced concrete beams tested in the experimental program include bar type, bar size, splice length, bar spacing, transverse reinforcement, and axial rigidity as described in detail in Chapter 3. The same mix design was used throughout the test program with the intent of keeping the concrete strength as constant. However, the concrete compressive strength varied from 3,990 to 5,400 psi which differed from the design value of 4,000 psi. Based on the results of various research studies (Canbay & Frosch, 2005; Zuo & Darwin, 2000), the net effect of the concrete strength on bond strength is proportional to the fourth root of the concrete compressive strength $\left(\sqrt[4]{f'_c}\right)$. Therefore, for the purpose of comparison, specimens that were cast in different series with different concrete compressive strengths will be normalized using the fourth root of the concrete compressive strength. The bar stresses at failure presented in this section are normalized to 4,000 psi concrete as follows:

$$f_{normalized} = f_s \cdot \sqrt[4]{\frac{4000}{f'_c}} \tag{C.18}$$

where:

$f_{normalized}$ = *normalized bar stress at failure (ksi) with design concrete compressive strength of f'_c = 4,000 psi*
f_s = *bar stress at failure (ksi) with provided concrete compressive strength of f'_c*
f'_c = *measured compressive strength of concrete (psi)*

C.5.1 Bar Type

C.5.1.1 Bond ratio. The effect of eleven different bar types on bond strength was investigated. Different bars may have different moduli of elasticity, coating thickness, deformation height, deformation spacing, and surface roughness. These differences resulted in different bond strengths among the bars tested as shown in Figure C.42. The bond ratio, which is the ratio of bond strength of the tested bar to the bond strength of the companion black bar, is plotted on the vertical axis. The darker color bars of each category represent the #5 bars while the lighter color bars next to it represent the #8 bars. Two specimens with #6 bars (ZC1) are labeled on Figure C.42. The lighter color bars but with dotted borders are the wider specimens that failed in face splitting (bars labeled as ZC1, ZC2, Z, and S2205 in Figure C.42).

As shown in Figure C.42, all coated bars have less bond strength than the black bar (bond ratio <1). Tin-plated zinc-clad bars had the lowest bond ratio followed by the

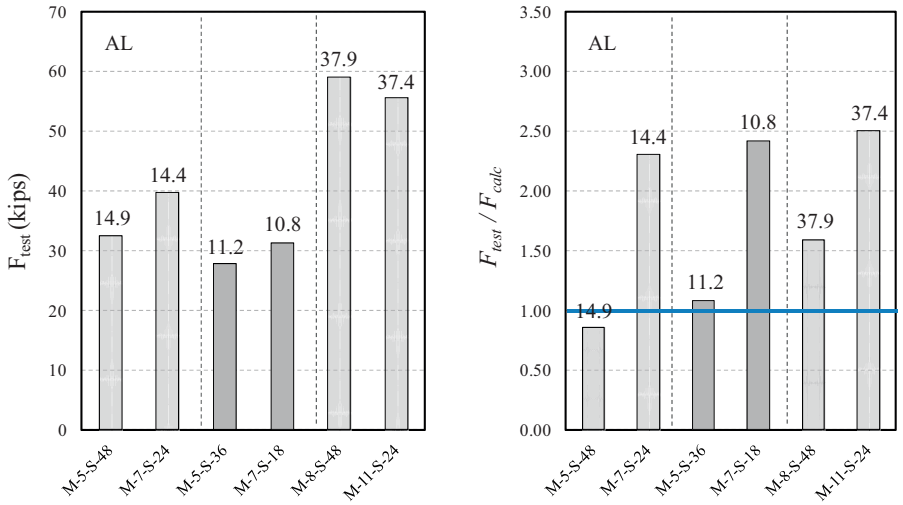

(a) Measured Bond Force (b) Test/Calculated Ratio of Bond Force

Figure C.33 Bond force of beams with identical bar axial rigidity.

un-plated zinc-clad bars. Epoxy-coated bars had approximately 90% of the bond strength of black bars while Zbars and hot-dip galvanized had on average approximately 4–6% higher bond strength than epoxy-coated bars. MMFX II and stainless-steel bars had on average comparable or slightly higher bond strength than black bars except XM-28 stainless steel which was comparable to the galvanized bar. The bond ratio increased as specimens became wider (larger clear spacing between bars) for all cases except the Zbar specimen.

The bond ratios of all tested specimens are also tabulated in Table C.3. Tin-plated zinc-clad specimen had on average 26% less bond strength than black bar. Un-plated zinc-clad specimen had on average 18% less bond strength than black bar. Specimens with these two zinc-clad bars clearly indicated less bond between the bars and concrete. Epoxy-coated, Zbar, and hot-dip galvanized bars had on average 11%, 6%, and 4% less bond strength than the black bar, respectively. On the other hand, MMFX II had 10% more bond strength than the black bar and all stainless steel bars except XM-28 stainless steel bar had comparable bond strength to the black bar. XM-28 stainless steel bar had on average comparable bond strength to hot-dip galvanized bar.

To further evaluate the differences in bond strength shown in Table C.3, the influence of surface roughness, relative rib area, and coating thickness to bond strength are investigated in the following sections.

C.5.1.2 Surface roughness. Abrams (1913) demonstrated that chemical adhesion and friction forces along the surface of the bar contribute to approximately 60% of the bond

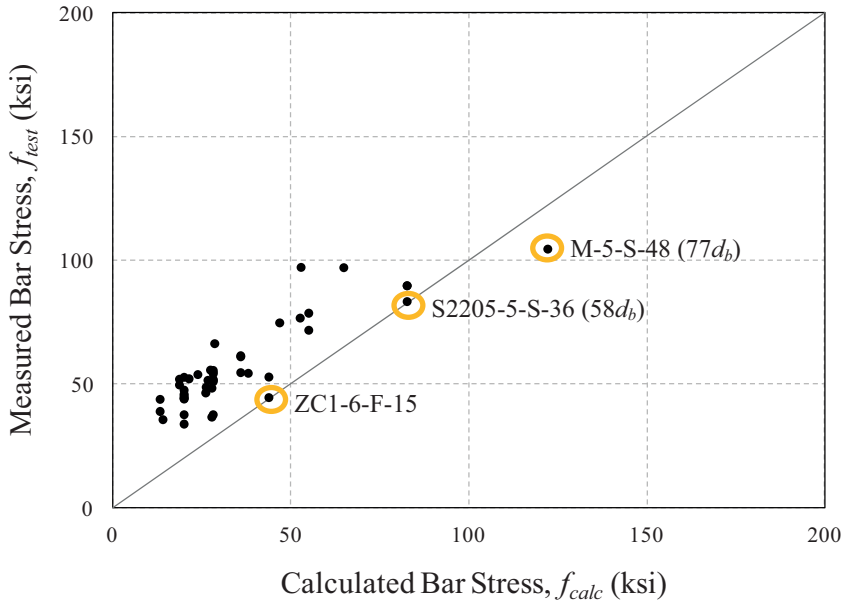

Figure C.34 Measured vs. calculated bar stresses by ACI 318-11.

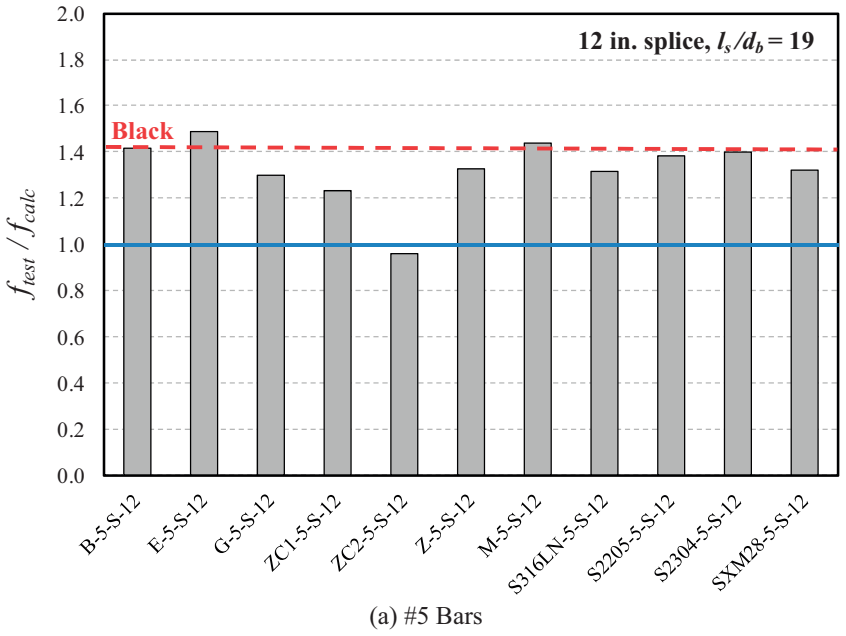

(a) #5 Bars

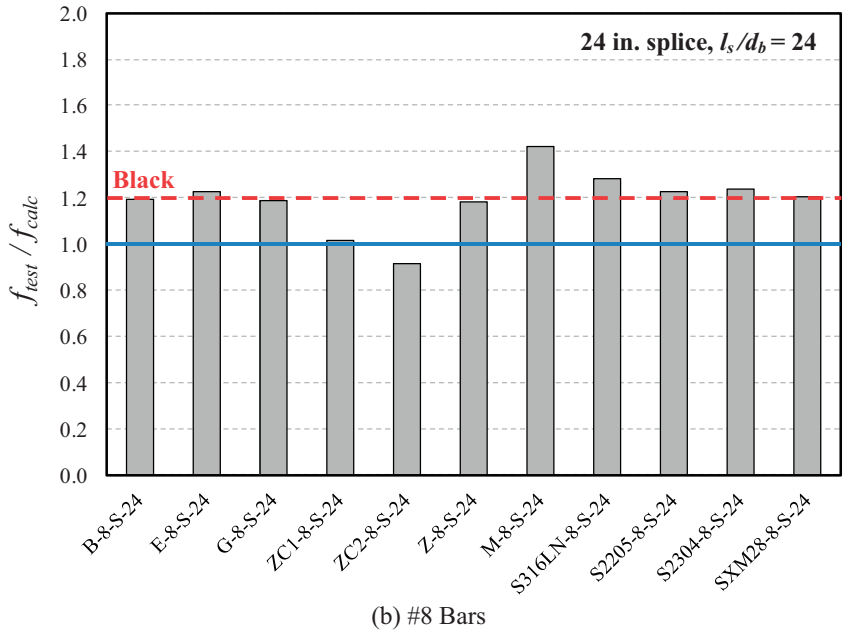

(b) #8 Bars

Figure C.35 Comparison of strength calculations of corrosion-resistant reinforcing bars by ACI 408R-03.

strength while bearing forces consist of 40% of the bond strength. Coating thickness and surface roughness are factors that contribute to chemical adhesion and friction forces while relative rib area influences bearing forces. Although, no research could be found that is focused on the relationship between surface roughness and bond strength, the influence of friction forces along the surface was studied by a few researchers (Cairns & Adullah, 1994; Idun & Darwin, 1999). Cairns and Adullah (1994) measured the coefficient of friction as 0.53 and 0.49 for uncoated and coated steel plates, respectively. Idun and Darwin (1999) had similar results measuring 0.56 and 0.49 for uncoated and coated reinforcing steel bar, respectively. They reported that the influence in this small difference of friction forces would be minimal when sufficient concrete cover or heavy confinement is provided.

The eleven bars tested in this program have different surface roughness which may affect adhesion and friction forces. To investigate the effect of surface roughness on bond strength, specimens having the same bar size, bar spacing, and splice length were compared.

Figure C.43(a) shows the normalized bar stress at failure plotted versus the surface roughness measured with a profiliometer (described in Chapter 2) for specimens with #5 bars, 1 in. clear spacing between bars, and a 12 in. splice length while Figure C.43(b) shows the same plot for the specimens

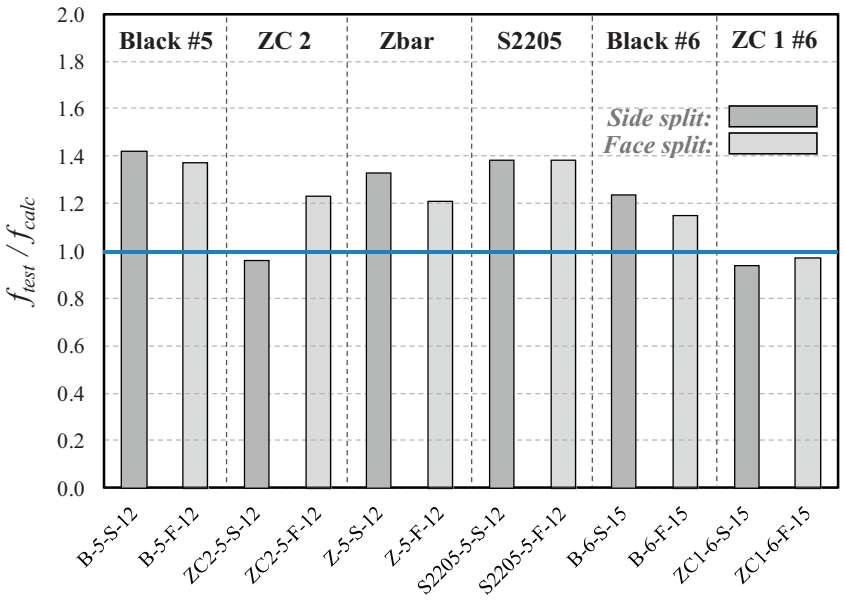

Figure C.36 Bond strength calculations of beams with different splitting failure modes by ACI 408R-03.

with #8 bars, 1 in. clear spacing between bars, and a 24 in. splice length. The number of peak to valley pairs defined per unit length on the surface of the bar was measured.

Although, there is more scatter for the larger bars (Figure C.43(b)), the two graphs clearly show a trend between the surface roughness and the bar stress reached at failure. As the surface roughness of the bar increases, the bond strength increases. All of the uncoated bars (black bar, stainless steel bars, and MMFX II bar) had more than 100 peak and valley pairs (Figure C.43) while all of the coated bars, had peak and valley pairs less than 100, except the hot-dip galvanized bar which had a coating thickness less than 5 mils.

From the observations made in this study by measuring the peak and valley pairs (as a measure of surface roughness) with a profiliometer, bar stresses reached at failure increased approximately 1 ksi for an increase of 20 peak and valley pairs.

C.5.1.3 Relative rib area. To investigate if different deformation heights and spacings affect the bearing resistance on the ribs, the ratio of the bearing area to the shearing area which is also known alternatively as "relative rib area" is investigated. The relative rib area shown in Figure C.44 is defined as follows (ACI 408, 2009):

$$R_r = \frac{Bearing\ \ Area}{Shearing\ \ Area} = \frac{A_r}{\pi d_b s_r} \approx \frac{h_r}{s_r} \qquad \text{(C.19)}$$

where:

R_r = *relative rib area*

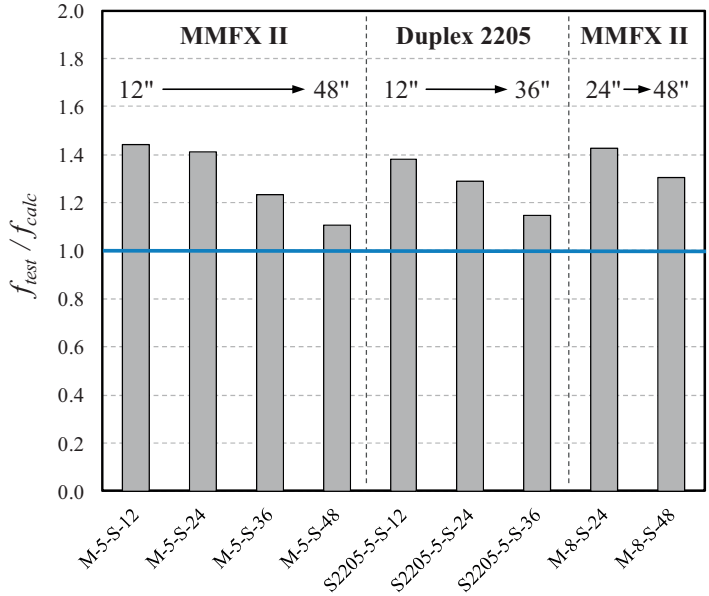

Figure C.37 Bond strength calculations of beams with varying splice lengths by ACI 408R-03.

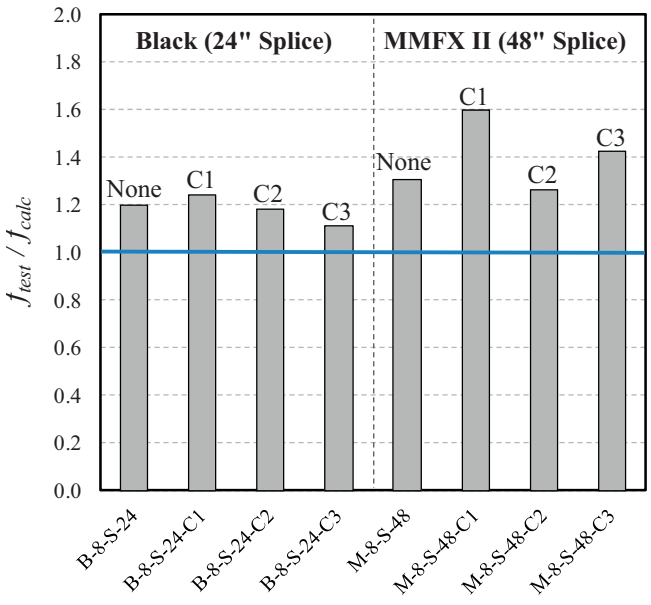

Figure C.38 Bond strength calculations of beams with confinement in splice region by ACI 408R-03.

A_r = *bearing area (in.^{2}) which is projected rib area normal to reinforcing bar axis*
h_r = *average height of deformation (in.)*
d_b = *nominal bar diameter (in.)*
s_r = *average center-to-center rib spacing (in.)*

The major deformation requirements in use today (ASTM A615, 2009) are based on research conducted by Clark (1946, 1949) at the National Bureau of Standards. Based on Clark's study of reinforcing bar patterns, a maximum average spacing of deformations equal to $0.7d_b$ and a minimum height of deformations equal to 0.04 for bars smaller than #4 bars, $0.045d_b$ for #5 bars, and $0.05d_b$ for larger bars were recommended. Clark's study also indicated that under some conditions, an increase in relative rib area will increase bond strength. Clark (1946) used the term, the ratio of the shearing area (bar perimeter times distance between ribs) to the rib bearing area (projected rib area normal to the bar axis) which is the inverse ratio of Equation (C.19) and provided recommendations from research to limit the ratio to a maximum of 10, and if possible 5 or 6. In terms of relative rib area defined by Equation (C.19), his recommendations suggest a minimum relative rib area of 0.1, with desirable values of 0.2 or 0.17. However, Clark's recommendations regarding the relative rib area (relatively high bearing area) were not included in the ASTM A615 (2009). The relative rib area (Equation (C.19)) for bars manufactured in the U.S. range from 0.057 to 0.084 (Darwin & Graham, 1993).

Kimura and Jirsa (1992) observed an increase in bond strength with increasing relative rib area. However, the relative rib area investigated in this study ranges from 0.06 to 0.4 where most of the specimens have a relative rib area greater than 0.1.

Darwin and Graham (1993) observed an increase in bond strength with increasing relative rib area when confinement is provided in the splice region. However, the study found that bond strength is independent of deformation pattern when bond strength is governed by splitting of the concrete with relatively low confinement. The relative rib area included in this study ranged between 0.05 to 0.2.

Figure C.45 shows the normalized bar stress at failure plotted versus the relative rib area for specimens with #5 bars and #8 bars. The deformation height and spacing was measured as explained in Chapter 2. Discarding the outlier specimen with tin-plated zinc-clad bars (Zinc-clad 2), no clear trend between bond strength and relative rib area of different reinforcement can be observed. The results are consistent with the view of ACI Committee 408 (ACI 408R-03) which does not include the effect of relative rib area for development length calculations when confinement is not

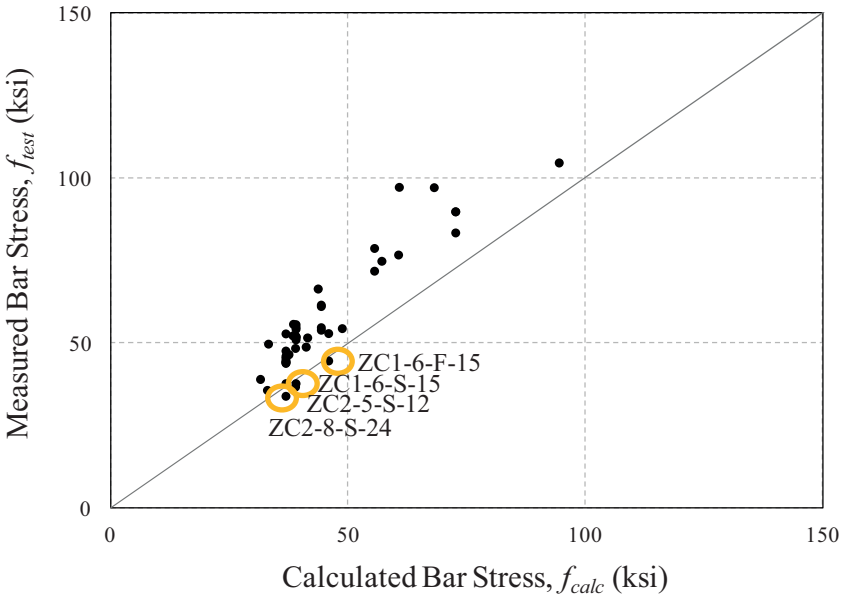

Figure C.39 Measured vs. calculated bar stresses by ACI 408R-03.

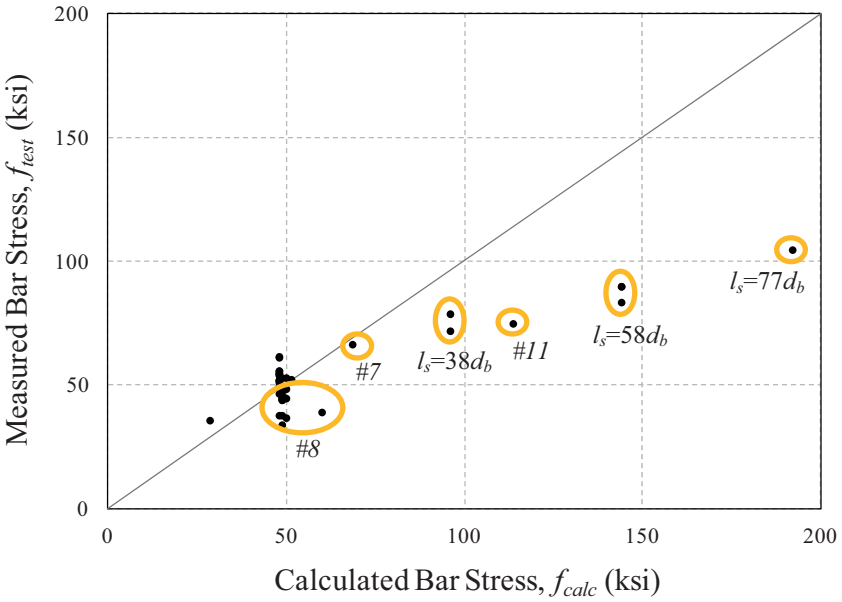

Figure C.40 Measured vs. calculated bar stresses by AASHTO-LRFD.

provided. The relative rib area is only included in calculations when transverse reinforcement is provided. Because the reinforcement included in this study, which are primarily manufactured in the U.S., have relatively low ratio of bearing area to shearing area (<0.1), the effect of bearing force is observed as minimal at best.

Considering the low relative rib area used in this study (<0.12), this finding was not unexpected. However, if confinement is provided in the splice region, it has been shown that bond strength increases with an increase in relative rib area (Darwin & Graham 1993; Zuo & Darwin, 1998, 2000). When this ratio (bearing area to shearing area) is between 0.1 and 0.2, bond strength increases as the ratio increases (Clark, 1946; Kimura & Jirsa, 1992). According to Kimura and Jirsa (1992), there is approximately a 0.25 ksi increase in bar stress for a 0.01 increase in relative rib area.

C.5.1.4 Coating thickness. To investigate if the coating thicknesses of the coated bars affects bond strength, coating thicknesses were measured with a magnetic pull-off dry-film gage as described in Chapter 2. Figure C.46 shows the normalized bar stress at failure plotted versus the coating thicknesses for specimens with #5 and #8 bars. The plots clearly show that there is a strong correlation between coating thickness and the bar stress achieved at failure.

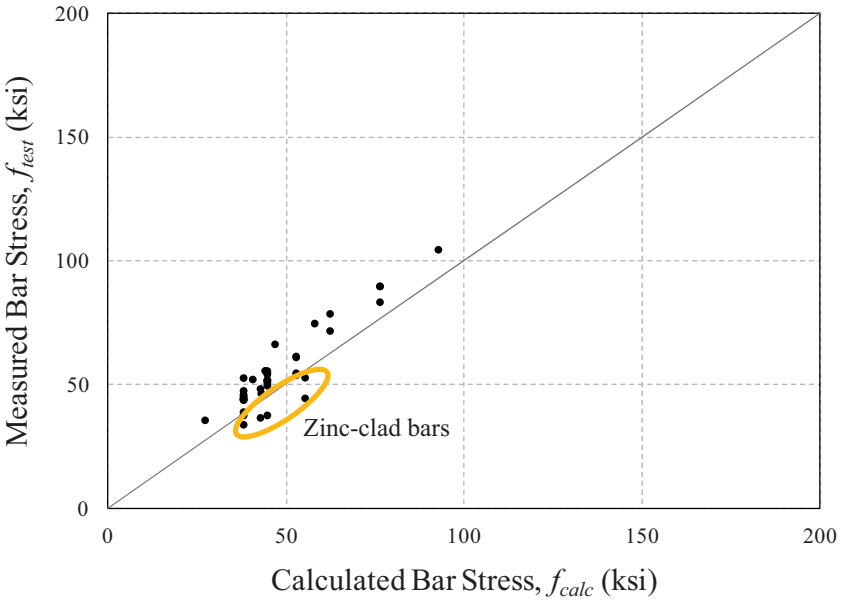

Figure C.41 Measured vs. calculated bar stresses by Canbay and Frosch (2005).

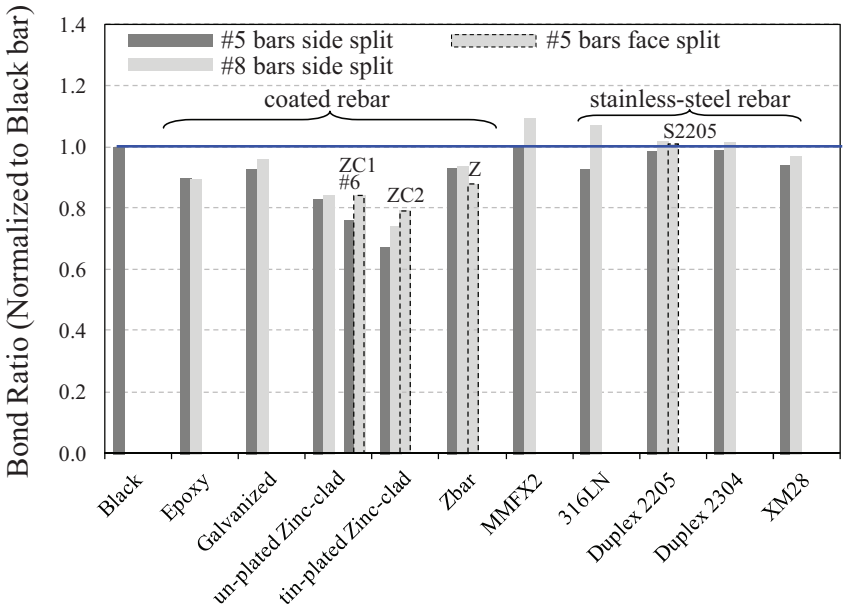

Figure C.42 Bond ratio of corrosion-resistant reinforcing bars.

As coating thickness increases, the bar stress achieved at failure (can also be expressed as bond strength) decreases.

Mathey and Clifton (1976) observed that bars with epoxy coatings between 1 and 11 mils in thickness had bond strengths about 6% lower than black bars. Johnston and Zia (1982) studied the effect of epoxy coating on bond strength and observed that bars with coating thicknesses between 6.7 and 11.1 mils had 15% lower bond strength compared to that of black bars. Treece and Jirsa (1989) tested 21 lap-splice beam specimens (17 specimens contained top-cast bars) in which 12 of the specimens contained epoxy-coated bars with coating thicknesses between 4.5 and 14 mils. An average reduction in bond strength of 35% compared to uncoated bars was observed in these tests, and this work became the basis of the development length modification factors for epoxy-coated bars in ACI 318 and the AASHTO bridge specifications.

Based on these observations and the test results of this study (Figure C.46), the trend of a 1 ksi decrease in bar stress for every 2 mils increase in coating thickness is found to be a reasonable estimate. For example, with the goal of achieving a bar stress of 60 ksi, a drop of 1 ksi is approximately 1.6%. If a coating has a thickness of 10 mils, there would be an approximately 8% decrease in bar stress reached at failure.

C.5.1.5 Summary. In summary, the surface roughness, relative rib area, and coating thickness were investigated to determine their influence on bond strength. Due to a relatively low bearing to shearing area (relative rib area) for the bars manufactured in U.S., no influence of the deformation height and spacing was observed. However, the surface roughness and coating thickness were observed to provide significant influence. In addition, both of these

TABLE C.3
Bond Ratio

Bar Type		#5		#6		#8		
		Side Split	Face Split	Side Split	Face Split	Side Split	Avg.	Min.
Black		1.00	1.00	1.00	1.00	1.00	1.00	1.00
Coated Bars	Epoxy	0.89	–	–	–	0.88	0.89	0.88
	Galvanized	0.92	–	–	–	0.99	0.96	0.92
	Zinc-clad 1	0.84	–	0.76	0.84	0.85	0.82	0.76
	Zinc-clad 2	0.68	0.79	–	–	0.76	0.74	0.68
	Zbar	0.94	0.88	–	–	0.99	0.94	0.88
MMFX II		1.00	–	–	–	1.19	1.10	1.00
Stainless Steel Bars	316LN	0.93	–	–	–	1.07	1.00	0.93
	Duplex 2205	0.98	1.01	–	–	1.03	1.01	0.98
	Duplex 2304	0.99	–	–	–	1.04	1.02	0.99
	XM-28	0.93	–	–	–	1.01	0.97	0.93

Note: Zinc-clad 1 (un-plated), Zinc-clad 2 (tin-plated), Zbar (dual-coated).

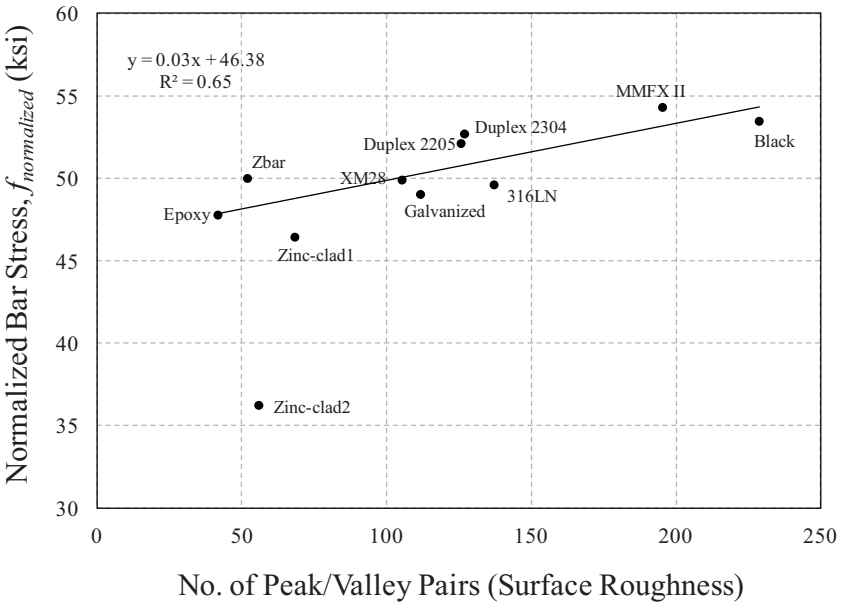

(a) Specimens with #5 Bars

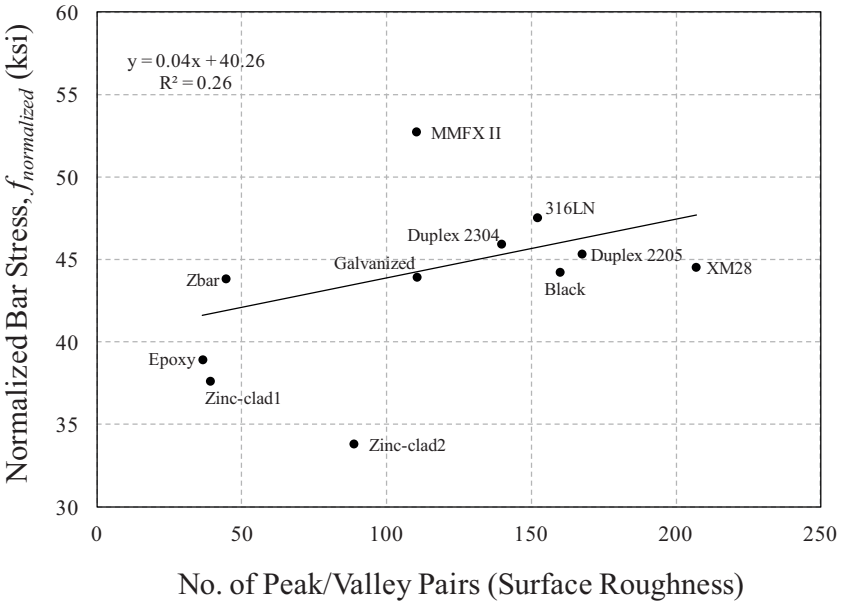

b) Specimens with #8 Bars

Figure C.43 Effect of surface roughness on bond strength.

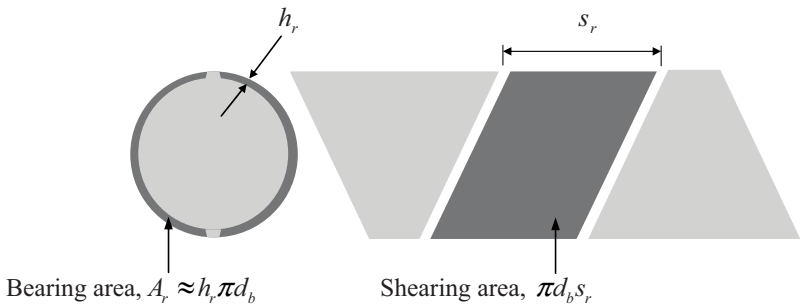

Figure C.44 Definition of relative rib area (ACI 408.3R-09).

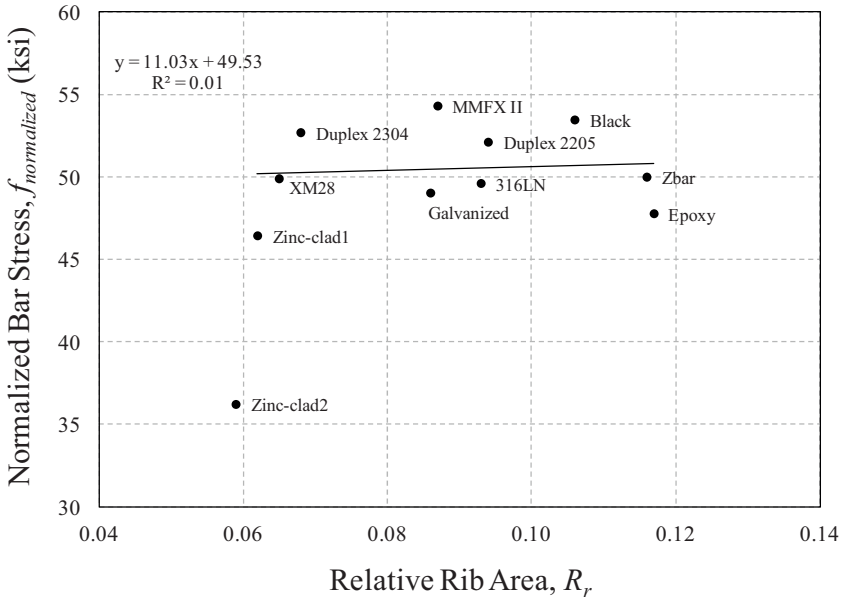

(a) Specimens with #5 Bars

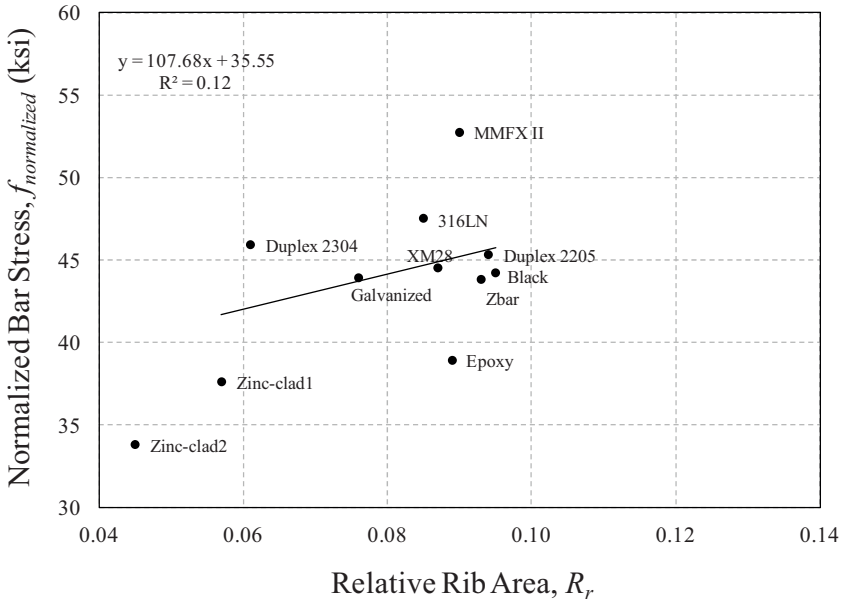

(b) Specimens with #8 Bars

Figure C.45 Effect of relative rib area on bond strength.

trends were fairly linear. For each parameter (surface roughness, relative rib area, and coating thickness), the increasing or decreasing trend for their influence on bond stresses as measured in this study are presented in Table C.4. The trends suggest that bond strength may be able to be predicted based on these measurements.

C.5.2 Bar Size

The effect of bar size on bond strength was investigated through testing four different bar sizes, #5, #7, #8, and #11 otherwise identical specimens. These specimens used the same splice length, bar spacing, and cover dimensions for the same bar type (MMFX II). The normalized bar stress reached at failure decreases as the bar diameter increases from 0.625 in. to 1.410 in as shown in Figure C.47. This relationship is also shown to be linear.

In terms of bond force obtained by the bar, the normalized bar forced reached at failure is plotted versus bar size for all the corrosion-resistant reinforcing bars used in current study (Figure C.48). Because, the splice lengths of the specimens presented in Figure C.48 also vary from 12 in. to 24 in., there is a wide range of scatter and may not completely represent the comparison between different bar

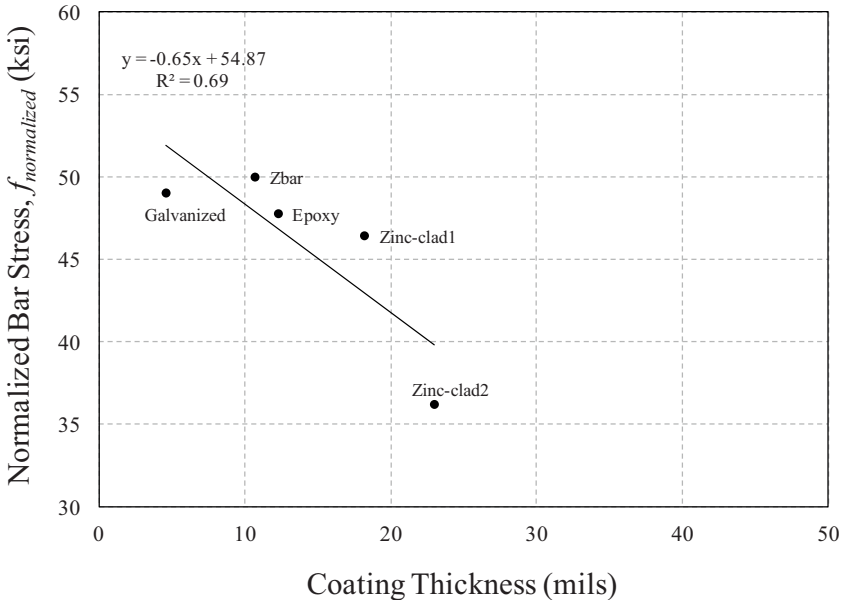

(a) Specimens with #5 Bars

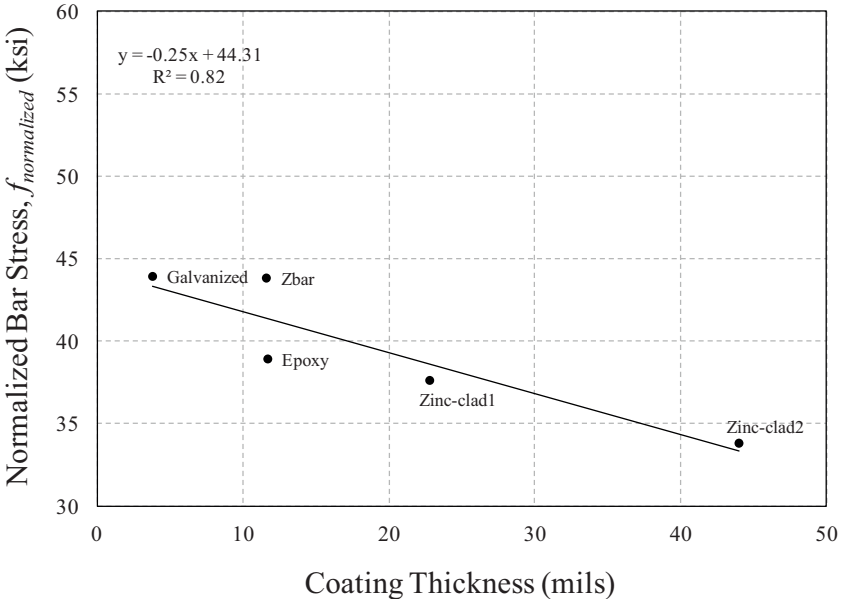

(b) Specimens with #8 Bars

Figure C.46 Effect of coating thickness on bond strength.

sizes correctly. However, the general trend is that the bond force increases as the bar diameter, d_b, increases.

C.5.3 Splice Length

The effect of splice length on bond strength is presented in Figure C.49. This plot presents #5 MMFX II bars with splice lengths varying from 12 to 48 in., #5 Duplex 2205 reinforcing bar with splice lengths varying from 12 to 36 in., and #8 MMFX II reinforcing bar with splice lengths varying from 24 to 48 in. MMFX II and Duplex 2205 reinforcing bars were selected for this study as these bars can reach high bar stresses at failure without yielding.

As shown in Figure C.49, the bar force reached at failure increases as the splice length increases. However, the strength gain reduces because the effectiveness of the splice decreases as the splice length increases. The increase in bond force is shown to decrease as the splice length is doubled from 12 to 24 in., tripled from 12 to 36 in., and quadrupled from 12 to 48 in.

This non-linear trend is clear when comparing with current design equations suggested by ACI 318-11 and ACI 408R-03 which were discussed earlier. Although, the bar stress at failure increases at a slower rate as the splice length increases, the current design equations estimate a linear relationship as shown in Figure C.50.

TABLE C.4
Influencing Parameters

Parameter	Influence	Change in Bar Stress	Percent Change (for 60ksi)
Surface Roughness (# of peak and valley)	chemical adhesion, friction forces	+1 ksi per 20 peak & valley	+1% per 10 peak & valley
Relative Rib Area (Equation (5–18))	bearing forces	+0.25 ksi per 0.01 increase	+1% per 0.02 increase
Coating Thickness (mils)	chemical adhesion, bearing forces	−1 ksi per 2 mils	−1% per 1 mils

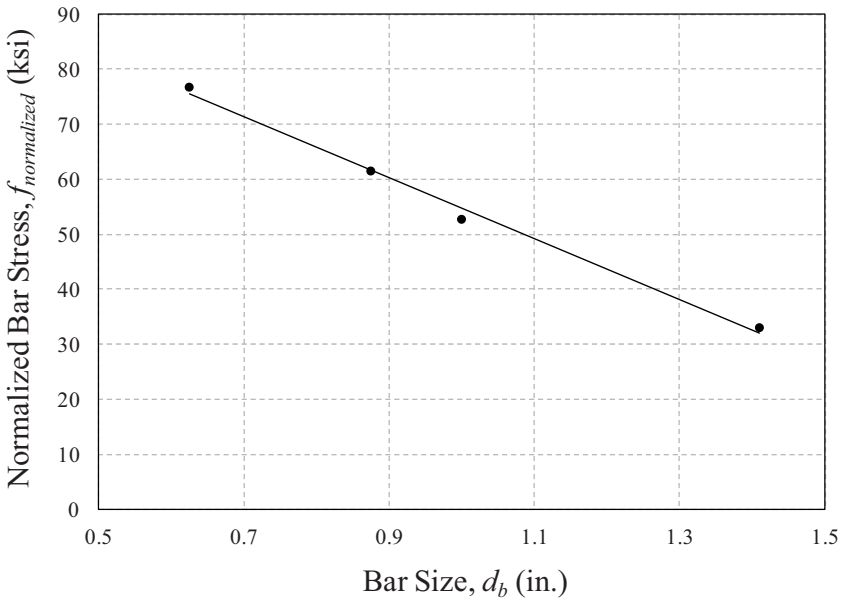

Figure C.47 Effect of bar size on bond strength (MMFX II bar).

Frosch and Pay (2006b) also observed that the relationship between bond strength and splice length is not linear by testing fiber reinforced polymer (FRP) reinforcing bars with long splice lengths. Frosch and Pay further investigated this relationship by including data from the ACI 408 database (ACI 408R-03) with steel reinforcement. To develop a model that can account for both FRP and steel reinforcement in bond force calculations, the concept of an equivalent splice length that considers the different axial stiffness of various reinforcement materials was introduced as follows:

$$L_{eq} = L_s \frac{E_b A_b}{E_{ref} A_{ref}} \tag{C.20}$$

where:

L_{eq} = *equivalent splice length (in.)*
L_s = *splice length (in.)*
E_b = *modulus of elasticity of spliced reinforcement (ksi)*
A_b = *area of spliced reinforcement (in.^{2})*
E_{ref} = *modulus of elasticity of reference reinforcement (ksi)*
A_{ref} = *area of reference reinforcement (in.^{2})*

To use the model suggested by Frosch and Pay (2006b) where the reference reinforcement was chosen as #5 wrapped and sand coated Glass FRP reinforcing bars, Equation (C.20) can be modified as the following term:

$$L_{eq} = L_s \frac{E_b A_b}{1800} \tag{C.21}$$

where:

L_{eq} = *equivalent splice length (in.)*
L_s = *splice length (in.)*
E_b = *modulus of elasticity of spliced reinforcement (ksi)*
A_b = *area of spliced reinforcement (in.^{2})*
E_{ref} = *5,800 ksi (wrapped and sand coated Glass FRP)*
A_{ref} = *0.31 in.^{2} (area of #5 bar)*

The bar force achieved at failure for the given equivalent splice length (Equation C.21) was suggested as follows (found from the best fit for the FRP and steel database):

$$F_b \cdot \sqrt[4]{\frac{4000}{f'_c}} = 2.1\sqrt{L_{eq}} \tag{C.22}$$

where:

F_b = *bar force achieved at failure (kips)*
L_{eq} = *equivalent splice length (in.)*

The descriptive equation by Frosch and Pay (2006b) is plotted in Figure C.50 for comparison with the test results of the MMFX II reinforcing bars and Duplex 2205 stainless bars in the current study. As shown, the simple model suggested by Frosch and Pay agrees well with the test results of the current experimental program. On the other hand, because the ACI 318-11 and ACI 408R-03 design expression assumes a linear relationship between bar stress achieved at failure and splice length, both equations

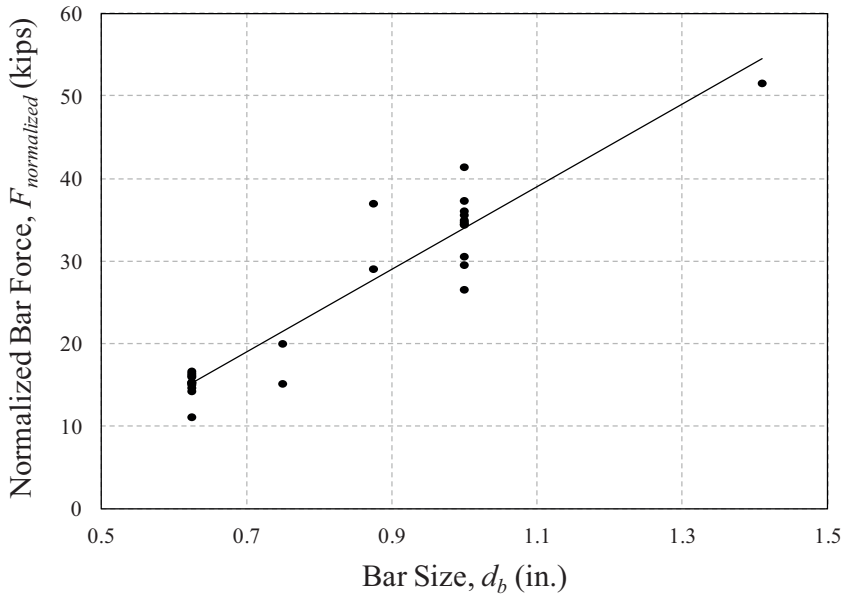

Figure C.48 Effect of bar size on bond force.

overestimate the bar stress at a splice length of 48 in. ($77d_b$) and are unconservative.

The bar stress distribution surrounding the splice region was also investigated through measurements using the digital image correlation (DIC) technique, optical motion tracking system, and DEMEC mechanical gages. From all three measurement techniques (Figure C.51(a) to Figure C.51(c)), the strain distribution demonstrates that the bond stress in the center of splice (24 in.) is small compared to the splice ends. And as the splice length is increased to 48 in., the region where the change in strain is small becomes longer, and only the splice ends produce high strains (Figure C.52).

As shown, the tensile strains are very low in the middle region and increase towards the end of the splice for both splices (24 in. and 48 in.). However, the region where the change in strain is small becomes longer as the splice length increases. This observation may explain why the splice strength does not increases linearly as the splice length increases.

C.5.4 Concrete Cover and Bar Spacing

The effect of concrete cover and bar spacing on bond strength was investigated by testing two different arrangements for specimens with #5 and #6 bars, respectively. For the #5 bars (12 in. splice), four different reinforcing materials were tested with the two different configurations, one with 1.5 in. top and side cover and a clear spacing of 1 in. between the bars, and the other with 0.75 in. top cover and

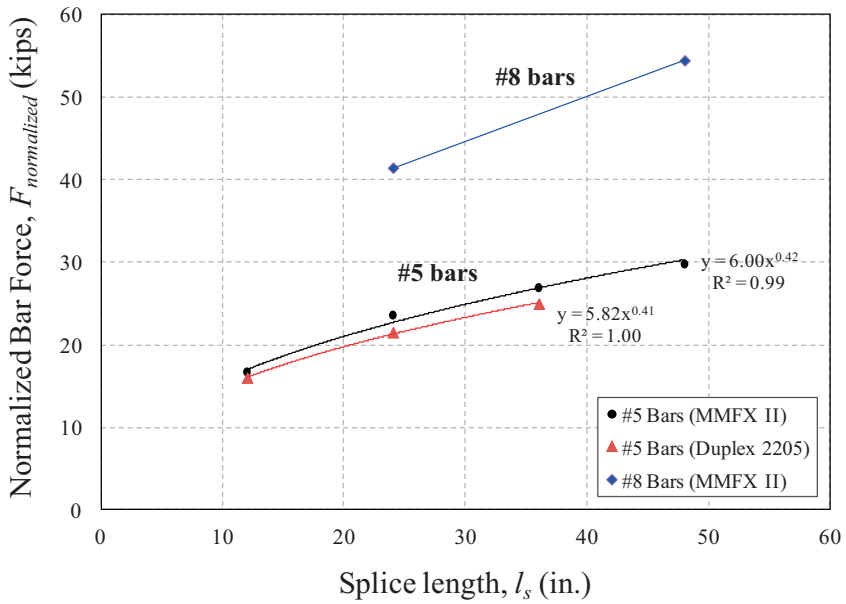

Figure C.49 Effect of splice length on bond force.

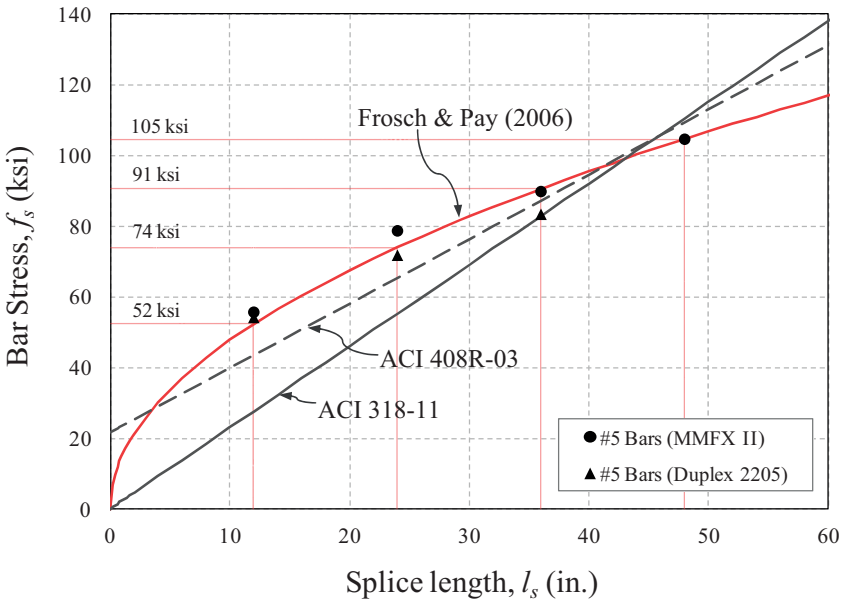

Figure C.50 Relationship between bar stress and splice length.

a center-to-center bar spacing of 6 in. For the #6 bars (15 in. splice), two different reinforcing materials were tested with the two different configurations, one with 1.5 in. top and side cover and a clear spacing of 1 in. between the bars, and the other with 1 in. top cover and a center-to-center bar spacing of 6 in.

The resistance of the concrete surrounding the reinforcing bars could be simplified as a surrounding-cylinder model suggested by various researchers (Orangun et al., 1977; Sozen & Moehle, 1990; Tepfers, 1973) to visualize the bursting-stress mechanism. This surrounding-cylinder model simplifies the bursting stress around the bar by considering the top, bottom, and side covers to be equivalent. The model also considers the clear separation between the bars as cover (two units of clear separation as equivalent to one unit of cover).

Using this concept of the surrounding-cylinder model that idealizes all covers to the concrete surface and clear separation between bars to be equivalent, the critical (minimum) cover taken as the smallest of top cover, side cover, and half of the clear spacing between the bars is used to discuss the test data in this study. The normalized bar stress plotted versus the minimum cover is shown in Figure C.53.

As shown in Figure C.53, the bond strength increases with increased spacing of the reinforcing bar (larger minimum cover assuming that clear separation between bars can theoretically be considered as a cover dimension). The minimum cover for side splitting is controlled by the clear spacing while for face splitting, it is controlled by the face cover. The identical trend is shown with the larger bars (#6 bar). Bond strength increases with an increase in cover dimension (all other variables are constant). However, the increase in bond strength with an increase in critical cover is less for the larger diameter bars. This finding is consistent with observations made by Ferguson and Thompson (1962).

C.5.5 Transverse Reinforcement

The influence of transverse reinforcement in the splice region was also investigated. The normalized bar stress plotted versus the amount of transverse reinforcement is shown in Figure C.54 while the normalized bar stress plotted versus the transverse reinforcement index is shown in Figure C.55. For the shorter splice of 24 in., there is a slight increase (7.5%) in bond strength when confinement is provided in the center only (C2). With the identical amount of transverse reinforcement (C1), when confinement is provided at the ends of the splice, a greater increase in bond strength was observed (13.7%). Finally, when additional confinement is provided at both the ends and center of the splice (C3), the bond strength increases 20% more than the case with no confinement (6.3% more than C1).

When the splice length increased to 48 in., it is seen that arrangement C2 and the control specimen with no transverse reinforcement have similar bond strengths (2.5% increase with confinement). This lack of influence occurs because the bar stress in the center of splice region essentially does not change for longer splices, and the bond stress is low in this region. By providing transverse reinforcement at the ends, a 30% increase in splice capacity was observed (arrangement C1 and C3). Arrangement C1 and C3 resulted in identical bond strengths. A summary of the influence of confinement is provided in Table C.5.

This trend is not captured by the current ACI 318-11 development length equations as shown in Figure C.56. While the measurements (Figure C.56(a)) show that the ratio of measured bond strength with confinement to the measured bond strength without confinement is similar between the C1 and C3 arrangement, the calculated ratios for these two cases are different (Figure C.56(b)). Because the design equations consider all transverse reinforcement equivalently, the expressions overestimate the influence of

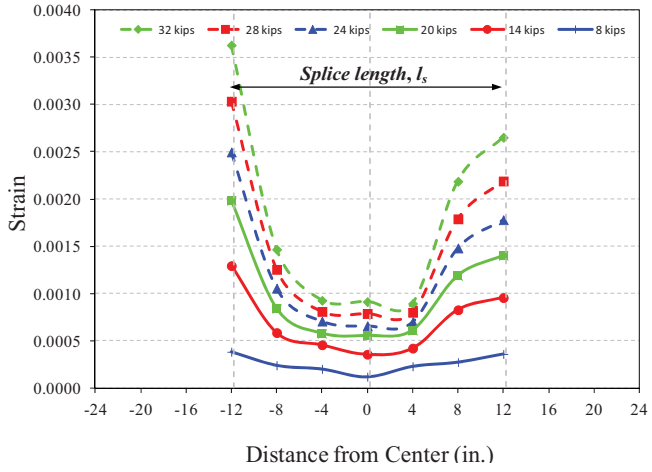

(a) Strain Measurements from DIC

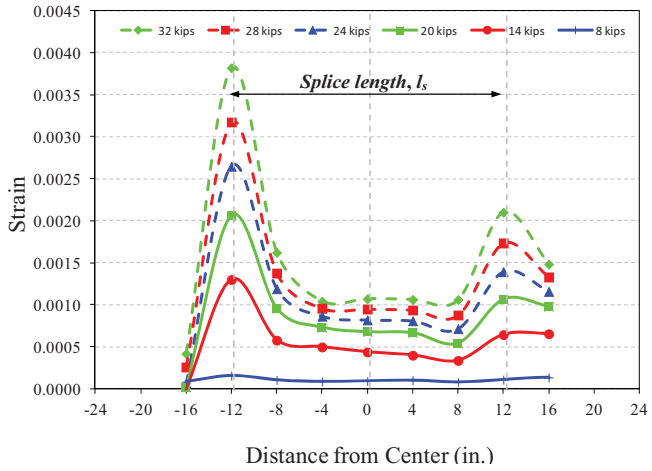

(b) Specimens Measurements from Optotrak

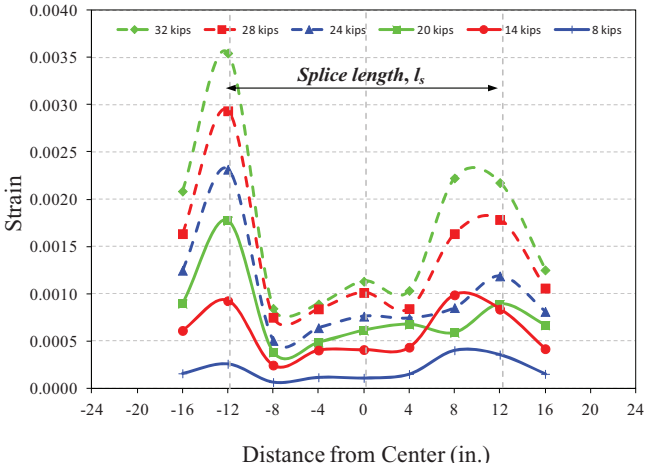

(c) Specimens Measurements from DEMEC Mechanical Gage

Figure C.51 Measured strain distribution along splice (specimen M-7-S-24).

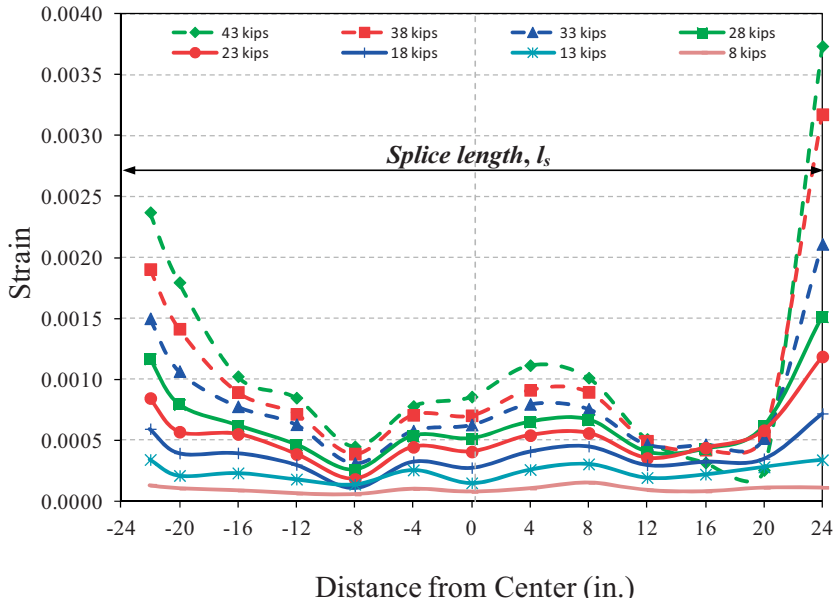

Figure C.52 Measured strain distribution along splice (M-8-S-48).

the center transverse reinforcement. In addition, while the measurements (Figure C.56(a)) show that the ratio of measured bond strength with confinement to the measured bond strength without confinement is similar between the no confinement case and C2 arrangement, the calculated ratios for these two cases are different (Figure C.56(b)).

C.5.6 Axial Rigidity

The effect of axial rigidity (AE) on bond strength was investigated by maintaining the modulus of elasticity of bar constant and pairing the bar size and splice length in three different combinations with the hypothesis that $A_1E_1L_1 = A_2E_2L_2$.

The normalized bar force plotted versus the product of axial rigidity (AE) and splice length is shown in Figure C.57. Although, there was some difference in bond force between the specimens with a 48 in. spliced #5 bar and a 24 in. spliced #7 bar, the other pairs had comparable bond force. As clearly shown, the bond force increases as AEL increases.

C.6. ANALYTICAL STUDY WITH EXISTING DATA

The analytical study regarding the various influencing factors that affect bond strength is enhanced by including additional splice beam test results from the ACI 408 Database 10-2001 (ACI 408R-03) and additional test data generated after that database was complied.

Based on the observations made from the previous section for the factors that influence bond strength, an objective is to develop an analytical model that can address the following key questions.

1. As surface roughness increases and coating thickness decreases, the bar stress achieved at failure increases. How should these aspects be considered in development length calculations for new materials?
2. As splice length increases, the bar stress reached at failure increases. However, the relationship between increasing the splice length and bond strength is not linear. Can a model be developed that consider this non-linear trend?
3. The stress distribution along long splices is not uniform. As a result, test results demonstrate that providing confinement in the middle of the splice region will not be fully effective. Can an analytical model be developed to accurately calculate splice strength with confinement?

An empirical method which combines the techniques of dimensional analysis and statistical regression analysis is applied to the complied data, similar to the approach Zsutty (1968) made for shear strength prediction with existing data.

C.6.1 Database of Lap-Spliced Beam Specimens

The ACI 408 Database 10-2001 (ACI 408R-03) includes a total of 478 (192 unconfined and 286 confined) uncoated, bottom cast, steel reinforced specimens which failed in splitting. Canbay and Frosch (2005) considered an additional 14 beams that contain conventional reinforcement that were unconfined, uncoated, and bottom cast.

Test data performed after 2005 were added in this evaluation and include 67 additional beams containing conventional reinforcing steel that is uncoated and bottom cast (21 unconfined and 46 confined). Test results from the current study include 39 beams (25 uncoated and 14 coated) that are unconfined and bottom cast and 6 confined beams that are uncoated and bottom cast. A total of 252 beams with no

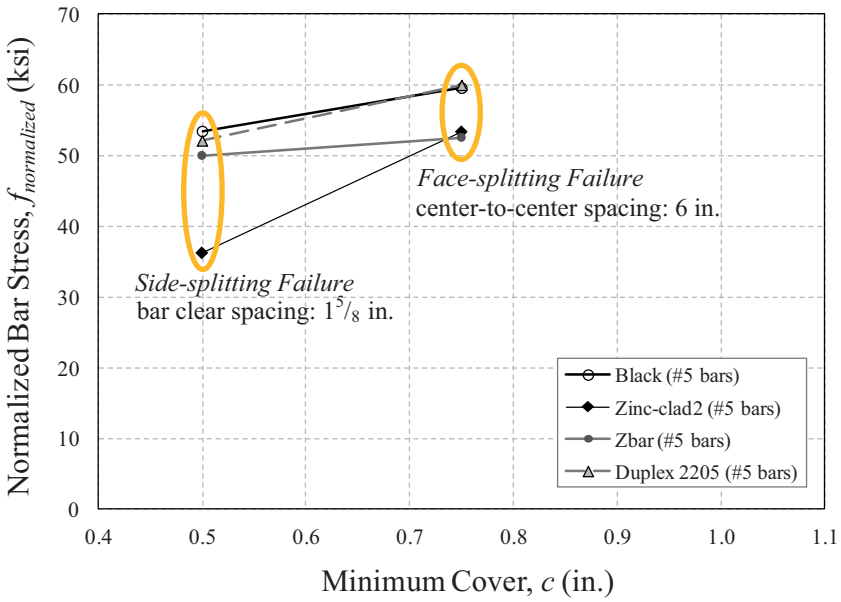

(a) Specimens with #5 Bars

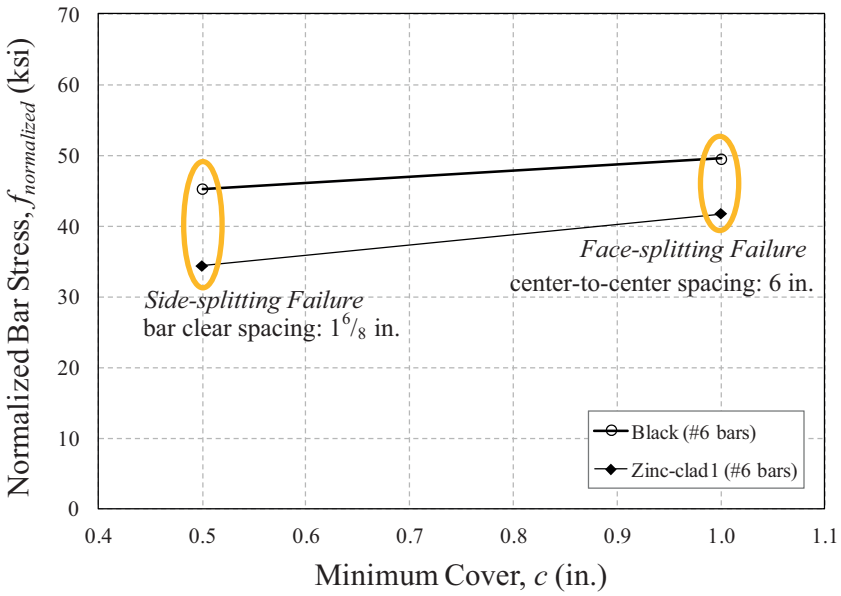

(b) Specimens with #6 bars

Figure C.53 Effect of minimum cover on bond strength.

confinement and 338 beams with confinement are analyzed. Summaries of the confined and unconfined lap-spliced beams used in the analysis are presented in Table C.6 and C.7, respectively. All beams included are splice tests loaded by four-point bending (with two concentrated loads from loading points and two reaction loads from supports) to create a constant moment region within the splice length.

The references, number of test specimens, and range of variables (splice length, bar diameter, concrete cover, and concrete compressive strength) are provided. In addition, for the purpose of comparing specimens with and without confinement, the number of specimens with identical dimensions (width and height), splice length, bar diameter, and concrete cover that can be paired together are listed in Table C.7. In other words, these are identical specimens except for the addition of confining reinforcement.

For unconfined lap-spliced beams, beams that yielded before bond failure were not included in the analysis because bar stresses at failure could have been higher in those beams if the yield strength of the reinforcing bars were higher. However, reinforcing bars that had a round-house stress-strain relationship that does not have a definite yield plateau were not considered to be yielded even if the bar stresses were

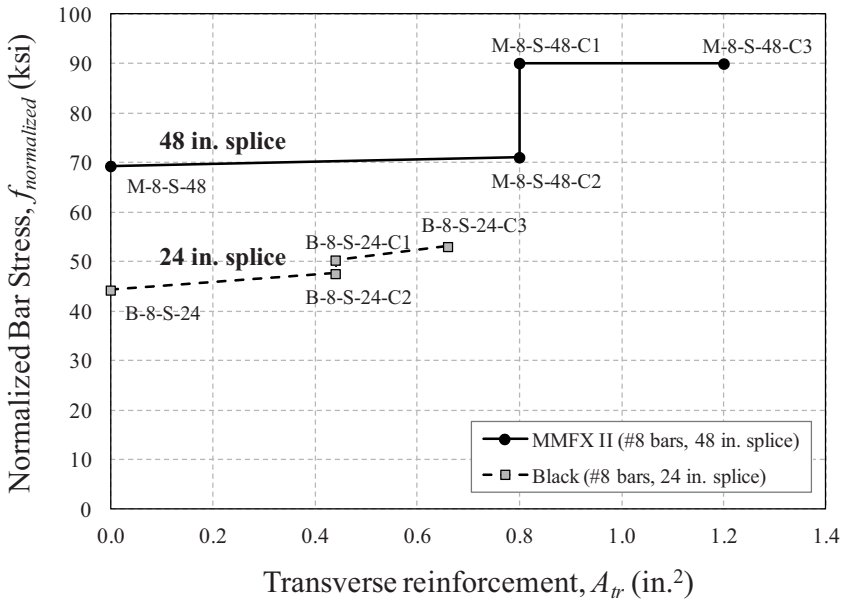

Figure C.54 Effect of transverse reinforcement on bond strength.

higher than the stresses at a tensile strain of 0.035 or stresses obtained from the 0.2% offset method. For these bars, stresses do not level out at yield and can be loaded to stresses beyond the yield strength.

The frequency distribution of the important parameters that will be analyzed from the combined database are presented in Figure C.58 to Figure C.63. The histograms show the distribution within the combined database of the splice to diameter ratio (l_s/d_b), diameter of the bars (d_b), concrete compressive strengths (f_c), and the cover dimensions (c_b, c_{si}, c_{so}). Because most of the splice tests were designed to produce a splitting failure before yield, 86% of the test data are concentrated between splice lengths of 10 to 40 bar diameter as shown in Figure C.58. However, the number of tests with a splice length to bar diameter ratio over 40 have increased within the past 10 years due to the increased interest in using high-strength reinforcing steel. With the use of high-strength reinforcing bars, tests are able to be designed to fail in splitting failure modes without necessarily yielding the bars.

Most of the test specimens in the combined database contained #6, #8, or #11 bars (80% of the data) as shown in Figure C.59. The current experimental program tested 20 beams reinforced with #5 bars which has contributed to the increase in number of specimens with #5 bars which are largely used in slabs and bridge decks.

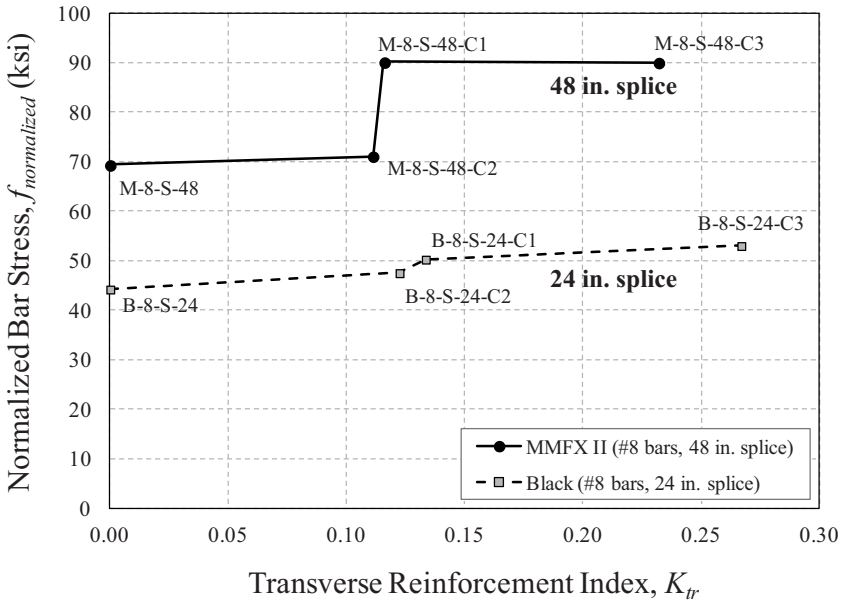

Figure C.55 Normalized bar stress vs. transverse reinforcement index.

TABLE C.5
Influence of Confinement

Bar Type	Splice Length	Effect of Stirrup Location	Arrangement	Increase in Splice Strength
Black	24 in.	Middle of Splice	None to C2	7.5%
			C1 to C3	6.3%
		Splice Ends	None to C1	13.7%
			None to C3	20%
MMFX II	48 in.	Middle of Splice	None to C2	2.5%
			C1 to C3	0%
		Splice Ends	None to C1	30%
			None to C3	30%

The majority of the tests in the database have concrete compressive strengths between 3,000 psi and 6,000 psi (68% of test data) as shown in Figure C.60. Similar to the increase in using high-strength reinforcing steel, the number of specimens with high-strength concrete is growing. Lap-splice beam specimens with concrete compressive strength higher than 6,000 psi is approximately 30%.

The distribution of bottom cover c_b, half of clear spacing c_{si}, and side cover c_{so} is presented in Figure C.61 through Figure C.63. Approximately 90% of the test specimens have a bottom cover c_b equal or less than 2 in. as shown in Figure C.61. The distribution of half the clear spacing between the bars c_{si} (Figure C.62) is larger than the distribution of the

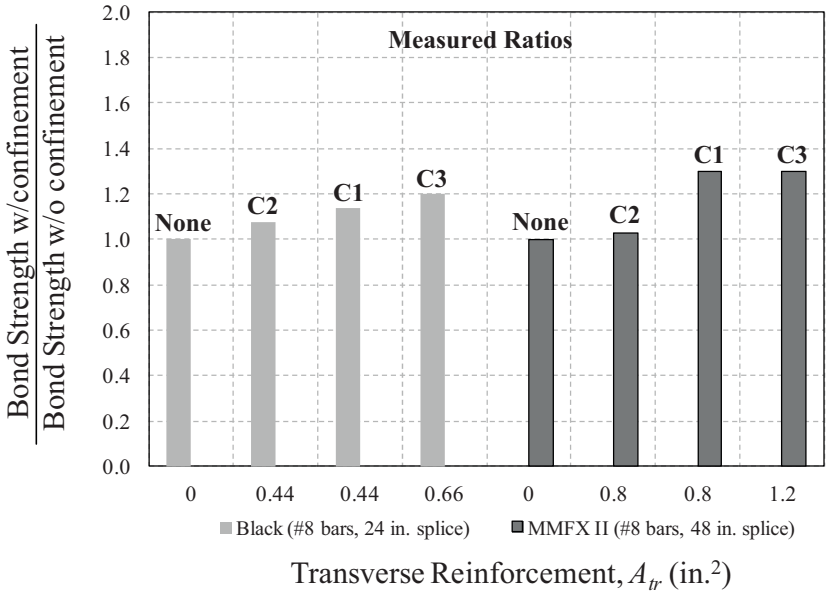

(a) Measured Ratios

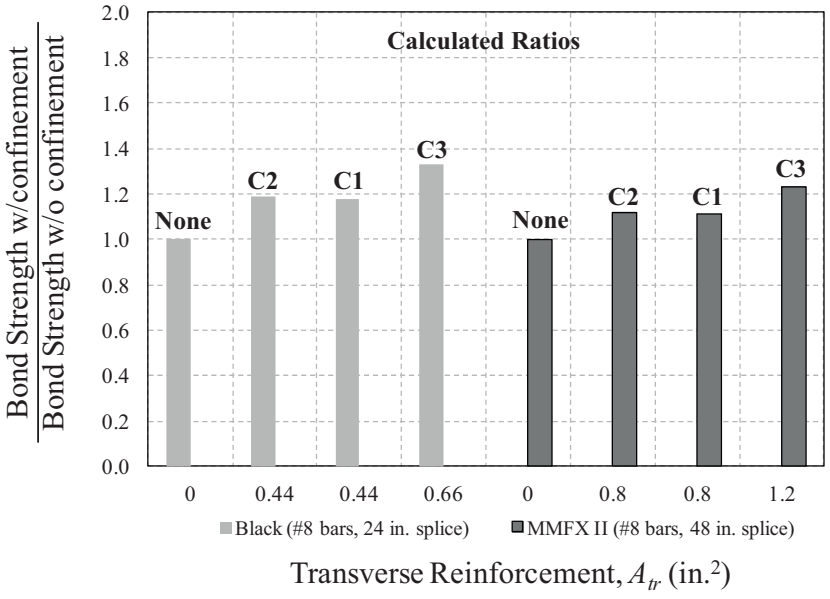

(b) Calculated Ratios

Figure C.56 Ratio of bond strength with and without confinement.

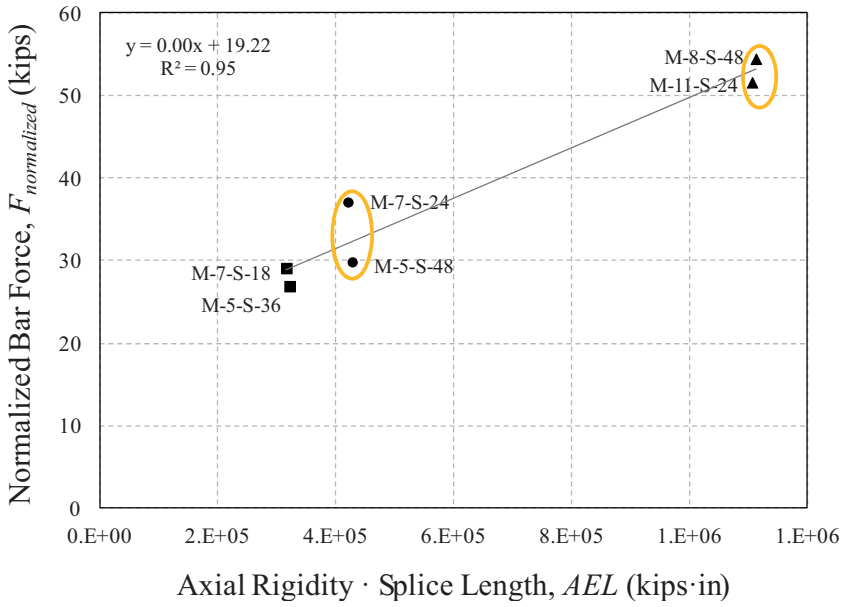

Figure C.57 Effect of axial rigidity on bond strength.

bottom cover c_b (Figure C.61). Number of specimens are available across a wide range.

A similar trend is shown for the side cover c_{so} distribution (Figure C.63) where approximately 40% of the specimens have side covers less than 1.5 in. and 66% of the data have side covers less than 2 in.

C.6.2 Influencing Factors

The bar stresses reached at splitting failure from the test results of the combined database are plotted against the concrete compressive strength f_c, splice length l_s, splice length to bar diameter ratio l_s/d_b, minimum cover dimensions c_{min}, minimum cover to bar diameter ratio c_{min}/d_b,

TABLE C.6
Summary of the Database with Unconfined Lap-Spliced Beams

Reference	No. of Tests	Splice Length l_s (in.)	Bar Diameter d_b (in.)	Concrete Cover c (in.)	Concrete Strength f'_c (psi)
Chinn, Ferguson, and Thompson (1955)	30	5.5 to 24.0	0.375 to 1.410	0.50 to 2.94	3,160 to 7,480
Chamberlin (1956)	1	12.0	0.500	0.50 to 2.00	4,540
Chamberlin (1958)	3	6.0	0.500	0.50 to 1.50	4,450
Ferguson and Breen (1965)	18	18.0 to 82.5	1.000 to 1.410	1.31 to 4.70	2,690 to 5,620
Ferguson and Thompson (1965)	4	49.4 to 63.3	1.410	1.50 to 10.15	2,730 to 3,410
Thompson, Jirsa, Breen, and Meinheit (1975)	11	12.0 to 60.0	0.750 to 1.690	1.00 to 4.00	2,870 to 4,710
Zekany, Neumann, Jirsa, and Breen (1981)	2	16.0 to 22.0	1.128 to 1.410	1.42 to 2.00	3,830 to 5,650
Cleary and Ramirez (1991)	4	10.0 to 12.0	0.750	2.00 to 3.25	3,990 to 8,200
Hadje-Ghaffari, Choi, Darwin, and McCabe (1990, 1991)	7	12.0 to 24.0	0.625 to 1.410	1.00 to 2.00	5,360 to 6,010
Hester, Salamizavaregh, Darwin, and McCabe (1991, 1993)	7	16.0 to 22.8	1.000	1.50 to 4.00	5,240 to 6,450
Rezansoff, Akanni, and Sparkling (1993)	4	29.5 to 44.3	0.992 to 1.177	0.99 to 2.00	3,730 to 4,030
Hwang, Lee, and Lee (1994)	4	11.8	1.130	1.13 to 1.14	9,240 to 12,180
Darwin, Tholen, Idun, and Zuo (1995)	13	16.0 to 40.0	0.625 to 1.410	1.02 to 3.06	3,830 to 5,250
Hamad, Mansour (1996)	3	11.8 to 13.8	0.551 to 0.787	0.79 to 4.69	2,900 to 3,350
Azizinamini, Pavel, Hatfield, and Ghosh (1999)	32	10.0 to 80.0	1.000 to 1.410	1.00 to 3.18	5,080 to 15,590
Zuo and Darwin (1998)	27	17.0 to 40.0	1.000 to 1.410	0.51 to 4.05	4,250 to 15,650
Hamad and Itani (1998)	8	12.0	0.984	1.50 to 1.58	7,590 to 11,120
Hamad and Machaka (1999)	3	12.0	0.984	1.02 to 1.10	6,770 to 13,460
Frosch and Pay (2006b)	1	12.0	1.000	0.50 to 1.50	4,020
El-Hacha, El-Agroudy, and Rizkalla (2006)	4	12.0 to 60.0	0.750	1.38 to 2.76	5,710 to 6,380
Seliem et al. (2009)	31	15.0 to 91.0	0.625 to 1.410	0.70 to 7.41	4,060 to 10,200
Richter (2012)	2	40.0	1.410	3.00 to 5.00	4,940 to 4,950
Sim (2014)	39	12.0 to 48.0	0.625 to 1.410	0.50 to 2.38	3,990 to 5,400
Totals	**252**	**5.5 to 91.0**	**0.375 to 1.690**	**0.50 to 10.15**	**2,690 to 15,650**

TABLE C.7
Summary of the Database with Confined Lap-Spliced Beams

Reference	No. of Tests	Tests with Pairs	Splice Length l_s (in.)	Bar Diameter d_b (in.)	Concrete Cover c (in.)	Concrete Strength f'_c (psi)
Mathey and Watstein (1961)	14	0	7.0 to 34.0	0.500 to 1.000	1.50 to 3.75	3,500 to 4,490
Ferguson and Breen (1965)	9	2	30.0 to 49.5	1.000 to 1.410	1.47 to 4.62	1,820 to 4,170
Thompson, Jirsa, Breen, and Meinheit (1975)	4	1	15.0 to 30.0	1.000 to 1.410	2.00	3,060 to 3,510
Zekany, Neumann, Jirsa, and Breen (1981)	10	10	16.0 to 22.0	1.130 to 1.140	1.50 to 2.00	3,750 to 5,700
DeVries, Moehle, and Hester (1991)	10	0	9.0 to 22.0	0.750 to 1.128	1.06 to 2.44	7,460 to 16,100
Rezansoff, Konkankar, and Fu (1991)	34	0	15.1 to 38.0	0.770 to 1.410	1.00 to 2.98	3,220 to 5,740
Hester, Salamizavaregh, Darwin, and McCabe (1991, 1993)	10	10	16.0 to 22.8	1.000	1.50 to 4.00	5,240 to 6,450
Rezansoff, Akanni, and Sparkling (1993)	11	0	11.8 to 44.3	0.992 to 1.177	0.50 to 2.00	3,630 to 4,090
Hwang, Lee, and Lee (1994)	4	4	11.8	1.130	1.13 to 1.14	9,000 to 11,680
Kadoriku (1994)	34	0	15.0 to 37.4	0.750	1.12 to 4.80	3,070 to 10,980
Darwin, Tholen, Idun, and Zuo (1995)	56	4	10.0 to 40.0	0.625 to 1.410	0.40 to 4.50	3,810 to 5,250
Hasan, Cleary, and Ramirez (1996)	1	0	12.0	0.875	2.38 to 4.63	3,900
Azizinamini, Pavel, Hatfield, and Ghosh (1999)	25	16	15.0 to 57.5	1.000 to 1.410	1.00 to 3.18	14,580 to 16,000
Zuo and Darwin (1998)	63	0	16.0 to 40.0	1.000 to 1.410	0.40 to 4.00	4,250 to 15,650
Hamad and Machaka (1999)	6	6	12.0	0.984	1.02 to 1.10	9,430 to 13,950
El-Hacha, El-Agroudy, and Rizkalla (2006)	3	0	24.0 to 72.0	1.000	1.38 to 4.87	5,710 to 6,870
Seliem et al. (2009)	38	38	27.0 to 91.0	1.000 to 1.410	1.38 to 7.52	4,060 to 10,200
Sim (2014)	6	6	24.0 to 48.0	1.000	0.50 to 1.5	4,400 to 5,400
Totals	**338**	**97**	**7.0 to 91.0**	**0.500 to 1.410**	**0.40 to 7.52**	**1,820 to 16,100**

bottom cover to bar diameter ratio c_b/d_b, half of clear spacing to bar diameter ratio c_{si}/d_b, and side cover to bar diameter ratio c_{so}/d_b. The influence of these parameters were studied to select the important parameters in constructing an analytical model. As shown in Figure C.64, there is almost no trend between the bar stresses reached at failure and the concrete compressive strength. However, there is higher correlation between the test data and splice length (Figure C.65). By using the ratio of splice length to bar diameter (l_s/d_b), this relationship increases as shown in Figure C.66.

Regarding the cover and spacing dimensions, the beam specimens in the database can be grouped into cases of a side splitting failure and a face splitting failure. However, to construct a simple model based on the analogy that bursting stresses around the reinforcing bars can be modeled as a surrounding-cylinder, half of the clear spacing between the bars is considered identical to the side and bottom covers. With this assumption, the minimum cover among the side cover, bottom cover, and half of the clear spacing was first investigated to study the bar stresses (Figure C.67 and Figure C.68).

Although, there is not strong correlation between the minimum cover dimension (c_{min}) and the bar stresses reached at failure (Figure C.67), the bar stresses reached at failure plotted against the minimum cover to bar diameter ratio (c_{min}/d_b) shown in Figure C.68 suggests that the fourth root

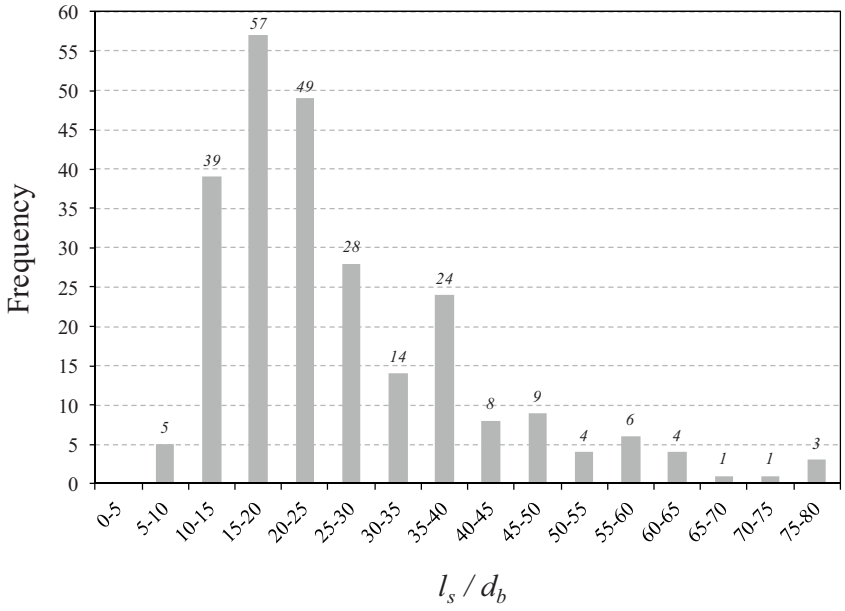

Figure C.58 Distribution of splice length/bar diameter (combined database).

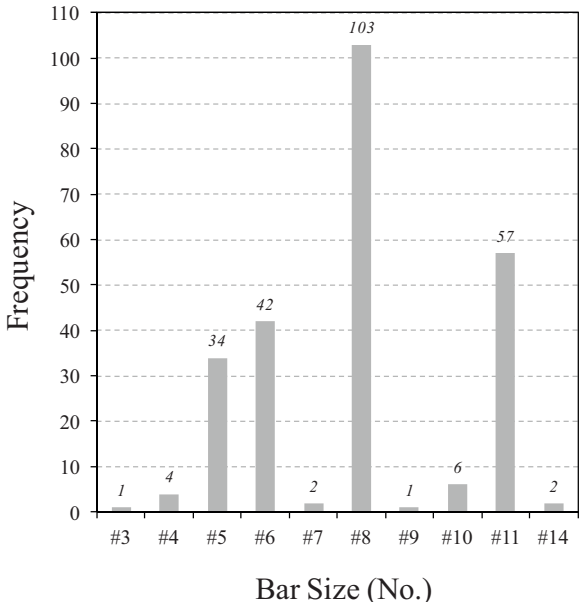

Figure C.59 Distribution of bar size (combined database).

of this ratio could be used to estimate the bar stresses. Again, there is significant scatter.

Other cover dimensions such as bottom cover to bar diameter ratio (c_b/d_b), half of clear spacing to bar diameter ratio (c_{si}/d_b), and side cover to bar diameter ratio (c_{so}/d_b) were further investigated. The trend between bottom cover to bar diameter ratio and bar stress was minor (Figure C.69). This is understandable because the distribution of bottom cover shown in Figure C.61 is concentrated on three different cover ranges that consist of 76% of all specimens.

The half of clear spacing to bar diameter ratio c_{si}/d_b (Figure C.70) and the side cover to bar diameter ratio c_{so}/d_b (Figure C.71), however, produced higher correlation with the bar stresses reached at failure than the minimum cover to bar diameter ratio c_{min}/d_b. These parameters will be considered further in constructing an analytical model.

C.6.3 Proposed Model

C.6.3.1 Dimensional and regression analysis. Dimensional analysis is useful when simplifying a complex relationship between different physical quantities to the simplest (or most economical) form (Sonin, 2001). The physical variables of interest are transformed (normalized) into dimensionless groups to determine relationships between the variables considering the fact that a physical relationship or a mathematical expression of the relationship must be dimensionally homogeneous and independent of the basic units (such as length, mass, or time) used to measure the physical quantities.

Similar to the approach Zsutty (1968) suggested to calculate shear strength, a simple analytical model has been developed to calculate bond strength using the technique of dimensional analysis. The fundamental physical dimensions (units) of force (F) and length (L) are used to categorize the test data as follows:

$$\begin{gathered} F_b = F \\ f'_c = F \cdot L^{-2} \\ l_s,\ d_b,\ c_{\min} = L \\ AE,\ F_{tr} = F \end{gathered} \tag{C.23}$$

where:

F_b = *bond force (kips)*
f'_c = *specified compressive strength of concrete (psi)*
l_s = *splice length (in.)*
d_b = *nominal diameter of bar (in.)*
c_{min} = *min(c_{so}, c_{si}, c_b) (in.)*
AE = *axial rigidity of bar (kips)*
F_{tr} = *contribution of transverse reinforcement (kips)*

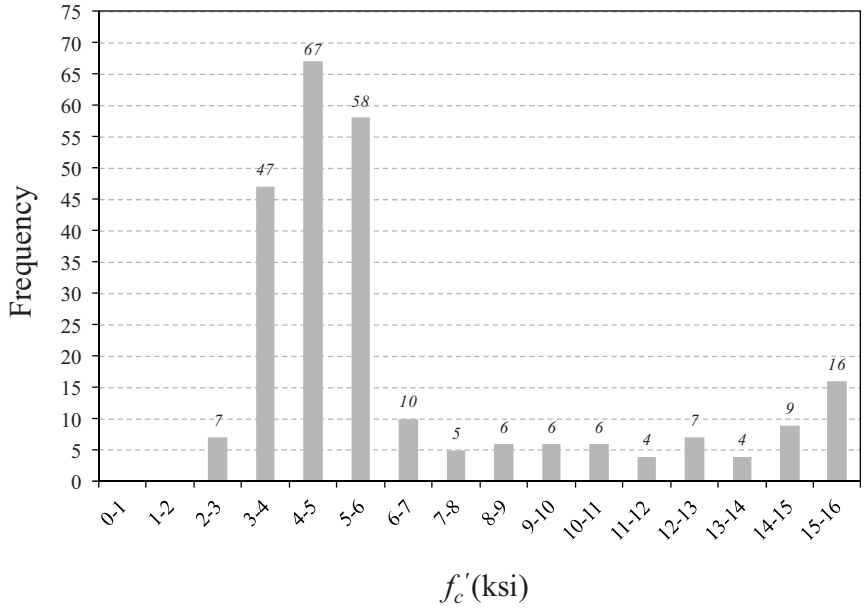

Figure C.60 Distribution of concrete compressive strength (combined database).

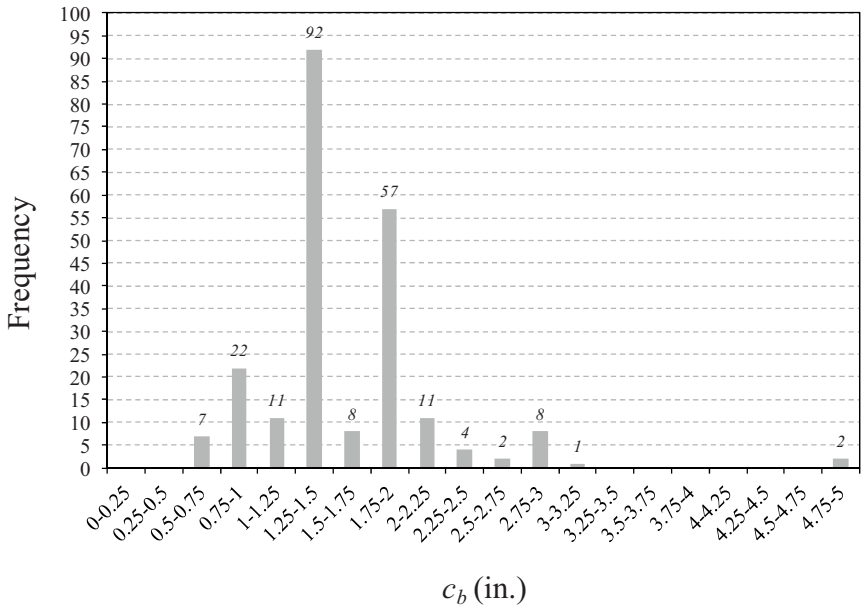

Figure C.61 Distribution of bottom cover (combined database).

Applying the Buckingham Π theorem which states that a physically meaningful equation involving n variables (that are considered pertinent to the problem) can be equivalently rewritten as an equation of n-k dimensionless parameters, where k is the number of fundamental dimensions. The same dimensions should present on the left and right sides of the equation to become a meaningful equation.

$n = 7$ *quantities* (F_b, f'_c, l_s, d_b, $c_{\min}$, F_{tr}, AE)
$k = 2$ basic dimensions (F, L)
$q = n(k = 7-2 = 5$ dimensionless ratios

Letting $f_b = k_b\left(f'_c\right)^b$ represent the bond stress in terms of concrete strength, with units of psi ($F{\cdot}L^{(2)}$) and $A_{ref}E_{ref}$ represent the axial rigidity of the reference reinforcing bar (which could be any size and type of bar such as glass fiber polymer (FRP) reinforcement), the 5 dimensionless ratios selected becomes:

$$\Pi_1 = \frac{F_b}{\pi d_b l_s f_b} \quad \Pi_2 = \frac{l_s}{d_b}$$

$$\Pi_3 = \frac{c_{\min}}{d_b} \quad \Pi_4 = \frac{F_{tr}}{\pi d_b l_s f_b}$$

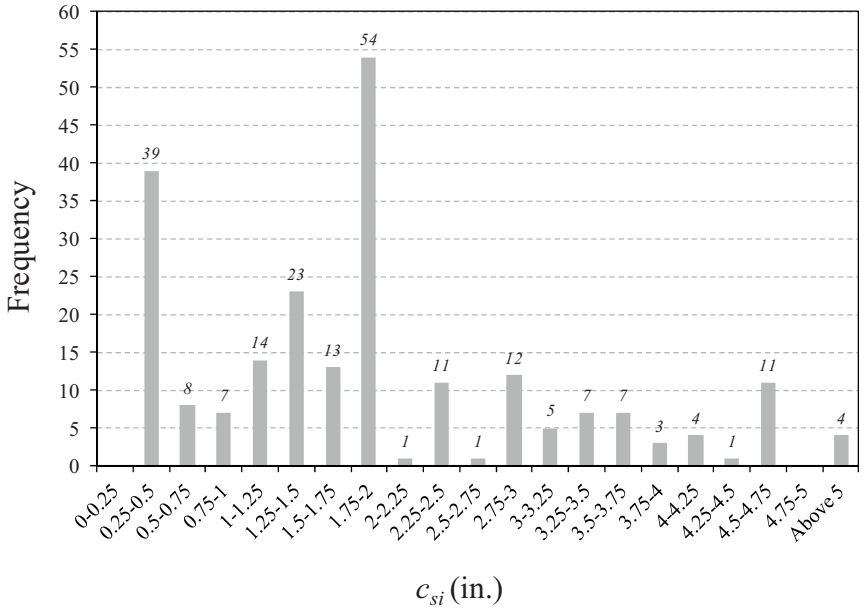

Figure C.62 Distribution of half of clear spacing (combined database).

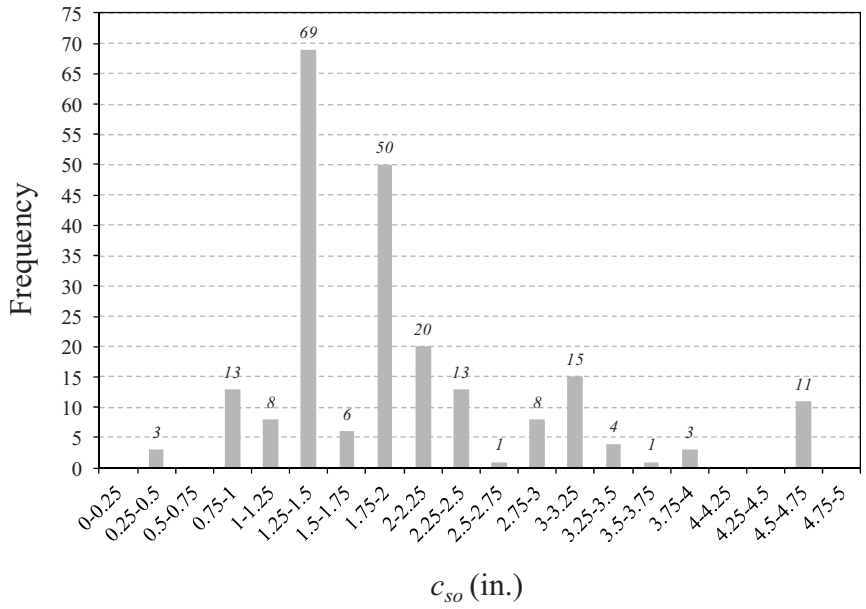

Figure C.63 Distribution of side cover (combined database).

$$\Pi_5 = \frac{AE}{A_{ref}E_{ref}}$$

The dimensionless ratio Π_5 is neglected in this analysis because the database only contains steel reinforcing bars with equivalent modulus of elasticity. In addition, the Π_5 term is not needed as the relationship between axial rigidity and bond strength was previously investigated by Frosch and Pay (2006b), and a model was suggested that fits well to the combined test data of steel reinforcing bars and FRP bars. To find a relationship between the dimensionless ratios for lap-spliced beam tests without confinement, the dimensionless ratio Π_4 for confinement is also not considered in the initial analysis. The contribution of confinement will be discussed separately later in this section. Therefore, the resulting dimensionless ratio equation becomes:

$$\frac{F_b}{\pi d_b l_s f_b} = \kappa\left(\frac{l_s}{d_b}\right)^{\alpha}\left(\frac{c_{\min}}{d_b}\right)^{\beta} \tag{C.24}$$

Using the relationship of $f_b = k_b\left(f_c'\right)^b$, the format of the bond stress equation becomes:

$$\frac{F_b}{\pi d_b l_s} = k\left(f_c'\right)^{b_1}\left(\frac{l_s}{d_b}\right)^{b_2}\left(\frac{c_{\min}}{d_b}\right)^{b_3} \tag{C.25}$$

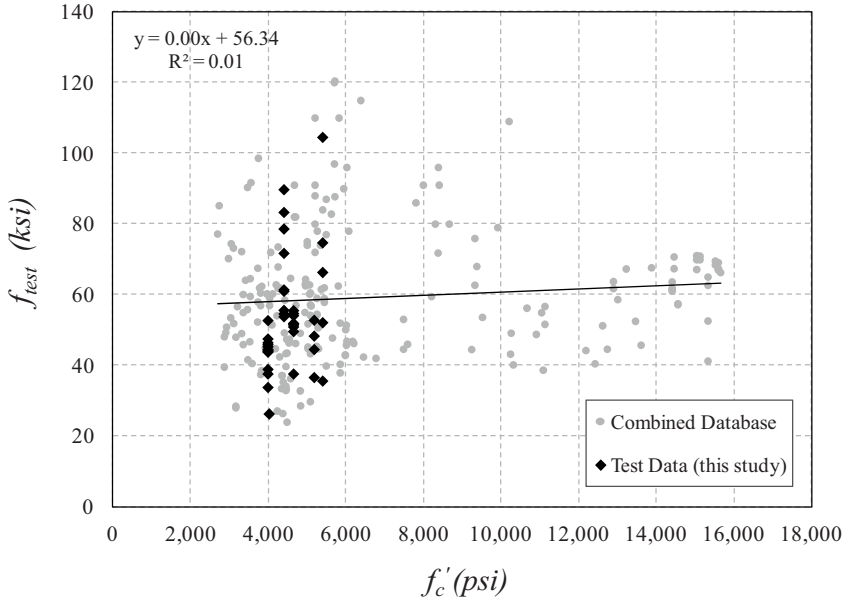

Figure C.64 Bar stress vs. concrete compressive strength.

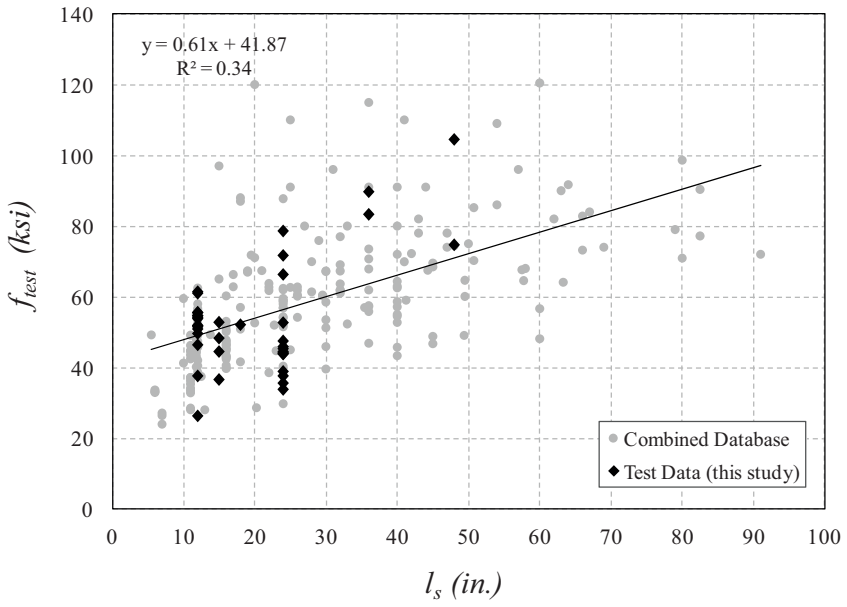

Figure C.65 Bar stress vs. splice length.

To find the constants, k, b_1, b_2, and b_3 by regression analysis of the test data, Equation (C.25) is transformed into logarithmic form as shown in Equation (C.26) which is a very common way to handle situations where a non-linear relationship exists between variables (for example, the non-linear relationship between bond stress and splice length), while still preserving the linear model.

$$\ln\left[\frac{F_b}{\pi d_b l_s}\right] = \ln(k) + b_1 \ln\left(f'_c\right) + b_2 \ln\left(\frac{l_s}{d_b}\right) + b_3\left(\frac{c_{\min}}{d_b}\right) \tag{C.26}$$

Regression analysis on the 252 beam tests data without confinement results in the following constants (constants rounded for simplicity):

$k = 0.35$ $b_1 = 0.25$ $b_2 = -0.5$ $b_3 = 0.25$

With the constants, Equation (C.25) becomes:

$$\frac{F_b}{\pi d_b l_s} = 0.35 \cdot \sqrt[f'_c]{4}\sqrt{\frac{d_b}{l_s}}\frac{c_{\min}}{d_b}\sqrt{4} \tag{C.27}$$

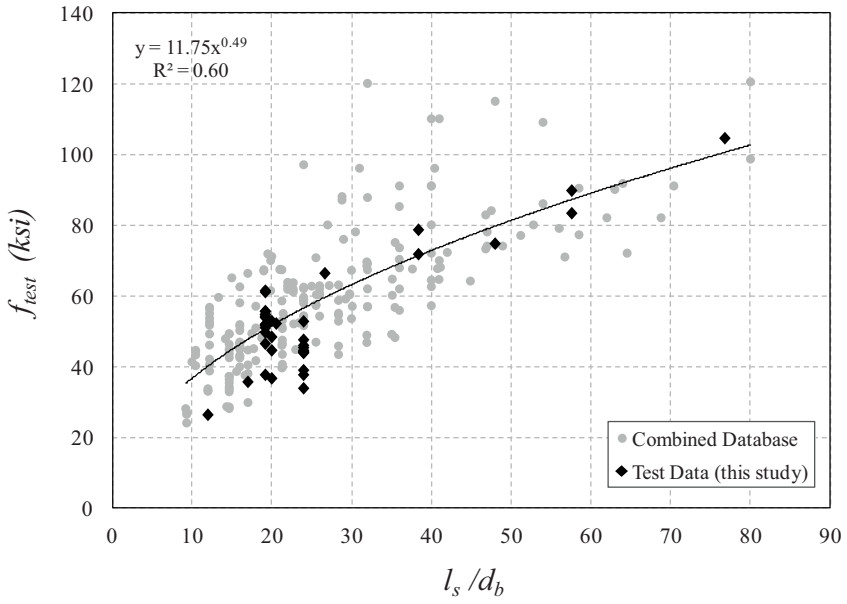

Figure C.66 Bar stress vs. splice length to bar diameter ratio.

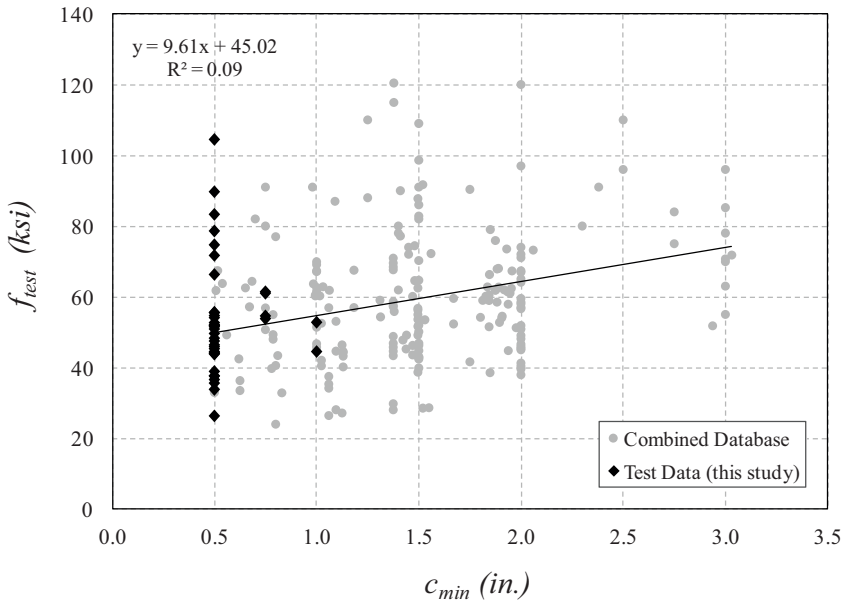

Figure C.67 Bar stress vs. minimum cover.

By arranging the expression presented in Equation (C.27) in terms of bar stress by substituting the area of the reinforcing bar, the following equation is developed:

$$f_b = 1.4 \cdot \sqrt[f'_c]{4} \sqrt{\frac{l_s}{d_b}} \sqrt[\frac{c_{min}}{d_b}]{4} \tag{C.28}$$

Solving Equation (C.28) for l_s/d_b, the development length to bar diameter ratio for beams without confinement can be computed as follows:

$$\frac{l_s}{d_b} = \frac{f_b^2}{2\sqrt{f'_c}} \frac{1}{\sqrt{\frac{c_{min}}{d_b}}} \tag{C.29}$$

where:

l_s = *splice or development length (in.)*
d_b = *nominal diameter of bar (in.)*

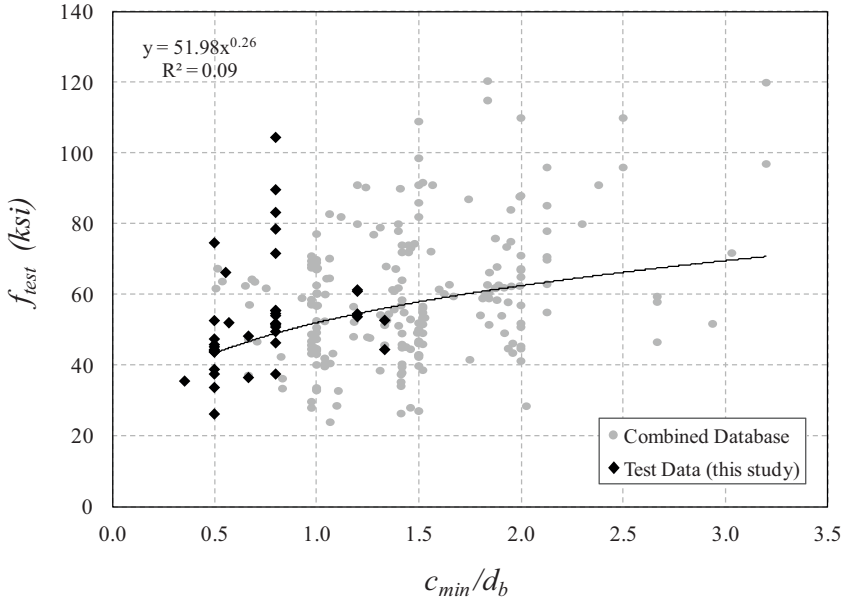

Figure C.68 Bar stress vs. minimum cover to bar diameter ratio.

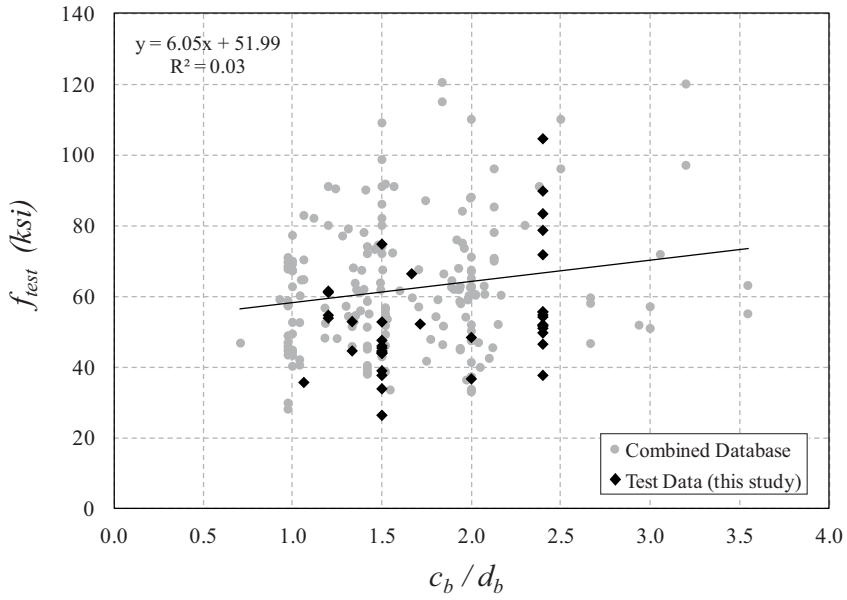

Figure C.69 Bar stress vs. bottom cover to bar diameter ratio.

f_b = *bar stresses at failure (psi)*
f'_c = *specified compressive strength of concrete (psi)*
c_{min} = *min(c_{so}, c_{si}, c_b) (in.)*
c_{so} = *side clear cover of reinforcing bars (in.)*
c_{si} = *half of clear spacing between bars (in.)*
c_b = *bottom clear cover of reinforcing bars (in.)*

The dimensional analysis and regression analysis demonstrates that the bar stress reached at failure has better correlation with the fourth root of concrete compressive strength, $\sqrt[4]{f'_c}$, than the square root of concrete compressive strength, $\sqrt{f'_c}$, which is consistent with observations from other research (ACI 408, 2003; Canbay & Frosch, 2005; Frosch & Pay, 2006b; Zuo & Darwin, 1998, 2000).

It is interesting to also note that bar stress at failure is proportional to square root of splice length which accounts for the non-linear trend between bond strength and splice length. This observation is also consistent with the analytical model proposed by Pay (2005) and the parametric analysis performed by Canbay and Frosch (2005), although the three models were developed by a different procedure.

Because the side cover to bar diameter ratio (c_{so}/d_b) was observed from the previous section to have a larger influence than the minimum cover to bar diameter ratio (c_{min}/d_b),

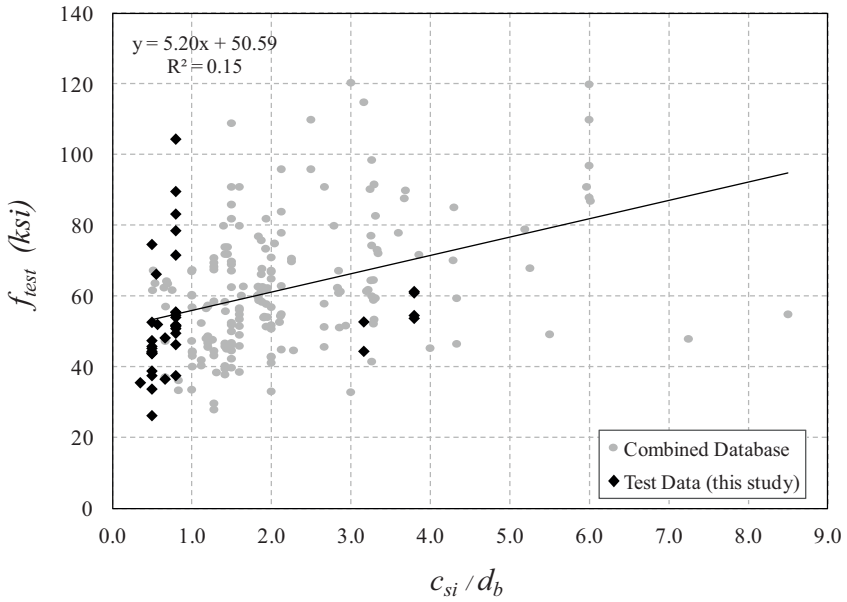

Figure C.70 Bar stress vs. half of clear spacing to bar diameter ratio.

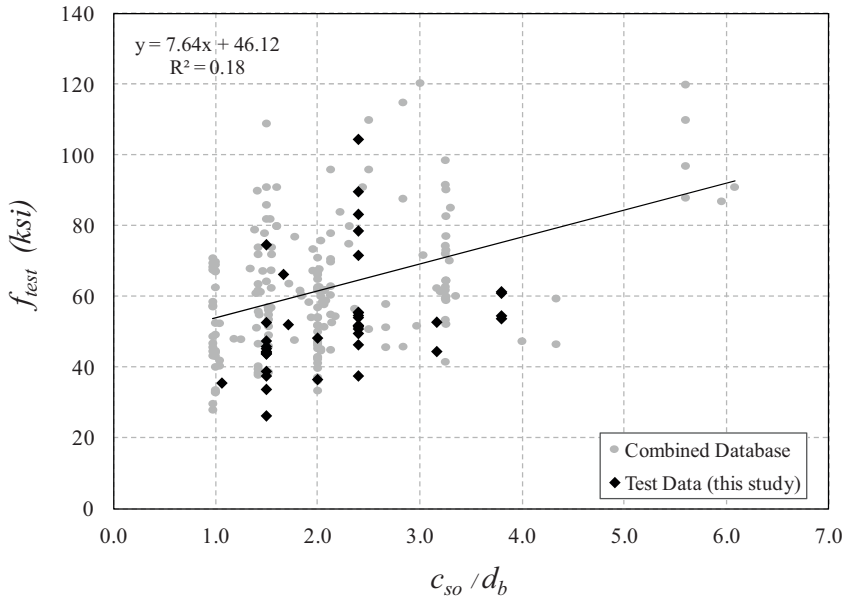

Figure C.71 Bar stress vs. side cover to bar diameter ratio.

Equation (C.25) was further investigated with c_{min}/d_b replaced with c_{so}/d_b. Through regression analysis, the exponents remain the same except the constant k which changes to 0.25. Equation (C.27) can be rewritten as follows:

$$\frac{F_b}{\pi d_b l_s} = 0.25 \cdot \sqrt[4]{f'_c}\sqrt{\frac{d_b}{l_s}}\sqrt[4]{\frac{c_{so}}{d_b}} \tag{C.30}$$

By arranging the expression presented in Equation (C.30) in terms of bar stress by substituting the area of the reinforcing bar, the following equation is developed:

$$f_b = \sqrt[4]{f'_c}\sqrt{\frac{l_s}{d_b}}\sqrt[4]{\frac{c_{so}}{d_b}} \tag{C.31}$$

Solving for l_s/d_b, the development length to bar diameter ratio for beams without confinement can be computed as follows:

$$\frac{l_s}{d_b} = \frac{f_b^2}{\sqrt{f'_c}}\frac{1}{\sqrt{\frac{c_{so}}{d_b}}} \tag{C.32}$$

where:

l_s = *splice or development length (in.)*
d_b = *nominal diameter of bar (in.)*
f_b = *bar stresses at failure (psi)*
f'_c = *specified compressive strength of concrete (psi)*
c_{so} = *side clear cover of reinforcing bars (in.)*

C.6.3.2 Comparisons with other descriptive equations. The proposed models (Equation C.28 and C.31) were compared with other descriptive expressions and design equations focused on bond strength and development length presented (Canbay & Frosch, 2005; Frosch & Pay, 2006b; Orangun et al., 1977; Zuo & Darwin, 2000).

Orangun, Jirsa, and Breen (1977). As discussed earlier, Orangun, Jirsa, and Breen (1977) studied the effect of splice length, concrete cover, bar diameter, concrete strength, transverse reinforcement, and the strength of anchored or developed bar to derive the expression shown in Equation (C.3). This expression became the basis of the ACI 318-11 equation discussed in Section 5.2.1.1. To compare bar stresses reached at failure, Equation (C.3) is re-arranged as follows for unconfined specimens:

$$f_s = \frac{4\sqrt{f'_c}}{\pi d_b^2}\left(1.2 + \frac{3C}{d_b} + \frac{50d_b}{l_d}\right) \tag{C.33}$$

where:

f_s = *bar stress at failure (ksi)*
f'_c = *concrete cylinder strength (psi)*
d_b = *nominal diameter of bar (in.)*
C = *the smaller of clear bottom cover to main reinforcement and half clear spacing between bars or splices (in.)*
l_d = *development length (in.)*

Zuo and Darwin (2000). Zuo and Darwin (2000) studied the effects of concrete strength, coarse aggregate quantity and type, and reinforcing bar geometry on bond strength. To compare bar stresses reached at failure, their expression which was obtained from regression analysis of unconfined specimens can be re-arranged as given by Equation (C.34). This expression is the basis of the ACI 408 approach discussed in Section 5.2.1.2.

$$f_s = \frac{\sqrt[4]{f'_c}}{A_b}[59.8l_s(c_{\min} + 0.5d_b) + 2350A_b]\left(0.1\frac{c_{\max}}{c_{\min}} + 0.9\right) \tag{C.34}$$

where:

$$0.1c_{max}/c_{min} + 0.9 \leq 1.25$$

where:

f_s = *bar stresses at failure (psi)*
f'_c = *specified compressive strength of concrete (psi)*
A_b = *area of spliced reinforcement (in.^{2})*
l_s = *splice or development length (in.)*
c_{max} = *maximum value of c_s or c_b(in.)*
c_{min} = *minimum value of c_s or c_b(in.)*
c_s = $\min(c_{si} + 0.25, c_{so})$
c_{si} = *half of clear spacing between bars (in.)*
c_{so} = *side clear cover of reinforcing bars (in.)*
c_b = *bottom clear cover of reinforcing bars (in.)*
d_b = *nominal diameter of bar (in.)*

Canbay and Frosch (2005). The descriptive equation suggested by Canbay and Frosch (2005) was previously discussed in Section 5.2.1.4 and is represented by Equation (C.13) for the computation of bar stress.

Frosch and Pay (2006b). The development length equation proposed by Frosch and Pay (2006b) which considers the modulus of elasticity of reinforcing bars (FRP and steel reinforcement), can be re-arranged to compute bar stress and is given as Equation (C.35).

$$f_b = \sqrt{\frac{E_b}{20,280}}\sqrt{\frac{l_s}{d_b}}\sqrt[4]{f'_c}\left(\frac{1}{0.2\frac{c}{d_b}+0.75}\right)\cdot\frac{1}{d_b} \qquad \text{(C.35)}$$

where:

f_b = *bar stresses at failure (ksi)*
E_b = *modulus of elasticity of the spliced reinforcement (ksi)*
l_s = *splice or development length (in.)*
d_b = *nominal diameter of bar (in.)*
f'_c = *specified compressive strength of concrete (psi)*
A_b = *area of spliced reinforcement (in.^{2})*
c = *minimum of c_{si} or c_b(in.)*
c_{si} = *half of clear spacing between bars (in.)*

Unlike design equations which are meant to provide conservative estimates of failure stresses, predictive (descriptive) equations are based on models that should provide reasonably accurate estimates of bar stresses at failure. For that reason, the test to calculated ratio should be greater than 1.0 when a design equation is used while the mean test to calculated ratio for large sample of tests should ideally be near 1.0 when calculated values are provided using descriptive equations.

Table C.8 presents the statistical comparison of the results of the various models. For this analysis, the test data collected from the combined database was compared with the calculated values from the equations. The mean, standard deviation, coefficient of variation (COV), and the product moment coefficient of correlation (r^2) are investigated for the ratio of test to calculated bar stresses at failure. A low coefficient of variation (COV) and high coefficient of correlation (r^2) indicate that the experimental data matches well with the calculated values. As the correlation gets closer to 1, the model is more reliable. The scatter of data is presented by the coefficient of variation (COV) which indicates the deviation of the data from its mean value.

TABLE C.8
Statistical Comparison of Descriptive Equations (Combined Database)

Model	Mean	Std. Dev.	COV	r^2
Orangun, Jirsa, and Breen (1977), Equation (C.33)	1.086	0.285	0.262	0.826
Zuo and Darwin (2000), Equation (C.34)	1.042	0.133	0.128	0.919
Canbay and Frosch (2005), Equation (C.13)	0.908	0.201	0.221	0.819
Frosch and Pay (2006b), Equation (C.35)	1.116	0.201	0.180	0.780
Proposed Model, Equation (C.28)	1.063	0.158	0.148	0.847
Proposed Model, Equation (C.31)	1.139	0.150	0.132	0.894

The models suggested by Canbay and Frosch (2005) and Frosch and Pay (2006b) have a lower standard deviation and coefficient of variation compared to the expression proposed by Orangun et al. (1977). The expressions proposed by Zuo and Darwin (2000) performed the best among these models with high correlation with the test data. However, the relatively simpler model proposed in this study (Equation C.29 and Equation C.32) performed similar to the model suggested by Zuo and Darwin (2000) and demonstrated comparable statistics with a small coefficient of variation (COV) and a high coefficient of correlation (r^2).

To investigate the consistency of the estimated bar stresses, the ratio of measured to calculated bar stresses (f_{test}/f_{calc}) is plotted against the calculated bar stresses (f_{calc}) for the various models shown in Table C.8. The Orangun et al. (1977) model shown in Figure C.72 demonstrates that the measured to calculated ratio (f_{test}/f_{calc}) decreases as the calculated stresses increase. In comparison, the model suggested by Zuo and Darwin (2000) in Figure C.73 shows less trend than the Orangun et al. (1977) model. The data has decreased scatter indicating that the stress calculations are matching well with the measured values. The Canbay and Frosch (2005) model shown in Figure C.74 also has less trend than the Orangun et al. (1977) model but there is a slight increase in the scatter compared to the model by Zuo and Darwin (2000). The model suggested by Frosch and Pay (2006b) (see Figure C.75) has approximately the same level of accuracy in calculating bar stresses. However, the results are more compressed to the left of the graph.

Finally, the models proposed in current study are shown in Figure C.76 which results in consistent calculations regardless of stress level. Both equations provides reasonable results compared to the measured values. In addition, the scatter is reduced relative to the other expressions.

In summary, Figure C.77 to Figure C.82 present the frequency of test specimens for the given range of test to calculated bar stress ratios (f_{test}/f_{calc}). All of the methods provide approximately a normal distribution. The Orangun et al. (1977) model (Figure C.77) estimates splice strengths in a wider range compared to other models. The Zuo and Darwin (2000) model provides excellent estimates of splice strengths with the majority of the results being in the range of 0.8 to 1.1 as shown in Figure C.78. The Canbay and Frosch (2005) model (Figure C.79) has more tests closer to 1

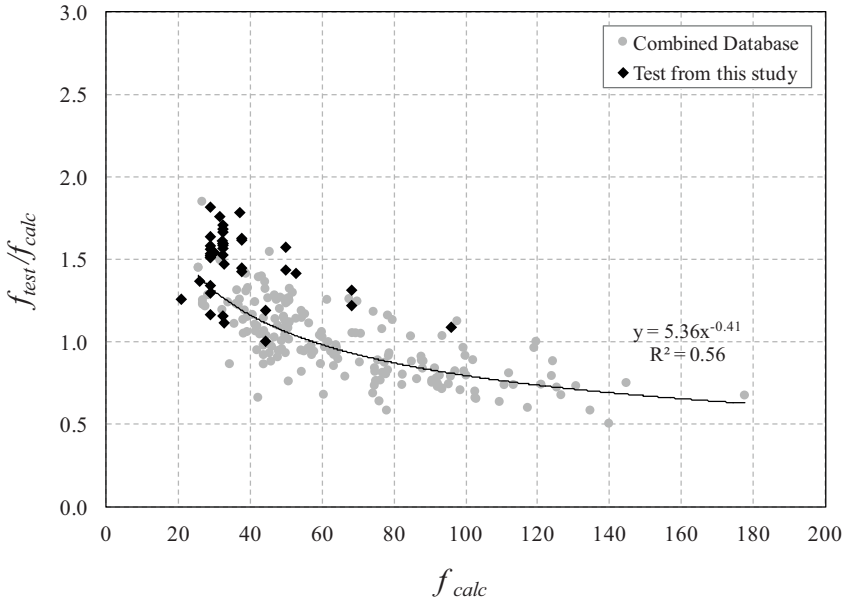

Figure C.72 Test to calculated ratios vs. Orangun et al. (1977) model.

compared to Orangun et al. (1977) model but results in a wider range of values compared to the Zuo and Darwin (2000) model. The Frosch and Pay (2006b) model (Figure C.80) is distributed well around 1 where most of the test/calculated values are between 0.9 and 1.3. Equation (C.28) of the current study has less scatter and test/calculated ratios concentrated near 1 (Figure C.81). Finally, as shown in Figure C.82, Equation (C.31) show improved results with test/calculated ratios primarily between 1.0 and 1.3.

C.6.3.3 Different bar type. The proposed model suggested by Equation (C.32) in the current study was derived from dimensional and regression analysis of available test data of steel reinforced specimens. Therefore, this equation is not meant to be used with other reinforcing materials. However, it is possible to slightly change Equation (C.32) with a simple modification factor for different types of reinforcing materials. By including a multiplier X based on test data for each type of reinforcement (similar to the approach used in design codes and the method suggested by Mosley (2000) for FRP reinforcement), the modified equation is shown below:

$$\frac{l_s}{d_b} = \frac{f_b^2}{\sqrt{f'_c}} \frac{1}{\sqrt{\frac{c_{so}}{d_b}}} X \tag{C.36}$$

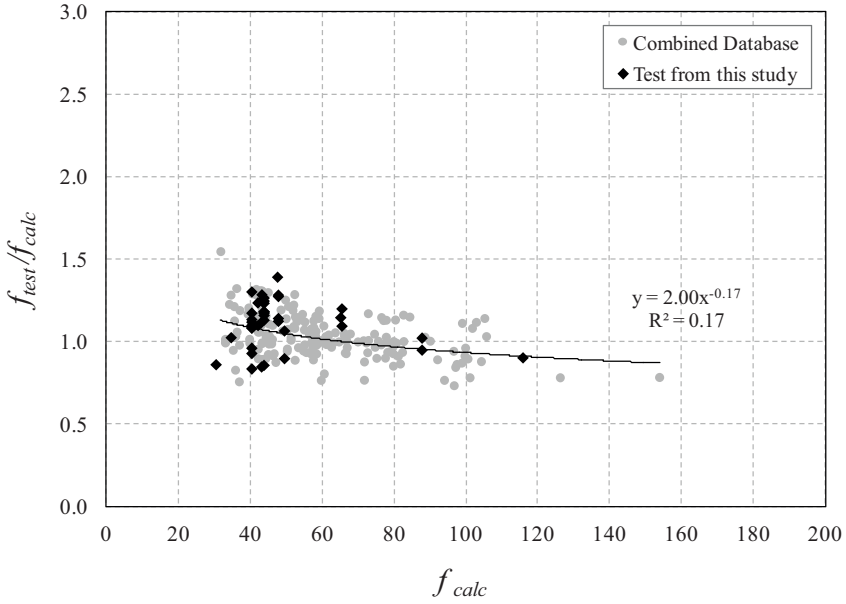

Figure C.73 Test to calculated ratios vs. Zuo and Darwin (2000) model.

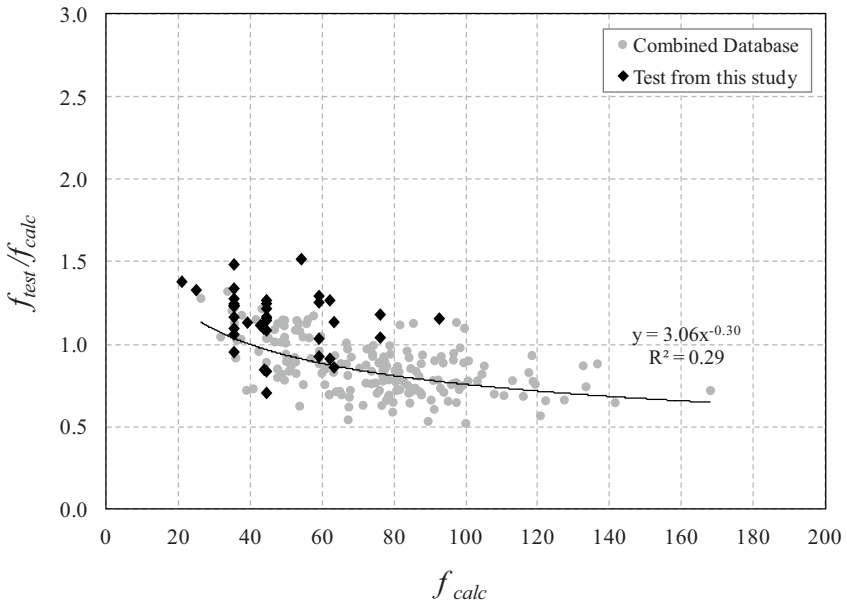

Figure C.74 Test to calculated ratios vs. Canbay and Frosch (2005) model.

Solving for X using the design dimensions for l_s, d_b, and c_{so} while taking the values of f_b and f_c as the calculated bar stress at failure and the average compressive strength at the time of testing, the X factors for each of the specimens tested in the experimental program were calculated and are provided in Table C.9. For the purpose of comparison, X values were determined for conventional black steel specimens. Considering that Equation (C.36) was derived from test data of conventional steel reinforced (black) specimens, the X factors for each bar type were normalized to the black bar. In addition, the average and maximum values of the normalized values are shown on Table C.9. The modification factors derived directly from taking the inverse of the bond ratios shown in Table C.3 are also presented.

The bond ratio of face split specimens are in most cases relatively higher than side split specimens. For that reason, the maximum modification factor was calculated by considering the minimum bond ratios of side split specimens. The bond ratios of the face split specimens in the current study were higher than the side split specimens except for one specimen with Zbar.

As shown in Table C.9, the normalized ratio derived from solving X in Equation (C.36) differs from the modification factor from the bond ratios in Table C.3.

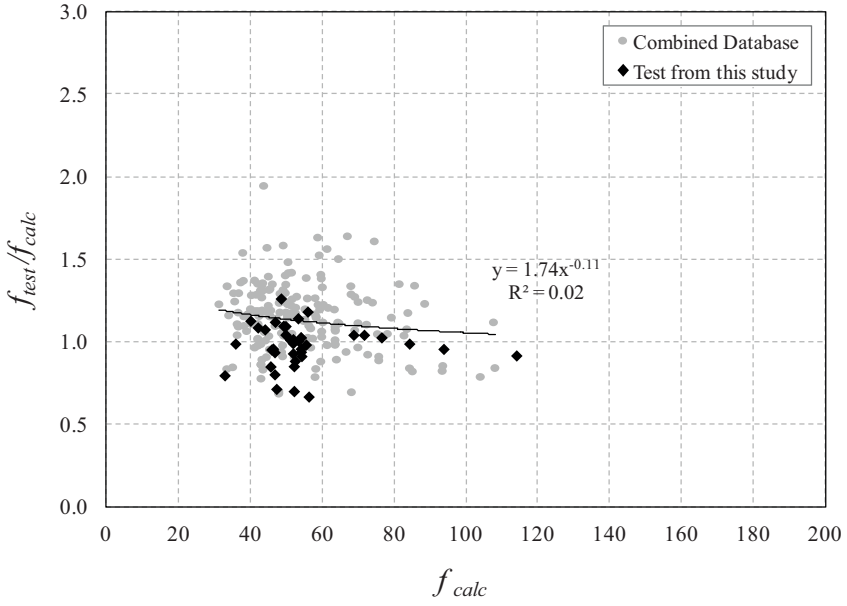

Figure C.75 Test to calculated ratios vs. Frosch and Pay (2006b) model.

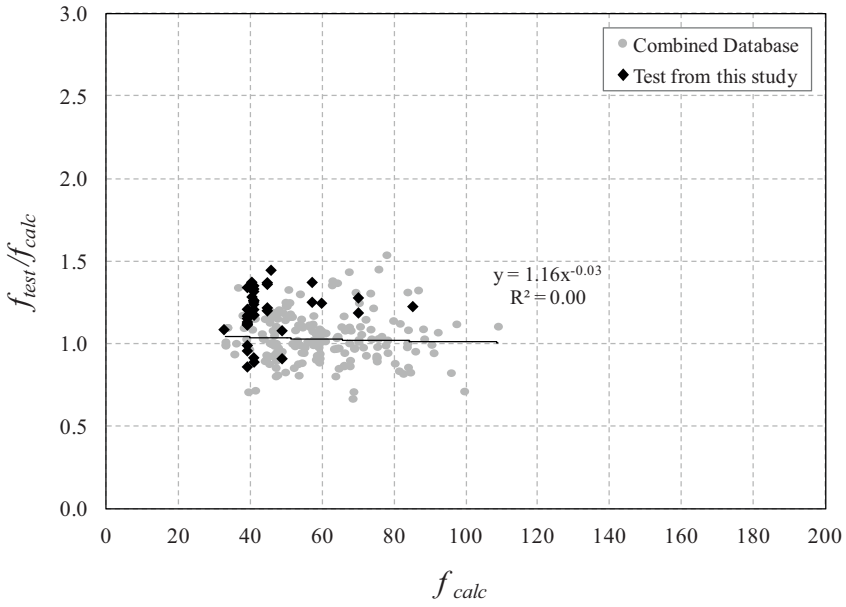

(a) Model from Equation (5-27)

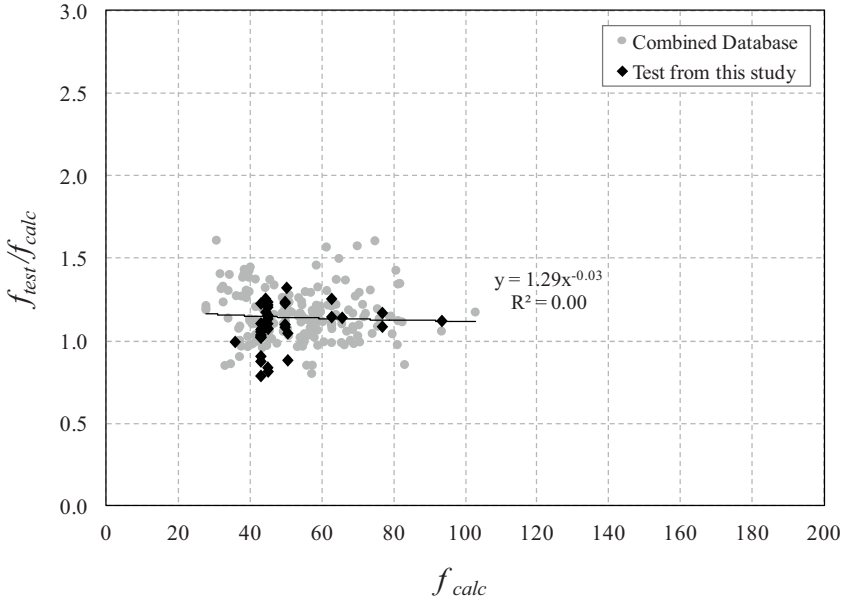

(b) Model from Equation (5-30)

Figure C.76 Test to calculated ratios vs. proposed model.

These results are different because the proposed model considers that bar stress is not linearly related to splice length but to the square root. For example, adding double the splice length does not result in double the bond strength. In other words, a multiplier of 2.0 only results in 1.41 more strength. Therefore, the square root of the normalized ratios calculated from the *X* factors is comparable with the modification factors directly calculated by taking the inverse of the bond ratios presented in Table C.3.

When the ACI 318 (2011) or AASHTO LRFD (2010) expressions are used, the multiplication factors would be different from the normalized ratio of *X* factors in Table C.9 because both design equations assume an linear relationship between bond strength and splice length. In other words, if a multiplier for the ACI 318 equation is derived the same way as *X* factors were found, the multiplier will be valid only for that specific stress level where the relative factor was found. Because, the relationship between bond strength and splice length is actually nonlinear, for each stress level, there should

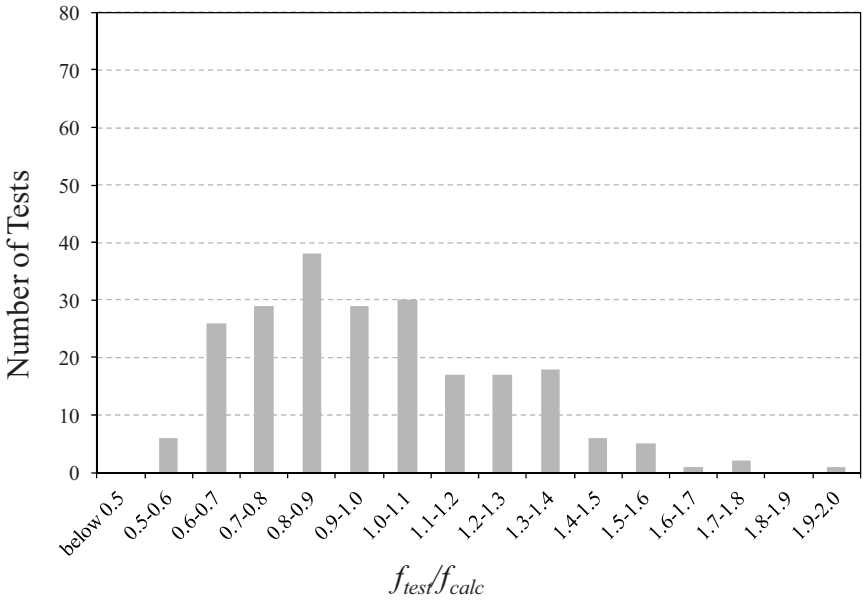

Figure C.77 Orangun, Jirsa, and Breen (1977) model with the combined database.

be a different multiplier to use the linear equation. The modification factor obtained from the X factors incorporate this nonlinear behavior because it was derived based on Equation (C.36) which already accounts for the nonlinear relationship between bond strength and splice length. Figure C.83 show the relationship between splice length and bar stress for the black, epoxy, and tin-plated zinc-clad (Zinc-clad 2) bars. Figure C.83(a) demonstrates the case when a linear multiplier is used for the ACI 318 equation. The linear multipliers are consisted with the modification factor in Table C.9 which is based on linear behavior. On the other hand, Figure C.83(b) presents the case when the nonlinear multiplier (derived from the proposed model) is used for the three bars.

As shown in Figure C.83(a) when a linear multiplier is used for the ACI 318 equation, the cross-over points move towards the left while as demonstrated in Figure C.83(b), when the nonlinear multiplier is used, the cross-over between the proposed model and ACI 318 equation occurs at approximately the same stress level. For that reason, when a linear multiplier is used, the discrepancy between the ACI 318 prediction (straight line) and the proposed model (curve) becomes higher. For example, to achieve a bar stress of 60 ksi, there is a large difference in the development length required based on the proposed model and ACI 318 equation for each bar when using a linear multiplier. However, when a nonlinear multiplier is used, the difference

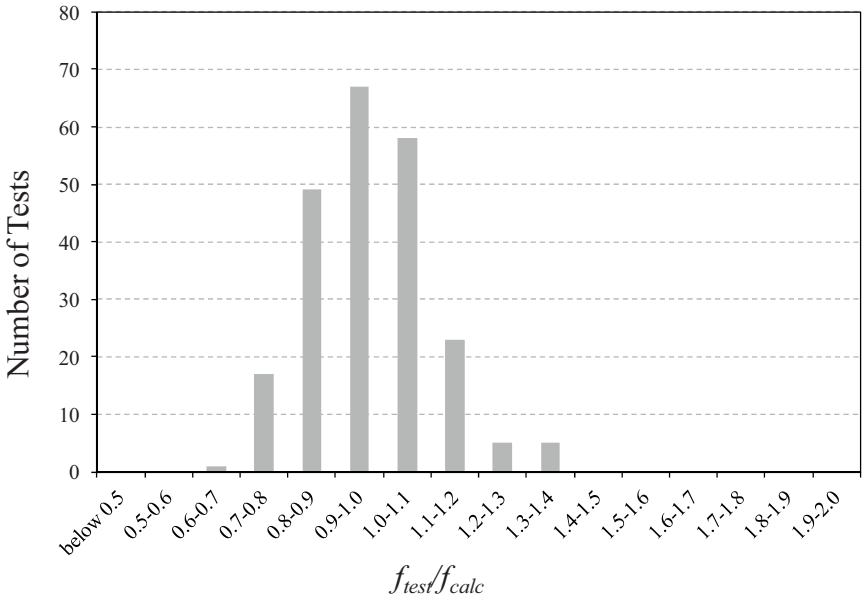

Figure C.78 Zuo and Darwin (2000) model with the combined database.

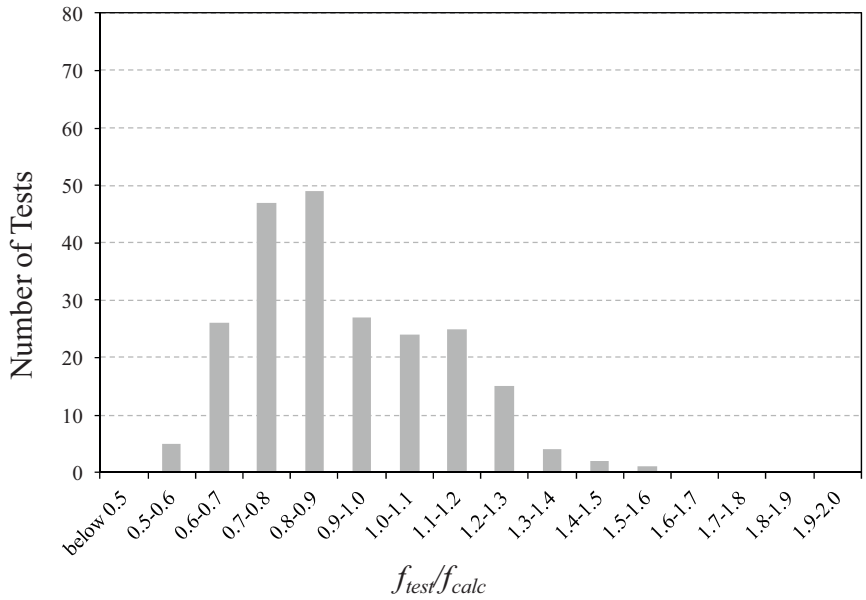

Figure C.79 Canbay and Frosch (2005) model with the combined database.

between the ACI 318 equation and the proposed model for the required development length to achieve bar stress of 60 ksi becomes smaller and relatively consistent. These two graphs clearly indicate that a nonlinear multiplier should be used for the ACI equation. Therefore, the X factors that account the nonlinear behavior is recommended as multiplication factors regardless of design method.

In evaluating the results of Table C.9, it is observed that the average ratio of all of the stainless steel bars have less than a 10% difference from the black bar. The relative ratios from Table C.3 are also less than 10% different. Therefore, these are considered to be effectively the same as black steel. MMFX II is considered also equivalent with a ratio less than 1.0. Both galvanized and Zbar resulted in similar values; the average ratios are within 10% and can be considered equivalent to black. The other coated bars on the other hand demonstrate variations from the black bar results. Epoxy and the Zinc-clad bars obviously require modification. Recommended factors are presented in Table C.10 for these as well as the rest of the bars.

Considering use of the modification factor ψ_b, the development length required for the various bars can be calculated as follows:

$$\frac{l_s}{d_b} = \frac{f_b^2}{\sqrt{f'_c}} \frac{1}{\sqrt{\frac{c_{so}}{d_b}}} \psi_b \tag{C.38}$$

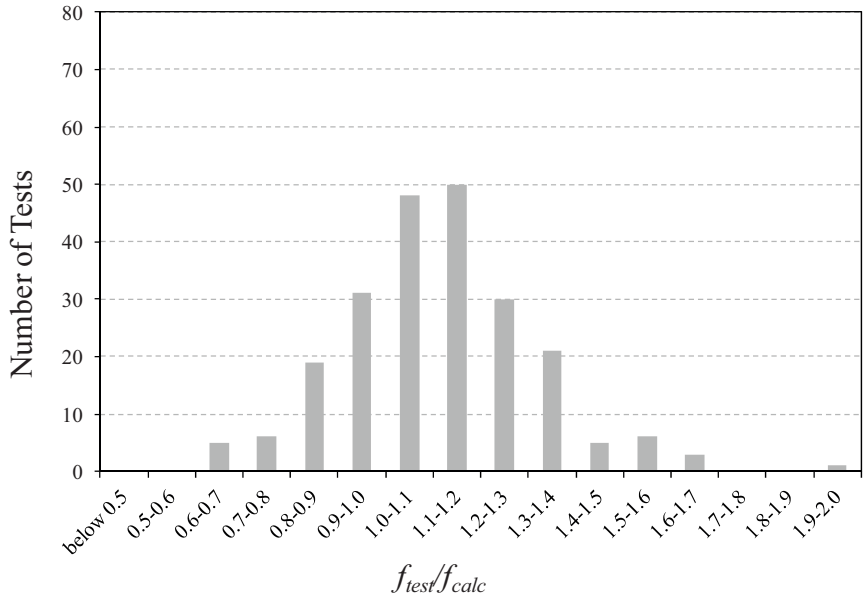

Figure C.80 Frosch and Pay (2006b) model with the combined database.

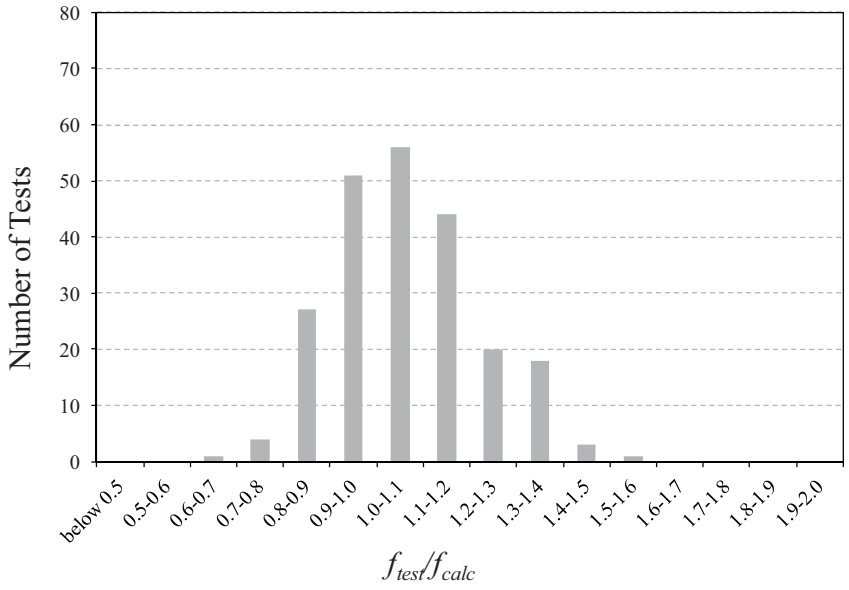

Figure C.81 Equation C.28 with the combined database.

where:

ψ_b = *modification factor for reinforcement type (Table C.10)*

The test to calculated bar stress at failure with and without the modification factor for each bar type is shown in Figure C.84. With inclusion of the modification factor, the test to calculated ratio, f_{test}/f_{calc} of all specimens is conservative (> 1.0).

C.6.3.4 Contribution of confinement in spliced region. The stress distribution along long splices is not uniform as discussed in Section C.5.3. Other research (Azizinamini et al., 1999; Ferguson & Briceno, 1969; Kluge & Tuma, 1945; Richter, 2012) has observed this behavior, and the measurements made in this study (Figure C.51 and Figure C.52) clearly support the non-uniform distribution. By testing three extreme layouts of confinement (Section 3.2.2.5), it was found that the contribution of the transverse reinforcement is not equivalent and depends on location within the splice. This variation in resistance has made it difficult to accurately quantify influence of the transverse reinforcement (Canbay & Frosch, 2005).

To better account for the varying contribution of the transverse reinforcement, the concept of using an effective splice length is considered. Based on observations from different research studies regarding the stress distribution along the splice length, bar stresses increase linearly providing uniform average bond stress for splice lengths up to $20d_b$. As splice lengths become greater than $20d_b$, the stress

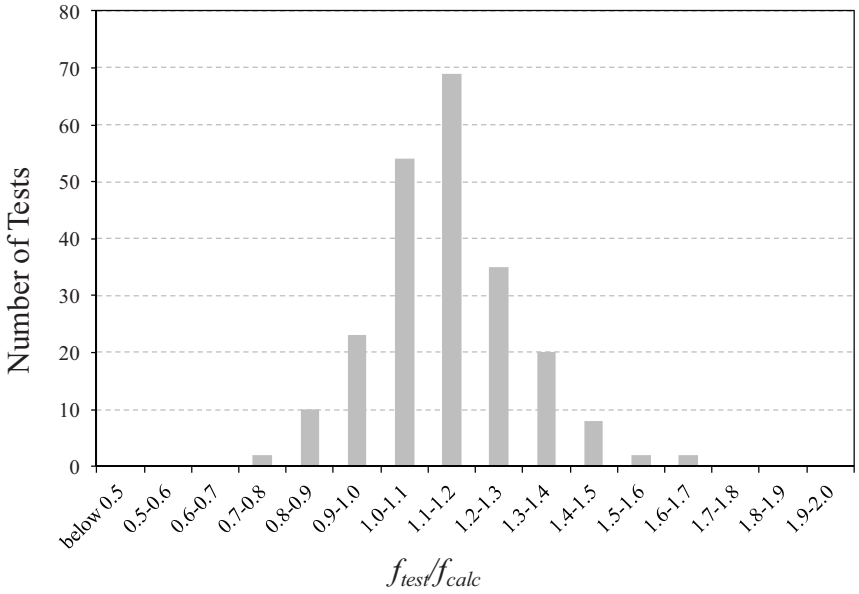

Figure C.82 Equation C.31 with the combined database.

TABLE C.9
***X* Factors Based on Experimental Results**

	Bar Type	#5		#8		Normalized Ratio from X factors		Modification Factor from Bond Ratio (Table C.3)	
		X factor	Normalized to Black	*X* factor	Normalized to Black	Avg.	Max	Avg.	Max
Black		0.66	1.00	0.95	1.00	1.00	1.00	1.00	1.00
Coated Bars	Epoxy	0.82	1.25	1.23	1.29	1.27	1.29	1.12	1.14
	Galvanized	0.78	1.19	0.96	1.01	1.10	1.19	1.04	1.09
	Zinc-clad I	0.87	1.33	1.31	1.38	1.35	1.38	1.22	1.32
	Zinc-clad II	1.43	2.18	1.63	1.71	1.94	2.18	1.35	1.47
	Zbar	0.75	1.14	0.97	1.02	1.08	1.14	1.03	1.06
MMFX II	0.64	0.97	0.67	0.70	0.84	0.97	0.91	1.00	
Stainless Steel Bars	316 LN	0.76	1.16	0.82	0.87	1.01	1.16	1.00	1.08
	Duplex 2205	0.69	1.05	0.90	0.95	1.00	1.05	0.99	1.02
	Duplex 2304	0.68	1.03	0.88	0.93	0.98	1.03	0.98	1.01
	XM-28	0.76	1.15	0.94	0.99	1.07	1.15	1.03	1.08

distribution begins to become nonlinear. Therefore, it was considered that transverse reinforcement within a $20d_b$ splice can be fully effective. On the other hand, for splices longer than $20d_b$, the section of the splice in the middle region is contributing much less to the bond strength (slight change in bar stress). Consequently, for splices longer than $20d_b$, the effective confinement length could be considered as only part of the splice length from each end.

Over this effective confinement length, the transverse confining force can be computed using the number of stirrups N_s in that region multiplied by $A_{tr}f_{yt}$ (force crossing the splitting plane of one stirrup). The influence on one bar in a splice can be computed by dividing this force by the number of developed or splice bars ($A_{tr}f_{yt}\ N_s/N_b$).

The influence of the force of one stirrup crossing the splitting plane to the measured contribution of confinement force is shown in Figure C.85. As discussed earlier (Section C.6.1), for the purpose of comparing specimens with and without confinement (listed in Table C.7), identical specimens (same dimensions, splice length, bar diameter, and concrete cover) except for the addition of confining reinforcement were evaluated. The measured contribution of confinement (Measured F_{tr}) was computed by subtracting the bar force obtained from the companion specimen without confinement ($A_s{\cdot}f_s$ without confinement) from the bar force obtained for the specimen with confinement ($A_s{\cdot}\ f_s$ with confinement). The bar force is the force measured at failure for one longitudinal bar in the splice. Therefore, F_{tr} is the extra force that can be developed in one longitudinal bar due to the addition of confinement.

The influence of $A_{tr}f_{yt}$ to one bar in the splice ($A_{tr}f_{yt}/N_b$) is shown in Figure C.86. It is difficult to visualize the direct influence of $A_{tr}f_{yt}$ or $A_{tr}f_{yt}/N_b$ on F_{tr} as shown in Figures C.85 or C.86 which considers a single stirrup. However, the contribution of this force to the measured confinement force (F_{tr}) becomes clearly evident by multiplying the number of stirrups, N_s used within the splice region (Figure C.87 and Figure C.88). Figures C.87 and C.88 also show that considering all the spliced longitudinal bars or only one spliced bar results in a similar trend.

For comparison, the influence of the transverse reinforcement index K_{tr} in ACI 318-11 to the measured confinement force F_{tr} is shown in Figure C.89. An increase in scatter is shown for this index compared to the index ($A_{tr}f_{yt}\ N_s/N_b$) used in Figure C.88.

The transverse reinforcement index K_{tr} in ACI 318-11 excluded the yield strength of the transverse reinforcement ($A_{tr}f_{yt}$) from the expression used in ACI 318-08 based on test results which demonstrated that transverse reinforcement rarely yields during a bond failure. Therefore, ACI did not want to suggest that f_{yt} was a parameter. However, while f_{yt} was removed from the equation, the coefficient 40 was based on $f_{yt}/1500$ using 60,000 psi for f_{yt}. Consequently, the expression is still inherently based on f_{yt}.

Unlike the test results which demonstrated that transverse reinforcement rarely yields, lap-splice beam tests carried out by Azizinamini et al. (1999) showed that the strain in stirrups can reach their yield strength. Specifically, stirrups located at the ends of the splice region reached yield strains. In addition, stirrups reached yield strength when the spliced bars failed in bond after yielding. These observations demonstrate that high-strength reinforcing bars that can reach high stress levels (stresses beyond 80 ksi without yielding the spliced bars) have the potential for the transverse reinforcement to reach its yield strain. Considering this background, the yield strength of the transverse reinforcement is considered as a basis for calculating the contribution of the confinement.

It is clearly shown in Figure C.87 that the confining force of one stirrup $A_{tr}f_{yt}$ multiplied by the number of stirrups N_s has a strong correlation to the measured confining force F_{tr}. To develop a model that computes the confining force on one bar, the force of all stirrups $A_{tr}f_{yt}\ N_s$ is divided by the number of spliced bars N_b (Figure C.88). As shown, $A_{tr}f_{yt}\ N_s/N_b$ directly correlates with the measured F_{tr}. The slope k of the relationship is approximately 0.5. Based on this

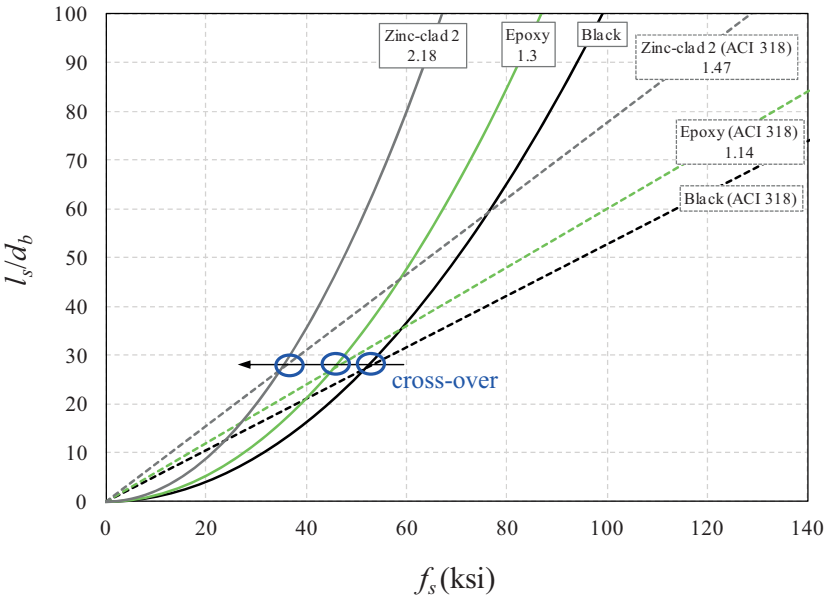

(a) Linear Multiplier to ACI 318 Equation

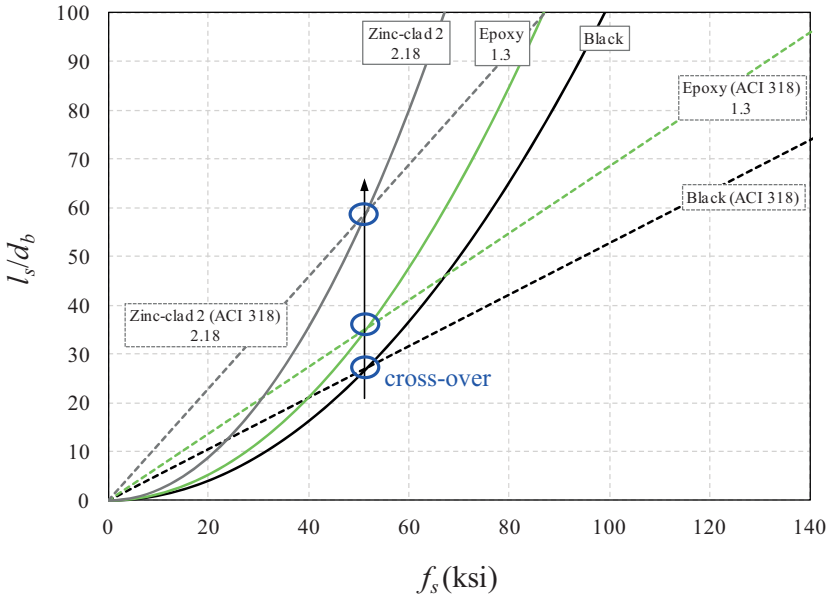

(b) Nonlinear Multiplier to ACI 318 Equation

Figure C.83 Linear and nonlinear multiplier for different bar types.

observation, the contribution of transverse reinforcement can be defined as follows:

$$F_{tr} = k \cdot \frac{A_{tr} f_{yt}}{N_b} \cdot N_s \qquad \text{(C.39)}$$

where:

F_{tr} = *contribution of transverse reinforcement in splice region (kips)*
k = *contribution factor (slope)*
A_{tr} = *total area of transverse reinforcement crossing the potential splitting plane* ($A_{tr} = A_{tr_{1bar}} \cdot N_l$) *(in.^{2})*
$A_{tr_{1bar}}$ = *area of one leg of transverse reinforcement (in.^{2})*
N_l = *number of legs of transverse reinforcement that cross the splitting plane*
f_{yt} = *yield strength of transverse reinforcement (ksi)*
N_s = *number of stirrups*
N_b = *number of spliced or developed bars*

The contribution factor k can account for the fact that lower stresses may occur in the transverse reinforcement when the splice bars are under low stress levels and not fully effective. In addition, this factor can also take account that only a certain number of stirrups at the splice ends will be effective in

TABLE C.10
Recommended Modification Factor

Bar Type		Modification Factor ψ_b
Black		1.0
Coated Bars	Epoxy	1.3
	Galvanized	1.0
	Zinc-clad I	1.4
	Zinc-clad II	2.0
	Zbar	1.0
MMFX II		1.0
Stainless Steel Bars	316 LN	1.0
	Duplex 2205	
	Duplex 2304	
	XM-28	

contributing to the splice strength. To evaluate the contribution factor further, Equation (C.39) was solved for k using the measured force F_{tr} from each test and the corresponding A_{tr}, f_{yt}, N_s, and N_b.

First, the contribution factor k was plotted against the splice length to diameter ratio, l_s/d_b, to determine if k varies for different splice lengths (Figure C.90).

The range of k values are spread wider when the splice length is shorter than $20d_b$, although only 3 points create the wider variation. The maximum k value is approximately 2.0 for specimens with splice lengths shorter than $20d_b$ while 1.0 for the case with splice lengths longer than $20d_b$. This observation from Figure C.89 can be tied together with the bar stress measurements that showed for longer splices, the section of the splice in the middle region is contributing less to bond strength. Again, the trend is not strong.

Secondly, the contribution factor k was plotted against bar stress achieved at failure f_s as shown in Figure C.91. As shown in Figure C.91(a), when the test specimen had splice lengths less than $20d_b$, most of the specimens had bar stresses less than 80 *ksi* and k values ranged from 0 to 2.0. Please note that only 3 points are greater than 1.0. On the other hand, when the splice length was greater than $20d_b$ (Figure C.91(b)), specimens had bar stresses ranging from 40 to 160 ksi. The k values can be grouped into two cases with bar stress achieved at failure lower and higher than 80 ksi. For splice lengths greater than $20d_b$ (Figure C.91(b)), it is shown that the range (scatter) of k values increases when bar stress achieved at failure is higher than 80 ksi.

Based on these observations, the contribution factor k can be conditionally defined to match all test data with different splice lengths and bar stress achieved at failure. Although the scatter or range may vary for different conditions, most of the test data demonstrate that the average value of k is 0.5. Consequently, the contribution factor k is selected as 0.5 to provide simplicity.

The proposed model in terms of bar force (Equation C.30) is used to investigate the effect of the transverse reinforcement. Equation (C.30) can be re-arranged as follows:

$$F_b = (\pi d_b l_s)0.25 \cdot \sqrt[4]{f'_c} \sqrt{\frac{d_b}{l_s}} \sqrt[4]{\frac{c_{so}}{d_b}} \qquad \text{(C.40)}$$

By adding Equation (C.39) to Equation (C.40) produces the bar force with confinement as follows:

$$F_s = F_b + F_{tr} \qquad \text{(C.41)}$$

where:

F_{tr} = *contribution of transverse reinforcement in splice region (kips)*

$= \frac{1}{2} \cdot \frac{A_{tr} f_{yt}}{N_b} \cdot N_s$

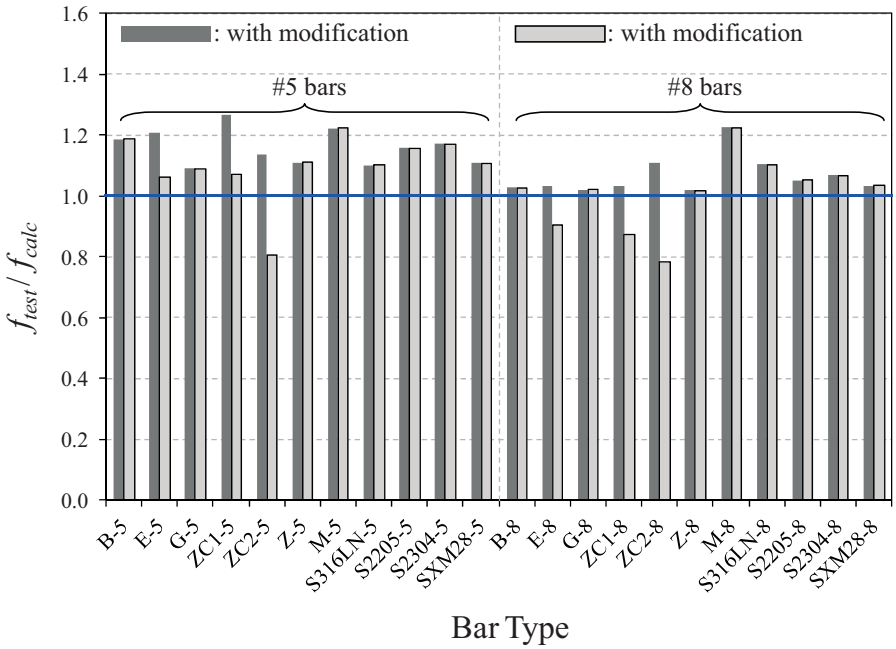

Figure C.84 Measured vs. calculated bar stress with bar type modification factor.

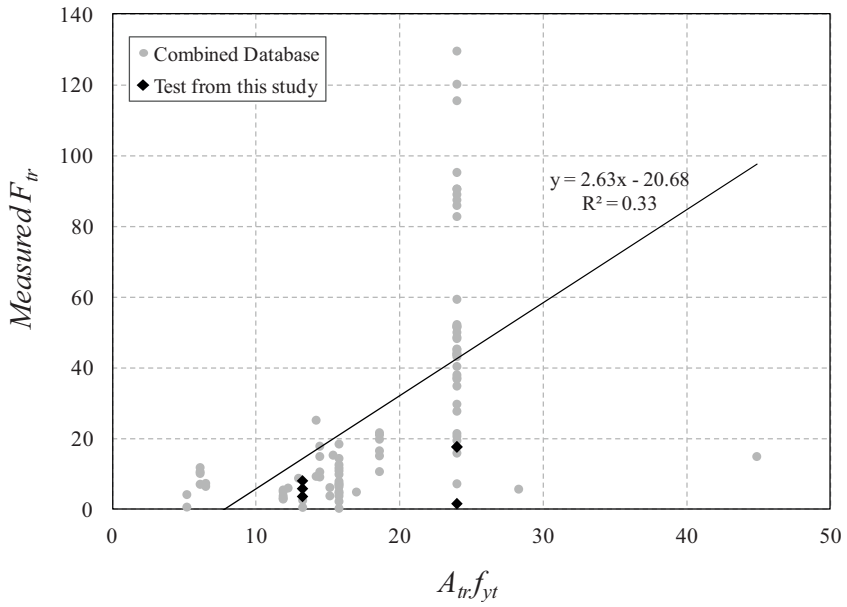

Figure C.85 Measured confinement contribution vs. force of one stirrup.

Equation (C.41) is evaluated through comparison with confined test results from the database with confinement (Table C.7) as shown in Figure C.92. For comparison, the ACI 318-11 expression which uses the transverse reinforcement index was also investigated.

The ACI 318-11 expression exhibits more scatter than the model and underestimates the contribution of the transverse reinforcement. Many of the test values were higher than the calculated values. Regarding the ACI 318-11 calculation, the $(c_b + K_{tr})/d_b$ term in Equation (C.9) shall not be greater than 2.5 to prevent pull-out failure modes. Therefore, specimens with no confinement which have $c_b/d_b = 2.5$ are calculated to have the same bar force both with and without confinement which resulted in a calculated $F_{tr} = 0$. These points are evident in Figure C.92 where the values in x axis are zero, but measured forces are plotted on the y axis. On the other hand, the proposed model estimated the additional splice strength fairly consistently with the measured values (Figure C.92(a)).

To investigate the consistency of the calculated bar stresses with confinement in the splice region, the ratio of the measured to calculated bar stresses (f_{test}/f_{calc}) is plotted against the calculated bar stresses (f_{calc}) in Figure C.93. The ACI 318-11 equation provides a strong trend as shown in Figure C.93(b). The measured to calculated ratio decreases as the calculated stresses increase. For low stresses, conservative calculations are evident. On the other hand, the proposed model provides significant improvement. The bar stresses with confinement obtained with the proposed

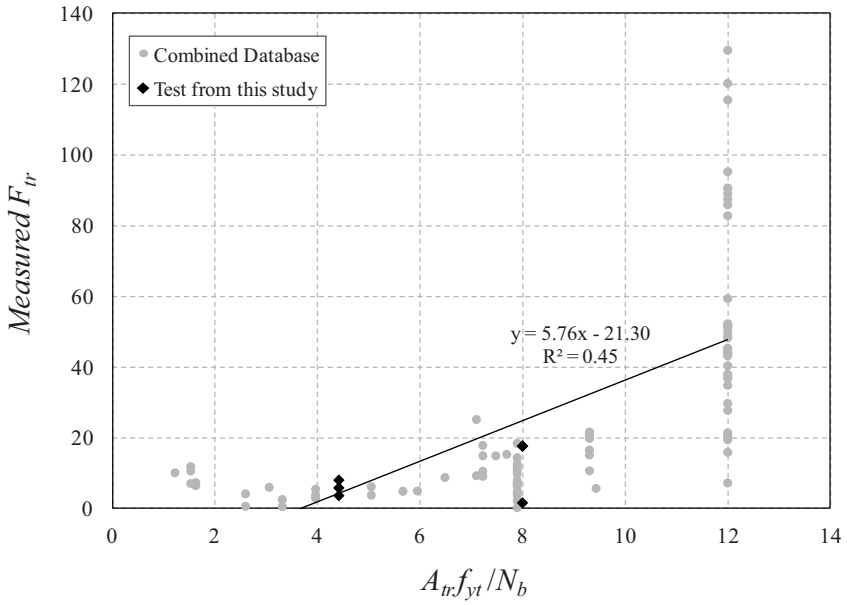

Figure C.86 Measured confinement contribution vs. force of one stirrup on one bar.

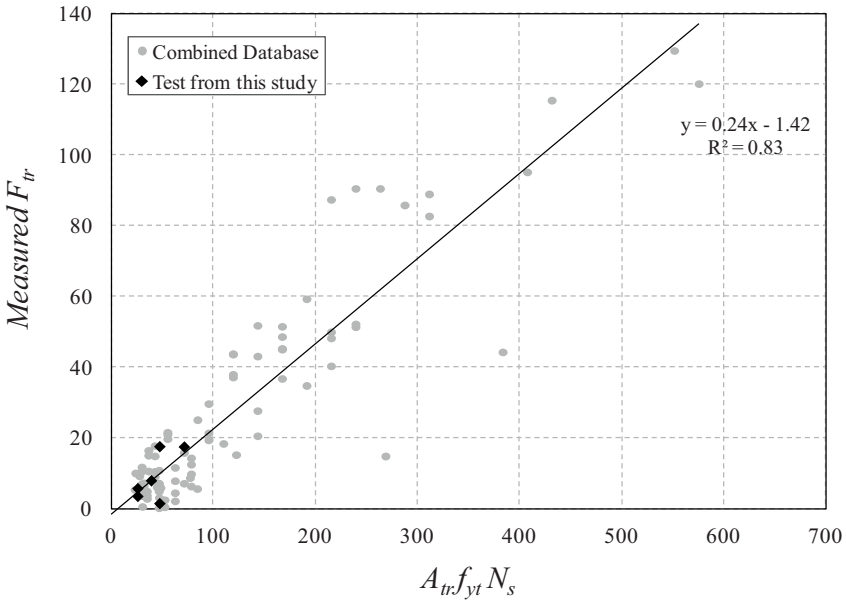

Figure C.87 Measured confinement contribution vs. force of all stirrups.

model has approximately the same level of accuracy for the range of computed stresses.

In summary, Figure C.94 present the frequency of test specimens for the given range of test to calculated bar stress ratios (f_{test}/f_{calc}). The ACI 318-11 expression estimates splice strengths with confinement in a wider range compared to the proposed model. The proposed model results in ratios closer to 1.0 compared to the ACI 318-11 expression which uses the transverse reinforcement index K_{tr}. As shown in Figure C.94, Equation (C.41) provides improved results with test to calculated ratios primarily between 0.9 and 1.2.

Table C.11 provides the statistical results of the proposed model (Equation (C.41)) and the ACI 318-11 calculation. The mean, standard deviation, coefficient of variation (COV), and the product moment coefficient of correlation (r^2) are investigated for the ratio of test to calculated bar stresses at failure. A low coefficient of variation (COV) and high coefficient of correlation (r^2) indicate that the experimental data matches well with the calculated values. As the correlation gets closer to 1, the model is shown to be more reliable. The proposed model clearly results in a smaller coefficient of variation (COV) and a higher coefficient of variation (r^2) than the ACI 318-11 procedure.

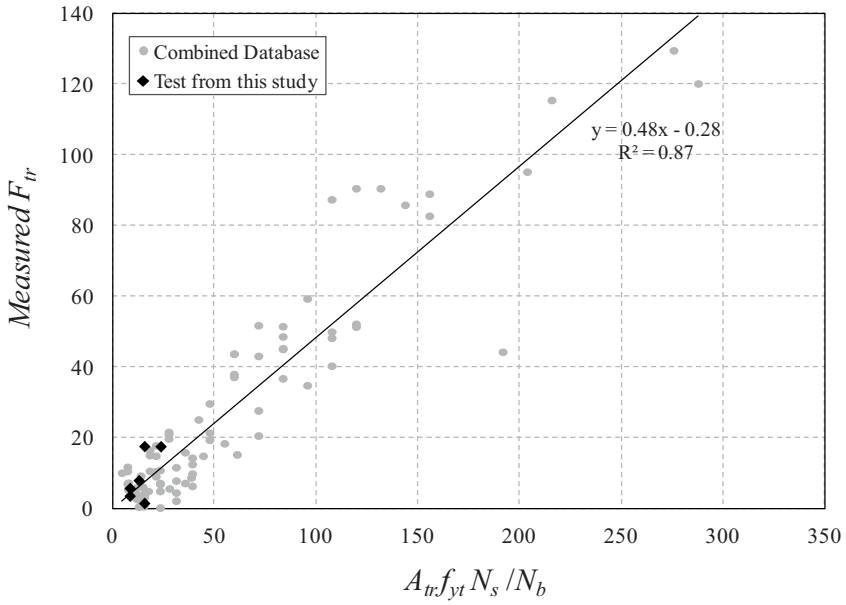

Figure C.88 Measured confinement contribution vs. force of stirrups on one bar.

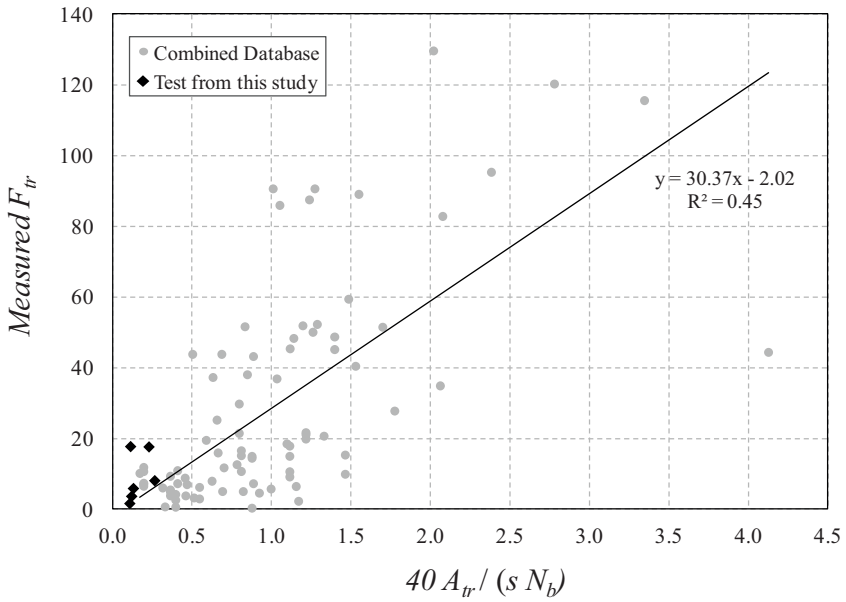

Figure C.89 Measured confinement contribution vs. K_{tr} index of ACI 318.

C.7. DESIGN RECOMMENDATIONS

Based on the analyses conducted with the combined database, a design model is proposed for the development length (splice length) calculations both with and without confinement. Modification factors are also provided to account for the various corrosion resistant reinforcing bars.

For the computation of development or splice length, Equations (C.30) and (C.39) are combined as follows:

$$F_s = (\pi d_b l_s)0.25 \cdot \sqrt[4]{f'_c}\sqrt{\frac{d_b}{l_s}}\sqrt[4]{\frac{c_{so}}{d_b}} + F_{tr} \qquad \text{(C.42)}$$

By dividing the area of the spliced bar, $\pi d_b^2/4$ on the left side of Equation (C.42) and solving for f_s gives the following equation:

$$f_s = \sqrt[4]{f'_c}\sqrt{\frac{l_s}{d_b}}\sqrt[4]{\frac{c_{so}}{d_b}} + \frac{4}{\pi d_b^2}\cdot\frac{1}{2}\frac{A_{tr}f_{yt}}{N_b}N_{s_{eff}} \qquad \text{(C.43)}$$

Solving Equation (C.43) for l_s/d_b results in:

$$\frac{l_s}{d_b} = \left[\left(f_s - \frac{4}{\pi d_b^2}\frac{1}{2}\frac{A_{tr}f_{yt}}{N_b}N_{s_{eff}}\right)\frac{1}{\sqrt[4]{f'_c}}\frac{1}{\sqrt[4]{c_{so}/d_b}}\right]^2 \qquad \text{(C.44)}$$

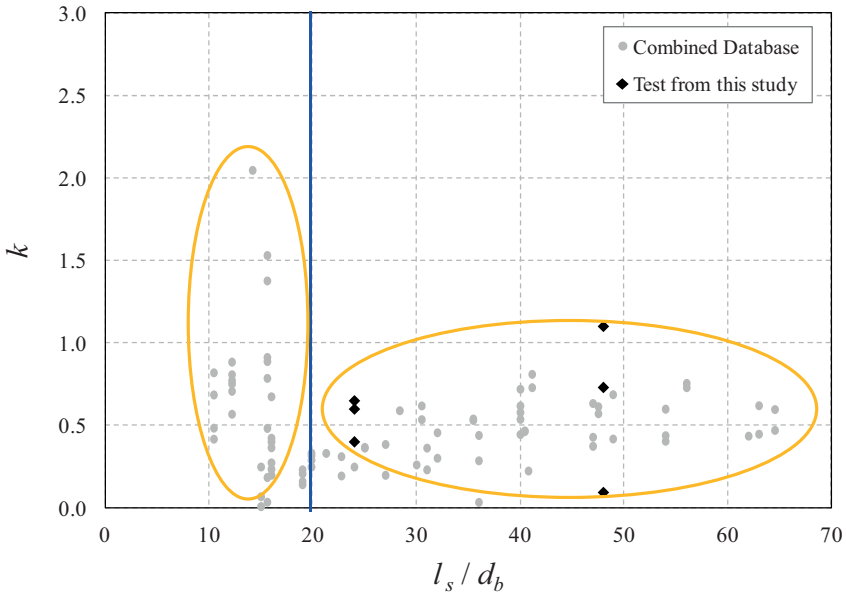

Figure C.90 Contribution factor k vs. splice length to bar diameter ratio.

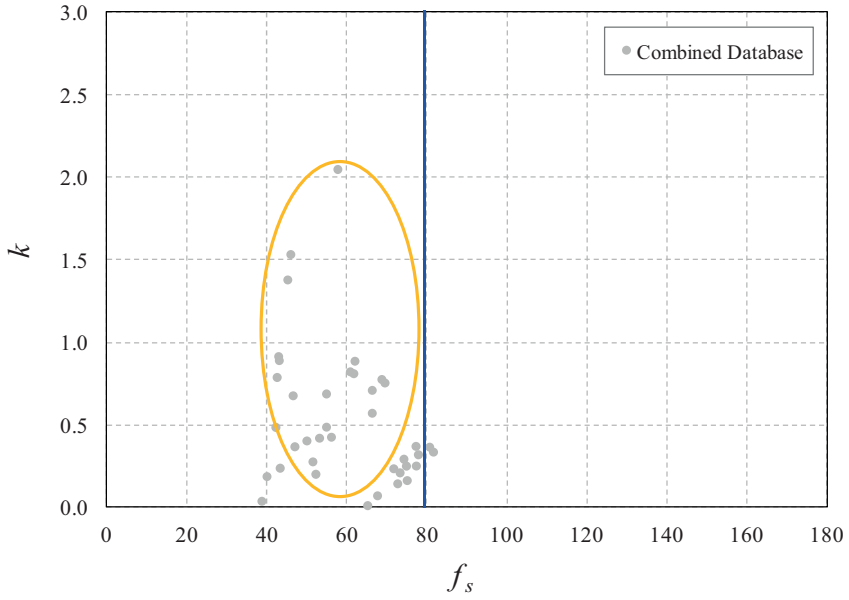

(a) $l_s / d_b \leq 20$

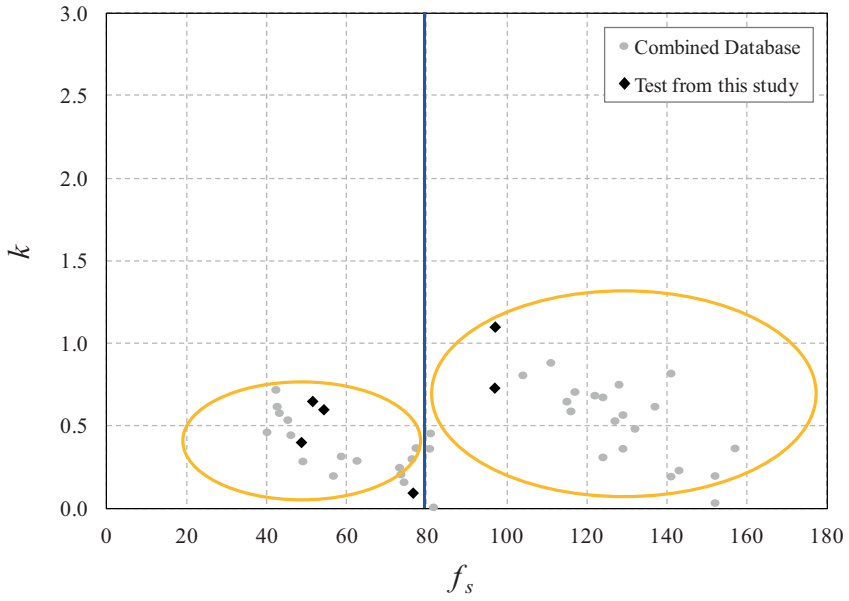

(b) $l_s / d_b > 20$

Figure C.91 Contribution factor k vs. bar stress at failure.

Therefore, the development length with confinement becomes:

$$l_s = \left[\frac{(f_s - f_{tr})^2}{\sqrt{f'_c}} \frac{1}{\sqrt{\frac{c_{so}}{d_b}}}\right] d_b \qquad \text{(C.45)}$$

Finally, to consider various types of reinforcing steel, a modification factor for reinforcement type can be added to Equation (C.45) resulting in the final expression given as Equation (C.46):

Splice (or development) length with confinement:

$$l_s = \left[\frac{(f_s - f_{tr})^2}{\sqrt{f'_c}} \frac{1}{\sqrt{\frac{c_{so}}{d_b}}}\right] d_b \cdot \psi_b \qquad \text{(C.46)}$$

where:

l_s = *splice or development length (in.)*
d_b = *nominal diameter of spliced bar (in.)*
f_s = *bar stress at failure (ksi)*
f_{tr} = *bar stress contribution from confinement (ksi)*
$= \frac{1}{2}\frac{A_{tr} f_{yt}}{A_b N_b} N_s$

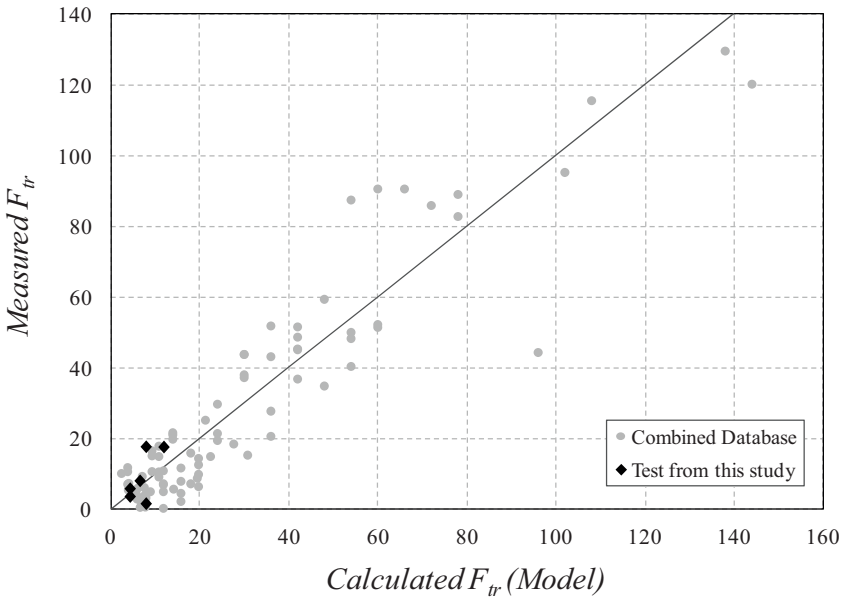

(a) Proposed Model

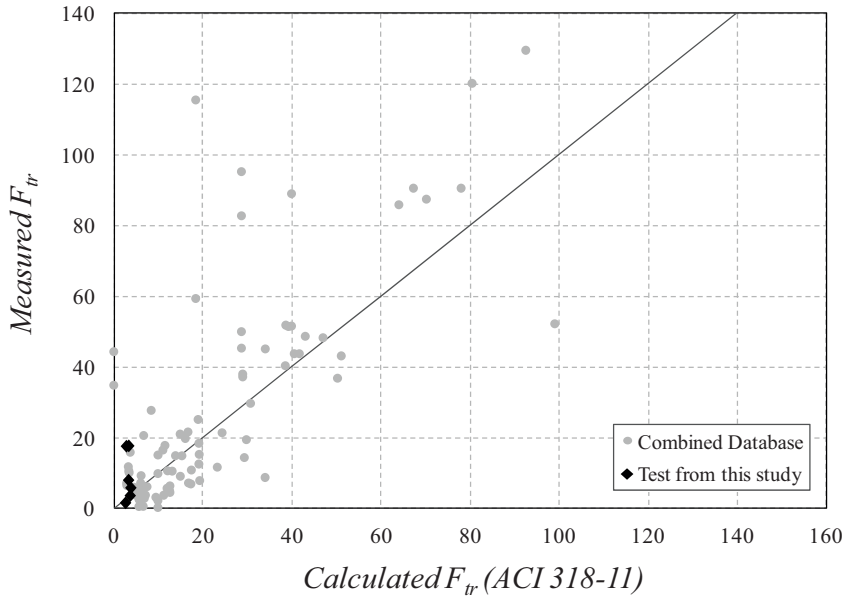

(b) ACI 318-11

Figure C.92 Confinement contribution from test vs. calculated.

A_b = *area of spliced bar (in.^{2})*
A_{tr} = *total area of transverse reinforcement crossing the potential splitting plane ($A_{tr} = A_{tr_{1bar}} \cdot N_l$) (in.^{2})*
$A_{tr_{1bar}}$ = *area of one transverse reinforcement (in.^{2})*
N_l = *number of legs of transverse reinforcement that cross the splitting plane*
f_{yt} = *yield strength of transverse reinforcement (ksi)*
N_s = *number of spliced bars*
N_b = *number of spliced or developed bars*
f'_c = *specified compressive strength of concrete (psi)*
c_{so} = *side cover (in.)*
ψ_b = *modification factor for different bar types (Factors for coated bars provided in Table 5.8)*

For conventional black steel, MMFX II steel, stainless steel reinforcement, galvanized reinforcement, and Zbar which have $\psi_b = 1.0$, the following simple equations are provided.

Without confinement:

$$l_s = \left[\frac{f_s}{\sqrt{f'_c}} \frac{1}{\sqrt{\frac{c_{so}}{d_b}}}\right] d_b \qquad \text{(C.47a)}$$

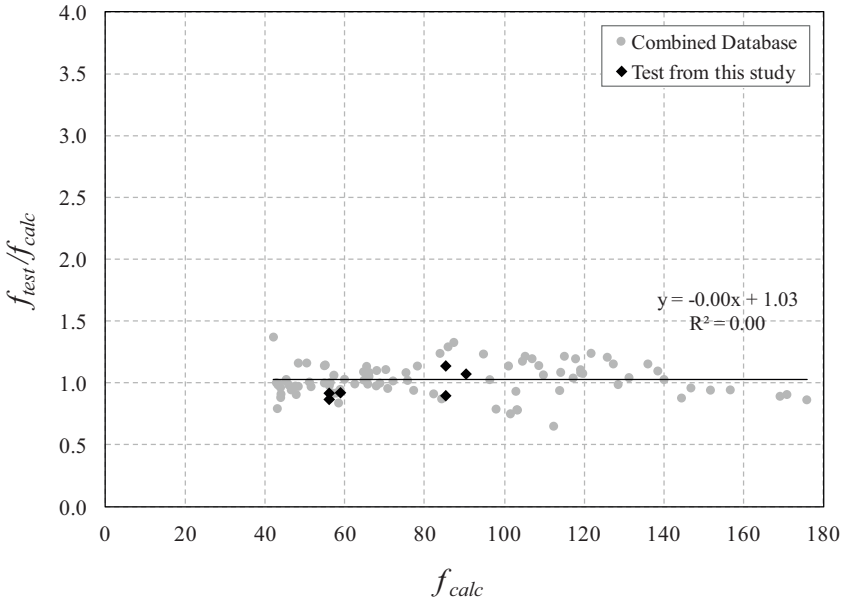

(a) Proposed Model

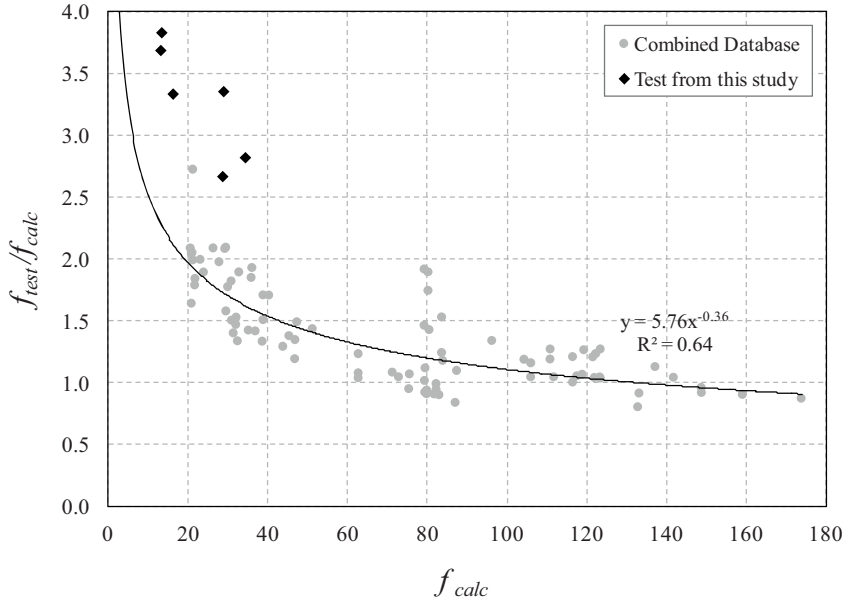

(b) ACI 318-11

Figure C.93 Test to calculated ratios vs. calculated stress.

With confinement:

$$l_s = \left[\frac{(f_s - f_{tr})^2}{\sqrt{f'_c}} \frac{1}{\sqrt{\frac{c_{so}}{d_b}}}\right] d_b \qquad \text{(C.47b)}$$

Because Equation (C.47) was developed from a regression analysis, the range of parameters for which it was developed is provided in Table C.12. As noted, a wide range of the parameters were considered.

It should be noted that the $\sqrt{c_{so}/d_b}$ can be conservatively simplified as 1.0 which further simplifies Equation (C.47) as follows:

Without confinement:

$$l_s = \frac{f_s}{\sqrt{f'_c}} d_b \qquad \text{(C.48a)}$$

With confinement:

$$l_s = \frac{(f_s - f_{tr})^2}{\sqrt{f'_c}} d_b \qquad \text{(C.48b)}$$

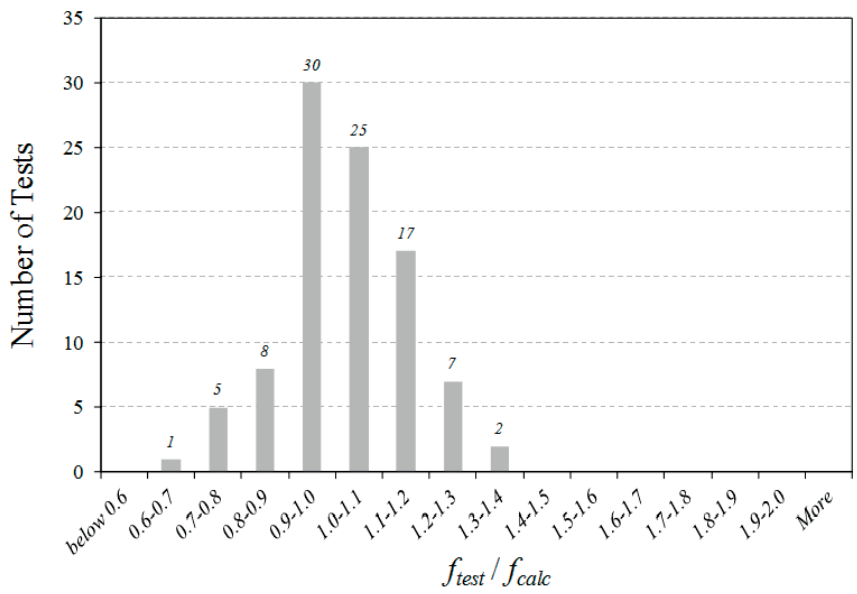

(a) Proposed Model

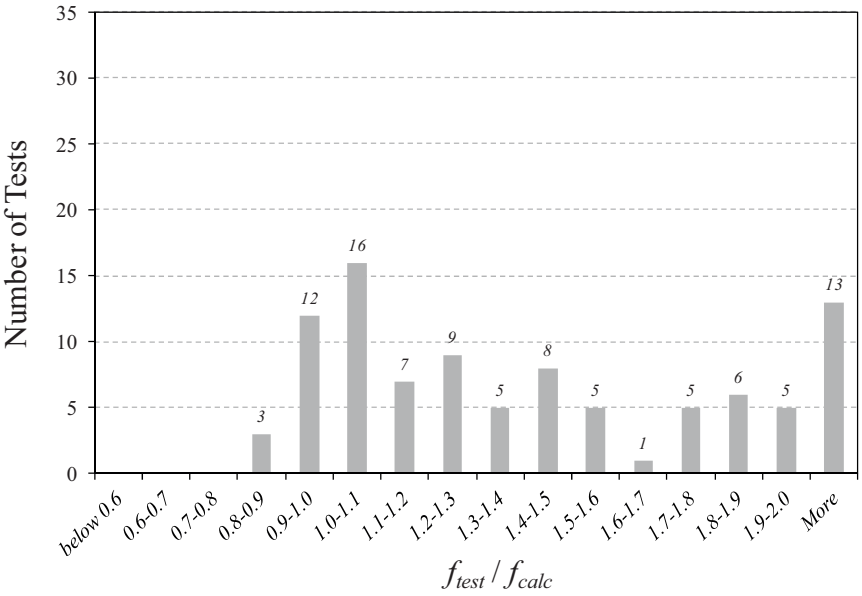

(b) ACI 318-11

Figure C.94 Frequency of test to calculated ratios.

where:

l_s = *splice or development length (in.)*
f_s = *bar stress at failure (ksi)*
$f_{tr} = \frac{1}{2} \cdot \frac{A_{tr} f_{yt}}{A_b N_b} \cdot N_s$
f'_c = *specified compressive strength of concrete (psi)*
d_b = *nominal diameter of spliced bar (in.)*

C.8. SUMMARY AND CONCLUSIONS

Forty five lap-splice beam specimens were tested to bars on bond performance. The effects of bar type, splice length, and transverse reinforcement on bond strength were investigated. In addition, the test data was combined with other data available in the literature to construct a simple model for

TABLE C.11
Statistical Comparison of Model for Confinement Contribution

Model	Mean	Std. Dev.	COV	r^2
Proposed Model, Equation (C.41)	1.023	0.132	0.129	0.933
ACI 318-11 (C.9)	1.497	0.616	0.412	0.780

TABLE C.12
Range of Test Data

	Splice Length l_s (in.)	Bar Diameter d_b (in.)	Concrete Side Cover c_{so} (in.)	Concrete Strength f'_c (psi)
Range	5.5 to 91.0	0.375 to 1.690	0.40 to 7.52	1,820 to 16,100

development and splice length that can consider the various types of reinforcing materials, a wide range of splice lengths, and the contribution of transverse reinforcement.

The following findings are based on analysis of the test results:

1. Stainless-steel, MMFX II microcomposite, hot-dip galvanized, and Zbar (dual-coated) reinforcing bars have bond strengths comparable to black bars.
2. Coated bars other than galvanized and dual-coated have reduced bond strengths. Epoxy-coated bars had on average 11% less bond strength than black. Un-plated zinc-clad and Tin-plated zinc-clad bar had on average 18% and 26% less bond strength than black bars, respectively.
3. Relative rib area had essentially no correlation with the bond strength of the bars tested. The relative rib area of the tested bars ranged from 0.059 to 0.117 for the #5 bars (only 3 bars larger than 0.1) and 0.045 to 0.095 for the #8 bars.
4. As the surface roughness of the uncoated bars increased, the bond strength increased. All uncoated bars in this study had at least a surface roughness of 100 peak and valley pairs. For every 20 peak and valley pair increase in surface roughness beyond 100, a 1 ksi increase in bar stress was observed.
5. Coated bars with a coating thickness greater than 10 mils were observed to have reduced bond strengths. For every 2 mils increase in thickness beyond 10 mils, a 1 ksi decrease in bar stress was observed.
6. As the splice length increased, the bar stress reached at failure increases nonlinearly. Bar stresses reached at bond failure, f_s, was observed to be increased proportional to the square root of splice length, $\sqrt{l_s}$.
7. Providing transverse reinforcement in the center of splice region is not effective. Only minimal increase in bond strength were observed using this configuration.
8. Confinement of the splice region can be used to increase bond strength. The additional force capacity of one splice bar is proportional to the force capacity of the transverse reinforcement crossing the splitting plane $A_{tr}f_{yt}N_s/N_b$. It is observed that the increased longitudinal force is 1/2 the transverse force F_{tr}.

TABLE C.13
Recommended Modification Factor

Bar Type		Modification Factor ψ_b
Black		1.0
Coated Bars	Epoxy	1.3
	Galvanized	1.0
	Zinc-clad I	1.4
	Zinc-clad II	2.0
	Zbar	1.0
MMFX II		1.0
Stainless Steel Bars	316 LN	1.0
	Duplex 2205	
	Duplex 2304	
	XM-28	

9. The following model is recommended for the calculation of development and splice lengths for both conventional black and corrosion resistant reinforcing steel:

$$l_s = \frac{\left(f_s - f_{tr}\right)^2}{\sqrt{f'_c}} d_b \cdot \psi_b \qquad \text{(C.49)}$$

where:

l_s = *splice or development length (in.)*
f_s = *bar stress at failure (ksi)*
f_{tr} = *bar stress contribution from confinement (ksi)* $= \frac{1}{2}\frac{A_{tr}f_{yt}}{A_b N_b} N_s$
A_b = *area of spliced bar (in.^{2})*
A_{tr} = *total area of transverse reinforcement crossing the potential splitting plane ($A_{tr} = A_{tr_{1bar}} \cdot N_l$) (in.^{2})*
$A_{tr_{1bar}}$ = *area of one transverse reinforcement (in.^{2})*
N_l = *number of legs of transverse reinforcement that cross the splitting plane*
f_{yt} = *yield strength of transverse reinforcement (ksi)*
N_s = *number of spliced bars*
N_b = *number of spliced or developed bars*
f'_c = *specified compressive strength of concrete (psi)*
d_b = *nominal diameter of spliced bar (in.)*
ψ_b = *modification factor for different bar types (Factors for coated bars provided in Table C.13)*

APPENDIX D: CRACKING—EXPERIMENTAL PROGRAM

D.1. INTRODUCTION

The objective of this phase of research is to investigate the cracking behavior of slabs reinforced with corrosion-resistant reinforcing steel. Although the reinforcing bars considered in this testing program are corrosion-resistant, the control of crack widths in reinforced concrete structures still remain important not only for aesthetics but also for durability. Twelve slab specimens were tested to 1) identify how cracking is affected by the distribution of the longitudinal reinforcement, 2) investigate if current crack width calculation procedures are adequate for these different products, and 3) evaluate crack widths at high stress levels considering that many of these material have higher strengths that may be utilized in design.

D.2. SPECIMEN DESIGN

D.2.1 Specimen Dimension

Structures such as bridge decks and parking garages in cold or marine environments can be susceptible to damage from cracking where water and chlorides can easily travel to the level of reinforcement causing corrosion. Therefore, the slab specimens were designed to represent a cut section of a bridge deck. Slabs were designed to have a depth of 8 in. which is a typical depth for bridge decks. The specimen width was selected as 36 in. to provide adequate space to allow various reinforcement layouts with different bar spacings. Three bar spacing of 6 in., 12 in, and 18 in. were selected as shown in Figure D.1. The maximum spacing of 18 in. was selected because this spacing represents the maximum allowed by code (AASHTO, 2010; ACI 318-11, 2011). To represent a bridge deck with constant bar spacing, reinforcement was spaced so that side cover of the exterior bars was the same distance as half of the clear spacing. All specimens included #5 reinforcing bars because these are commonly used in bridge decks. Previous studies (Broms & Lutz, 1965; Frosch, 1999; Hognestad, 1962; Karr & Mattock, 1963) indicate that the bar size is not a primary factor influencing crack spacing and widths. Therefore, variations in bar size were not considered.

A typical test specimen is illustrated in Figure D.2. The total length of the slab was designed to be 16 ft, and a constant moment region of 8 ft was provided to develop a sufficient number of cracks such that differences caused by various reinforcement arrangements could be observed. Loading was applied 2 ft from supports, and the reinforcement was developed 2 ft further from the loading point to ensure that bond failure does not occur prior to yielding the reinforcement resulting in a development length of 48 in. ($77d_b$). The specimens were loaded at the ends of the specimen to develop tension and cracking at the top surface of the constant moment region providing ease in both mapping and measuring cracks.

D.2.2 Specimen Variables

The variables tested include the type of reinforcement and reinforcement spacing as listed in Table D.1. Specimens are identified by the initial of the reinforcement type followed by the spacing of the reinforcement in inches. Because, crack spacings and crack widths can vary due to the difference in bond strength, the various reinforcing steel were chosen based on the bond test results of lap-spliced beams. Stainless steel reinforcement (XM-28 and Duplex 2205; lower modulus of elasticity than black), high-strength reinforcement (MMFX II), dual coated (Zbar), epoxy-coated reinforcement, and unplated zinc-clad reinforcement (Zinc-clad 1) were tested.

To compare the crack performance of the various reinforcement, the primary spacing was selected as 12 in. Slab specimens with black reinforcement were considered control specimens.

To verify that crack spacings and widths are directly related to the reinforcement spacing, two additional bar spacings of 6 in. and 18 in. were investigated. While testing this variable, high-strength steels (MMFX II and Duplex 2205 stainless steel) were evaluated. These specimens are of significance as there are only limited test results (Shahrooz, Miller, Harries, & Russell, 2011) with crack measurements at higher bar stresses ($>$ 60 ksi). Understanding cracking

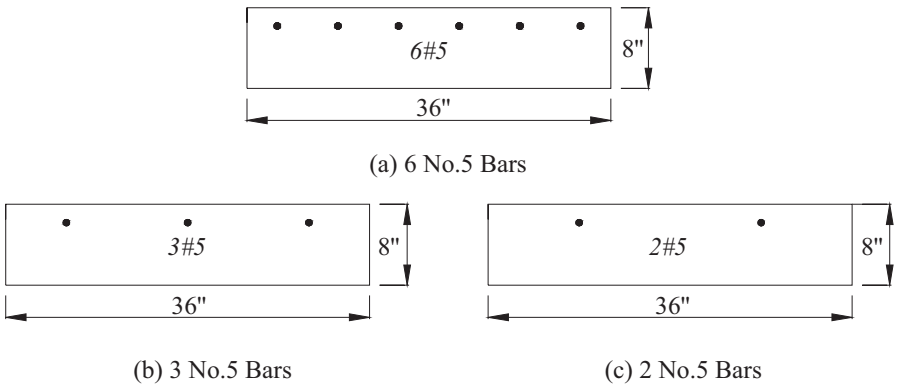

(a) 6 No.5 Bars

(b) 3 No.5 Bars

(c) 2 No.5 Bars

Figure D.1 Cross section details.

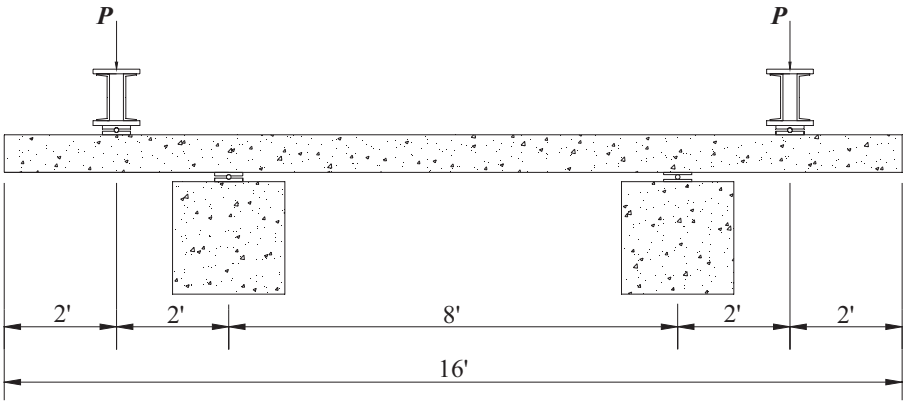

Figure D.2 Slab specimen test setup.

behavior at higher stresses is valuable as designs may want to take advantage of the higher yield strengths many of these materials provide.

D.3. MATERIALS

D.3.1 Concrete

Specimens were cast in three different batches (Table D.2) of the same concrete mix design, all of which had a target strength of 4000 psi. The concrete was provided by a local ready-mix concrete supplier, Irving Materials Inc. (IMI), located approximately 1.5 miles from the Bowen Laboratory. The selected design was a seven bag mix classified as INDOT (Indiana Department of Transportation) Class C.

The concrete mix proportions, batch weights per cubic yard, and the actual slump measurement prior to casting are provided in Table D.3. Each cast required six cubic yards of concrete. A target slump of 5 in. was requested for each of the casts and was measured upon arrival at the laboratory. Actual values achieved are listed.

The compressive strength of concrete cylinders for each concrete batch was monitored by testing three standard 6 by 12 in. cylinders at 3, 7, 14, and 28 days after casting. Additional tests were performed on the day that specimen testing ended. A 600 kip capacity Forney F-60C-DFM/I compression testing machine was used for the tests. The cylinders were capped with neoprene pads and loaded in compression at a loading rate of 35 psi/sec (approximately 59,000 lb/min) in accordance with ASTM C39 (2012). All cylinders were made during each cast and cured 7 days in an identical manner as the slab specimens (covered with wet burlap and plastic sheathing). Cylinder molds were removed when the formwork for the specimens were removed.

In addition, split-tensile strength was monitored by testing three standard 6 by 12 in. cylinders at 7 and 28 days after casting and on the day that specimen testing ended. Load was applied at a rate of 150 psi/min (approximately 17,000 lb/min), the average rate in accordance with ASTM C496 (2011). The compressive strength growth curves for each cast are provided in Figure D.3, and a summary of results is given in Table D.4.

D.3.2 Reinforcing Steel

Seven types of reinforcement (#5 deformed bars) were used for the slab test. Two types of stainless steel (Duplex 2205 and XM-28), MMFX II, epoxy-coated, dual coated (with zinc and epoxy), unplated zinc-clad, and conventional black reinforcing bars were included. The measured mechanical properties used for the slab specimens are reported in Chapter 2.

TABLE D.1
Slab Specimen Details

Specimen	Reinforcement Type	Reinforcement Spacing (in.)
B-6	Black	6
B-12		12
B-18		18
E-12	Epoxy	12
ZC1-12	Zinc-clad 1	12
Z-12	Zbar	12
M-6	MMFX II	6
M-12		12
M-18		18
S2205-18	Duplex 2205	18
XM28-12	XM-28	12
XM28-18		18

TABLE D.2
Cast Data

Casting Data	Cast 1	Cast 2	Cast 3
Slab Specimens	B-6	B-12	B-18
	M-6	E-12	S2205-18
	M-12	ZC1-12	XM28-18
	M-18	Z-12	XM28-12
Date of Casting	03/12/12	03/23/12	04/24/12
Curing Time and time before stripping forms	7	7	7

TABLE D.3
Mix Proportions per Cubic Yard

Material	Cast 1	Cast 2	Cast 3
Cement (lbs/yd^3) (ASTM C-150 Type 1)	658	658	658
Coarse Aggregate (lbs/yd^3) (#8 Stone, Vulcan Materials, Lafayette, IN)	1800	1800	1800
Fine Aggregate (lbs/yd^3) (#23 Sand, Vulcan Materials, Lafayette, IN)	1200	1240	1240
Water (lbs/yd^3)	250	275	240
Water Reducer (oz/yd^3) (BASF Glenium 3030 NS)	2	2	2
Air Entrainer (oz/yd^3) (ASTM C-260)	0.5	0.6	0.65
Water-to-Cement Ratio	0.38	0.42	0.36
Measured Slump (in.)	5	4	5

D.4. SPECIMEN CONSTRUCTION

D.4.1 Formwork and Reinforcing Steel Layout

Four specimens were cast simultaneously using two sets of formwork constructed as shown in Figure D.4(a). All forms were constructed with a 3/4 in. plywood and 2×4 in. lumber. The base form had a width of 8 ft and a length of 17 ft which was constructed with four 4×8 ft plywood sheets (3/4 in. thickness) and a 1×8 ft plywood section in the center. The center divider, side forms, and end forms were assembled and attached to the base using lag screws to allow ease in formwork removal. The 2×4 in. studs and 2×4 in. lumber at the base was spaced at 12 in. All joints between the forms were sealed with silicon caulking and backing rods to prevent leakage during casting.

After the formwork was completed, form oil was sprayed one day prior to the cast before rebar placement. The same formwork was reused for the second and third casting operations.

The slabs contained only longitudinal reinforcement located on the tension side. To provide the correct bar spacing and a cover of 1.5 in., the reinforcement was tied on continuous chairs. The longitudinal tension reinforcement was placed on 1.5 in. chairs, because the slabs were to be bottom cast and flipped prior to loading. The chairs were tied to the formwork with steel wires, and small wood blocks were placed at the gap between the chairs and formwork to maintain the correct location and dimensions during casting. The chairs were placed at locations 2 ft and 5 ft from the end of the specimen to limit the effect of the chairs on the slab cracking pattern. Figure D.4(b) shows the various reinforcement layouts with bar spacing of 6 in. (6 bars), 12 in. (3 bars), and 18 in. (2 bars).

D.4.2 Casting, Curing, and Storage

Specimens in each series were cast simultaneously from the same batch of concrete. Concrete was placed in two lifts directly from the chute of the ready-mix truck into the forms and consolidated using internal vibrators. The slabs were screeded first with magnesium screeds. Then, the surface was finished using a magnesium bull float as shown in Figure D.5(a). Four coil loop inserts manufactured from Dayton Superior Co. (Type B-16, 0.5" diameter, 4" insert length) were installed for lifting purposes as shown in Figure D.5(b). After initial set of the concrete, the slabs were covered with wet burlap, and plastic sheets were placed on top of the burlap to prevent moisture loss during curing. The specimens were cured for 7 days to minimize shrinkage cracking. Immediately following the end of wet curing, the forms were removed.

Concrete cylinders were also cast at the same time and placed into the cylinder molds with steel scoups in two lifts.

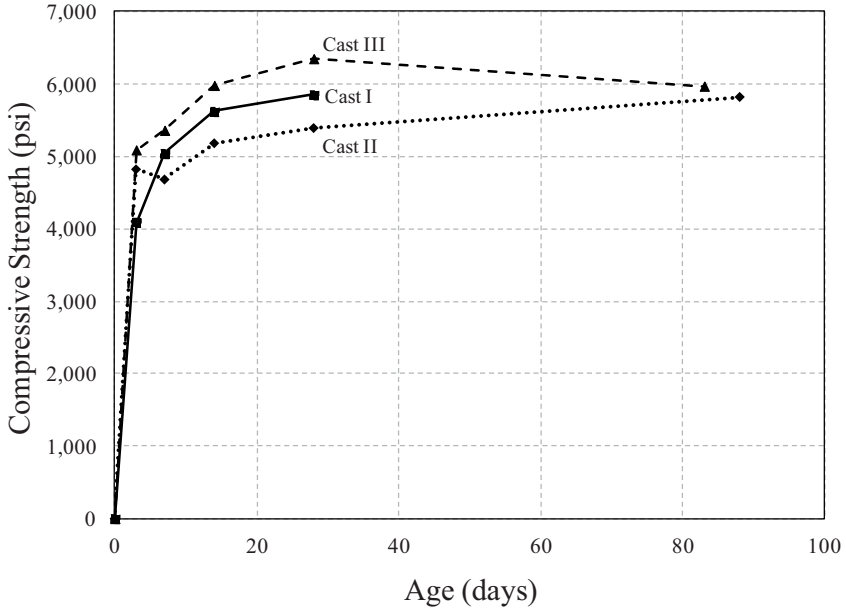

Figure D.3 Concrete strength growth.

TABLE D.4
Concrete Compressive and Split-Tensile Strength Data

	Cast 1				Cast 2				Cast 3			
	Compressive Strength, f_c'		Split-Tensile Strength, f_t'		Compressive Strength, f_c'		Split-Tensile Strength, f_t'		Compressive Strength, f_c'		Split-Tensile Strength, f_t'	
Age	Ea.	Avg.	Ea.	Avg.	Ea.	Avg.	Ea.	Avg.	Ea.	Avg.	Ea.	Avg.
3	4,060	4,090	–	–	4,340	4,280	–	–	5,100	5,090	–	–
	4,170				4,310				4,980			
	4,050				4,190				5,180			
7	5,150	5,040	450	470	4,760	4,680	480	470	5,380	5,360	480	470
	4,970		530		4,590		450		5,070		450	
	5,010		430		4,690		470		5,630		470	
14	5,490	5,620	–	–	4,890	5,180	–	–	5,960	5,980	–	–
	5,590				5,270				6,090			
	5,770				5,380				5,880			
28	5,780	5,850	580	530	5,280	5,390	530	540	6,320	6,350	520	540
	5,790		470		5,510		570		6,340		504	
	5,960		550		5,370		520		6,380		590	
Test End	–	–	–	–	5,710	5,820	490	450	5,720	5,970	490	510
					5,340		420		6,270		480	
					5,900		440		5,930		540	

(a) Slab Formwork

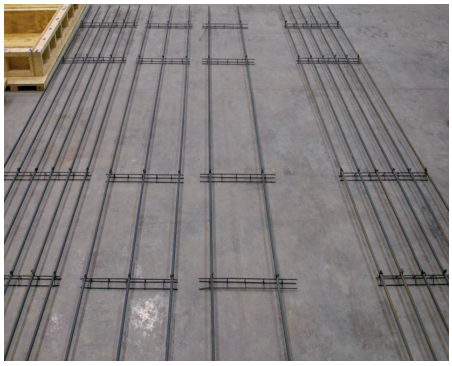

(b) Reinforcing Steel Layout

Figure D.4 Formwork and reinforcing steel.

(a) Finishing Procedure

(b) Lifting Inserts and Slab Storage

Figure D.5 Construction and storage.

Figure D.6 Slab specimen test setup.

The cylinders were consolidated using an internal vibrator. The identical curing procedure for the slab specimens was followed for the cylinders, and the molds were removed after 7 days of curing. The test specimens and cylinders were stored for 28 days prior to testing. Due to the limitation in storage space at the lab, the specimens were stacked with 4×4 blocks located at the loading and support location as shown in Figure D.5(b).

D.5. TEST SETUP AND TEST PROCEDURE

The testing setup was designed to load the slabs at the ends producing a constant moment region in the center. The slabs were supported by concrete blocks as shown in Figure D.6. At the reactions, steel bearing plates were attached to the concrete block and the test specimen using hydrostone to provide uniform load distribution and control bearing stresses in the concrete. A roller support was obtained by placing a 1 in. diameter and 36 in. long steel rod between $0.5 \times 12 \times 36$ in. flat steel plates while a pin support was obtained by placing a 1 in. diameter and 36 in. long steel rod between $0.75 \times 12 \times 36$ in. steel plates that were grooved 0.25 in.

The load for the slab specimens in which the calculated yield capacities were below 20 kips were applied in one kip intervals. Slab specimens that had calculated yield capacities below 30 kips used a two kips load increment. One specimen with high-strength steel with a 6 in. bar spacing was excepted to exceed 40 kips to yield, therefore, a four kips load interval was used. The load from each ram was monitored by load cells manufactured from Tokyo Sokki Kenkyujo Co., Ltd. or from Honeywell Inc. The model number, output range, output sensitivity of hydraulic rams and load cells are provided in Table D.5. The loading system was calibrated on a Baldwin 120-kip capacity universal testing machine with an Instron control and data acquisition system.

Deflections were monitored using ten string potentiometers manufactured by UniMeasure Inc. (range and sensitivity listed in Table D.5). Two string potentiometers were installed at midspan, two at each support, and two at loading points. Load and deflection data were collected through a VISHAY data acquisition System 7000-128-SM and monitored at 0.1-second intervals during testing using VISHAY StrainSmart Ver. 4.7.25. The string potentiometers for deflection measurements

TABLE D.5
Summary of Instrumentation

Type of Application	Manufacturer	Model	Accuracy or Range	Sensitivity
Data Acquisition	Vishay	System 7000-128-SM	Measurement accuracy of ±0.05%	–
Hydraulic Ram	Enerpac	RCH-603	60 ton capacity 3 in. stroke	–
Load Cell	Tokyo Sokki	KCB-500kN	±125,000 lb	1.080 mV/V
	Honeywell	3632-100k	±100,000 lb	2.194 mV/V
String Potentiometer	UniMeasure	PA-10-DS	±10 in.	94.61mV/V/in.
		PA-25-DS	±25 in.	39.08mV/V/in.
Crack width microscope	Edmunds Industrial Optics	50X Direct Measuring	Reading accuracy of 1/1000 in.	–

Figure D.7 Measuring cracks during testing (specimen B-12).

were calibrated using a Fowler Trimos height gage (Model 600+, 24 in. travel) with an accuracy of 0.00005 in.

At each load stage, cracks were marked and crack widths in the constant moment region were measured using an Edmund Direct Measuring 50X pocket microscope (Figure D.7). The microscopes allowed for crack measurement within an accuracy of 1/1000 of an inch.

A crack was considered a primary crack if it connected through the full width in transverse direction. The width of each primary crack was measured in three different locations on the top surface including at least one above a reinforcing bar and another above the midpoint between the reinforcement within the constant moment region. In addition, crack widths on the side surface were measured on both sides at the depth where the bar was located.

APPENDIX E: CRACKING—TEST RESULTS AND ANALYSIS

E.1. INTRODUCTION

The experimental results of each slab specimen are presented to evaluate the effect of bar type and bar spacing on crack widths and crack spacings. Further analysis was performed to identify if current crack width calculations are adequate for various reinforcement. Based on the analysis, recommendations are provided for the control of crack widths for different bar types.

E.2. EXPERIMENTAL RESULTS

E.2.1 Load-Deflection Behavior

The load-deflection behavior of the tested slab specimens was similar. The load-deflection plots clearly demonstrate the three distinct stages shown commonly in flexural tests: behavior before cracking, behavior after cracking up to yielding, and behavior after yielding. Up to cracking, the stiffness of the specimens is primarily controlled by the concrete and each of the specimens behaved similarly up to first cracking in this range. Therefore, each of the specimens behaved similarly up to first cracking in this range as shown in Figure 6.1.

After flexural cracking, a stage where stiffness of the structure is governed primarily by the reinforcement, specimens with wider bar spacings (less reinforcement) displayed a reduction in stiffness as shown in Figure E.1 and Figure E.2. Specimens with identical bar spacings, however, behaved similarly until yielding of reinforcement (Figure E.3). The stiffness drops after cracking, but the behavior remains approximately linear up to yielding. Bar stresses in linear elastic region obtained by both cracked transformed section analysis and moment-curvature analysis using the Hognestad (1951) concrete model and the stress-strain relationship of rebar provide difference in bar stresses less than 1 ksi.

The load-deflection plot in Figure E.3 indicates that black bar and Zbar have similar yield strengths, epoxy and MMFX II bars have higher yield strengths, while zinc-clad has a lower yield strength. In addition, the load-deflection plot shows a flat region for the materials that have a definite yield plateau which include all bars except for the MMFX II which has a roundhouse stress-strain curve and does not contain a distinct modulus. These results are consistent with the material strengths shown in Table 2.3.

E.2.2 Crack Patterns

Cracks were marked at each load increment, and crack widths were measured. Transverse cracks first appeared 1 ft from the support in the constant moment region. This location is where the chair was located, 5 ft from the end of the specimen. The number of primary cracks developed in the constant moment region subsequently increased as load was increased. However, after a certain load was reached, the number of primary cracks within the constant moment region did not increase further. After all primary cracks formed, crack widths became wider as the load increased and the number and depths remained relatively the same until yielding. This stage of behavior is also referred to as the equilibrium stage when redistribution of concrete stresses stabilize. The stress level when all primary cracks formed was in the range of 40-80 ksi for the slab specimens tested (side cover ranging from 3 to 9 in.).

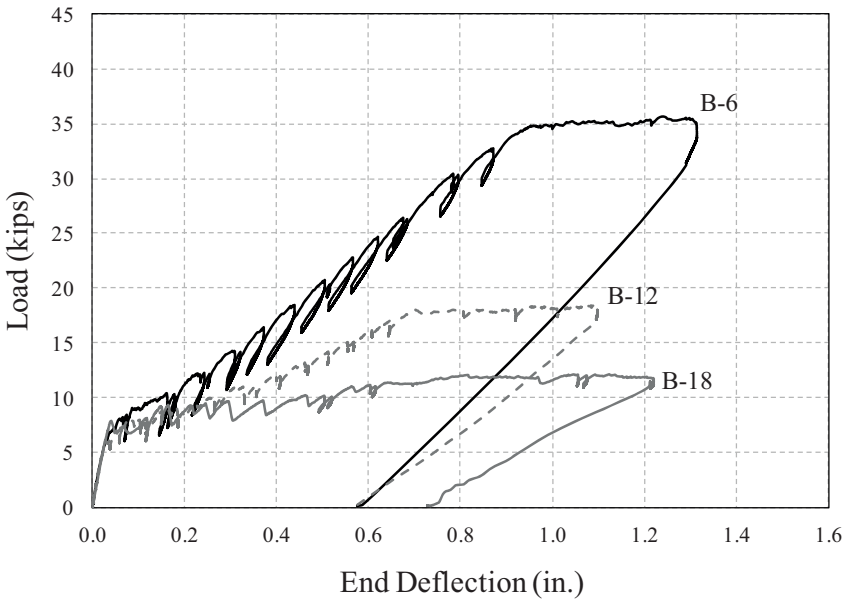

Figure E.1 Load-deflection response (black).

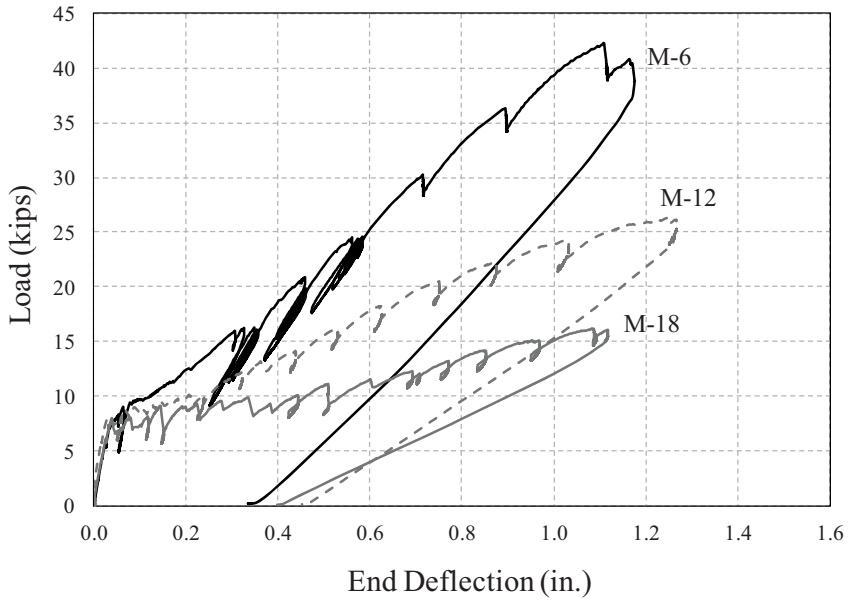

Figure E.2 Load-deflection response (MMFX II).

Various studies (Broms, 1965b; Hognestad, 1962; Karr & Mattock, 1963; Kaar & Hognestad, 1965) also confirmed that after all primary cracks have formed, their number remained essentially unchanged at higher stresses. The critical stress range has been previously reported to be approximately 20–30 ksi with cover thicknesses ranging from 1.25 to 3.0 in. and about 50 ksi at a thickness of 6 in. according to Broms (1965a).

Slab specimens with MMFX II bars with varying bar spacings were cast at the same time. Interestingly, the results of these slab specimens show that all primary cracks were entirely formed when the bar stresses were approximately the same even though different bar spacings were used. In order words, regardless of the reinforcement ratio, primary cracks have all formed when the reinforcing steel reached a critical bar stress. Beyond that stress level, as load increases, the number of cracks did not increase and the cracks did not propagate deeper but only wider.

Transverse cracks outside the support region usually appeared after several primary cracks developed in the constant moment region. The number of these cracks increased only after all of the primary cracks in the constant moment region were formed. As the load approached yield, transverse cracks outside the support region inclined towards the supports. In addition, on top of the reinforcing bars, longitudinal splitting cracks formed as load approached yield for specimens with 12 in. and 18 in. bar spacings as shown in Figure E.4. These longitudinal

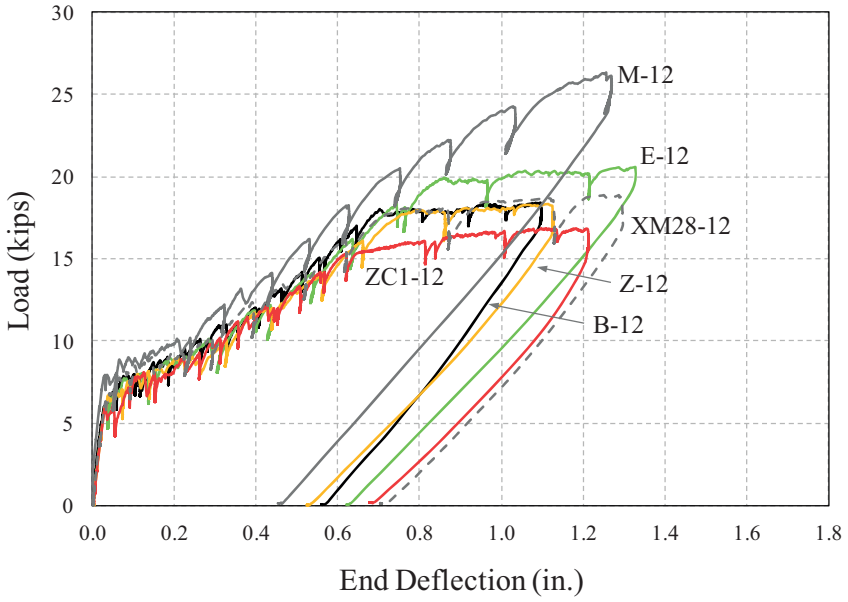

Figure E.3 Load-deflection response with varying reinforcement.

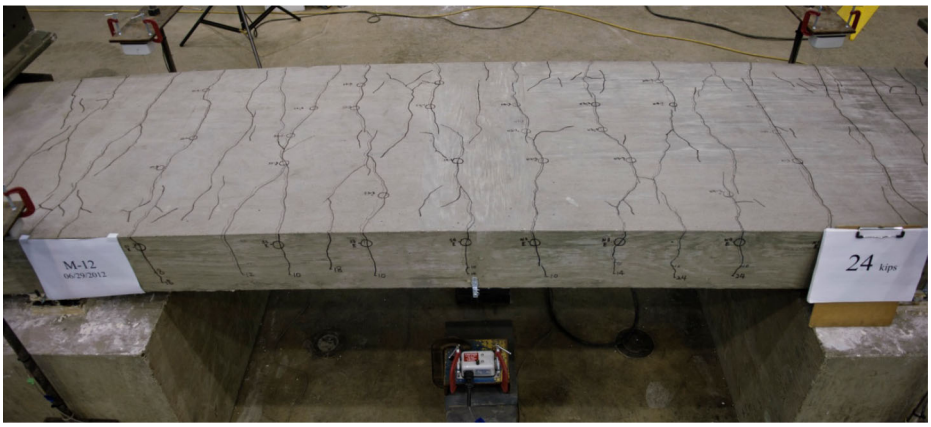

Figure E.4 Crack patterns (specimen M-12).

secondary cracks at high stress levels have also been observed by a number of researchers (Broms, 1965b; Bianchini, Kesler, & Lott, 1968; Blackman, 2002).

After completion of testing, the spacing of primary cracks (cracks that traverse the full width of slabs) were measured at the mid height of the slab. The minimum, maximum, and average spacing of the primary cracks are summarized in Table E.1. Figure E.5 and Figure E.6 show the comparison of slabs with various bar spacings containing conventional black steel. As the reinforcing bar spacing increases, the number of primary crack decreases. Longitudinal splitting cracks were formed on top of the reinforcement for the slab specimens with 18 in. spacing prior to yielding similar to that shown in Figure E.4.

E.2.3 Crack Widths

E.2.3.1 Bar spacing. Two sets of specimens (one with black bar and the other with MMFX II) were designed to evaluate the influence of reinforcement distribution on crack width. Each set consisted of three different reinforcing steel spacings: 6 in., 12 in., and 18 in. The crack widths were measured from three different locations for every primary crack. These measurements are provided in Appendix C. Because, all specimens were tested beyond yield, bar stresses were calculated by moment-curvature analysis using the Hognestad (1951) concrete model and the stress-strain relationship of the reinforcement including the elastic, plastic, and an ascending strain-hardening region.

TABLE E.1
Number and Spacing of Primary Cracks

Specimen	Number of Primary Cracks	Minimum Spacing (in.)	Maximum Spacing (in.)	Average Spacing (in.)	Standard Deviation (in.)
B-6	15	3.2	10.6	6.3	2.0
M-6	16	2.2	14.4	6.2	2.2
B-12	12	5.4	14.1	8.8	2.4
E-12	12	4.3	15.5	8.1	2.7
ZC1-12	11	5.0	17.8	9.7	2.8
Z-12	11	3.8	15.2	8.9	2.6
M-12	11	4.7	13.2	9.2	2.3
XM28-12	11	4.7	13.4	8.5	2.6
B-18	10	4.4	18.4	10.2	4.3
M-18	10	3.7	14.2	8.9	2.7
S2205-18	10	4.3	15.4	9.9	3.2
XM28-18	10	6.1	12.9	9.1	1.8

Figure E.7 and Figure E.8 plot the average and maximum crack widths on the top surface of the slabs for each stress level for slabs with Black and MMFX II steel, respectively. As evident, both black bars and MMFX II bars demonstrate that the average and maximum crack widths increase as the bar spacing increases (reinforcement area decreases). Regarding Figure E.7, the average and maximum crack widths of specimens with black bars at 6 in. and 12 in. are similar while a separation is shown for black bars spaced at 18 in. spacing. Note that yield is evident by the change in slope becoming vertical for the plots in Figure E.7. However, MMFX II specimens shown in Figure E.8 behaved slightly different demonstrating that crack widths are more similar between the specimens with 12 in. and 18 in. bar spacings while there is separation between the 6 in. bar spacing case and other spacings.

In addition, because MMFX II bars have higher yield stress than black bars and do not have a definite yield plateau, the change in slope does not become vertical for these specimens as shown in Figure E.7.

To understand the behavior better and compare the measurements for different bar spacing at the same bar stress, the measured crack widths at different stress levels were interpolated and Table E.2 to Table E.5 summarize the results by normalizing these measured crack widths (interpolated) to measured crack widths at a 6 in. bar spacing. As shown, average and maximum crack widths at an 18 in. bar spacing are approximately twice the crack widths at a 6 in. bar spacing for both black and MMFX II bars.

Figure E.9 and Figure E.10 provide 3D plots which present crack widths for each stress level for varying bar spacings. The 3D plot clearly shows that as bar spacing

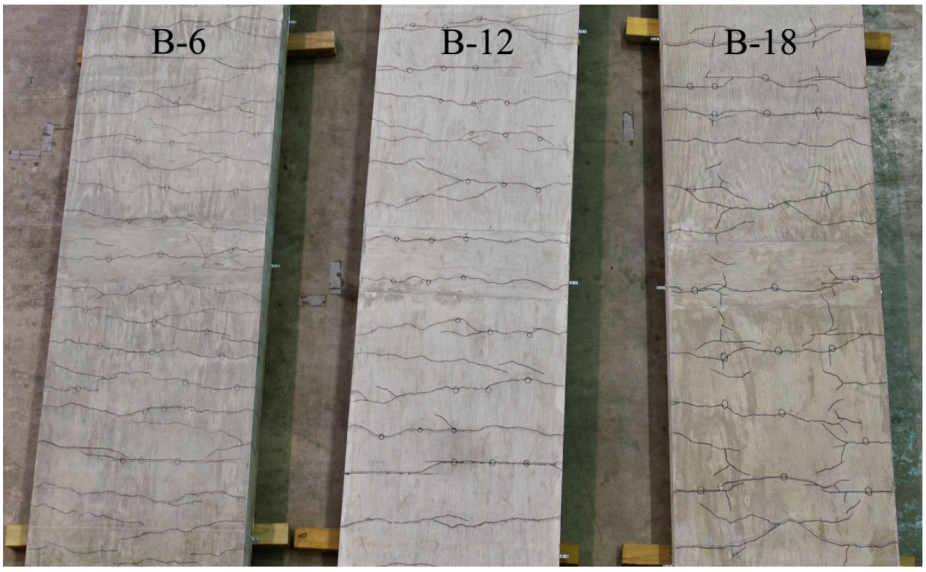

Figure E.5 Comparison of slabs with varying bar spacing (black).

increases, the crack widths increase for the same steel stress level. In addition, both the figures and tables demonstrate that first cracking occurred at higher stress levels as the bar spacing increased.

Figure E.11 and Figure E.12 also show the effect of bar spacing on crack widths. For each stress increment and as bar spacing increases, both the average and maximum crack widths increase for black bars and MMFX II steel. The trend, however, is non-linear. As the bar spacing increased to 18 in., much higher crack widths are noted for the specimens with black bars. On the other hand, specimens with MMFX II bars provide a difference non-linear trend.

E.2.3.2 Bar type. Six specimens were designed to evaluate the influence of bar type on crack widths. The specimens included #5 bars at a 12 in. spacing. Crack widths were measured from three different locations for each primary crack. Steel stress was calculated using moment-curvature analysis. The crack widths measurements for these specimens are provided in Appendix C.

Figure E.13 presents the average and maximum crack widths measured for the specimens with a 12 in. bar spacing. The slab specimens with black, epoxy, and MMFX II bars up to a steel stress of 75 ksi have comparable crack widths, while the test specimens with Zbar and XM-28 bars behave similarly and have wider crack widths than slabs with black bar at the same steel stress up to 60 ksi. The slabs with zinc-clad bars had the widest cracks at the same steel stress for both maximum and average crack widths.

Table E.6 and 6.7 provide the results in tabular format. To evaluate relative differences, the measured crack widths are interpolated for each stress level and crack widths are

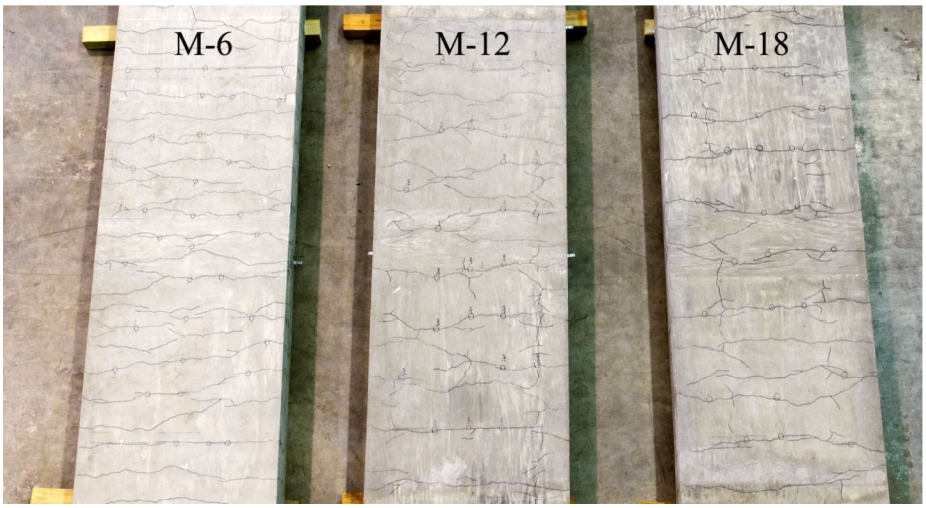

Figure E.6 Comparison of slabs with varying bar spacing (MMFX II).

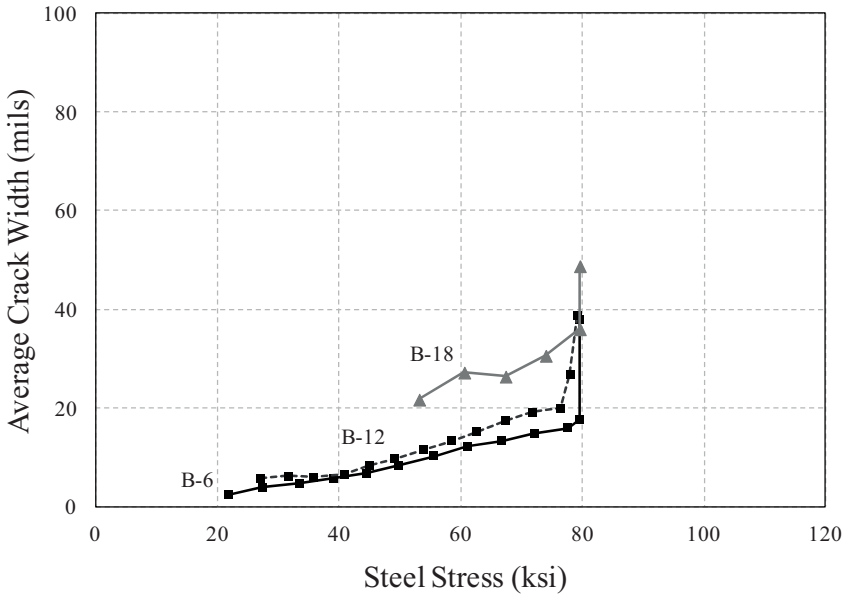

(a) Average Crack Widths

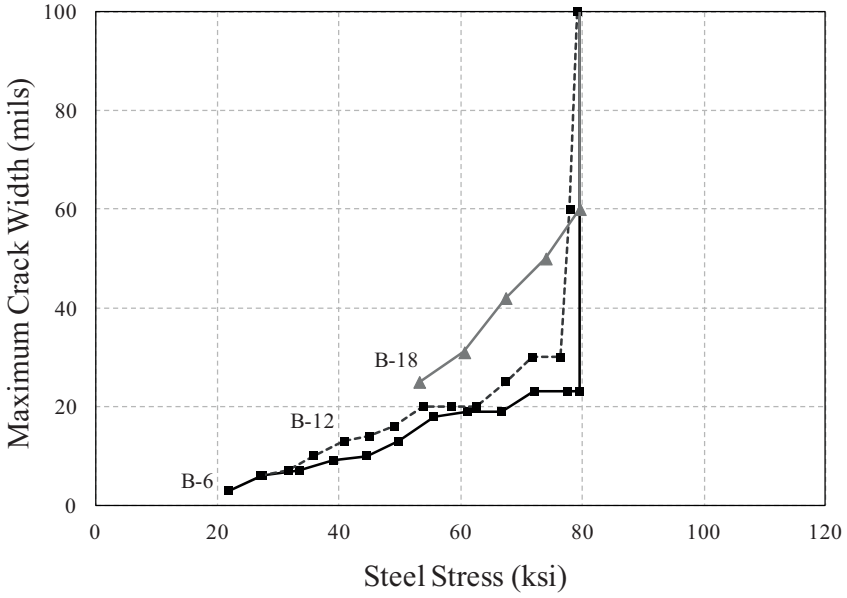

(b) Maximum Crack Widths

Figure E.7 Crack widths for varying bar spacing (black).

normalized to those of black bars. The crack widths of specimens with zinc-clad bars were twice as large as the slabs with black bars.

Figure E.14 plots average and maximum crack widths measured for an additional set of specimens with different bar types at 18 in. bar spacings. Because XM-28 and Duplex 2205 does not have a definite yield plateau and have a roundhouse look stress-strain curve, the crack widths increases nonlinearly as the bar stress increases after each material pass their yield strength (strength at 0.0035 strain) which is 60 ksi and 71 ksi, respectively. In addition, although slabs with MMFX II bars at 6 in. and 12 in. bar spacings produced crack widths comparable to slabs with black bars, specimens with MMFX bars at an 18 in. spacing resulted in the smallest crack widths compared to the other bars including black bars at every stress level. XM-28 and Duplex 2205 stainless steel had comparable crack widths with the black bar before reaching their yield strength.

Table E.8 and Table E.9 summarize the crack widths and normalized them to those of black bars. Slabs with XM-28 and Duplex 2205 stainless steel have similar crack widths to black bars at an 18 in. bar spacing while as previously discussed, the slab with MMFX II bars had relatively smaller crack widths than black at 18 in. bar spacing.

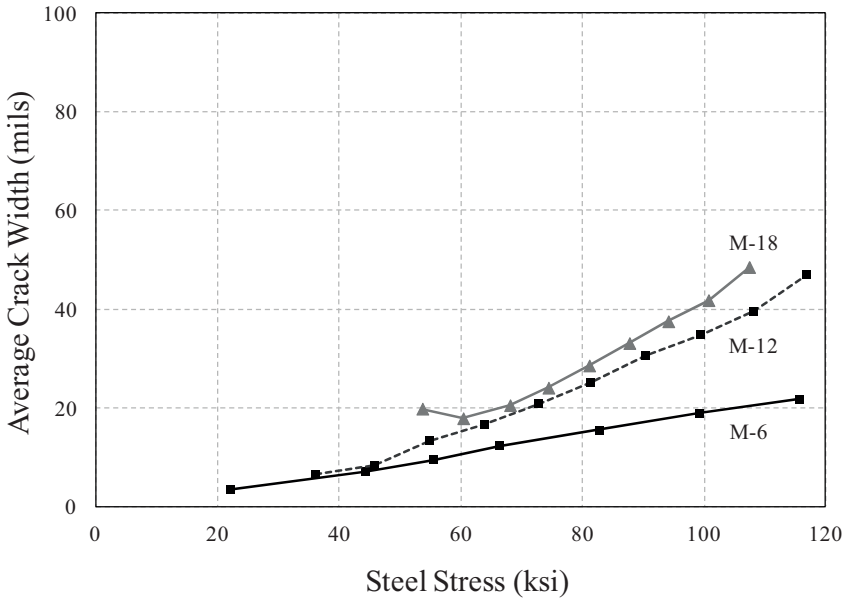

(a) Average Crack Widths

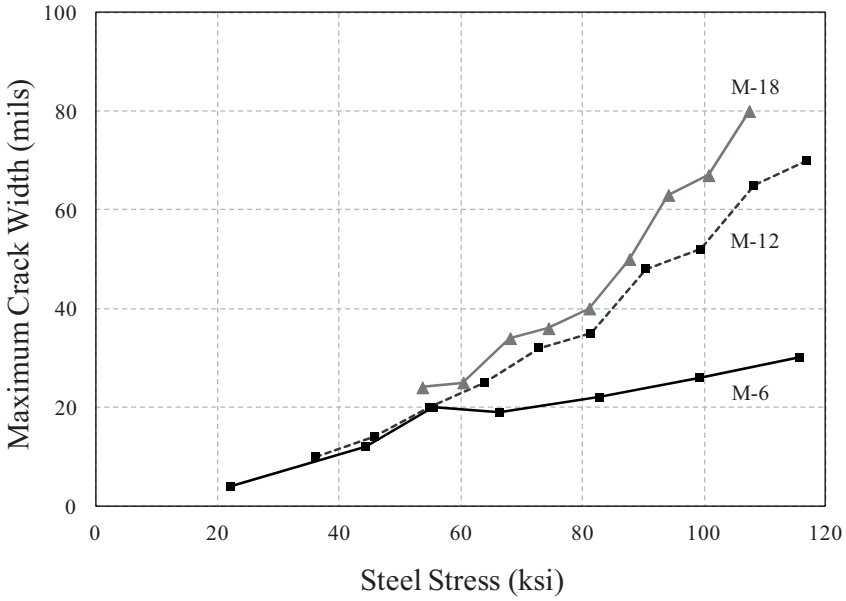

(b) Maximum Crack Widths

Figure E.8 Crack widths for varying bar spacing (MMFX II).

From reviewing Table E.6 through Table E.9, it is observed that the MMFX II bar with a 12 in. spacing behaved similar to the black bar (crack widths normalized to black: avg. ratio: 1.08, max ratio: 1.05) while the MMFX II bar with an 18 in. spacing had smaller crack widths compared to the black (avg. ratio: 0.76, max ratio: 0.77). This behavior was unexpected. Regarding the XM-28 bar, the specimen with a 12 in. spacing had larger crack widths than black (avg. ratio: 1.60, max ratio: 1.46) while the specimen with an 18 in. spacing had comparable crack widths with black (avg. ratio: 1.03, max ratio: 1.12). The relative ratios of the XM-28 to MMFX II for the 12 in. and 18 in. specimens, however, are similar. From review of Figure E.13 and Figure E.14, it is possible that the measured crack widths of the black bar specimen may be an outlier. As shown for the 12 in. specimen (Figure E.13), the black bar specimen lines up with the MMFX II specimen. However, for the 18 in., the crack widths are higher. It was expected that the black and MMFX II would have performed similarly. If the crack widths of the black bars are considered as those of the MMFX II, the XM-28 ratio would be computed as an average of 1.27 and a maximum of 1.487 and in better alignment with the 12 in. specimens. This connection would produce an average ratio of 1.36 and maximum ratio of 1.45 for the Duplex 2205 bars.

TABLE E.2
Average Crack Widths for Varying Bar Spacing (Black)

	Bar Spacing					
	6 in.		12 in.		18 in.	
Steel Stress (ksi)	w_6 (mils)	w_6/w_6	w_{12} (mils)	w_{12}/w_6	w_{18} (mils)	w_{18}/w_6
25	3.3	1.00				
30	4.2	1.00	6.0	1.41		
35	4.9	1.00	6.0	1.21		
40	5.9	1.00	6.3	1.08		
45	6.7	1.00	8.4	1.25		
50	8.4	1.00	10.1	1.20		
55	10.1	1.00	12.0	1.19	23.0	2.28
60	11.7	1.00	14.0	1.19	26.7	2.28
65	13.0	1.00	16.3	1.25	26.6	2.05
70	14.3	1.00	18.4	1.29	28.0	1.96
75	15.5	1.00	19.7	1.28	31.5	2.04
80	17.7	1.00			36.0	2.03
Avg.		**1.00**		**1.24**		**2.11**

E.3. ANALYSIS OF TEST RESULTS

E.3.1 Crack Spacing

Up to the 1960s, test variables such as bar diameter, effective reinforcement ratio, or effective concrete area in tension was considered as important parameters to control crack widths (these were used in the CEB code). However, Hognestad (1962) observed that bar size, concrete strength, reinforcement ratio, and effective reinforcement ratio do not demonstrate a clear relationship with crack width measurements. Although, Hognestad (1962) stated that relationships between steel stress, crack spacing, and crack width hardly have a place in practical design criteria (which are the parameters used in current code), he did observe that the concrete cover has a high correlation to crack width measurements. Further studies at PCA laboratories by Karr and Mattock (1963) similarly focused on the influence of area of concrete surrounding each reinforcing bar to crack width measurements. This parameter was also used in the Gergely and Lutz (1968) crack width equation and adopted

TABLE E.3
Maximum Crack Widths for Varying Bar Spacing (Black)

	Bar Spacing					
	6 in.		12 in.		18 in.	
Steel Stress (ksi)	w_6 (mils)	w_6/w_6	w_{12} (mils)	w_{12}/w_6	w_{18} (mils)	w_{18}/w_6
25	4.7	1.00				
30	6.4	1.00	6.6	1.03		
35	7.5	1.00	9.4	1.25		
40	9.2	1.00	12.5	1.36		
45	10.0	1.00	14.0	1.40		
50	13.0	1.00	16.4	1.26		
55	17.9	1.00	20.0	1.12	26.5	1.48
60	19.0	1.00	20.0	1.05	30.5	1.61
65	17.7	1.00	22.4	1.27	38.1	2.15
70	23.0	1.00	27.9	1.21	45.2	1.96
75	23.0	1.00	30.0	1.30	51.8	2.25
80	23.0	1.00			60.0	2.61
Avg.		**1.00**		**1.22**		**2.01**

TABLE E.4
Average Crack Widths for Varying Bar Spacing (MMFX II)

	Bar Spacing					
	6 in.		12 in.		18 in.	
Steel Stress (ksi)	w_6 (mils)	w_6/w_6	w_{12} (mils)	w_{12}/w_6	w_{18} (mils)	w_{18}/w_6
25	4.0	1.00				
30	4.8	1.00				
35	5.6	1.00				
40	6.4	1.00	7.2	1.13		
45	7.3	1.00	8.2	1.13		
50	8.3	1.00	10.6	1.28		
55	9.4	1.00	13.3	1.42	19.5	2.08
60	10.6	1.00	15.2	1.43	18.0	1.69
65	11.9	1.00	17.2	1.44	19.5	1.63
70	13.0	1.00	19.5	1.50	21.6	1.66
75	14.0	1.00	21.9	1.57	24.5	1.75
80	14.9	1.00	24.5	1.64	27.8	1.87
85	15.9	1.00	27.3	1.72	31.3	1.96
90	17.0	1.00	30.3	1.79	34.7	2.04
95	18.0	1.00	32.7	1.81	38.1	2.11
100	19.1	1.00	35.1	1.84	41.4	2.17
105	19.9	1.00	37.8	1.90	46.1	2.32
110	20.7	1.00	41.1	1.98		
115	21.6	1.00	45.4	2.10		
Avg.		**1.00**		**1.61**		**1.94**

TABLE E.5
Maximum Crack Widths for Varying Bar Spacing (MMFX II)

	Bar Spacing					
	6 in.		12 in.		18 in.	
Steel Stress (ksi)	w_6 (mils)	w_6/w_6	w_{12} (mils)	w_{12}/w_6	w_{18} (mils)	w_{18}/w_6
25	5.0	1.00				
30	6.8	1.00				
35	8.6	1.00				
40	10.4	1.00	11.6	1.11		
45	12.4	1.00	13.6	1.10		
50	16.0	1.00	16.7	1.04		
55	19.6	1.00	20.1	1.02	24.2	1.23
60	19.6	1.00	22.8	1.17	24.9	1.27
65	19.1	1.00	25.9	1.35	30.4	1.59
70	19.7	1.00	29.8	1.52	34.6	1.76
75	20.6	1.00	32.8	1.59	36.4	1.77
80	21.5	1.00	34.5	1.61	39.3	1.83
85	22.5	1.00	40.2	1.78	45.9	2.04
90	23.8	1.00	47.4	2.00	54.7	2.30
95	25.0	1.00	50.0	2.00	63.5	2.54
100	26.2	1.00	52.9	2.02	66.6	2.54
105	27.4	1.00	60.3	2.20	75.4	2.75
110	28.6	1.00	66.0	2.31		
115	29.9	1.00	68.9	2.31		
Avg.		**1.00**		**1.63**		**1.97**

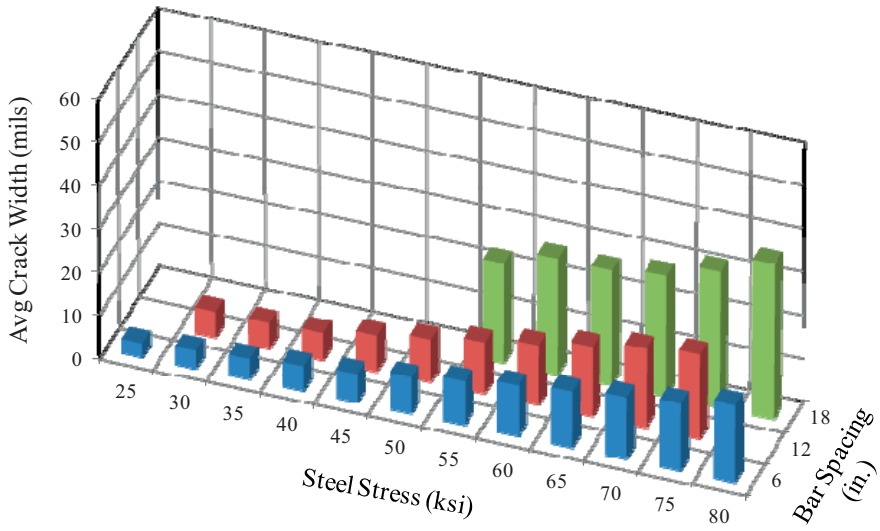

(a) Average Crack Widths

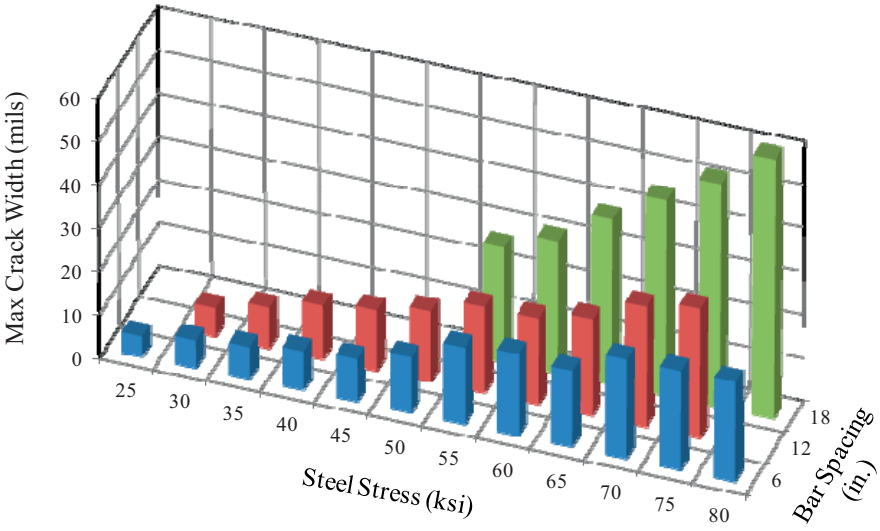

(b) Maximum Crack Widths

Figure E.9 3-D plot of crack widths for varying bar spacing (black).

by the ACI Building Code in 1971 through the use of z-factor method.

On the other hand, Broms (1965b) developed a simple method for the calculation of crack width and crack spacing in reinforced concrete members. This simple physical model was re-evaluated by Frosch (1999) and was adopted by ACI 318 in 1999 and by AASHTO in 2005 to control crack widths through limiting the maximum spacing of flexural reinforcement. The model is based on the concept that the crack width is a function of the crack spacing and reinforcing steel strain. To demonstrate how crack spacing is associated with the concrete cover, Broms used the analogy of a load transferring stress circle to explain whether a new tensile crack could be a primary crack or a secondary crack. When multiple bars are used, the diameter of the stress circles will overlap with each other, and if the primary crack spacing is larger than twice the thickness of the side cover, the tensile crack would be considered a primary crack otherwise, it would be considered a secondary crack. Based on this analogy, Broms suggested that the theoretical minimum crack spacing will be equal to the thickness of the controlling cover (measured from the center of reinforcing bar located closest to the concrete surface, Figure E.15), while the maximum crack spacing will be twice this value.

The measured average crack spacing of the twelve slab specimens in this test program was compared with the theoretical crack spacing model proposed by Broms (1965a) using the controlling cover. Table E.10 shows the controlling cover distance, the calculated average crack spacing, and the measured average spacing of primary cracks. This data is

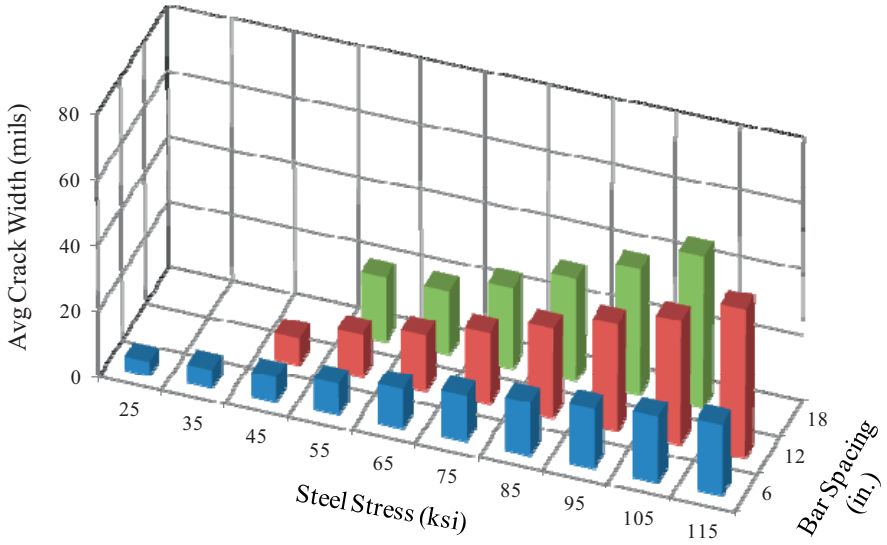

(a) Average Crack Widths

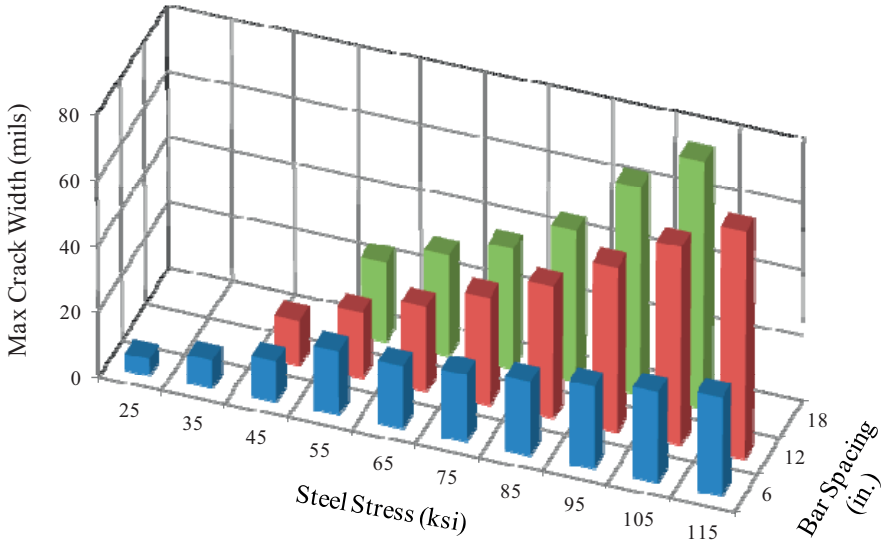

(b) Maximum Crack Widths

Figure E.10 3-D plot of crack widths for varying bar spacing (MMFX II).

compared in Figure E.16 with the theoretical minimum, maximum, and average spacing of the model.

Figure E.16 reveals the trend that as the bar spacing increases, the measured primary crack spacing increases. Thus, as the bar spacing increases, wider crack widths will be present. If the elongation of concrete between cracks is neglected (small compared to the elongation of reinforcement), the number of tensile cracks multiplied by the average crack widths will be the total elongation of the reinforcement. Therefore, as the primary crack spacing increases (less cracks form), wider cracks would be observed to produce the same elongation for the corresponding stress. Test results from the previous section showed that the average and maximum crack widths increases as the bar spacing increases which is consistent with the results shown in Figure E.16 where the primary crack spacing increases as bar spacing increases. Broms (1965b) observed that the measured average crack spacing is twice the controlling cover distance, higher than the theoretical value of 1.5. Similar results were observed for the slab specimens with 6 in. bar spacing (3 in. side cover) in this study. However, as the bar spacing increased, the measured average spacing became closer to the calculated minimum, equivalent to the controlling cover distance.

The crack spacing model suggested by Broms (1965b) was based on the test results of tension and flexural specimens which had small side covers (only 4 out of 50 specimens had a side cover of 6 in.). Therefore, although the model has shown good or conservative estimates with test results for smaller side covers and bar spacings, the model can be

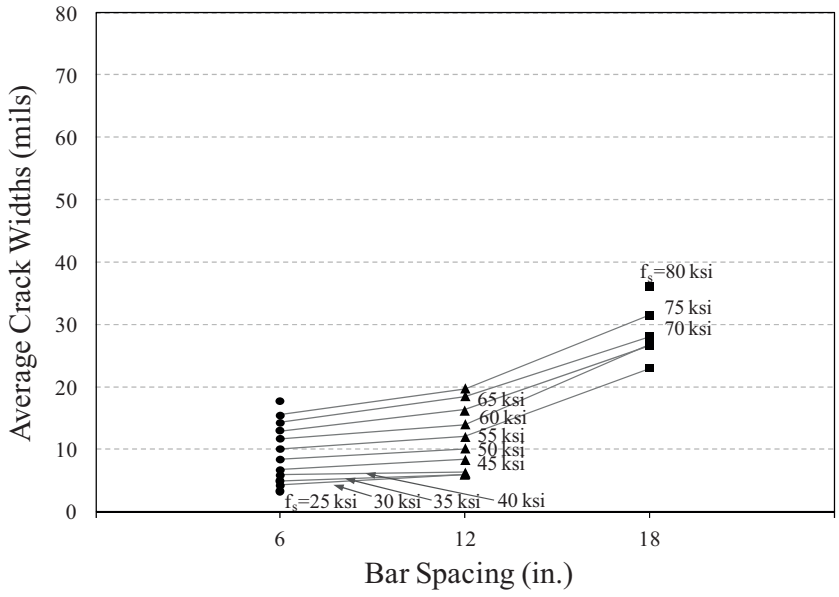

(a) Average Crack Widths

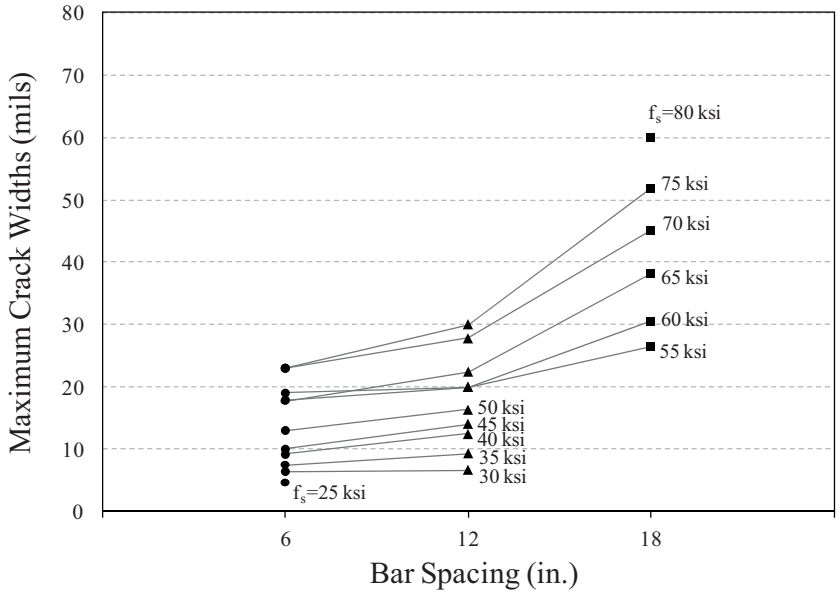

(b) Maximum Crack Widths

Figure E.11 Effect of bar spacing to crack widths (black).

modified for wider specimens such as slabs with larger side covers and bar spacings.

To re-evaluate the relationship between crack spacing and the controlling cover, test data from previous works were reviewed. A total number of 107 specimens are evaluated. A summary of the crack width test specimens are presented in Table E.11. Tests of 50 specimens consisting of slabs (6 to 15 in. wide, 6 in. deep) and beams (6×15 and 6×23 in.) tested by Clark (1956), 8 beam specimens (8×16 in.) tested by Hognestad (1962), 13 test specimens including both beams (rectangular or T-beam) and slabs (24×8 in.) evaluated by Karr and Mattock (1963), 14 tension and flexural specimens (round shape and squared shape) by Broms (1965b), 10 slab specimens (36×8 in.) tested previously at Purdue by Blackman (2002), and 12 slabs specimens from this study are included.

Figure E.17 shows the measured average crack spacings from these test data. There is an increasing trend up to a controlling cover of 6 in. Broms (1965b) reported that the measured average crack spacings were about twice the controlling cover (grey triangles). Specimens tested by Hognestad (grey diamonds) also demonstrate that the

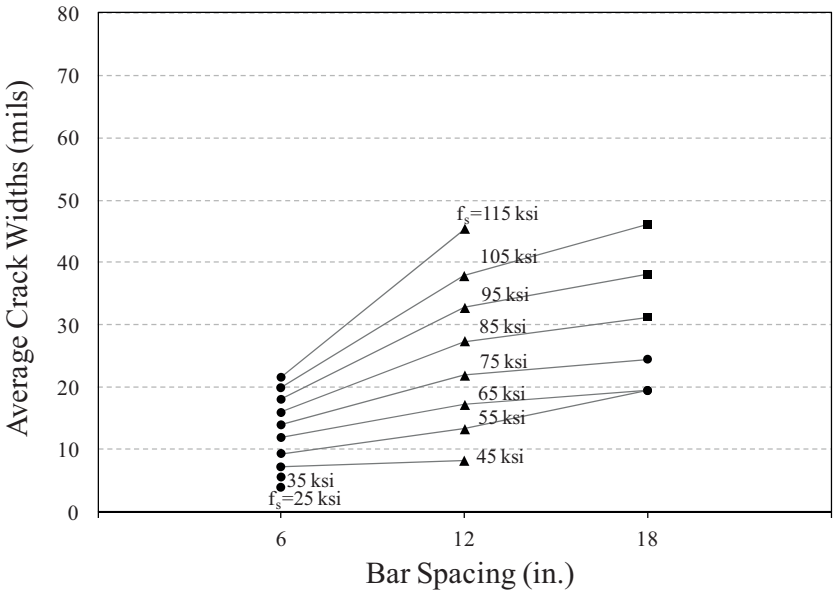

(a) Average Crack Widths

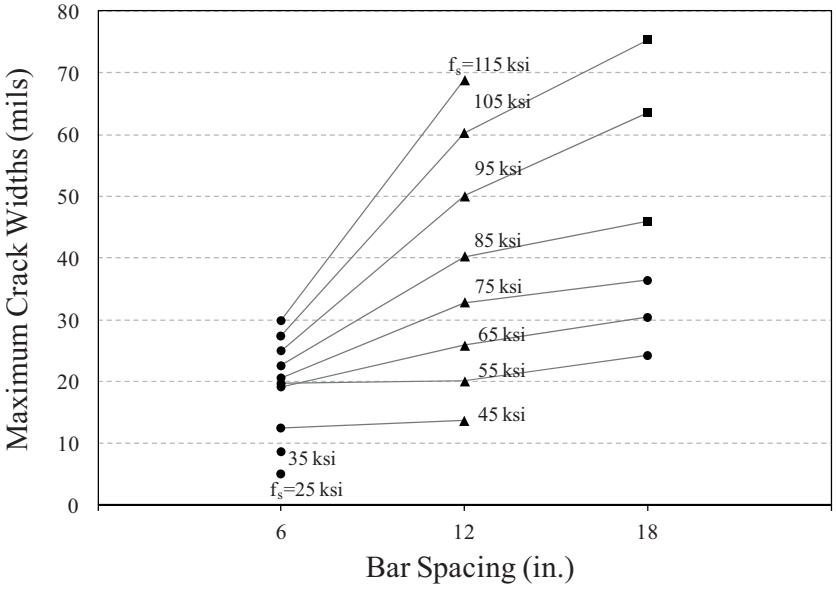

(b) Maximum Crack Widths

Figure E.12 Effect of bar spacing to crack widths (MMFX II).

measured data is close to twice the controlling cover. The majority of the data from Clark (1956) (grey circles) show that the average test results match well with the theoretical average ($S_{avg} = 1.5d^*$). Test results from Karr and Mattock demonstrated that their beam specimens with small controlling covers produced larger crack spacings than the calculated average of $1.5d^*$ while the measured crack spacings were smaller than the calculated average and closer to the theoretical minimum value for controlling covers larger than 4 in.

Similar to the results shown by Karr and Mattock, tests performed previously at Purdue (black diamonds) by Blackman (2002) and current study (black triangles) demonstrate that slab specimens with a controlling cover less than 6 in. have wider crack spacings than the theoretical average while slab specimens that have a controlling cover more than 6 in. have smaller crack spacings than the calculated average. The ratio of average measured crack spacings to controlling cover is 2.0 for specimens with controlling cover less than 6 in., 1.5 for slabs with a controlling cover of 6 in., and 1.0 for specimens with a controlling cover of 9 in. In other words, the average crack spacing is approximately 9 in. when the side cover is 6 in. and remains 9 in. although

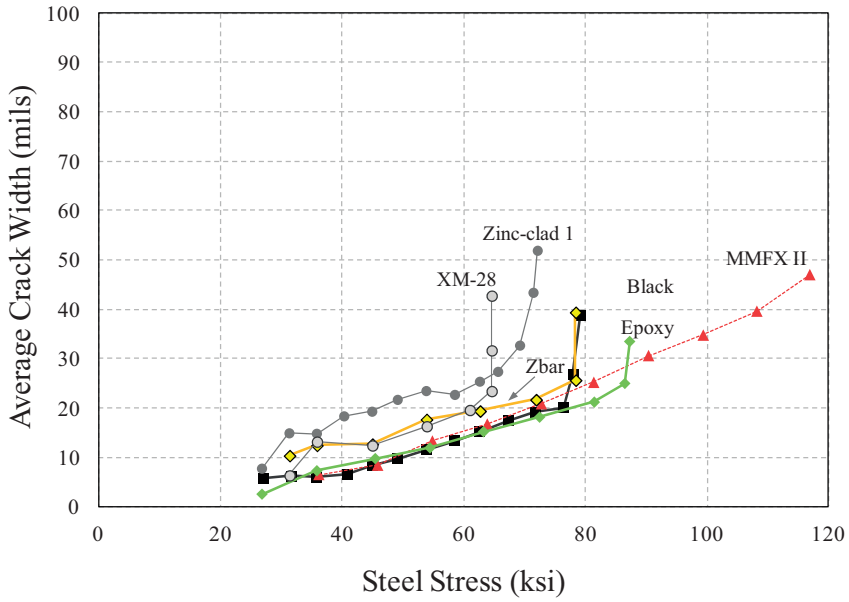

(a) Average Crack Widths

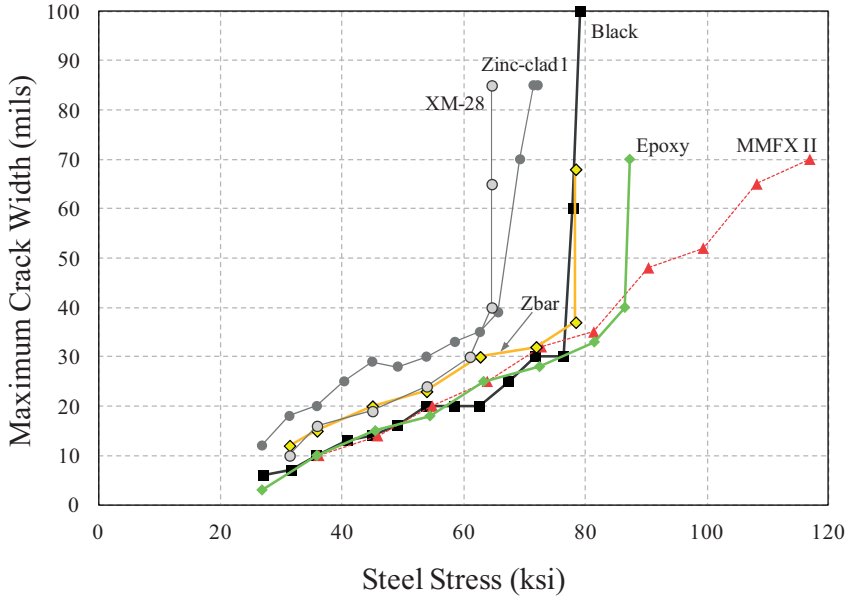

(b) Maximum Crack Widths

Figure E.13 Crack widths for various bar types with 12 in. bar spacing.

the controlling cover increases. This can be viewed that there is an upper limit in the transfer length, a length necessary to transfer bond stress between the reinforcement and concrete. The transfer length is used in the bond-slip models (Burns, 2011) to control crack widths and by the *fib* Model Code for Concrete Structures (2010). For design purpose, the current study suggests that average crack spacing of 1.5 multiplied by the controlling cover distance can be used up to a controlling cover of 6 in. and remain constant for larger controlling covers.

E.3.2 Crack Widths

E.3.2.1 Bar spacing. Crack widths calculated using the crack model by Frosch (1999) were compared with crack widths measured for the three different bar spacings (Table E.12 and Table E.13). The values given in these tables have been averaged over all stress levels. Individual comparisons between calculated and measured crack widths for each stress level is provided in Appendix C. The calculated crack widths are generally greater than the measured crack widths. This result is reasonable as the model neglects the concrete

TABLE E.6
Average Crack Widths for Various Bar Types (12 in. Bar Spacing)

	Bar Type											
	Black		Epoxy		Zinc-clad		Zbar		MMFX II		XM-28	
Steel Stress (ksi)	w_b (mils)	w_b/w_b	w_e (mils)	w_e/w_b	w_{zc} (mils)	w_{zc}/w_b	w_z (mils)	w_z/w_b	w_m (mils)	w_m/w_b	w_{xm} (mils)	w_{xm}/w_b
30	6.0	1.00	4.1	0.69	12.6	2.11						
35	6.0	1.00	6.8	1.13	14.8	2.47	12.0	2.01			11.8	1.97
40	6.3	1.00	8.3	1.31	18.0	2.84	12.5	1.98	7.2	1.14	12.8	2.02
45	8.4	1.00	9.6	1.14	19.2	2.30	12.7	1.51	8.2	0.98	12.4	1.48
50	10.0	1.00	10.8	1.08	21.9	2.19	15.5	1.55	10.6	1.06	14.6	1.46
55	12.0	1.00	12.0	1.00	23.2	1.93	17.9	1.49	13.3	1.11	16.8	1.40
60	14.0	1.00	13.9	1.00	23.5	1.69	18.8	1.35	15.2	1.09	19.1	1.37
65	16.3	1.00	15.7	0.97	26.8	1.65	19.9	1.23	17.2	1.06	23.8	1.47
70	18.4	1.00	17.3	0.94	36.0	1.95	21.2	1.15	19.5	1.06		
75	19.7	1.00	19.0	0.96			23.6	1.20	21.9	1.11		
Avg.		**1.00**		**1.02**		**2.12**		**1.50**		**1.08**		**1.60**

tensile strain to provide conservative estimates. In general, the estimated values became more accurate as bar spacing decreased (except from the black bars as the spacing decreased from 18 in. to 12 in.).

It is also observed that the maximum crack widths are better estimated than the average crack widths for both black and MMFX II steel. This result is similar to test results reported by Blackman (2002). In addition, although the model was developed for black bars, the model also estimates the crack widths in a similar fashion for MMFX II steel because the two bar type have comparable bond strengths as discussed in the previous chapter.

Figure E.18 to Figure E.20 plot the measured crack widths versus the calculated crack widths for black bars and MMFX II bars with 6 in., 12 in., and 18 in. spacings. Measurements prior to yield was considered only. Both black and MMFX II performed similarly except for the 18 in. specimen. Specimens with a 6 in. spacing show that the measured maximum crack widths match well with the calculated values (Figure E.18). Specimens with a 12 in. spacing (Figure E.19) show conservative results (measured crack width $<$ calculated crack width). The same trend is shown for specimens with a 18 in. spacing (Figure E.20). The measured crack width is smaller than the calculated crack widths for specimens with a 18 in. spacing. However, there is difference in crack widths between the black and MMFX II specimen.

The total elongation of a reinforcing bar is the product of number of primary cracks and the average crack widths as shown in Equation (E.1) where the concrete elongation is neglected. The number of primary cracks, N within length, L is equal to the average crack spacing, S_{cavg}. Therefore, Equation (E.2) can be rewritten as Equation (E.3). For a given strain, this relationship indicates that crack widths will increase linearly as crack spacings increase.

$$N \cdot w_{c_{avg}} = \varepsilon_s \cdot L \tag{E.1}$$

$$w_{c_{avg}} = \varepsilon_s \cdot \frac{L}{N} \tag{E.2}$$

$$w_{c_{avg}} = \varepsilon_s \cdot S_{c_{avg}} \tag{E.3}$$

where:

N = *number of primary cracks within length L*
$w_{c_{avg}}$ = *average crack widths*
ε_s = *reinforcing steel strain*
L = *length of interest (in.)*
$S_{c_{avg}}$ = *average crack spacing*

Based on this model, test results which indicate that crack width estimations become more conservative as the bar spacing increases can be expected because the model is based on the concept that the crack spacing linearly increases as the controlling cover increases. However, observations from tests show that the measured crack spacings remain approximately constant while the controlling cover increases from 6 in. to 9 in. Therefore, conservative results are not unexpected for larger bar spacings.

Figure E.21 shows the relationship between crack widths and the two parameters: bar spacing and concrete bottom cover. Test data from other researchers (Blackman, 2002; Clark, 1956; Hognestad, 1962; Karr & Mattock, 1963) have been included. For comparison, crack widths measured at the same bar stress (40 ksi) are collected. In addition, only average crack widths measured across the tension face are considered. A total number of 88 specimens are evaluated. Measurements that exceed the crack widths calculated by the model (Frosch, 1999; contour lines) have a positive sign next to the dots.

In addition, the measured crack widths are labeled next to the dots for data exceeding more than 50% of the model value. Approximately 55% of the measurement data exceeded the model value. However, only 5% of them had a value 50% larger than calculated. Of particular interest was the influence of the two parameters (bar spacing and concrete bottom cover) on crack widths. Controlling cover distance in Equation (E.4) incorporates these two important parameters and they serve as the basis of crack width calculations. Figure E.21 displays that the measured data increases (the color of the dots gets darker) both as bar spacing and concrete cover increases. These parameters are clearly correlated with crack widths.

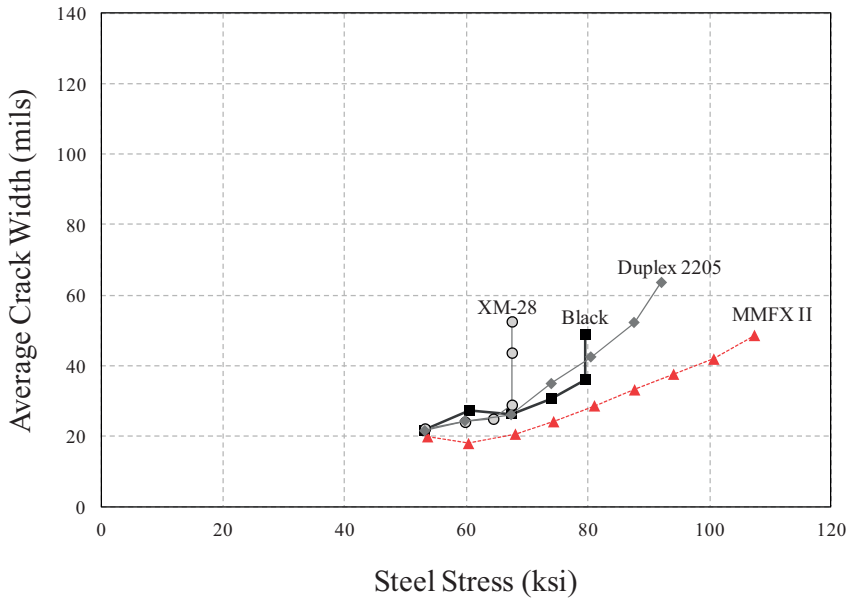

(a) Average Crack Widths

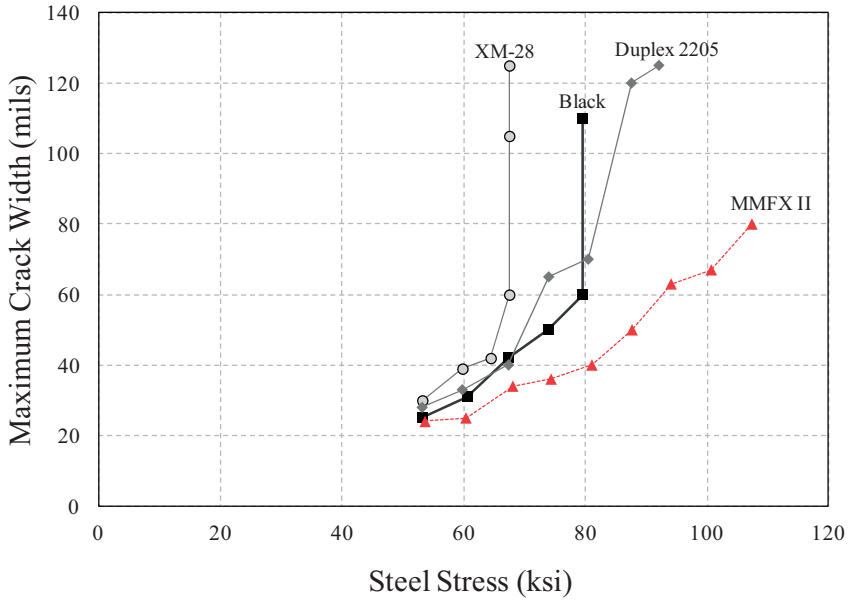

(b) Maximum Crack Widths

Figure E.14 Crack widths for various bar types with 18 in. bar spacing.

$$d^* = \max\left(\sqrt{d_c^2 + d_s^2}, \sqrt{d_c^2 + \left(\frac{s}{2}\right)^2}\right) \qquad \text{(E.4)}$$

where:

d^* = *controlling cover distance*
d_c = *bottom cover measured from the center of bar*
d_s = *side cover measured from the center of bar*
s = *center to center bar spacing*

Figure E.22 plots the average crack widths measured on the tension face at a steel stress of 40 ksi for various controlling cover distances. There is definitely an increasing trend in crack widths as the controlling cover increases. There is only one data point shown plotted that has a controlling cover greater than 7 in. The current study includes specimens that have a controlling cover of 9.2 in., however, the first crack was observed at a stress higher than 40 ksi. For that reason, no data from current study is included for that controlling cover dimension.

TABLE E.7
Maximum Crack Widths for Various Bar Types (12 in. Bar Spacing)

	Bar Type											
	Black		Epoxy		Zinc-clad		Zbar		MMFX II		XM-28	
Steel Stress (ksi)	w_b (mils)	w_b/w_b	w_e (mils)	w_e/w_b	w_{zc} (mils)	w_{zc}/w_b	w_z (mils)	w_z/w_b	w_m (mils)	w_m/w_b	w_{xm} (mils)	w_{xm}/w_b
30	6.6	1.00	5.4	0.82	16.1	2.44						
35	9.4	1.00	9.3	0.99	19.6	2.09	14.4	1.54			14.8	1.58
40	12.5	1.00	12.1	0.97	24.6	1.97	17.3	1.38	11.6	0.93	17.4	1.39
45	14.0	1.00	14.7	1.05	29.0	2.07	20.0	1.43	13.6	0.97	19.0	1.36
50	16.4	1.00	16.5	1.01	28.3	1.73	21.7	1.32	16.7	1.02	21.8	1.33
55	20.0	1.00	18.4	0.92	30.7	1.54	23.9	1.19	20.1	1.00	24.9	1.25
60	20.0	1.00	22.4	1.12	33.7	1.68	27.9	1.39	22.8	1.14	29.1	1.46
65	22.4	1.00	25.6	1.14	38.1	1.70	30.5	1.36	25.9	1.15	41.1	1.83
70	27.9	1.00	27.2	0.97	74.8	2.68	31.6	1.13	29.8	1.07		
75	30.0	1.00	29.4	0.98			34.4	1.15	32.8	1.09		
Avg.		**1.00**		**1.00**		**1.99**		**1.32**		**1.05**		**1.46**

Figure E.23 to Figure E.25 plot the measured average crack widths for higher steel stresses where there is lack of test data in the general literature. Although, only data from this study is included for 60 and 70 ksi, it is shown that the measured average crack widths become smaller than the calculated crack widths at higher stresses for specimens with larger controlling covers. As discussed earlier, the crack spacing does not increase linearly as the controlling cover increases for large controlling covers. Therefore, crack width calculations can be adjusted for controlling covers greater than 6 in. by limiting the crack spacing as shown (the red solid line). While this limit can be provided, it should be noted that the model produced conservative results (average measured values fall within calculated minimum and maximum) and a limit is not required.

E.3.2.2 Bar type. Crack widths calculated using the crack model by Frosch (1999) were compared with crack widths measured for the six different bar types at a 12 in. bar spacing in Figure E.26 and the four different bar types at an 18 in. bar spacing in Figure E.27. Measurements made prior to yielding are plotted. The calculated crack widths are conservative for all bar types except the un-plated zinc-clad (Zinc-clad 1) bar. Specimens containing MMFX II and epoxy-coated bars (12 mils coating thickness) behaved similarly to specimens containing black reinforcing bars.

However the data indicated that crack widths in specimens designed with Zbar, XM-28, Duplex 2205, and un-plated zinc-clad bars have larger crack widths compared to similar specimens designed with black bars. For the Duplex 2205 which has a roundhouse stress-strain curve, maximum crack widths increased nonlinearly at high stresses as shown in Figure E.27(b). For the 12 in. bar spacing, average and maximum measured crack widths increased linearly, consistent with the theoretical model (Figure E.26). Similar results are observed for the 18 in. bar spacings with the exception of the Duplex 2205 (Figure E.27 (b)).

Table E.14 and Table E.15 summarize the ratio of calculated to measured average and maximum crack widths. In addition, the tables present the ratios of the calculated to measured crack width normalized to that of black bars. The values presented have been averaged over all stress levels. The calculated to measured crack width ratios indicate that the calculations overestimate crack widths except for the un-plated zinc-clad bars.

Because average and maximum crack widths measured for various specimens behave similarly increasing linearly as shown in Figure E.26, crack widths can be computed by

TABLE E.8
Average Crack Widths for Various Bar Types (18 in. Bar Spacing)

	Bar Type							
	Black		MMFX II		Duplex 2205		XM-28	
Steel Stress (ksi)	w_b (mils)	w_b/w_b	w_m (mils)	w_m/w_b	w_{s2205} (mils)	w_{s2205}/w_b	w_{xm28} (mils)	w_{xm28}/w_b
55	23.0	1.00	19.5	0.85	22.3	0.97	22.7	0.99
60	26.7	1.00	18.0	0.67	24.4	0.91	24.1	0.90
65	26.6	1.00	19.5	0.73	25.5	0.96	25.7	0.96
70	28.0	1.00	21.6	0.77	29.5	1.05		
75	31.5	1.00	24.5	0.78	36.1	1.14		
80	36.3	1.00	27.8	0.77	41.9	1.15		
Avg.		**1.00**		**0.76**		**1.03**		**0.95**

TABLE E.9
Maximum Crack Widths for Various Bar Types (18 in. Bar Spacing)

	Bar Type							
	Black		MMFX II		Duplex 2205		XM-28	
Steel Stress (ksi)	w_b (mils)	w_b/w_b	w_m (mils)	w_m/w_b	w_{s2205} (mils)	w_{s2205}/w_b	w_{xm28} (mils)	w_{xm28}/w_b
55	26.5	1.00	24.2	0.91	29.4	1.11	32.5	1.23
60	30.5	1.00	24.9	0.82	33.2	1.09	39.1	1.28
65	38.1	1.00	30.4	0.80	37.8	0.99	45.3	1.19
70	45.2	1.00	34.6	0.77	49.8	1.10		
75	51.8	1.00	36.4	0.70	65.8	1.27		
80	60.7	1.00	39.3	0.65	69.6	1.15		
Avg.		**1.00**		**0.77**		**1.12**		**1.23**

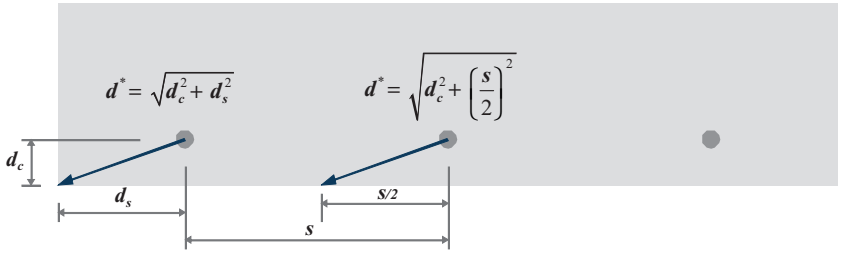

Figure E.15 Controlling cover distance.

multiplying factors to the crack widths computed for black bars. In addition, crack spacings were observed to not change dramatically as the bar spacing change from 12 in. to 18 in. Therefore, a simple multiplication factor for each bar type can be considered in computing crack widths.

Table E.16 provides the normalized ratios of average and maximum crack widths measurements for each bar type. The relative ratios of each bar are obtained by normalizing the average and maximum crack widths to that of black bar at each stress level as shown in Table E.6 through Table E.9. Figure E.13 and Figure E.14 illustrate the trends.

Considering Table E.16, Figure E.13 and Figure E.14, the recommended modification factor X_{crack} for crack width calculations are provided in Table E.17. For specimens not tested, the crack width results from the bond specimens presented in Appendix B were also considered. Bars that resulted in ratios equal or less than 10% difference from the black bar are considered to be effectively the same as black steel. Therefore, epoxy (12 mil), hot-dip galvanized, MMFX II bars are considered to have a multiplication factor of 1.0. Based on the crack width measurements from both slab specimens and bond specimens, to be conservative, all stainless steel bars are recommended to have a multiplication factor of 1.3.

TABLE E.10
Controlling Cover Distance and Measured Average Spacing

Specimen	Controlling Cover Distance, d^* (in.)	Calculated Average Spacing (in.)	Measured Average Spacing (in.)
B-6	3.5	5.3	6.3
M-6			6.2
B-12	6.3	9.4	8.8
E-12			8.1
ZC1-12			9.7
Z-12			8.9
M-12			9.2
XM28-12			8.5
B-18	9.2	13.8	10.2
M-18			8.9
S2205-18			9.9
XM28-18			9.1

E.4. SUMMARY AND CONCLUSIONS

Twelve slabs reinforced with black steel bars and six different corrosion-resistant bars were tested to evaluate the influence of various materials on cracking. In addition, the effect of the spacing of the reinforcement and the effect of

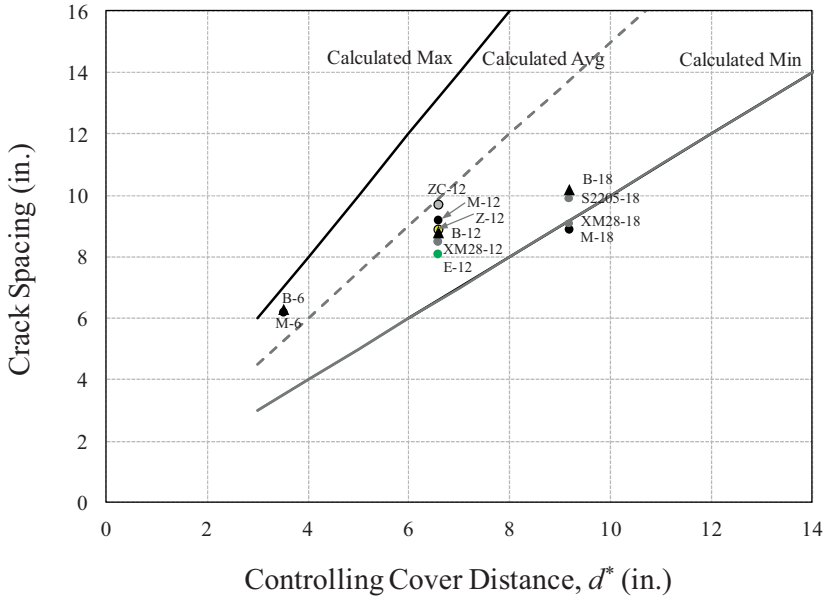

Figure E.16 Measured and calculated average crack spacings.

TABLE E.11
Summary of the Test Database with Crack Widths

Reference	No. of Tests	Bottom Cover d_c (in.)	Side Cover d_s (in.)	Bar Spacing s (in.)	Controlling Cover Distance d^* (in.)	Bar Stress at Measurements f_s (ksi)
Clark (1956)	50	0.69 to 2.7	1.44 to 3.75	2.5 to 9.0	1.77 to 4.61	15 to 45
Hognestad (1962)	8	0.8125 to 4.8125	1.8125	4.375	2.33 to 5.29	30
Karr and Mattock (1963)	13	1.625 to 2.0	1.625 to 6.0	3.25 to 12.0	2.30 to 6.32	40
Broms (1965b)	14	1.5 to 4.05	2.0 to 5.5	1.0 to 6.0	1.40 to 6.00	32 to 70
Blackman (2002)	10	1.5	3.0 to 9.0	6.0 to 18.0	3.35 to 9.12	25 to 55
Sim and Frosch (2014)	12	1.5	3.0 to 9.0	6.0 to 18.0	3.35 to 9.12	27 to 117
Totals	**107**	**0.69 to 4.8125**	**1.44 to 9.0**	**1.0 to 18.0**	**1.40 to 9.12**	**15 to 117**

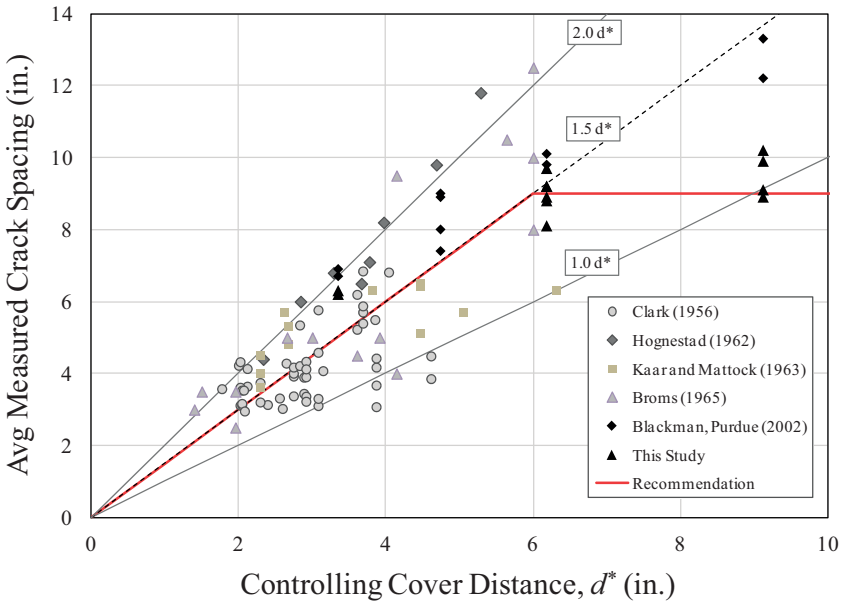

Figure E.17 Average measured crack spacings vs. the controlling cover.

high reinforcement stresses that can be obtained by high-strength reinforcement were considered.

The following findings were based on the test results of this study:

1. The bar types affected the spacing and width of primary cracks. For the control of crack widths, it is recommended that crack widths be calculated based on black bars and multiplying the factors in Table E.17. Design code approaches can directly incorporate these factors to reduce the spacing of these bars by dividing the black bar spacing by these factors.
2. Spacing of the reinforcement affected both crack spacing and crack widths. As the reinforcement spacing increased, the number of primary cracks decreased and the crack spacing increased. This trend is consistent with previous test results.
3. Crack spacing and crack width, however, did not increase significantly after spacing of reinforcement became greater than 12 in. For design purposes, the crack spacing can be considered to be constant for bar spacing greater than 12 in. For a given stress, this results in the same crack widths for spacings greater than 12 in.
4. Crack widths of high-strength bars (MMFX II and stainless steel) which have a roundhouse stress-strain curve will increase nonlinearly at high stresses ($>$ 80 ksi). However, the crack widths of high-strength bars can be conservatively calculated using the model for conventional black bars up to bar stresses of 80 ksi.

TABLE E.12
Ratio of Calculated to Measured Crack Width (Black)

	Calculated/Measured Crack Width	
Bar Spacing (in.)	**Average**	**Maximum**
6	1.23	1.10
12	1.78	1.55
18	1.30	1.27

TABLE E.13
Ratio of Calculated to Measured Crack Width (MMFX II)

	Calculated/Measured Crack Width	
Bar Spacing (in.)	**Average**	**Maximum**
6	1.17	1.03
12	1.38	1.16
18	1.54	1.37

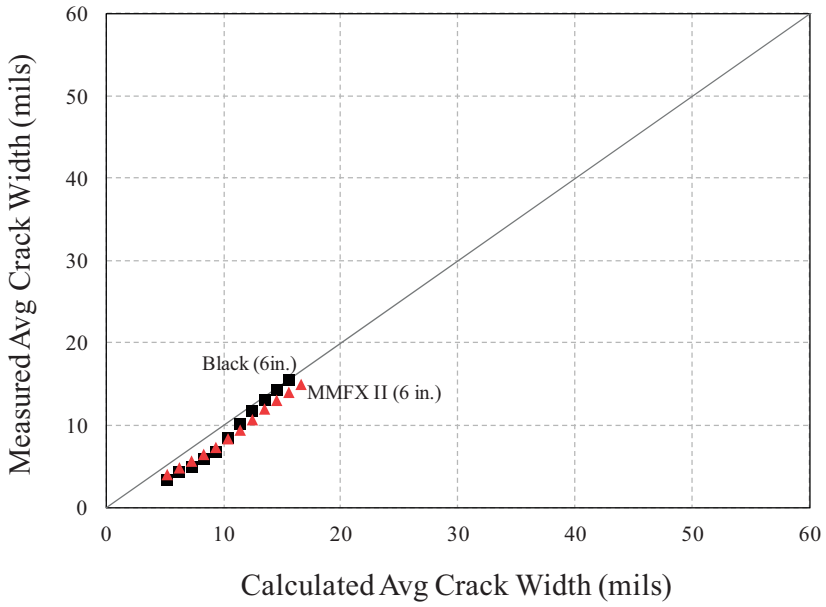

(a) Average Crack Widths

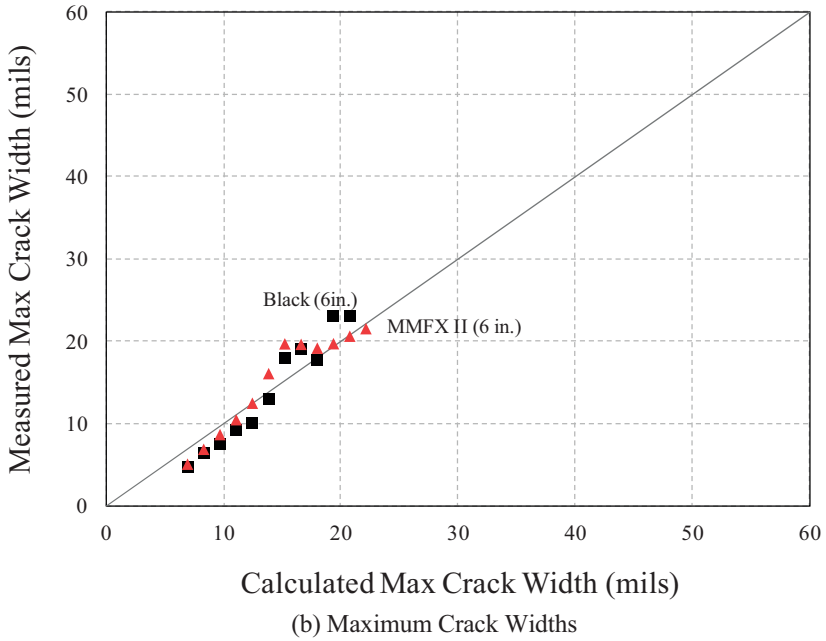

(b) Maximum Crack Widths

Figure E.18 Measured vs. calculated maximum crack widths (6 in.).

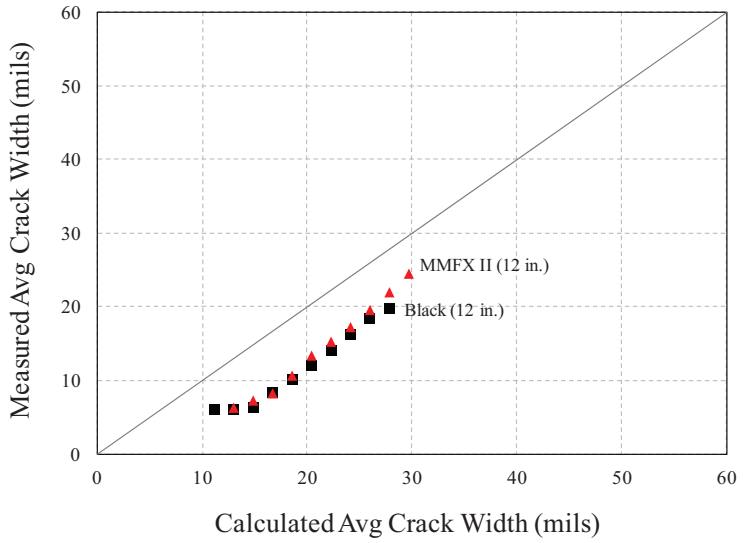

(a) Average Crack Widths

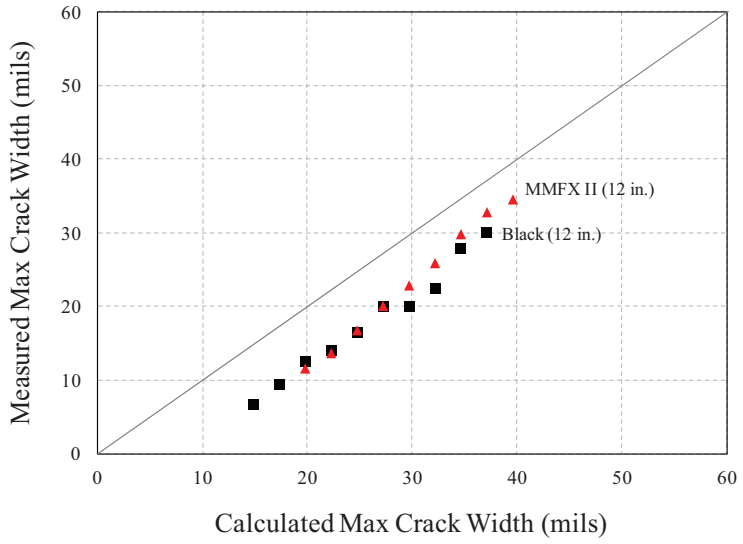

(b) Maximum Crack Widths

Figure E.19 Measured vs. calculated maximum crack widths (12 in.).

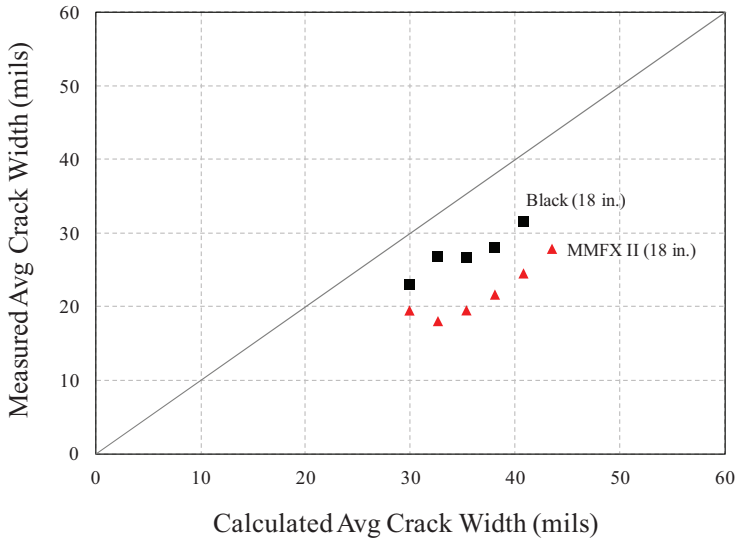

(a) Average Crack Widths

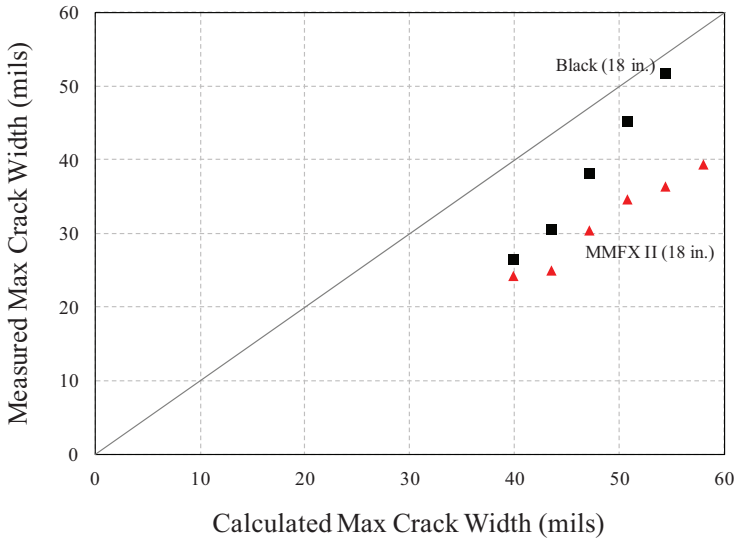

(b) Maximum Crack Widths

Figure E.20 Measured vs. calculated maximum crack widths (18 in.).

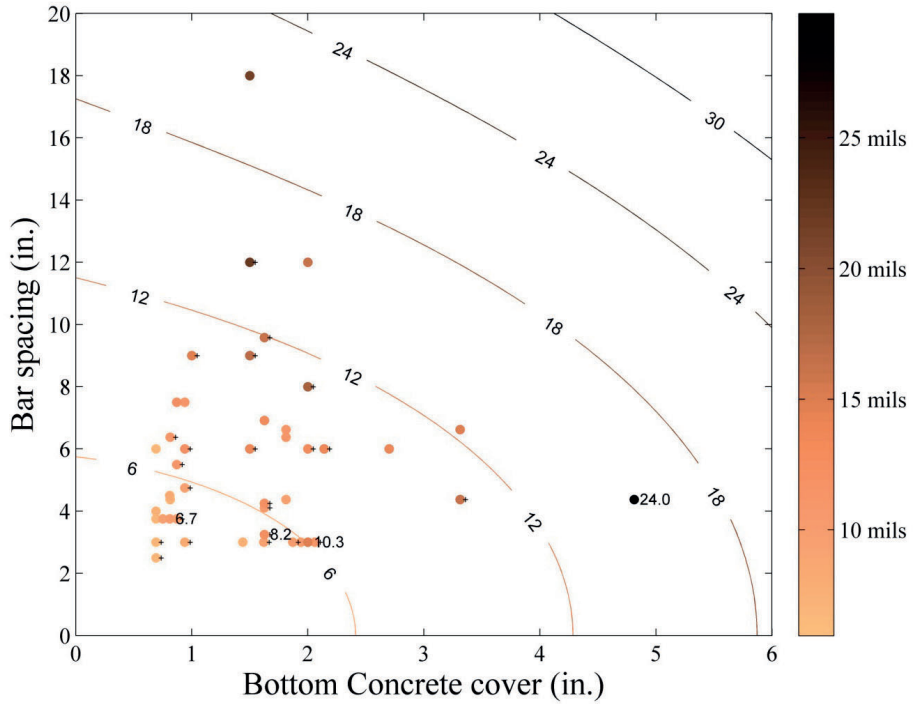

Figure E.21 Effect of bar spacing and bottom cover to average measured crack widths.

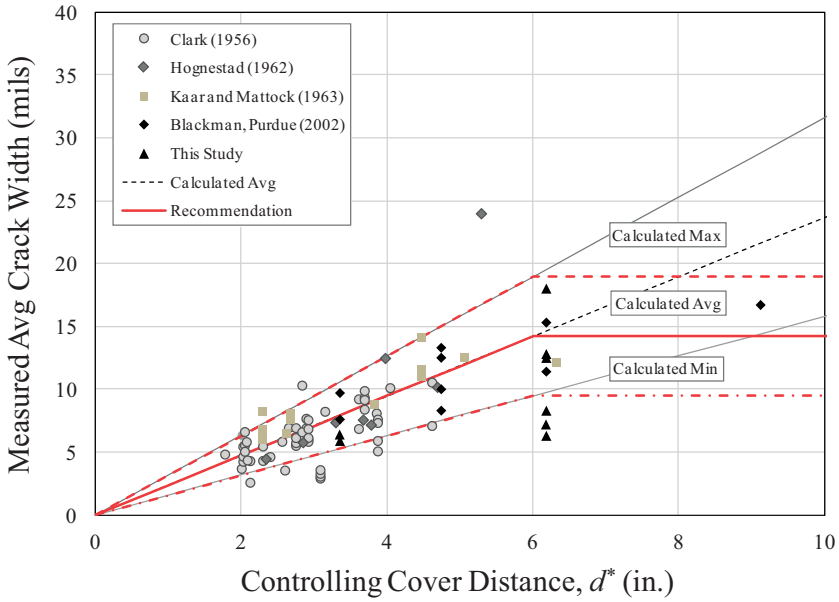

Figure E.22 Measured average crack width vs. controlling cover (40 ksi).

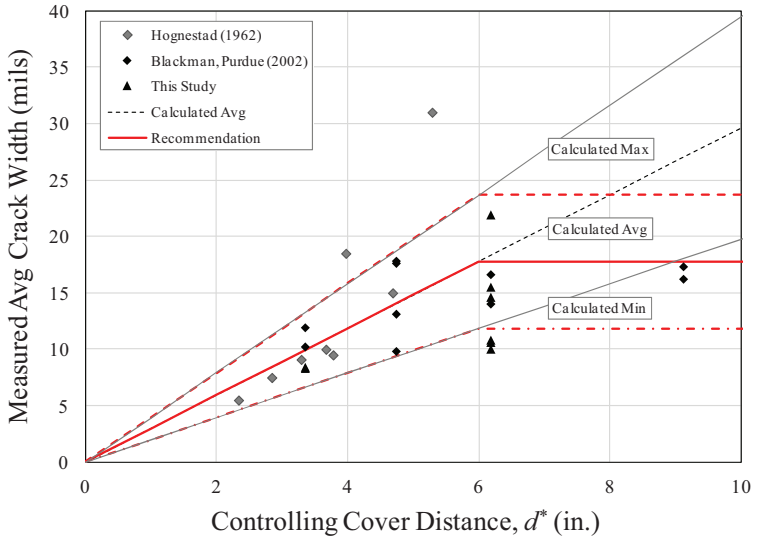

Figure E.23 Measured average crack width vs. controlling cover (50 ksi).

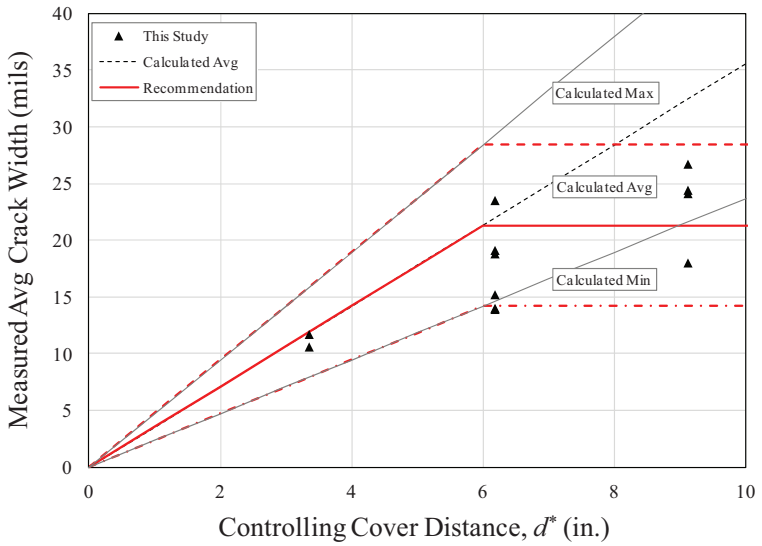

Figure E.24 Measured average crack width vs. controlling cover (60 ksi).

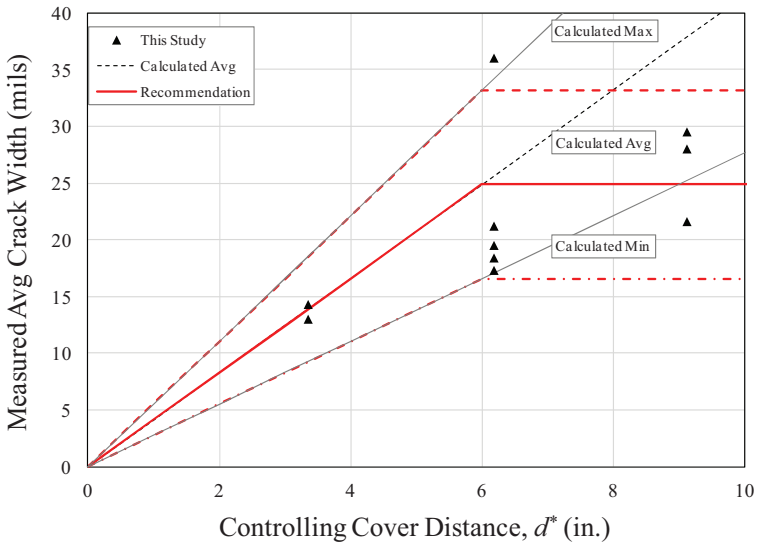

Figure E.25 Measured average crack width vs. controlling cover (70 ksi).

TABLE E.14
Calculated/Measured Crack Width of Varying Reinforcements (12 in.)

	Calculated/Measured Crack width		Normalized Calculated/Measured	
Reinforcing Steel Type	**Average**	**Maximum**	**Average**	**Maximum**
Black	1.78	1.55	1.00	1.00
MMFX II	1.61	1.16	0.90	0.75
Epoxy	1.77	1.59	0.99	1.02
Z-bar	1.19	1.12	0.67	0.72
Zinc-clad 1	0.86	0.81	0.48	0.52
XM-28	1.18	1.07	0.66	0.69

TABLE E.15
Calculated/Measured Crack Width of Varying Reinforcements (18 in.)

	Calculated/Measured Crack width		Normalized Calculated/Measured	
Reinforcing Steel Type	**Average**	**Maximum**	**Average**	**Maximum**
Black	1.28	1.22	1.00	1.00
MMFX II	1.54	1.37	1.20	1.13
Duplex 2205	1.16	0.97	0.91	0.79
XM28	1.35	1.13	1.05	0.93

TABLE E.16
Maximum Crack Width Ratio of Varying Reinforcements

		12 in. Bar Spacing		18 in. Bar Spacing	
Bar Type		**Avg.**	**Max**	**Avg.**	**Max**
Black		1.00	1.00	1.00	1.00
Coated Bars	Epoxy	1.02	1.00	–	–
	Zinc-clad	2.12	1.99	–	–
	Zbar	1.50	1.32	–	–
MMFX II		1.08	1.05	0.76	0.77
Stainless Steel Bars	Duplex 2205	–	–	1.03	1.12
	XM-28	1.60	1.46	0.95	1.23

TABLE E.17
Recommended Modification Factor for Crack Width Calculations

Bar Type		**Modification Factor X_{Crack}**
Black		1.0
Coated Bars	Epoxy (12 mils)	1.0
	Galvanized	1.0
	Zinc-clad	2.0
	Zbar	1.3
MMFX II		1.0
Stainless Steel Bars	316 LN	1.3
	Duplex 2205	
	Duplex 2304	
	XM-28	

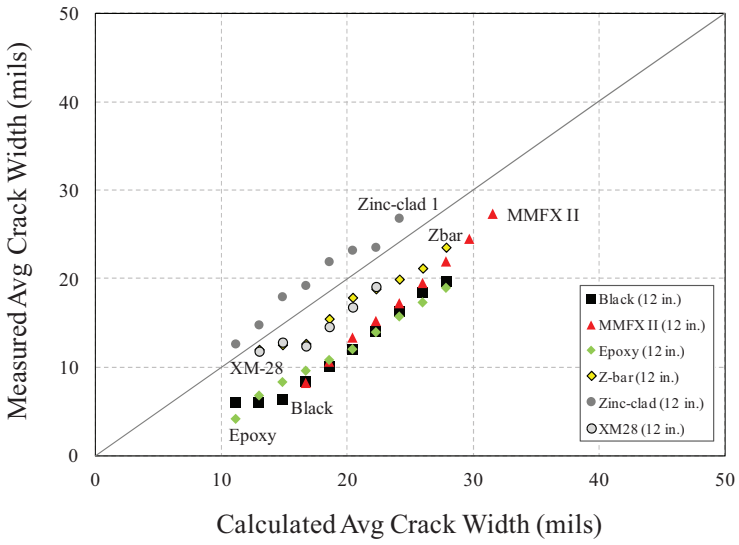

(a) Average Crack Widths

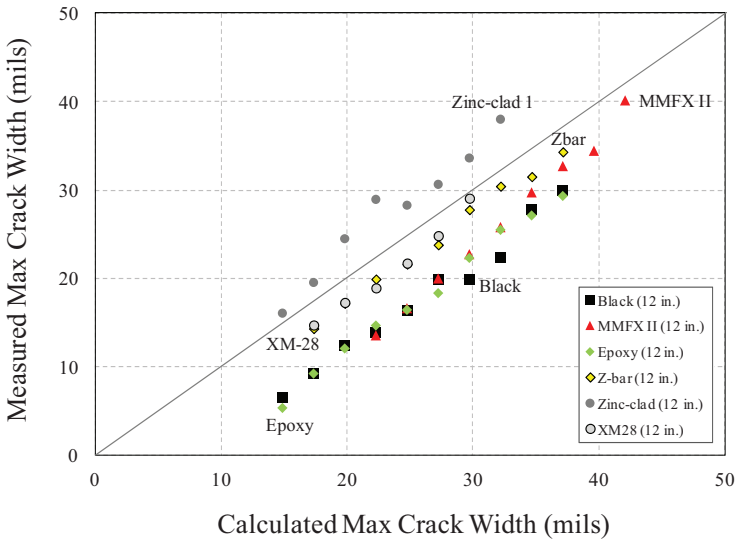

(b) Maximum Crack Widths

Figure E.26 Measured vs. calculated crack widths with various bar types (12 in.).

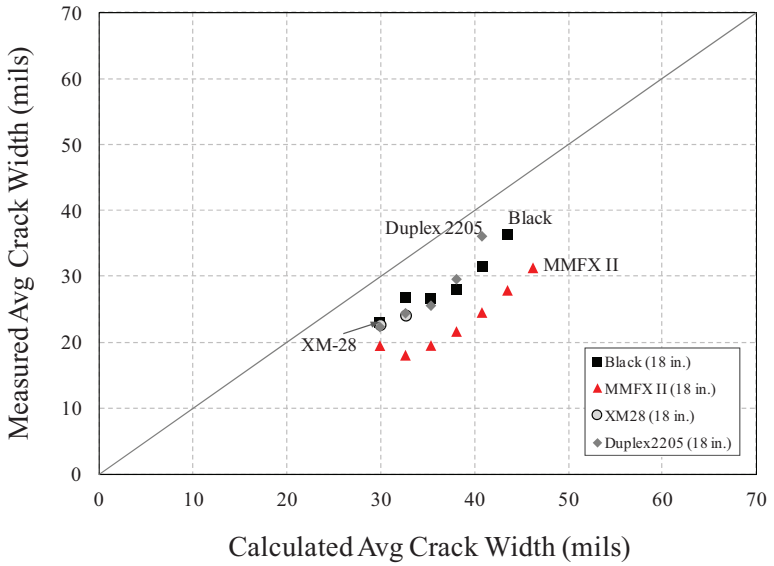

(a) Average Crack Widths

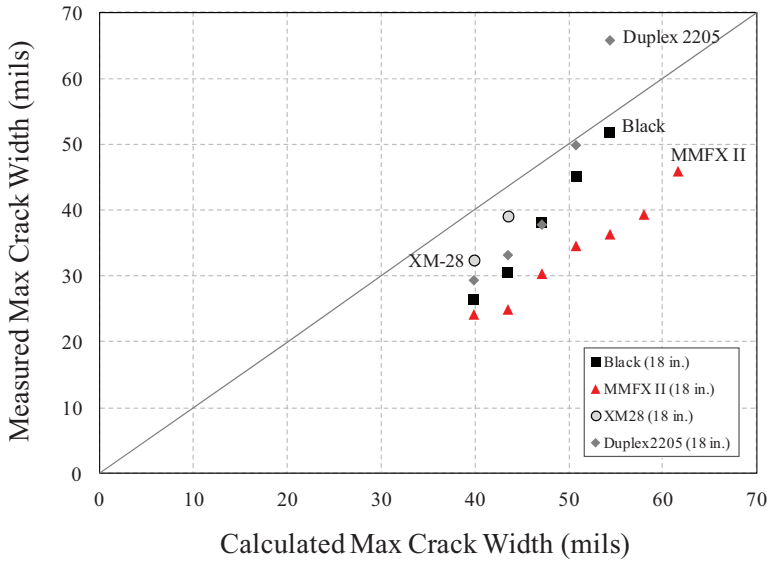

(b) Maximum Crack Widths

Figure E.27 Measured vs. calculated crack widths with various bar types (18 in.).

F.1. INTRODUCTION

The objective of this experimental program is to evaluate the corrosion-resistance of various types of reinforcing steel which could be used in concrete bridge decks. Epoxy-coated steel, hot-dip galvanized steel, two types of zinc-clad steel (un-plated and tin-plated), dual-coated steel (Zbar), MMFX II microcomposite steel, and four different types of stainless steel (316LN, Duplex 2205, Duplex 2304, and XM 28) were selected for study. The performance of these materials was compared with conventional black steel which was used as the control.

Reinforcement in concrete can corrode due to carbonation or chloride attack. Concrete with a low water/cement ratio, good compaction and quality curing is beneficial because it can reduce the carbonation process at the level of reinforcing bar by providing a less permeable concrete. However, bridge decks in marine environment or in cold climates where de-icing salts are used are subjected to chlorides. Chloride ions concentrated on the surface of the bar may act as catalysts to corrosion by breaking down the passive film on the reinforcing bars. Bridge decks typically include two layers of reinforcement in which chloride ions can reach the top mat of the reinforcement which depassivates this layer prior to the bottom layer. In this case, rebar on top can becomes an anode while the rebar on bottom becomes a cathode. Due to electrical continuity typically formed in bridge deck from chairs, an electrochemical cell is created between the two layers which is commonly referred to macrocell corrosion.

Macrocells have become the most commonly used laboratory test specimen to investigate corrosion of reinforcing steel in bridge decks. A number of laboratory test methods have been developed using this type of specimen and they have been standardized in ASTM G109 (2007) and ASTM A955 (2009).

ASTM G109 (2007) introduce a test method to investigate the effects of chemical admixtures on the corrosion of metal in concrete. The test method allows to assess the corrosivity of admixture in a chloride environment and also to evaluate materials intended to inhibit chloride-induced corrosion of steel in concrete. The ASTM G109 macrocell is uncracked (Figure F.1(a)).

ASTM A955 (2009) provides the standard specification that covers deformed and plain stainless-steel bars for concrete reinforcement. In Annex A3 of ASTM A955, "cracked beam" macrocells developed at the University of Kansas is introduced. This macrocell inserts stainless shim plates down to the bar level to create artificial cracks as shown in Figure F.1(b).

These standard macrocells shown in Figure F.1 have a number of limitations which include: uncracked specimens (ASTM G109), artificial cracks formed by stainless steel shim plates (ASTM A955) only down to the top bar, and no transverse reinforcement (ASTM G109 and ASTM A955).

However, most of the transverse cracks in bridge decks are caused at early ages due to restrained shrinkage and extended the full depth of the deck (Frosch, Blackman, & Radabaugh, 2003; Frosch, Bice, & Erickson, 2006a; shown in Figure 1.3).

F.1.1 Macrocell Action

The bottom layer of reinforcement in macrocells introduced in ASTM is twice the area of the top reinforcement to preferably derive corrosion of the top mat. However, in this study, the reinforcement layer were maintained as the same area to be more consistent with bridge deck design as well as to not setup a preference in corrosion performance.

F.1.1.1 Carbonation. Carbonic dioxide (CO_2) dissolves in water (Equation (F.1)) to form carbonic acid (H_2CO_3) and this reacts with the calcium hydroxides ($Ca(OH)_2$) in

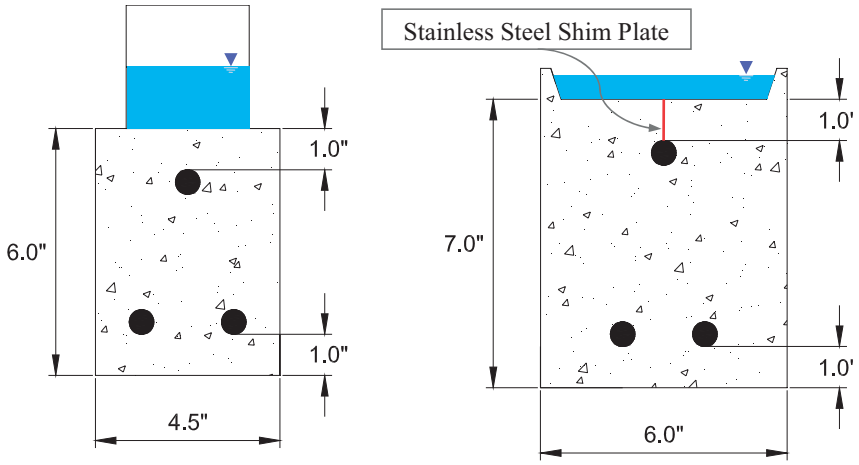

(a) ASTM G109 Macrocell (b) ASTM A955 Macrocell

Figure F.1 Macrocells from standard specifications.

concrete (Equation (F.2)) forming calcium carbonate ($CaCO_3$). In this chemical process, the pH of the pore water in concrete severely drops from 12–13 to 8–9. Due to the drop in pH of the pore water, the protective passivation layer on the steel is removed which enables oxygen and water to reach the base steel causing corrosion of reinforcement.

$$CO_2 + H_2O \rightarrow H_2CO_3 \quad \text{(F.1)}$$

$$H_2CO_3 + Ca(OH)_2 \rightarrow CaCO_3 + 2H_2O \quad \text{(F.2)}$$

Concrete with a low water/cement ratio, good compaction and quality curing can reduce the rate of carbonation, and increase the time for carbonation to reach the level of the reinforcing steel (Mindess, Young, & Darwin, 2002).

F.1.1.2 Chloride attack. Chloride ions concentrated on the surface of the steel may act as catalysts to corrosion by breaking down the passive film on the reinforcing steel. Chloride ions can penetrate through the passive layer of steel without causing an overall drop in pH (as occurs by carbonation) and open a path for oxygen and water to reach the steel. The chloride ions activate a local area of steel forming an anode where the remaining steel (with a passive layer) becomes a cathode. Once an anode is formed on the reinforcing bar, the electrochemical process of electron transfer occurs internally through the steel, which is called microcell corrosion as shown in Figure F.2. The problem with microcell corrosion is that the chloride ions are not consumed because HCl in Equation (F.4) breaks into H^+ and Cl^- ions again. This causes the process of so-called autocatalytic corrosion that continuously breaks down the passive film of reinforcing steel without the need for the addition of more chloride ions.

$$Fe^{2+} + 2Cl^- \rightarrow FeCl_2 \quad \text{(F.3)}$$

$$FeCl_2 + 2H_2O \rightarrow Fe(OH)_2 + 2HCl \quad \text{(F.4)}$$

As the passive layer of steel is removed by chloride ions, a galvanic cell can also be set-up where the top mat of reinforcement becomes an anode and the bottom mat turns into a cathode in reinforced concrete structures such as bridge decks that include two layers of reinforcing bars which are electrically connected as shown in Figure F.2. In these structures, the top and bottom mat can be connected by stirrups or rebar chair which allow transfer of electrons while the moist concrete acts as a salt bridge permitting anions to move in the reverse direction. This process creates an electrochemical connection as shown in Figure F.2. The following equations (Equation (F.5) and (F.6)) represent the ionic and electron flow of a corrosion cell that is activated in macrocell corrosion

$$\text{Anodic Reaction : (Oxidation)} Fe \rightarrow Fe^{2+} + 2e^- \quad \text{(F.5)}$$

$$\text{Cathodic Reaction : (Oxygen reduction)} 4e^- + 2H_2O + O_2 \rightarrow 4OH^- \quad \text{(F.6)}$$

In summary, if a cracked concrete structure is exposed to excessive chlorides from de-icing salts or from a marine environment and is supplied with water and oxygen, microcell and/or macrocell corrosion will take place and corrode the reinforcing bars as shown in Figure F.2.

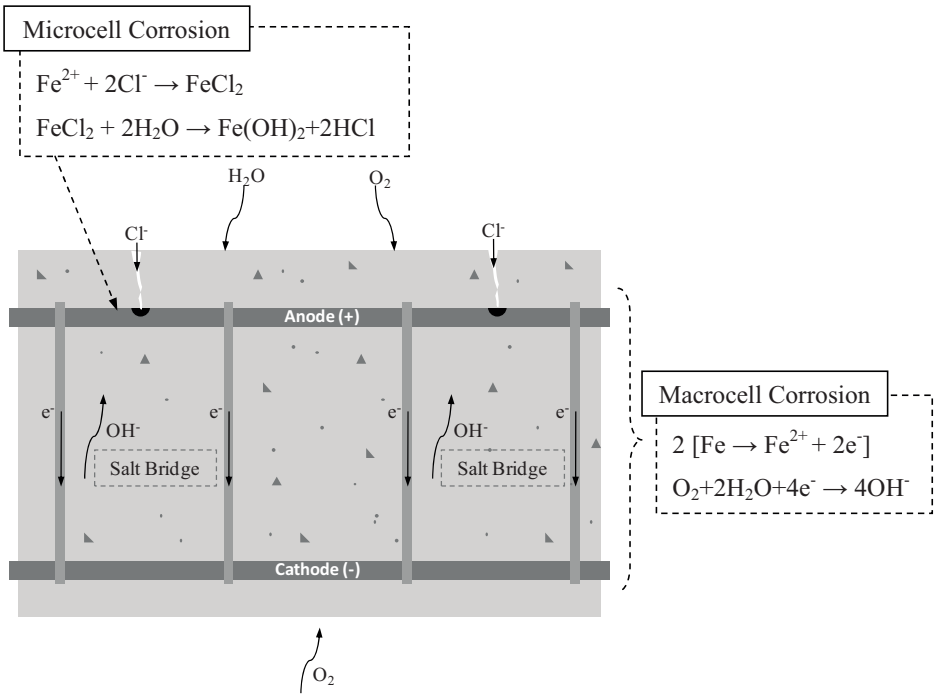

Figure F.2 Chloride attack and macrocell corrosion of reinforcing steel.

F.1.2 Types of Corrosion in Bridge Decks

F.1.2.1 Crevice corrosion. Crevice corrosion is basically initiated by the migration of chloride ions into a crevice (Fontana, 1986). Although, there are differences in metal and oxygen concentration between the crevice and its exterior surface, crevice corrosion is not caused solely because of the difference in geometry. The electrochemical process of oxidation and oxygen reduction initially starts inside and outside the crevice uniformly. After a certain period, the oxygen within the crevice is depleted and oxygen reduction ceases in the crevice, in other words, stops corrosion.

However, because the oxygen depletes inside the crevice while metal continues to dissolve, the positive charge (Fe^{2+}) within the crevice is overloaded and necessitated to be balanced with other ions. With the presence of chloride ions, the increased concentration of metal ion can be balanced and form metal chloride. Furthermore, metal chloride within the crevice will hydrolyze in water as follows:

$$FeCl_2 + 2H_2O \rightarrow Fe(OH)_2 + 2HCl \qquad (F.7)$$

In this process, chloride ions are not consumed. They react automatically with the metal ions again and accelerate the dissolution process, which becomes autocatalytic corrosion. Therefore, although the geometry of the crevice decreases the oxygen reduction rate, the geometry itself will not cause corrosion unless there are chlorides at the exterior of the crevice which later initiates and accelerates the autocatalytic corrosion process. Crevice corrosion can take place in bridge decks where transverse bars and longitudinal bars are tied together creating a crevice at the intersection of the bars and chloride ions exist from the use of de-icing salts or salts from a marine environment.

F.1.2.2 Pitting corrosion. Pitting corrosion is a self-initiating form of a localized corrosion that creates pits (holes) on the metal surface. Once a pit is formed and corrosion starts within the hole, more chloride ions react with the metal ions inside the localized pit and create an autocatalytic corrosion process similar to the crevice corrosion mechanism. Although, the mechanism is identical to crevice corrosion where chloride ion concentration accelerates the corrosion process, pitting corrosion does not necessarily require a crevice to initiate. Pitting corrosion will initiate at a local area where the rate of metal dissolution is momentarily higher than other locations. As a result, chloride ions migrate to this point and start the corrosion process. Moreover, once a cavity is formed, the pit develops downwards from the horizontal surfaces because they generally became stable when growing in the direction of gravity. Pitting corrosion is likely to be present in bridge decks where the chloride ions can be carried locally to the reinforcing steel through transverse cracks formed on the top surface. At this stage, pitting corrosion can formulate at any location where chloride ions are locally concentrated.

F.1.2.3 Galvanic or two-metal corrosion. When two dissimilar metals are exposed to a corrosive environment and one material is more likely to be corrosion-resistant than the other, electric currents can be driven between the two metals due to the difference in the potential developed (Fontana, 1986). The more noble metal becomes the anode while the less noble metal becomes a cathode. The conductive (moist concrete paste) carries the current between these electrodes like a dry-cell battery. This type of electrochemical process is defined as galvanic or two-metal corrosion. Bridge decks with two mats of reinforcement (top and bottom) are likely to develop galvanic corrosion problems. Differences in potential can be developed during de-passivation of the reinforcement in one layer and not the other. In addition, dissimilar material used in the different layers can lead to this type of corrosion.

F.2. SPECIMEN DESIGN

F.2.1 Introduction

A first generation of cracked macrocells developed at Purdue (Hoffman, 2008) focused on forming cracks representative of full depth shrinkage cracks by stressing the specimens using a uniform tensile force. For this study, macrocell testing was focused on evaluating different types of corrosion-resistant reinforcing bar for use in bridge decks. Bridge decks normally have both longitudinal and transverse reinforcement tied together in a mat. Unlike conventional macrocell test specimens which only have longitudinal reinforcement, it was desired to include transverse steel tied together to the longitudinal steel similar to a real bridge deck. This creates a unique condition that better represents field conditions: Specifically, 1) shrinkage cracks are likely to crack at locations where transverse steel is located, 2) longitudinal and transverse steel electronically connect the reinforcement, and 3) the intersection of the longitudinal and transverse reinforcement form locations where crevice corrosion is likely.

In this study, 112 macrocell specimens were designed to evaluate corrosion resistance of different reinforcing bars in concrete.

F.2.2 Overall Dimension

The macrocell specimen used in this study (Figure F.3) was modified from several ASTM standard specimens. The specimens simulate restrained shrinkage cracks that form through the full depth of a specimen. The cracks are developed through applying tensile forces to the longitudinal reinforcement which is extended through the specimen. The specimens also include transverse reinforcement tied to the longitudinal reinforcement to represent a typical steel mat used in bridge decks. The transverse reinforcement also assists in the formation of cracks at the location of the transverse steel. As noted previously, the intersection of the longitudinal and transverse reinforcement provides a location where crevice corrosion between the bars can occur.

The dimensions are identical to the first generation macrocell specimens developed at Purdue (Hoffman, 2008). The only difference from the first generation is the inclusion of transverse reinforcement. Details of the specimens

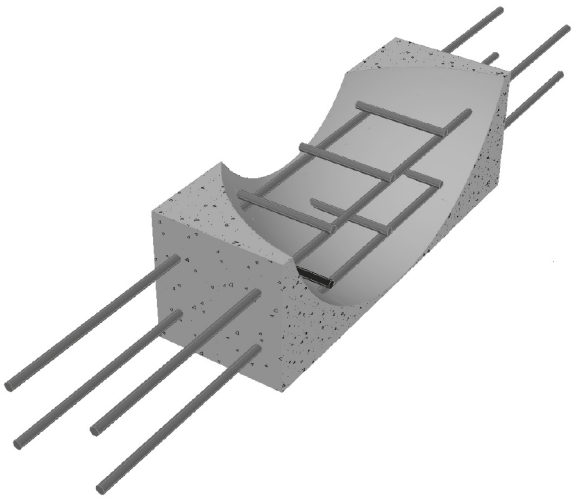

Figure F.3 Concept of modified macrocell corrosion specimen.

are shown in Figure F.4. The specimens were designed to have a depth of 8 in. to simulate the thickness of a typical bridge deck. A length of 24 in. was selected to allow the formation of multiple cracks within the specimen. All bars are #4 which is commonly used in bridge decks especially for the longitudinal reinforcement. The longitudinal bars are spaced at 5 in. while the transverse bars are spaced at 6 in. as shown. Due to the presence of transverse reinforcement, the dimensions of the specimens, and the spacing of the reinforcement, it is expected that three full depth cracks will form.

F.2.3 Cover

Concrete cover to the top reinforcement is an important parameter which contributes to the durability of the deck. According to Russell (2004), up to the 1970s, the recommended minimum cover was 2 in. while most typical bridge decks were reported to only include a 1.5 in. cover.

The current AASHTO LRFD Bridge Design Specifications (2010) follow the previous recommendations from 2002 and require a minimum cover of 2.5 in. for concrete that is exposed to deicing salts. This cover can be decreased to 1.5 in. if epoxy-coated reinforcement is used. Although, a 1 in. cover is used for many of the existing macrocell laboratory testing methods (ASTM G109 or ASTM A955), a 2 in. cover was chosen for this test program that represents the current field practices.

F.2.4 Crack Widths

Cracked specimens were designed to represent field conditions with full depth cracks. The average target crack width was set to 0.020 in. because this is a typical crack width measured in bridge decks from previous studies (Hoffman, 2008).

F.3. SPECIMEN VARIABLES

The variables tested in this experimental program includes the type of reinforcement, crack condition, bar combination, and tie material as provided in Table F.1. All modified macrocell specimens have both longitudinal and transverse steel tied together to create a crevice corrosion condition (Series I through IV). The cracks formed in macrocells will create a pitting corrosion condition for both longitudinal and transverse steel inside the specimens (Series II). Uncracked specimens were cast as a control specimen to this condition (Series I). Series III in test matrix represents the galvanic condition with two different material used. In addition, different tie material were tested in Series IV.

The designation used to identify each specimen consists of three parts which are separated by dashes. If the specimens are cracked, the first part of the notation system is labeled C. This is then followed by the type of reinforcement. Following the material, a label B is used for specimen that include a combination of corrosion-resistant steel in the top mat and conventional black steel in the bottom. In general, specimens are tied with plastic ties to eliminate corrosion from the tie wire. However, as a sub-variable, several macrocells were tied with either conventional black tie wire or stainless tie wire to investigate the influence of tie material. For this case, the third designation is labeled BT(black tie) or ST(stainless tie) corresponding to the tie material used.

The macrocell corrosion specimens in this study allow evaluation of the following test configurations:

- Uncracked (Series I) and Cracked (Series II)
- Identical reinforcement in top and bottom layers (Series II)

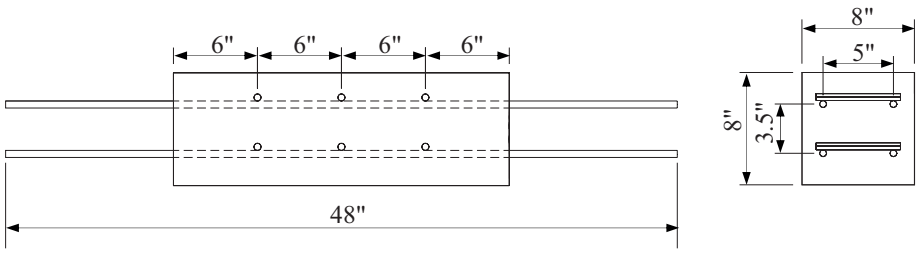

Figure F.4 Cross-section and side-view of specimen.

TABLE F.1
Corrosion Specimen Test Matrix

Series	No.	Designation	Bar Type	Cracked Condition	Bar Combination	Tie
I	1-3	SXM28	XM-28	Uncracked	Top: "test" bar	Plastic
	4-6	S316LN	316LN		Bottom: "test" bar	
	7-9	S2205	Duplex 2205			
	10-12	S2304	Duplex 2304			
	13-15	M	MMFX			
	16-18	Z	ZBar			
	19-21	E	Epoxy			
	22-24	G	Galvanized			
	25-27	ZC1	Zinc-clad 1			
	28-30	ZC2	Zinc-clad 2			
	31-33	B	Black Bar			
II	34-36	C-SXM28	XM-28	Cracked	Top: "test" bar	Plastic
	37-39	C-S316LN	316LN		Bottom: "test" bar	
	40-42	C-S2205	Duplex 2205			
	43-45	C-S2304	Duplex 2304			
	46-48	C-M	MMFX			
	49-51	C-Z	ZBar			
	52-54	C-E	Epoxy			
	55-57	C-G	Galvanized			
	58-60	C-ZC1	Zinc-clad 1			
	61-63	C-ZC2	Zinc-clad 2			
	64-66	C-B	Black Bar			
III	67-69	C-SXM28-B	XM-28	Cracked	Top: "test" bar	Plastic
	70-72	C-S316LN-B	316LN		Bottom: black bar	
	73-75	C-S2205-B	Duplex 2205			
	76-78	C-S2304-B	Duplex 2304			
	79-81	C-M-B	MMFX			
	82-84	C-Z-B	ZBar			
	85-87	C-E-B	Epoxy			
	88-90	C-G-B	Galvanized			
	91-93	C-ZC1-B	Zinc-clad 1			
	94-96	C-ZC2-B	Zinc-clad 2			
IV	97-98	C-SXM28-ST	XM-28	Cracked	Top: "test" bar	Stainless or Black
	99-100	C-SXM28-BT			Bottom: "test" bar	
	101-102	C-S2205-ST	Duplex 2205			
	103-104	C-S2205-BT				
	105-107	C-E-BT	Epoxy			
	108-109	C-B-BT	Black Bar			
	110-112	C-B-ST				

and Corrosion resistant bars on the top and black bars in the bottom (Series III)

- Ordinary black ties (Series IV) and stainless steel ties (Series IV). All other specimens are tied with plastic ties. (Series I through III)

F.4. MATERIALS

F.4.1 Concrete

All macrocells were cast at the same time which had a target strength of 4000 psi. Concrete was provided by a local ready-mix concrete supplier, Irving Materials Inc. (IMI). The selected concrete design was a seven bag mix classified as INDOT (Indiana Department of Transportation) Class C. The concrete mix proportions, batch weights per cubic yard, and the actual slump measurement prior to casting are provided in Table F.2. Five and a half cubic yards of

TABLE F.2
Mix Proportions per Cubic Yard

Material	Cast1
Cement (lbs) (ASTM C-150 Type 1)	658
Coarse Aggregate (lbs) (#8 Stone, Vulcan Materials, Lafayette, IN)	1800
Fine Aggregate (lbs) (#23 Sand, Vulcan Materials, Lafayette, IN)	1200
Water (lbs)	220
Water Reducer (oz) (BASF Glenium 3030 NS)	2
Air Entrainer (oz) (ASTM C-260)	0.6
Water-to-Cement Ratio	0.36
Measured Slump (in.)	6

concrete were delivered and a slump of 6 in. was measured upon arrival at the laboratory.

The compressive strength of the concrete was monitored by testing three standard 6 by 12 in. cylinders at 7, 14, 21, and 28 days after casting. Additional tests were performed on the day the macrocells were initiated for corrosion testing. A 600 kip capacity Forney F-60C-DFM/I compression testing machine was used for these tests. The cylinders were capped with neoprene pads and loaded in compression at a loading rate of 35 psi/sec (approximately 59000 lb/min) in accordance with ASTM C39 (2012). All cylinders were made at the time of casting and cured 7 days covered with wet burlap and plastic sheathing in an identical manner as the macrocell specimens. Cylinder molds were removed when the formwork for the specimens were removed. The compressive strength growth curve is shown in Figure F.5, and a summary of the results are provided in Table F.3.

In addition, the split-tensile strength of concrete cylinders was monitored by testing three standard 6 by 12 in. cylinders at 7, 14, 21, and 28 days after casting and on day that corrosion testing began. Load was applied at a rate of 150 psi/min (approximately 17000 lb/min) in accordance with ASTM C496 (2011). Test results are summarized in Table F.3.

F.4.2 Reinforcing Steel

Eleven types of reinforcement (#4 deformed bars) were used for the macrocell corrosion test. The chemical composition of the uncoated corrosion-resistant reinforcing steel and the mechanical properties measured are provided in Chapter 2 (Table 2.2 and Table 2.3).

F.5. SPECIMEN CONSTRUCTION

F.5.1 Damage on Coated Reinforcement

The amount of damage on coated reinforcing steel applied in this study was based on damage limits for epoxy-coated reinforcing steel.

ASTM A755 (2007), "Standard Specification for Epoxy-Coated Steel Reinforcing Bars," specifies that the damaged coating shall not exceed 1% of the bar surface area in any linear foot length of coated bar. A coated bar with coating damage not exceeding the 1% limit is acceptable on the condition that all of the damaged coating is repaired before shipping while a coated bar with damaged coating that exceeds the 1% limit is unacceptable.

ASTM D3963 (2001), "Standard Specification for Fabrication and Jobsite Handling of Epoxy-Coated Steel Reinforcing Bars," requires that the total damaged area surface area (prior to repair) shall not exceed 2% of the bar surface area in any linear foot of the bar. Coating damage should be repaired if the sum of all damaged areas exceeds the 2% limit.

Samples and Ramirez (1999) reported that damage to the coating during fabrication, transportation, and placement is approximately 1/3 of the total damage that epoxy-coated rebars will experience, while 2/3 of the total damage occurs during casting of concrete. Therefore, damage significantly greater than 2% is likely.

This study selected the damage amount on epoxy-coated rebar prior to casting to be 1% per linear foot. This amount was selected which is consistent with the maximum amount allowed by ASTM A755 with assumptions that additional damage during casting could be developed.

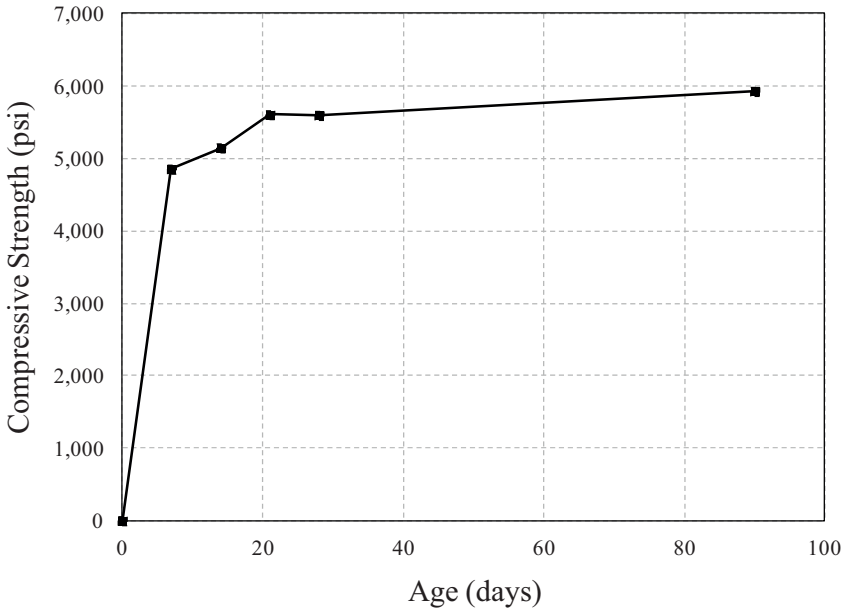

Figure F.5 Concrete strength growth.

TABLE F.3
Concrete Compressive and Split-Tensile Strength Data

Age	Compressive Strength		Split-Tensile Strength	
	Ea.	Avg.	Ea.	Avg.
7	4,920	4,850	540	560
	4,870		570	
	4,770		560	
14	5,180	5,150	640	610
	5,030		560	
	5,230		620	
21	5,670	5,600	600	610
	5,520		610	
	5,630		640	
28	5,730	5,590	520	540
	5,440		590	
	5,620		500	
90	5,990	5,930	530	470
	5,860		440	
	5,940		440	

Unlike other studies where the damage on coated bars is created through drilling holes or cutting out section of the coating, this research focused on controlling the impact force that creates the designed damaged area on an epoxy-coated rebar. In other words, because other coated rebars have different coating thickness and may have higher or lower resistance to coating damage than an epoxy-coated rebar, the impact load causing damage load was controlled instead of the amount (area) of damage. Therefore, different levels of damage occurred where coating with higher resistance to damage would have less damage.

To create 1% damage per linear one foot on an epoxy-coated rebar, a steel channel was dropped from a constant height (4 ft from base) using a load guillotine as shown in Figure F.6(a). The height that developed 1% damage on epoxy-coated rebar was determined and used to create damage on all other coated bars (hot-dip galvanized, unplated zinc-clad, tin-plated zinc-clad, and Zbar).

The steel channel was welded with two C shaped steel sections: C6 × 13 and C5 × 9 as shown in Figure F.6(b).

The size of damage created by dropping the steel section as shown in Figure F.7 from a 4 ft height on epoxy-coated reinforcing bar was 0.125 in. by 0.5 in. The damage was created using the 6 in. channel legs every 6 in. apart on longitudinal reinforcement in which the transverse reinforcement was tied (Figure F.8). On the transverse reinforcement, the welded steel beam was flipped so that the 5 in. channel legs created damage 5 in. apart, located at the damage intersection of the longitudinal reinforcement.

F.5.2 Formwork and Reinforcement

Formwork was constructed to cast 112 specimens at the same time. One set of formwork was designed to cast 14 specimens. A total of 8 sets of forms were constructed. Three sets are shown in Figure F.9. The base form consists of two 4 by 8 ft plywood sheets (3/4 in. thickness). All wall forms were assembled using 3/4 in. plywood and 2 by 4 in. lumber which provides 14 individual boxes as shown in Figure F.9. Holes were drilled in the formwork to allow inserting the reinforcing steel and provide the correct cover dimensions. The bars extended outside the macrocell specimens to allow for cracking of the specimens. A plywood end wall was installed as shown in Figure F.9(a) to provide an end stop when the reinforcing steel was slide through the holes which provided accurate placement of the reinforcement.

For ease of vibrating, screeding, and finishing during construction, an additional platform was installed for a walkway on top of the extended reinforcement located above the base formwork. After the formwork was completed, form oil was sprayed prior to rebar placement.

The longitudinal bars were inserted first, and the transverse bars were then tied to them as shown in Figure F.10. All transverse bars that were cut at the ends were repaired before placement. The cut ends of epoxy-coated and dual-coated (Zbar) bars were re-sealed with the patch kit that the manufacturer provided. The cut ends of hot-dip galvanized and zinc-clads were sealed with high-performance zinc spray (93% zinc in the dry film) which was recommended by the manufacturer and is widely used for re-coating or touching-up the damaged surfaces.

(a) Load Guillotine (b) Welded C Shapes

Figure F.6 Load guillotine and welded C shapes.

Figure F.7 Creating coating damage.

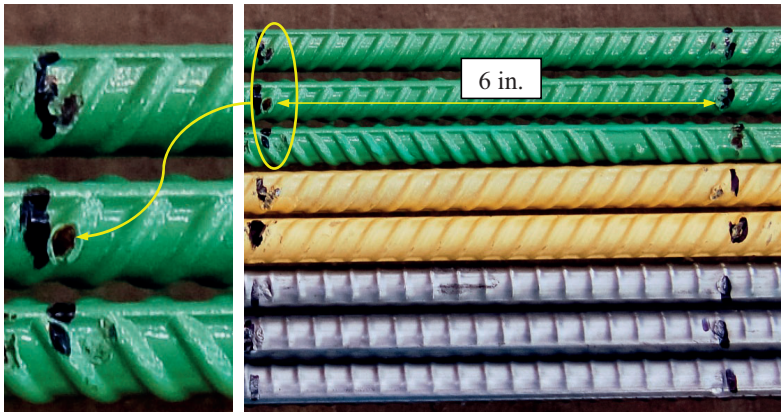

Figure F.8 Damage on coatings.

All specimens except the macrocells which were cast to evaluate the tie material were tied with plastic zip ties. The joints between the forms and gaps between the holes and reinforcement were sealed with silicon caulking and backing rods to prevent leakage during casting.

F.5.3 Casting and Curing

Concrete was placed from the chute of the ready-mix truck into the formwork and consolidated using vibrators. The macrocells were screeded as shown in Figure F.11 and finished using magnesium floats. After initial set, the

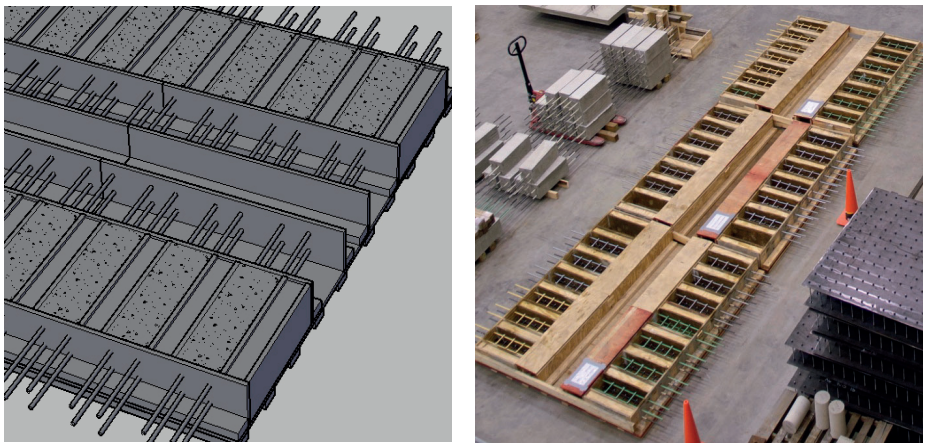

(a) Detailed concept of formwork (b) Formwork and reinforcement

Figure F.9 Formwork preparation.

(a) Stainless Steel Mats

(b) Plastic Ties

Figure F.10 Steel reinforcement.

specimens were covered with wet burlap and plastic sheets were placed on top of the burlap to prevent moisture loss during curing. The specimens were wet cured for 7 days to minimize shrinkage cracking. and the burlap was kept wet during the 7 days of curing period. Immediately following the end of wet curing, the forms were removed. Concrete cylinders were also cast at the same time and placed into the cylinder molds with steel scoups in two lifts. The cylinders were consolidated using an internal vibrator as well. An identical curing procedure was followed for the cylinders, and the molds were removed after 7 days of wet curing. The test specimens and cylinders were stored for 28 days prior to testing.

F.6. SPECIMEN PREPARATION

F.6.1 Cracking

An identical loading system that was used in previous studies (Hoffman, 2008) at Purdue was used to crack the macrocell specimens. The loading system is designed to produce equal tension in each reinforcing bar which is transferred to the concrete specimen and produces a full depth crack through the cross section. An overview of the loading setup is shown in Figure F.12.

The four reinforcing bars were gripped by angled mechanical wedges manufactured from Howlett Machine Works which were designed to fit #4 reinforcing bars. Detailed views of the threaded rod, bearing plate, and transfer steel plates with wedges in the conical holes are shown in Figure F.13. During tensioning, the wedges were held within the steel plates that were machined to have conical holes. These plates were attached to a Dywidag bar on either side of the specimen which were anchored between two steel abutments as shown in Figure F.12. The abutments (steel beams) were tensioned down to the strong floor with Dywidag threaded rods.

Tension was applied using a center-hole hydraulic ram installed between the abutment and anchor plate. Bearing plates and high strength nuts were used on either end of the rods to attach to the abutment and the specimen transfer plate.

(a) Screeding

(b) Floating

Figure F.11 Specimen construction.

Figure F.12 Loading system for macrcocell cracking.

First cracks typically occurred halfway between the macrocell specimen ends when the applied force was between 22 to 29 kips which provides a tensile stress approximately 350 to 460 ksi in the concrete. Shortly afterwards, the next cracks formed halfway between the first crack and the specimen ends. These crack locations match well with theory. However, the macrocells also included transverse reinforcement in the center of specimen

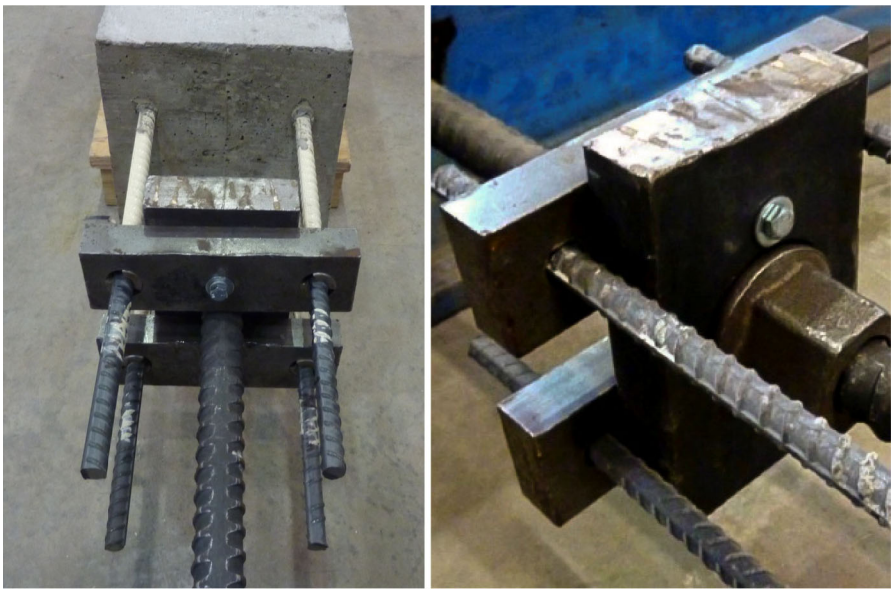

Figure F.13 Details of load transfer.

and halfway between the ends and center (6 in. from the ends and 6 in. from the center) which resulted in a majority of the specimens having a total number of three cracks formed at the location of transverse reinforcement. Specimens that include reinforcement which has less bond strength than black steel such as zinc-clad reinforcing bars developed only one crack in the center of the specimen. To have the cracks remained open to a target width of 0.020 in., specimens were loaded past the yield point of the steel.

For specimens which do not identical reinforcing steel in the top and bottom mats, a special loading set-up was required because of the different mechanical properties of the two layers. Therefore, to stress the rebars beyond yield and let cracks remain open, specimens that had different bars were pulled with two different hydraulic rams as shown in Figure F.14. The two mats were pulled with different forces. For example, where top bars were corrosion-resistant steel that had a higher yield strength than black bars, the two top bars could be pulled with more force after the two bottom bars yielded. The objective of the special loading system was to provide uniform crack widths throughout the full depth.

The specimen was rotated 90 degrees while stressing because the distance between the top and bottom mat was smaller than the distance between the bars in the mat. The alignment provided adequate space for the two rods and bearing plates used for tensioning. A conical hole to hold the wedges was directly machined in the bearing plates for this loading system as shown in Figure F.15.

Figure F.16 shows the histogram of average crack widths produced in the 79 cracked specimens (33 specimens were uncracked). The widths of cracks from all specimens ranged from 0.005 in. to 0.079 in. where 86% of the crack widths fell within the range of 0.015 in. to 0.035 in. The overall average of all cracks were 0.020 in. The final crack widths of each tensile crack formed in the macrocell specimens are tabulated in Appendix D.

F.6.2 Additional Preparation

After the macrocells were cracked, acrylic clear plastic dams (7 in. × 20 in. and 3 in. tall) were attached to the top surface of each specimens with silcone to allow ponding of a salt water. Tensile cracks on the sides and bottom of specimens were

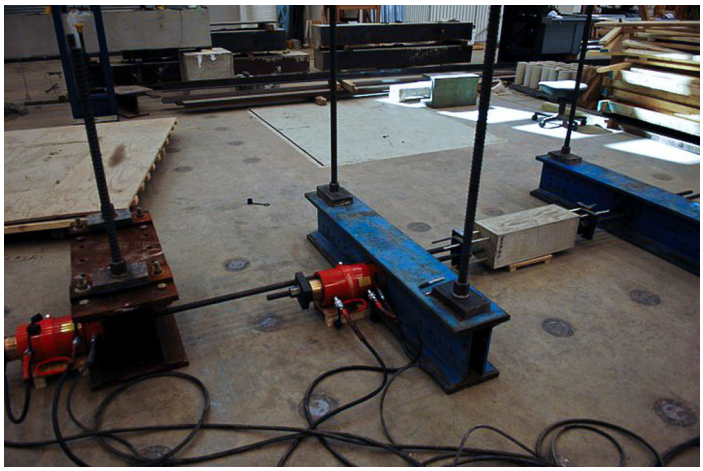

Figure F.14 Loading system for specimens with dissimilar bars.

Figure F.15 Typical cracked specimen with dissimilar bars.

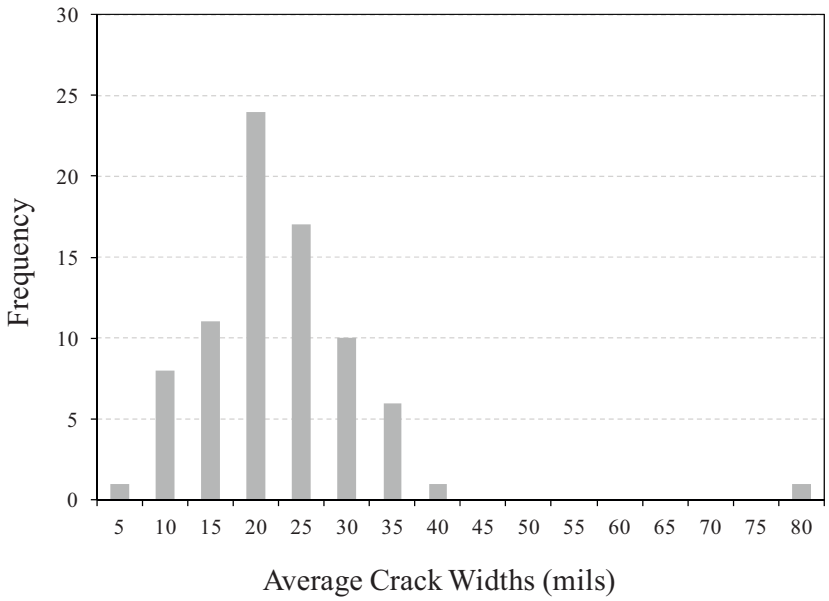

Figure F.16 Average crack widths formed on macrocell specimens.

sealed with silcone to prevent leakage during salt water ponding. After the cracks were sealed, the sides and top surface outside the dam for each specimen were sealed with a waterproofing epoxy (Sikagard 62) in accordance with the ASTM G109 standard. Figure F.17 shows an example of macrocell specimens with the plastic dam attached and all sides sealed with a water proofing epoxy. By sealing all four side surfaces, the macrocell specimens simulate an infinite slab where concrete extends in all directions which allow for only vertical flow of moisture through the specimen.

The protruding steel reinforcing bars which were designed to be 12 in. long for stressing operations were cut to 6 in. length and painted with a rust-resisting paint (Rust-Oleum® Stops Rust®) to prevent corrosion of the reinforcement from the outside. Previous research studies reported that inaccurate macrocell readings were observed due to the corrosion of the exposed reinforcing bars. After the corrosion test was initiated and under a year of testing, the rust-preventing paint on some exposed rebars were peeling from unintended salt water contact or salt water vapor. Therefore, all exposed bars were additionally painted with the identical waterproofing epoxy product which was applied to the sides and top surface outside the dam.

Figure F.17 Macrocells under preparation for corrosion testing.

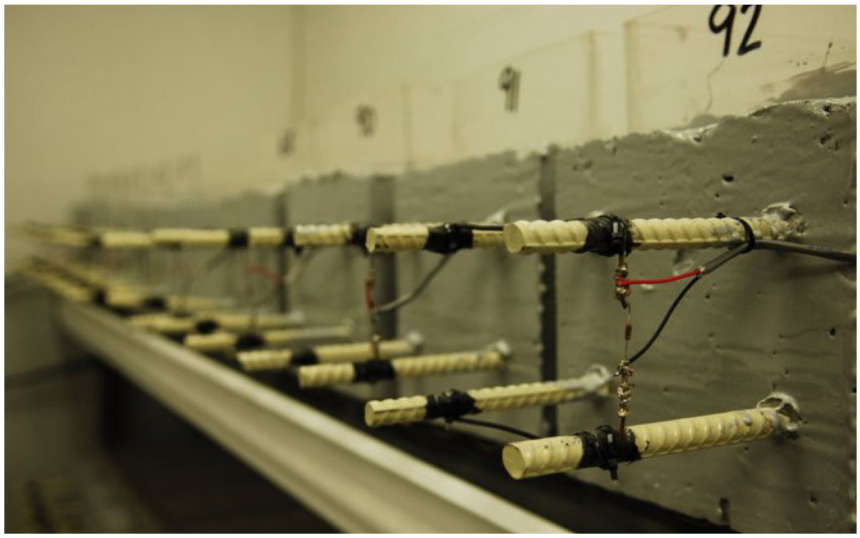

Figure F.18 Electrical connections of macrocell corrosion test.

F.7. TEST SETUP AND PROCEDURE

The top reinforcing bars were electrically connected with a 14 gage copper wire wrapped tightly around the bars. These copper wires were sealed with electrical tape and additionally attached to the rebar with plastic ties. The two bottom reinforcing bars were connected in an identical fashion. The corrosion circuit was completed by connecting a 100-ohm resistor across the two mats. The precision of the resistor used was within 0.1 ohm. The actual resistance for each resistor was measured and recorded prior to the initiation of corrosion testing, and the measured values were used in calculations to obtain current values. The voltage drop across the resistor of each macrocell specimen was collected through an 18 gauge copper wire connected between the specimens and Campbell Scientific AM16/32 Multiplexers. The voltage data of all specimens were recorded every 6 hours automatically by a Campbell Scientific CR10X Datalogger which was connected to the five multiplexers. The electrical connection of a typical specimen is shown in Figure F.18, and the connection to the datalogger is shown in Figure F.19.

The testing procedure is identical to ASTM G109 including the sodium chloride concentration of 3%-by-weight solution and the test regime with a two week wet cycle followed by a two week of dry cycle. The corrosion test was initiated on September 10, 2011. Salt solutions were prepared one day prior to the start day of each wet cycle, and a salometer was used to prepare the 3%-by-weight solution. These salt solutions were maintained in plexiglass dams for two weeks. During the wet cycles, the depth of ponding was monitored and more solution was added when required. After the wet cycle, the salt solution was removed with a vacuum to initiate the two week dry cycle. This four week cycle is maintained throughout the corrosion testing program. Figure F.20 shows the macrocell specimens under a wet cycle.

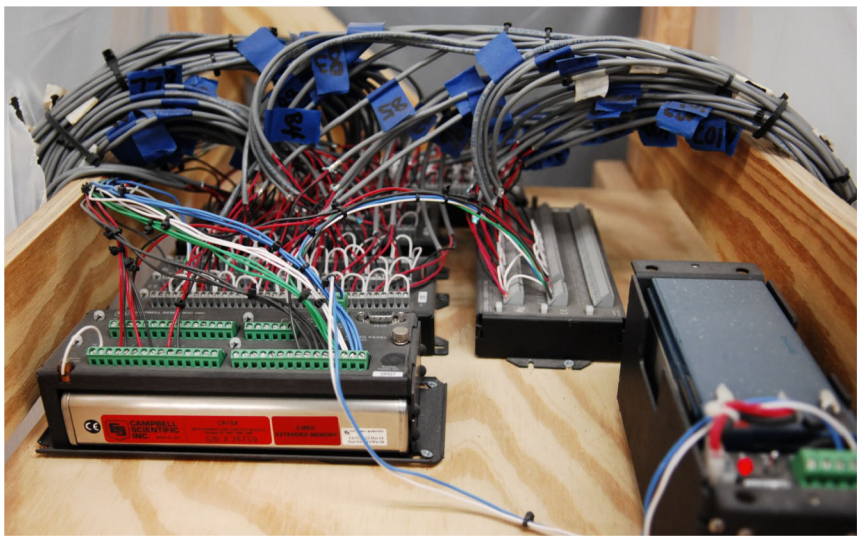

Figure F.19 Datalogger and multiplexers.

Figure F.20 Macrocells under wet cycle.

G.1. INTRODUCTION

The results of 112 macrocell tests are presented to evaluate the corrosion resistance of 11 different reinforcing bars. Results presented include the electrical current measurements, total charge (total corrosion) calculated from the electrical current measurements and autopsy results of the reinforcing bars removed from the concrete after a year of testing.

The test results are presented in the order of the test configurations as follows.

Cracking: Two configurations are considered: (1) Uncracked (Series I) and (2) Cracked (Series II). The uncracked specimens allow evaluating conditions in a bridge deck between cracks (consistent with ASTM G109 specimens). The cracked specimens allow evaluating conditions at and between cracks.

Bottom bars: Two configurations are considered: (1) Identical Mats - Identical reinforcement in top and bottom layers (Series II) and (2) Black Bottom - Corrosion resistant bars on the top and black bars in the bottom (Series III).

Tie material: Two tie material are specifically evaluated: (1) Ordinary black ties (Series IV) and (2) Stainless ties (Series IV). All other specimens are tied with plastic ties (Series I through III).

By using Ohm's law ($V = Ir \cdot R$), macrocell currents can be calculated using the measured voltage drop and known resistance measured from each resistor. The electrical current is the rate of change (slope) in corrosion. Therefore, the total charge (in coulombs) defined by the ASTM G109 can be calculated by integrating the measured electrical current over time as follows:

$$TC_j = TC_{j-1} + \left[(t_j - t_{j-1}) \cdot \left(\frac{i_j + i_{j-1}}{2}\right)\right] \qquad \text{(G.1)}$$

where:

TC = *total charge or total corrosion (coulombs = amps in seconds)*
t_j = *time (seconds) at which measurement of the current is carried out*
i_j = *macrocell current (amps) at time, t_j*

The current and total charge plots shown in the following sections are obtained by averaging the data of 3 identical specimens. The voltage drop of each specimen was recorded every 6 hours and averaged for each day.

G.2. EXPERIMENTAL RESULTS

G.2.1 Currents

The currents of uncracked specimens are shown in Figure G.1(a) and electrical measurements of cracked specimens are shown in Figure G.1(b). As evident, the un-plated zinc-clad, tin-plated zinc-clad, galvanized, and black reinforcing bars in cracked specimens produce currents immediately after the initiation of a wet-cycle. A slight change in currents is observed for the uncracked black control specimen after 200 days of testing, but the electrical current is very small compared to that measured in the cracked specimens.

Figure G.2 plots the electrical currents of the cracked specimens with identical mats and the black bottom mat specimens. It is evident that when two different types of steel are coupled higher currents are measured. This indicates that the macrocells are more likely to corrode when different material is used in the top and bottom mats. As shown in Figure G.2(b), not only are the galvanized and zinc-clad bars actively corroding as expected, the stainless steel reinforcing bars and the MMFX II bar also exhibit corrosion currents. The positive currents of the stainless steel reinforcement and MMFX II bars indicate that the bottom black bars are acting as an anode and corroding preferentially.

Figure G.3 presents the influence of different tie material. When black ties are used instead of plastic ties, more corrosion activity is measured. While essentially no electrical currents are measured when stainless ties are used with stainless steel reinforcing bars (Figure G.3(b)), stainless steel bars with black ties show corrosion activities. Both stainless steel ties and black ties used together with black bars have higher currents than black bars with plastic ties.

G.2.2 Total Charge

G.2.2.1 Cracking. The results of the total charge for coated (non-metallic or metallic) and chromium containing (four stainless steels and MMFX II) corrosion-resistant reinforcing steel are plotted in Figure G.4 and Figure G.5, respectively, focusing on the comparison between the uncracked and cracked specimens. In these figures, the reinforcement in the mats is identical. It is evident that the corrosion is delayed when the specimens are not cracked.

Among coated reinforcing steel, epoxy and dual-coated (Zbar) perform considerably well compared to the control black bar. All metallic coated reinforcing steel (galvanized and two zinc-clads) have higher total charge than black steel. Further investigation is required to determine whether the charge is originating from the sacrificial action of zinc corrosion or steel corrosion. Among the zinc applied reinforcing steel, the total charge is highest in the tin-plated zinc-clad, followed by the galvanized, and then the un-plated zinc-clad.

All four stainless steels also perform significantly better compared to the control black bar. MMFX II microcomposite steel, however, demonstrates more corrosion than the stainless steel reinforcement. This result is expected because the steel includes less chromium. In addition, the MMFX II reinforcement also retains its mill scale. However, for MMFX II, it is evident that the initiation of corrosion is delayed as compared to the black bar.

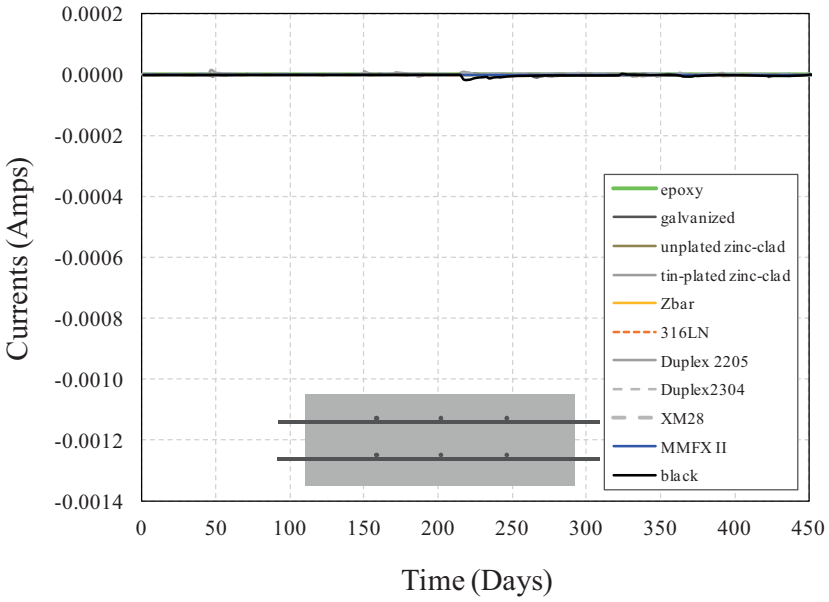

(a) Uncracked

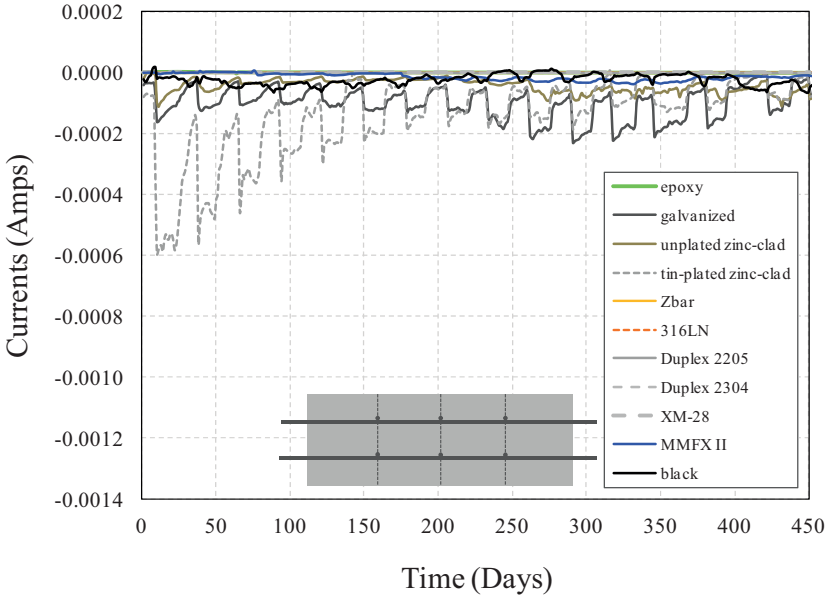

(b) Cracked

Figure G.1 Influence of cracking.

G.2.2.2 Reinforcement material in mats (identical or dissimilar material). The results of the total charge for coated (non-metallic or metallic) and chromium containing (four stainless steels and MMFX II) corrosion-resistant reinforcing steel are plotted in Figure G.6 and Figure G.7. The plots compare the results of specimens where the bars in both mats are identical and where black bars are used in the bottom mat. In these figures, all specimens are cracked. The black control case where both the top and bottom mats are reinforced with black bars are also shown.

When black bars are used as the bottom mat, the total corrosion increases compared relative to when the top and the bottom mats are both reinforced with the same corrosion-resistant bars. Figure G.6(b) clearly demonstrates that the currents of galvanized and zinc-clad specimens increase dramatically when coupled with black bottom bars.

In addition, when both mats are reinforced with stainless steel bars, essentially no corrosion activity is shown and looks good otherwise. MMFX II and black bars on both mats produce a negative charge as shown in Figure G.7(a). However, Figure G.7(b) indicates that all specimens

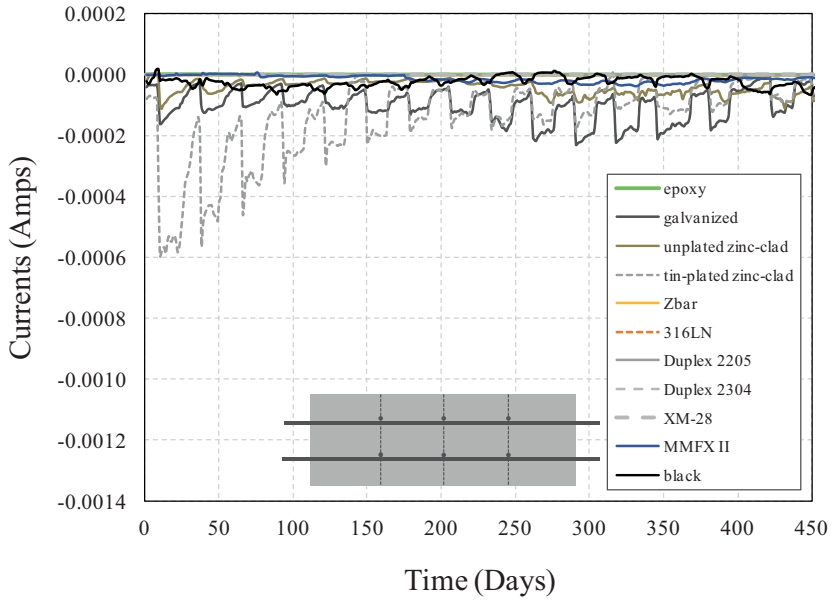

(a) Identical Mats

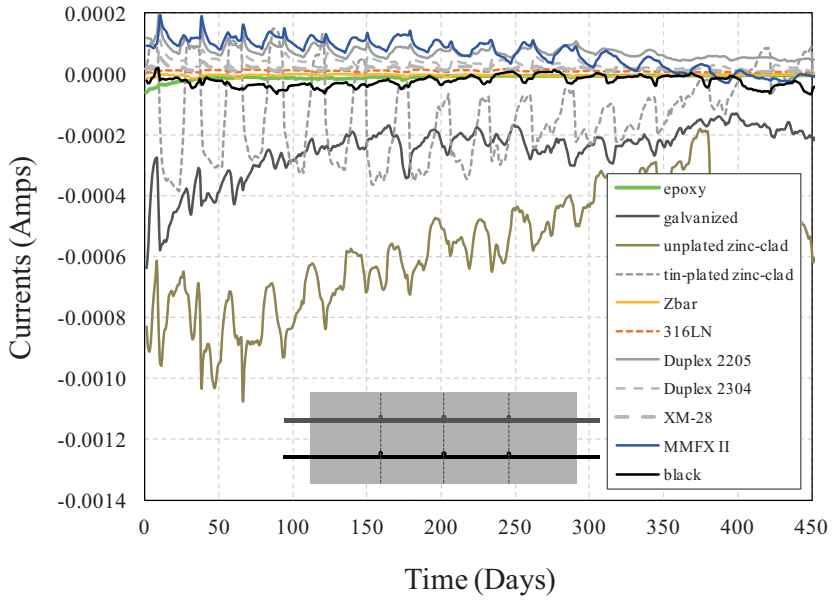

(b) Black Bottom

Figure G.2 Influence of reinforcing material in mats (cracked specimens).

with chromium containing bars (stainless steel and MMFX II) produce a positive charge flow which indicates that the bottom black bars are corroding preferentially.

G.2.2.3 Tie material. All longitudinal and transverse steel used in the specimens were tied with plastic ties except specimens that were designed to evaluate the influence of the tie material. Stainless steel bars tied with both black and stainless ties, epoxy-coated bars tied with black ties, and control black bars tied with black ties and stainless ties were evaluated. The total corrosion of these specimens is shown in Figure G.8. All specimens shown are cracked.

Specimens with stainless steel bars tied with black ties exhibited corrosion while the specimens with stainless ties did not. Although, the total corrosion measured was relatively low, epoxy-coated reinforcing steel with black ties also exhibited corrosion. When stainless steel ties are used instead of black ties, the total charge can be reduced.

The test results demonstrate that the material used for ties can influence corrosion of the reinforcing steel. The results also indicate that corrosion-resistant reinforcing steel should not be tied with conventional black ties. Macrocell corrosion can occur through electrical connectivity. In addition, galvanic coupling of the tie with the base metal of

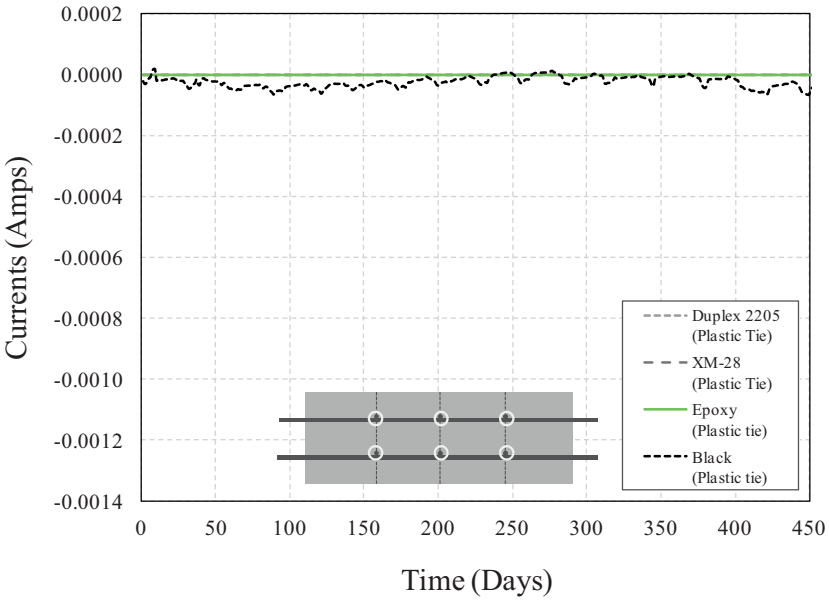

(a) Plastic Ties

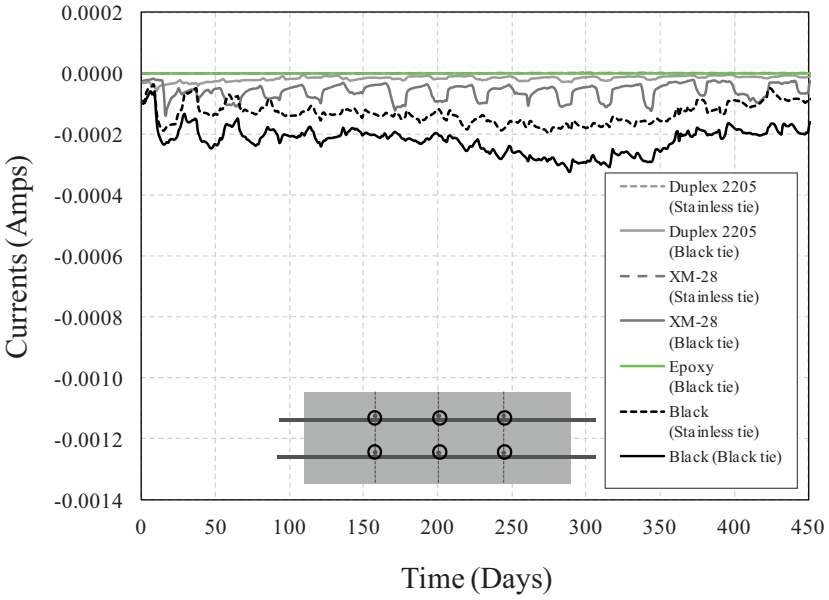

(b) Steel Ties

Figure G.3 Influence of tie material (cracked specimens).

the bar has the potential to cause local corrosion of the base metal.

G.2.3 Autopsy Results

After 503 days of exposure, macrocell specimens selected for autopsy were removed from corrosion testing to examine the rebar for evidence of corrosion. Although corrosion inside the concrete can be evaluated through the electric current measurement, the recorded voltages can be caused by corrosion from the exposed reinforcement which is unintended (the exposed reinforcement was coated with rust resisting paint and later coated with water proof epoxy to minimize this potential). In addition, as previously discussed, some specimens indicated positive currents (bottom bars serving as anode) while other specimens indicated negative currents (bottom bars as cathode). Therefore, visual examination was necessary after corrosion testing to verify the electrical current measurements and evaluate the degree of corrosion exhibited on the bars.

Specimens were cut open from Jan 25, 2013 to Feb 24, 2013. One specimen for each test parameter (three specimens were constructed with identical conditions) was

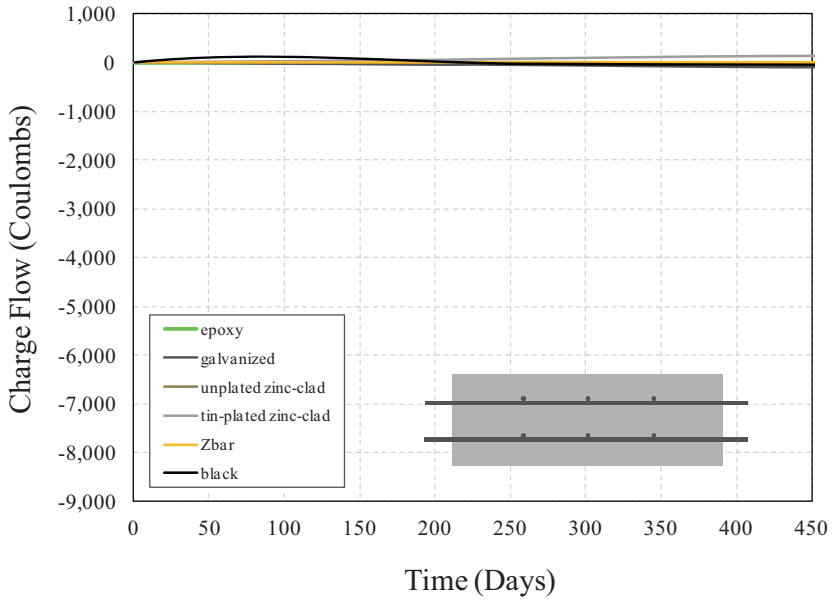

(a) Uncracked

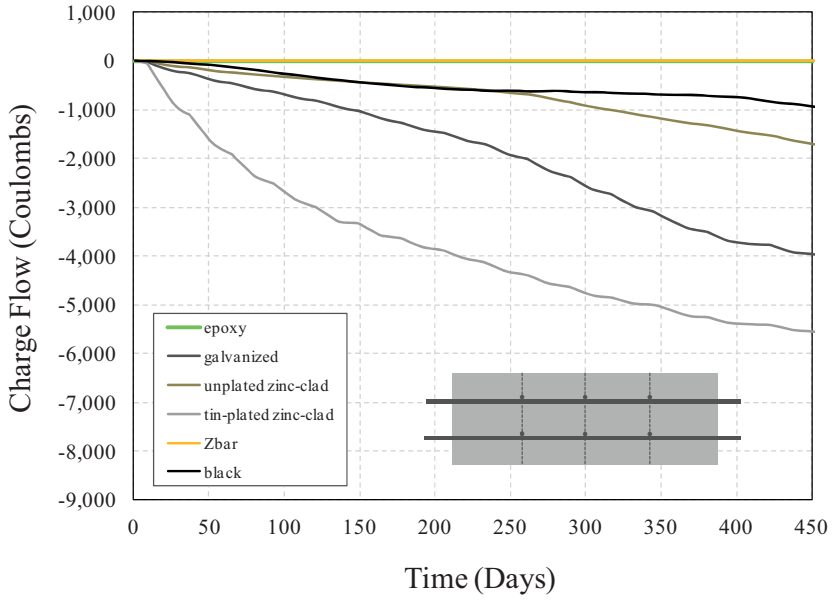

(b) Cracked

Figure G.4 Influence of cracking (coated rebar).

cut open with special care to avoid disturbing the corrosion products that may have formed on the reinforcement. A circular saw was used to make eight cuts to extract the four longitudinal bars from both the top and bottom mats. The saw cuts were made right next to the bars and slightly under the bars, and the concrete was chipped out from the four sides using a pry-bar or a chisel. The bars were easily removed from the concrete by tapping the protruding portion of rebar or by striking the concrete portion with a hammer. In addition, all transverse steel from both the top and bottom mats at the location of cracks were removed after the longitudinal steel was removed. All photos shown in this section will have an overall view of both top and bottom mats. A close-up view will be presented for corrosion spots or locations where further discussions are necessary (specified by circles).

G.2.3.1 Cracking

G.2.3.1.1 Uncracked specimens. Light corrosion was observed on the top longitudinal bars of conventional black bar and MMFX II bar as shown in Figure G.9 and Figure G.10, respectively. On the other hand, all stainless

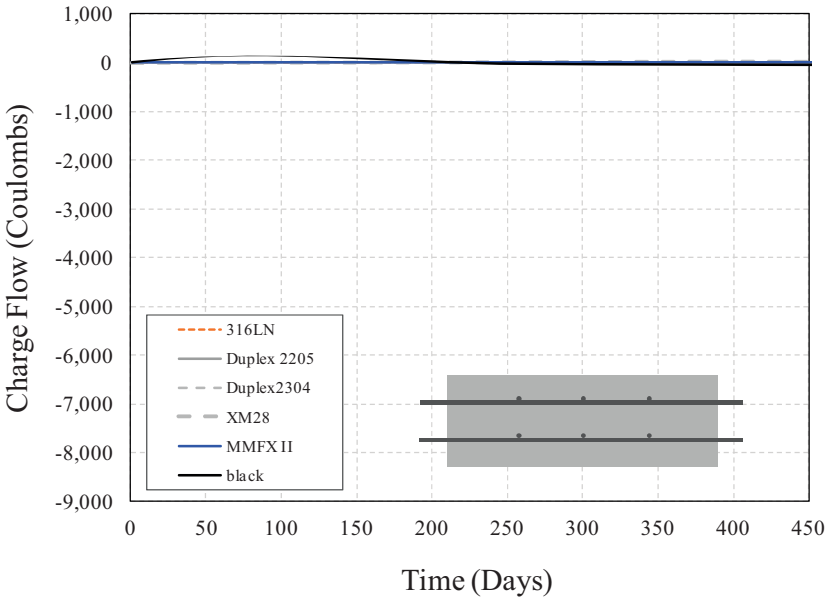

(a) Uncracked

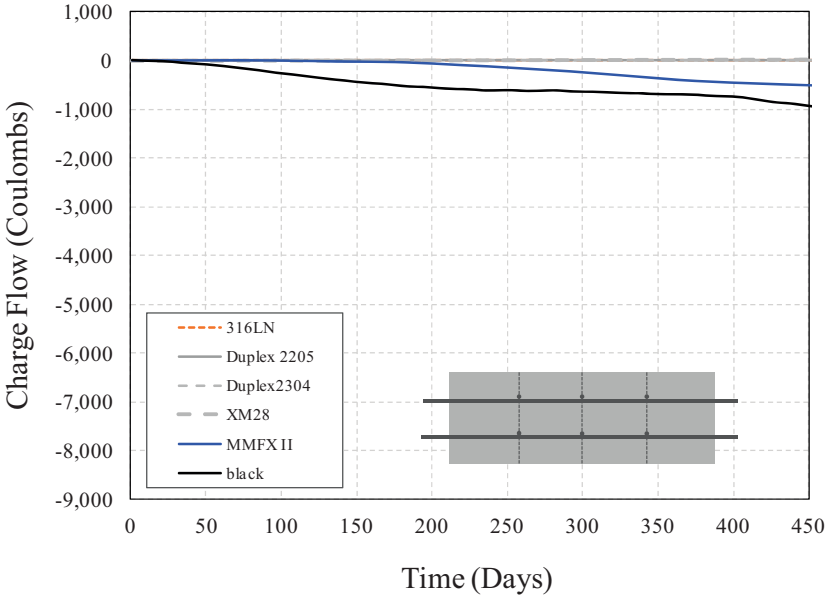

(b) Cracked

Figure G.5 Influence of cracking (rebar with chromium).

steel reinforcement showed no visual corrosion (Figure G.11 and Figure G.12). However, discoloration was observed on XM-28 stainless steel as shown in Figure G.11(b). It should be noted that Duplex 2205 stainless steel shown on Figure G.12(a) was originally dark in color and not shiny as other stainless steel bars.

Epoxy-coated reinforcement on Figure G.13 had a small spot showing corrosion rust of base metal. However, it was located where the coating was damaged prior to the testing. Galvanized, un-plated zinc-clad, and tin-plated zinc-clad reinforcing steel did not have an evidence of white corrosion rust (from zinc oxides) or underlying base metal corrosion (from iron oxides) but Figure G.14 to Figure G.16 illustrate that the outer layer of the shiny pure zinc has been consumed. This zinc consumption is assumed to be mainly from the reaction of the zinc coating with the concrete during hydration rather than entirely from zinc reacting as a sacrificial anode because electrical currents demonstrated less corrosion activities. Zbars showed no visual corrosion (Figure G.17).

As previously discussed, the uncracked specimens indicated only minimal to no corrosion based on the electrical current measurement. These autoposy results confirm those measurements.

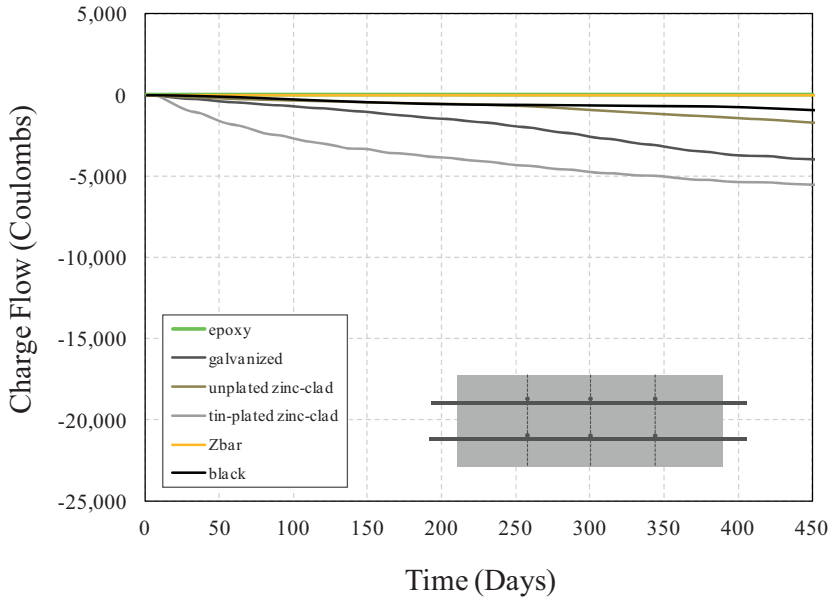

(a) Identical Mats

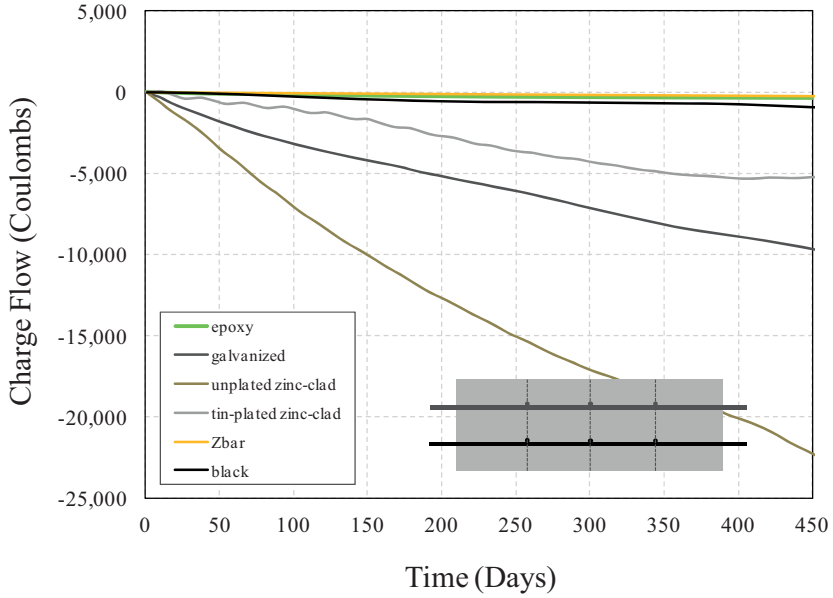

(b) Black Bottom

Figure G.6 Influence of reinforcing material in mats (coated rebar).

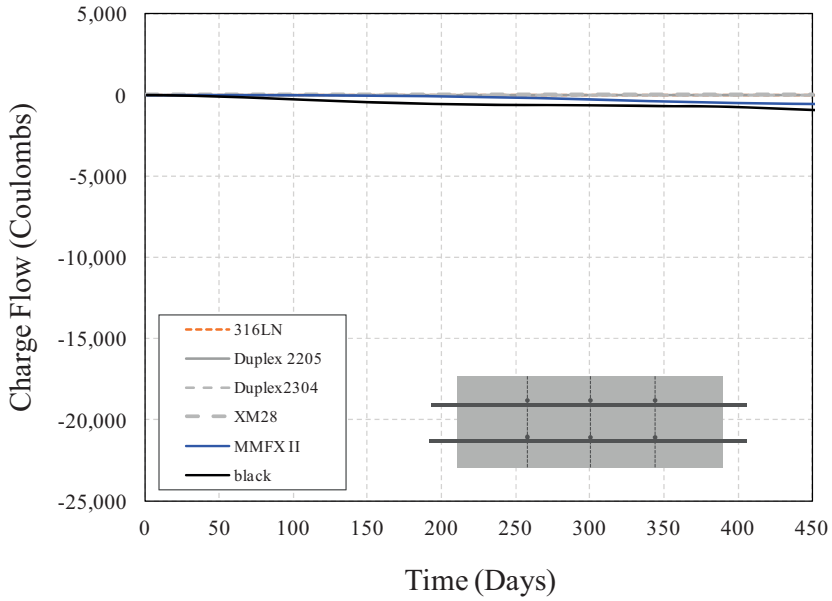

(a) Identical Mats

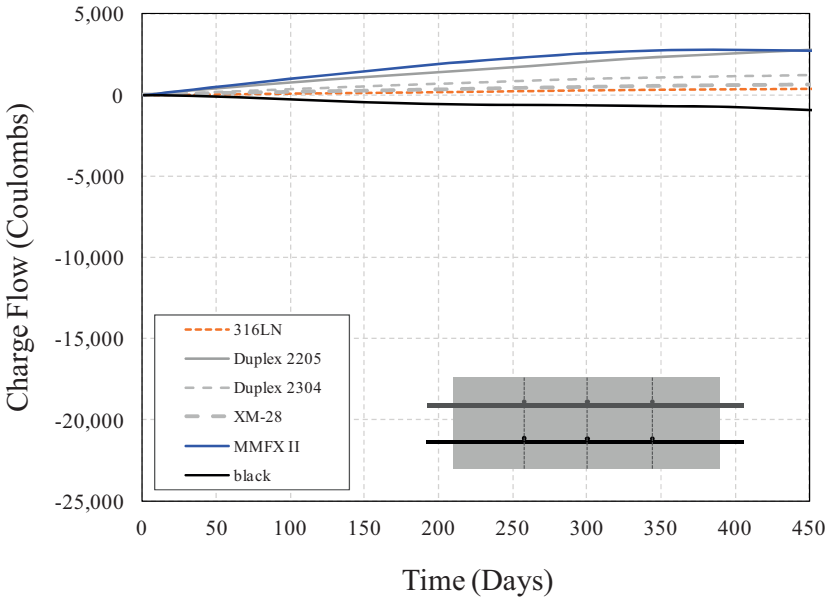

(b) Black Bottom

Figure G.7 Influence of reinforcement layer materials (rebar with chromium).

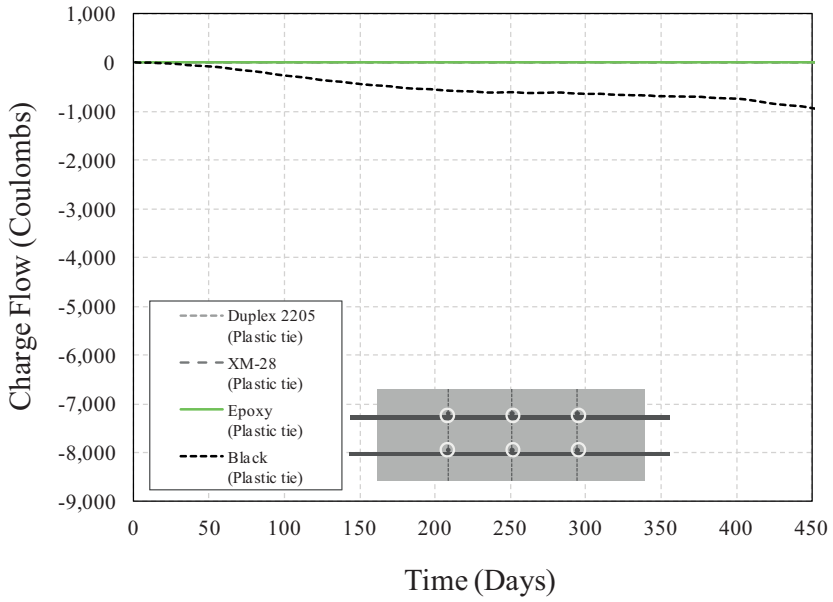

(a) Plastic Ties

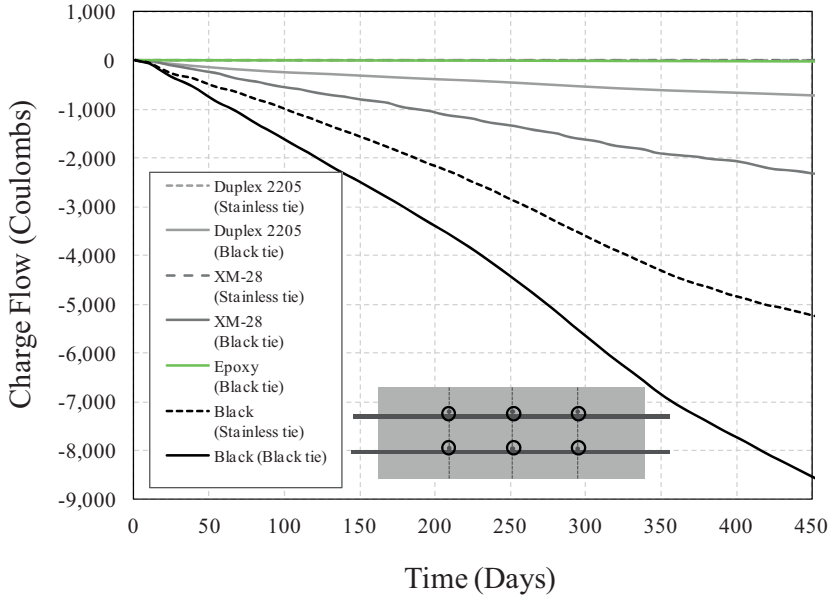

(b) Steel Ties

Figure G.8 Influence of tie material (cracked specimens).

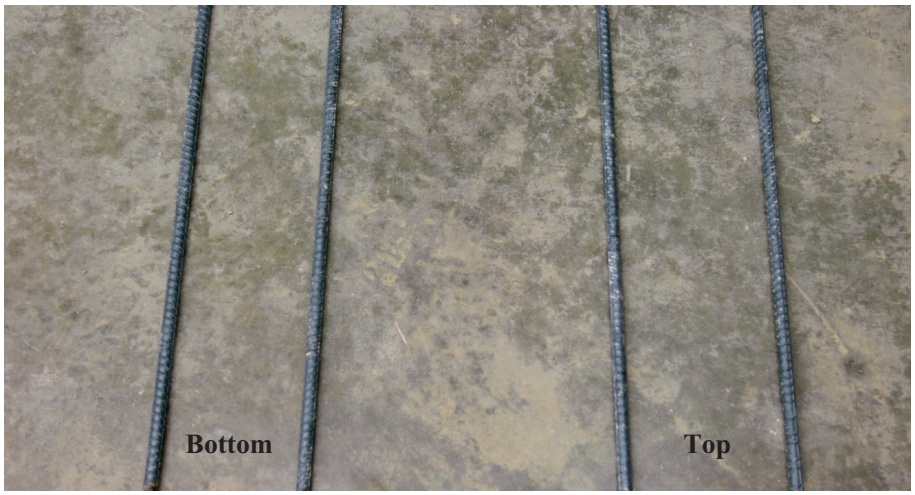

(a) Overall View

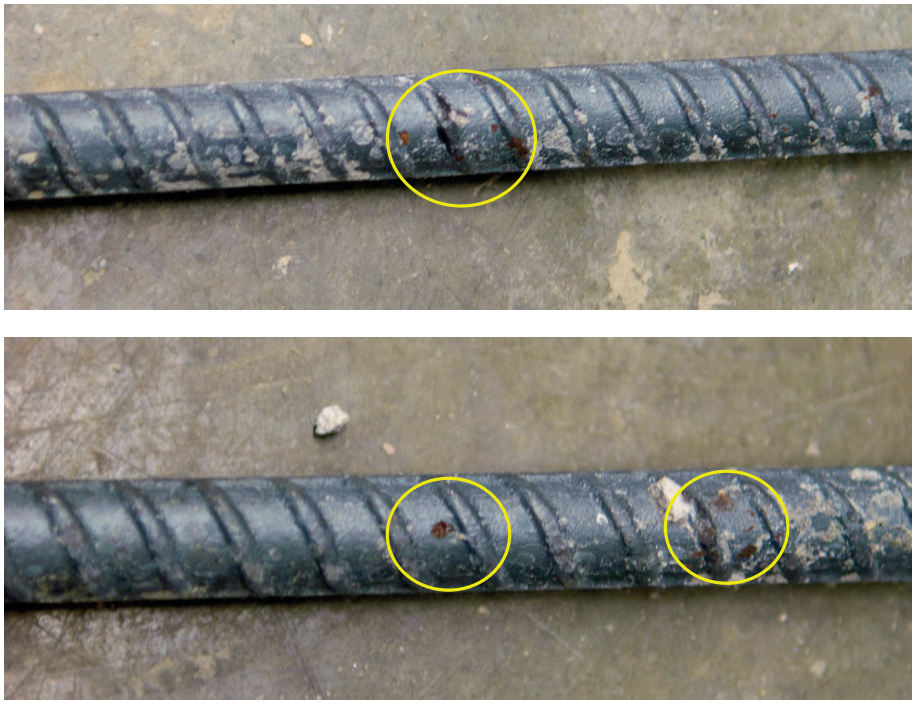

(b) Light Corrosion on Black Bar

Figure G.9 Black bars (uncracked).

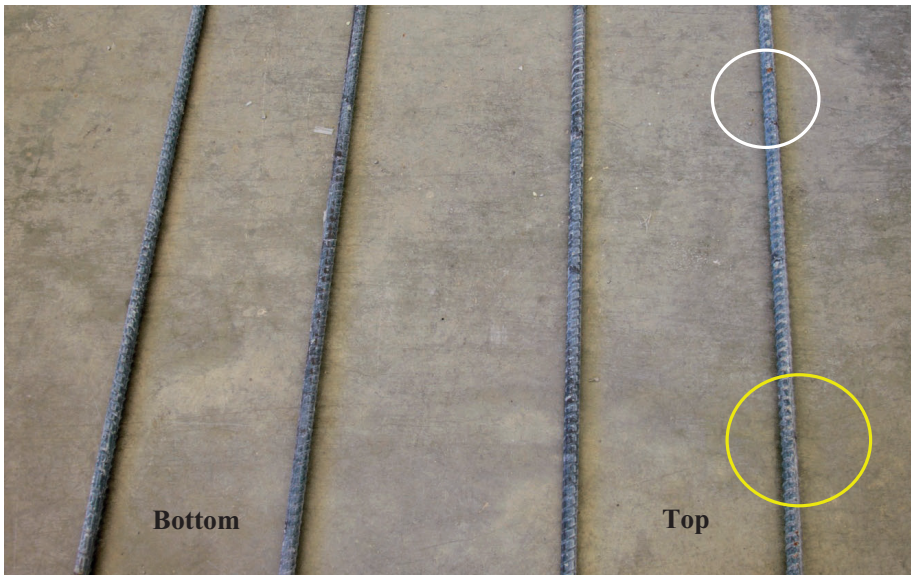

(a) Overall View

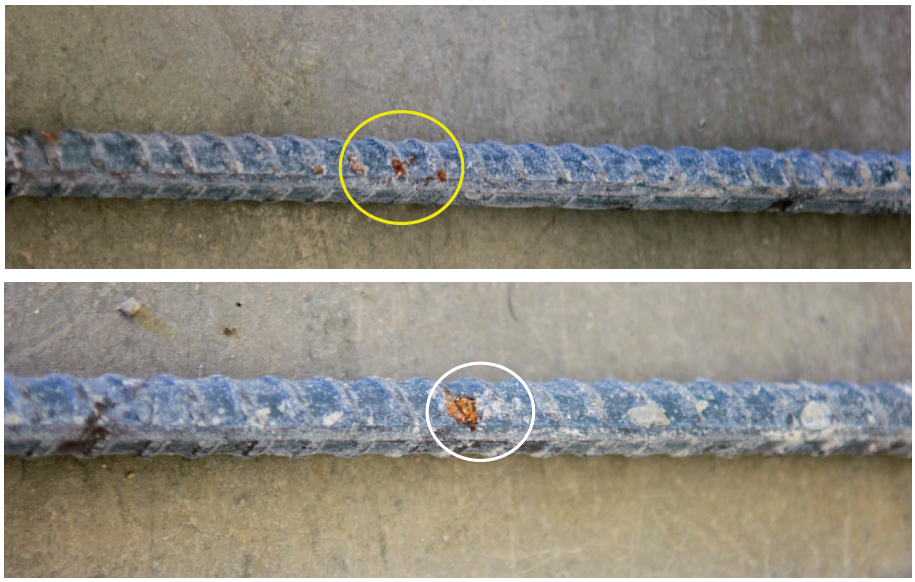

(b) Light Corrosion on Top Longitudinal Bars

Figure G.10 MMFX II bars (uncracked).

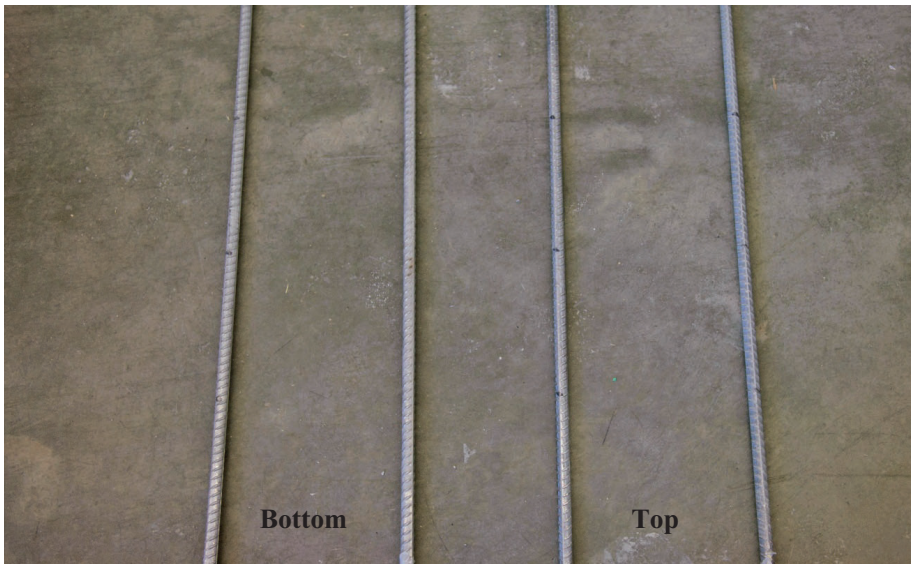

(a) 316LN

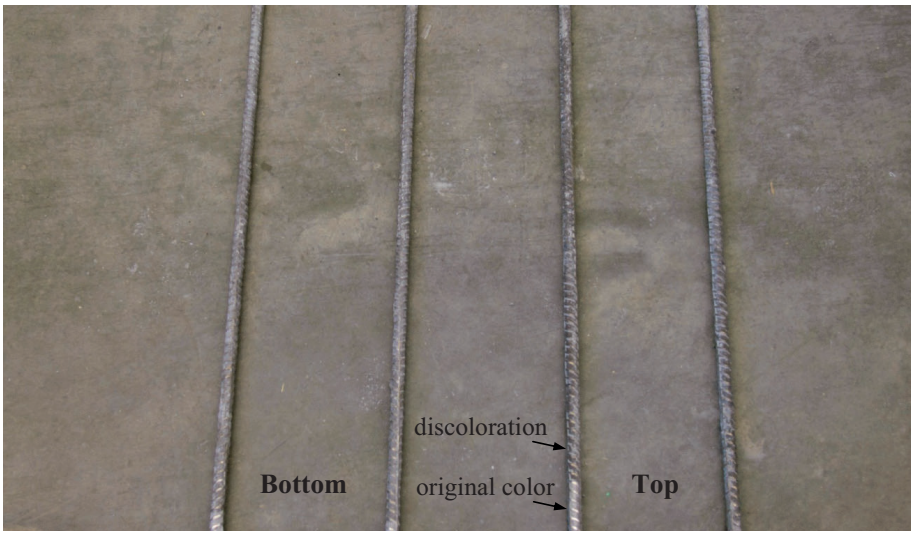

(b) XM-28

Figure G.11 316LN and XM-28 (uncracked).

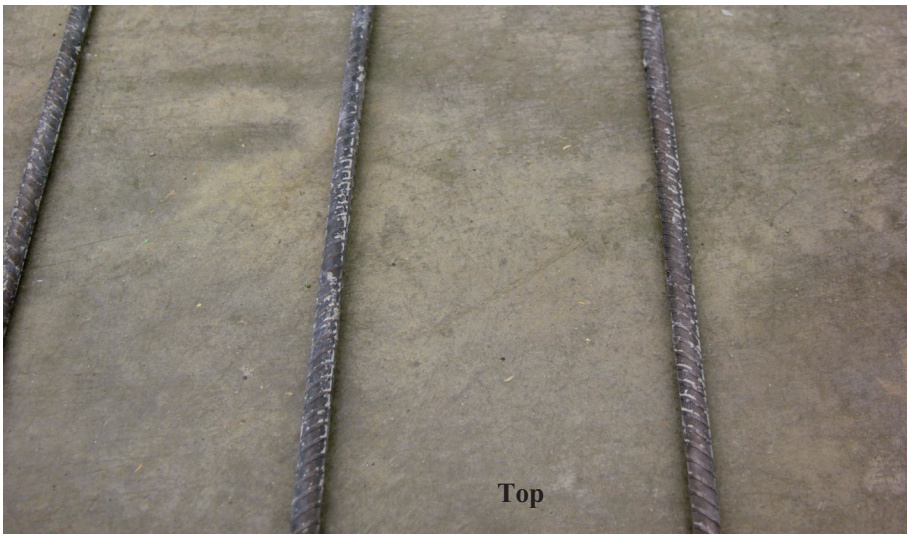

(a) Duplex 2205

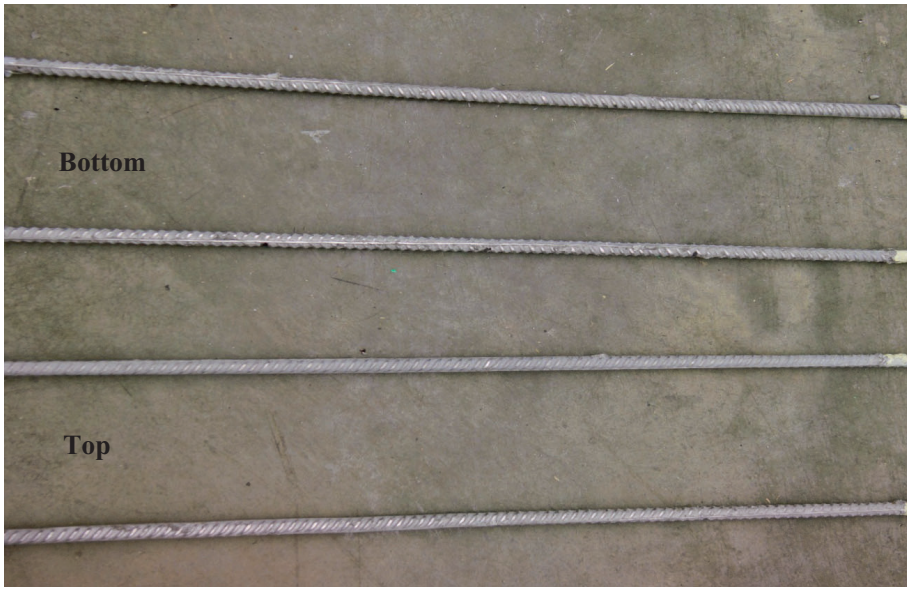

(b) Duplex 2304

Figure G.12 Duplex stainless steel bars (uncracked).

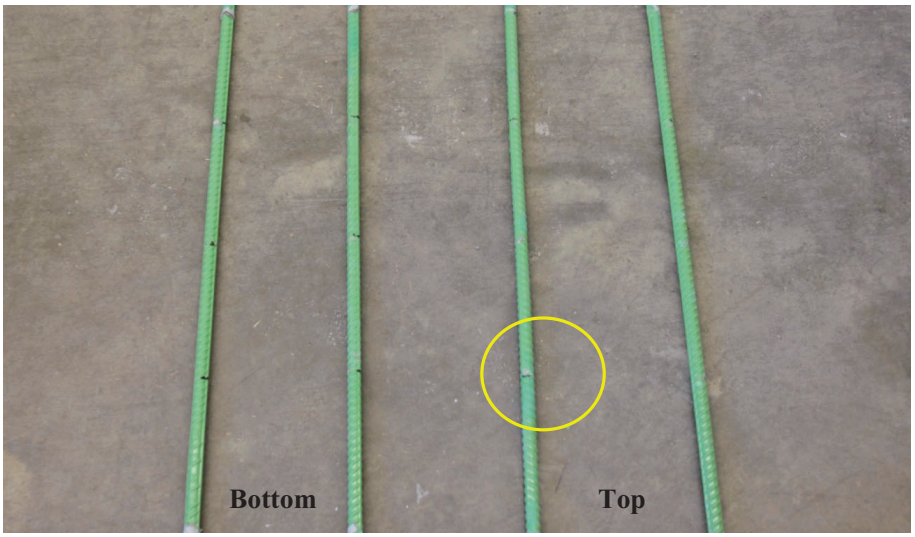

(a) Epoxy-coated

(b) Corrosion on Damaged Epoxy-coated Bar

Figure G.13 Epoxy-coated bars (uncracked).

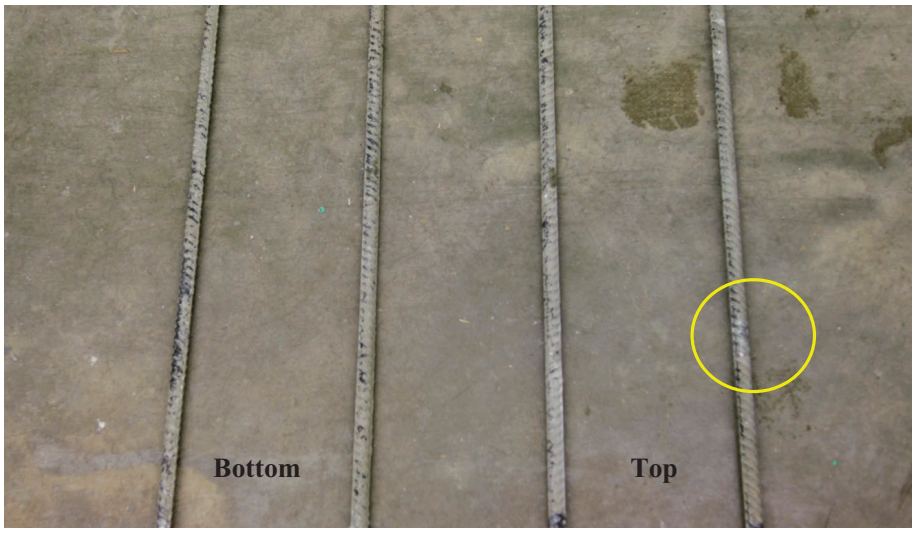

(a) Overall View

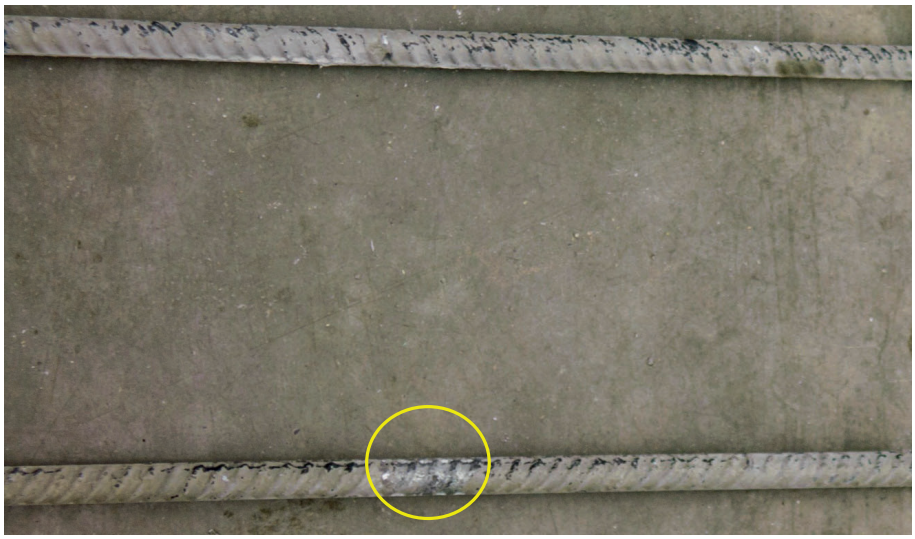

(b) Remaining Pure Zinc Outer Layer

Figure G.14 Galvanized bars (uncracked).

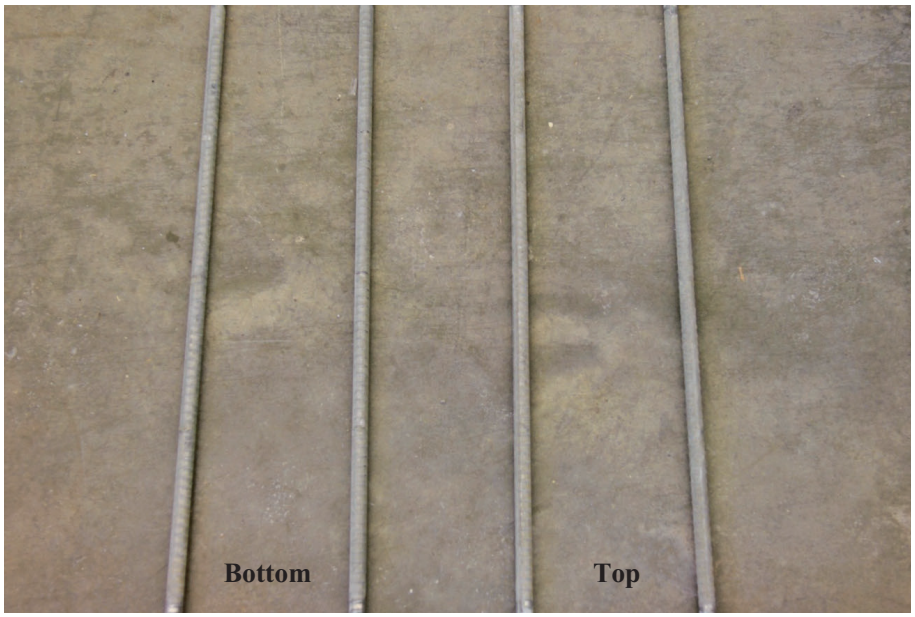

(a) Overall View

(b) Remaining Pure Zinc Outer Layer

Figure G.15 Un-plated zinc-clad bars (uncracked).

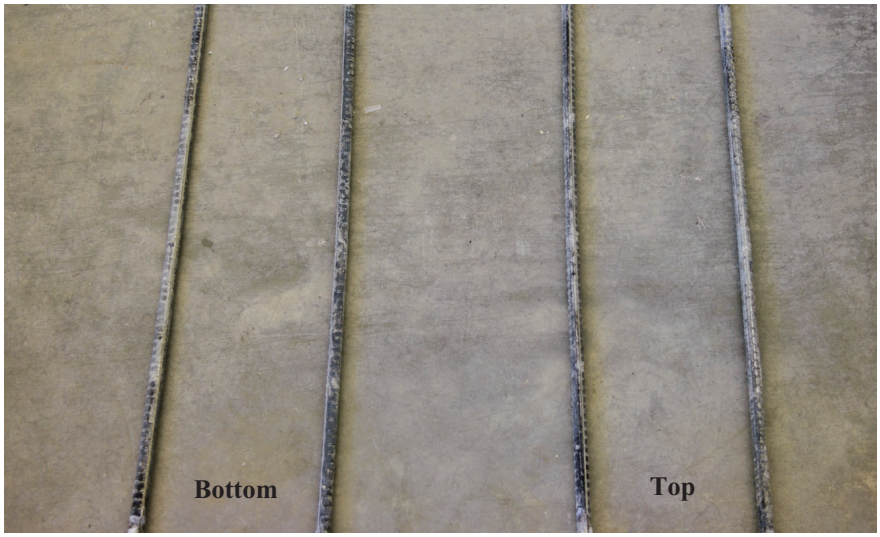

(a) Overall View

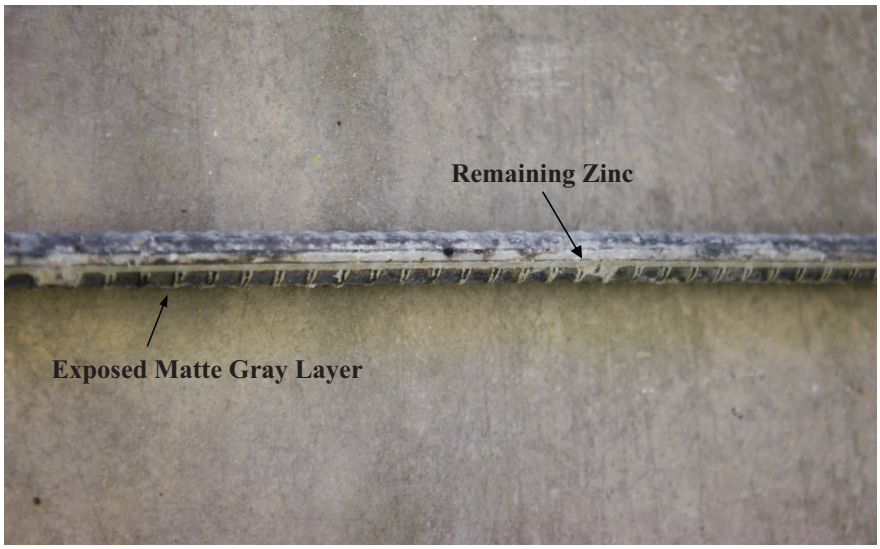

(b) Remaining Pure Zinc Layer and Exposed Matte Gray Intermetallic Layer

Figure G.16 Tin-plated zinc-clad bars (uncracked).

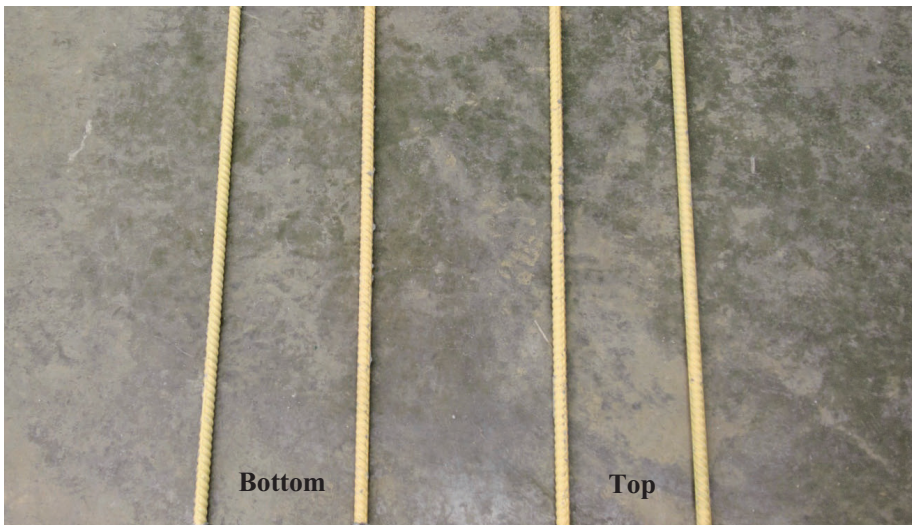

Figure G.17 Dual-coated zbars (uncracked).

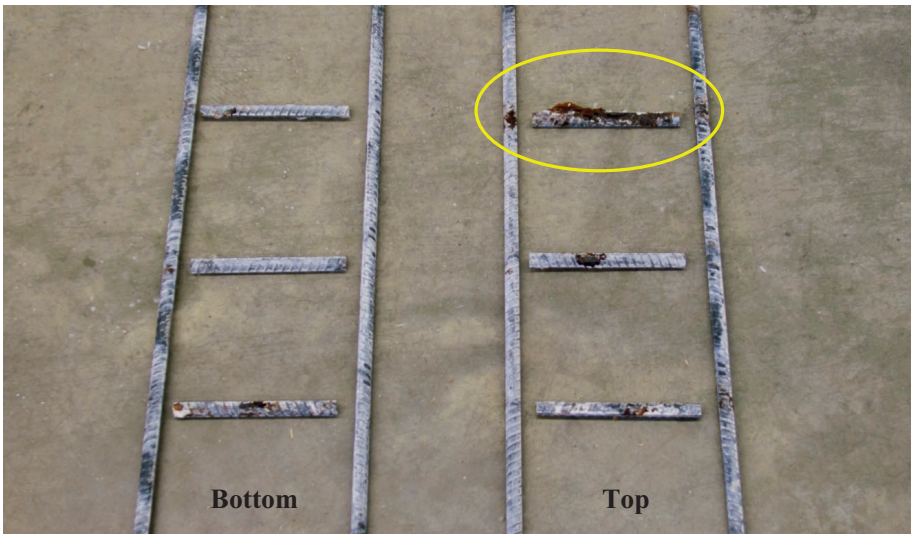

(a) Overall View

(b) Corrosion Shown at Crack Location (Top Transverse Bars)

Figure G.18 Black bars (cracked).

G.2.3.1.2 Cracked specimens. Figure G.18 and Figure G.19 present the autopsy results of the conventional black steel and MMFX II microcomposite steel, respectively. Both black steel and MMFX II had corrosion products in both the top and bottom mats. However, more corrosion products from iron oxides were located on the top mats which is consistent with the electrical measurements that indicated negative currents. In addition, from both figures, it is shown that the top longitudinal bars are corroded at the intersection of bars.

Figure G.20 to Figure G.23 present autopsy results of the stainless steel reinforcement. The 316LN and Duplex 2304 stainless steel did not display any evidence of corrosion. However, the Duplex 2205 stainless steel (Figure G.21) was discolored (it should be noted that Duplex 2205 was originally dark in color and not shiny) from its original color as shown in Figure G.21(b). The XM-28 stainless steel exhibited more discolored locations (Figure G.23), and Figure G.23(b) reveals a spot with a reddish corrosion product on the transverse steel. It should be noted that the XM-28 significantly changed color relative to its original appearance as shown in Figure G.23(c).

Figure G.24 show the corrosion observed on the epoxy-coated bar. Although corrosion was limited to a local area, corrosion of the underlying base metal was observed at the ends of the transverse steel (all ends were patched and

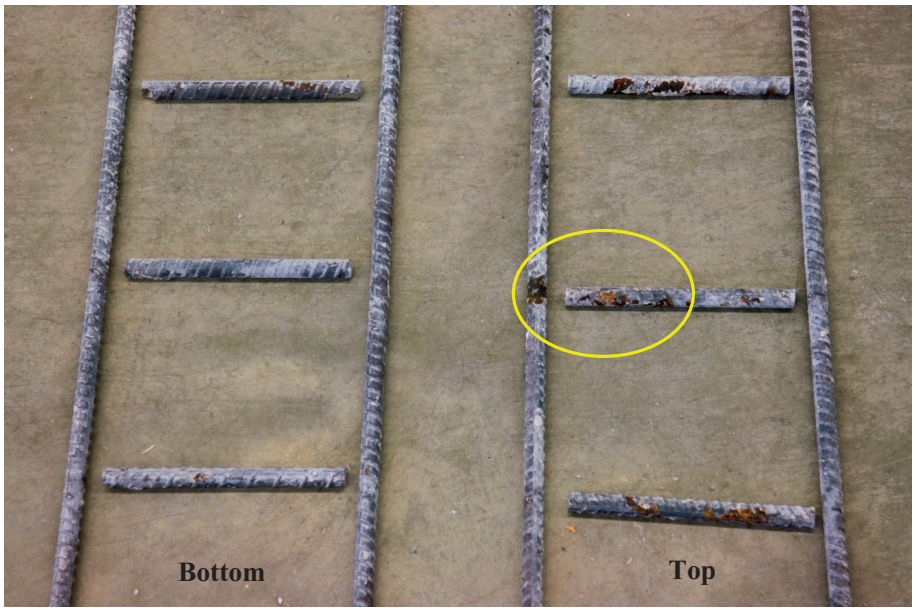

(a) Overall View

(b) Corrosion on MMFX II bars

Figure G.19 MMFX II bars (cracked).

repaired prior to casting) where the coating peeled as shown in Figure G.24(b). In addition, due to corrosion of the base metal underneath the epoxy coating, a spot where the coating was bulging was observed.

Figure G.25 to Figure G.27 shown autopsy results of hot-dip galvanized, un-plated zinc-clad, and tin-plated zinc-clad steel reinforcement. In contrast to the uncracked specimens, white corrosion products from zinc oxide were observed in all three cases. A greater amount of the white product was noted at the location of the cracks and especially on the transverse steel which was located parallel to the cracks. Figure G.25(b) show white corrosion product on the galvanized steel (transverse bar) and a small reddish corrosion spot demonstrating underlying base metal corrosion. Figure G.26(b) clearly demonstrates the top transverse steel under cracks contain more white corrosion products. Figure G.27(b) shows not only the white corrosion product from the zinc oxide but also the zinc-clad cover of the transverse steel which was consumed. In addition, the zinc-cladding peeled off while removing the transverse steel from the macrocell specimen which revealed a light reddish product on the base metal.

Cracked specimens with dual-coated Zbars did not show significant corrosion, but corrosion was observed at the location where damage was introduced prior to testing (Figure G.28(b)). The zinc under the epoxy layer was consumed and red iron oxide products are shown which indicates corrosion of base metal.

(a) Overall View

(b) No Corrosion Observed

Figure G.20 316LN stainless steel bars (cracked).

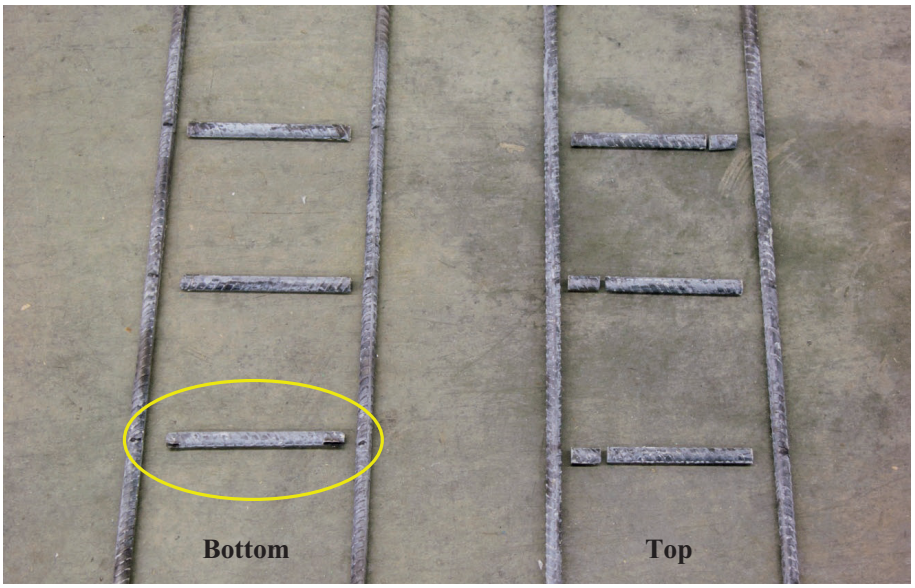

(a) Overall View

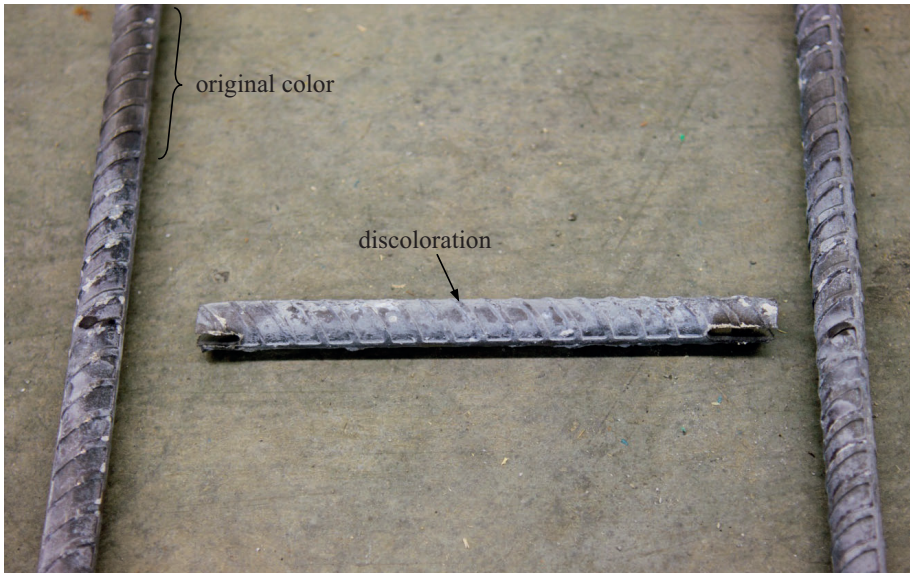

(b) Discoloration of Transverse Bar

Figure G.21 Duplex 2205 stainless steel bars (cracked).

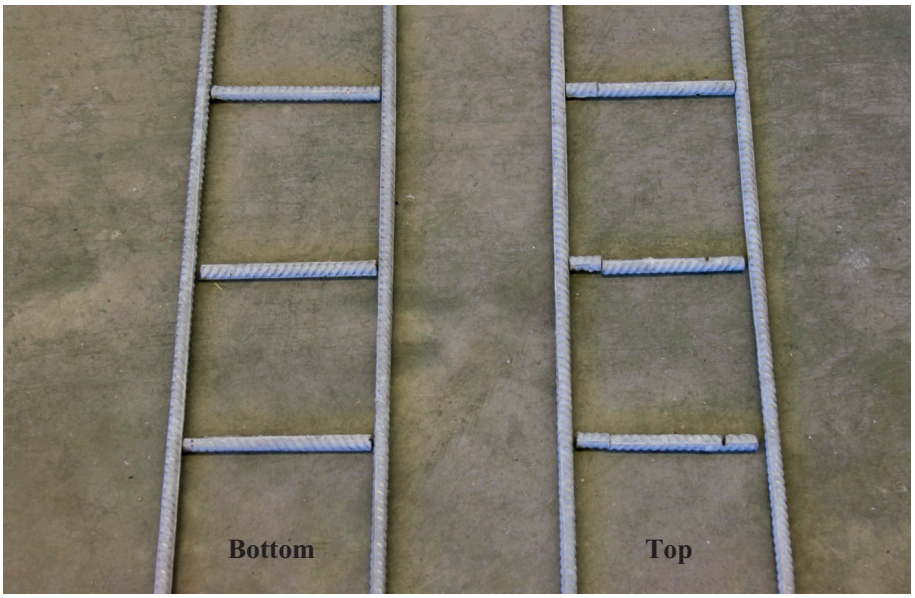

(a) Overall View

(b) No Corrosion Observed

Figure G.22 Duplex 2304 stainless steel bars (cracked).

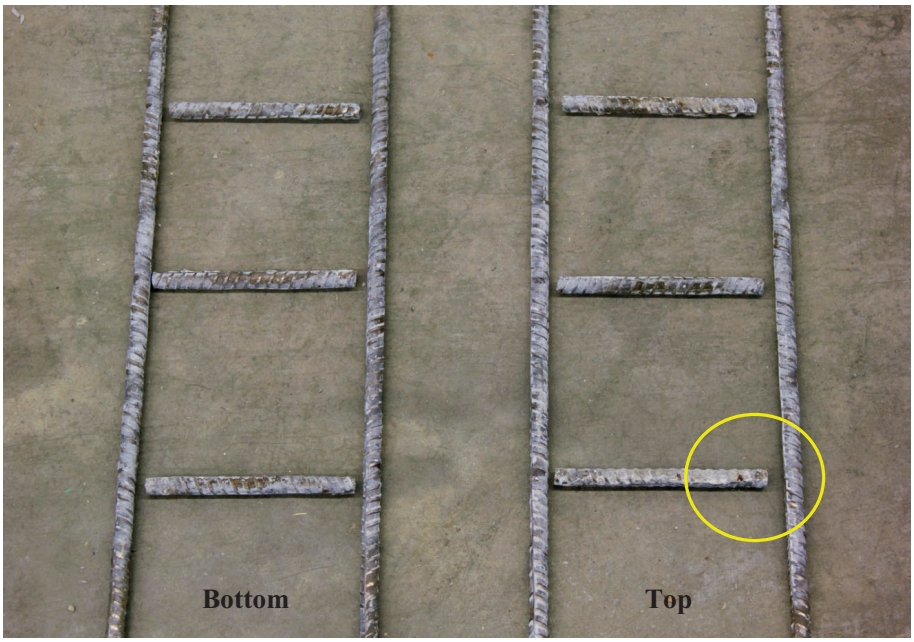

(a) Overall View

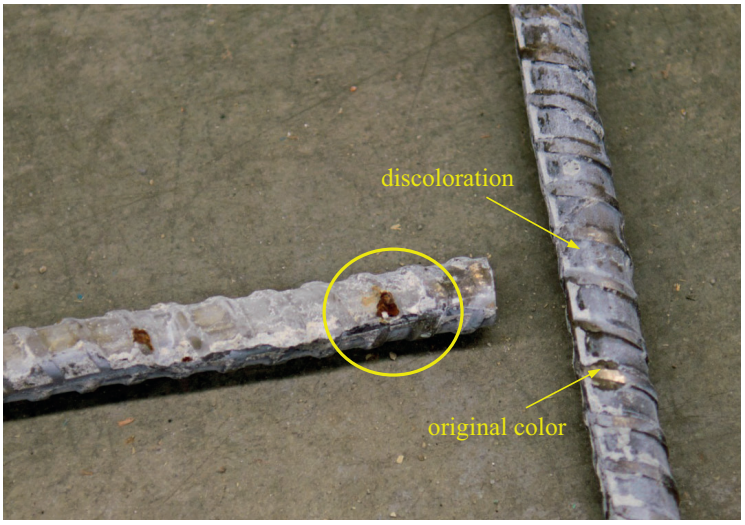

(b) Discoloration and Corrosion Products

(c) Original

Figure G.23 XM-28 stainless steel bars (cracked).

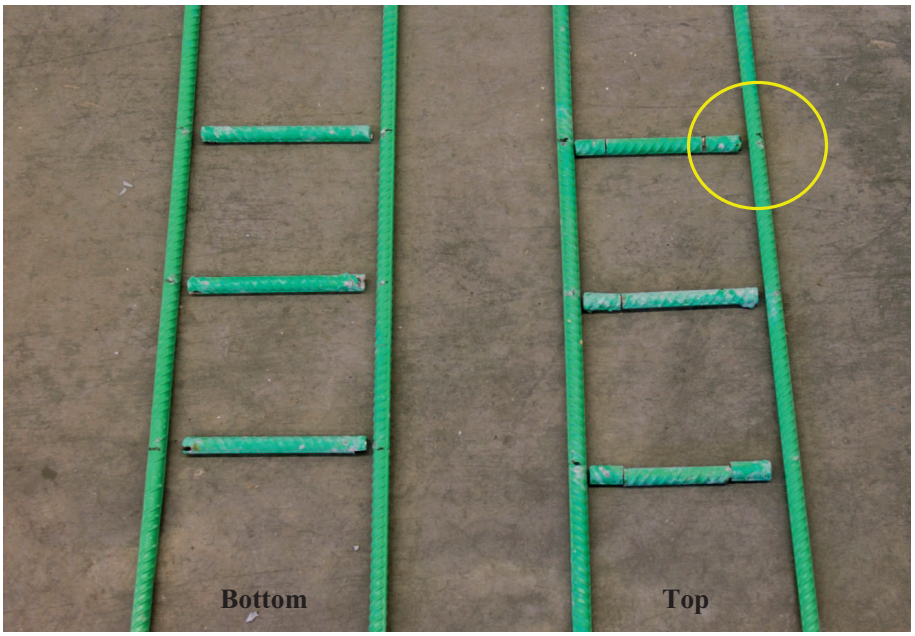

(a) Overall View

(b) Corrosion on Epoxy-coated Bar

Figure G.24 Epoxy-coated bars (cracked).

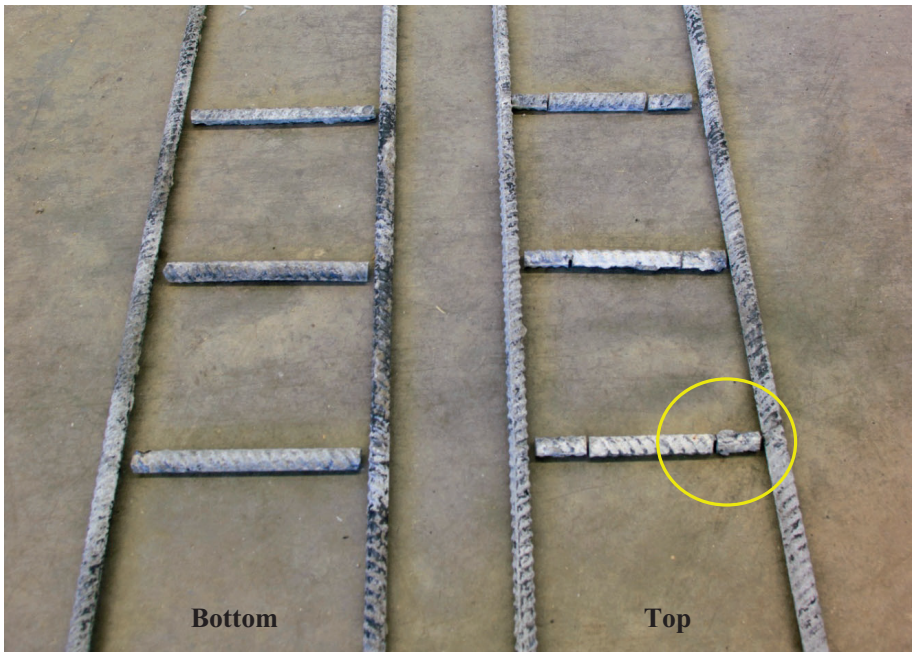

(a) Overall View

(b) White Corrosion products of Zinc and Corrosion spot of Underlying Base Metal

Figure G.25 Galvanized bars (cracked).

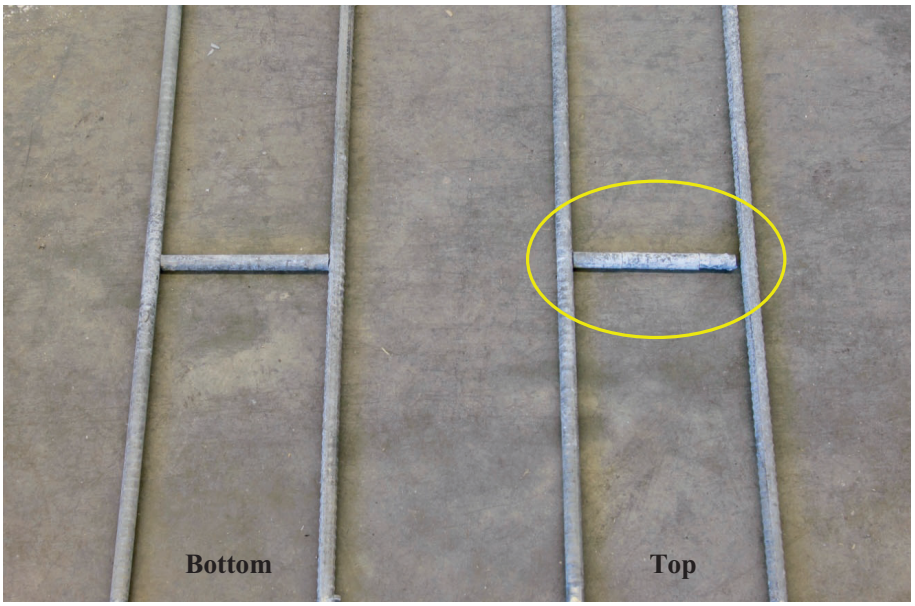

(a) Overall View

(b) White Corrosion Products from Zinc Corrosion

Figure G.26 Un-plated zinc-clad bars (cracked).

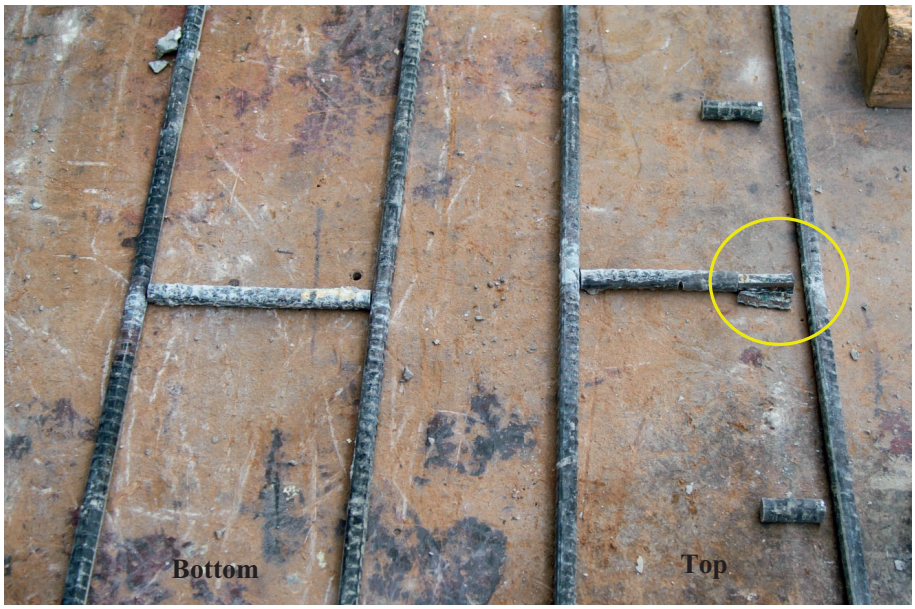

(a) Overall View

(b) White Corrosion of Zinc, Consumed Zinc Cover, and Peeled off Cover

Figure G.27 Tin-plated zinc-clad bars (cracked).

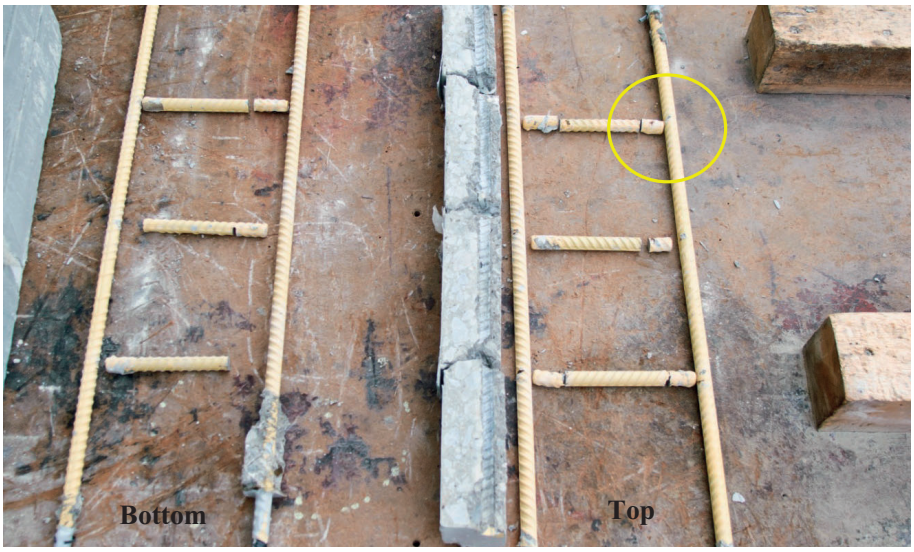

(a) Overall View

(b) Corrosion on damaged area

Figure G.28 Dual-coated zbars (cracked).

G.2.3.1.3 Summary. In summary, cracked specimens demonstrated more corrosion products than uncracked specimens. In most cases, corrosion was observed where cracks were located. Therefore, the corrosion products were typically observed on the transverse steel in a larger area than the longitudinal steel. The longitudinal steel had majority of the corrosion at the intersection of bars at the cracked locations.

Reddish-brown iron oxide corrosion products were observed in both black and MMFX II microcomposite reinforcements in cracked specimens. Stainless steel reinforcement performed well. However, Duplex 2205 and XM-28 in cracked specimens were discolored and evidences of corrosion of the steel was observed in the XM-28. White corrosion products were evident in the cracked specimens with metallic coated reinforcement (galvanized and zinc-clads). Non-metallic coated reinforcement (epoxy and Zbar) in cracked specimens performed relatively well displaying local corrosion spots at the ends of transverse steel and close to damaged areas.

G.2.3.2 Reinforcement material in mats (identical or dissimilar material). The autopsy results of specimens with corrosion-resistant steel used in the top mats while black

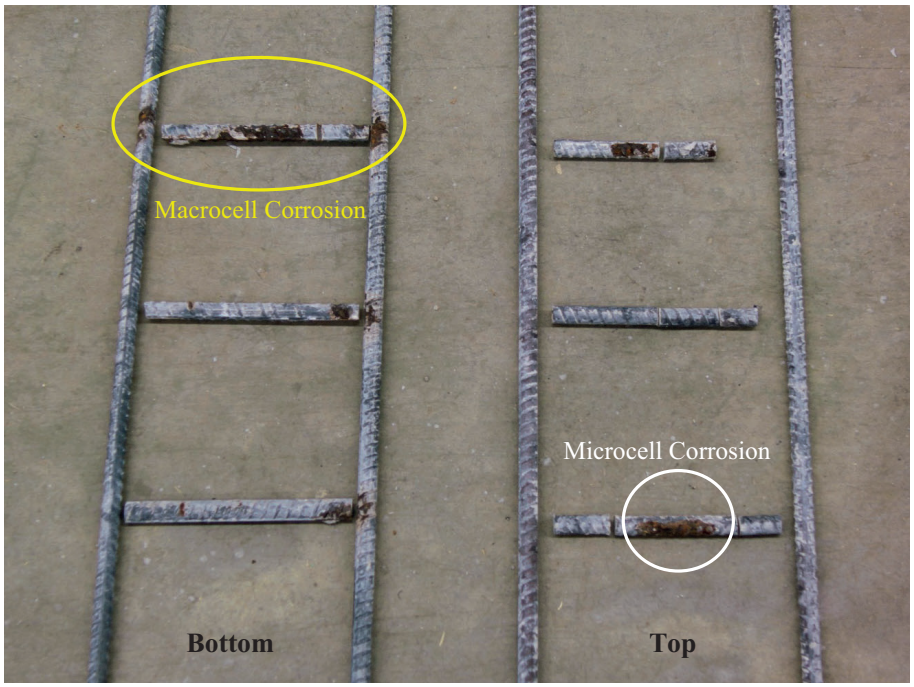

(a) Overall View

(b) Corrosion on Bottom Black Bars

Figure G.29 MMFX II and black bars (cracked). *(Figure continued on next page.)*

(c) Overall View of Corrosion on Bottom Black Bar

(d) Close up View of Corrosion on Bottom Black Bar

(e) Microcell Corrosion on Top MMFX II bar

Figure G.29 *Continued.*

bars were used for bottom mats are presented. The electrical current measurements discussed previously indicated that the total charge (total corrosion) was much higher for specimens with mats made of dissimilar materials. In addition, coated (nonmetallic or metallic) reinforcement indicated a negative charge (bottom bars acting as the cathode) while chromium based reinforcement (MMFX II and stainless steels) indicated a positive charge (bottom bars acting as the anode). The difference in electron flow as well as increased corrosion activity of these specimens was of particular interest. The autopsy results can clearly shed light on and verify these trends as suggested by the electrical measurements.

Figure G.29 shows corrosion products on the specimen with MMFX II steel. Although, the MMFX II steel in the top mat locally corroded (Figure G.29 (a), white circle), this is considered to be microcell corrosion since there is no corrosion observed at the intersection with the longitudinal MMFX II bars. On the other hand, corrosion is observed on both the longitudinal and transverse black bottom bars, especially at their intersection (Figure G.29(a), yellow circle). Based on the positive charge flow measured by the macrocells for these specimens, it appears that the MMFX II steel was more noble than the black reinforcement. Therefore, the black bars provided galvanic protection to the MMFX II bars. However, at locations away from the

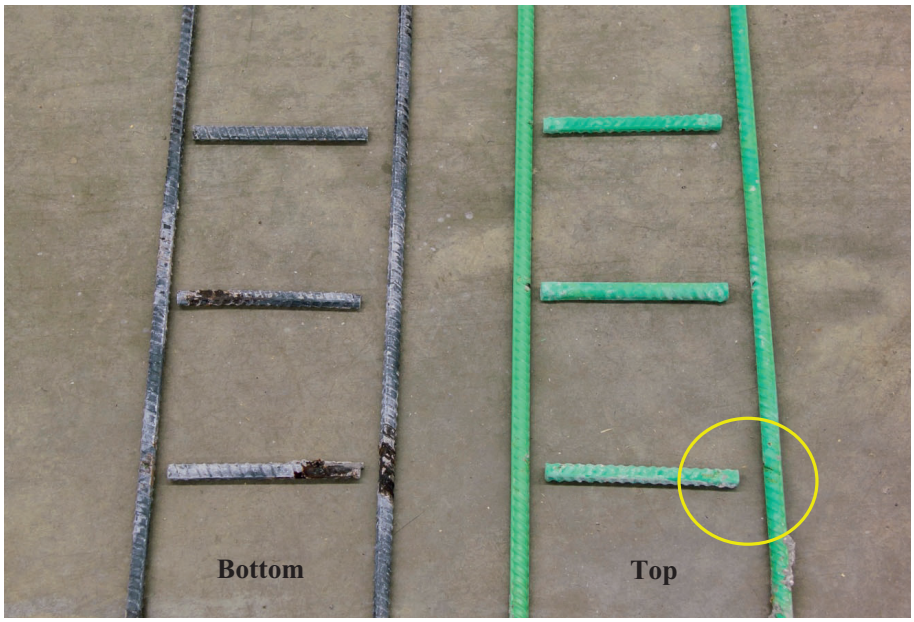

(a) Overall View

(b) Corrosion on Epoxy-Coated Steel

Figure G.30 Epoxy-coated and black bars (cracked).

coupling, microcell corrosion of MMFX II bars occurred (Figure G.29(e)).

Figure G.30(b) shows blisters on the epoxy-coated rebar where it was connected to the transverse steel. The ends of the transverse steel which was repaired with the epoxy patch material prior to testing was observed to have the coatings peeled off. Metallic coated reinforcement with zinc demonstrated white corrosion products from zinc oxides (Figure G.31 to Figure G.33). Figure G.31(b) reveals white corrosion products on the galvanized bar including reddish-brown iron oxide from the underlying base metal. Specifically, the reddish-brown corrosion products were evident locally on both the transverse and longitudinal steel where they were tied together which appears to be crevice corrosion. Both the unplated zinc-clad (Figure G.32) and tin-plated zinc-clad (Figure G.33) bars acted as a sacrificial anode; no visual corrosion was observed on the bottom black bar mats. However, Figure G.32(b) and Figure G.33(b) reveal that the zinc-clads were reacting fast and being consumed after 456 days of corrosion testing. Figure G.34(b) shows corrosion rust of base metal from a damaged spot on dual-coated, Zbar.

As shown in Figure G.35 to Figure G.38, the stainless steel reinforcement does not indicate any visual corrosion (although there is discoloration on Duplex 2205 and XM-28). These stainless steel are noble and due to galvanic coupling, drive the bottom black bars to act as the anode. Unlike conventional test programs where cracks are formed only to the top bar, the cracks in these specimens were full

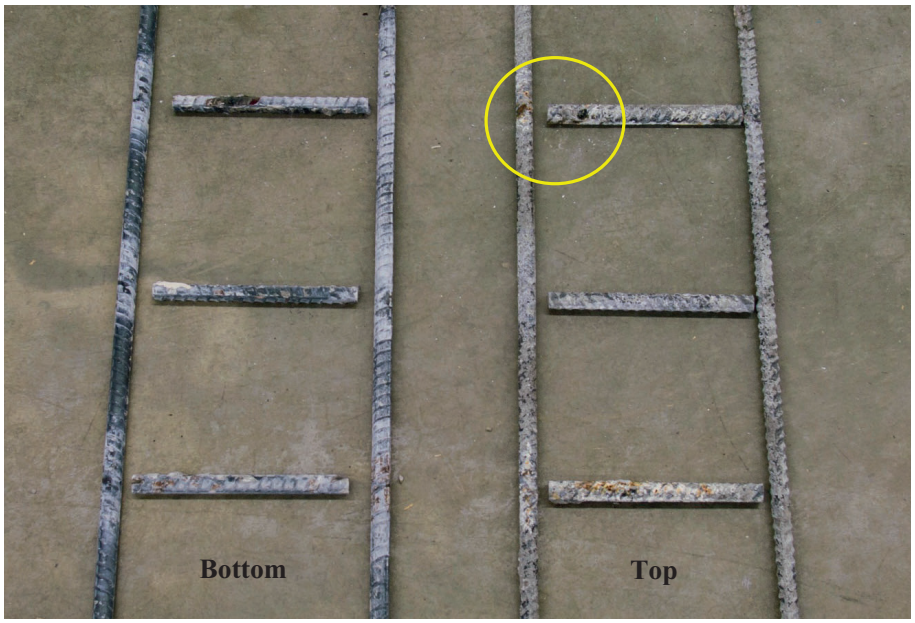

(a) Overall View

(b) White Corrosion and Iron Oxide Corrosion on Galvanized Bar

Figure G.31 Galvanized and black bars (cracked).

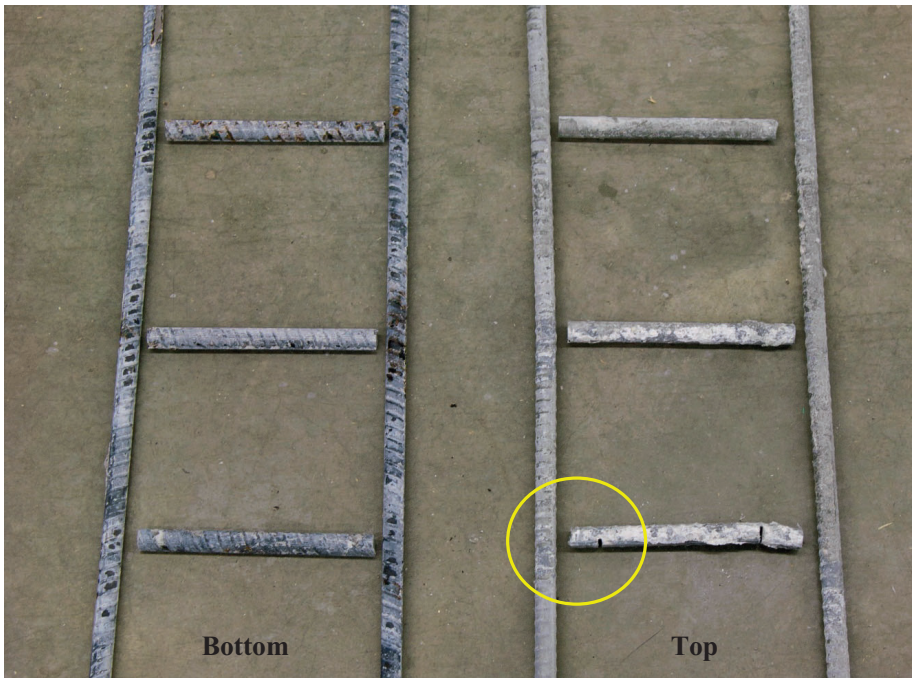

(a) Overall View

(b) White Corrosion and Consumption of Zinc-clad on Transverse Steel

Figure G.32 Un-plated zinc-clad and black bars (cracked).

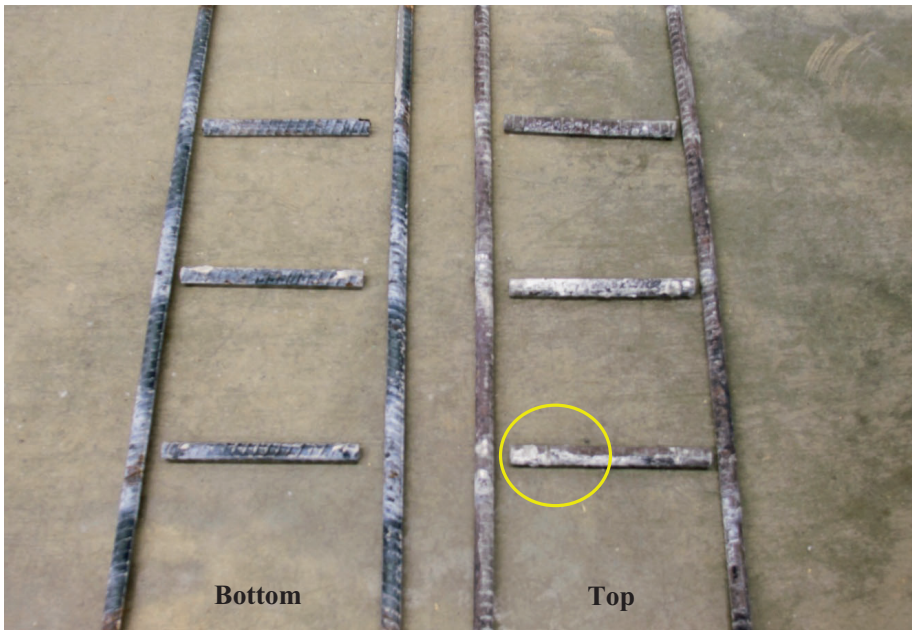

(a) Overall View

(b) White Corrosion and Consumption of Tin-Plated Zinc Clad

Figure G.33 Tin-plated zinc-clad and black bars (cracked).

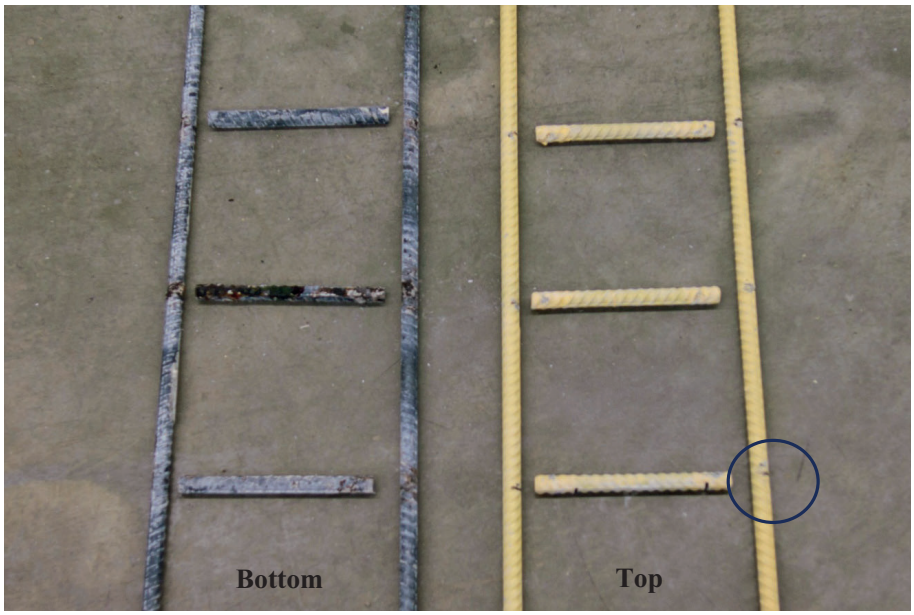

(a) Overall View

(b) Corrosion of Base Metal at Damaged Location

Figure G.34 Dual-coated zbar and black bars (cracked).

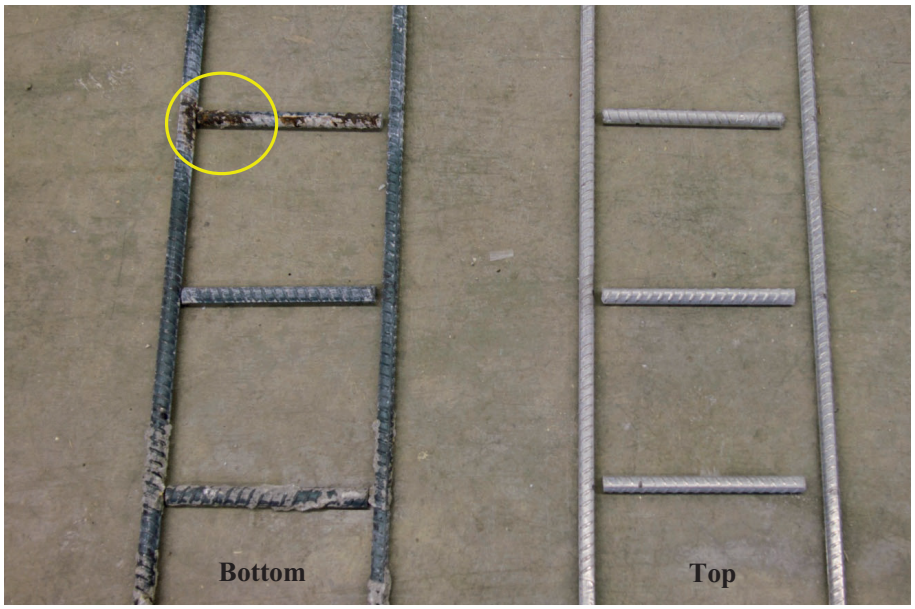

(a) Overall View

(b) Corrosion on Bottom Black Bars

Figure G.35 316LN stainless steel and black bars (cracked).

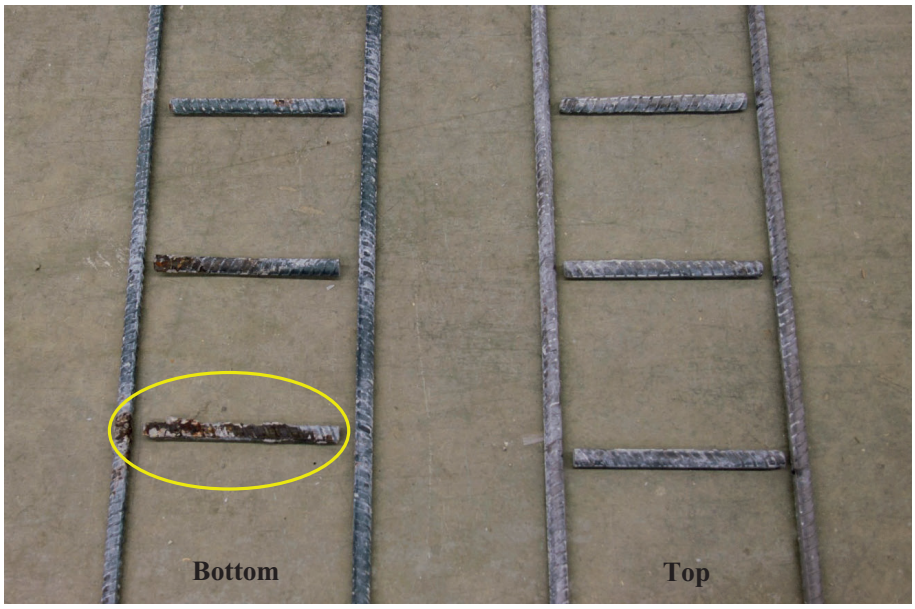

(a) Overall View

(b) Corrosion on Bottom Black Bars

Figure G.36 Duplex 2205 stainless steel and black bars (cracked).

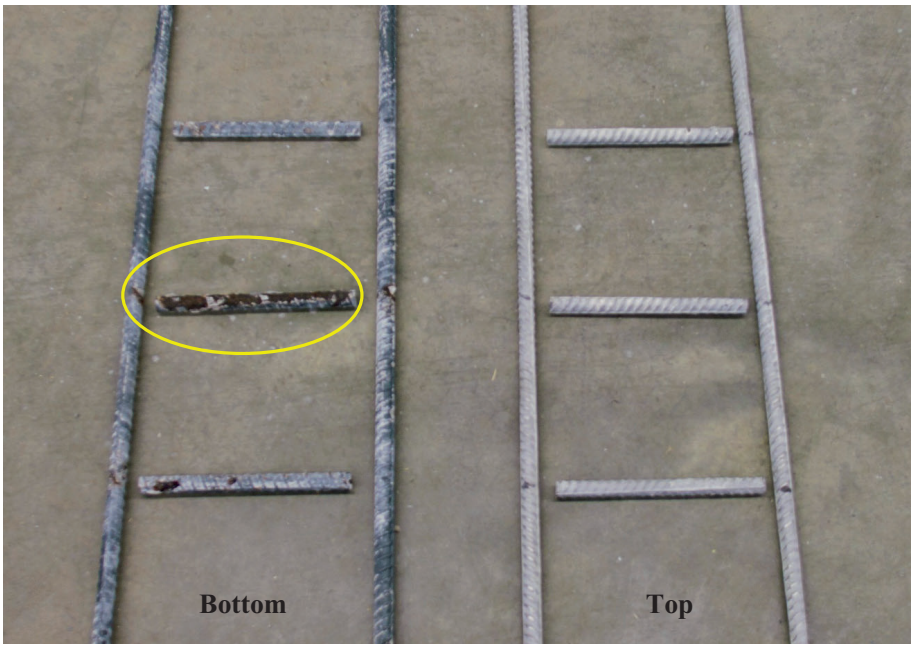

(a) Overall View

(b) Corrosion on Bottom Black Bars

Figure G.37 Duplex 2304 stainless steel and black bars (cracked).

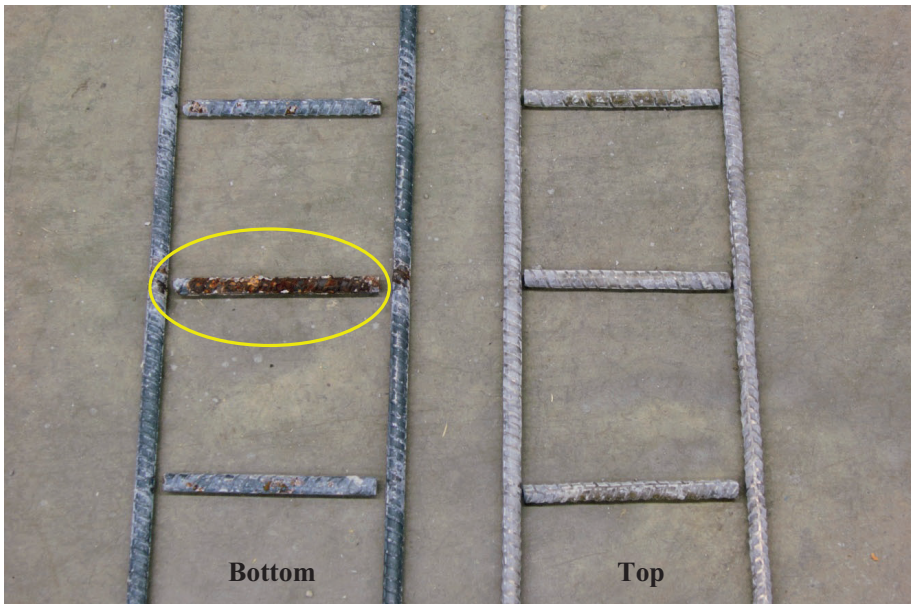

(a) Overall View

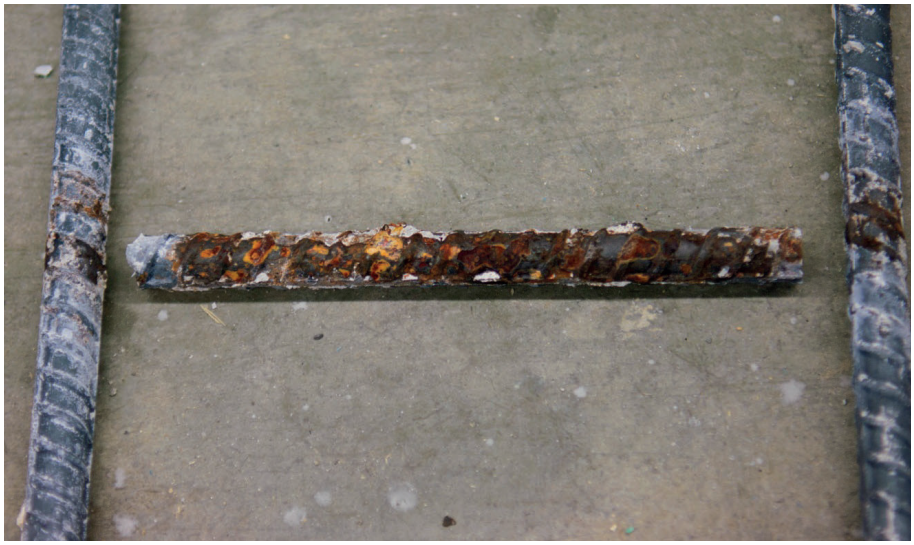

(b) Corrosion on Bottom Black Bars

Figure G.38 XM-28 stainless steel and black bars (cracked).

depth. Therefore, depassivation of the bottom mat was possible as chlorides could easily reach the bottom mat. This unequal potential drove corrosion of the bottom mat. All black bars revealed reddish-brown or blackish iron oxide corrosion products on the full section of transverse steel and locally on the longitudinal steel where it was connected to the transverse steel.

In summary, Figure G.30 to Figure G.34 presented the autopsy results of the coated reinforcement while Figure G.35 to Figure G.38 presented the autopsy results of the chromium based reinforcement. By comparing the visual appearance of the bottom black bars with the top bars, it is clearly observed that the coupling with MMFX II microcomposite steel and stainless steel (Figure G.29, and Figure G.35 to Figure G.38) forces the bottom black bars to corrode more than when the black bottom bars are coupled with the coated reinforcement (Figure G.30 to Figure G.34). In addition, more reddish-brown or blackish iron oxide corrosion products were observed on the transverse steel located parallel to the cracks relative to the longitudinal steel. Corrosion on the longitudinal steel was located primarily where it was connected to the transverse steel.

G.2.3.3 Tie material. Details of corrosion on the black bars tied with black and stainless steel ties are shown in Figure G.39. Regarding the total corrosion of black bars,

(a) Black Bar with Black Tie

(a) Black Bar with Stainless Tie

Figure G.39 Black bars with steel ties (cracked).

when stainless steel ties are used instead of black ties, the total charge was measured to be relatively lower (Figure G.8). However, the autopsy results (Figure G.40 and Figure G.41) indicate that both cases are comparable in terms of corrosion. Both cases where steel ties are used have relatively more corrosion rust than when plastic ties are used as shown in Figure G.42.

Figure G.43 shows the XM-28 stainless steel bar tied with black and stainless ties. As evident, the XM-28 stainless steel tied with a black tie has reddish brown corrosion products both on the stainless steel bar and the black tie while the stainless steel bar tied with a stainless tie have no visual corrosion. Figure G.44 and Figure G.45 show the top and bottom mats of the longitudinal and transverse steel removed from the macrocells. While only light corrosion (Figure G.45(b)) was observed in stainless reinforcement with stainless ties, reddish-brown corrosion products were observed in stainless reinforcement tied with black ties, particularly at the location where the transverse steel and longitudinal steel was tied together (Figure G.44(b)). Figure G.46 show the XM-28 stainless bars tied with plastic ties. A few spots on the transverse steel had corrosion products, but no corrosion was observed on the longitudinal steel as shown in the case with black tie (Figure G.44(b)).

To examine whether the corrosion products shown in Figure G.44(b) are from the XM-28 stainless steel bar or from the tie material, both the longitudinal bar and transverse bar were further investigated using a Omano binocular microscope. The images were captured using the OptixCam digital camera which was mounted to the

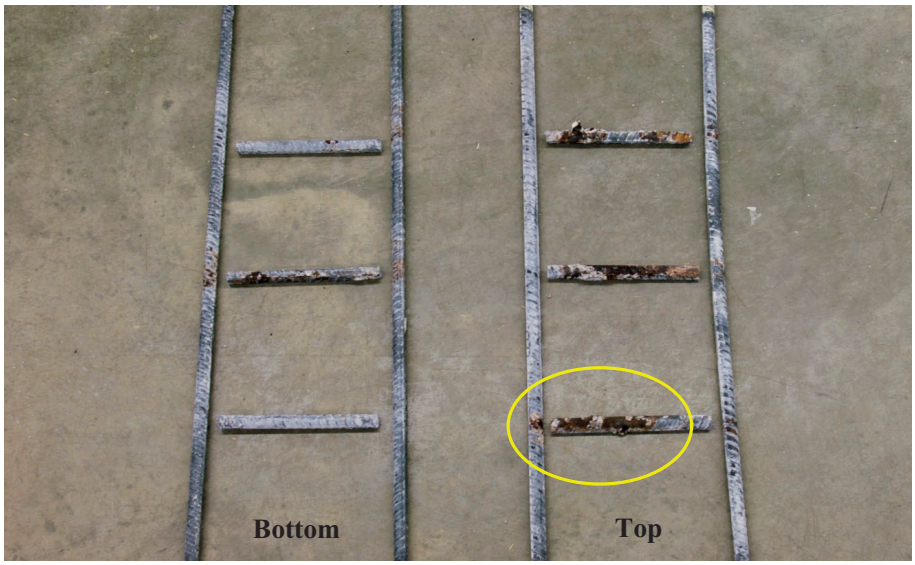

(a) Overall View

(b) Corrosion on Top Longitudinal and Transverse Steel

Figure G.40 Black bars with black ties (cracked).

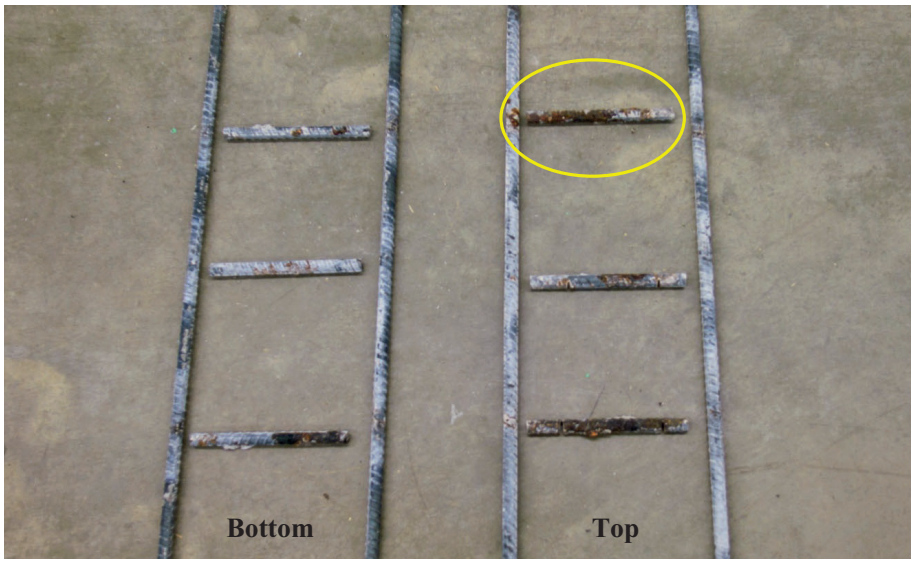

(a) Overall View

(b) Corrosion on Top Longitudinal and Transverse steel

Figure G.41 Black bars with stainless ties (cracked).

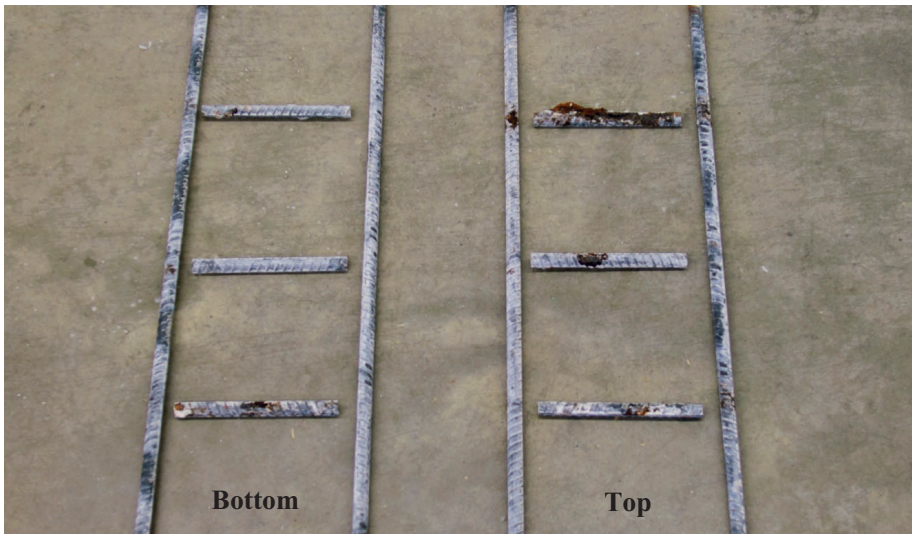

(a) Overall View

(b) Black Bars with Plastic Ties

Figure G.42 Black bars with plastic ties (cracked).

(a) XM-28 Bar with Black Tie

(b) XM-28 Bar with Stainless Tie

Figure G.43 XM-28 stainless steel with steel ties (cracked).

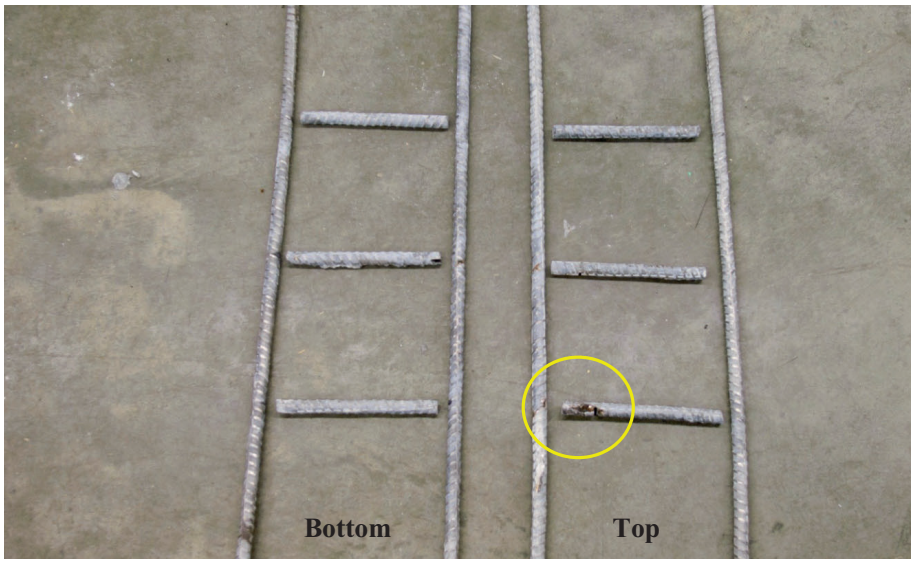

(a) Overall View

(b) Corrosion where Stainless Steel was Tied with Black Tie

Figure G.44 XM-28 stainless steel bars with black ties (cracked).

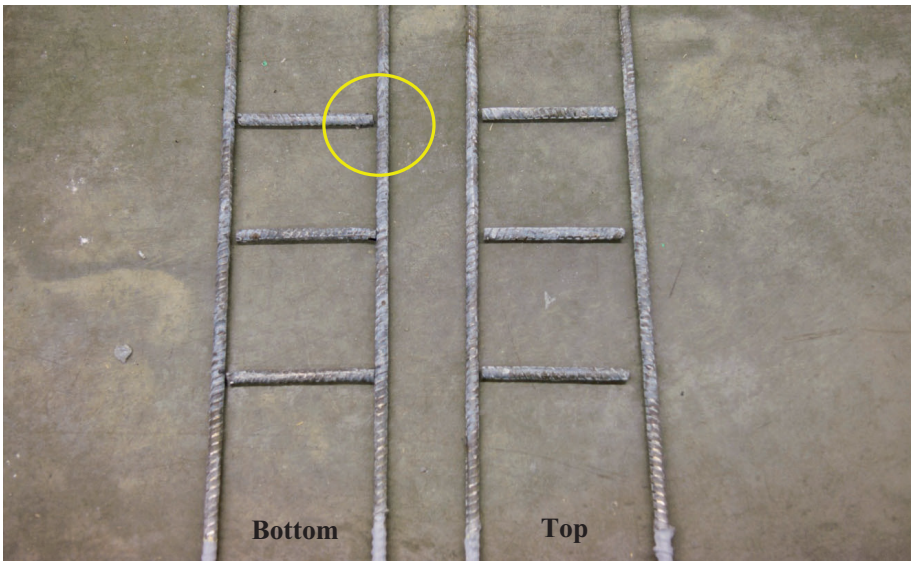

(a) Overall View

(b) Light Corrosion on Bottom Transverse Steel

Figure G.45 XM-28 stainless steel bars with stainless ties (cracked).

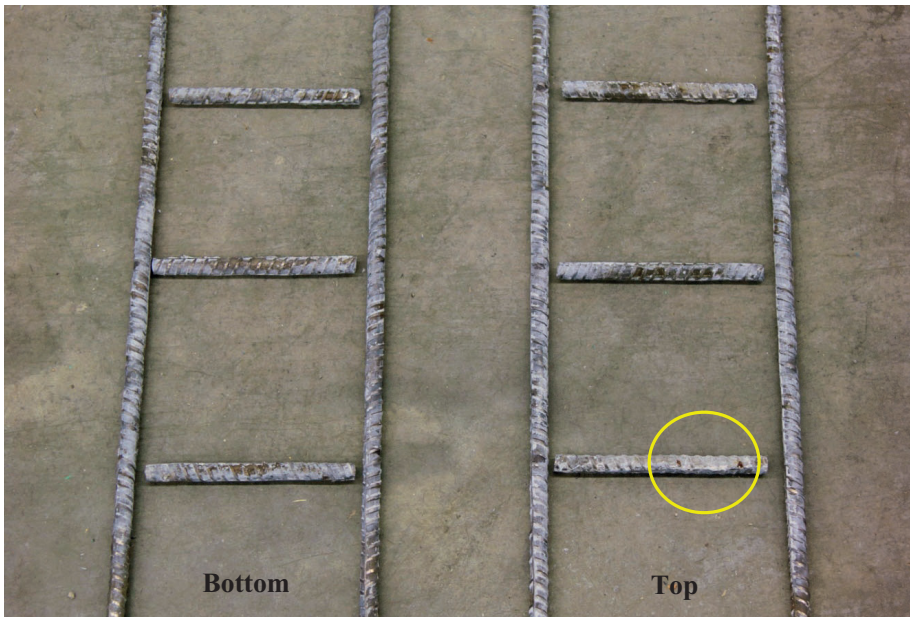

(a) Overall View

(b) Corrosion Products on Transverse Steel

Figure G.46 XM-28 stainless steel bars with plastic ties (cracked).

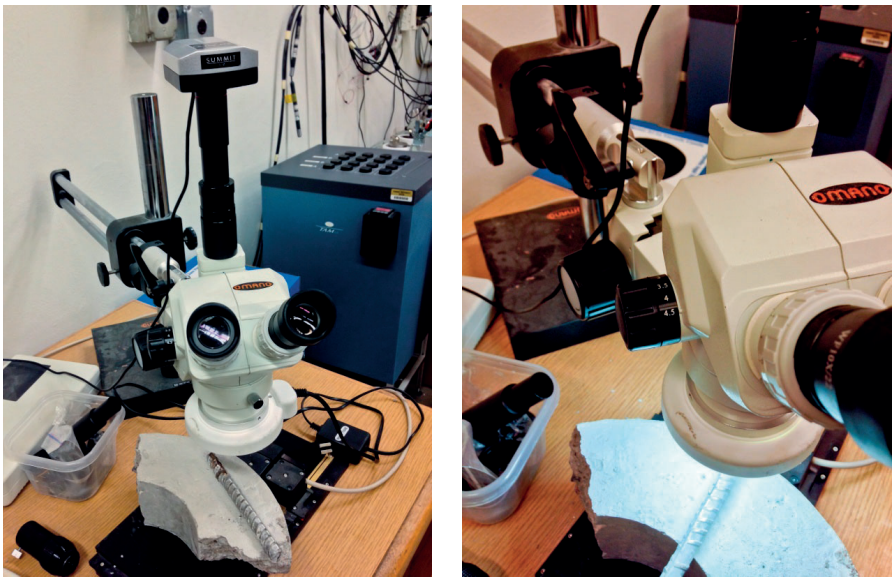

(a) Digital Microscope Camera

(b) Hydrochloric Acid Cleaning

Figure G.47 Preparation for a microscopic view on corrosion of XM-28.

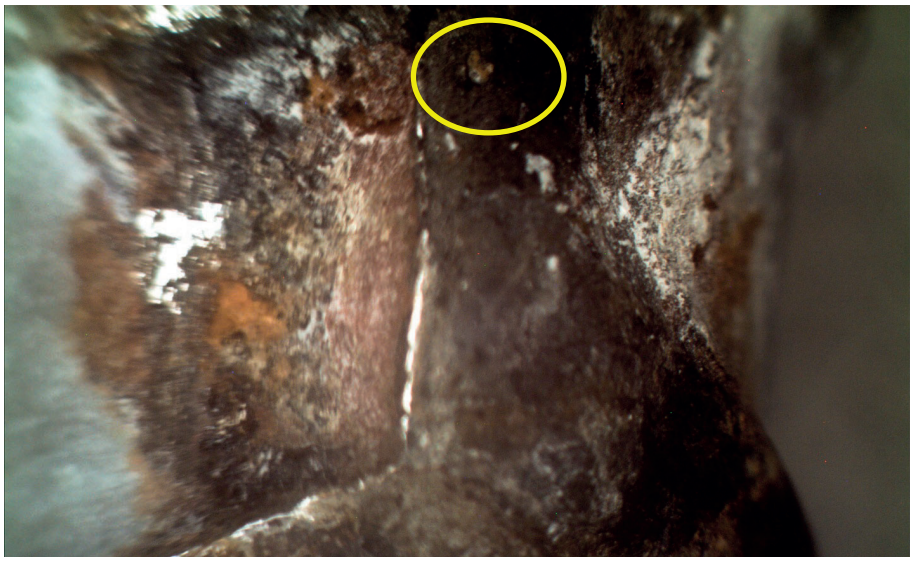

(a) Pitting Corrosion on Transverse Steel

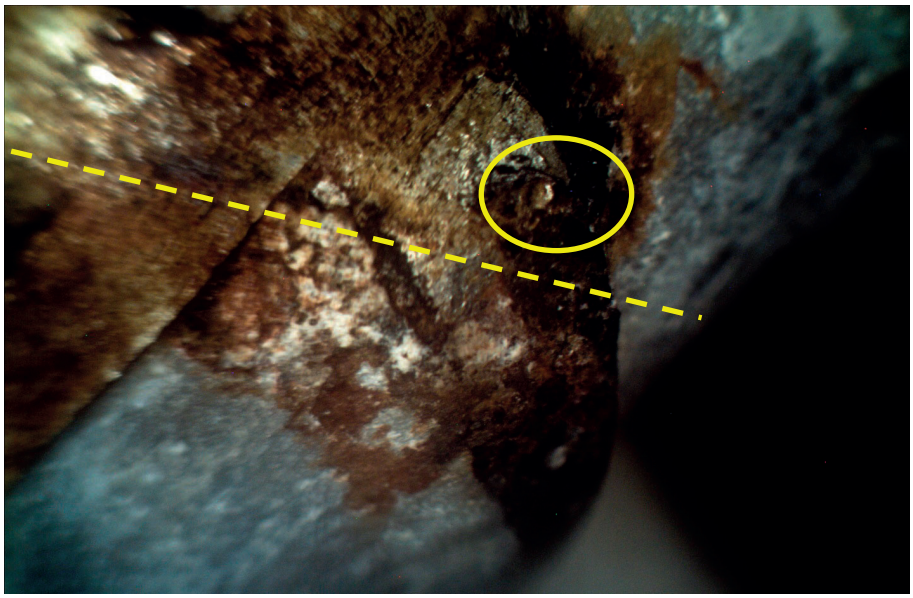

(b) Pitting Corrosion above Tie Location on Longitudinal Steel

Figure G.48 Pitting corrosion observed on XM-28 (before cleaning).

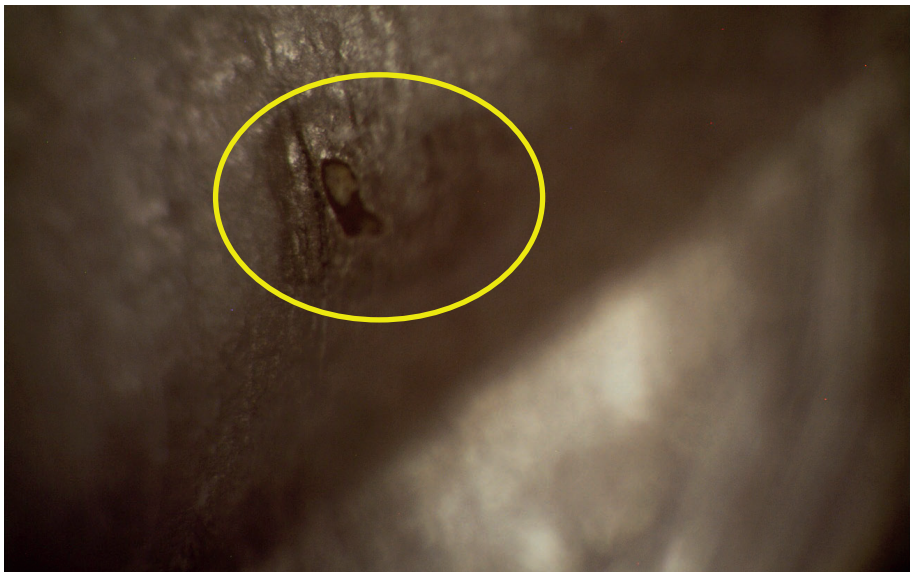

(a) Pitting Corrosion on Transverse Steel

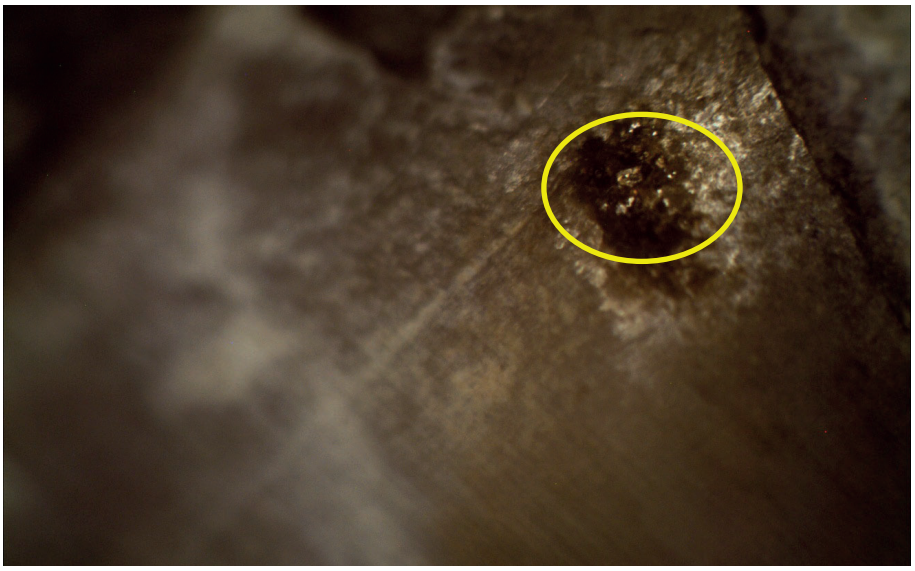

(b) Pitting Corrosion on Longitudinal Steel

Figure G.49 Pitting corrosion observed on XM-28 (after cleaning).

(a) Corrosion on Transverse Bar with Black Tie

(b) Corrosion on Longitudinal Bar with Black Ties

Figure G.50 Epoxy-coated bar with black ties (cracked). *(Figure continued on next page.)*

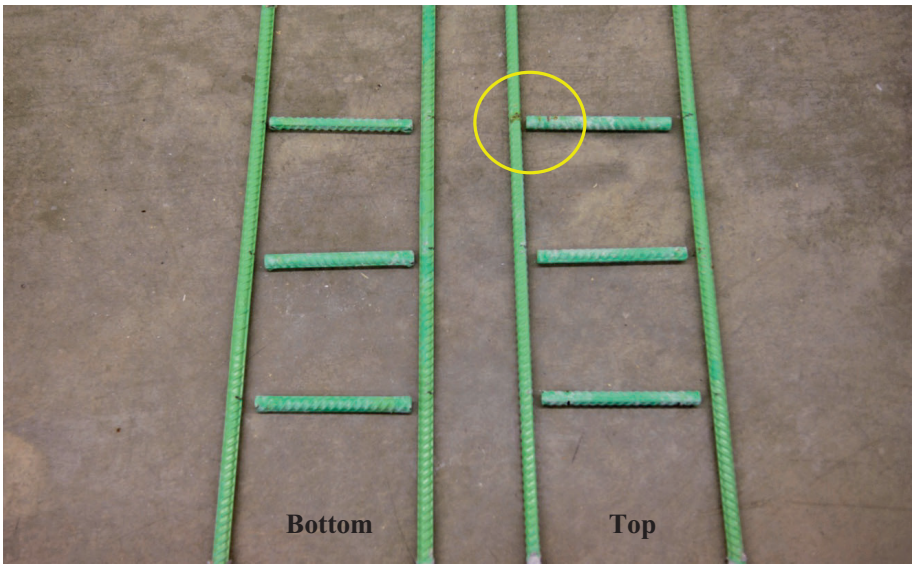

(c) Overall View

(d) Corrosion Where Steel Was Tied with Black Tie

Figure G.50 *Continued.*

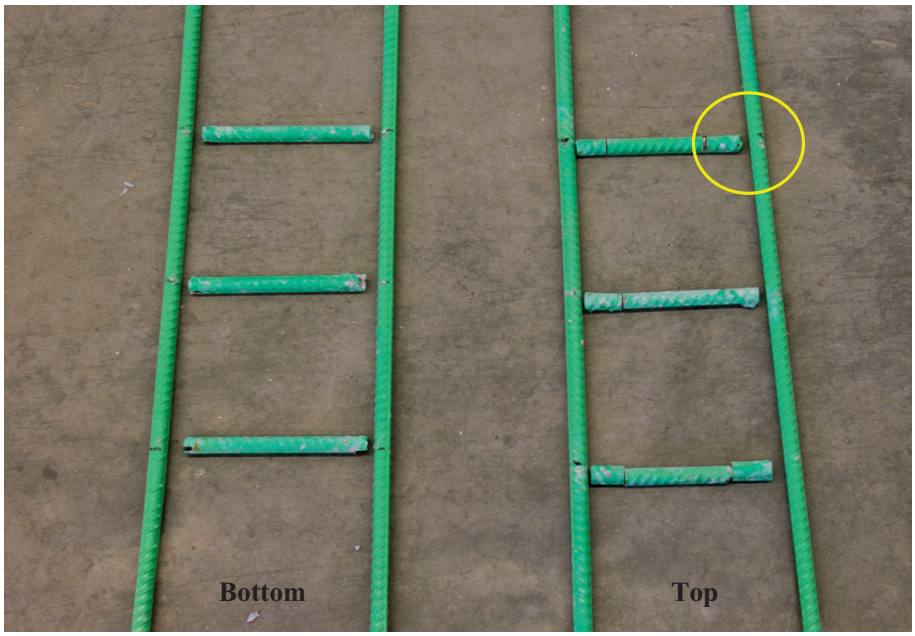

(a) Overall View

(b) Plastic Tie Location

Figure G.51 Epoxy-coated bar with plastic ties (cracked).

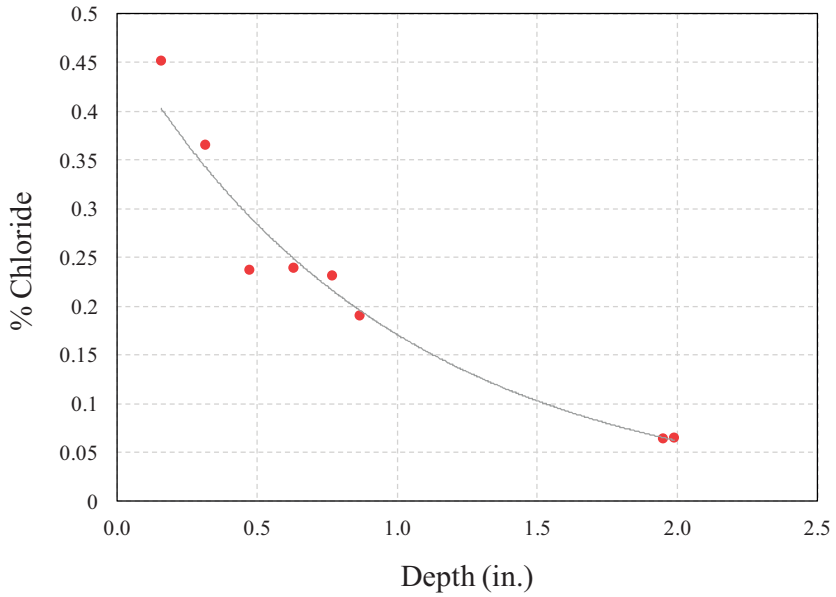

Figure G.52 Chloride content in uncracked black specimen at 537 days.

microscope as shown in Figure G.47. The corrosion products on XM-28 stainless steel were observed before cleaning the rust and after cleaning the surface with hydrochloric acid (Figure G.47(b)). Figure G.48 and Figure G.49 show the pits observed through the microscope before and after the hydrochloric acid cleaning process, respectively. On both longitudinal and transverse steel, pits were found. Of special note, the pit found on the longitudinal steel near the tie location is shown on Figure G.48(b) which verifies that localized corrosion of the XM-28 stainless steel occurred. It is evident that stainless steel reinforcement with black ties resulted in corrosion of both the ties and more importantly the primary reinforcement.

Although, the total corrosion measured was relatively low for epoxy-coated reinforcing steel with black ties (Figure G.8), light corrosion was observed where the transverse and longitudinal steel was tied together as shown in Figure G.50. Blisters and bulging of the epoxy coating is observed on the longitudinal bar at the intersection with the transverse bar (Figure G.50(b) and Figure G.50(d)). Although light corrosion is shown on epoxy-coated bar with plastic ties (Figure G.51), it is limited to the ends of transverse bar where the coatings were peeled off and a spot on the longitudinal bar where the coating was bulging. As seen in Figure G.51(b), the transverse bar underneath the plastic tie has no corrosion products or marks when the tie was taken off.

In summary, while corrosion is evident at the connection of the black tie to the black bar, much more corrosion is evident when a stainless tie is used with a black bar. It also appears that galvanic coupling of the dissimilar materials resulted in increased corrosion of the reinforcing bar at the location of the tie. These test specimens clearly illustrates not only the reinforcing material should be corrosion-resistant, but the tie material should be of identical material or inert to prevent galvanic coupling.

G.2.4 Chloride Concentrations

The chloride content of one uncracked macrocell specimen with black bars was measured at 8 different levels after 537 days of testing. The chloride concentrations and depth profile is shown in Figure G.52. A sample was taken out from a macrocell specimen during autopsy to the level of reinforcement (2 in. depth from top surface). The sample was grinded for each level to obtain at least 3 grams of ground powder from each depth. Then, an automated titration system developed by the concrete materials group at Purdue (Di Bella, Villani, Hausheer, & Weiss, 2012) was used to measure the chloride concentrations. The chloride measured at the bar level was 0.06% weight of concrete after 537 days of testing.

G.3. ANALYSIS OF TEST RESULTS

G.3.1 Visual Examination

The corroded surface area of all longitudinal and transverse steel removed from the specimens was measured. The percentage of corroded surface area from each specimen is provided in Table G.1. The percentage of corrosion from each mat is calculated as the corroded surface area relative to the total area of 103.7 in.^{2} (which is the surface area of the entire mat: two 24 in. long #4 bars and three 6 in. long #4 bars).

The intensity of corrosion damage may vary with each corroded area. Large corroded areas can have light corrosion while small corroded areas may have heavy corrosion. Therefore, the damage level from visual observations was rated on a scale of 0 to 10 where 0 designates no damage and 10 indicates the highest level of damage. The size of the affected region based on the color of corrosion products was the basis in evaluating the damage level. However, only reddish-brown (from red iron oxide) and blackish (from black iron oxide) corrosion were considered in this evaluation. White corrosion products of zinc oxides that were produced from the hot-dip galvanized reinforcing steel and zinc-clad

TABLE G.1
Corroded Surface Area and Visual Rating

Corroded Surface Area (in.^{2})/Visual Rating Score (*0–10*)														
			Top Bars						Bottom Bars					
			Longitudinal		Transverse				Longitudinal		Transverse			
Cracked Condition	**No.**	**Bar Type**	**L**	**R**	**F**	**M**	**B**	**Top Mat Corrosion (%)**	**L**	**R**	**F**	**M**	**B**	**Bottom Mat Corrosion (%)**
Uncracked	1	XM-28						–						–
	6	316LN						–						–
	9	Duplex 2205						–						–
	11	Duplex 2304		0.01 ***5***				**0.01**						–
	13	MMFX II		0.05 ***5***				**0.05**						–
	16	Zbar						–						–
	21	Epoxy						–						–
	23	Galvanized						–						–
	25	Zinc-clad 1						–						–
	28	Zinc-clad 2						–						–
	32	Black						–		0.04 ***2***				**0.04**
Cracked—Identical Mats	34	XM-28			0.07 ***5***			**0.07**						–
	38	316LN						–						–
	41	Duplex 2205						–						–
	44	Duplex 2304						–						–
	47	MMFX II	0.51 ***10***		1.03 ***9***	2.88 ***10***	0.84 ***9***	**5.1**				0.04 ***5***	0.12 ***6***	**0.15**
	51	Zbar			0.59 ***5***		0.02 ***5***	**0.59**						–
	53	Epoxy	0.01 ***4***	0.02 ***8***	0.04 ***3***	0.02 ***3***	0.04 ***3***	**0.13**						–
	56	Galvanized			0.01 ***5***			**0.01**						–
	59	Zinc-clad 1						–						–
	61	Zinc-clad 2						–						–
	64	Black	1.15 ***9***	0.56 ***4***	0.2 ***7***	1.37 ***10***	2.37 ***10***	**5.5**	0.61 ***6***		1.05 ***10***	0.06 ***6***	0.06 ***10***	**1.7**
Cracked—Dissimilar Mats	67	XM-28						–	0.53 ***8***	0.27 ***8***	0.33 ***8***	3.79 ***10***	0.1 ***5***	**4.8**
	72	316LN						–	0.48 ***8***			0.02 ***5***	2.07 ***9***	**2.5**
	73	Duplex 2205						–		0.7 ***10***	2.3 ***10***	0.99 ***9***	0.15 ***4***	**4.0**
	78	Duplex 2304						–	0.27 ***8***	0.27 ***8***	0.27 ***10***	2.22 ***9***	0.09 ***2***	**3.0**
	80	MMFX II				1.35 ***10***	0.59 ***10***	**1.9**	0.67 ***9***	1.85 ***10***	0.64 ***8***	0.3 ***10***	2.34 ***10***	**5.6**
	83	Zbar						–	0.33 ***7***	0.33 ***7***	0.1 ***7***	2.7 ***10***		**3.3**
	85	Epoxy	0.05 ***4***	0.004 ***2***			0.01 ***3***	**0.06**	0.28 ***5***	2.63 ***9***	1.7 ***9***	1.02 ***9***		**5.4**
	90	Galvanized	0.15 ***10***	0.15 ***1***	0.11 ***3***		0.65 ***4***	**1.0**		0.6 ***2***	0.2 ***1***	0.1 ***3***	0.54 ***8***	**1.4**
	91	Zinc-clad 1						–	0.69 ***5***	0.99 ***7***	0.09 ***4***	0.05 ***9***	0.26 ***8***	**2.0**
	96	Zinc-clad 2						–	0.34 ***3***	0.86 ***5***		0.05 ***4***	0.3 ***10***	**1.5**
Cracked—Tie Material	98	XM-28 ST						–						–
	100	XM-28 BT	0.13		0.37			**0.48**		0.06		0.04		**0.10**

Continued.

Table G.1.—*Continued.*

Cracked Condition	No.	Bar Type	Corroded Surface Area (in.^{2})/Visual Rating Score (*0–10*)											
			Top Bars						Bottom Bars					
			Longitudinal		Transverse				Longitudinal		Transverse			
			L	R	F	M	B	Top Mat Corrosion (%)	L	R	F	M	B	Bottom Mat Corrosion (%)
			4		***4***					***8***		***2***		
	101	Duplex 2205 ST						–						–
	103	Duplex 2205 BT						–						–
	107	Epoxy BT	0.09	0.2	0.02	0.04	0.01	**0.35**						–
			9	***9***	***1***	***2***	***2***							
	109	Black ST	1.13	0.89	5.65	1.48	3.95	**12.6**	0.06	0.35	0.31	2.24	0.85	**3.7**
			9	***7***	***10***	***10***	***10***		***3***	***3***	***10***	***10***	***6***	
	111	Black BT	0.55	0.1	3.53	5.18	3.31	**12.2**	0.72	0.45	0.01	0.49	0.08	**1.7**
			10	***4***	***10***	***10***	***10***		***5***	***5***	***2***	***10***	***10***	

Notes:

1. L: Left, R: Right, F: Front, M: Middle, B: Back.
2. The percentage of corrosion was calculated as corroded area relative to the total surface area of 103.7 in.^{2} (entire mat of two longitudinal #4 bars (2ft length) and three transverse #4 bars (6 in. length)).
3. Visual rating scores (0-10 scale) and total scores are in italic, bold font.

reinforcing steels were not considered in this rating. These products indicate sacrificial action of the zinc and are not damage to the reinforcement.

Table G.2 provides the percentage of corroded surface area for both the top and bottom mats and provides the total score for the visual examination. The total score was calculated by multiplying each corroded surface area by its visual rating scale shown in Table G.1 and summing all of the individual scores for both the top and bottom bars.

G.3.1.1 Cracking. For the uncracked specimens, only the Duplex 2304 stainless steel bar and MMFX II bar had corrosion of the top bars. Black bars had light corrosion on the bottom bars as shown in Table G.2. For the cracked specimens, XM-28, MMFX II, Zbar, epoxy-coated, galvanized, and black bar had corrosion on the top bars. As clearly seen, cracked specimens have a higher total score than uncracked specimens. The cracked specimens with black reinforcing steel and MMFX II microcomposite reinforcing steel have high scores compared to the specimens of the other bars. The 316LN, Duplex 2205, and Duplex 2304 stainless steel bars as well as the zinc-clad bars did not show any sign of corrosion from iron oxides (rust). As previously noted, white corrosion products from zinc oxides were not included in the visual rating.

G.3.1.2 Reinforcement material in mats (identical or dissimilar material). It is evident that when black bars are used in the bottom mat, the visual examination scores are much higher than for the case with both mats identical. Although, some research (Bertolini et al. 1998; Qian et al., 2006) reports that stainless steel reinforcing steel does not have galvanic coupling issues, the electrical current measurements and the visual examination in this study clearly demonstrates that more corrosion damage is observed when different types of steel are used in the top and bottom mats. In all cases of dissimilar mats, the black steel in the bottom mat corroded preferentially to the top mat. Among chromium containing corrosion-resistant reinforcing steel, MMFX II microcomposite steel resulted in the most black bar corrosion. Regarding stainless steel reinforcement, galvanic corrosion was also observed with the highest being XM-28 followed in order by Duplex 2205, Duplex 2304, and 316LN stainless steel.

Metallic coated reinforcement such as hot-dip galvanized bars and the two zinc-clad bars provided the least amount of corrosion of the bottom black bars suggesting that the zinc on the top mat is protecting the black bars through sacrificial action (acting as an anode). However, it is difficult to compare corrosion of metallic coated reinforcement with other non-metallic coated reinforcement or chromium based reinforcement because they function differently. For galvanically protected reinforcement, corrosion of the zinc protects the base material.

G.3.1.3 Tie material. Similar to the electrical current measurement results, when the longitudinal and transverse steel is tied with black or stainless ties (cracked - tie material in Table G.1 and Table G.2), more corrosion was observed than when plastic ties were used (cracked - identical mats in Table G.1 and Table G.2). Although the amount of corrosion is small for the specimen with epoxy-coated and stainless steel bars using black ties, increased corrosion occured. As previously noted in the visual examination results, it is not recommended to use dissimilar metallic tie materials.

G.3.2 Corrosion Rate

Corrosion rates were calculated based on the electrical measurements made from the macrocell specimens. Calcu-

TABLE G.2
Summary of Visual Examination

Cracked Condition	Bar Type	Top Mat Corrosion (%)	Bottom Mat Corrosion (%)	Total Score
Uncracked	XM-28	–	–	–
	316LN	–	–	–
	Duplex 2205	–	–	–
	Duplex 2304	0.01	–	0.1
	MMFX II	0.05	–	0.3
	ZBar	–	–	–
	Epoxy	–	–	–
	Galvanized	–	–	–
	Zinc-clad 1	–	–	–
	Zinc-clad 2	–	–	–
	Black Bar	–	0.04	0.1
Cracked—Identical Mats	XM-28	0.07	–	0.4
	316LN	–	–	–
	Duplex 2205	–	–	–
	Duplex 2304	–	–	–
	MMFX II	5.1	0.15	51
	ZBar	0.59	–	3.1
	Epoxy	0.13	–	0.5
	Galvanized	0.01	–	0.1
	Zinc-clad 1	–	–	–
	Zinc-clad 2	–	–	–
	Black Bar	5.5	1.7	66
Cracked—Dissimilar Mats	XM-28	–	4.8	47
	316LN	–	2.5	3.9
	Duplex 2205	–	4.0	39
	Duplex 2304	–	3.0	27
	MMFX	1.9	5.6	52
	ZBar	–	3.3	32
	Epoxy	0.06	5.4	50
	Galvanized	1.0	1.4	6.3
	Zinc-clad 1	–	2.0	11
	Zinc-clad 2	–	1.5	5.5
Cracked—Tie Material	XM-28 ST	–	–	–
	XM-28 BT	0.48	0.10	2.6
	Duplex 2205 ST	–	–	–
	Duplex 2205 BT	–	–	–
	Epoxy BT	0.35	–	2.7
	Black ST	12.6	3.7	154
	Black BT	12.2	1.7	137

lations were made based on ASTM G102 (2010) to convert the corrosion current density (Equation (G.2)) to mass loss rates (corrosion rate) shown in Equation (G.3). The calculation method is based on Faraday's Law of Electrolysis which gives the quantitative relationship between the mass of a substance altered at an electrode to the electrical charge transferred at the electrode.

$$i_{cor} = \frac{I_{cor}}{A} \tag{G.2}$$

where:

i_{cor} = *corrosion current density* ($\mu A/cm^2$)
I_{cor} = *current at anode reinforcement* (μA)
A = *surface area of anode reinforcements* (cm^2)

$$CR = \frac{i_{cor} W}{F \rho n} \tag{G.3}$$

where:

CR = *corrosion rate (mils/year or mm/year)*
W = *atomic weight of element (g)*
F = *Faraday's constant (96,485 Coulombs per mole)*
ρ = *density of metals and alloys* (g/cm^3)
n = *valance of the element (for oxidation in corrosion process)*

ASTM G102 provides guidance on the calculation of the corrosion rates of metals and a variety of alloys using

TABLE G.3
Parameters for Corrosion Rate Calculation

Bar type	EW	ρ (g/cm³)	Corrosion Rate (mils/year)		Corrosion rate (μm/year)	
			K_1	C	K_1	C
Black	27.9	7.87	0.1288	0.457	3.27	11.6
Epoxy	27.9	7.87	0.1288	0.457	3.27	11.6
Galvanized	32.7	7.13	0.1288	0.591	3.27	15.0
Zinc-clad 1	32.7	7.13	0.1288	0.591	3.27	15.0
Zinc-clad 2	32.7	7.13	0.1288	0.591	3.27	15.0
Zbar	32.7	7.13	0.1288	0.591	3.27	15.0
MMFX II	26.4	7.87	0.1288	0.432	3.27	11.0
316LN	25.5	7.9	0.1288	0.416	3.27	10.6
S2205	24.7	7.8	0.1288	0.408	3.27	10.3
S2304	24.6	7.8	0.1288	0.406	3.27	10.3
XM-28	25.2	7.75	0.1288	0.419	3.27	10.6

Notes: Units of K_1: $(mils/y) \cdot g/(\mu A \cdot cm)$ or $(\mu m/y) \cdot g/(\mu A \cdot cm)$.
Units of C: $(mils/y) \cdot cm^2/\mu A$ or $(\mu m/y) \cdot cm^2/\mu A$.

Equation (G.3). By simply changing Faraday's constant which is in Columbs (amps in seconds) to a year conversion (Equation (G.4)), corrosion rates can be expressed in either mils/year or mm/year. In addition, depending on the chemical composition of the alloy, ASTM G102 demonstrates methods to calculate the equivalent weight (Equation (G.5)) of alloys based on their atomic weight and numbers of electrons required to oxidize an atom of the element in the corrosion process. The equivalent weight of various alloys are provided in ASTM G102 and the density of various metals and alloys are provided in ASTM G1 (2011) which can be used in calculating corrosion rates. Equation (G.3) can be re-written as follows which is provided in ASTM G102:

$$CR = K_1 \frac{i_{cor}}{\rho} EW \tag{G.4}$$

where:

K_1 = *conversion factor (1/F)0.1288 (mpy · g/(μA · cm)) to obtain corrosion rates in mils/year 3.27 × 10⁻³ (mm/y · g/(μA · cm)) to obtain corrosion rates in mm/year*
EW = *equivalent weight*

$$= \frac{W}{n}$$

$$= \frac{1}{\sum \frac{n_i f_i}{W_i}}$$

n_i = *valence of the i^{th} element of the alloy*
f_i = *mass fraction of the i^{th} element of the alloy*
W_i = *atomic weight of the i^{th} element of the alloy*

A single constant can be obtained by multiplying the conversion factor and equivalent weight and dividing it by each density. This constant can be multiplied by the current density (measured) to obtain the corrosion rate of the reinforcing steel used in this study.

$$CR = C \cdot i_{cor} \tag{G.5}$$

where:

$$C = K_1 \frac{EW}{\rho}$$

Table G.3 provides the equivalent weight, density, conversion factor, and constant C (Equation (G.5)) of each of the reinforcing steels used in this study. The equivalent weight of stainless steel and MMFX II reinforcing steel were calculated based on the chemical composition of the major chemical elements (Chromium, Nickel, Molybdenum, Manganese, and Iron). The equivalent weight of hot-dip galvanized, zinc-clad reinforcing steel, and dual-coated Zbar were based on the calculations for zinc assuming that zinc is the major component which reacts in the corrosion process. The equivalent weight of epoxy-coated reinforcing steel was assumed to be identical as the weight for conventional black steel because the non-metallic coating does not chemically react during corrosion. To be consistent with other chapters, the units used in this study for the corrosion rate is mils per year.

The corrosion rate increased as specimens were cracked as shown in Figure G.53. The rates increased more as specimens were coupled in a galvanic condition (black bars in bottom mat) as shown in Figure G.54. Finally, when black ties are used instead of plastic ties, it is seen in Figure G.55 that the black ties increase the corrosion rate.

G.3.3 Ranking of Corrosion Resistant Reinforcement

G.3.3.1 Evaluation of cracked specimens with identical mats. The visual examination scores that were calculated by multiplying the corroded surface area to each visual rating scores and the total charge flow (total corrosion) which indicates the number of electrons removed from the anode for the cracked specimens with identical mats normalized to black steel and are presented in Figure G.56. Although, the total corrosion measured for the galvanized and zinc-clad bars are higher than other bars as shown in Figure G.56(b), this is due to the sacrificial action of zinc and is not related to the iron oxide corrosion of steel. Because black and MMFX II had very high corrosion scores relative to the other bars, it is difficult to distinguish the difference between other bars. Therefore, the visual rating and the electrical measurements for cracked specimens are provided in Table G.4 and Table G.5.

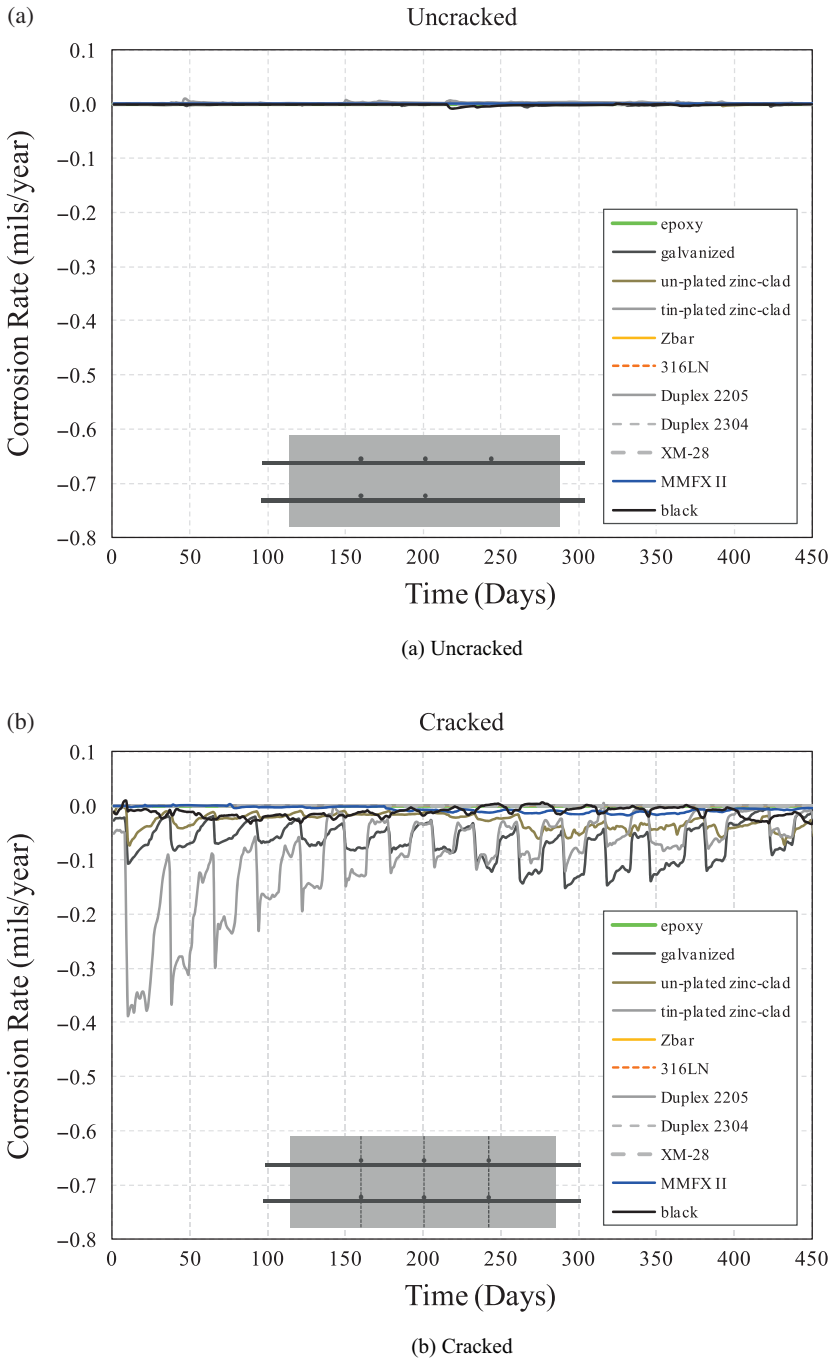

Figure G.53 Influence of cracking on corrosion rates.

Thirty-nine specimens were autopsied, and there are some discrepancies between the measurements and visual ratings. The visual examination includes evaluation of both macrocell and microcell corrosion products which may not necessarily be measured by the electrical connection of the macrocells. Because it is difficult to identify and clearly separate microcell and macrocell corrosion products, relatively higher scores may be rated by the visual examination as compared to the electrical measurements from the macrocell. Overall, however, the autopsy results correspond well with the electrical measurements and provide a similar ranking order (highest to lowest percentage of corrosion) when excluding the zinc containing bars as shown in Table G.4 and Table G.5.

The 316LN, Duplex 2304, and Duplex 2205 stainless steel bars as well as the zinc-clad bars did not display any visual corrosion (iron oxide steel corrosion) on the bars. To assist in providing ranked order for better performing

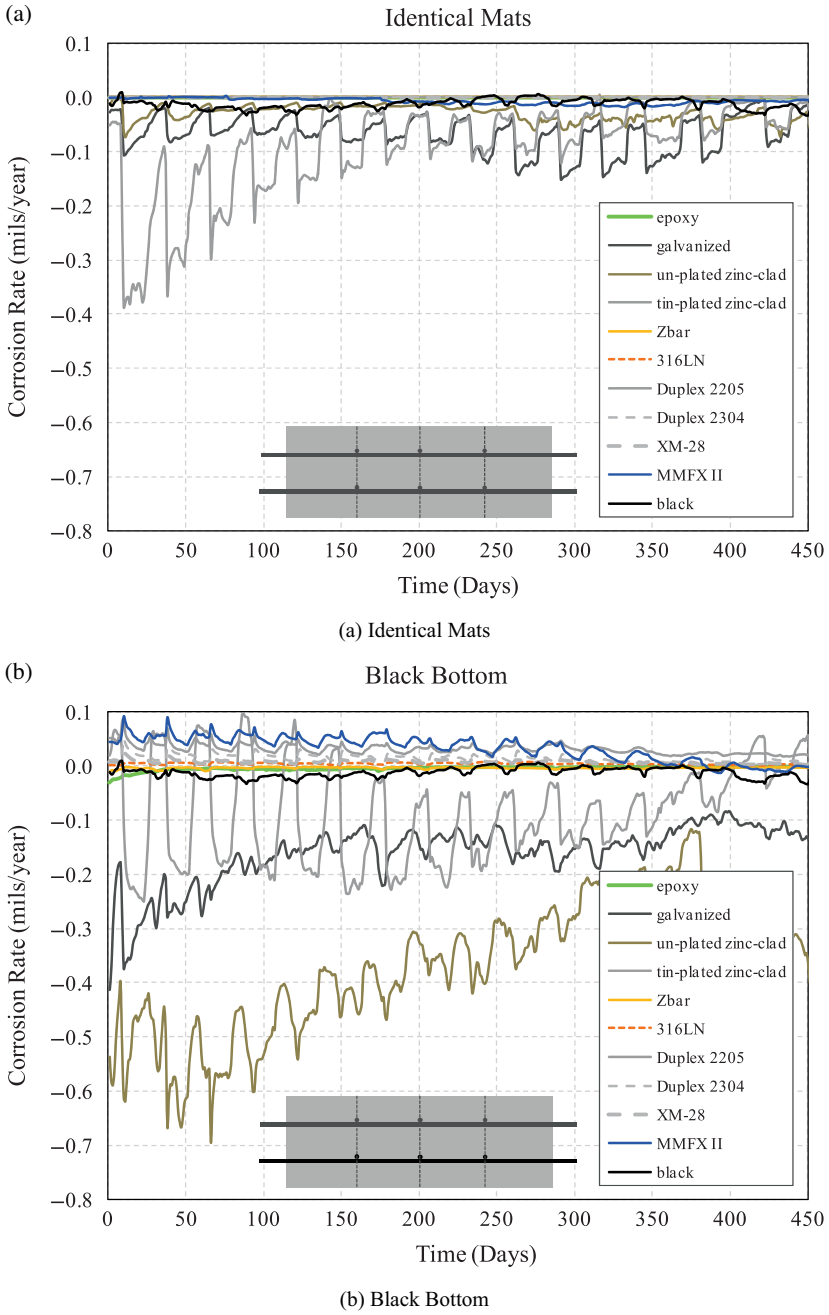

Figure G.54 Influence of reinforcing material in mats on corrosion rates.

(more corrosion-resistant) bars, the electrical current measurements are listed in Table G.5. Based on the total corrosion measurements, among stainless steel bars, 316LN performed best followed by Duplex 2304, Duplex 2205, and XM-28. In addition, zinc-clad bars exhibited more total corrosion compared to galvanized bars which is understandable because the zinc coating ranged from 18-44 mils for the zinc-clad bars with only 4-5 mils for the galvanized bars. In addition, the zinc-clad bars are almost pure zinc. Overall, zinc-clad bars had less visual corrosion than the galvanized bars.

Unlike the total corrosion measurements, Zbar and epoxy-coated bar were the only two bars that were ranked differently in the visual examination. More corrosion was observed on the Zbar compared to the epoxy-coated bar during the visual examination. However, as shown in Figure G.28(b), the corrosion was near the ends of the transverse bars which were cut to 6 in. length and repaired with the approved touch-up patching kit. The corrosion, while in the region that was painted, occurred at the location of the designed damage where the bar was influenced only by the damage as the cut end was located further away. The epoxy-coated bar shown in Figure G.24(b) not only had corrosion at the ends of the transverse bar but also on the longitudinal bar. Because no corrosion was observed

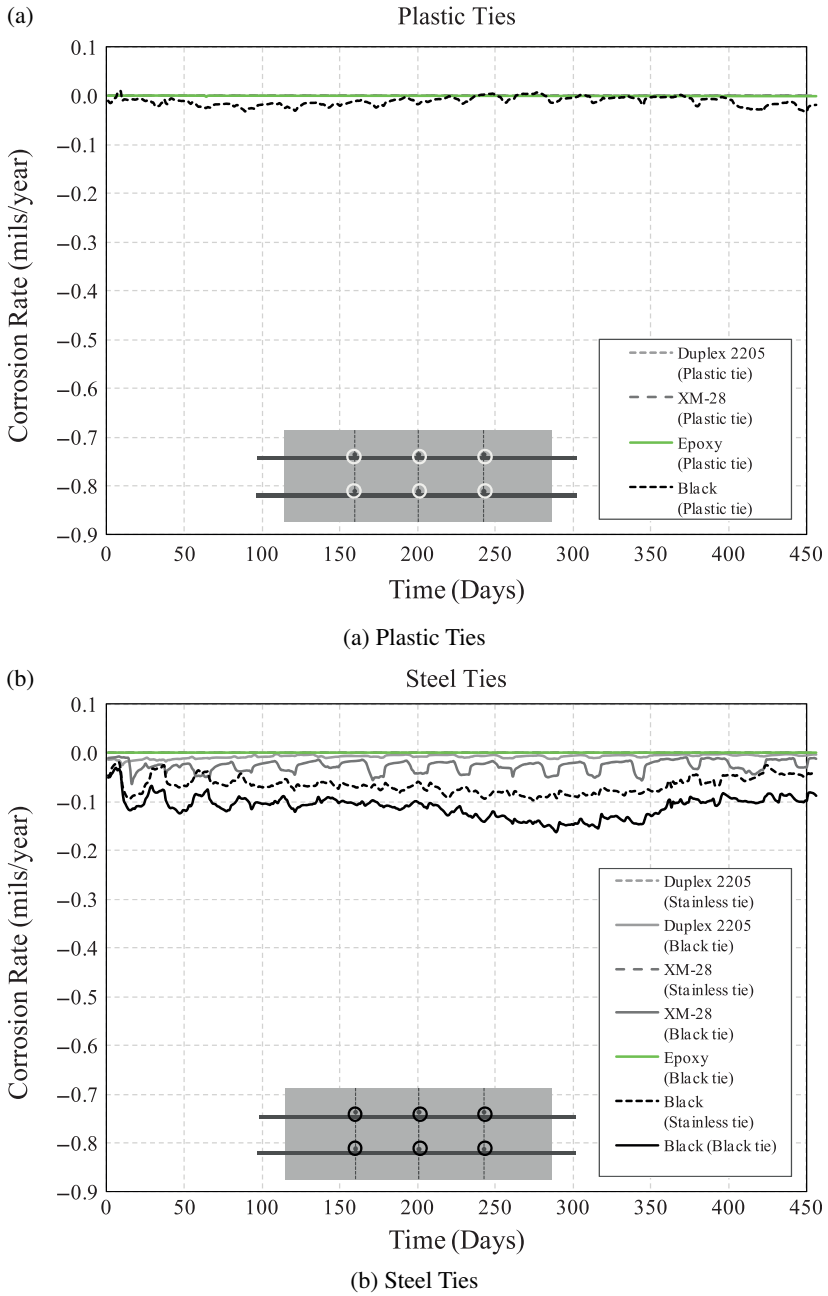

Figure G.55 Influence of tie material on corrosion rates.

on the longitudinal bar of Zbar, although the visual corrosion scores were higher, Zbar is believed to provide better performance than the epoxy-coated bar. In addition, total corrosion measurements for the Zbar (Table G.5) indicate that less macrocell corrosion actually occurred for the Zbar (half the value).

G.3.3.2 Evaluation of cracked specimens with dissimilar mats. The visual examination scores and total charge flow (total corrosion) for the cracked specimens with dissimilar mats are presented in Figure G.57. Table G.6 and Table G.7 present the actual values for the visual examination score and total charge, respectively, sorted from the highest to lowest. For specimens with dissimilar mats, corrosion was primarily observed on the black bars located in the bottom mat. Therefore, the visual examination score presented in Figure G.57(a) does not indicate the corrosion of the corrosion-resistant bars but rather the corrosion on the black bar. This plot indirectly demonstrates the nobleness of the bars. For example, the specimen with 316LN in top mat and black bars in the bottom mat had the least corrosion observed on the black bar indicating 316LN is the most noble bar among the corrosion-resistant bars.

With this perspective, regarding the stainless steel bars, 316LN is the best performing bar (most noble; most corrosion-resistant) followed by Duplex 2304, Duplex 2205, and XM-28

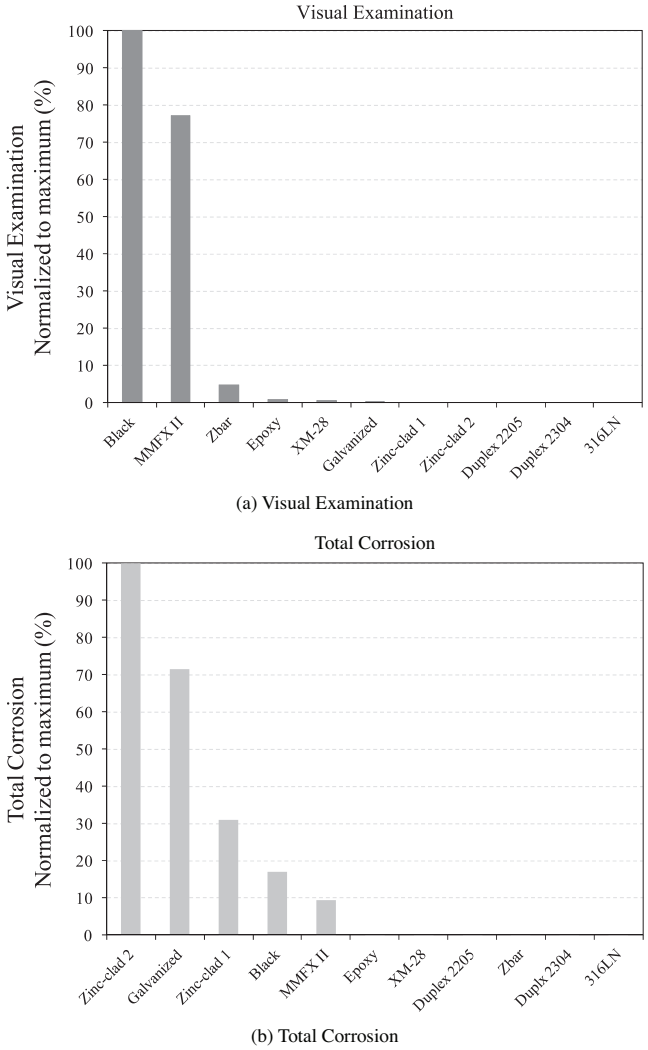

Figure G.56 Evaluation of corrosion resistance (cracked—identical mats).

stainless steel bar. Zinc-clad bars are also more corrosion-resistant (more zinc active; sacrificial; corrosion-resistant) than the galvanized bars potentially due to the thick zinc coating and the richness of the zinc. The rankings are consistent with the observation for the cracked specimens with identical mats. The specimen with Zbar had less corrosion on the black bar compared to the epoxy-coated bar. Therefore, Zbar is assisting in the protection of the black bar even considering that only small regions of zinc were exposed. This bar provided better protection than the epoxy-coated bar. It should be noted that epoxy coating can electrically isolate the mats preventing macrocell corrosion as long as the barrier is not compromised.

G.3.3.3 Summary of ranking. Based on evaluation of the visual examination score and the total charge (total corrosion) measurements, the better performing (more corrosion-resistant) reinforcing bars are ranked in Table G.8. Rankings were based on the visual examination of cracked specimens with identical mats. Specimens that did not have any iron-oxide corrosion were ranked based on the total corrosion measurements. In addition, the results from the cracked specimens with dissimilar mats were used to assist in providing a ranked order because the nobleness of bar could be assessed.

This ranking is based on the test results and visual examination conducted at 503 days of exposure. Extended exposure testing is required as visual corrosion was not evident on a number of bars. This ranking is preliminary and may change in the future when results from extended exposure are available.

G.4. Summary and Conclusions

Macrocell specimens with 11 different corrosion-resistant reinforcing bars were tested to evaluate corrosion resistance of the various materials with a focus on typical bridge deck construction. Of particular interest was the influence on corrosion of full depth cracks which are typical in bridge decks, corrosion at the intersection of longitudinal and transverse reinforcing mats, the effect of galvanic coupling where dissimilar materials are used in the top and bottom reinforcement mats, and the influence of tie material. The cracks for cracked specimens were formed full-depth,

TABLE G.4
Rankings Based on Visual Examination

Cracked Condition	Bar Type	Visual Examination
Cracked—Identical Mats	Black	66
	MMFX II	51
	Zbar	3.1
	Epoxy	0.5
	XM-28	0.4
	Galvanized	0.1
	Zinc-clad 1	0
	Zinc-clad 2	0
	Duplex 2205	0
	Duplex 2304	0
	316LN	0

TABLE G.5
Rankings Based on Total Corrosion Measurements

Cracked Condition	Bar Type	Total Corrosion (C)
Cracked—Identical Mats	Zinc-clad 2	5,573
	Galvanized	3,994
	Zinc-clad 1	1,727
	Black	947
	MMFX II	529
	Epoxy	10
	XM-28	9
	Duplex 2205	8
	Zbar	5
	Duplex 2304	2
	316LN	1

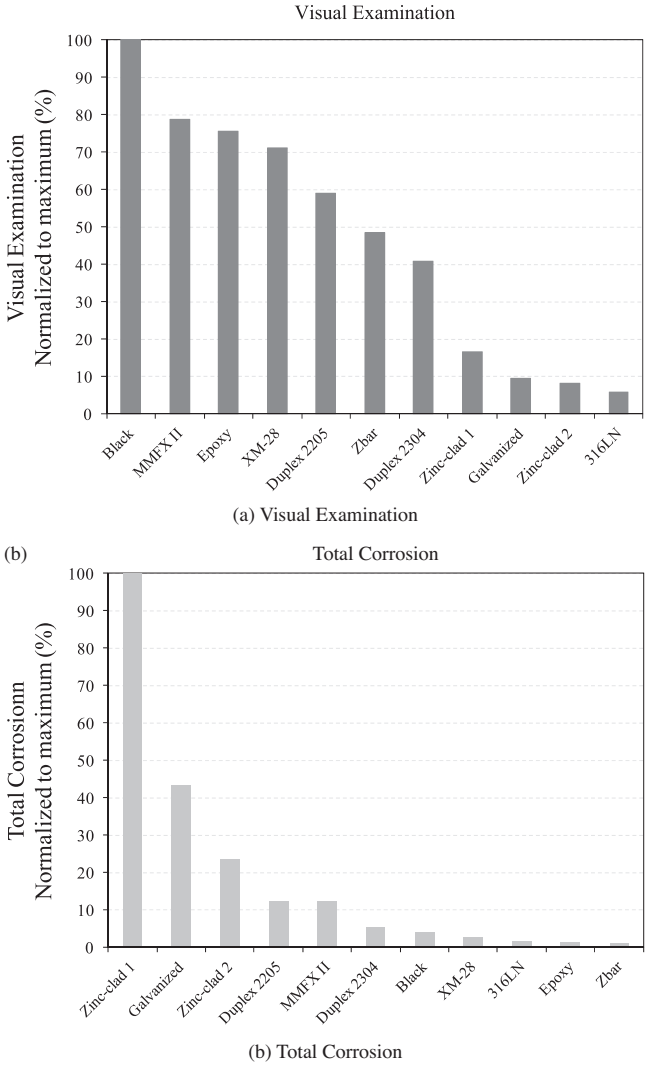

Figure G.57 Evaluation of corrosion resistance (cracked—dissimilar mats).

TABLE G.6
Ranks Based on Visual Examination (Dissimilar Mat)

Cracked Condition	Bar Type	Visual Examination
Cracked—Dissimilar Mats	Black	66
	MMFX II	52
	Epoxy	50
	XM-28	47
	Duplex 2205	39
	Zbar	32
	Duplex 2304	27
	Zinc-clad 1	11
	Galvanized	6.3
	Zinc-clad 2	5.5
	316LN	3.9

TABLE G.7
Ranks Based on Total Corrosion Measurements (Dissimilar Mat)

Cracked Condition	Bar Type	Total Corrosion (C)
Cracked—Dissimilar Mats	Zinc-clad 1	22,532
	Galvanized	9,744
	Zinc-clad 2	5,336
	Duplex 2205	2,781
	MMFX II	2,752
	Duplex 2304	1,212
	Black	947
	XM-28	660
	316LN	381
	Epoxy	355
	Zbar	220

TABLE G.8
Performance of Corrosion-Resistant Reinforcement

Rank	Bar Type	Corrosion Performance
1	316LN	Best
2	Duplex 2304	
3	Duplex 2205	
4	Zinc-clad	
5	Galvanized	
6	XM-28	
7	Zbar	
8	Epoxy	
9	MMFX II	
10	Black	Worst

uniformly, and with an average crack width of 0.020 in. Cracks were normally formed at the location where the transverse steel was tied to the longitudinal steel.

Based on the results of this study, the following conclusions are made:

1. While all uncracked specimens showed relatively very low currents at 503 days of exposure, cracked specimens demonstrated high corrosion activity which was electronically measured by the macrocell test and confirmed by visual examination through an autopsy of the specimen.
2. Autopsy results demonstrated that most of the longitudinal steel (secondary reinforcement in a bridge deck) corroded at the intersection with the transverse steel (primary reinforcement in a bridge deck) while the transverse reinforcement corroded over its entire length. The transverse steel, typically located parallel to the cracks, was under direct chloride exposure over its entire length while the longitudinal steel had direct exposure only at the location of the cracks.
3. When corrosion-resistant chromium based reinforcing steel is used in the top mat and black bars are used in bottom mats, a galvanic couple resulted where the bottom black steel corroded to protect the top corrosion-resistant reinforcement. This galvanic couple occurred because the cracks in the macrocells were formed full depth where chlorides can easily reach the bottom black bars from the first day of testing. This condition is realistic as bridge decks have full-depth cracks which are formed at early ages (<28 days) due to restrained shrinkage. Both

the electrical current measurements and autopsy results demonstrated that mixing reinforcement where black bars are provided in the bottom mat is detrimental to corrosion resistance.

4. Specimens that were tied with black ties indicated more corrosion than specimens with plastic ties. In addition, tying reinforcing steel with dissimilar metallic materials results in galvanic coupling. When stainless steel tie were used to connect black reinforcement, increased damage of the black bars resulted. In addition, black ties used to connect stainless bars resulted in crevice corrosion and pitting of the stainless steel bar. Only similar metallic or inert (plastic) materials should be used to tie reinforcement.
5. Based on corrosion testing and the visual examination at 503 days, a preliminary ranking of corrosion performance was developed and is provided in Table G.8.

APPENDIX H: SURFACE ROUGHNESS, COATING THICKNESS, AND RELATIVE RIB AREA OF CORROSION-RESISTANT REINFORCING BARS

TABLE H.1
Surface Roughness of #5 Bar

Bar Type	Surface Roughness	Measurements 1	2	3	4	5	Avg.
Black	R_{max}	972	1564	873	1140	1092	1128
	P_c	267	273	248	159	197	229
Epoxy	R_{max}	264	344	287	691	561	429
	P_c	32	57	57	38	25	42
Hot-Dip Galvanized	R_{max}	502	922	955	700	1289	874
	P_c	95	165	114	102	83	112
Zinc-clad 1	R_{max}	174	186	536	396	395	337
	P_c	44	44	70	114	70	68
Zinc-clad 2	R_{max}	302	143	384	314	903	409
	P_c	51	76	44	44	64	56
Zbar	R_{max}	325	485	727	419	282	448
	P_c	38	44	76	64	38	52
MMFX II	R_{max}	778	860	754	1063	1094	910
	P_c	203	184	184	203	203	195
316LN	R_{max}	1206	968	854	1138	1101	1053
	P_c	108	127	197	114	140	137
Duplex 2205	R_{max}	875	1056	1090	687	942	930
	P_c	140	146	95	121	127	126
Duplex 2304	R_{max}	1927	973	818	251	900	974
	P_c	146	159	127	108	95	127
XM-28	R_{max}	870	950	861	1007	1185	975
	P_c	108	114	108	95	102	105

Notation:
R_{max} = *maximum roughness depth (μin.).*
P_c = *number of peak/valley pairs.*

TABLE H.2
Surface Roughness of #8 Bar

Bar Type	Surface Roughness	Measurements 1	2	3	4	5	Avg.
Black	R_{max}	1452	2090	1737	1519	1610	1682
	P_c	190	140	159	108	203	160
Epoxy	R_{max}	539	454	376	295	608	454
	P_c	25	44	25	32	57	37
Hot-Dip Galvanized	R_{max}	431	931	872	403	608	649
	P_c	102	95	83	171	102	111
Zinc-clad 1	R_{max}	471	268	120	163	143	233
	P_c	57	25	19	44	51	39
Zinc-clad 2	R_{max}	387	227	329	191	131	253
	P_c	95	76	114	95	64	89
Zbar	R_{max}	369	518	543	486	404	464
	P_c	51	25	32	64	51	45
MMFX II	R_{max}	898	1593	1576	1612	1203	1376
	P_c	95	95	102	146	114	110
316LN	R_{max}	805	783	1037	809	828	852
	P_c	114	184	146	152	165	152
Duplex 2205	R_{max}	1017	701	695	1117	816	869
	P_c	190	159	190	121	178	168
Duplex 2304	R_{max}	738	675	733	612	779	707
	P_c	159	159	133	140	108	140
XM-28	R_{max}	797	611	542	374	1066	678
	P_c	184	152	184	267	248	207

Notation:
R_{max} = *maximum roughness depth (μin.).*
P_c = *number of peak/valley pairs.*

TABLE H.3
Coating Thickness of Coated Reinforcing Bars

Bar Type	Bar Size	Coating Thickness (mils) 1	2	3	4	5	Avg.
Epoxy	#4	12	10	9	11.5	14.5	11.4
	#5	12	13	12	10.5	14	12.3
	#8	12	12	11	11.5	12	11.7
Hot-Dip Galvanized	#4	8.5	2.4	3.5	6	5	5.1
	#5	3.8	7	3	5.5	3.5	4.6
	#8	6	3	4.5	2.3	3	3.8
Zinc-clad 1	#4	22	23	22	23	28	23.6
	#5	15	20	18	18	20	18.2
	#8	20	24	24	23	23	22.8
Zinc-clad 2	#4	28	24	24	24	28	25.6
	#5	20	20	23	22	30	23.0
	#8	45	40	50	40	45	44.0
Zbar	#4	16	16	17	13	18	16.0
	#5	11	11	12	9.5	10	10.7
	#8	10.5	9	14	19	10.5	12.6

TABLE H.4
Rib Height of Coated Reinforcing Bars (#5 Bars)

Bar Type	Readings	Measurement Locations 1	2	3	4	5	Rib Height (mils)
Black	1	35	48	41	50	40	46
	2	36	48	47	46	37	
	3	42	46	50	52	50	
	Avg.	38	47	46	49	42	
Epoxy	1	50	52	54	51	47	51
	2	47	51	56	49	46	
	3	52	50	48	51	47	
	Avg.	50	51	53	50	47	
Hot-Dip Galvanized	1	34	37	36	34	43	37
	2	34	33	39	38	43	
	3	36	37	35	43	41	
	Avg.	35	36	37	38	42	
Zinc-clad 1	1	–	29	29	34	–	31
	2	–	30	34	28	–	
	3	–	28	30	37	–	
	Avg.	–	29	31	33	–	
Zinc-clad 2	1	–	21	37	36	–	29
	2	–	20	36	34	–	
	3	–	16	26	31	–	
	Avg.	–	19	33	34	–	
Zbar	1	39	52	55	54	46	51
	2	35	54	54	54	48	
	3	52	49	51	54	54	
	Avg.	42	52	53	54	49	

TABLE H.5
Rib Height of Chromium Containing Bars (#5 Bars)

Bar Type	Readings	Measurement Locations 1	2	3	4	5	Rib Height (mils)
MMFX II	1	42	41	38	44	42	40
	2	44	41	40	43	38	
	3	36	39	40	39	39	
	Avg.	41	40	39	42	40	
316LN	1	23	36	32	31	23	30
	2	24	37	31	29	22	
	3	19	26	34	33	26	
	Avg.	22	33	32	31	24	
Duplex 2205	1	42	45	43	45	40	43
	2	44	45	44	44	40	
	3	36	42	45	42	39	
	Avg.	41	44	44	44	40	
Duplex 2304	1	26	38	42	26	18	28
	2	14	32	40	18	15	
	3	21	22	41	28	13	
	Avg.	20	31	41	24	15	
XM-28	1	23	36	32	31	23	30
	2	24	37	31	29	22	
	3	19	26	34	33	26	
	Avg.	22	33	32	31	24	

TABLE H.6
Relative Rib Area of Coated Reinforcing Bars (#5 Bars)

Bar Type	Readings	Longitudinal Rib Width (in.) Top	Bot	Area (in.^{2})	Rib Height (in.)	Rib Spacing (in.)	Relative Rib Area
Black	1	111	172	0.012	0.046	0.393	0.106
	2	106	160				
	3	105	165				
	Avg.	107	166				
Epoxy	1	107	170	0.014	0.051	0.395	0.117
	2	106	171				
	3	110	175				
	Avg.	108	172				
Hot-Dip Galvanized	1	56	148	0.008	0.037	0.405	0.086
	2	73	152				
	3	79	159				
	Avg.	69	153				
Zinc-clad 1	1	116	173	0.014	0.031	0.427	0.062
	2	142	210				
	3	122	208				
	Avg.	127	197				
Zinc-clad 2	1	115	187	0.012	0.029	0.421	0.059
	2	143	210				
	3	92	200				
	Avg.	117	199				
Zbar	1	111	188	0.015	0.051	0.399	0.116
	2	100	182				
	3	96	193				
	Avg.	102	188				

TABLE H.7
Relative Rib Area of Chromium Containing Bars (#5 Bars)

Bar Type	Readings	Longitudinal Rib Width (in.) Top	Bot	Area (in.^{2})	Rib Height (in.)	Rib Spacing (in.)	Relative Rib Area
MMFX II	1	106	177	0.012	0.040	0.424	0.087
	2	120	174				
	3	122	182				
	Avg.	116	178				
316LN	1	76	90	0.005	0.032	0.323	0.093
	2	67	101				
	3	74	97				
	Avg.	72	96				
Duplex 2205	1	83	141	0.009	0.043	0.427	0.094
	2	78	139				
	3	85	136				
	Avg.	82	139				
Duplex 2304	1	–	150	0.010	0.028	0.368	0.068
	2	–	212				
	3	–	175				
	Avg.	–	179				
XM-28	1	88	154	0.008	0.030	0.419	0.065
	2	104	159				
	3	85	167				
	Avg.	92	160				

TABLE H.8
Rib Height of Coated Reinforcing Bars (#8 Bars)

Bar Type	Readings	Measurement Locations 1	2	3	4	5	Rib Height (mils)
Black	1	70	72	64	67	53	65
	2	69	72	69	67	52	
	3	60	67	57	62	58	
	Avg.	66	70	63	65	54	
Epoxy	1	52	60	60	60	58	61
	2	53	63	66	61	62	
	3	61	59	60	67	62	
	Avg.	55	61	62	63	61	
Hot-Dip Galvanized	1	46	60	59	54	56	57
	2	45	62	53	57	55	
	3	56	64	54	60	54	
	Avg.	49	62	55	57	55	
Zinc-clad 1	1	58	55	42	51	34	46
	2	53	50	45	44	29	
	3	33	44	58	46	35	
	Avg.	48	50	48	47	33	
Zinc-clad 2	1	40	38	35	33	31	34
	2	40	39	36	33	31	
	3	52	34	22	30	26	
	Avg.	44	37	31	32	29	
Zbar	1	67	65	65	69	61	65
	2	66	67	67	67	58	
	3	61	68	66	64	58	
	Avg.	65	67	66	67	59	

TABLE H.9
Rib Height of Chromium Containing Bars (#8 Bars)

Bar Type	Readings	Measurement Locations 1	2	3	4	5	Rib Height (mils)
MMFX II	1	61	62	65	70	67	63
	2	62	62	66	68	66	
	3	60	58	51	61	69	
	Avg.	61	61	61	66	67	
316LN	1	69	66	65	72	63	68
	2	70	68	66	70	62	
	3	67	67	65	75	65	
	Avg.	69	67	65	72	63	
Duplex 2205	1	52	61	61	60	50	61
	2	57	60	61	60	55	
	3	56	69	65	67	57	
	Avg.	55	63	62	62	54	
Duplex 2304	1	61	50	47	48	45	48
	2	58	50	47	48	55	
	3	50	42	42	53	38	
	Avg.	56	47	45	50	46	
XM-28	1	69	66	65	72	63	68
	2	70	68	66	70	62	
	3	67	67	65	75	65	
	Avg.	69	67	65	72	63	

TABLE H.10
Relative Rib Area of Coated Reinforcing Bars (#8 Bars)

Bar Type	Readings	Longitudinal Rib Width (in.) Top	Bot	Area (in.^{2})	Rib Height (in.)	Rib Spacing (in.)	Relative Rib Area
Black	1	98	198	0.019	0.065	0.616	0.095
	2	108	198				
	3	104	188				
	Avg.	103	195				
Epoxy	1	109	215	0.020	0.061	0.616	0.089
	2	105	208				
	3	120	213				
	Avg.	111	212				
Hot-Dip Galvanized	1	106	215	0.017	0.057	0.671	0.076
	2	87	200				
	3	86	190				
	Avg.	93	202				
Zinc-clad 1	1	145	325	0.023	0.046	0.677	0.057
	2	172	318				
	3	200	356				
	Avg.	172	333				
Zinc-clad 2	1	97	208	0.012	0.034	0.674	0.045
	2	104	240				
	3	96	270				
	Avg.	99	239				
Zbar	1	105	214	0.021	0.065	0.628	0.093
	2	87	212				
	3	86	216				
	Avg.	93	214				

TABLE H.11
Relative Rib Area of Chromium Containing Bars (#8 Bars)

Bar Type	Readings	Longitudinal Rib Width (in.) Top	Bot	Area (in.^{2})	Rib Height (in.)	Rib Spacing (in.)	Relative Rib Area
MMFX II	1	76	152	0.015	0.063	0.646	0.090
	2	90	163				
	3	74	154				
	Avg.	80	156				
316LN	1	74	121	0.010	0.051	0.564	0.085
	2	71	119				
	3	80	111				
	Avg.	75	117				
Duplex 2205	1	142	221	0.022	0.061	0.570	0.094
	2	140	212				
	3	137	230				
	Avg.	140	221				
Duplex 2304	1	–	310	0.023	0.048	0.670	0.061
	2	–	248				
	3	–	163				
	Avg.	–	240				
XM-28	1	136	255	0.024	0.068	0.689	0.087
	2	128	212				
	3	131	223				
	Avg.	132	230				

APPENDIX I: CRACK MEASUREMENT, CRACK PATTERNS, AND AS-BUILT DIMENSIONS OF LAP-SPLICE BEAM SPECIMENS

TABLE I.1
Crack Measurements (B-6-S-15)

		Crack Width (1/1000 in.)							
		Crack No.							
Load, P (kips)	**Bar Stress (ksi)**	**1**	**2**	**3**	**4**	**5**	**6**	**Avg. Crack Width (mils)**	**Max Crack Width (mils)**
8	17.1		3			3	3	0	3
10	21.4		3			3	4	3.0	4
12	25.7	4	4			3	5	3.3	5
14	30.1	5	5	5	3	6	5	4.0	6
16	34.4	6	6	5	3	7	6	4.8	7
18	38.9	6	7	5		5	7	5.5	7
20	43.0	9	7	5		9	7	6.0	9
22	47.4	10	10	10		10	10	7.4	10

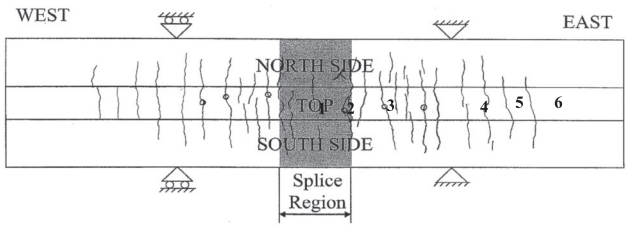

Figure I.1 Crack pattern and measurement locations (B-6-S-15).

TABLE I.2
Crack Measurements (ZC1-6-S-15)

		Crack Width (1/1000 in.)					
		Crack No.					
Load, P (kips)	**Bar Stress (ksi)**	**1**	**2**	**3**	**4**	**Avg. Crack Width (mils)**	**Max Crack Width (mils)**
8	17.2				3	3	3
10	21.4	4			5	4.5	5
12	25.7	6			6	6	6
14	30.2	7	7	7	7	7	7
16	34.5	7	7	8	7	7.25	8

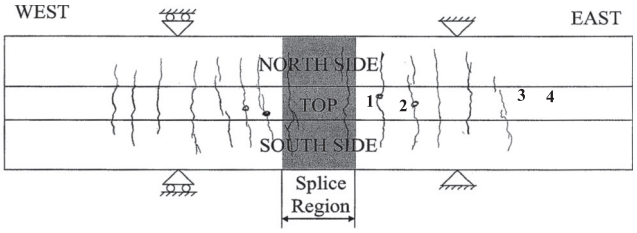

Figure I.2 Crack pattern and measurement locations (ZC1-6-S-15).

TABLE I.3
Crack Measurements (B-6-S-15)

		Crack Width (1/1000 in.)							
		Crack No.							
Load, P (kips)	Bar Stress (ksi)	1	2	3	4	5	6	Avg. Crack Width (mils)	Max Crack Width (mils)
10	20.1	4	3			4	4	3.8	4
12	24.2	5	5	4	5	4	5	4.7	5
14	28.2	5	6	5	6	4	7	5.5	7
16	32.2	7	6	6	8	4	8	6.5	8
18	36.2	10	7	7	10	4	7	7.5	10
20	40.2	10	10	10	10	7	10	9.5	10
22	44.3	10	10	10	10	10	10	10.0	10
24	48.3	10	10	10	12	10	10	10.3	12

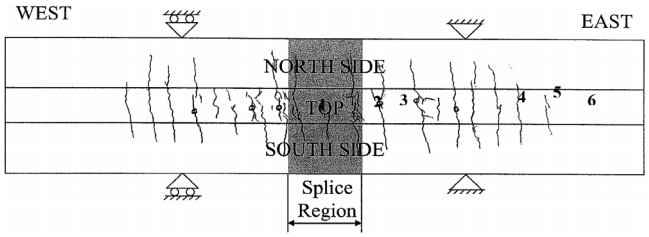

Figure I.3 Crack pattern and measurement locations (B-6-S-15).

TABLE I.4
Crack Measurements (ZC1-6-F-15)

		Crack Width (1/1000 in.)					
		Crack No.					
Load, P (kips)	Bar Stress (ksi)	1	2	3	4	Avg. Crack Width (mils)	Max Crack Width (mils)
8	16.1	5	4	3	3	3.75	5
10	20.1	6	5	4	7	5.5	7
12	24.2	10	10	4	10	8.5	10
14	28.2	10	10	10	10	10	10
16	32.2	14	10	12	12	12	14
18	36.2	15	12	15	12	13.5	15
20	40.3	15	12	15	15	13.5	15
22	44.5	15	15	15	15	15	15

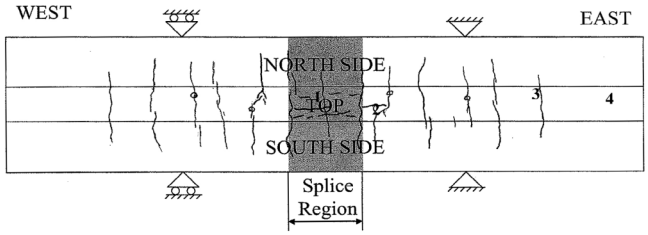

Figure I.4 Crack pattern and measurement locations (ZC1-6-F-15).

TABLE I.5
Crack Measurements (B-5-S-12)

		Crack Width (1/1000 in.)					
		Crack No.					
Load, P (kips)	Bar Stress (ksi)	1	2	3	4	Avg. Crack Width (mils)	Max Crack Width (mils)
6	18.2	2			2	2	2
7	21.3	3	2	2	3	3	3
8	24.3	4	3	3	4	4	4
9	27.3	4	4	4	4	4	4
10	30.4	6	4	4	5	5	6
11	33.6	6	5	5	5	5	6
12	36.7	7	6	5	6	6	7
13	39.8	7	6	6	6	6	7
15	45.9	15	10	10	10	11	15
16	48.9	20	15	15	15	16	20

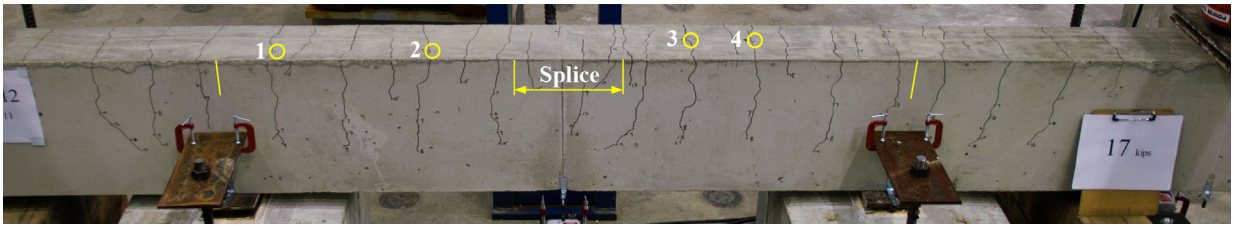

Figure I.5 Crack pattern and measurement locations (B-5-S-12).

TABLE I.6
Crack Measurements (E-5-S-12)

		Crack Width (1/1000 in.)							
		Crack No.							
Load, P (kips)	Bar Stress (ksi)	1	2	3	4	5	6	Avg. Crack Width (mils)	Max Crack Width (mils)
6	18.2	2	2	2					
7	21.3	3	3	3	3	3	3	2	2
8	24.3	4	3	4	4	4	4	3	3
9	27.3	5	4	5	5	5	5	4	4
10	30.4	6	5	5	6	5	6	5	5
11	33.6	7	5	6	7	6	7	6	6
12	36.7	10	6	6	7	6	10	6	7
13	39.8	15	10	7	10	7	10	8	10
15	45.9	15	10	10	10	10	15	10	15
16	48.9	15	10	10	10	10	15	12	15

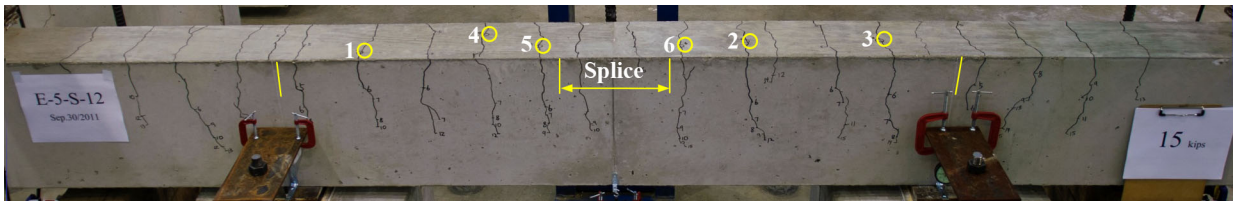

Figure I.6 Crack pattern and measurement locations (E-5-S-12).

TABLE I.7
Crack Measurements (G-5-S-12)

		Crack Width (1/1000 in.)						
		Crack No.						
Load, P (kips)	Bar Stress (ksi)	1	2	3	4	5	Avg. Crack Width (mils)	Max Crack Width (mils)
6	18.2							
7	21.3	4	3				4	4
8	24.3	4	4	3	3		4	4
9	27.3	5	5	5	4		5	5
10	30.4	6	5	5	5		5	6
11	33.6	6	6	6	6	4	6	6
12	36.7	7	7	6	6	5	6	7
13	39.8	7	7	7	7	6	7	7
14	45.9	10	7	7	8	7	8	10
15	48.9	10	7	8	8	7	8	10

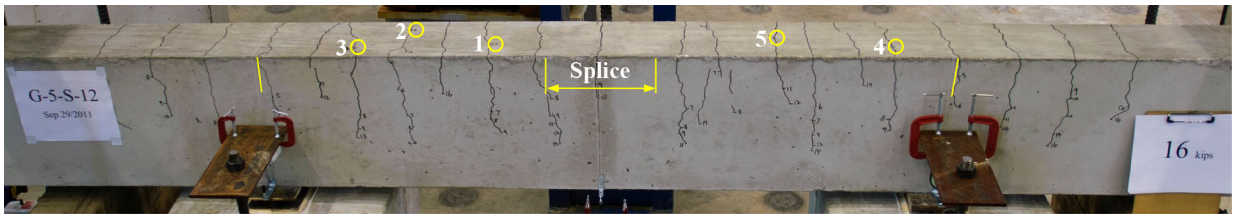

Figure I.7 Crack pattern and measurement locations (G-5-S-12).

TABLE I.8
Crack Measurements (ZC1-5-S-12)

		Crack Width (1/1000 in.)					
		Crack No.					
Load, P (kips)	Bar Stress (ksi)	1	2	3	4	Avg. Crack Width (mils)	Max Crack Width (mils)
6	18.2	3				3	3
7	21.3	4	4			4	4
8	24.3	5	5	4	4	5	5
9	27.3	6	5	4	5	5	6
10	30.4	7	6	6	6	6	7
11	33.6	9	7	7	7	8	9

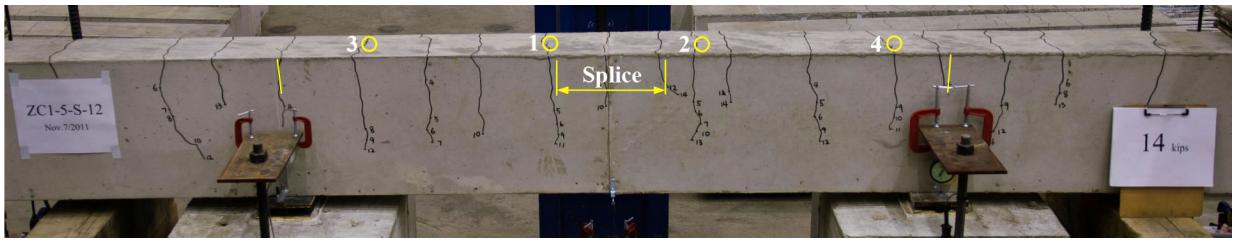

Figure I.8 Crack pattern and measurement locations (ZC1-5-S-12).

TABLE I.9
Crack Measurements (ZC2-5-S-12)

		Crack Width (1/1000 in.)					
		Crack No.					
Load, P (kips)	Bar Stress (ksi)	1	2	3	4	Avg. Crack Width (mils)	Max Crack Width (mils)
6	18.2						
7	21.3						
8	24.3						
9	27.3	7	6	7		7	7
10	30.4	10	6	8		8	10
11	33.6	12	6	10	4	8	12

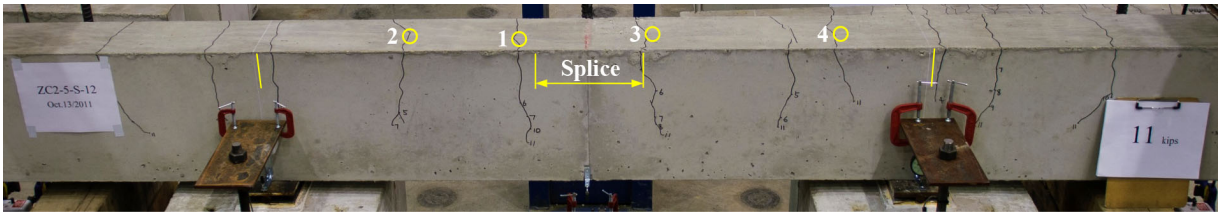

Figure I.9 Crack pattern and measurement locations (ZC2-5-S-12).

TABLE I.10
Crack Measurements (Z-5-S-12)

		Crack Width (1/1000 in.)					
		Crack No.					
Load, P (kips)	Bar Stress (ksi)	1	2	3	4	Avg. Crack Width (mils)	Max Crack Width (mils)
6	18.3	2	–	–	–		
7	21.3	3	3	3	3	2	2
8	24.3	4	4	4	4	3	3
9	27.4	5	5	5	5	4	4
10	30.4	6	6	6	6	5	5
11	33.6	6	7	7	6	6	6
12	36.8	7	7	8	6	7	7
13	39.6	7	8	9	7	7	8
14	42.7	10	9	10	7	8	9
15	45.8	12	10	12	8	9	10
16	48.8	13	10	15	8	11	12

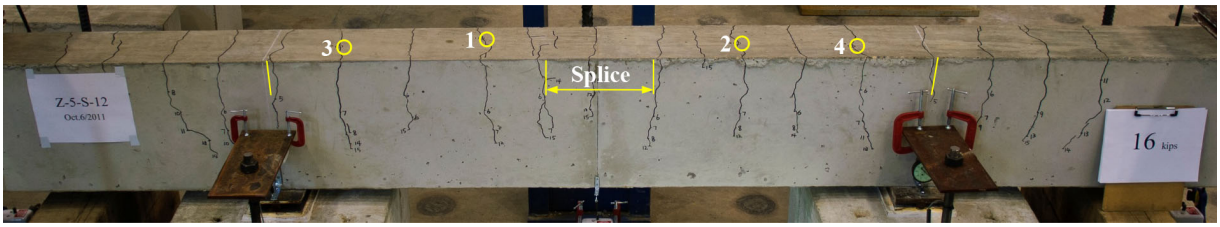

Figure I.10 Crack pattern and measurement locations (Z-5-S-12).

TABLE I.11
Crack Measurements (M-5-S-12)

		Crack Width (1/1000 in.)							
		Crack No.							
Load, P (kips)	Bar Stress (ksi)	1	2	3	4	5	6	Avg. Crack Width (mils)	Max Crack Width (mils)
6	18.3	3	2.5					2.8	3.0
8	24.4	4	4	4	5	3.5		4.1	5.0
10	30.5	5.5	6	5	6	5		5.5	6.0
12	36.5	6	7	6	7	6	4	6.0	7.0
14	42.7	7	8	7	8	7	4.5	6.9	8.0
16	49.0	8	9	8	10	8	5	8.0	10.0

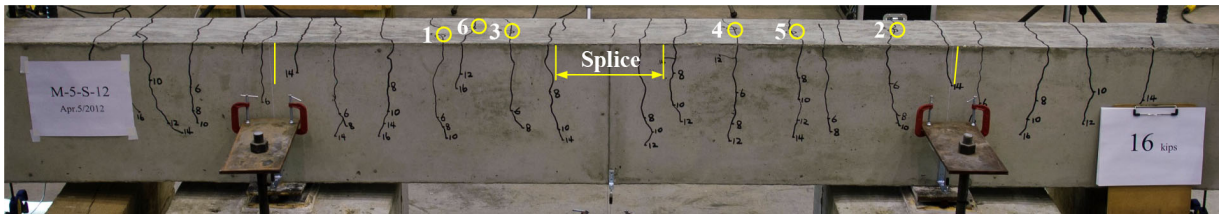

Figure I.11 Crack pattern and measurement locations (M-5-S-12).

TABLE I.12
Crack Measurements (S316LN-5-S-12)

		Crack Width (1/1000 in.)					
		Crack No.					
Load, P (kips)	Bar Stress (ksi)	1	2	3	4	Avg. Crack Width (mils)	Max Crack Width (mils)
6	18.2	3	–	–	–	3	3
7	21.2	4	2	–	–	3	4
8	24.2	5	4	–	–	5	5
9	27.2	5	5	3		4	5
10	30.3	6	5	4	4	5	6
11	33.3	6	6	4	6	6	6
12	36.9	7	7	5	7	7	7
13	39.8	8	7	5	7	7	8
14	42.9	8	7	6	8	7	8
15	46.0	10	9	6	9	9	10
16	49.0	12	10	7	12	10	12

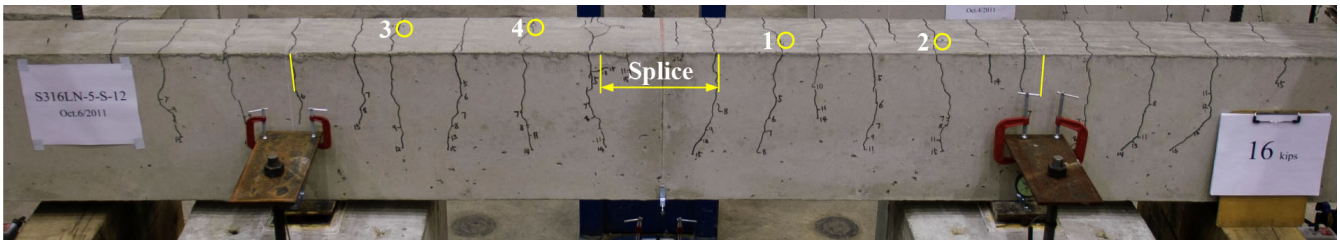

Figure I.12 Crack pattern and measurement locations (S316LN-5-S-12).

TABLE I.13
Crack Measurements (S2205-5-S-12)

		Crack Width (1/1000 in.)						
		Crack No.						
Load, P (kips)	Bar Stress (ksi)	1	2	3	4	5	Avg. Crack Width (mils)	Max Crack Width (mils)
6	18.1	3	3				3	3
7	21.1	4	4	2	3	–	3	4
8	24.1	5	5	4	4	3	4	5
9	27.1	6	5	5	4	3	5	6
10	30.1	7	6	6	5	3	5	7
11	33.1	10	7	7	5	3	6	10
12	36.4	10	10	10	5	3	8	10
13	39.4	10	10	10	6	7	9	10
14	42.3	10	10	10	6	10	9	10
15	45.3	15	10	10	7	10	10	15
16	48.4	15	15	15	10	10	13	15

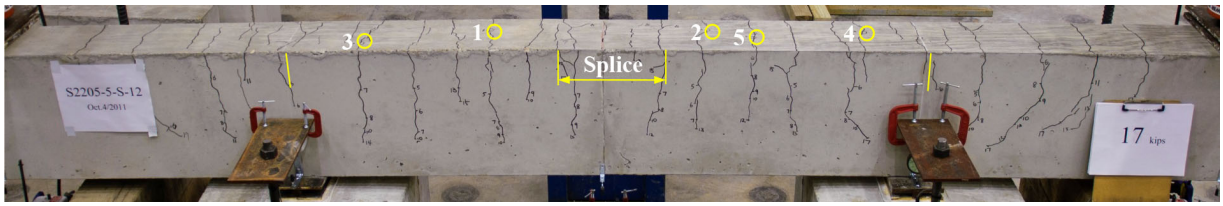

Figure I.13 Crack pattern and measurement locations (S2205-5-S-12).

TABLE I.14
Crack Measurements (S2304-5-S-12)

		Crack Width (1/1000 in.)							
		Crack No.							
Load, P (kips)	Bar Stress (ksi)	1	2	3	4	5	6	Avg. Crack Width (mils)	Max Crack Width (mils)
6	18.2	2	–	–	–	–	–	2	2
7	21.2	3	2	2	3	3		3	3
8	24.2	4	4	3	4	4	4	4	4
9	27.2	5	5	3	5	4	5	5	5
10	30.3	6	6	4	6	5	6	6	6
11	33.3	7	6	4	7	6	7	6	7
12	36.3	7	7	4	7	7	7	7	7
13	39.9	10	10	6	10	10	10	9	10
14	42.8	10	10	7	10	10	10	10	10
15	46.0	15	10	10	10	10	10	11	15
16	49.0	15	10	10	10	10	10	11	15
17	51.9	15	10	10	15	15	10	13	15

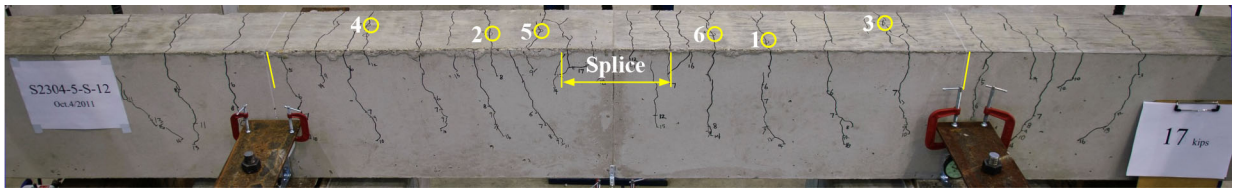

Figure I.14 Crack pattern and measurement locations (S2304-5-S-12).

TABLE I.15
Crack Measurements (SXM28-5-S-12)

		Crack Width (1/1000 in.)					
		Crack No.					
Load, P (kips)	Bar Stress (ksi)	1	2	3	4	Avg. Crack Width (mils)	Max Crack Width (mils)
6	18.2						
7	21.3	2				2	2
8	24.3	3	4			4	4
9	27.3	4	5	4	4	4	5
10	30.4	4	5	4	5	5	5
11	33.4	5	6	6	5	6	6
12	36.8	6	7	6	6	6	7
13	39.7	7	7	7	7	7	7
14	42.7	7	8	7	7	7	8
15	45.9	8	8	7	8	8	8
16	49.0	10	10	9	9	10	10

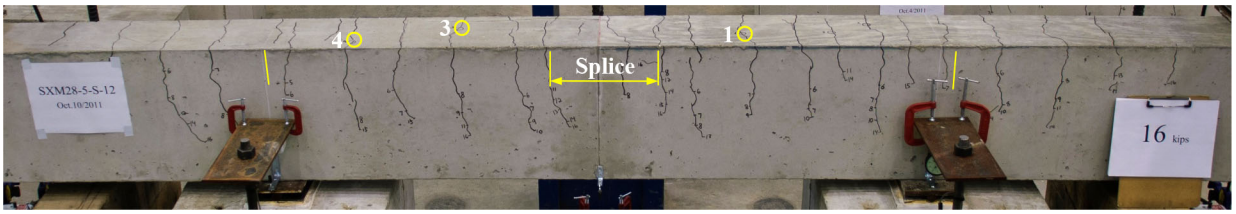

Figure I.15 Crack pattern and measurement locations (SXM28-5-S-12).

TABLE I.16
Crack Measurements (B-8-S-24)

		Crack Width (1/1000 in.)						
		Crack No.						
Load, P (kips)	Bar Stress (ksi)	1	2	3	4	5	Avg. Crack Width (mils)	Max Crack Width (mils)
10	12.7	2	2				2.0	2.0
12	15.2	2.5	2.5				2.5	2.5
14	17.8	3	3				3.0	3.0
16	20.4	4	3	4			3.7	4.0
18	23.0	5	3.5	4	5		4.4	5.0
20	25.7	5	4	5	6		5.0	6.0
22	28.3	6	4	6	7	5	5.6	7.0
24	30.9	6	5	7	9	6	6.6	9.0
26	33.4	7	5	8	10	6	7.2	10.0
28	36.0	7	6	9	12	7	8.2	12.0
32	41.4	9	7	10	16	8	10.0	16.0

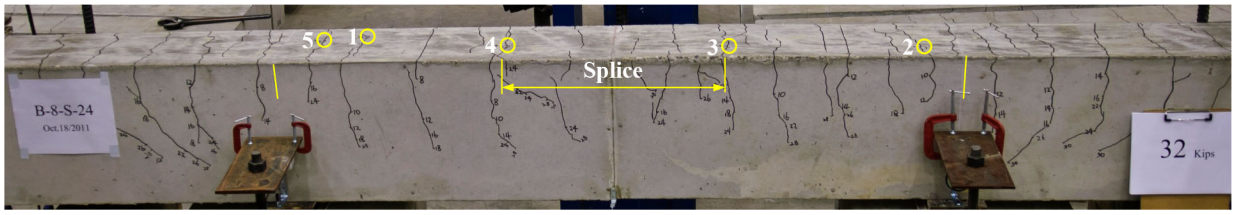

Figure I.16 Crack pattern and measurement locations (B-8-S-24).

TABLE I.17
Crack Measurements (E-8-S-24)

		Crack Width (1/1000 in.)					
		Crack No.					
Load, P (kips)	Bar Stress (ksi)	1	2	3	4	Avg. Crack Width (mils)	Max Crack Width (mils)
10	12.7	3	3	–	–	3.0	3.0
12	15.2	3	4	3.5	–	3.5	4.0
14	17.8	4	5	4	4	4.3	5.0
16	20.4	5	5	4.5	4	4.6	5.0
18	22.9	6	5	5	5	5.3	6.0
20	25.6	7	6	5.5	5.5	6.0	7.0
22	28.2	8	6	5.5	6	6.4	8.0
24	30.7	9	6	6	7	7.0	9.0
26	33.4	10	6.5	6	8	7.6	10.0
28	36.0	12	7	7	9	8.8	12.0

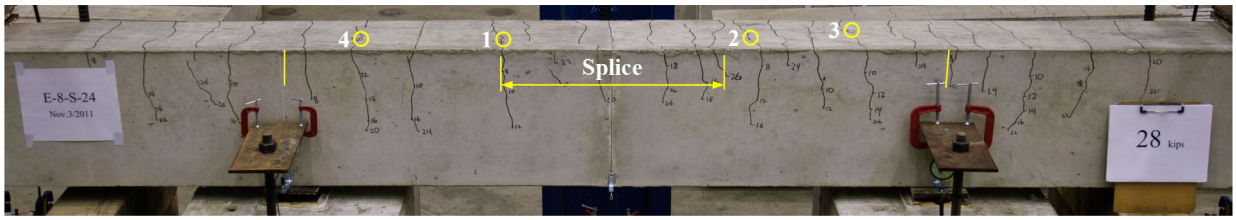

Figure I.17 Crack pattern and measurement locations (E-8-S-24).

TABLE I.18
Crack Measurements (G-8-S-24)

		Crack Width (1/1000 in.)							
		Crack No.							
Load, P (kips)	Bar Stress (ksi)	1	2	3	4	5	6	Avg. Crack Width (mils)	Max Crack Width (mils)
10	12.7								
12	15.3	2	2	3				2.3	3.0
14	18.0	3.5	3	4	3.5			3.5	4.0
16	20.4	4	3.5	4.5	4	4	4	4.0	4.5
18	23.0	4.5	3.5	5	5	4.5	4	4.4	5.0
20	25.7	5	4	6	5	5	4.5	4.9	6.0
22	28.3	5.5	4.5	7	5.5	5.5	5	5.5	7.0
24	30.9	6	4.5	8	6	6	5	5.9	8.0
26	33.5	6.5	5.5	9	7	6.5	5.5	6.7	9.0
28	36.1	7	6	10	8	7	6	7.3	10.0

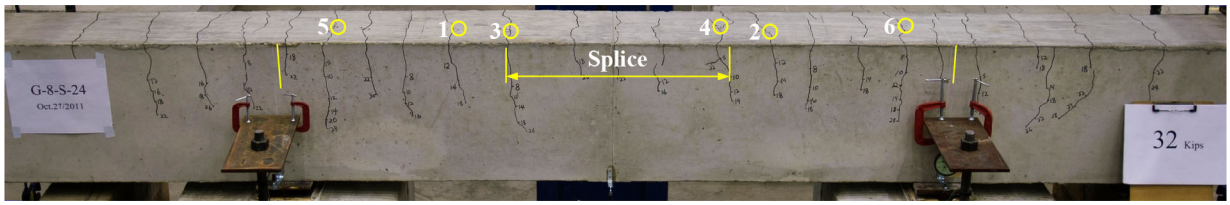

Figure I.18 Crack pattern and measurement locations (G-8-S-24).

TABLE I.19
Crack Measurements (ZC1-8-S-24)

		Crack Width (1/1000 in.)					
		Crack No.					
Load, P (kips)	Bar Stress (ksi)	1	2	3	4	Avg. Crack Width (mils)	Max Crack Width (mils)
10	12.7	4	3.5	3.5	4	3.8	4.0
12	15.3	5	4	5	5.5	4.9	5.5
14	18.0	6	5.5	6	5.5	5.8	6.0
16	20.4	6.5	6	7	6.5	6.5	7.0
18	23.0	7	7	8	7	7.3	8.0
20	25.7	7	8	9	8	8.0	9.0
22	28.3	8	9	10	9	9.0	10.0
24	30.9	9	9	12	10	10.0	12.0
26	33.5	10	10	16	12	12.0	16.0

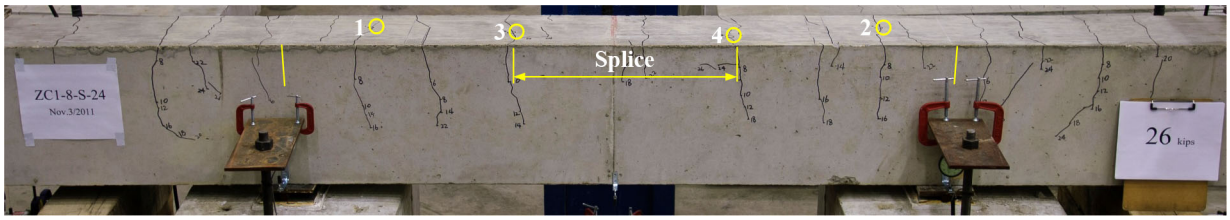

Figure I.19 Crack pattern and measurement locations (ZC1-8-S-24).

TABLE I.20
Crack Measurements (ZC2-8-S-24)

		Crack Width (1/1000 in.)					
		Crack No.					
Load, P (kips)	Bar Stress (ksi)	1	2	3	4	Avg. Crack Width (mils)	Max Crack Width (mils)
10	12.7	4	5	–	–	4.5	5.0
12	15.3	6	6	–	–	6.0	6.0
14	17.8	7	7	4	–	6.0	7.0
16	20.7	8	8	5	–	7.0	8.0
18	23.2	9	9	6	–	8.0	9.0
20	25.8	10	10	7	–	9.0	10.0
22	28.5	12	12	8	3	8.8	12.0
24	31.0	12	13	9	4	9.5	13.0

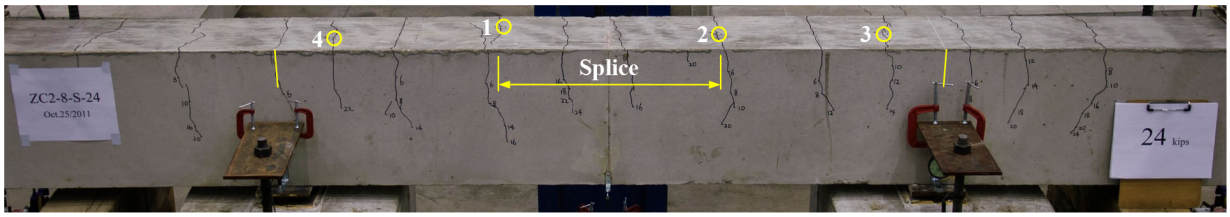

Figure I.20 Crack pattern and measurement locations (ZC2-8-S-24).

TABLE I.21
Crack Measurements (Z-8-S-24)

		Crack Width (1/1000 in.)					
		Crack No.					
Load, P (kips)	Bar Stress (ksi)	1	2	3	4	Avg. Crack Width (mils)	Max Crack Width (mils)
10	12.7	3	3			3.0	3.0
12	15.9	4	3.5			3.8	4.0
14	17.9	5	5			5.0	5.0
16	20.5	5	5	4	4	4.5	5.0
18	23.0	6	6	5	5	5.5	6.0
20	25.7	7	6	5	5	5.8	7.0
24	30.8	7	7	6	6	6.5	7.0
26	33.4	8	8	6	7	7.3	8.0
28	36.0	9	9	7	7	8.0	9.0
30	38.7	10	10	7	8	8.8	10.0
32	41.3	12	12	7	8	9.8	12.0

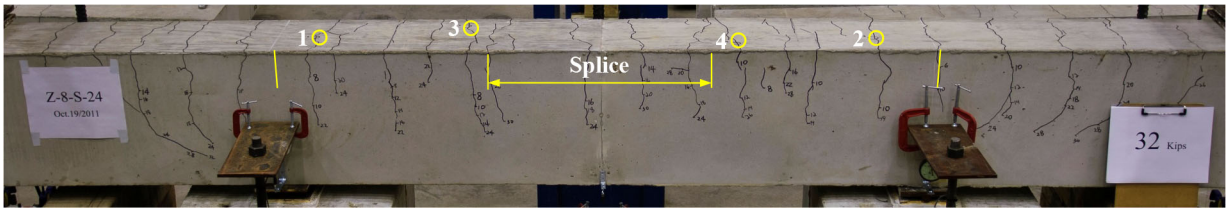

Figure I.21 Crack pattern and measurement locations (Z-8-S-24).

TABLE I.22
Crack Measurements (M-8-S-24)

		Crack Width (1/1000 in.)							
		Crack No.							
Load, P (kips)	Bar Stress (ksi)	1	2	3	4	5	6	Avg. Crack Width (mils)	Max Crack Width (mils)
10	12.7								
12	15.3	2	2	–	–	–	–	2.0	2.0
14	17.8	3	3	–	–	–	–	3.0	3.0
16	20.6	3.5	3	3.5	–	–	–	3.3	3.5
18	23.2	4	4	4	4	–	–	4.0	4.0
20	25.8	5	4.5	4	4	–	–	4.4	5.0
22	28.4	5.5	5	5	4	–	–	4.9	5.5
24	31.1	6	5	5.5	5	–	–	5.4	6.0
26	33.7	7	5.5	6	5.5	6	6	6.0	7.0
28	36.4	8	6	6.5	6	6	7	6.6	8.0
30	39.0	10	6	6.5	6	6	8	7.1	10.0
32	41.7	10	6.5	7	6	6.5	9	7.5	10.0

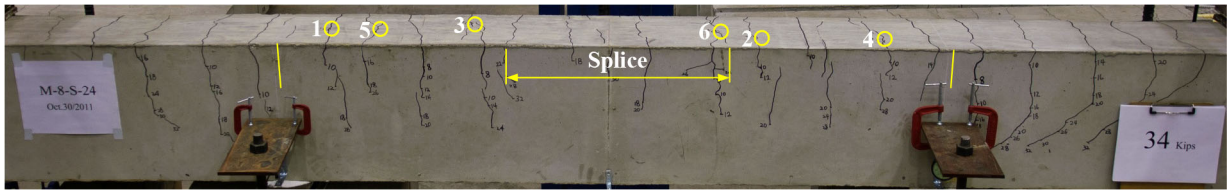

Figure I.22 Crack pattern and measurement locations (M-8-S-24).

TABLE I.23
Crack Measurements (S316LN-8-S-24)

		Crack Width (1/1000 in.)						
		Crack No.						
Load, P (kips)	Bar Stress (ksi)	1	2	3	4	5	Avg. Crack Width (mils)	Max Crack Width (mils)
10	12.6	2	2	–	–	–	2.0	2.0
12	15.2	3	3	3	–	–	3.0	3.0
14	17.7	3	4	4	–	–	3.7	4.0
16	20.3	4	5	4.5	–	–	4.5	5.0
18	22.9	4	6	5	–	–	5.0	6.0
20	25.4	4.5	7	5	4	6	5.3	7.0
22	28.1	5	8	6	5	7	6.2	8.0
24	30.6	6	10	6	6	7	7.0	10.0
26	33.4	7	12	8	7	8	8.4	12.0
28	35.9	8	13	9	8	10	9.6	13.0
30	38.6	8	14	10	9	12	10.6	14.0
32	41.2	9	16	12	10	13	12.0	16.0

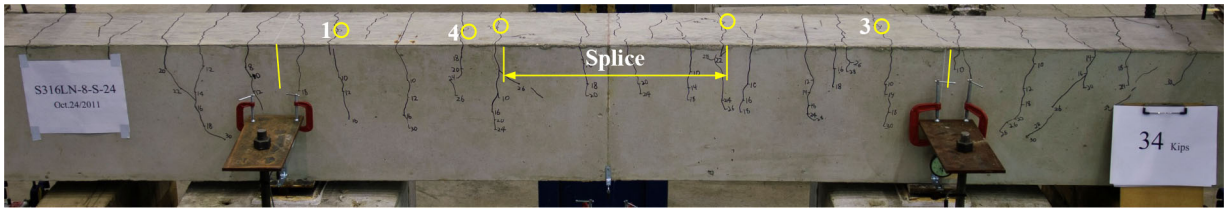

Figure I.23 Crack pattern and measurement locations (S316LN-8-S-24).

TABLE I.24
Crack Measurements (S2205-8-S-24)

		Crack Width (1/1000 in.)						
		Crack No.						
Load, P (kips)	Bar Stress (ksi)	1	2	3	4	5	Avg. Crack Width (mils)	Max Crack Width (mils)
10	12.5	2	3				2.5	3.0
12	15.0	3	3.5	3			3.2	3.5
14	17.7	4	4.5	4			4.2	4.5
16	20.2	5	5	4.5	4		4.6	5.0
18	22.7	5.5	6	5.5	4.5		5.4	6.0
20	25.2	6	7	6	4.5		5.9	7.0
22	27.9	7	8	7	5	6	6.6	8.0
24	30.4	8	9	8	5.5	6	7.3	9.0
26	33.0	10	12	9	6	6.5	8.7	12.0
28	35.7	12	13	10	6.5	7	9.7	13.0

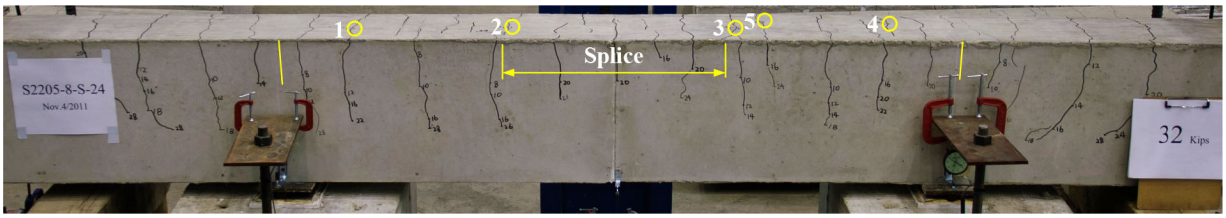

Figure I.24 Crack pattern and measurement locations (S2205-8-S-24).

TABLE I.25
Crack Measurements (S2304-8-S-24)

		Crack Width (1/1000 in.)						
		Crack No.						
Load, P (kips)	Bar Stress (ksi)	1	2	3	4	5	Avg. Crack Width (mils)	Max Crack Width (mils)
10	12.5	2	–	3	–	–	2.5	3.0
12	15.1	2.5	2	3.5	3.5	2	2.7	3.5
14	17.7	3	3	4	4	3	3.4	4.0
16	20.4	4	4	5	5	3.5	4.3	5.0
18	23.0	5	5	6	6	4	5.2	6.0
20	25.5	5.5	5	7	6.5	5	5.8	7.0
22	28.2	6	5.5	8	7	5.5	6.4	8.0
24	30.7	6	6	10	8	6	7.2	10.0
26	33.2	7	6.5	12	9	6	8.1	12.0
28	35.9	8	7	13	10	6	8.8	13.0
30	38.5	9	8	16	12	7	10.4	16.0

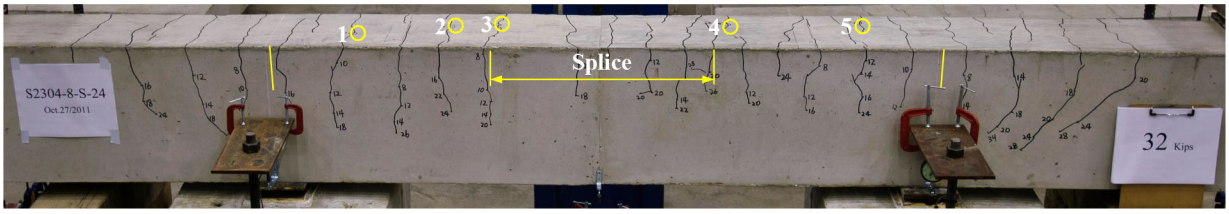

Figure I.25 Crack pattern and measurement locations (S2304-8-S-24).

TABLE I.26
Crack Measurements (XM28-8-S-24)

		Crack Width (1/1000 in.)							
		Crack No.							
Load, P (kips)	Bar Stress (ksi)	1	2	3	4	5	6	Avg. Crack Width (mils)	Max Crack Width (mils)
10									
12									
14	17.8	2	4	3	4			3.3	4.0
16	20.8	3	5	4	4			4.0	5.0
18	23.4	4	6	4	5			4.8	6.0
20	26.0	4	7	5	5			5.3	7.0
22	28.6	4	8	6	6	4	5	5.5	8.0
24	31.3	5	10	7	7	4	6	6.5	10.0
26	33.8	5	12	8	7	5	6	7.2	12.0
28	36.5	6	16	10	8	5	7	8.7	16.0

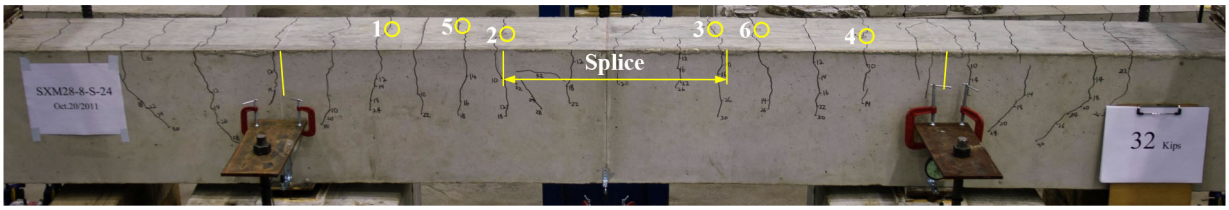

Figure I.26 Crack pattern and measurement locations (XM28-8-S-24).

TABLE I.27
Crack Measurements (B-5-F-12)

		Crack Width (1/1000 in.)							
		Crack No.							
Load, P (kips)	Bar Stress (ksi)	1	2	3	4	5	6	Avg. Crack Width (mils)	Max Crack Width (mils)
8	22.5	3	3					3.0	3.0
10	28.1	4.5	5	4.5	4			4.5	5.0
12	33.7	6	7	6	5.5	6	6	6.1	7.0
13	36.5	7	8	6.5	6	7	7	6.9	8.0
14	39.3	7	9	7	6.5	8	7	7.4	9.0
15	42.1	7	10	7	7	8	7	7.7	10.0
16	45.1	7	10	8	8	9	8	8.3	10.0
17	47.8	8	10	9	8	10	9	9.0	10.0
18	50.4	10	11	10	9	10	10	10.0	11.0
19	53.6	10	12	10	9	10	11	10.3	12.0
20	56.2	11	13	10	10	12	12	11.3	13.0

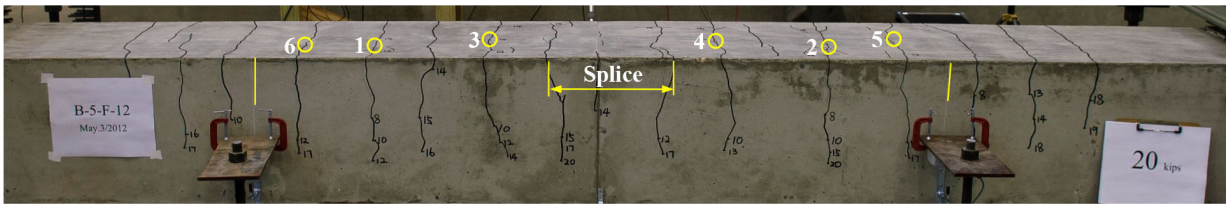

Figure I.27 Crack pattern and measurement locations (B-5-F-12).

TABLE I.28
Crack Measurements (ZC2-5-F-12)

		Crack Width (1/1000 in.)					
		Crack No.					
Load, P (kips)	Bar Stress (ksi)	1	2	3	4	Avg. Crack Width (mils)	Max Crack Width (mils)
8	22.5	7	7	6	3	5.8	7.0
9	25.3	8	9	7	6	7.5	9.0
10	28.1	9	10	9	8	9.0	10.0
11	30.9	10	11	10	10	10.3	11.0
12	33.7	11	13	10	11	11.3	13.0
13	36.5	12	14	13	13	13.0	14.0
14	39.3	13	16	13	13	13.8	16.0
15	42.1	16	17	16	16	16.3	17.0

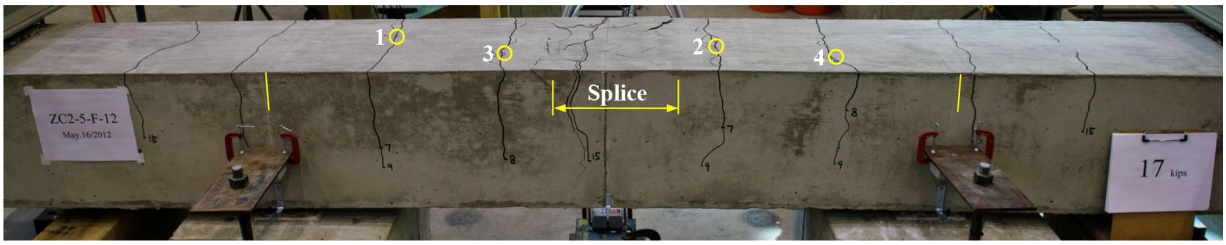

Figure I.28 Crack pattern and measurement locations (ZC2-5-F-12).

TABLE I.29
Crack Measurements (Z-5-F-12)

		Crack Width (1/1000 in.)							
		Crack No.							
Load, P (kips)	Bar Stress (ksi)	1	2	3	4	5	6	Avg. Crack Width (mils)	Max Crack Width (mils)
8	22.5	4	5					4.5	5.0
10	25.3	4.5	6	4				4.8	6.0
12	28.1	5	7	5	6			5.8	7.0
13	30.9	6	8	6	6			6.5	8.0
14	33.7	6	9	6	7			7.0	9.0
15	36.5	7	10	7	8	6	5	7.2	10.0
16	39.3	9	11	7	9	7	6	8.2	11.0
17	42.1	10	13	9	10	7	7	9.3	13.0

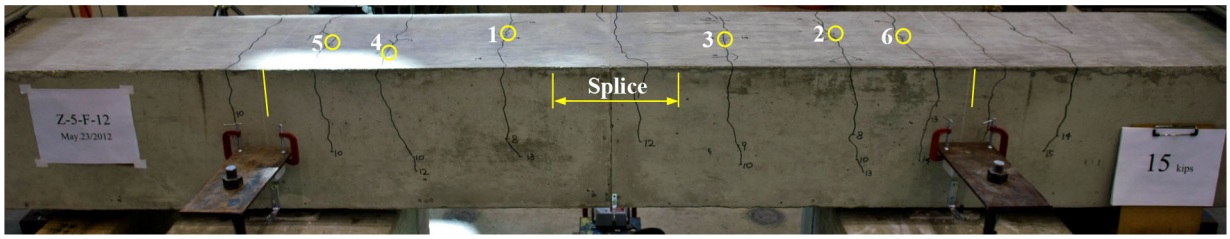

Figure I.29 Crack pattern and measurement locations (Z-5-F-12).

TABLE I.30
Crack Measurements (S2205-5-F-12)

		Crack Width (1/1000 in.)							
		Crack No.							
Load, P (kips)	Bar Stress (ksi)	1	2	3	4	5	6	Avg. Crack Width (mils)	Max Crack Width (mils)
9	25.1	4	4	3.5	4			3.9	4.0
10	27.9	5.5	6	5.5	6			5.8	6.0
11	30.7	7	6.5	7	7			6.9	7.0
12	33.5	7	7	8	8			7.5	8.0
13	36.3	7	8	9	9	7	7	7.8	9.0
14	39.1	7	8	9	9	8	8	8.2	9.0
15	41.9	7	9	10	10	9	9	9.0	10.0
16	44.6	7	10	11	11	10	10	9.8	11.0
17	47.6	7	12	12	12	11	12	11.0	12.0

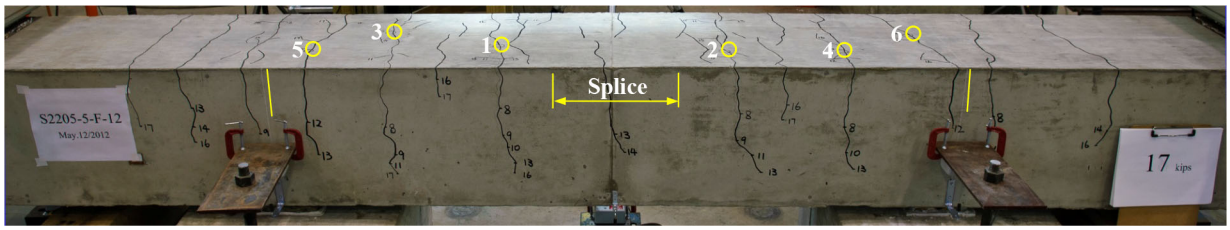

Figure I.30 Crack pattern and measurement locations (S2205-5-F-12).

TABLE I.31
Crack Measurements (B-8-S-24-C1)

		Crack Width (1/1000 in.)							
		Crack No.							
Load, P (kips)	Bar Stress (ksi)	1	2	3	4	5	6	Avg. Crack Width (mils)	Max Crack Width (mils)
8	10.1	2	2	2				2.0	2.0
10	12.7	2.5	2.5	2.5	2			2.4	2.5
12	15.2	3	3	3	3	2.5		2.9	3.0
14	17.9	3.5	3.5	3.5	3.5	3		3.4	3.5
16	20.4	4	4	4	4	3.5		3.9	4.0
18	23.0	4.5	4.5	5	5.5	4		4.7	5.5
20	25.5	5	5	5.5	6	5	5	5.3	6.0
24	28.0	6	6	7	7	6	7	6.5	7.0
28	30.7	7	7	8	9	7	8	7.7	9.0
32	35.8	8	7	9	13	8	10	9.2	13.0
36	41.2	9	8	10	14	9	13	10.5	14.0
38	46.4	10	9	10	15	10	14	11.3	15.0

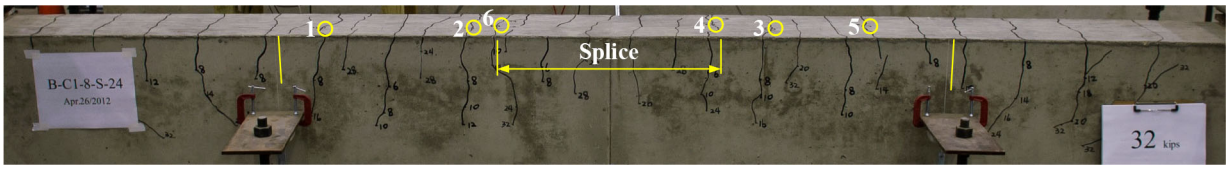

Figure I.31 Crack pattern and measurement locations (B-8-S-24-C1).

TABLE I.32
Crack Measurements (B-8-S-24-C2)

		Crack Width (1/1000 in.)							
		Crack No.							
Load, P (kips)	Bar Stress (ksi)	1	2	3	4	5	6	Avg. Crack Width (mils)	Max Crack Width (mils)
8	10.1	2						2.0	2.0
12	15.2	3	2.5	3	3	3		2.9	3.0
16	20.4	4	4	3.5	3.5	4		3.8	4.0
20	25.5	5	5	5	4.5	5		4.9	5.0
24	30.7	6	7	6	5.5	7	4	6.3	7.0
28	35.8	7	8	7	6	9	5	7.4	9.0
32	41.2	8	10	8	7	12	5.5	9.0	12.0

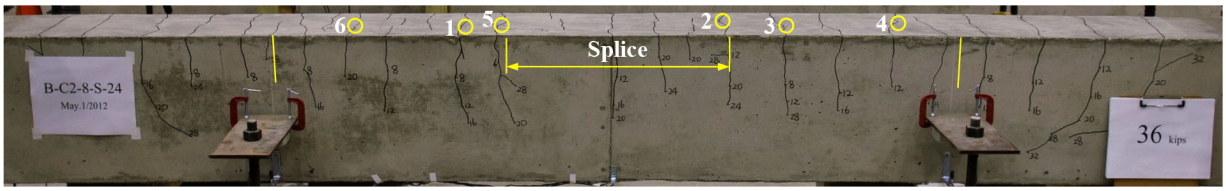

Figure I.32 Crack pattern and measurement locations (B-8-S-24-C2).

TABLE I.33
Crack Measurements (B-8-S-24-C3)

		Crack Width (1/1000 in.)							
		Crack No.							
Load, P (kips)	Bar Stress (ksi)	1	2	3	4	5	6	Avg. Crack Width (mils)	Max Crack Width (mils)
10	12.7	2						2.0	2.0
12	15.2	2.5	2.5					2.5	2.5
14	17.9	3	3	3	3			3.0	3.0
16	20.4	3.5	4	4	4	3		3.7	4.0
18	23.0	4	4.5	4	4.5	4	4	4.2	4.5
20	25.5	4.5	5	5	6	4	5	4.9	6.0
22	28.0	5	6	5.5	5.5	5	6	5.5	6.0
24	30.7	5.5	6	5.5	6	6	7	6.0	7.0
26	33.2	5.5	7	6	7	6	8	6.6	8.0
28	35.8	6	7	6	7	7	9	7.0	9.0
30	38.6	6	7	6	7	7	10	7.2	10.0
32	41.2	7	8	7	8	8	11	8.2	11.0
36	43.9	8	9	8	9	9	12	9.2	12.0

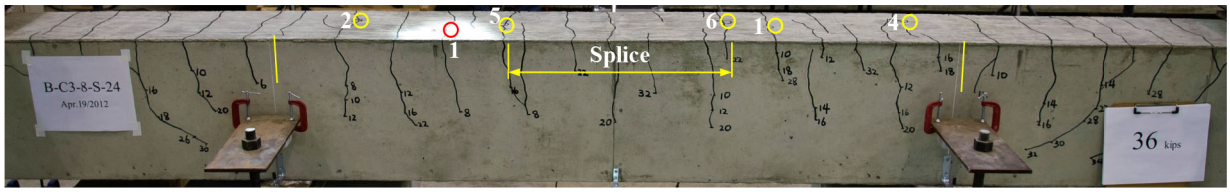

Figure I.33 Crack pattern and measurement locations (B-8-S-24-C3).

TABLE I.34
Crack Measurements (M-5-S-24)

		Crack Width (1/1000 in.)							
		Crack No.							
Load, P (kips)	Bar Stress (ksi)	1	2	3	4	5	6	Avg. Crack Width (mils)	Max Crack Width (mils)
6	18.3	2	2	–	–	–	–	2.0	2.0
8	24.4	4	3.5	3.5	3	–	–	3.5	4.0
10	30.5	5	5	5	5	5	6	5.2	6.0
12	36.5	6	6	7	6	6	7	6.3	7.0
14	42.7	8	8	8	8	7	9	8.0	9.0
16	49.0	9	9	9	9	8	11	9.2	11.0
18	55.3	10	10	10	10	10	12	10.3	12.0
20	61.4	10	12	12	12	12	13	11.8	13.0
22	67.6	13	13	13	13	13	14	13.2	14.0

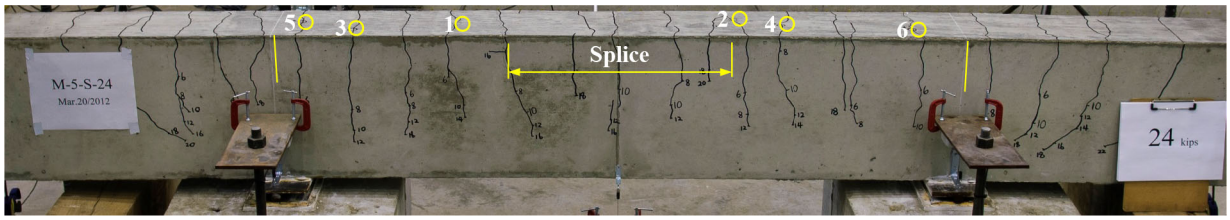

Figure I.34 Crack pattern and measurement locations (M-5-S-24).

TABLE I.35
Crack Measurements (M-5-S-36)

		Crack Width (1/1000 in.)							
		Crack No.							
Load, P (kips)	Bar Stress (ksi)	1	2	3	4	5	6	Avg. Crack Width (mils)	Max Crack Width (mils)
6	18.3	2	2	–	–	–	–	2.0	2.0
8	24.4	4	4	3.5				3.8	4.0
10	30.5	5	5	4.5	2	2	3	3.6	5.0
12	36.5	6	7	6	3.5	3.5	4	5.0	7.0
14	42.7	7	8	7	5	4	5	6.0	8.0
16	49.0	9	11	10	6	5	7	8.0	11.0
18	55.3	10	12	10	7	6	7	8.7	12.0
20	61.4	12	13	11	13	7	10	11.0	13.0
22	67.6	13	14	12	14	8	11	12.0	14.0
24	73.8	13	16	14	18	10	12	13.8	18.0

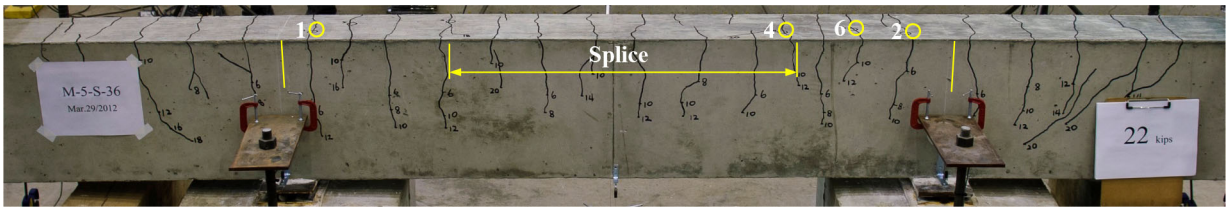

Figure I.35 Crack pattern and measurement locations (M-5-S-36).

TABLE I.36
Crack Measurements (S2205-5-S-24)

		Crack Width (1/1000 in.)							
		Crack No.							
Load, P (kips)	Bar Stress (ksi)	1	2	3	4	5	6	Avg. Crack Width (mils)	Max Crack Width (mils)
6	18.1								
8	24.1	4	4	4	4.5			4.1	4.5
10	30.2	5	5	5	6	5.5		5.3	6.0
12	36.6	7	6	6.5	7	7	6	6.6	7.0
14	42.6	8	8	7	10	8	7	8.0	10.0
16	48.6	10	10	10	12	9	7	9.7	12.0
18	54.7	12	10	11	13	12	8	11.0	13.0

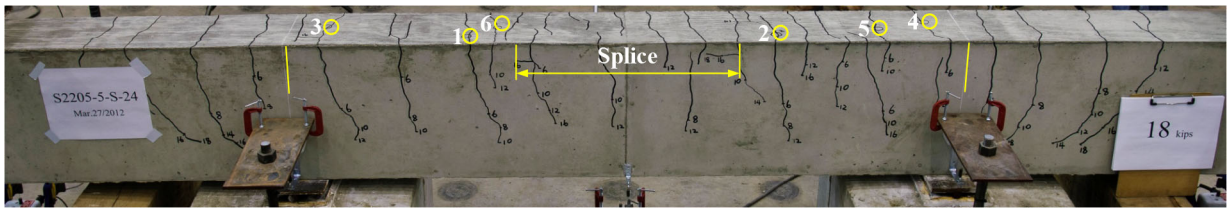

Figure I.36 Crack pattern and measurement locations (S2205-5-S-24).

TABLE I.37
Crack Measurements (S2205-5-S-36)

		Crack Width (1/1000 in.)							
		Crack No.							
Load, P (kips)	Bar Stress (ksi)	1	2	3	4	5	6	Avg. Crack Width (mils)	Max Crack Width (mils)
6	18.1	3	3					3.0	3.0
8	24.1	4	5	3	3			3.8	5.0
10	30.2	6	7	5	4			5.5	7.0
12	36.6	7	7	6	5.5			6.4	7.0
14	42.6	9	9	8	7			8.3	9.0
16	48.6	10	10	11	9			10.0	11.0
18	54.7	13	13	13	10			12.3	13.0
20	60.8	18	16	16	10	12	13	14.2	18.0
22	66.9	25	20	25	13	14	14	18.5	25.0

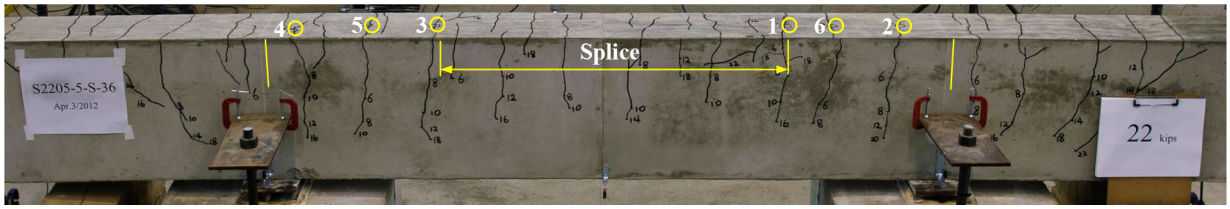

Figure I.37 Crack pattern and measurement locations (S2205-5-S-36).

TABLE I.38
Crack Measurements (M-5-S-48)

		Crack Width (1/1000 in.)							
		Crack No.							
Load, P (kips)	Bar Stress (ksi)	1	2	3	4	5	6	Avg. Crack Width (mils)	Max Crack Width (mils)
6	18.2	2						2.0	2.0
10	30.3	4	3	5	5	3		4.0	5.0
12	36.4	5	4	6	6	4	6	5.2	6.0
16	48.7	6	7	7	6	6	7	6.5	7.0
20	60.9	8	8	10	7	8	10	8.5	10.0
24	73.4	10	13	13	9	10	13	11.3	13.0
28	85.6	10	16	20	10	15	17	14.7	20.0
32	97.6	13	22	24	15	15	22	18.5	24.0

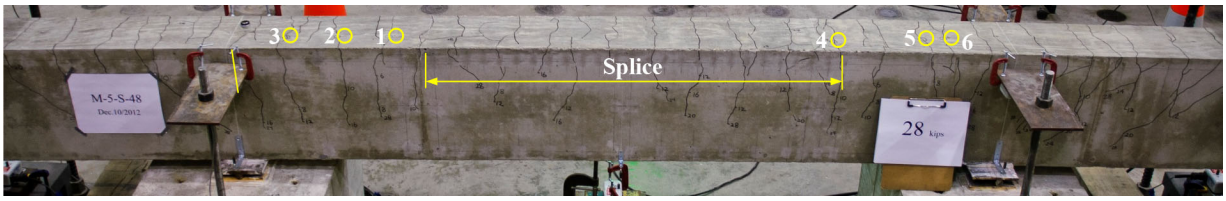

Figure I.38 Crack pattern and measurement locations (M-5-S-48).

TABLE I.39
Crack Measurements (M-7-S-24)

		Crack Width (1/1000 in.)							
		Crack No.							
Load, P (kips)	Bar Stress (ksi)	1	2	3	4	5	6	Avg. Crack Width (mils)	Max Crack Width (mils)
8	12.8	3	4					3.5	4.0
14	22.4	6	7	6	5			6.0	7.0
16	25.6	8	7	7	5		4	6.2	8.0
20	32.3	10	8	9	8		5	8.0	10.0
24	38.9	12	10	11	9		7	9.8	12.0
28	45.4	13	12	12	9	7	9	10.3	13.0
32	51.8	16	13	13	10	9	11	12.0	16.0

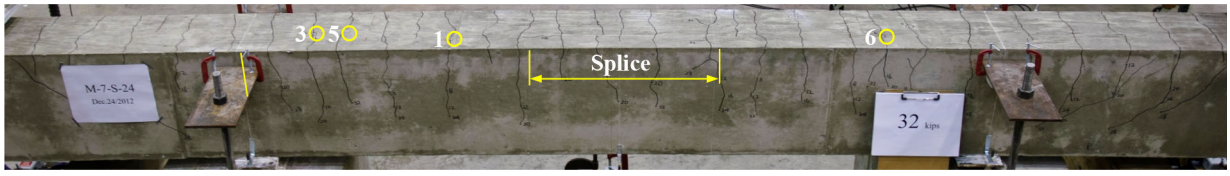

Figure I.39 Crack pattern and measurement locations (M-7-S-24).

TABLE I.40
Crack Measurements (M-7-S-18)

		Crack Width (1/1000 in.)							
		Crack No.							
Load, P (kips)	Bar Stress (ksi)	1	2	3	4	5	6	Avg. Crack Width (mils)	Max Crack Width (mils)
8	12.8	2						2.0	2.0
10	16.0	3	3	3	4			3.3	4.0
12	19.2	4	4	3.5	5	4		4.1	5.0
14	22.4	5	4.5	4	6	4		4.7	6.0
16	25.6	6	5	5	6.5	5	6	5.6	6.5
18	28.8	7	6	6	7	6	7	6.5	7.0
20	32.3	8	7	8	8	8	8	7.8	8.0
22	35.5	10	8	9	9	8	10	9.0	10.0
24	38.9	10	9	10	10	9	12	10.0	12.0
26	42.0	10	9	12	11	9	13	10.7	13.0
28	45.4	11	10	13	12	10	15	11.8	15.0

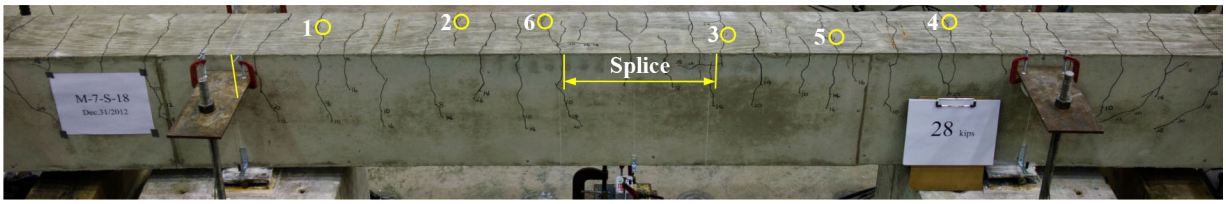

Figure I.40 Crack pattern and measurement locations (M-7-S-18).

TABLE I.41
Crack Measurements (M-8-S-48)

		Crack Width (1/1000 in.)						
		Crack No.						
Load, P (kips)	**Bar Stress (ksi)**	**1**	**2**	**3**	**4**	**5**	**Avg. Crack Width (mils)**	**Max Crack Width (mils)**
8	10.0							
13	16.2	3	4	3			3.3	4.0
18	22.4	4	6	4	4	4	4.4	6.0
23	29.0	5	7	5	5	6	5.6	7.0
28	35.1	7	9	6	6	7	7.0	9.0
33	41.5	7	10	7	10	8	8.4	10.0
38	47.9	9	11	10	10	11	10.2	11.0
43	54.2	10	15	11	12	14	12.4	15.0

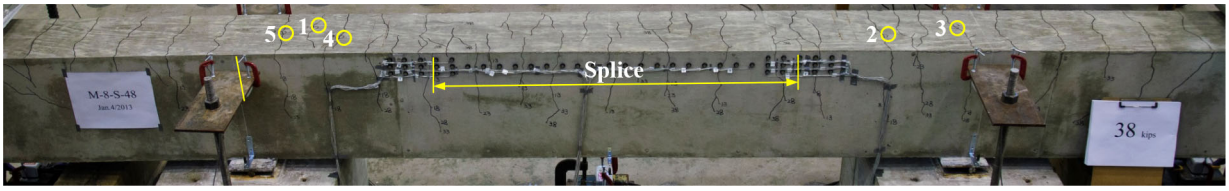

Figure I.41 Crack pattern and measurement locations (M-8-S-48).

TABLE I.42
Crack Measurements (M-11-S-24)

		Crack Width (1/1000 in.)						
		Crack No.						
Load, P (kips)	**Bar Stress (ksi)**	**1**	**2**	**3**	**4**	**5**	**Avg. Crack Width (mils)**	**Max Crack Width (mils)**
8	5.2							
13	8.5	3	2				2.5	3.0
18	11.8	3.5	3	3			3.2	3.5
23	15.1	4	4	4			4.0	4.0
28	18.5	5	5	5	4		4.8	5.0
33	21.9	6	6	6	5	6	5.8	6.0
38	25.3	7	7	7	6	7	6.8	7.0
43	28.6	8	8	8	7	8	7.8	8.0
48	31.9	9	10	10	8	9	9.2	10.0

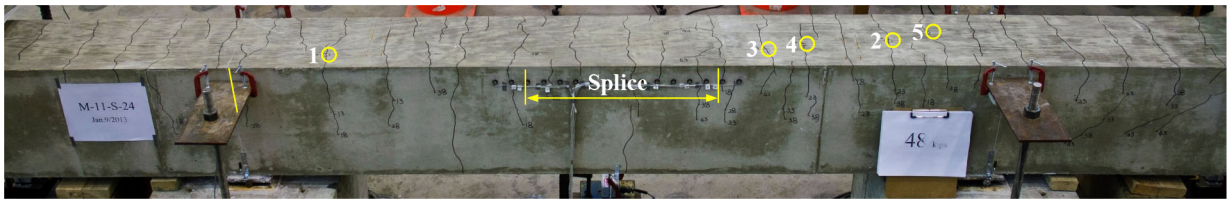

Figure I.42 Crack pattern and measurement locations (M-11-S-24).

TABLE I.43
Crack Measurements (M-8-S-48-C1)

		Crack Width (1/1000 in.)						
		Crack No.						
Load, P (kips)	Bar Stress (ksi)	1	2	3	4	5	Avg. Crack Width (mils)	Max Crack Width (mils)
8	10.0	2	2				2.0	2.0
13	16.2	3	4	3	3		3.3	4.0
18	22.4	4	4	5	4	3	4.0	5.0
23	29.0	5	6	7	7	4	5.8	7.0
28	35.2	7	7	11	10	7	8.2	11.0
33	41.5	8	8	13	13	8	9.7	13.0
38	47.9	9	9	16	16	9	11.2	16.0
43	54.2	10	10	20	20	11.5	13.6	20.0

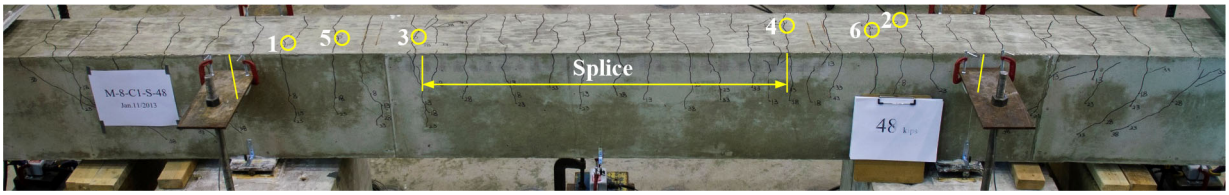

Figure I.43 Crack pattern and measurement locations (M-8-S-48-C1).

TABLE I.44
Crack Measurements (M-8-S-48-C2)

		Crack Width (1/1000 in.)						
		Crack No.						
Load, P (kips)	Bar Stress (ksi)	1	2	3	4	5	Avg. Crack Width (mils)	Max Crack Width (mils)
8	10.0							
13	16.2	4	4	4			4.0	4.0
18	22.4	5	5	5	5	5	5.0	5.0
23	29.0	6	7	7	9	7	7.2	9.0
28	35.2	9	11	9	12	10	10.2	12.0
33	41.5	10	11	10	14	13	10.8	14.0
38	47.9	13	12	12	20	18	13.8	20.0
43	54.2	14	13	13	25	23	16.2	25.0

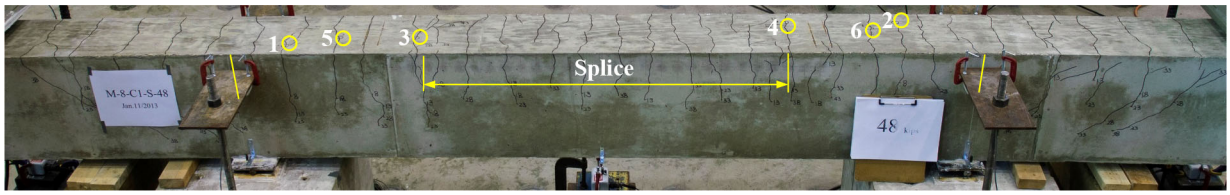

Figure I.44 Crack pattern and measurement locations (M-8-S-48-C2).

TABLE I.45
Crack Measurements (M-8-S-48-C3)

		Crack Width (1/1000 in.)							
		Crack No.							
Load, P (kips)	Bar Stress (ksi)	1	2	3	4	5	6	Avg. Crack Width (mils)	Max Crack Width (mils)
8	10.0								
13	16.2	4	4					4.0	4.0
18	22.4	5	5	4	5			4.8	5.0
23	29.0	7	7	5	6			6.3	7.0
28	35.2	8	10	7	10	7	7	8.2	10.0
33	41.5	10	15	9	12	10	8	10.7	15.0
38	47.9	11	19	10	13	11	8	12.0	19.0
43	54.2	12	24	11	16	12	9	14.0	24.0
48	60.8	14	26	12	16	13	11	15.3	26.0

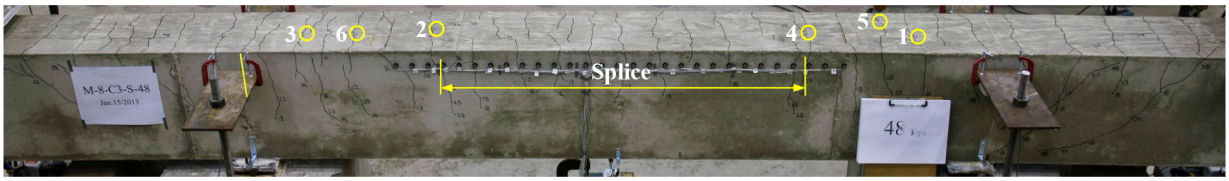

Figure I.45 Crack pattern and measurement locations (M-8-S-48-C3).

TABLE I.46
As-Built Specimen Dimensions After Testing (Series II)

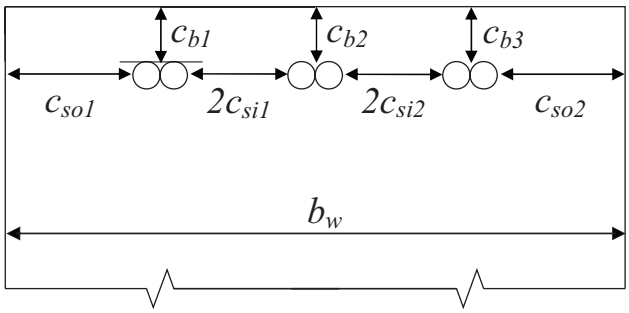

	Cover and Spacing Dimensions (in.) (Nearest 16th of an inch)							
Specimen	c_{b1}	c_{b2}	c_{b3}	c_{so1}	$2c_{si1}$	$2c_{si2}$	c_{so2}	b_w **(in.)**
B-5-S-12	1.531	1.438	1.375	1.625	1.063	0.938	1.438	8.813
E-5-S-12	1.375	1.500	1.313	1.375	1.125	1.250	1.313	8.813
G-5-S-12	1.469	1.531	1.375	1.500	1.000	1.125	1.500	8.875
ZC1-5-S-12	1.406	1.531	1.469	1.250	1.188	1.000	1.563	8.750
ZC2-5-S-12	1.156	1.500	1.219	1.438	1.063	1.063	1.500	8.813
Z-5-S-12	1.438	1.531	1.469	1.500	1.000	0.813	1.688	8.750
M-5-S-12	1.438	1.281	1.250	1.375	1.000	0.750	1.875	8.750
S316LN-5-S-12	1.250	1.531	1.188	1.375	1.000	1.375	1.250	8.750
S2205-5-S-12	1.250	1.406	1.469	1.438	1.188	0.813	1.563	8.750
S2304-5-S-12	1.344	1.531	1.188	1.313	1.000	1.250	1.563	8.875
SXM28-5-S-12	1.438	1.375	1.469	1.313	1.188	1.250	1.313	8.813

TABLE I.47
As-Built Specimen Dimensions After Testing (Series III)

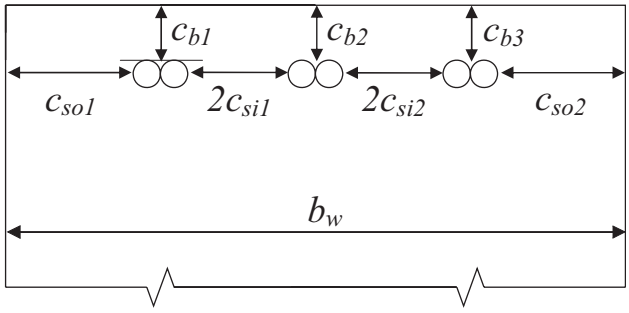

	Cover and Spacing Dimensions (in.) (Nearest 16th of an inch)							
Specimen	c_{b1}	c_{b2}	c_{b3}	c_{so1}	$2c_{si1}$	$2c_{si2}$	c_{so2}	b_w **(in.)**
B-8-S-24	1.375	1.531	1.438	1.250	1.250	1.250	1.375	11.125
E-8-S-24	1.438	1.500	1.438	1.375	1.063	1.438	1.125	11.000
G-8-S-24	1.563	1.469	1.531	1.438	1.063	1.313	1.250	11.063
ZC1-8-S-24	1.469	1.500	1.531	1.063	1.063	1.500	1.438	11.063
ZC2-8-S-24	1.469	1.531	1.500	1.688	1.188	1.125	1.000	11.000
Z-8-S-24	1.500	1.531	1.438	1.188	1.188	1.500	1.250	11.125
M-8-S-24	1.469	1.313	1.344	1.313	1.125	1.250	1.313	11.000
S316LN-8-S-24	1.469	1.438	1.500	1.500	1.375	1.000	1.188	11.063
S2205-8-S-24	1.375	1.563	1.469	1.625	1.125	1.375	1.000	11.125
S2304-8-S-24	1.469	1.469	1.469	1.188	1.250	1.250	1.375	11.063
SXM28-8-S-24	1.500	1.469	1.469	1.250	1.375	1.250	1.125	11.000

TABLE I.48
As-Built Specimen Dimensions After Testing (Series IV)

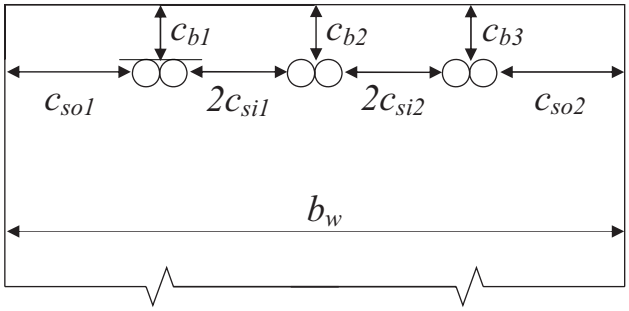

Specimen	Cover and Spacing Dimensions (in.) (Nearest 16th of an inch)							
	c_{b1}	c_{b2}	c_{b3}	c_{so1}	$2c_{si1}$	$2c_{si2}$	c_{so2}	b_w (in.)
B-5-F-12	0.750	0.813	0.750	2.563	4.750	4.500	2.375	17.938
ZC2-5-F-12	0.688	0.688	0.750	2.375	4.875	4.625	2.375	18.000
Z-5-F-12	0.813	0.750	0.813	2.625	4.563	4.938	2.125	18.000
S2205-F-12	0.750	0.750	0.750	2.375	4.625	4.563	2.688	18.000
B-8-S-24-C1	1.375	1.563	1.500	1.500	1.000	1.000	1.563	11.063
B-8-S-24-C2	1.500	1.375	1.500	1.500	0.938	0.938	1.625	11.000
B-8-S-24-C3	1.500	1.438	1.438	1.500	1.000	0.813	1.688	11.000
M-5-S-24	1.313	1.563	1.438	1.563	1.000	0.938	1.500	8.750
M-5-S-36	1.438	1.500	1.375	1.375	0.938	1.000	1.688	8.750
S2205-5-S-24	1.438	1.500	1.375	1.313	0.938	1.125	1.625	8.750
S2205-5-S-36	1.438	1.438	1.438	1.500	1.000	0.938	1.563	8.750

APPENDIX J: CRACK MEASUREMENTS, CRACK PATTERNS, AND CALCULATED BAR STRESSES OF SLAB SPECIMENS

TABLE J.1
Crack Measurements (B-6)

	Top Surface Crack Width (1/1000 in.) Crack No.																													
	S1			S2			S3			S4			S5			N1			N2			N3			N4			N5			N6		
Load, *P* (kips)	1	2	3	1	2	3	1	2	3	1	2	3	1	2	3	1	2	3	1	2	3	1	2	3	1	2	3	1	2	3	1	2	3
8	2															3																
10	4	5	3	2	3	4	4	4	4							5	5	6	4	5	4	4	4	3	4	3	3	4	4	3			
12	5	6	4	4	4	5	4	5	4	4	5	4				5	5	7	5	6	5	4	5	3	4	4	5	5	5	4			
14	5	7	4	5	6	6	5	7	5	5	6	5	5	6	4	6	7	9	5	7	6	6	6	4	5	5	6	6	6	5	6	6	6
16	7	8	5	6	7	9	6	7	5	7	7	7	6	7	5	8	8	10	5	8	6	7	7	5	6	6	6	7	7	6	7	6	7
18	10	11		10	10	10	8	8	6	9	9	9	8	8	7	10	10	13	5	9	7	8	8	5	7	7	8	10	9	7	9	6	8
20	10	14		12	12	11	10	10	8	11	10	11	8	10	9	13	10	18	8	10	9	10	9	8	10	9	10	11	12	10	10	6	10
22	13	14		15	12	13	11	12	10	12	12	11	9	13	10	15	12	19	10	13	10	12	13	9	11	10	13	16	15	12	12	8	11
24	14	18		17	13	13	14	13	10	15	14	11	12	14	11	16	14	19	10	12	15	13	12	10	12	13	15	17	15	12	13	9	11
26	17	23		16	15	15	16	14	9	17	14	13	14	16	13	18	20	20	10	15	15	14	13	10	14	13	16	18	17	14	14	9	14
30	17			17	17	15	17	15	11	18	15	14	15	18	13		20	23	13	18	16	16	15	12	16	17	16	18	20	17	16	9	15
32	20			20	17	16	18	19	15	22	18	15	16	20	15			23	14	20	17	16	16	15	19	19	20	22	22	17	18	10	15
34.7	125	83	120	50	35	48	20	21	18	24	23	18	19	22	26	58	125	74	20	23	22	20	16	19	22	20	25	38	35	29	21	10	21

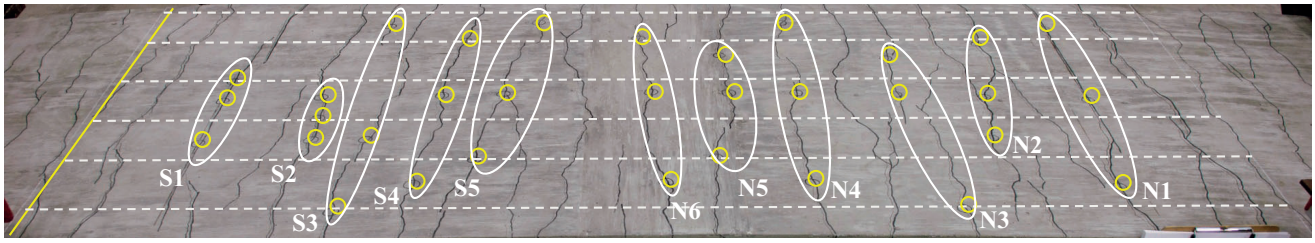

Figure J.1 Crack pattern and measurement locations (B-6).

TABLE J.2
Summary of Crack Widths (B-6)

Top Surface Crack Width						Side Crack Width (at bar level)			
Load, P (kips)	Bar Stress (ksi)	Avg. Crack Width (1/1000)	Max Crack Width (1/1000)	No. of Primary Cracks	Cracks outside Constant Moment	Load, P (kips)	Bar Stress (ksi)	Avg. Crack Width (1/1000)	Max Crack Width (1/1000)
8	21.9	2.5	3.0	2		8	21.9		
10	27.4	3.9	6.0	11		10	27.4	3.1	4.0
12	33.6	4.7	7.0	13	2	12	33.6	3.7	5.0
14	39.1	5.7	9.0	15	2	14	39.1	4.6	7.0
16	44.5	6.7	10.0	15	2	16	44.5	5.7	9.0
18	49.9	8.4	13.0	15	4	18	49.9	6.7	11.0
20	55.6	10.3	18.0	15	4	20	55.6	7.8	11.0
22	61.2	12.1	19.0	15	4	22	61.2	9.4	15.0
24	66.7	13.3	19.0	15	4	24	66.7	10.3	15.0
26	72.1	14.9	23.0	15	5	26	72.1	12.6	18.0
30	77.6	16.0	23.0	15	5	30	77.6	13.6	20.0
32	79.5	17.7	23.0	15	5	32	79.5	16.6	24.0
34.7	79.5	37.9	125.0	15	5	34.7	79.5	27.0	64.0

TABLE J.3
Calculated Bar Stress (B-6)

Load History		Transformed Section Analysis			Moment-Curvature Analysis							
P (kips)	*M (k-in)*	f_s *(ksi)*	e_s	e_c	*c (in.)*	ϕ *(1lin.)*	e_c	C_c *(in.)*	y_{bar} *(in.)*	*M (k-in)*	f_s *(ksi)*	Δf_s *(ksi)*
8	192	21.9	0.00076	0.00027								
9	219	25.0	0.00086	0.00031	4.00	0.000033	0.00013	43.2	2.661	209.5		
10	240	27.4	0.00095	0.00034	1.62	0.000251	0.00041	52.1	1.070	293.7	33.6	6.17
12	288	32.9	0.00113	0.00040	1.62	0.000251	0.00041	52.1	1.070	293.7	33.6	0.69
14	336	38.4	0.00132	0.00047	1.62	0.000294	0.00048	60.6	1.072	341.6	39.1	0.71
16	384	43.9	0.00151	0.00054	1.63	0.000336	0.00055	69.0	1.074	388.8	44.5	0.65
18	432	49.4	0.00170	0.00060	1.63	0.000377	0.00062	77.4	1.076	435.6	49.9	0.55
20	480	54.8	0.00189	0.00067	1.64	0.000422	0.00069	86.2	1.079	485.2	55.6	0.79
22	528	60.3	0.00208	0.00074	1.65	0.000465	0.00077	94.9	1.082	533.6	61.2	0.90
24	576	65.8	0.00227	0.00081	1.65	0.000509	0.00084	103.5	1.085	581.3	66.7	0.95
26	624	71.3	0.00246	0.00087	1.66	0.000552	0.00092	111.8	1.088	627.8	72.1	0.86
28	672	76.8	0.00265	0.00094	1.67	0.000594	0.00099	120.3	1.091	674.8	77.6	0.83
30	720	82.3	0.00284	0.00101	0.82	0.003736	0.00304	123.2	0.497	723.2	79.5	2.76
32	768	87.7	0.00303	0.00107	0.82	0.003736	0.00304	123.2	0.497	723.2	79.5	8.24
34.7	832.1	95.1	0.00328	0.00116	0.82	0.003736	0.00304	123.2	0.497	723.2	79.5	15.56

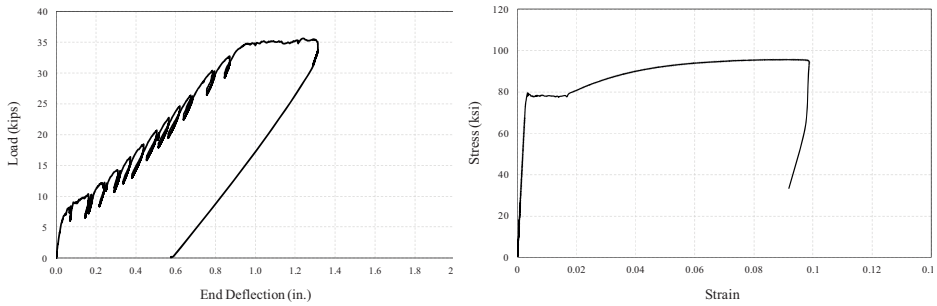

Figure J.2 Load-deflection and stress-strain relationship (B-6).

TABLE J.4
Crack Measurements (M-6)

	Top Surface Crack Width (1/1000 in.) Crack No.																													
	Crack No.																													
	S1			S2			S3			S4			S5			N1			N2			N3			N4			N5		
Load, *P* (kips)	**1**	**2**	**3**	**1**	**2**	**3**	**1**	**2**	**3**	**1**	**2**	**3**	**1**	**2**	**3**	**1**	**2**	**3**	**1**	**2**	**3**	**1**	**2**	**3**	**1**	**2**	**3**	**1**	**2**	**3**
8	4	4	4													2	3	4												
16	10	10	10	12	10	8	9	7	6	5	5	6	7	6	8	7	10	10	6	7	6	6	7	6	5	6	4	5	7	3
20	14	20	13	15	15	10	11	8	7	7	8	10	10	7	11	12	10	13	8	7	6	7	9	7	6	8	6	6	9	4
24	18	19	17	17	15	13	15	12	11	9	10	13	12	13	14	14	15	17	12	11	7	10	10	13	8	9	9	9	11	6
30	18	19	22	19	19	17	18	13	15	12	15	16	18	13	20	17	19	19	15	17	10	10	13	16	12	13	13	11	15	10
36	20	25	26	24	23	20	21	19	20	13	18	17	20	18	20	20	22	23	18	20	12	18	19	20	15	16	16	15	18	12
42	23		25	30	28	23	25	22	23	15	20	20	23	22	20	25	24	27	20	23	15	17	23	25	17	20	20	19	20	15

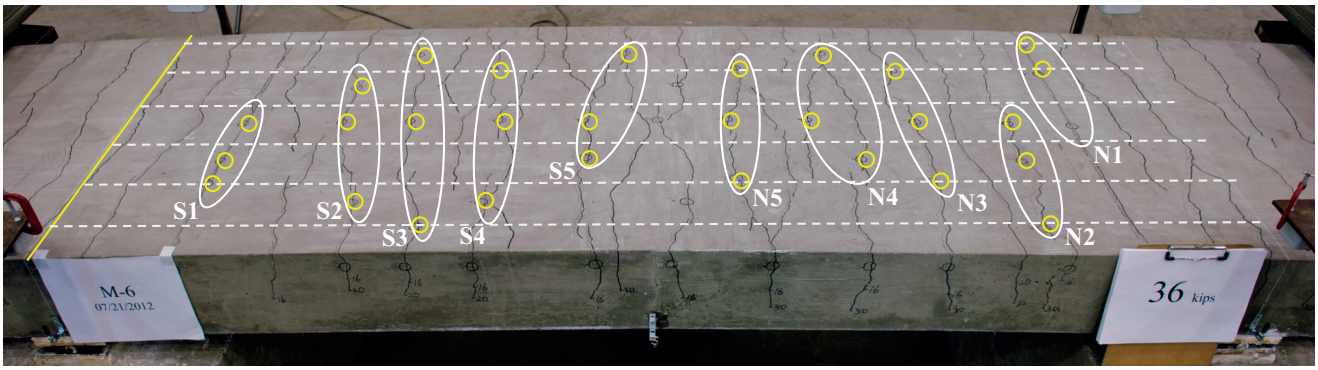

Figure J.3 Crack pattern and measurement locations (M-6).

TABLE J.5
Summary of Crack Widths (M-6)

Top Surface Crack Width						Side Crack Width (at bar level)			
Load, *P* (kips)	Bar Stress (ksi)	Avg. Crack Width (1/1000)	Max Crack Width (1/1000)	No. of Primary Cracks	Cracks outside Constant Moment	Load, *P* (kips)	Bar Stress (ksi)	Avg. Crack Width (1/1000)	Max Crack Width (1/1000)
8	22.2	3.5	4.0	2		8	22.2	3.5	4.0
16	44.4	7.1	12.0	13	2	16	44.4	7.1	12.0
20	55.5	9.5	20.0	15	3	20	55.5	9.5	20.0
24	66.4	12.3	19.0	15	4	24	66.4	12.3	19.0
30	82.8	15.5	22.0	17	4	30	82.8	15.5	22.0
36	99.2	18.9	26.0	17	4	36	99.2	18.9	26.0
42	115.6	21.7	30.0	17	4	42	115.6	21.7	30.0

TABLE J.6
Calculated Bar Stress (M-6)

Load History	Transformed Section Analysis	Moment-Curvature Analysis										
P (kips)	*M (k-in)*	f_s *(ksi)*	e_s	e_c	*c (in.)*	ϕ *(1/in.)*	e_c	C_c *(in.)*	y_{bar} *(in.)*	*M (k-in)*	f_s *(ksi)*	Δf_s *(ksi)*
8	192	21.9	0.00076	0.00027								
9	219	25.0	0.00086	0.00031	4.00	0.000033	0.00013	43.2	2.661	209.5		
16	384	43.9	0.00151	0.00054	1.63	0.000332	0.00054	68.8	1.078	387.5	44.4	0.51
20	480	54.8	0.00189	0.00067	1.61	0.000435	0.00070	86.0	1.061	484.5	55.5	0.63
24	576	65.8	0.00227	0.00081	1.59	0.000548	0.00087	102.9	1.044	580.2	66.4	0.58
30	720	82.3	0.00284	0.00101	1.56	0.000746	0.00116	128.4	1.016	724.6	82.8	0.58
36	864	98.7	0.00340	0.00121	1.52	0.000991	0.00151	153.8	0.984	868.6	99.2	0.53
42	1008	115.2	0.00397	0.00141	1.48	0.001316	0.00195	179.2	0.945	1012.1	115.6	0.43

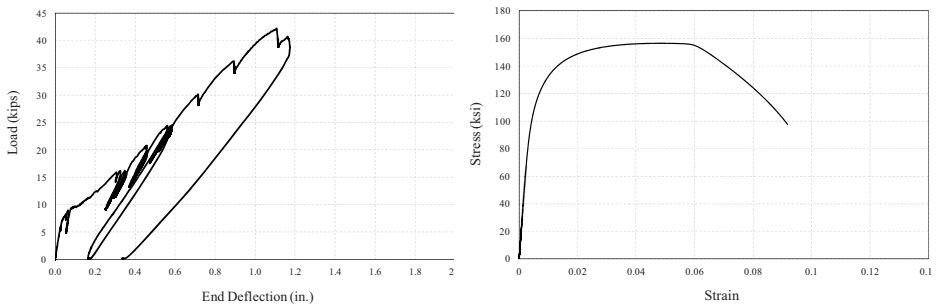

Figure J.4 Load-deflection and stress-strain relationship (M-6).

TABLE J.7
Crack Measurements (B-12)

	Top Surface Crack Width (1/1000 in.)																														
	Crack No.																														
	S1			S2			S3			S4			S5			N1			N2			N3			N4			N5			N6		
Load, *P* (kips)	1	2	3	1	2	3	1	2	3	1	2	3	1	2	3	1	2	3	1	2	3	1	2	3	1	2	3	1	2	3	1	2	3
7	7	7	7													5	6	5															
8	10	10	10	5	6	6	2	3	2							6	9	7	3	6	4												
9	10	13	12	7	6	7	6	7	6	5	6	5				7	10	7	4	7	5	3	6	6				3	3	3			
10	13	14	13	10	7	10	7	9	7	6	8	7				8	10	10	5	10	7	5	7	7	7	7	6	10	9	7			
11	13	16	15	13	10	10	7	10	7	6	10	8				9	10	10	7	10	8	6	8	8	8	10	6	14	14	10			
12	18	20	16	15	13	13	10	13	12	10	16	10	10	10	9	13	13	12	8	15	8	7	10	10	8	11	7	15	16	10	7	8	9
13	20	20	18	17	15	13	15	15	13	12	17	10	13	10	10	13	13	13	10	16	9	8	17	13	12	11	10	16	18	13	9	10	12
14	20	20	20	15	17	18	18	18	15	13	18	12	15	12	13	16	13	14	10	20	13	8	18	16	12	13	13	18	20	16	10	13	12
15	21	23	23	17	18	19	20	20	15	14	22	15	15	12	14	16	18	17	13	20	15	10	25	19	15	16	15	20	25	20	12	15	17
16	21	25	24	17	22	19	20	30	20	16	22	20	19	18	16	16	18	18	13	20	13	12	25	20	16	16	16	25	30	20	13	16	16
17	25	25	23	20	21	18	20	25	19	13	14	21	20	20	18	20	19	19	13	18	13	14	23	24	20	20	19	25	30	22	16	22	20
18	60	55	60	20	23	22	25	25	20	18	25	23	25	24	25			20	20	24	19	18	25	25	20	22	20	30	40	30	17	25	24
18.3	90	90	100	25	30	30	25	27	25	20	30	23	70	60	68			27	20	30	14	19	28	28	20	23	22	60	78	50	20	25	23

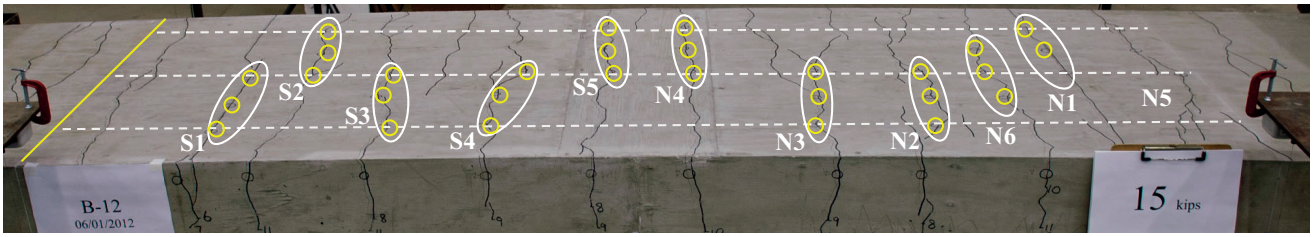

Figure J.5 Crack pattern and measurement locations (B-12).

TABLE J.8
Summary of Crack Widths (B-12)

	Top Surface Crack Width					Side Crack Width (at bar level)			
Load, *P* (kips)	Bar Stress (ksi)	Avg. Crack Width (1/1000)	Max Crack Width (1/1000)	No. of Primary Cracks	Cracks outside Constant Moment	Load, *P* (kips)	Bar Stress (ksi)	Avg. Crack Width (1/1000)	Max Crack Width (1/1000)
6	27.2	5.7	6.0	1		6	27.2		
7	31.7	6.2	7.0	2		7	31.7	4.3	6.0
8	35.9	5.9	10.0	5		8	35.9	5.0	8.0
9	40.9	6.4	13.0	8		9	40.9	6.0	9.0
10	45	8.4	14.0	11		10	45.0	7.3	10.0
11	49.2	9.7	16.0	12	2	11	49.2	8.5	10.0
12	53.9	11.6	20.0	12	2	12	53.9	9.6	14.0
13	58.6	13.4	20.0	12	4	13	58.6	10.8	16.0
14	62.7	15.1	20.0	12	4	14	62.7	12.8	18.0
15	67.4	17.5	25.0	12	4	15	67.4	13.8	18.0
16	71.9	19.2	30.0	12	4	16	71.9	16.0	20.0
17	76.5	20.0	30.0	12	4	17	76.5	18.0	25.0
18	78	26.7	60.0	12	4	18	78.0	25.2	65.0
18.3	79.2	38.7	100.0	12	4	18.3	79.2	31.1	70.0

TABLE J.9
Calculated Bar Stress (B-12)

Load History		Transformed Section Analysis					Moment-Curvature Analysis					
P (kips)	*M (k-in)*	f_s *(ksi)*	e_s	e_c	*c (in.)*	ϕ *(1/in.)*	e_c	C_c *(in.)*	y_{bar} *(in.)*	*M (k-in)*	f_s *(ksi)*	Δf_s *(ksi)*
8	192	35.9	0.00124	0.00033								
9	219	40.9	0.00141	0.00037	4.00	0.000033	0.00013	43.2	2.661	209.5		
10	240	44.8	0.00155	0.00041	1.29	0.000319	0.00041	41.9	0.852	240.7	45.0	0.16
11	264	49.3	0.00170	0.00045	1.29	0.000349	0.00045	45.8	0.853	263.2	49.2	0.11
12	288	53.8	0.00186	0.00049	1.29	0.000383	0.00050	50.2	0.855	288.3	53.9	0.12
13	312	58.3	0.00201	0.00053	1.30	0.000417	0.00054	54.5	0.856	313.2	58.6	0.31
14	336	62.8	0.00216	0.00058	1.30	0.000447	0.00058	58.3	0.858	335.2	62.7	0.04
15	360	67.3	0.00232	0.00062	1.30	0.000480	0.00063	62.6	0.860	359.7	67.4	0.09
16	384	71.8	0.00247	0.00066	1.31	0.000513	0.00067	66.9	0.861	384.0	71.9	0.17
17	408	76.2	0.00263	0.00070	1.31	0.000546	0.00072	71.1	0.863	408.1	76.5	0.23
18	432	80.7	0.00278	0.00074	0.62	0.002972	0.00185	72.6	0.398	432.6	78.0	2.71
18.3	439.2	82.1	0.00283	0.00075	0.59	0.003495	0.00206	73.7	0.374	439.9	79.2	2.86

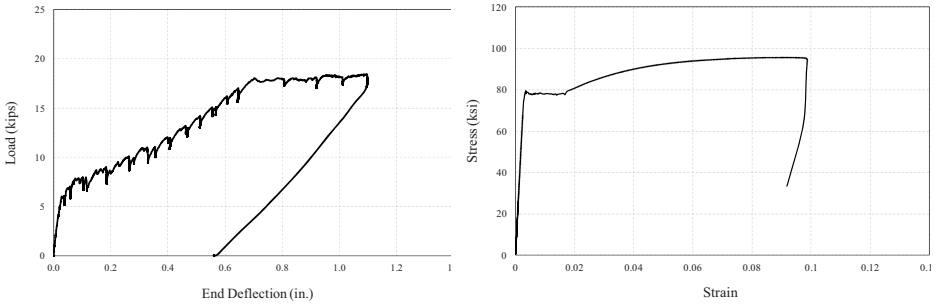

Figure J.6 Load-deflection and stress-strain relationship (B-12).

TABLE J.10
Crack Measurements (E-12)

	Top Surface Crack Width (1/1000 in.) Crack No.																												
	S1			S2			S3			S4			S5			N1			N2			N3			N4			N5		
Load, *P* (kips)	**1**	**2**	**3**	**1**	**2**	**3**	**1**	**2**	**3**	**1**	**2**	**3**	**1**	**2**	**3**	**1**	**2**	**3**	**1**	**2**	**3**	**1**	**2**	**3**	**1**	**2**	**3**	**1**	**2**	**3**
6	3	3	3													2	2	2												
8	5	10	9	5	6	8										8	10	10	5	7	4									
10	6	15	13	9	11	12	9	10	7	13	10	5				8	12	12	10	12	7	10	10	9	6	8	9			
12	12	17	14	15	18	15	15	13	10	13	12	7	5	6	5	10	15	14	12	18	11	10	15	12	7	10	10			
14	19	20	17	16	20	18	18	20	13	15	15	12	11	12	8	13	18	19	15	25	15	20	20	13	10	15	15	8	5	10
16	21	23	17	20	23	20	23	25	17	15	18	12	15	14	15	14	20	19	18	28	22	20	20	16	12	18	15	15	10	18
18	25	33	21	25	22	23	25	29	20	20	18	18	15	18	20	15	25	23	18	31	25	25	25	25	15	19	15	15	11	16
19.6	25	36	20	30	26	27	25	30	24	25	25	18	23	18	20	27	27	25	25	40	30	30	33	25	18	22	20	20	15	19
20.1	50	70	35	34	32	28	40	35	34	26	25	20	28	22	22	25	50	40	25	40	38	53	65	48	20	22	20	20	16	20

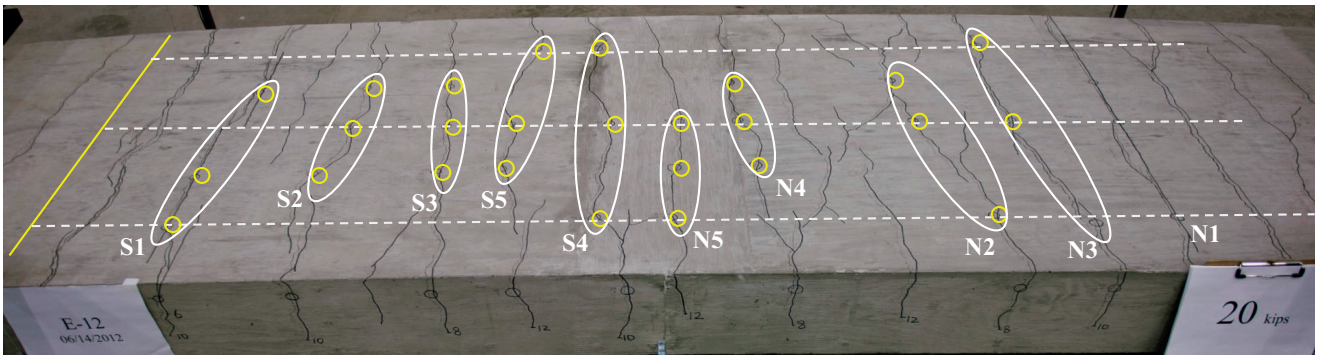

Figure J.7 Crack pattern and measurement locations (E-12).

TABLE J.11
Summary of Crack Widths (E-12)

Top Surface Crack Width					Side Crack Width (at bar level)				
Load, P (kips)	Bar Stress (ksi)	Avg. Crack Width (1/1000)	Max Crack Width (1/1000)	No. of Primary Cracks	Cracks outside Constant Moment	Load, P (kips)	Bar Stress (ksi)	Avg. Crack Width (1/1000)	Max Crack Width (1/1000)
6	26.9	2.5	3.0	2		6	26.9	2.5	3.0
8	35.9	7.3	10.0	6		8	35.9	7.3	10.0
10	45.5	9.7	15.0	10	1	10	45.5	9.7	15.0
12	54.5	11.9	18.0	13	2	12	54.5	11.9	18.0
14	63.3	15.2	25.0	13	2	14	63.3	15.2	25.0
16	72.5	18.1	28.0	13	2	16	72.5	18.1	28.0
18	81.5	21.2	33.0	13	3	18	81.5	21.2	33.0
19.6	86.5	24.9	40.0	13	3	19.6	86.5	24.9	40.0
20.1	87.3	33.4	70.0	13	3	20.1	87.3	33.4	70.0

TABLE J.12
Calculated Bar Stress (E-12)

Load History		Transformed Section Analysis			Moment-Curvature Analysis							
P (kips)	*M (k-in)*	f_s *(ksi)*	e_s	e_c	*c (in.)*	ϕ *(1lin.)*	e_c	C_c *(in.)*	y_{bar} *(in.)*	*M (k-in)*	f_s *(ksi)*	Δf_s *(ksi)*
8	192	35.9	0.00124	0.00033								
9	219	40.9	0.00141	0.00037	4.00	0.000033	0.00013	43.2	2.661	209.5		
10	240	44.8	0.00155	0.00041	1.29	0.000321	0.00041	42.3	0.855	243.5	45.5	0.68
12	288	53.8	0.00186	0.00049	1.30	0.000385	0.00050	50.7	0.858	291.1	54.5	0.65
14	336	62.8	0.00216	0.00058	1.30	0.000448	0.00058	58.8	0.860	338.0	63.3	0.49
16	384	71.8	0.00247	0.00066	1.31	0.000514	0.00067	67.4	0.863	386.8	72.5	0.71
18	432	80.7	0.00278	0.00074	1.32	0.000580	0.00076	75.8	0.867	434.7	81.5	0.77
19.2	460.2	86.0	0.00297	0.00079	1.19	0.000774	0.00092	80.5	0.779	464.9	86.5	0.54
20	480	89.7	0.00309	0.00082	0.65	0.003205	0.00207	81.2	0.411	483.4	87.3	2.35

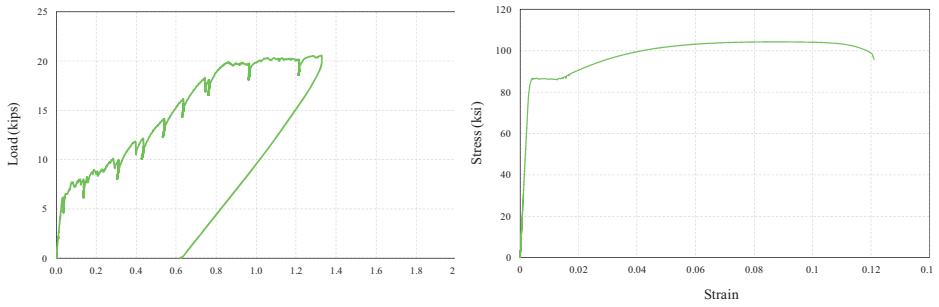

Figure J.8 Load-deflection and stress-strain relationship (E-12).

TABLE J.13
Crack Measurements (ZC1-12)

	Top Surface Crack Width (1/1000 in.)																							
	Crack No.																							
	S1			S2			S3			S4			N1			N2			N3			N4		
Load, *P* (kips)	1	2	3	1	2	3	1	2	3	1	2	3	1	2	3	1	2	3	1	2	3	1	2	3
6	4	5	5										10	10	12									
7	13	15	14										11	18	18									
8	20	20	20	5	11	13							19	19	20	7	13	10						
9	20	25	24	10	18	15							22	25	23	14	17	16	15	13	17			
10	22	26	25	10	20	18	10	12	10				25	25	29	15	20	19	25	15	20			
11	25	25	26	10	25	19	17	15	13				25	28	28	20	22	20	25	20	26			
12	25	30	30	10	25	20	22	20	17				25	28	30	20	25	25	20	24	25			
13	27	33	30	15	28	20	23	23	15				30	28	33	22	27	25	24	26	26	5	8	7
14	30	33	33	17	30	23	23	25	17				35	32	34	30	30	28	25	28	30	7	11	10
15	30	34	35	17	30	30	28	30	24	18	25	17	39	36	38	30	32	31	30	30	34	12	10	15
16		40	40	17	40	30	30	40	25	22	28	16	70	50	55	33	36	32	30	30	35	15	18	18
16.6		50	60	17	40	40	55	60	45	21	35	25	80	70	85	40	45	44	35	42	46	19	22	20
16.7				19	55	35	65	60	65	28	50	50	85	80	85	55	59	50	50	55	57	30	25	30

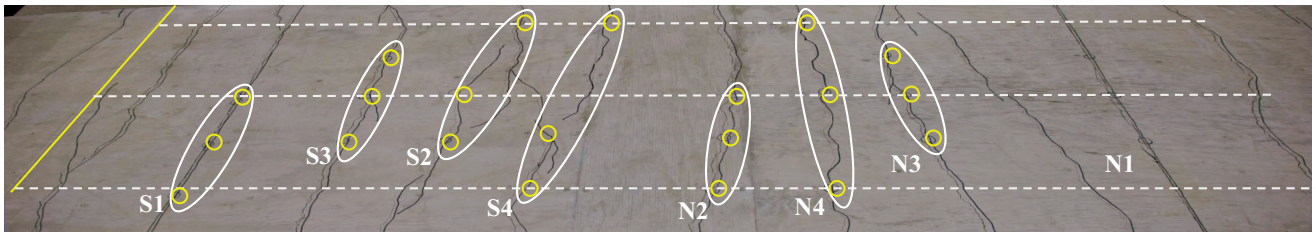

Figure J.9 Crack pattern and measurement locations (ZC1-12).

TABLE J.14
Summary of Crack Widths (ZC1-12)

Top Surface Crack Width						Side Crack Width (at bar level)			
Load, *P* (kips)	Bar Stress (ksi)	Avg. Crack Width (1/1000)	Max Crack Width (1/1000)	No. of Primary Cracks	Cracks outside Constant Moment	Load, *P* (kips)	Bar Stress (ksi)	Avg. Crack Width (1/1000)	Max Crack Width (1/1000)
6	26.9	7.7	12.0	2		6	26.9	5.3	8.0
7	31.4	14.8	18.0	2		7	31.4	10.8	12.0
8	35.9	14.8	20.0	4		8	35.9	11.1	15.0
9	40.4	18.3	25.0	7		9	40.4	15.0	18.0
10	45.0	19.2	29.0	8		10	45.0	16.0	20.0
11	49.2	21.6	28.0	9		11	49.2	18.3	23.0
12	53.9	23.4	30.0	10	2	12	53.9	19.8	25.0
13	58.6	22.6	33.0	11	2	13	58.6	18.5	25.0
14	62.7	25.3	35.0	11	2	14	62.7	20.7	30.0
15	65.7	27.3	39.0	11	2	15	65.7	22.6	35.0
16	69.3	32.6	70.0	11	2	16	69.3	28.3	50.0
16.6	71.5	43.3	85.0	11	2	16.6	71.5	36.0	60.0
16.7	72.2	51.8	85.0	11	2	16.7	72.2	46.3	75.0

TABLE J.15
Calculated Bar Stress (ZC1-12)

Load History		Transformed Section Analysis			Moment-Curvature Analysis							
P (kips)	*M* (k-in)	f_s (ksi)	e_s	e_c	*c* (in.)	φ (1lin.)	e_c	C_c (in.)	y_{bar} (in.)	*M* (k-in)	f_s (ksi)	Δf_s (ksi)
8	192	35.9	0.00124	0.00033								
9	219	40.9	0.00141	0.00037	4.00	0.000033	0.00013	43.2	2.661	209.5		
10	240	44.8	0.00155	0.00041	1.29	0.000319	0.00041	41.9	0.852	240.7	45.0	0.16
11	264	49.3	0.00170	0.00045	1.29	0.000349	0.00045	45.8	0.853	263.2	49.2	0.11
12	288	53.8	0.00186	0.00049	1.29	0.000383	0.00050	50.2	0.855	288.3	53.9	0.12
13	312	58.3	0.00201	0.00053	1.30	0.000417	0.00054	54.5	0.856	313.2	58.6	0.31
14	336	62.8	0.00216	0.00058	1.30	0.000447	0.00058	58.3	0.858	335.2	62.7	0.04
15	360	67.3	0.00232	0.00062	0.80	0.001330	0.00106	61.1	0.522	361.0	65.7	1.60
16	384	71.8	0.00247	0.00066	0.61	0.002598	0.00159	64.4	0.395	384.7	69.3	2.45
16.6	397.2	74.2	0.00256	0.00068	0.56	0.003361	0.00189	66.5	0.359	397.9	71.5	2.72
16.7	401.8	75.1	0.00259	0.00069	0.55	0.003622	0.00199	67.2	0.350	402.3	72.2	2.83

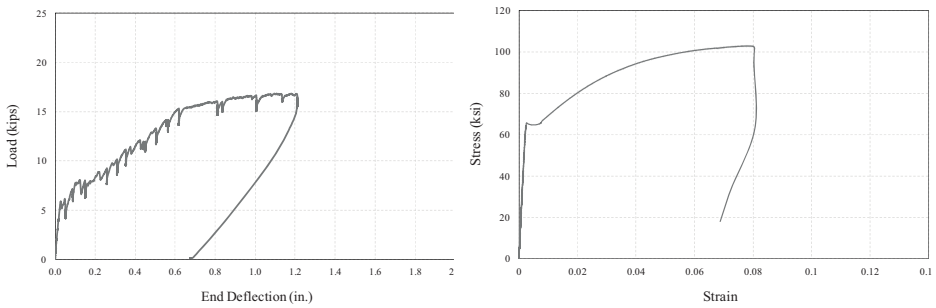

Figure J.10 Load-deflection and stress-strain relationship (ZC1-12).

TABLE J.16
Crack Measurements (Z-12)

	Top Surface Crack Width (1/1000 in.)																										
	Crack No.																										
	S1			S2			S3			S4			S5			N1			N2			N3			N4		
Load, *P* (kips)	1	2	3	1	2	3	1	2	3	1	2	3	1	2	3	1	2	3	1	2	3	1	2	3	1	2	3
7	10	12	12													9	9	10									
8	13	14	15	10	13	9										14	12	13	10	14	12						
10	15	16	20	12	13	14	10	13	8	11	15	10				15	18	18	10	15	10	10	13	10	8	10	10
12	21	19	23	13	23	17	18	20	13	18	20	16				20	23	19	17	22	15	15	21	16	12	13	10
14	25	23	30	19	28	22	18	20	13	17	20	19	13	8	10	24	24	22	20	26	17	14	20	23	15	19	14
16	27	25	32	20	30	23	22	20	20	16	20	20	13	15	13	26	28	27	22	31	17	16	24	26	18	18	16
17.9	32	30	35	22	35	27	25	25	22	18	27	26	19	18	20	30	32	32	25	37	18	21	29	27	20	23	17
18.0	55	60	60	43	54	45	68	44	48	20	35	35	20	19	28	35	40	35	24	36	19	24	33	35	50	50	48

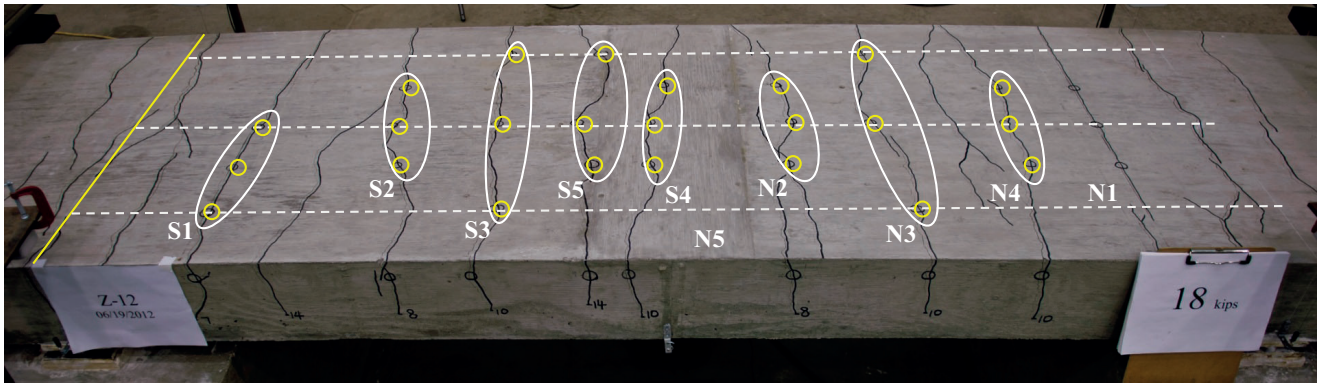

Figure J.11 Crack pattern and measurement locations (Z-12).

TABLE J.17
Summary of Crack Widths (Z-12)

Top Surface Crack Width						Side Crack Width (at bar level)			
Load, *P* (kips)	Bar Stress (ksi)	Avg. Crack Width (1/1000)	Max Crack Width (1/1000)	No. of Primary Cracks	Cracks outside Constant Moment	Load, *P* (kips)	Bar Stress (ksi)	Avg. Crack Width (1/1000)	Max Crack Width (1/1000)
7	31.4	10.3	12.0	2		7	31.4	5.8	8.0
8	35.9	12.4	15.0	4		8	35.9	8.3	12.0
10	45.0	12.7	20.0	10		10	45.0	11.2	15.0
12	53.9	17.7	23.0	10	1	12	53.9	15.3	20.0
14	62.7	19.4	30.0	11	2	14	62.7	16.6	25.0
16	71.9	21.7	32.0	11	2	16	71.9	19.6	26.0
17.9	78.4	25.6	37.0	11	2	17.9	78.4	22.8	30.0
18.0	78.4	39.4	68.0	11	2	18.0	78.4	32.4	50.0

TABLE J.18
Calculated Bar Stress (Z-12)

Load History		Transformed Section Analysis			Moment-Curvature Analysis							
P (kips)	*M (k-in)*	f_s *(ksi)*	e_s	e_c	*c (in.)*	φ *(1lin.)*	e_c	C_c *(in.)*	y_{bar} *(in.)*	*M (k-in)*	f_s *(ksi)*	Δf_s *(ksi)*
8	192	35.9	0.00124	0.00033								
9	219	40.9	0.00141	0.00037	4.00	0.000033	0.00013	43.2	2.661	209.5		
10	240	44.8	0.00155	0.00041	1.29	0.000319	0.00041	41.9	0.852	240.7	45.0	0.16
12	288	53.8	0.00186	0.00049	1.29	0.000383	0.00050	50.2	0.855	288.3	53.9	0.12
14	336	62.8	0.00216	0.00058	1.30	0.000447	0.00058	58.3	0.858	335.2	62.7	0.05
16	384	71.8	0.00247	0.00066	1.31	0.000513	0.00067	66.9	0.861	384.0	71.9	0.17
17.9	429.6	80.3	0.00277	0.00074	0.82	0.001566	0.00128	73.0	0.532	430.4	78.4	1.83
18.0	432.72	80.9	0.00279	0.00074	0.69	0.002371	0.00162	72.9	0.441	433.5	78.4	2.42

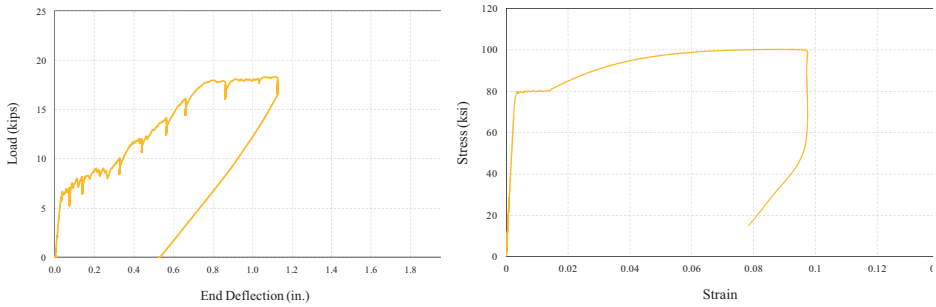

Figure J.12 Load-deflection and stress-strain relationship (Z-12).

TABLE J.19
Crack Measurements (M-12)

	Top Surface Crack Width (1/1000 in.) Crack No.																						
	S1			S2			S3			S4			N1			N2			N3			N4		
Load, *P* (kips)	**1**	**2**	**3**	**1**	**2**	**3**	**1**	**2**	**3**	**1**	**2**	**3**	**1**	**2**	**3**	**1**	**2**	**3**	**1**	**2**	**3**	**1**	**2**	**3**
8	6	7	5										5	10	6									
10	12	8	6	7	10	10	6	5	6	7	5	9	7	14	10	11	7	11	11	6	7	10	10	6
12	15	9	13	14	16	20	10	10	10	13	7	13	10	20	16	14	12	16	16	10	13	17	15	10
14	19	10	18	16	16	25	13	12	13	15	10	18	12	22	20	20	16	22	22	15	18	17	18	14
16	30	18	23	17	20	32	20	16	15	22	15	22	13	25	25	23	18	24	24	20	23	21	18	16
18	30	26	25	22	22	35	25	16	18	27	18	30	16	35	29	26	23	30	30	25	26	25	20	25
20	37	26	33	25	25	44	28	20	20	30	19	48	20	42	35	29	30	36	36	33	30	30	33	25
22	40	29	38	25	29	52	30	27	24	30	23	45	30	42	40	43	33	40	40	35	34	35	45	25
24	40	33	50	30	38	65	40	30	25	35	20	48	31	48	43	40	43	45	45	40	40	50	46	25
26	40	40	65	30	35	70	43	37	25	40	35	65	40	60	53	40	45	60	60	65	45	50	55	30

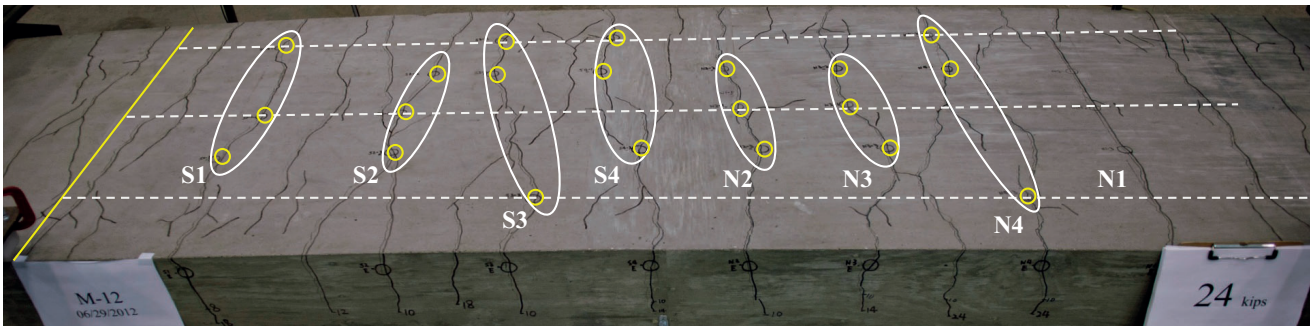

Figure J.13 Crack pattern and measurement locations (M-12).

TABLE J.20
Summary of Crack Widths (M-12)

Top Surface Crack Width						Side Crack Width (at bar level)			
Load, *P* (kips)	Bar Stress (ksi)	Avg. Crack Width (1/1000)	Max Crack Width (1/1000)	No. of Primary Cracks	Cracks outside Constant Moment	Load, *P* (kips)	Bar Stress (ksi)	Avg. Crack Width (1/1000)	Max Crack Width (1/1000)
8	36.2	6.5	10.0	2		8	36.2	5.8	6.0
10	45.9	8.4	14.0	10		10	45.9	7.8	12.0
12	54.9	13.3	20.0	10		12	54.9	11.0	15.0
14	63.9	16.7	25.0	11	2	14	63.9	14.4	23.0
16	72.8	20.8	32.0	11	2	16	72.8	18.1	25.0
18	81.4	25.2	35.0	12	2	18	81.4	21.9	35.0
20	90.4	30.6	48.0	12	4	20	90.4	27.3	45.0
22	99.4	34.8	52.0	12	4	22	99.4	32.9	50.0
24	108.2	39.6	65.0	12	4	24	108.2	37.6	60.0
26	116.9	47.0	70.0	12	4	26	116.9	41.5	60.0

TABLE J.21
Calculated Bar Stress (M-12)

Load History		Transformed Section Analysis			Moment-Curvature Analysis							
P (kips)	*M (k-in)*	f_s *(ksi)*	e_s	e_c	*c (in.)*	*φ (1lin.)*	e_c	C_c *(in.)*	y_{bar} *(in.)*	*M (k-in)*	f_s *(ksi)*	Δf_s *(ksi)*
8	192	35.9	0.00124	0.00033								
9	219	40.9	0.00141	0.00037	4.00	0.000033	0.00013	43.2	2.661	209.5		
10	240	44.8	0.00155	0.00041	1.30	0.000318	0.00041	42.7	0.862	245.2	45.9	1.03
12	288	53.8	0.00186	0.00049	1.28	0.000397	0.00051	51.1	0.848	293.7	54.9	1.09
14	336	62.8	0.00216	0.00058	1.27	0.000482	0.00061	59.5	0.835	342.2	63.9	1.15
16	384	71.8	0.00247	0.00066	1.25	0.000573	0.00072	67.7	0.822	390.1	72.8	1.06
18	432	80.7	0.00278	0.00074	1.23	0.000672	0.00083	75.7	0.807	436.5	81.4	0.70
20	480	89.7	0.00309	0.00082	1.21	0.000787	0.00095	84.1	0.791	485.3	90.4	0.75
22	528	98.7	0.00340	0.00090	1.19	0.000916	0.00109	92.4	0.774	533.7	99.4	0.71
24	576	107.6	0.00371	0.00099	1.16	0.001066	0.00124	100.6	0.755	581.5	108.2	0.53
26	624	116.6	0.00402	0.00107	1.14	0.001242	0.00141	108.8	0.735	629.4	116.9	0.34

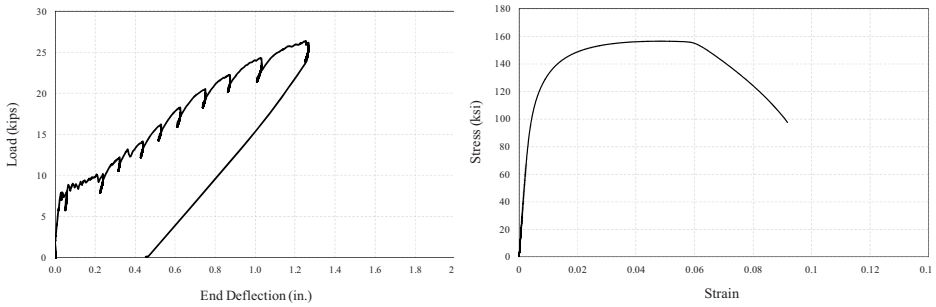

Figure J.14 Load-deflection and stress-strain relationship (M-12).

TABLE J.22
Crack Measurements (XM28-12)

	Top Surface Crack Width (1/1000 in.)																							
	Crack No.																							
	S1			S2			S3			S4			S5			N1			N2			N3		
Load, *P* (kips)	1	2	3	1	2	3	1	2	3	1	2	3	1	2	3	1	2	3	1	2	3	1	2	3
8	10	9									8	10	9			8	9					8	9	
10	11	13	7	5	3	7					10	11	13	7	5	10	13	10	13	8	10	10	13	10
12	17	14	15	10	5	15	6	20	6	4	12	17	14	15	10	18	18	14	19	12	14	18	18	14
14	18	20	18	13	9	20	6.5	22	12	10	14	18	20	18	13	25	20	18	21	17	20	25	20	18
16	25	23	22	16	10	22	10	27	12	16	16	25	23	22	16	25	27	20	25	19	24	25	27	20
18.2	40	30	22	20	10	25	15	35	17	23	18.2	40	30	22	20	35	43	30	30	25	30	35	43	30
18.5	57	35	30	25	25	30	18	38	20	27	18.5	57	35	30	25	55	63	33	36	40	42	55	63	33

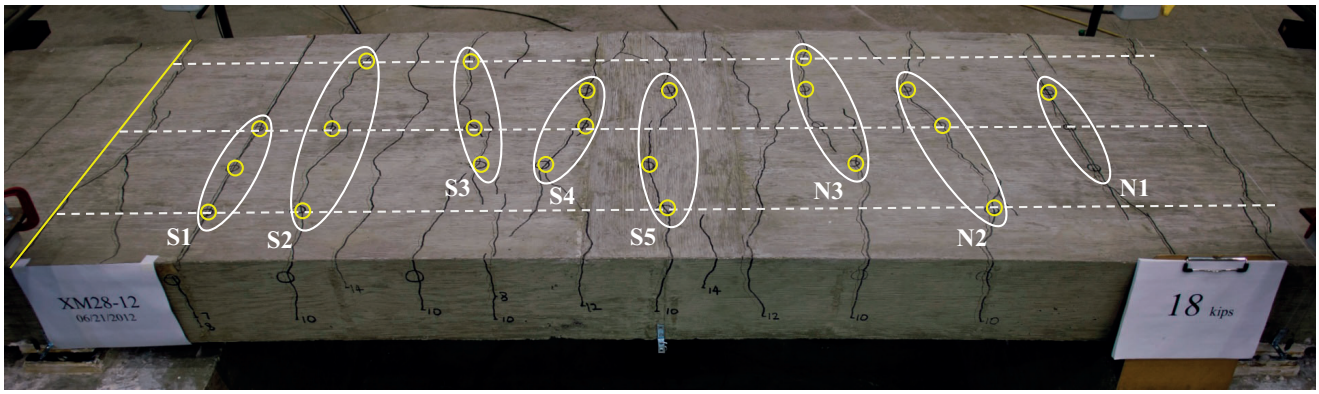

Figure J.15 Crack pattern and measurement locations (XM28-12).

TABLE J.23
Summary of Crack Widths (XM28-12)

Top Surface Crack Width						Side Crack Width (at bar level)			
Load, *P* (kips)	Bar Stress (ksi)	Avg. Crack Width (1/1000)	Max Crack Width (1/1000)	No. of Primary Cracks	Cracks outside Constant Moment	Load, *P* (kips)	Bar Stress (ksi)	Avg. Crack Width (1/1000)	Max Crack Width (1/1000)
7	31.4	6.3	10.0	2		7	13.5		
8	35.9	13.2	16.0	3		8	18.0	9.0	10.0
10	45.0	12.4	19.0	9		10	45.2	9.2	13.0
12	53.9	16.3	24.0	10		12	54.2	12.9	20.0
14	61.0	19.6	30.0	10	2	14	61.5	16.8	25.0
16	64.6	23.4	40.0	12	2	16	65.2	20.2	27.0
18.2	64.6	31.7	65.0	12	2	18.2	65.2	26.9	43.0
18.8	64.6	42.8	85.0	12	2	18.8	65.2	35.8	63.0

TABLE J.24
Calculated Bar Stress (XM28-12)

Load History		Transformed Section Analysis			Moment-Curvature Analysis							
P (kips)	*M (k-in)*	f_s *(ksi)*	e_s	e_c	*c (in.)*	φ *(1lin.)*	e_c	C_c *(in.)*	y_{bar} *(in.)*	*M (k-in)*	f_s *(ksi)*	Δf_s *(ksi)*
7	168	31.4	0.00108	0.00029								
8	192.0	35.9	0.00124	0.00033	4.00	0.000033	0.00013	43.2	2.661	209.5		
10	240	44.8	0.00155	0.00041	1.29	0.000319	0.00041	41.9	0.852	240.7	45.0	0.16
12	288	53.8	0.00186	0.00049	1.29	0.000383	0.00050	50.2	0.855	288.3	53.9	0.12
14	336	62.8	0.00216	0.00058	0.71	0.001558	0.00111	56.7	0.466	337.0	61.0	1.77
16	384	71.8	0.00247	0.00066	0.40	0.007541	0.00301	60.1	0.244	362.4	64.6	7.15
18.2	436.8	81.6	0.00281	0.00075	0.40	0.007541	0.00301	60.1	0.244	362.4	64.6	17.02
18.8	451.2	84.3	0.00291	0.00077	0.40	0.007541	0.00301	60.1	0.244	362.4	64.6	19.71

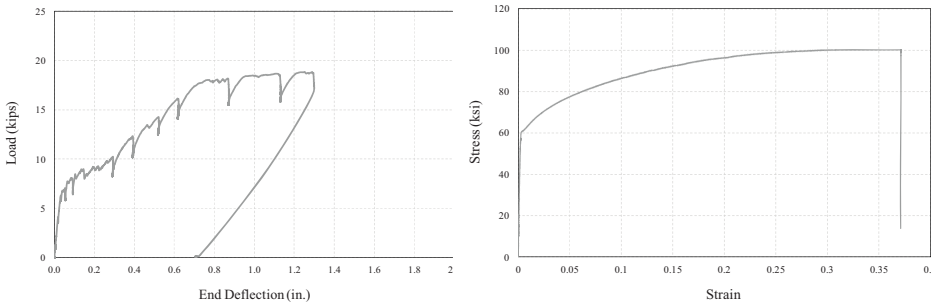

Figure J.16 Load-deflection and stress-strain relationship (XM28-12).

TABLE J.25
Crack Measurements (B-18)

	Top Surface Crack Width (1/1000 in.)																				
	Crack No.																				
	S1			S2			S3			N1			N2			N3			N4		
Load, *P* (kips)	**1**	**2**	**3**	**1**	**2**	**3**	**1**	**2**	**3**	**1**	**2**	**3**	**1**	**2**	**3**	**1**	**2**	**3**	**1**	**2**	**3**
8	20	18	24							23	25	20									
9	30	18	31							26	30	28									
10	32	23	33	20	20	16	42	27	28	32	36	35	22	24	20	36	17	19	23	25	23
11	32	24	43	20	24	20	50	30	32	33	43	42	28	27	26	40	19	20	29	32	28
12	35	24	60	22	25	27	55	33	36	50	52	49	30	30	30	46	22	26	33	35	35
12.1	35	26	65	35	60	55	57	33	38	100	110	105	33	30	33	45	28	29	33	38	35

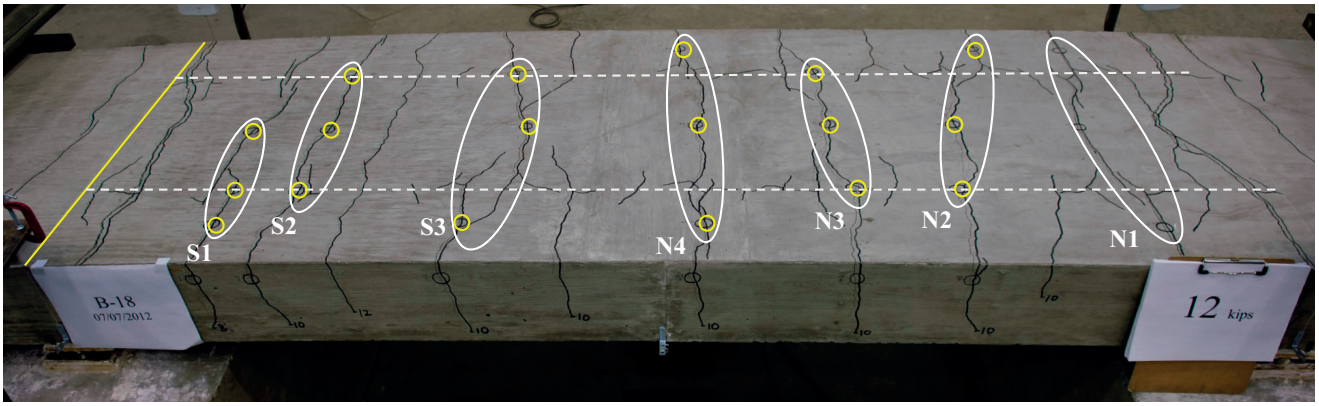

Figure J.17 Crack pattern and measurement locations (B-18).

TABLE J.26
Summary of Crack Widths (B-18)

Top Surface Crack Width						Side Crack Width (at bar level)			
Load, *P* (kips)	Bar Stress (ksi)	Avg. Crack Width (1/1000)	Max Crack Width (1/1000)	No. of Primary Cracks	Cracks outside Constant Moment	Load, *P* (kips)	Bar Stress (ksi)	Avg. Crack Width (1/1000)	Max Crack Width (1/1000)
8	53.2	21.7	25.0	2		8	53.2	21.7	25.0
9	60.6	27.2	31.0	2		9	60.6	27.2	31.0
10	67.4	26.3	42.0	10		10	67.4	26.3	42.0
11	74.0	30.6	50.0	10	1	11	74.0	30.6	50.0
12	79.6	36.0	60.0	10	2	12	79.6	36.0	60.0
12.1	79.6	48.7	110.0	10	2	12.1	79.6	48.7	110.0

TABLE J.27
Calculated Bar Stress (B-18)

Load History		Transformed Section Analysis			Moment-Curvature Analysis							
P (kips)	*M (k-in)*	f_s *(ksi)*	e_s	e_c	*c (in.)*	φ *(1lin.)*	e_c	C_c *(in.)*	y_{bar} *(in.)*	*M (k-in)*	f_s *(ksi)*	Δf_s *(ksi)*
8	192	53.2	0.00183	0.00039								
9	219	60.6	0.00209	0.00044	4.00	0.000033	0.00013	43.2	2.661	209.5		
10	240	66.4	0.00229	0.00049	1.09	0.000455	0.00050	42.2	0.720	245.5	67.4	0.96
11	264	73.1	0.00252	0.00054	1.09	0.000500	0.00054	46.2	0.720	268.5	74.0	0.88
12	288	79.7	0.00275	0.00058	0.84	0.000962	0.00081	50.6	0.551	298.3	79.6	0.18
12.1	290.4	80.4	0.00277	0.00059	0.70	0.001435	0.00100	50.6	0.456	300.7	79.6	0.79

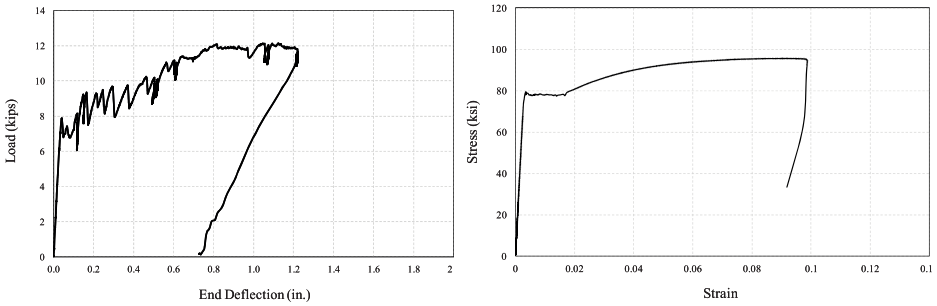

Figure J.18 Load-deflection and stress-strain relationship (B-18).

TABLE J.28
Crack Measurements (M-18)

	Top Surface Crack Width (1/1000 in.)																							
	Crack No.																							
	S1			S2			S3			S4			N1			N2			N3			N4		
Load, *P* (kips)	1	2	3	1	2	3	1	2	3	1	2	3	1	2	3	1	2	3	1	2	3	1	2	3
8	20	24	20										15	20	20									
9	22	25	23	12	10	10							15	23	21									
10	25	30	34	28	25	16	15	14	18	16	18	18	22	28	22	7	15	12	26	27	26	16	18	17
11	33	33	36	30	35	20	16	14	19	22	20	18	25	30	32	10	18	15	32	30	29	19	23	19
12	35	36	40	36	40	28	20	22	22	25	26	27	30	35	30	15	20	20	36	35	35	20	26	27
13	40	42	42	40	50	30	22	23	30	33	30	31	30	35	35	20	25	25	50	40	35	24	33	30
14	45	40	60	50	53	30	25	25	32	34	35	35	40	40	45	21	28	25	63	40	40	26	34	35
15	50	40	65	60	55	30	30	30	35	38	38	40	40	43	55	30	33	30	67	40	50	30	35	40
16	55	48	70	60	58	40	40	40	42	40	44	44	47	50	54	35	40	40	80	45	48	45	40	60

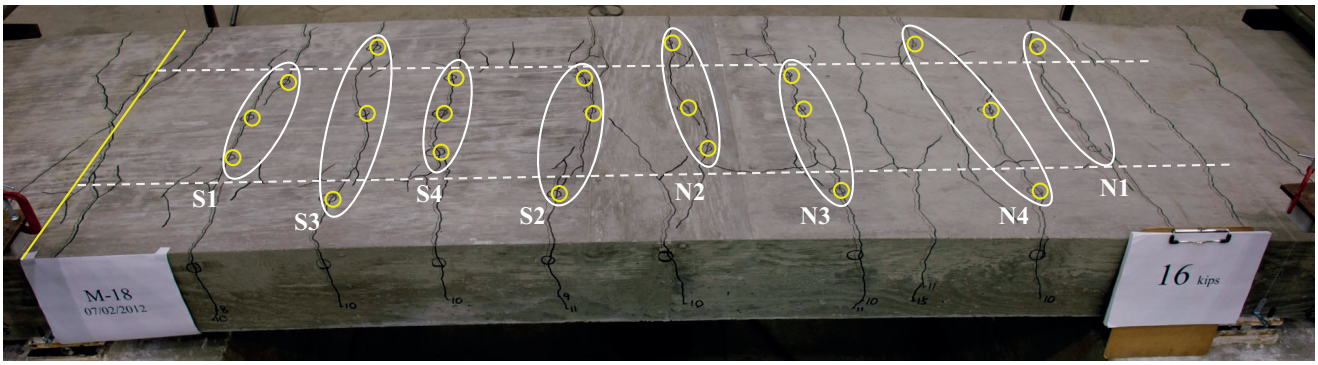

Figure J.19 Crack pattern and measurement locations (M-18).

TABLE J.29
Summary of Crack Widths (M-18)

Top Surface Crack Width						Side Crack Width (at bar level)			
Load, *P* (kips)	**Bar Stress (ksi)**	**Avg. Crack Width (1/1000)**	**Max Crack Width (1/1000)**	**No. of Primary Cracks**	**Cracks outside Constant Moment**	**Load, *P* (kips)**	**Bar Stress (ksi)**	**Avg. Crack Width (1/1000)**	**Max Crack Width (1/1000)**
8	53.7	19.8	24.0	2		8	53.7	14.8	18.0
9	60.4	17.9	25.0	3		9	60.4	15.2	20.0
10	68.1	20.5	34.0	9		10	68.1	16.6	27.0
11	74.4	24.1	36.0	9		11	74.4	19.3	30.0
12	81.1	28.6	40.0	10	2	12	81.1	26.0	35.0
13	87.7	33.1	50.0	10	2	13	87.7	29.6	40.0
14	94.1	37.5	63.0	10	2	14	94.1	33.1	40.0
15	100.7	41.8	67.0	10	2	15	100.7	35.8	48.0
16	107.4	48.5	80.0	10	2	16	107.4	43.1	50.0

TABLE J.30
Calculated Bar Stress (M-18)

Load History		Transformed Section Analysis			Moment-Curvature Analysis							
***P* (kips)**	***M* (k-in)**	**f_s (ksi)**	**e_s**	**e_c**	**c (in.)**	**φ (1lin.)**	**e_c**	**C_c (in.)**	**y_{bar} (in.)**	***M* (k-in)**	**f_s (ksi)**	**Δf_s (ksi)**
8	192	53.2	0.00183	0.00039								
9	219	60.6	0.00209	0.00044	4.00	0.000033	0.00013	43.2	2.661	209.5		
10	240	66.4	0.00229	0.00049	1.05	0.000495	0.00052	42.2	0.691	246.3	68.1	1.66
11	264	73.1	0.00252	0.00054	1.03	0.000559	0.00058	46.1	0.681	269.2	74.4	1.32
12	288	79.7	0.00275	0.00058	1.02	0.000631	0.00064	50.3	0.672	293.5	81.1	1.35
13	312	86.4	0.00298	0.00063	1.01	0.000711	0.00071	54.4	0.661	317.7	87.7	1.33
14	336	93.0	0.00321	0.00068	0.99	0.000792	0.00079	58.3	0.651	341.0	94.1	1.04
15	360	99.7	0.00344	0.00073	0.97	0.000889	0.00087	62.5	0.639	365.5	100.7	1.08
16	384	106.3	0.00367	0.00078	0.96	0.000995	0.00095	66.6	0.626	390.0	107.4	1.09

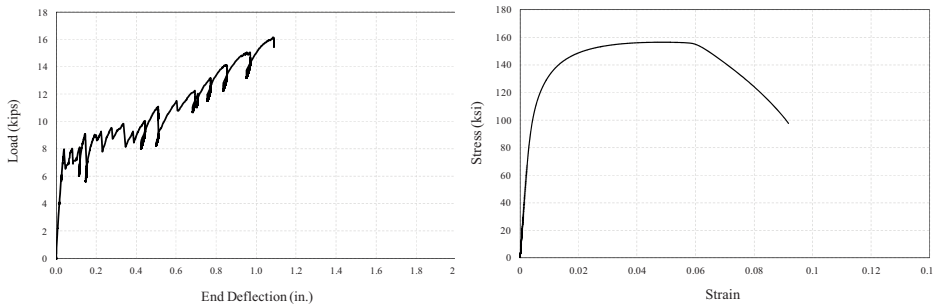

Figure J.20 Load-deflection and stress-strain relationship (M-18).

TABLE J.31
Crack Measurements (S2205-18)

	Top Surface Crack Width (1/1000 in.)																				
	Crack No.																				
	S1			S2			SH*			N1			N2			N3			N4		
Load, *P* (kips)	1	2	3	1	2	3	1	2	3	1	2	3	1	2	3	1	2	3	1	2	3
8	28	18	22							23	23	15									
9	33	20	26	29	8	29				26	28	20									
10	40	28	27	38	15	37				26	35	22	27	23	15	24	12	22			
11	42	30	35	43	21	46				41	65	30	27	30	18	33	18	32	40	37	40
12	47	35	49	56	30	59				54	70	45	35	32	20	39	28	34	45	41	45
13	60	35	58	65	35	77				65	120	50	35	45	27	45	30	40	50	53	50
14	93	58	65	78	52	85				73	125	50	54	49	30	60	35	52	70	60	55

*SH: Shrinkage crack (specimen that was stored at the bottom of the stack during early age).

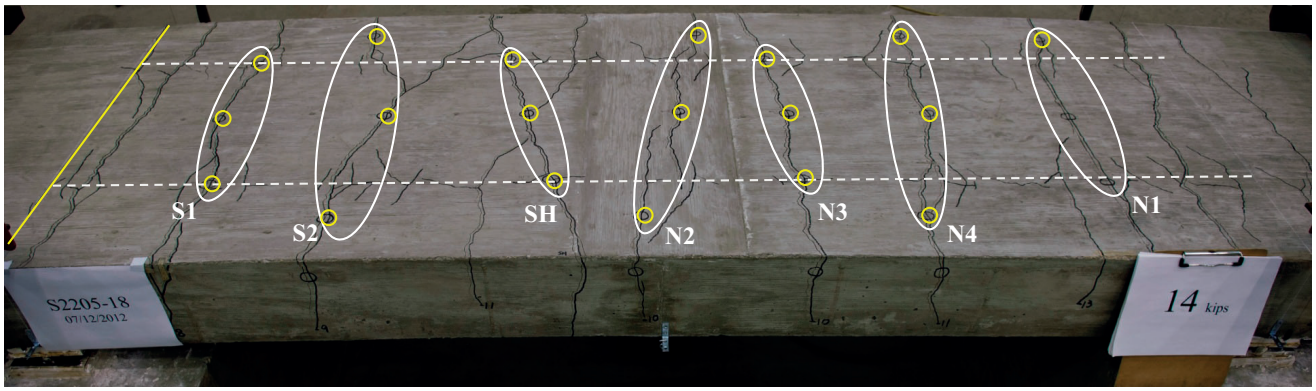

Figure J.21 Crack pattern and measurement locations (S2205-18).

TABLE J.32
Summary of Crack Widths (S2205-18)

Top Surface Crack Width						Side Crack Width (at bar level)			
Load, *P* (kips)	Bar Stress (ksi)	Avg. Crack Width (1/1000)	Max Crack Width (1/1000)	No. of Primary Cracks	Cracks outside Constant Moment	Load, *P* (kips)	Bar Stress (ksi)	Avg. Crack Width (1/1000)	Max Crack Width (1/1000)
8	53.2	21.5	28.0	3		8	53.2		
9	59.8	24.3	33.0	4		9	59.8	17.5	25.0
10	67.4	26.1	40.0	6		10	67.4	19.5	32.0
11	74.0	34.9	65.0	10	1	11	74.0	27.8	37.0
12	80.5	42.4	70.0	10	1	12	80.5	32.6	44.0
13	87.6	52.2	120.0	10	1	13	87.6	39.0	62.0
14	92.1	63.6	125	10	1	14	92.1	45.3	62.0

TABLE J.33
Calculated Bar Stress (S2205-18)

Load History		Transformed Section Analysis			Moment-Curvature Analysis							
P (kips)	*M (k-in)*	f_s *(ksi)*	e_s	e_c	*c (in.)*	φ *(1lin.)*	e_c	C_c *(in.)*	y_{bar} *(in.)*	*M (k-in)*	f_s *(ksi)*	Δf_s *(ksi)*
8	192	53.2	0.00183	0.00039								
9	219	60.6	0.00209	0.00044	4.00	0.000033	0.00013	43.2	2.661	209.5		
10	240	66.4	0.00229	0.00049	1.09	0.000455	0.00050	42.2	0.720	245.5	67.4	0.97
11	264	73.1	0.00252	0.00054	1.09	0.000500	0.00054	46.2	0.720	268.5	74.0	0.88
12	288	79.7	0.00275	0.00058	1.09	0.000544	0.00060	50.2	0.721	291.9	80.5	0.79
13	312	86.4	0.00298	0.00063	1.10	0.000593	0.00065	54.5	0.723	317.0	87.6	1.23
14	336	93.0	0.00321	0.00068	0.97	0.000842	0.00082	59.1	0.637	346.1	92.1	0.90

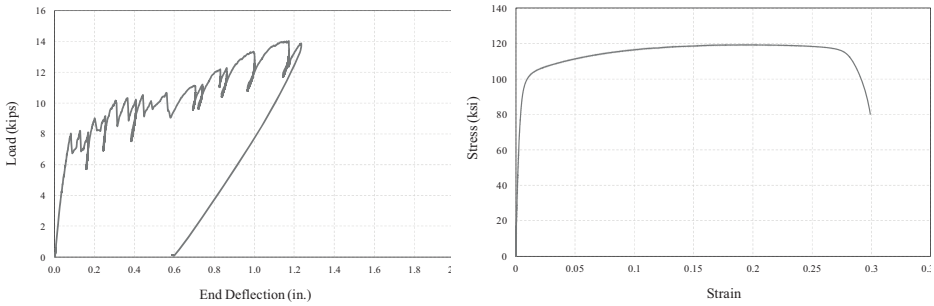

Figure J.22 Load-deflection and stress-strain relationship (S2205-18).

TABLE J.34
Crack Measurements (XM28-18)

	Top Surface Crack Width (1/1000 in.)																					
	Crack No.																					
	S1			S2			S3			S4			N4			N2			N3			N4		
Load, *P* (kips)	**1**	**2**	**3**	**1**	**2**	**3**	**1**	**2**	**3**	**1**	**2**	**3**	**1**	**2**	**3**	**1**	**2**	**3**	**1**	**2**	**3**	**1**	**2**	**3**
8	23	16	30										26	21	17									
9	30	18	39	25	22	18	26	27	25				34	23	20	22	14	18						
10	35	20	42	37	26	20	30	27	32	19	16	20	35	29	22	23	17	20	21	12	21			
11	43	23	51	37	33	27	35	32	36	26	20	28	60	34	22	28	17	24	27	12	26	20	16	17
12	95	48	105	60	60	43	37	47	43	45	27	40	56	55	45	30	20	28	35	24	37	22	22	25
12.1	110	60	125	70	70	47	42	55	46	60	32	47	80		65	37	30	33	42	24	40	30	38	26

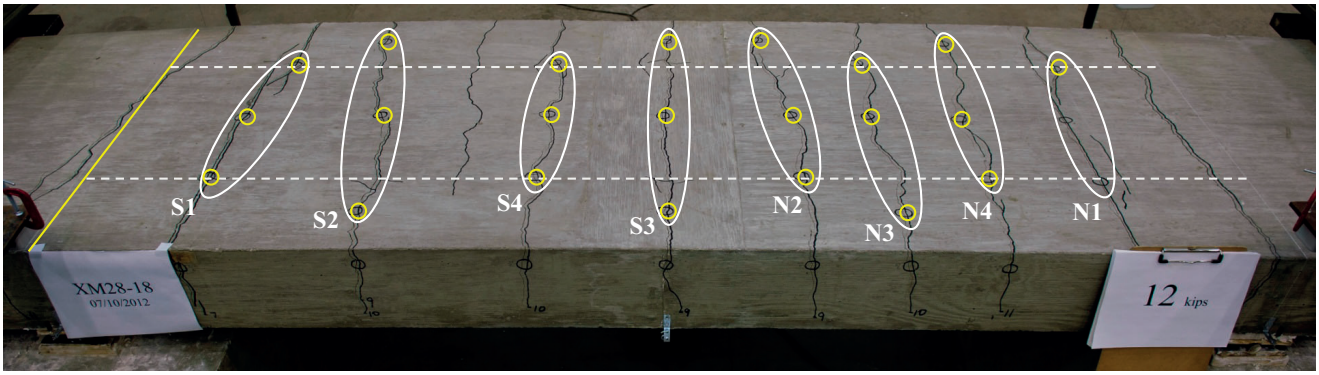

Figure J.23 Crack pattern and measurement locations (XM28-18).

TABLE J.35
Summary of Crack Widths (XM28-18)

Top Surface Crack Width						Side Crack Width (at bar level)			
Load, *P* (kips)	Bar Stress (ksi)	Avg. Crack Width (1/1000)	Max Crack Width (1/1000)	No. of Primary Cracks	Cracks outside Constant Moment	Load, *P* (kips)	Bar Stress (ksi)	Avg. Crack Width (1/1000)	Max Crack Width (1/1000)
8	53.2	22.2	30.0	2		8	53.2	19.3	22.0
9	59.8	24.1	39.0	5		9	59.8	19.2	30.0
10	64.4	25.0	42.0	7		10	64.4	21.5	34.0
11	67.5	28.9	60.0	10		11	67.5	23.7	42.0
12	67.5	43.7	105.0	10		12	67.5	37.2	85.0
12.2	67.5	52.6	125.0	10		12.2	67.5	43.3	95.0

TABLE J.36
Calculated Bar Stress (XM28-18)

Load History		Transformed Section Analysis			Moment-Curvature Analysis							
P (kips)	*M (k-in)*	f_s *(ksi)*	e_s	e_c	*C (in.)*	φ *(1lin.)*	e_c	C_c *(in.)*	y_{bar} *(in.)*	*M (k-in)*	f_s *(ksi)*	Δf_s *(ksi)*
8	192	53.2	0.00183	0.00039								
9	219	60.6	0.00209	0.00044	4.00	0.000033	0.00013	43.2	2.661	209.5		
10	240	66.4	0.00229	0.00049	0.32	0.006134	0.00199	39.7	0.206	240.7	64.0	2.48
11	264	73.1	0.00252	0.00054	0.28	0.010945	0.00301	41.5	0.168	252.1	66.9	6.21
12	288	79.7	0.00275	0.00058	0.28	0.010945	0.00301	41.5	0.168	252.1	66.9	12.85
12.2	292.8	81.1	0.00280	0.00059	0.28	0.010945	0.00301	41.5	0.168	252.1	66.9	14.18

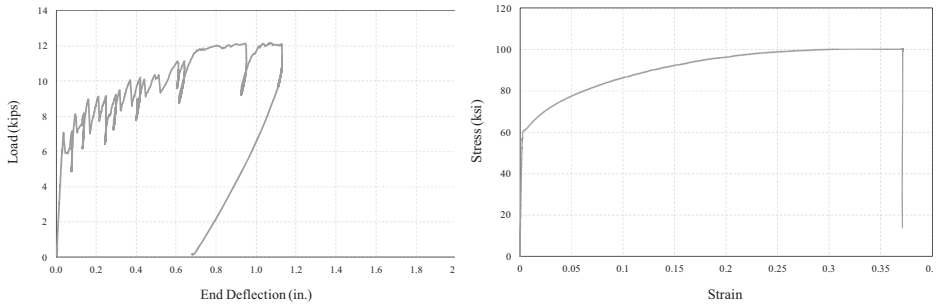

Figure J.24 Load-deflection and stress-strain relationship (XM28-18).

APPENDIX K: MACROCELL SPECIMEN CRACKING DATA

TABLE K.1
Macrocell Specimen Cracking Data

Specimen ID	Specimen No.	Crack Widths (mils) 1	2	3	Avg.
C-SXM28	34	24	24	16	21
	35	24	24	16	21
	36	24	16	16	18
C-316LN	37	12	16	8	12
	38	–	16	16	16
	39	16	16	8	13
C-S2205	40	16	24	8	16
	41	8	24	24	18
	42	16	24	8	16
C-S2304	43	24	24	24	24
	44	31	24	31	29
	45	16	24	16	18
C-M	46	8	8	8	8
	47	8	16	16	13
	48	16	8	8	11
C-Z	49	8	20	24	17
	50	31	8	12	17
	51	12	24	8	14
C-E	52	16	24	16	18
	53	31	31	16	26
	54	8	4	16	9
C-G	55	31	39	31	34
	56	16	24	24	21
	57	24	31	24	26
C-ZC1	58	–	31	–	31
	59	–	24	–	24
	60	–	31	–	31
C-ZC2	61	–	79	–	79
	62	–	31	–	31
	63	–	39	–	39
C-B	64	24	16	8	16
	65	31	31	31	31
	66	31	24	31	29
C-SXM28-B	67	16	16	24	18
	68	16	16	16	16
	69	8	24	16	16
C-S316LN-B	70	4	4	4	4
	71	8	4	4	5
	72	8	4	4	5
C-S2205-B	73	8	16	16	13
	74	8	8	8	8
	75	8	16	16	13
C-S2304-B	76	8	16	16	13
	77	16	16	24	18
	78	16	24	24	21
C-M-B	79	16	8	8	10
	80	8	8	8	8
	81	8	8	8	8
C-Z-B	82	16	16	8	13
	83	24	16	8	16
	84	31	24	8	21

Continued.

Table K.1.—*Continued.*

Specimen ID	Specimen No.	Crack Widths (mils)			Avg.
		1	2	3	
C-E-B	85	39	8	–	24
	86	24	16	–	20
	87	24	24	8	18
C-G-B	88	24	16	8	16
	89	16	24	24	21
	90	16	24	8	16
C-ZC1-B	91	8	–	24	16
	92	39	39	24	34
	93	24	24	31	26
C-ZC2-B	94	16	24	8	16
	95	16	8	8	10
	96	24	31	8	21
C-SXM28-ST	97	8	8	4	7
	98	16	16	16	16
C-SXM28-BT	99	16	24	24	21
	100	24	24	16	21
C-S2205-ST	101	31	16	16	21
	102	16	24	24	21
C-S2205-BT	103	24	16	24	21
	104	24	24	16	21
C-E-BT	105	16	31	31	26
	106	16	24	16	18
	107	24	16	8	16
C-B-BT	108	24	24	24	24
	109	31	24	24	26
C-B-ST	110	31	24	24	26
	111	31	24	24	26
	112	31	24	24	26

About the Joint Transportation Research Program (JTRP)

On March 11, 1937, the Indiana Legislature passed an act which authorized the Indiana State Highway Commission to cooperate with and assist Purdue University in developing the best methods of improving and maintaining the highways of the state and the respective counties thereof. That collaborative effort was called the Joint Highway Research Project (JHRP). In 1997 the collaborative venture was renamed as the Joint Transportation Research Program (JTRP) to reflect the state and national efforts to integrate the management and operation of various transportation modes.

The first studies of JHRP were concerned with Test Road No. 1—evaluation of the weathering characteristics of stabilized materials. After World War II, the JHRP program grew substantially and was regularly producing technical reports. Over 1,500 technical reports are now available, published as part of the JHRP and subsequently JTRP collaborative venture between Purdue University and what is now the Indiana Department of Transportation.

Free online access to all reports is provided through a unique collaboration between JTRP and Purdue Libraries. These are available at: http://docs.lib.purdue.edu/jtrp

Further information about JTRP and its current research program is available at: http://www.purdue.edu/jtrp

About This Report

An open access version of this publication is available online. This can be most easily located using the Digital Object Identifier (doi) listed below. Pre-2011 publications that include color illustrations are available online in color but are printed only in grayscale.

The recommended citation for this publication is:

Frosch, R. J., Labi, S., & Sim, C. (2014). *Increasing bridge deck service life: Volume I—Technical evaluation* (Joint Transportation Research Program Publication No. FHWA/IN/JTRP-2014/16). West Lafayette, IN: Purdue University. http://dx.doi.org/10.5703/1288284315516